NASA CP-001

77N17996

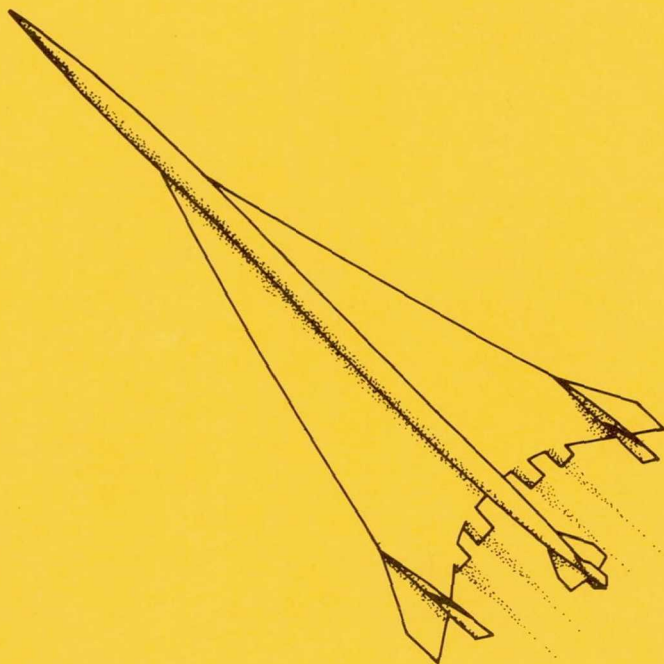# PROCEEDINGS OF THE SCAR CONFERENCE

PART 1

Held at
LANGLEY RESEARCH CENTER
Hampton, Virginia,
November 9-12, 1976

NASA CP-001

PROCEEDINGS OF THE SCAR CONFERENCE

PART 1

Held at
Langley Research Center
Hampton, Virginia
November 9-12, 1976
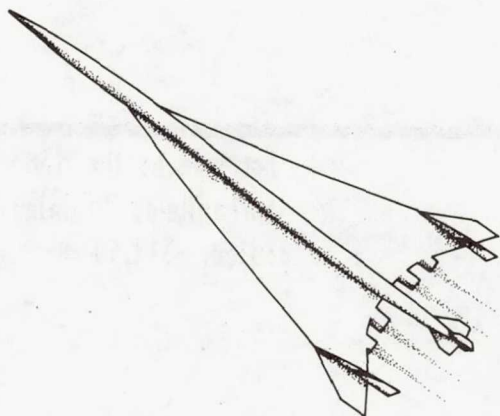
PREFACE

Since 1972 the Supersonic Cruise Aircraft Research (SCAR) Program has provided an accelerated and focused technology effort which has resulted in development of improved analytical techniques, design procedures, and an expanded experimental data base. Major advances have been achieved and were reported to the technical community at the SCAR Conference held at Langley Research Center, November 9-12, 1976.

This document is a compilation of papers presented by 49 speakers representing airframe and engine manufacturers, the Federal Aviation Administration, and four NASA research centers.

The Conference was organized in six sessions as follows:

I. Aerodynamics

II. Stability and Control

III. Propulsion

IV. Environmental Factors

V. Airframe Structures and Materials

VI. Design Integration

Papers and the authors thereof are grouped by session and identified in the CONTENTS. The order of papers is the actual order of speaker appearance at the Conference. The Lockheed-California Company four-part oral presentation in the Design Integration session has been consolidated into one paper by the three speakers.

The size of the compilation necessitated publication in two parts (Parts I and II). A list of attendees, by organizational affiliation, is included at the back of Part II.

We would like to express appreciation to session chairmen and speakers whose efforts contributed to the technical excellence of the Conference.

C. Driver
Conference Chairman

Hal T. Baber, Jr.
Conference Coordinator

Page intentionally left blank

CONTENTS

Part I

SESSION I - AERODYNAMICS
Chairman: Robert E. Bower

Part II*

SESSION IV - ENVIRONMENTAL FACTORS
Chairman: Harry W. Johnson

SESSION V - AIRFRAME STRUCTURES AND MATERIALS
Chairman: Richard R. Heldenfels

*Papers 22 to 47 are presented under separate cover.

SESSION VI - DESIGN INTEGRATION
Chairman: William S. Aiken, Jr.

TOWARD A SECOND GENERATION FUEL EFFICIENT

SUPERSONIC CRUISE AIRCRAFT

SCAR PROGRAM OVERVIEW

F. Edward McLean
NASA Langley Research Center

INTRODUCTION

In 1971, after some 10 years of effort, the United States Government canceled this Nation's program to develop a supersonic transport aircraft. Soon after program cancellation, however, the Government took some limited steps to keep its options open for possible future consideration of such an aircraft. First, during 1971 and 1972, the Government provided funding support for the continuation, completion, and reporting of some basic tests on materials, noise, sealants, etc. which were in progress at the close of the SST program. Then, in July of 1972, the Government initiated, within NASA, an Advanced Supersonic Technology (AST) Program. This Program, which became the NASA Supersonic Cruise Aircraft Research (SCAR) Program in 1973, was established to promote further basic supersonic research, and to provide an advanced technology base for application to possible future supersonic aircraft.

During its first 4 years of operation, the NASA AST/SCAR Program has involved the research efforts of 60 research organizations throughout the Country and has provided research data for some 300 technical reports. The Program has also made substantial progress in the identification of research solutions to the critical problems which inhibit the full acceptability of supersonic cruise flight.

The purpose of this Overview is to consider briefly the objectives, research elements, and distribution of research effort within the NASA AST/SCAR Program. Subsequent papers (papers 1 to 47) will provide details of some of the SCAR research efforts and point out the potential impact of the SCAR research results on the performance of future supersonic cruise aircraft.

DISCUSSION

SCAR Program Objectives

Among the principal factors which led to the 1971 cancellation of the United States SST Program were

1. Concerns over the marginal SST performance and economic potentials that appeared possible within the then-available technology base

2. Concerns over the possible noise and pollution impacts of SST type aircraft

In order for the United States Government or industry to make rational decisions in the consideration of future supersonic aircraft, it is necessary to know whether acceptable research solutions can be found to these technical concerns. This, then, is the principal objective of the NASA SCAR Program:

<u>To provide the data needed to make rational decisions in the consideration of future military and civil supersonic aircraft</u>

These data will be provided through the generation of an expanded supersonic technology base and the necessary research required to assess and minimize environmental impact.

SCAR Program Elements

All the configurational and operational features of a supersonic cruise aircraft directly influence the aircraft performance and contribute to its environmental impact. Consequently, to meet the SCAR Program objectives, a research plan was adopted which involves the simultaneous upgrading of the state of the art in all disciplinary research areas associated with supersonic flight. This approach leads to the SCAR Program elements illustrated in the left side of figure 1. Focused research efforts are carried out in the disciplinary areas of Aerodynamics, Controls, Propulsion, Stratospheric Emissions, and Structures and Materials. In each of these research areas, improved solutions to known supersonic problems are sought through in-house NASA research, NASA/Industry contracts, and NASA grants. Some examples of these disciplinary research efforts and results will be presented in subsequent papers (papers 1 to 38).

There are complex interdisciplinary relationships in the evolution of a supersonic cruise aircraft. Consequently, a disciplinary breakthrough or technology advance does not necessarily apply fully in a practical supersonic aircraft design. The SCAR Program has adopted the Systems Integration Studies approach, illustrated in the center of figure 1, to sort out these complex interdisciplinary relationships and assess the traded impact of the disciplinary technology advances. As illustrated in the figure, disciplinary research results are fed into Systems Integration Study teams which consider the impact of the research results on a baseline supersonic cruise aircraft concept. Currently, industry Systems Integration Study teams at Boeing, Douglas, and Lockheed, and a NASA/Vought in-house team are performing these integration/technology impact studies with the support of propulsion teams at Pratt & Whitney and General Electric. Some results of these studies will be presented in papers 39 to 47.

As illustrated in the right side of figure 1, the ultimate goal of the SCAR Disciplinary Research and Systems Integration Studies is to introduce into the development base an advanced supersonic technology which could lead to a supersonic cruise aircraft which is acceptable in every respect.

SCAR Distribution of Research Effort

Since the NASA AST/SCAR Program was initiated in 1972, approximately
$34 million of basic research and technology funding has been provided by the
U.S. Congress to carry out the supersonic research program. The distribution
of this funding among the SCAR Disciplinary Research areas and SCAR Systems
Integration Studies is illustrated in figure 2. The numbers in parentheses
represent cumulative values since the start of the AST/SCAR Program. A contin-
uous program has been manintained in all areas except Emissions. This latter
element of disciplinary research was made the responsibility of the NASA Office
of Space Sciences in Fiscal Year 1976.

CONCLUDING REMARKS

This Overview has discussed the objectives, Program elements, and distribu-
tion of research effort in the NASA AST/SCAR Program since its inception in
July of 1972. The remainder of this document will provide examples of the
research effort and results of the first 4 years of the Program.
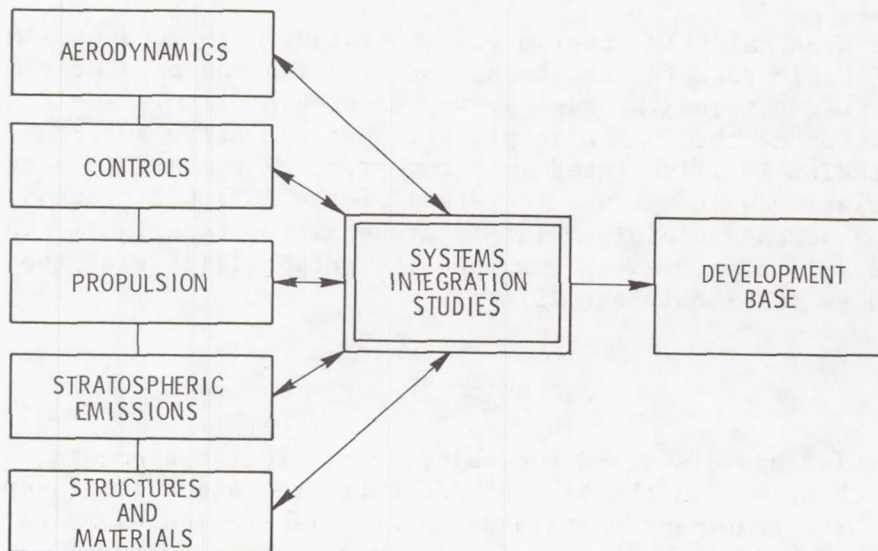
Figure 1.- SCAR Program elements.
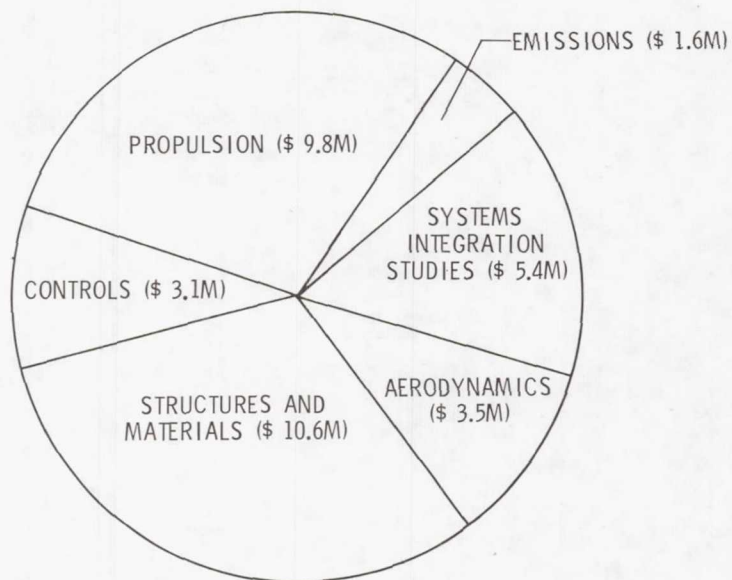
Figure 2.- Distribution of SCAR R&T effort.
(Total R&T funding to date $34.0M.)

SESSION I — AERODYNAMICS

Page intentionally left blank

INTRODUCTION

Robert E. Bower
NASA Langley Research Center

The emergence of computerized supersonic design and analysis methods a decade ago led to the evolution of highly efficient supersonic cruise configurations. As shown in figure 1, the NASA-generated SCAT 15F arrow-wing configuration represents a substantial improvement in lift-drag ratio relative to first-generation transports. This "baseline" configuration represents a point of departure for the discussion of aerodynamics in this conference.

During the past 4 years, the SCAR aerodynamics effort has stressed both theoretical and experimental programs throughout a broad Mach number range. Refined linearized-theory design and analysis methods, treated in paper 1, by Miller, and in paper 2, by Erickson, have improved the usability and accuracy of linearized methods and extended design capability to more complete configurations. Advanced methods, including the effects of wing leading-edge separation and vortex flows, are important in defining detailed loadings at high angles of attack for structural design. Paper 3, by Gloss, describes a new method which considers these effects. Supersonic finite-difference methods, such as described by Townsend in paper 4, show high promise in defining local flow details in regions of aircraft where the assumptions inherent in linearized theory break down. A summary of the state of the art of theoretical methods is presented by Bobbitt in paper 5 together with key experimental-theoretical comparisons.

The SCAR experimental aerodynamics program is addressing the important problems of improved low-speed lift characteristics for highly swept, low-aspect-ratio wings, a data base for an $M = 2.2$ transport, and new configuration concepts for aircraft up to $M = 3.0$. The status of this effort is summarized in figure 2. In paper 6, Coe describes the NASA in-house program directed at the generation of low-speed lift to keep take-off field length and approach speeds low. The SCAT 15F wing is oversized by 20 percent in order to meet these off-design constraints. Coe's paper shows that important performance gains can be realized by using conventional high-lift devices and powered-lift concepts. With the possible application of powered lift, however, comes the concern of over-the-wing engine location in the critical areas of subsonic cruise and transonic acceleration. Mercer (paper 7) presents experimental results obtained in the Langley 16-foot transonic tunnel on these engine location effects. In the final paper of this session (paper 8), Roensch, of McDonnell Douglas Corporation, presents experimental results obtained at transonic and supersonic speeds at the NASA Ames Research Center on an $M = 2.2$ design.

Although not reported in this conference, in-house testing continues on advanced blended arrow-wing configurations. Features of these configurations are improved aerodynamic efficiency, lower sonic boom, and more efficient propulsion integration, including thrust vectoring for low-speed lift enhancement.
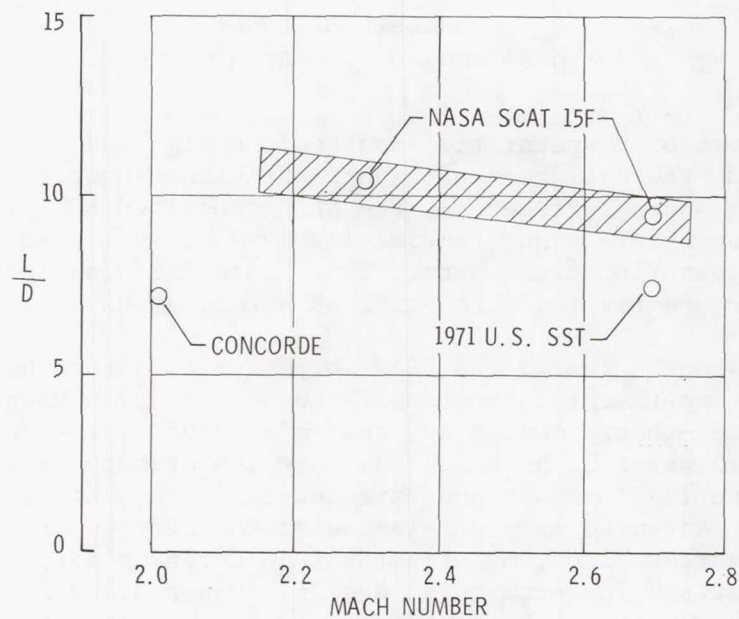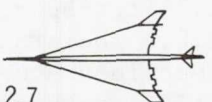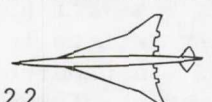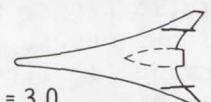
Figure 1.- Impact of supersonic design and analysis methods.

	SCAT 15F M = 2.7			ARROW WING (DOUGLAS) M = 2.2			ADVANCED ARROW M = 3.0		
	LOW SPEED	TRAN-SONIC	SUPER-SONIC	LOW SPEED	TRAN-SONIC	SUPER-SONIC	LOW SPEED	TRAN-SONIC	SUPER-SONIC
AERO PERFORMANCE	●	○	○		●	●	●	○	○
LOADS	●	●			●	●	○	○	○
PROPULSION EFFECTS	●	●	●	○	●	●	●	○	○
WING DESIGN VALIDATION		○	○		●	●			○

○ PLANNED
● TESTS COMPLETE

Figure 2.- Status of SCAR experimental aerodynamics program.

8

A LINEARIZED THEORY METHOD OF CONSTRAINED OPTIMIZATION FOR

SUPERSONIC CRUISE WING DESIGN

David S. Miller and Harry W. Carlson
NASA Langley Research Center

and

Wilbur D. Middleton
Boeing Commercial Airplane Company

SUMMARY

A linearized theory wing design and optimization procedure which allows physical realism and practical considerations to be imposed as constraints on the optimum (least drag due to lift) solution is discussed and examples of application are presented. In addition to the usual constraints on lift and pitching moment, constraints can also be imposed on wing surface ordinates and wing upper surface pressure levels and gradients. The design procedure also provides the capability of including directly in the optimization process the effects of other aircraft components such as a fuselage, canards, and nacelles.

INTRODUCTION

Because of their versatility, speed, and convenience, linearized theory computer methods have been widely employed for aerodynamic design and analysis. The close correspondence between the small disturbance assumptions of the theory and the small disturbance requirements for high aerodynamic efficiency makes the methods particularly attractive for supersonic cruise vehicles. The greatest advantage of the linearized methods lies in a unique capability for direct design and optimization made possible by the provision for linear addition and superposition of basic solutions; similar design and optimization capability for nonlinear methods does not presently exist.

Foremost among the linearized theory design methods are those which provide for the definition of wing lifting surface shapes for minimization of drag due to lift, typically the largest contribution to cruise vehicle inviscid drag. The first computerized wing design procedure (ref. 1) calculated the optimum (least drag for a given lift) combination of three simple analytic loadings (uniform, linear chordwise, and linear spanwise) and the resulting wing surface shape for an arbitrary planform wing. The original procedure was extended (ref. 2) to include constraints on pitching moment and root chord z-ordinate; with these additional two constraints, the original set of three component loadings was increased to eight to allow for effective optimization. In rather extensive applications of the method certain numerical deficiencies were revealed and techniques to overcome them were incorporated into the procedure

9

(ref. 3). In order to integrate the resulting optimum wing designs into the complete airplane environment, other design procedures such as wing-nacelle reflexing (ref. 4) and fuselage camber shaping (refs. 5 and 6) were developed.

Wing design and configuration studies conducted in the past (refs. 7, 8, and 9) have indicated that the theoretical benefits predicted by linear theory design and optimization procedures are generally not fully realized. It became apparent that there was a need for considerations of additional restraints in the design process to avoid highly distorted surface shapes as well as local pressure levels and gradients which depart from physical realism and from the linear theory assumptions.

As a part of a computational system for the aerodynamic design and analysis of supersonic airplanes (ref. 10), a wing design procedure has been developed which employs a constrained optimization process for determining the wing surface shape to support a minimum drag pressure distribution. In addition to the usual constraints of desired lift and pitching moment, other optional constraints are available to impose physical realism and practical design considerations on the linearized theory solution. These new options include the application of equality constraints on surface ordinates at specified planform locations and inequality constraints on upper surface pressure levels and gradients. Special attention has been given to include directly in the optimization process the major effects of other aircraft components such as a fuselage, canards, and nacelles.

A general description of the new constrained optimization procedure is presented along with examples of calculated results to illustrate the design capability of the system. Particular attention is given to the control over the design afforded by the various constraint options.

SYMBOLS

ΔC_D incremental drag coefficient due to lift

C_L lift coefficient

$C_{L, design}$ lift coefficient for which the warped wing surface is designed to produce minimum drag

$C_{m,o}$ pitching-moment coefficient at zero lift

C_p pressure coefficient

c_r wing root chord length (see fig. 7)

$(L/D)_{max}$ maximum lift-drag ratio

M Mach number

10

z   wing camber surface ordinate

z^* wing camber surface ordinate constraints (see fig. 7)

DISCUSSION

The Aerodynamic Design and Analysis System

The wing design and optimization capability described herein is provided by one element of a set of computer program modules contained in an integrated supersonic aerodynamic design and analysis system shown in figure 1. Details of the system are given in reference 10. The fundamental concept of the system is that complete airplane solutions can be assembled by superposition of individual contributions evaluated by means of linear theory and the supersonic area rule. An executive "driver" controls the execution and sequencing of several basic aerodynamic programs which perform analysis or design functions shown in the figure. The major role of the analysis programs is to produce loading information and total integrated aerodynamic forces for a given aircraft; however, several of these same programs are used to provide input to the wing design program.

The remainder of this paper will describe the wing design and optimization method and present examples of typical results.

Wing Design and Optimization Procedure

The wing design solution determines an optimum (least drag due to lift) pressure distribution and the corresponding mean camber surface shape. The procedure can be divided into two computational tasks.

The first task requires some method of computing the wing surface shape which would support a prescribed wing loading. Any reliable supersonic lifting surface method could be employed; a vortex lattice method is presently being used. As illustrated in figure 2, the wing planform is divided into a large number of grid elements and a matrix of aerodynamic influence functions relating wing loading and wing surface is calculated. For a given set of wing loadings, a set of corresponding wing camber surfaces is readily obtained. The lift, pitching moment, and drag are then calculated for each of the loadings. Using superposition principles, the individual loadings and camber surfaces are combined assuming that each loading has an unknown strength to be determined. This formulation gives the total wing loading, camber surface, lift, and pitching moment as linear functions of the unknown strengths and the total drag due to lift as a quadratic function of these unknowns. Refer to reference 3 for a detailed description of the formulation.

The second task is to determine values for the unknown strengths which will give minimum drag and satisfy certain constraints. The drag to be minimized is quadratic in terms of the unknown strengths, and the constraints are linear; thus, application of Lagrange's method of undetermined multipliers

11

reduces the solution of the constrained optimization problem to the solution of a set of linear algebraic equations for determining the unknown loading strengths. The imposition of inequality constraints is achieved by automated successive applications of the optimization process as set forth in reference 10.

The present capabilities of the computer implemented wing design procedure are shown in figure 3. The set of loadings available for optimization are of two types: Basic lifting surface loadings and configuration related loadings. The basic loadings are analytic functions of planform position and have unknown overall strengths to be determined. The second type of loading is configuration related because it accounts for the effect of another configuration component interacting with the wing. Each of these configuration dependent loadings has two contributions: One which is generated by the configuration component and is of fixed distribution and strength, and one which is generated by an incremental wing camber surface (reflexing) to have the same distribution but unknown strength. The strength of the second contribution of the pair is determined in the optimization process to provide whatever degree of counteraction or augmentation of the component induced loadings that may be required for drag minimization. Presently, three configuration related loadings are available to account for the effects of fuselage upwash, fuselage volume, and nacelles. An example of wing-nacelle interference will be presented later to illustrate this capability.

The use of linear theory methods to design wings which have reasonable camber surface shapes, produce flows that are physically attainable, and yield certain desired aerodynamic characteristics requires that restrictions be placed on the theoretical solution. The restraints available are shown in figure 3 and are imposed mathematically as equality or inequality constraints. Desired aerodynamic characteristics of lift and pitching moment may be specified and are treated as equality constraints. For the wing upper surface, values for minimum pressure level and maximum pressure gradient may be specified. These pressure values, which need not be constant but may vary over the wing planform, are not to be exceeded by the solution and thus are treated as inequality constraints. In almost every practical wing design, regions exist where surface ordinates must be specified such as at wing-body junctions or hinge lines. To insure these criterions can be satisfied, wing surface ordinate values (which may be specified at up to five planform locations) are treated as equality constraints.

Application to Lifting Surface Design

The benefits which may be obtained from employment of linearized theory methods for wing camber surface design are perhaps best illustrated in data obtained more than a decade ago in an experimental program which first demonstrated a truly successful application of the design concepts. Data from this study are presented in figure 4. For this investigation, an arrow wing with a 70° leading-edge sweep angle was constructed with a camber surface corresponding to a simple two-component loading (uniform and linear chordwise) designed to minimize drag at a Mach number of 2.05 and a lift coefficient of 0.16. For comparison purposes, a flat wing of the same planform and an additional twisted

and cambered wing with one half the camber surface severity (a design lift coefficient of 0.08) of the first were included in the test program.

In figure 4, the maximum lift-drag ratio achieved for each wing as well as the moment coefficient at zero lift is shown as a function of the design lift coefficient which serves as an index of the camber surface severity illustrated in the inset sketches. The test results indicated not only that improvements in lift-drag ratio approaching a value of 1 (or about 12.5 percent) might be attainable but also that a substantial additional reduction in trim drag might be afforded by the self-trimming moment provided.

The data obtained in this study also point out the need for the application of appropriate constraints in the design process. Note that the experimental $(L/D)_{max}$ does not continue to increase up to the optimum design lift coefficient of 0.16 indicated by the theory. This discrepancy is probably due to a camber surface severity which violates to too large a degree the assumptions of linearized theory. In this investigation, consideration was given to placement of restraints on the pressure distribution by the simple expedient of limiting lifting pressures to those permitted by the simple two-component loading. An indication that this rather arbitrary constraint is not the most appropriate and probably is too restrictive is given by the fact that greater benefits were achieved by a wing with a considerable flat-plate loading contribution, a loading with high peaks and large gradients.

As pointed out previously, the newer design methods reported in reference 10 now provide the designer with a wide range of choices for application of needed restraints and at the same time offer a large enough number of candidate loadings to maintain a viable optimization process. Some indication of the theoretical potential for lifting efficiency improvement offered by these expanded capabilities is given in figure 5. The drag-due-to-lift factor, $\Delta C_D/C_L^2$, a measure of the degree of optimization achieved, is shown for a series of wing designs in which the design loadings vary from a simple uniform distribution to a complex 10-term optimum. A design Mach number of 2.05 and a design lift coefficient of 0.16 were imposed for all results presented. The order in which the loadings are added is shown in the inset sketches. For any given design, the loading shown directly above the bar has been considered in addition to all the loadings to the left in arriving at an optimum combination.

Data are shown for an unrestrained solution and for a solution to which both pressure and camber surface ordinates restraints are imposed. The pressure level and gradient restraints were determined from an assessment of attainable values based on an examination of pressure data obtained in an experimental investigation (ref. 11). The ordinate restraints imposed are, in the belief of the authors, a reasonable compromise between indicated theoretical efficiencies and practical aircraft design realities. Levels of these restraints applicable to a given design problem are, of course, a matter subject to the judgment of the program user. For both unrestrained and restrained solutions, rather dramatic improvements over the uniform load case are shown for only a few additional loadings. Beyond that, the benefits increase more gradually. It will be noted that as the number of loadings is increased the imposition of restraints exerts a greater influence on the solution. The more loadings there are, the greater will be the opportunity for pressure peaks,

13

steep gradients, and severe camber shapes to arise in the theoretical solution, and thus the greater will be the need for imposition of realistic restraints. These data indicate that even with the restraints applied, there is a potential for a 32-percent improvement over the uniform load case and about a 15-percent improvement over the two-loading case used in the experimental program previously discussed. The amount of this additional theoretical potential which can actually be achieved in practice remains to be determined by experimentation.

Theoretical levels of lifting efficiency which may be approached through application of the new design methods may be placed in better perspective by comparison with known standards as has been done in figure 6. Here, the theoretical goals for a 10-loading cambered wing with and without restraints is compared with theoretical and experimental data for a flat wing and for the two-loading wing. Flat wing theoretical values are given for full leading-edge suction and for no leading-edge suction. In this and other experiments, little evidence of leading-edge suction is found. Theoretical results for the two-loading wing indicate that the use of wing twist and camber can more than make up for the loss of suction. However, only about half of this gain is realized experimentally. The 10-loading theoretical data indicate a further potential gain. Only a relatively small penalty is predicted for imposition of what are believed to be realistic restraints. There is clearly a need for further investigation of this subject.

Application to Configuration Integration

The problem under discussion up to this point, that of optimizing the lifting efficiency as measured by the drag-due-to-lift factor or the untrimmed lift-drag ratio, does not take into account all the factors that must be considered in a real configuration design process. Another major consideration is that of providing the pitching-moment characteristics necessary to trim the aircraft for steady level flight without excessive drag penalties. Earlier in this paper, it was pointed out that for one example of the application of wing design methods, an increase in $C_{m,o}$ as well as an increase in untrimmed L/D resulted. This increase in moment coefficient at zero lift, which acts to reduce the control surface deflection required for trimmed flight at supersonic speeds and thus reduce trim drag, was in that case a byproduct of the drag optimization.

The new wing design methods allow moment considerations to be included as a fundamental part of the optimization process. An example of the use of the design program for the definition of wing surfaces providing for drag minimization subject to specified moment constraints is shown in figure 7. Because of the close interrelationship, camber surface ordinate restraints as well as moment restraints are treated in a single illustration.

The plot on the left of the figure shows the effect on drag-due-to-lift factor, $\Delta C_D/C_L{}^2$, of constraining the pitching moment at zero lift, $C_{m,o}$, to values between 0 and 0.06. No z-ordinate constraint is applied and, as depicted in the wing surface sketches, the root chord region exhibits large shape changes across the range of $C_{m,o}$ values. It should be noted that the more reasonable

14

surface shapes and the near minimum values of drag due to lift both occur in the vicinity of $C_{m,o}$ values estimated to be desirable for acceptable trimming characteristics.

The plot on the right of figure 7 illustrates the effect on drag due to lift and on surface shape of varying the value of a single z-ordinate constraint while maintaining a $C_{m,o}$ of 0.04. The ordinate constraint is applied on the root chord at 67 percent of its length and surface ordinate, z^*, values range from -20 percent to 10 percent of the root chord length. An examination of the results indicates that a z^*/c_r constraint value of about -0.1 probably provides a reasonable compromise between a practical wing shape and a minimization of drag due to lift.

The primary point of the example presented here lies, however, not in the specific results obtained but in the demonstration of the improved design capability.

As previously discussed, the present wing design procedure has the capability of including the effects of other aircraft components directly in the optimization process. To illustrate this capability, two approaches for designing a wing-nacelle combination will be discussed. One approach utilizes the well-known method of wing-nacelle reflexing and the other approach employs the present wing design procedure. For illustrative purposes, both procedures are applied to the design of a delta wing in the presence of two nacelles and results for a design Mach number of 2.0 and a design lift coefficient of 0.10 are shown in figure 8.

The method of wing-nacelle reflexing is described in detail in reference 4 and will only be outlined here. The process of reflexing begins with the selection of an optimum wing alone design which has desired aerodynamic characteristics (open circle on solid line). The addition of the nacelles introduces a pressure field acting on the wing which requires a reduction in other loadings and corresponding changes in the camber surface to preserve the design lift. This results in a decrease in both $C_{m,o}$ and $\Delta C_D / C_L^2$ (open circle on dashed line). Wing reflexing is then applied to alter the basic wing surface in the region influenced by the nacelle pressure field to cancel or augment to varying degrees the nacelle effects. A wing reflexing which cancels all the nacelle induced loading, restores the original loading distribution, and reproduces the original value of $C_{m,o}$ is referred to as 100 percent reflexing (shaded circle on dashed line). As indicated in the figure, although drag penalties above the minimum point may be small for this 100-percent reflexing, the use of larger values of positive reflexing to achieve moments in the desirable trim range may bring about large penalties.

The present design procedure differs from the simple reflexing procedure because the entire wing is redesigned with the fixed nacelle loading and reflex (camber induced) loading as well as all the other loadings included in the optimization process. In the range of desirable pitching-moment characteristics, the present procedure provides substantial improvements in drag due to lift over the simple reflexing method.

Constraint Selection Considerations

As previously discussed, a new broad range of controls over the wing design process is now provided in a linearized theory method for drag-due-to-lift minimization. The constraints provided have been identified, and examples of their application given, but little has been said about the establishment of these constraints. It is this aspect of the problem which most severely taxes the knowledge and skill of the program user, calling on the art as well as the science of aerodynamics.

Some of the considerations involved in the selection of restraints applicable to a wing designed for a given Mach number, lift coefficient, and pitching moment may be discussed with the aid of figure 9. Near the wing leading edge in the vicinity of the fuselage juncture, it may be necessary to impose pressure level limitations to prevent a strong sidewash directed toward the fuselage which could create an inboard shock on being redirected by the fuselage surface. Pressure level constraints may also be required along the leading edge to avoid flow separation due to the large flow turning angles associated with high-pressure levels. At the trailing edge, some measure of C_p control may be needed to alleviate trailing-edge shock strength which could, under some circumstances, lead to flow separation well ahead of that location. In addition, pressure level and gradient constraints may be imposed on the entire wing surface or on suspected trouble spots as may be desired. A more complete discussion of the pressure restraint application in the design process and of criteria for establishment of specific restraint levels is given in reference 12. Some degree of control over fuselage floor angle and ground clearance may be afforded by strategic placement of ordinate constraints beginning at the wing-fuselage juncture. Ordinate constraints may also be useful in providing for straight hinge lines, although much of this can be accomplished by wing surface shearing (discussed in ref. 5).

Other Design Factors

Although the wing design procedure discussed in this paper is probably the most versatile and most comprehensive of its type, all aspects of wing design are by no means encompassed. Some of the more obvious aspects worthy of considerations are listed in figure 10. Linear theory methods provide no means of accounting for shock waves; thus, for example, to detect and control the strength of a forward shock (shown in the sketch) one must resort to empirical information, nonlinear solutions (see ref. 13), and, in many instances, wind-tunnel testing. Several researchers have proposed the utilization of vortex lift as an efficient means of producing low drag lift (see ref. 14); however, more knowledge and better computational methods must be acquired to design for vortex lift. The present procedure has no capability for taking advantage of various flow-control devices or accounting for propulsion-system integration effects which have been demonstrated to be beneficial if properly applied. These are but a few of the items which should be incorporated into future wing design procedures.

CONCLUDING REMARKS

A linearized theory wing design and optimization procedure which allows physical realism and practical considerations to be imposed as constraints on the optimum (least drag due to lift) solution has been presented and discussed. In addition to the usual constraints on lift and pitching moment, constraints can also be imposed in wing surface ordinates and wing upper surface pressure levels and gradients. The design procedure also provides the capability of including directly in the optimization process the effects of other aircraft components such as a fuselage, canards, and nacelles.

The capability and versatility of the design and optimization procedure have been illustrated by examples of its application to an arrow planform wing and a delta wing nacelle configuration. The results indicate a substantial theoretical potential for further gains in supersonic cruise vehicle aerodynamic performance. Experimental studies, however, are required to determine achievable levels and to provide empirical design criteria needed in more refined implementations of the method.

REFERENCES

1. Carlson, Harry W.; and Middleton, D.: A Numerical Method for the Design
   of Camber Surfaces of Supersonic Wings With Arbitrary Planforms. NASA
   TN D-2341, 1964.

2. Sorrells, Russell B.; and Miller, David S.: Numerical Method for Design
   of Minimum-Drag Supersonic Wing Camber With Constraints on Pitching
   Moment and Surface Deformation. NASA TN D-7097, 1972.

3. Carlson, Harry W.; and Miller, David S.: Numerical Methods for the Design
   and Analysis of Wings at Supersonic Speeds. NASA TN D-7713, 1974.

4. Mack, Robert J.: A Numerical Method for Evaluation and Utilization at
   Supersonic Nacelle-Wing Interference. NASA TN D-5057, 1969.

5. Carlson, Harry W.; and McLean, F. Edward: Current Methods for Prediction
   and Minimization of Lift-Induced Drag at Supersonic Speeds. NASA TM
   X-1275, 1966.

6. Dollyhigh, Samuel M.; Morris, Odell A.; and Adams, Mary S.: Experimental
   Effects of Fuselage Camber on Longitudinal Aerodynamic Characteristics
   of a Series of Wing-Fuselage Configurations at a Mach Number of 1.41.
   NASA TM X-3411, 1976.

7. Carlson, Harry W.: Aerodynamic Characteristics at Mach Number 2.05 of a
   Series of Highly Swept Arrow Wings Employing Various Degrees of Twist
   and Camber. NASA TM X-332, 1960.

8. McLean, F. Edward; and Fuller, Dennis E.: Supersonic Aerodynamic Charac-
   teristics of Some Simplified and Complex Aircraft Configurations Which
   Employ Highly Swept Twisted-and-Cambered Arrow-Wing Planforms. Vehicle
   Design and Propulsion. American Inst. Aero. and Astronautics. November
   1963, pp. 98-103.

9. Mack, Robert J.: Effects of Leading-Edge Sweep Angle and Design Lift
   Coefficient on Performance of a Modified Arrow Wing at a Design Mach
   Number of 2.6. NASA TN D-7753, 1974.

10. Middleton, W. D.; Lundry, J. L.; and Coleman, R. G.: A Computational
    System for Aerodynamic Design and Analysis of Supersonic Aircraft.
    Parts 1, 2, and 3. NASA CR-2715, CR-2716, and CR-2717, 1976.

11. Carlson, Harry W.: Pressure Distributions at Mach Number 2.05 on a Series
    of Highly Swept Arrow Wings Employing Various Degrees of Twist and
    Camber. NASA TN D-1264, 1962.

12. Rettie, Ian H.: Computer-Aided Aerodynamic Design for Supercruise. Proc.
    Design Conference Technology for Supersonic Cruise Military Aircraft,
    1976. Vol. I (Available from AFFDL/FX, Wright-Patterson AFB, Ohio,
    4543).

18

13. Townsend, James C.: The Role of Finite-Difference Methods in Design and
     Analysis for Supersonic Cruise. Proceedings of the SCAR Conference,
     NASA CP-001, 1977. (Paper no. 4 of this compilation.)

14. Gloss, Blair B.; and Johnson, Forrester T.: Development of an Aerodynamic
     Theory Capable of Predicting Surface Loads on Slender Wings With Vortex
     Flow. Proceedings of the SCAR Conference, NASA CP-001, 1977. (Paper
     no. 3 of this compilation.)
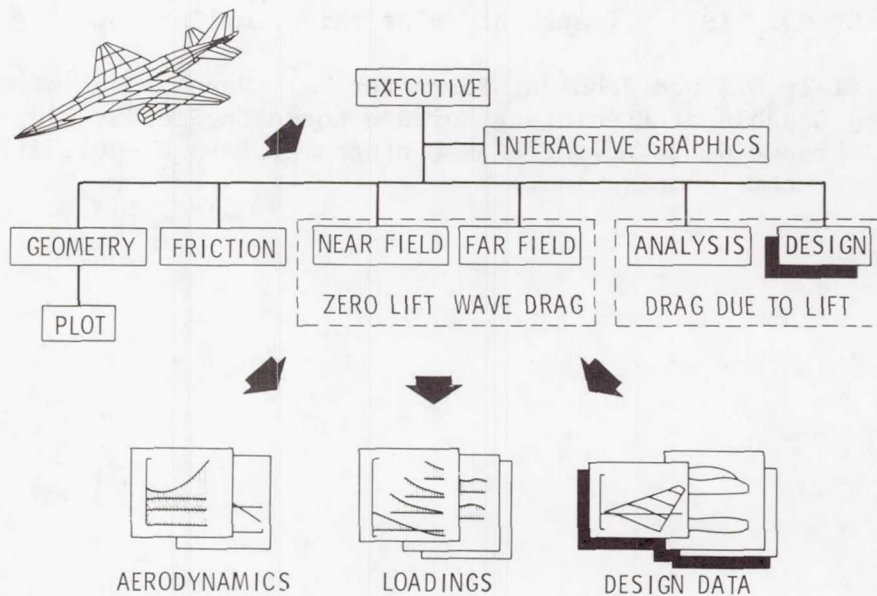
Figure 1.- Integrated supersonic design and analysis system.
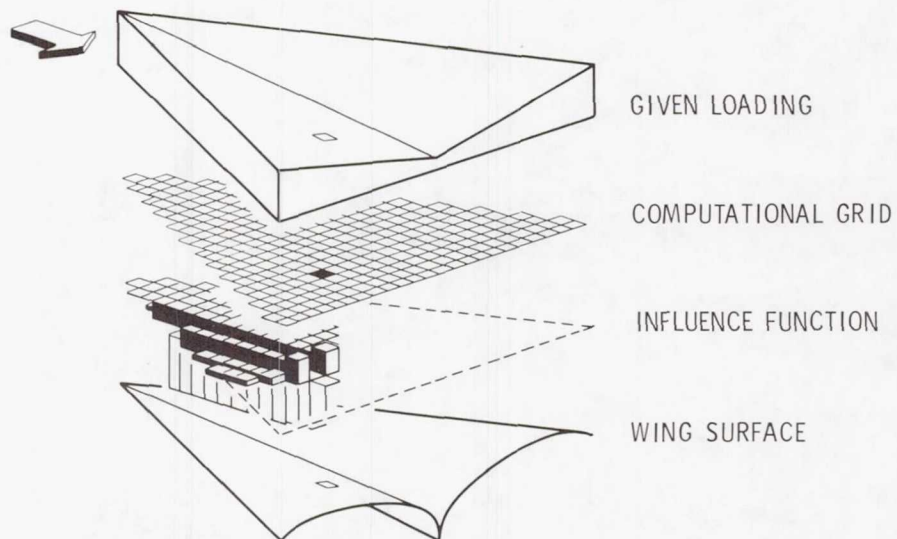
Figure 2.- Fundamental approach for wing surface design.
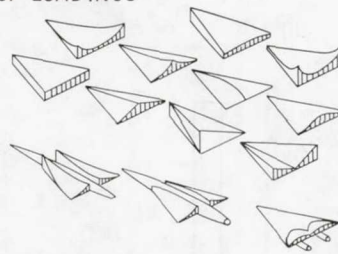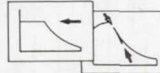
Figure 3.- System for optimization of configuration lifting efficiency.
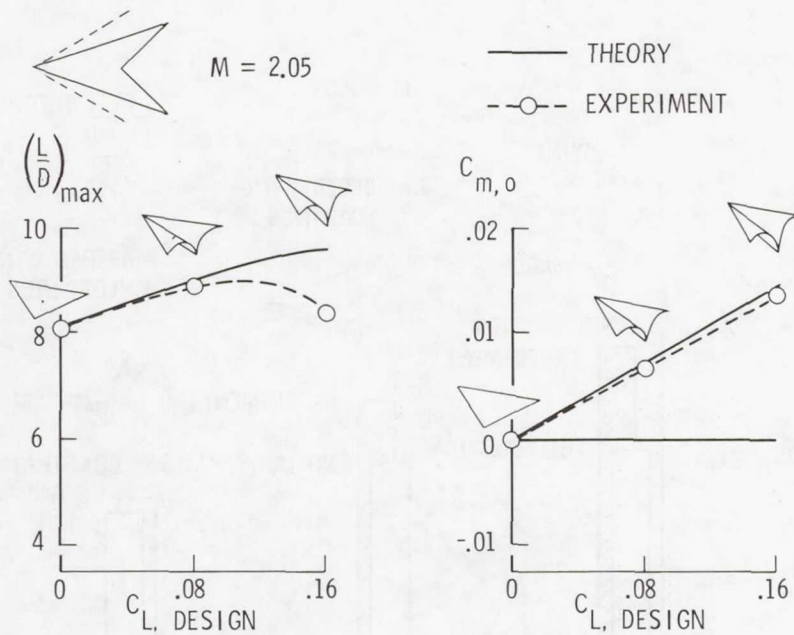
Figure 4.- Example of wing design for drag minimization.
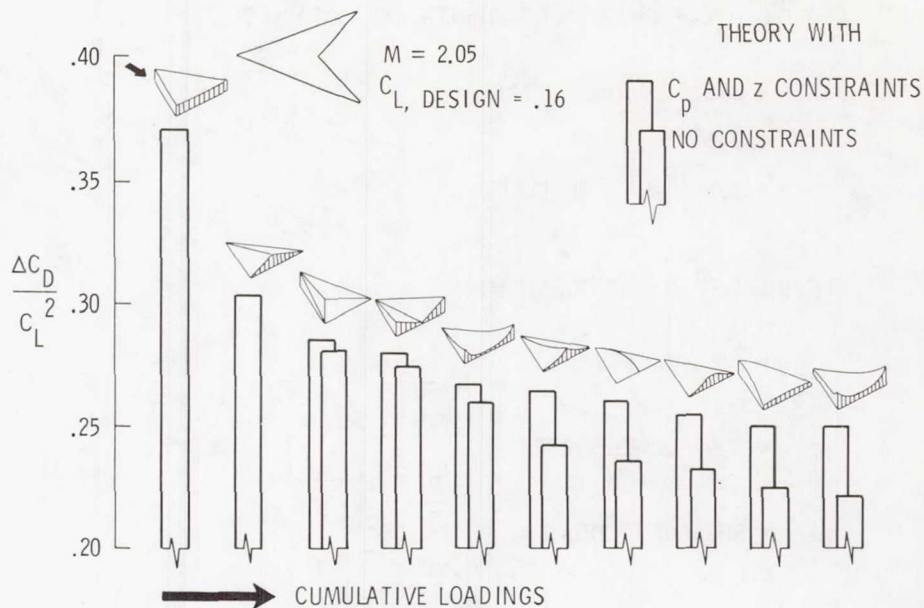
Figure 5.- Theoretical effect of optimized loadings on drag due to lift.
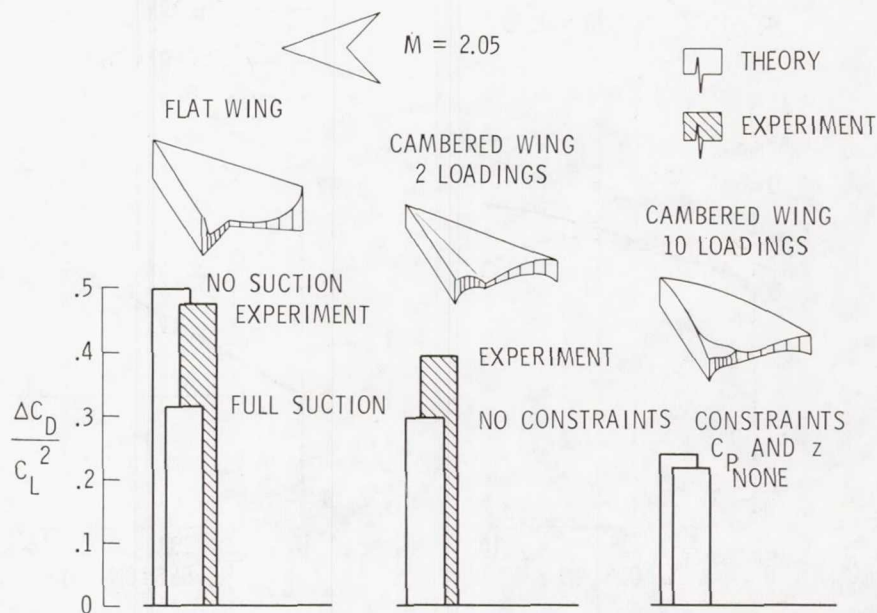
Figure 6.- Theoretical potential for wing design improvement.

22

M = 2.05; $C_{L,DESIGN}$ = .16

8 LOADINGS; C_P CONSTRAINTS

MOMENT CONSTRAINT
(z^* UNCONSTRAINED)

ORDINATE CONSTRAINT
$\left(C_{m,o} = .04\right)$

$\dfrac{\Delta C_D}{C_L^2}$

.4

.3

.2

DESIRABLE RANGE

DESIRABLE RANGE

0   .02   .04   .06

$C_{m,o}$

-.2   -.1   0   .1

z^*/c_r
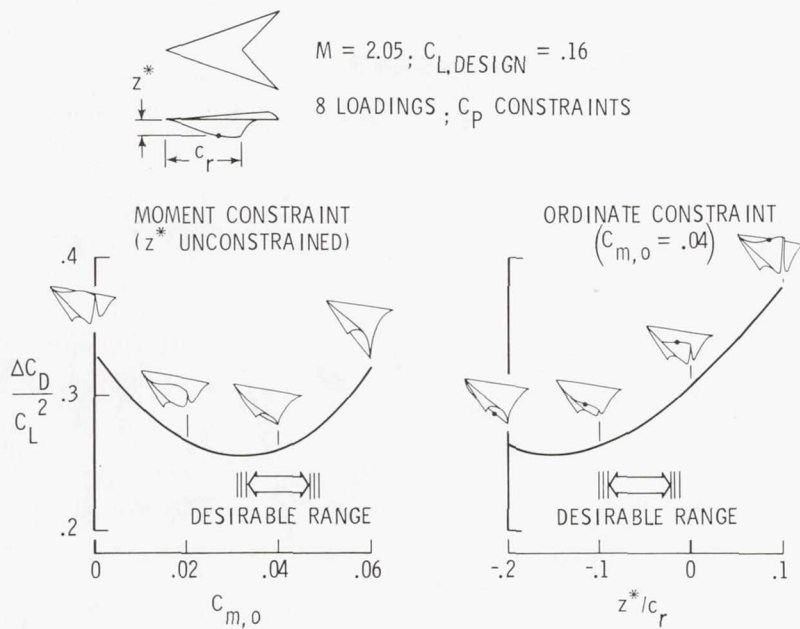
Figure 7.- Influence of moment and surface ordinate constraints.

M = 2.0, $C_{L,DESIGN}$ = 0.1

$\dfrac{\Delta C_D}{C_L^2}$

.45

.40

.35

.30

POSITIVE REFLEX

WING ALONE
BASIC OPTIMIZED SURFACE

WING NACELLE
BASIC SURFACE WITH REFLEX

WING NACELLE
REOPTIMIZED SURFACE

DESIRABLE RANGE

0   .004   .008   .012

$C_{m,o}$
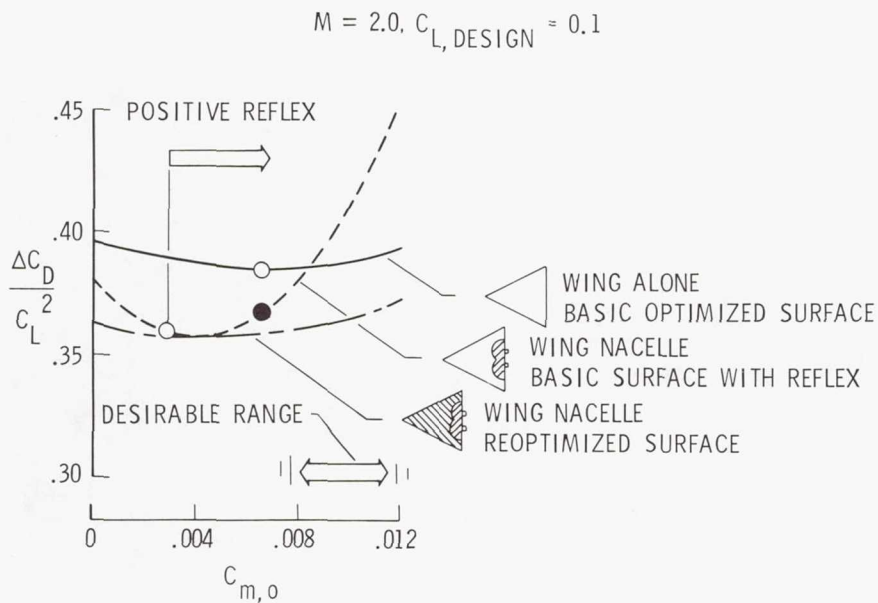
Figure 8.- Nacelle effects on wing design.

23

DESIGN CONDITIONS
- MACH NUMBER
- LIFT
- PITCHING MOMENT

LEADING EDGE C_P CONSTRAINT

OVERALL C_P AND dC_P/dx CONSTRAINT

INBOARD SHOCK C_P CONSTRAINT

TRAILING EDGE C_P CONSTRAINT

HINGE LINE ORDINATE CONSTRAINT

SIDE OF BODY ORDINATE CONSTRAINTS
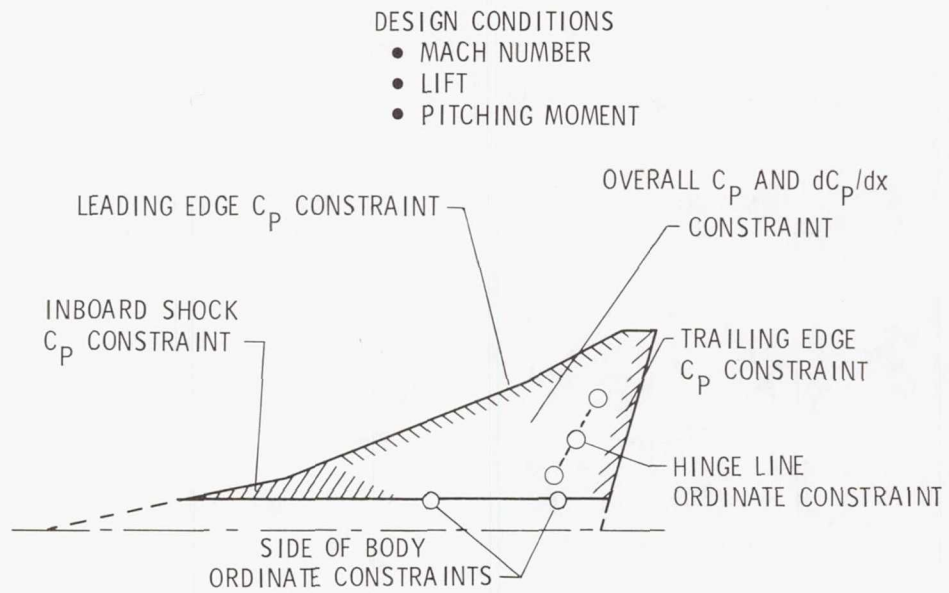
Figure 9.- Typical wing design constraint imposition.

- SHOCK DETECTION AND CONTROL

VORTEX LIFT

- UTILIZATION OF VORTEX LIFT

- APPLICATION OF FLOW CONTROL DEVICES

- PROPULSION SYSTEM INTEGRATION
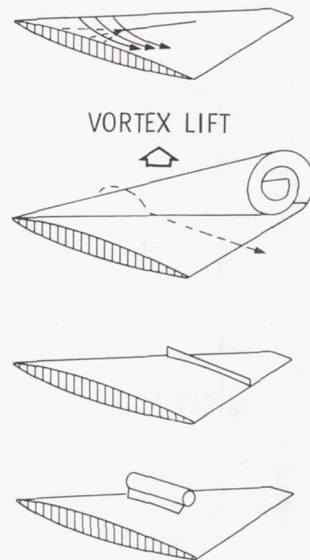
Figure 10.- Other design considerations.

ADVANCED SURFACE PANELING METHOD FOR

SUBSONIC AND SUPERSONIC FLOW[*]

Larry L. Erickson
NASA Ames Research Center

Forrester T. Johnson and F. Edward Ehlers
Boeing Commercial Airplane Co.

SUMMARY

Numerical results illustrating the capabilities of an advanced aerody-
namic surface paneling method are presented. The method is applicable to both
subsonic and supersonic flow, as represented by linearized potential flow
theory. The method is based on linearly varying sources and quadratically
varying doublets which are distributed over flat or curved panels. These
panels can be applied to the true surface geometry of arbitrarily shaped
three-dimensional aerodynamic configurations. The method offers the user a
variety of modeling options and is both stable and accurate, the numerical
results displaying a marked insensitivity to panel arrangement.

INTRODUCTION

This paper summarizes the general features of an advanced aerodynamic
surface paneling method and gives results for both subsonic and supersonic
steady flow. The work was originally motivated by limitations in the Woodward-
type aerodynamic method used in FLEXSTAB. Although the FLEXSTAB aerodynamic
model has several unique capabilities for three-dimensional configurations
(e.g., subsonic and supersonic flow, steady and low-frequency unsteady motion
(ref. 1)), it also has several faults that are typical of other paneling
schemes. For example, results are often sensitive to the manner in which the
paneling is laid out, and localized changes in panel density often require
corresponding changes to be made over the entire planform. Equally important,
the aerodynamic model for fuselage-type components is based on a slender body
of revolution plus an interference shell, as shown in figure 1(a). This model-
ing restriction often results in crude approximations to the geometry of air-
craft, especially fighter-type aircraft.

The goal of this development work is to produce a reliable subsonic/
supersonic panel method that accurately represents the actual surface geometry
of realistic aircraft as shown in figure 1(b). To produce such a method

---

[*]This work was performed under contract NAS2-7729 for NASA Ames Research
Center.

requires flat and curved panels that can be arbitrarily oriented in space (e.g., panels should incline toward the flow direction and panel side edges should not have to be parallel to the flow). To be usable and reliable, the method must produce accurate results that are not sensitive to the size, shape, and arrangement of the paneling; in turn, this capability makes automated paneling practical. In addition, the method must be efficient. The results indicate that these requirements can be met for both subsonic and supersonic analysis problems (specify shape, solve for pressure) and for subsonic design problems (specify pressure, solve for shape).

SYMBOLS

Values are given in SI units. The calculations were made in U.S. customary units.

A_{ij} influence coefficient matrix relating singularity strength parameters to perturbation velocities, m^{-1}

b wing span, m

$[C]$ matrix relating doublet strength coefficients and doublet singularity parameters

C_L lift coefficient

C_{L_α} lift curve slope

C_m pitching moment coefficient

$C_p = \dfrac{p - p_\infty}{q_\infty}$ pressure coefficient

$\Delta C_p = C_{p_\ell} - C_{p_u}$

c local chord

c_ℓ section lift coefficient

K kernel function in equation (4), m^{-2}

k panel number

L body length, m

M Mach number

N number of singularity parameters associated with panel K; also, number of chordwise and streamwise panels in figure 5.

N_o aerodynamic center location as fraction of local chord

$\vec{n}$ unit normal to aerodynamic surface

P_j the set of N points corresponding to the μ_j in equation (2)

p pressure, N/m^2

q dynamic pressure, N/m^2

R see equation (3)

r body radius, m

S_k area of integration over panel k, m^2

$\vec{U}_\infty$ free-stream velocity vector, m/sec

$U_\infty = |\vec{U}_\infty|$

$\vec{V}$ total velocity vector, m/sec

$\vec{v}^k_{i(j)}$ perturbation velocity vector at field point i due to the N singularity parameters μ_j associated with panel k, m/sec

W_j weighting values used in equation (3)

x, y coordinates in chordwise and spanwise directions, respectively, m

α angle of attack, degrees or radians

Γ bound circulation

$\mu(\xi, \eta)$ doublet strength distribution, m^2/sec

μ_j doublet singularity parameter, m^2/sec

$\mu_o, \cdots \mu_{\eta\eta}$ coefficients in the expression for $\mu(\xi, \eta)$

ξ, η, ζ local orthogonal coordinate axes associated with individual panels, m

ϕ perturbation potential, m^2/sec; also, circumferential angle in figures 15 and 16

ρ fluid density, kg/m^3

$\sigma(\xi, \eta)$ source strength distribution, m/sec

Subscripts:

i	field point
j	singularity parameter or singularity parameter point
ℓ	lower surface
u	upper surface
∞	free-stream value

Operator:

$\vec{\nabla}$	gradient (with respect to field point coordinates), m^{-1}

GENERAL FEATURES OF THE METHOD

The approach is fundamentally the same for both subsonic and supersonic flow. (More specific details of the mathematics are given in refs. 2 and 3.) As in several other methods, it is based on the singular source and doublet solutions to the linearized subsonic and supersonic potential flow equations. The primary differences in the present method are (1) the use of higher order forms for the spatial distribution of these singularity strengths, and (2) the retention of curvature effects for the panels on which these singularities are distributed. Specifically, the sources are assumed to have a linear strength distribution and the doublets have a quadratic strength distribution over the panels. (Both triangular and quadrilateral panels are allowed.) The panels can be used for both actual surface paneling, or for mean surface paneling as indicated in figure 1(b). Velocity or mass flux (ref. 3) type boundary conditions can be imposed on either the mean or actual surface boundary; alternately, potential-type boundary conditions can be imposed on the interior of closed bodies. These alternatives are sketched in figure 2, and are illustrated by later examples. Initial results indicate the modeling technique of figure 2(b) is generally the best choice for closed bodies — it gives accurate results and requires considerably fewer calculations than velocity-type boundary conditions.

For both subsonic and supersonic flow, the integrations giving the panel influence coefficients have been obtained in closed form. This has the following advantages over a numerical integration form:

1. The influence coefficients can generally be computed faster and more accurately. This is especially true for regions in which the integral is singular.

2. The coding is much simpler, especially for nonstreamwise side edges. In the supersonic case, all Mach cone/panel intersections are automatically treated.

28

CHARACTER OF THE NUMERICAL MODELS

Networks

For user convenience, the numerical model is cast in the form of panel networks. These networks are a collection of either source or doublet panels and are independently defined over various portions of the aircraft surface as illustrated in figure 3.

Associated with each network are discrete sets of standard points. As described later, some points are used for expressing the source and doublet singularity strength distributions in terms of singularity parameters whose values are to be determined. An equal number of points are used as control points. Control points located at panel centers are used to impose local boundary conditions expressed in terms of either velocity or velocity potential. Additional control points along network edges are used to match the flow properties along common edges of adjacent networks.

The edge control points are also used to impose auxiliary conditions such as the Kutta condition at subsonic trailing edges and for the design case to ensure the proper closure of surfaces (e.g., to specify trailing edge thickness).

Four basic network types are used: source/analysis, doublet/analysis, source/design and doublet/design. In addition, variations of these four types are used for special purposes such as wake paneling. The features that distinguish one network type (and variations thereof) from another are the number and location of the singularity parameter points and the control points (ref. 2, appendices B and C). Particular combinations of singularity parameter points and control points are selected for their ability to produce stable numerical results for the boundary value problem under consideration.

To apply the method, the user must represent the aircraft surface (and the wake for subsonic flow) as a collection of paneled networks, and specify the network type(s) and appropriate boundary conditions. For each network, the code then sets up all the proper singularity parameter and control point locations.

Singularity Strength and Singularity Parameters

A brief description of the singularity strength definition for both source and doublet networks is given in reference 2. An expanded explanation is given here for the specific case of a doublet/analysis network.

Figure 4(a) shows a network comprised of 25 panels. (The surface shape of these panels is obtained by least square fitting a paraboloid to corner points of neighboring panels (ref. 2). Also shown are the locations of the 49 singularity parameter points; one point is at the center of each panel and the

other points are distributed along the network edges. For this particular network, the control points are arranged in a nearly identical fashion.[1]

Associated with each panel k of the network is a six-degree-of-freedom quadratic-doublet strength distribution of the form

$$\mu^k(\xi,\eta) = \mu_o{}^k + \mu_\xi{}^k \xi + \mu_\eta{}^k \eta + \frac{1}{2} \mu_{\xi\xi}^k \xi^2 + \mu_{\xi\eta}^k \xi\eta + \frac{1}{2} \mu_{\eta\eta}^k \eta^2 \qquad (1)[2]$$

In equation (1), ξ and η are local orthogonal coordinates that lie in a reference plane associated with panel k, as illustrated in figure 4(b). (This plane is tangent to the curved panel at the panel center and is nearly parallel to the plane passing through the midpoints of the line segments connecting the corner points of the curved panel.) For each panel, the six coefficients in equation (1) are expressed in terms of selected subsets of the network singularity parameters. For panel k, this subset consists of N singularity parameters μ_j that are associated with panel k and with the panels directly adjacent to panel k.[3] For convenience, the N points at which these singularity parameters are defined are designated P_j. In equation form,

$$\left\{ \begin{array}{c} \mu_o{}^k \\ \mu_\xi{}^k \\ \mu_\eta{}^k \\ \mu_{\xi\xi}^k \\ \mu_{\xi\eta}^k \\ \mu_{\eta\eta}^k \end{array} \right\} = \underset{k}{\overset{6\times N}{[C]}} \; \underset{k}{\overset{N\times 1}{\left\{ \mu_j \right\}}} \qquad (2)$$

Thus, for panel 13 of figure 4(a), $k = 13$, $N = 9$, and $j = (17\text{-}19, 24\text{-}26, 31\text{-}33)$.

The linear relationship given by equation (2) is determined by the method of weighted least squares. That is, for each panel k, the expression

$$R^k = \frac{1}{2} \sum_j W_j [\mu^k(\xi_j,\eta_j) - \mu_j]^2 \qquad (3)$$

---

[1]The only difference is that the edge control points are inset slightly from the network edge; this is done to prevent the influence coefficients from becoming infinite.

[2]The symbol k is a superscript, not an exponent.

[3]Only these neighboring points are used in order to localize any irregularities that may appear in the total solution.

is minimized with respect to the six coefficients appearing in $\mu^k(\xi_j, \eta_j)$. The summation in equation (3) ranges over the points P_j. The weight W_k is given a much larger value than the weights $W_{j \neq k}$. This forces the least squares fit of equation (1) (to the N singularity parameters at points P_j) to be best at panel k. This is illustrated in figure 4(c) for k = 13. (In practice $W_k = 10^8$ and $W_{j \neq k} = 1$ are used.)

Note that the sole reason for the above least squares procedure is to express the assumed panel doublet strength distribution in terms of a neighboring subset of the unknown singularity parameters. This procedure is required because the higher order form for $\mu^k(\xi, \eta)$ given by equation (1) associates more than one coefficient with a single panel. If a constant strength distribution were chosen, that is, $\mu^k(\xi, \eta) = \mu_o{}^k$, then there would be only one coefficient per panel. Consequently, the coefficients $\mu_o{}^k$ themselves could be taken as the basic unknowns. (In fact, this is the concept employed by the Woodward constant pressure panels.)

Because of the least squares formulation, the singularity strength $\mu^k(\xi, \eta)$ of a panel is defined beyond the panel boundary. For the purpose of computing influence coefficients, however, the range of ξ and η is confined to the panel interior and boundary. This range is illustrated in figure 4(c) by the solid portion of the curve for $\mu^{13}(\xi, \eta)$.

Note that the doublet singularity strengths of adjacent panels are not forced to be continuous at the panel edges. For sufficiently dense paneling, however, the strengths are nearly continuous. Thus, the appearance of doublet strength mismatches at panel edges provides a valuable indicator of locally inadequate paneling. (This is illustrated below by the results for the randomly paneled swept wing.)

Influence Coefficients and Determination of the Singularity Parameters

Having each of the panel singularity strength distributions expressed in terms of the unknown singularity parameters enables the perturbation potentials and velocities to be computed in terms of these parameters. Imposing boundary conditions then yields a set of influence coefficient equations from which the singularity parameters can be computed. The discussion below illustrates this for boundary conditions expressed in terms of velocity.

The symbol $\vec{v}^k_{i,(j)}$ is used to denote the perturbation velocity at field point i due to panel k; the subscript (j) indicates that the velocity depends on several singularity parameters μ_j (at points P_j). This velocity is computed from the doublet singularity strength $\mu^k(\xi, \eta)$ and the doublet velocity potential $K(\xi_i - \xi, \eta_i - \eta)$ by an integral of the form (ref. 4, p. 166)

$$\vec{v}^k_{i(j)} = \iint_{S_k} \mu^k(\xi, \eta) \; \vec{\nabla} K(\xi_i - \xi, \; \eta_i - \eta) d\xi \; d\eta \qquad (4)$$

31

where (ξ_i, η_i) is the field point i, and the gradient operator is taken with respect to the field point coordinates (i.e., $\partial/\partial\xi_i$, etc.). The expression for the velocity kernel K differs for subsonic and supersonic flow, as does the region of integration S_k. For subsonic flow, S_k is the entire panel area. For supersonic flow, S_k is that portion of the panel that lies in the upstream Mach cone emanating from the field point.

The result of the integration in equation (4) is that the right-hand side of the equation becomes a linear algebraic equation in the network singularity parameters μ_j.[4] For the single network of figure 4(a), the total velocity at any control point i, due to all the panels, is given by

$$\vec{V}_i = \vec{U}_\infty + \sum_{k=1}^{k=25} \vec{v}^k_{i(j)} = \vec{V}_i(\mu_j) \tag{5}$$

where $\vec{U}_\infty$ is the free-stream velocity vector. Imposing the boundary condition $\vec{V}_i \cdot \vec{n}_i = 0$, where $\vec{n}_i$ is the unit normal vector at control point i, gives

$$\sum_{k=1}^{25} \vec{v}^k_{i(j)} \cdot \vec{n}_i = -\vec{U}_\infty \cdot \vec{n}_i \qquad i = 1, \ldots 49$$

When cast in matrix form, this equation becomes

$$\underset{49\times49}{\left[A_{ij} \right]} \left\{ \begin{matrix} \mu_1 \\ \cdot \\ \cdot \\ \cdot \\ \mu_{49} \end{matrix} \right\} = - \left\{ \begin{matrix} \vec{U}_\infty \cdot \vec{n}_1 \\ \cdot \\ \cdot \\ \cdot \\ \vec{U}_\infty \cdot \vec{n}_{49} \end{matrix} \right\} \tag{6}$$

Each row i of the influence coefficient matrix A_{ij} represents a boundary condition imposed at one of the 49 control points. Each column j corresponds to one of the 49 singularity parameters μ_j. The matrix A_{ij} is constructed one row (control point) at a time. For each row, one cycles through the panels and enters the contributions of each panel to the appropriate columns of A_{ij}. For example, panel 13 of figure 4(a) would contribute a value to columns 17-19, 24-26, and 31-33. (Other panels would also contribute values to some of these same columns, and these values would be added to those from panel 13.)

For more than a single network, the procedure is exactly the same except that the matrices in equation (6) expand in size so as to incorporate all the panels, all the singularity parameters, and all the control points of every network. (At this point the networks effectively lose their distinct identities.) The general form of equation (6) is then

---

[4]This integration, and a similar one for the linear source distribution, has been carried out analytically for both subsonic and supersonic flows. See references 2 and 3, respectively.

$$\begin{matrix} \text{M×M} & \text{M×1} & \text{M×1} \\ [A] & \{\mu\} = & \{b\} \end{matrix} \qquad\qquad (7)$$

where M is the total number of singularity parameters (and control points) for all the networks. Hence $\{\mu\}$ can be solved for, and then the velocities can be calculated from $\vec{V}_i(\mu_j)$ as indicated by equation (5). (The value $k = 25$ appearing in equation (5) would be replaced with the total number of panels in all the networks.) Knowing the velocities, the pressures can then be calculated from appropriate velocity-pressure relationships.

RESULTS AND DISCUSSION

The following numerical results are presented to illustrate the various capabilities of the method.

Subsonic Flow[5]

Localized panel density changes.- Figure 5 shows the right half of an aspect-ratio-two wing modeled as three doublet/analysis mean surface networks and two wake networks. The panel density in wing networks I and II is held fixed while the panels in wing network IV vary from 4 to 144, with corresponding changes made to the trailing wake network (number V). The lift curve slope and chordwise center of pressure location N_o are only slightly affected by this large change in local panel density. Another feature illustrated by this example is that panel edges from adjacent networks are not required to be aligned. For $N = 4$ in fact, none of the panel edges internal to network IV are aligned with those from networks I and II.

When this set of cases was first run it was expected that only cases $N = 2$ and $N = 6$ would be successful because these are the only arrangements in which network IV has edge control points directly opposite those of networks I and II. It was somewhat surprising to discover how forgiving the numerics actually are to such network mismatches.

Convergence behavior.- The aspect-ratio-two wing was also used to study solution convergence behavior. In this case, single doublet/analysis networks were used for the wing. One network used uniform panel spacing and the other used cosine spacing, as shown in figure 6(a). The variation in lift coefficient with number of panels is shown in figure 6(b), along with the highly accurate and converged solution of Rowe (ref. 6). The convergent character of the panel solutions is clearly seen. The cosine spacing probably converges faster than the uniform spacing because of the greater panel density at the wing leading edge and tip where pressure gradients are largest. Chordwise variations in $\Delta C_p = C_{p_\ell} - C_{p_\mu}$ at $y/(b/2) = 0.5$ are shown in figures 6(c)

[5]All the cases shown are for incompressible flow. The method is easily extended to compressible flow by stretching the aircraft geometry in the streamwise direction by the Prandtl-Glauert rule (ref. 5, p. 84).

and 6(d) for the cosine and uniform spacing cases, respectively, along with results from reference 6. Again, cosine spacing gives more accurate results than uniform spacing for a given number of panels.

Insensitivity to panel arrangement.- Figure 7 illustrates the insensitivity of the method to extremes in panel size, shape and arrangement. A swept wing has been paneled in a regular and in a random fashion, and the vortex spline method of reference 7 was used to calculate results for the regular paneling. A doublet/analysis network of the present method was used for the random paneling. The spanwise lift distributions computed by the two methods are nearly identical as seen in figure 7(b). Chordwise pressure distributions at $y/(b/2) = 0$ are plotted in figure 7(c). Here, the results of the present method differ from those of the reference solution towards the leading edge where the pressure gradient becomes large. Note that the pressures predicted by the present method are actually discontinuous at panel edges. When the panel density is sufficiently fine, these discontinuities essentially vanish. The large mismatches are an indication of locally inadequate panel density over the forward portion of the wing. This agrees with figure 7(a), where it is seen that only two panels are used between the leading edge and about the 30% chord line.

The above examples of random paneling and of localized panel density changes (fig. 5) demonstrate the extreme forgiveness of the method to irregular paneling, a feature that greatly enhances its practical usability for applications involving complex geometries where regular, evenly spaced paneling cannot always be constructed.

Alternative surface paneling models.- The preceding examples of lifting surfaces are all mean surface models. In figure 8, results are presented for three different upper and lower surface paneling models of an aspect-ratio-two, 12% thick rectangular wing.

The first model was somewhat similar to that of the reference solution and employed a source/analysis network on the wing surface combined with a doublet/analysis network lifting system on the camber surface. Zero normal velocity was prescribed at control points of both networks. The second model used a doublet/analysis network on the wing surface with zero total potential specified on the interior side of the surface. For this formulation it was necessary to close the wing by paneling the tip. The third model (pioneered by Morino (ref. 8) employed superimposed source/analysis and doublet/analysis networks on the wing surface. Zero perturbation potential was specified on the interior side of the wing surface and the source strengths were set equal to the negative of the normal component of free-stream velocity (see fig. 2(b). This model appeared to be somewhat more forgiving than the previous model regarding closed surfaces and it was unnecessary to panel the tip.

The last two models have certain advantages over the first. The influence coefficients require the computation of a scalar ϕ rather than a vector $\vec{\nabla}\phi$; moreover, the scalar is a lower order expression, which is cheaper to compute. The influence coefficients need not be saved for postprocessing since surface velocities can be calculated directly from doublet strength gradient. This fact also implies that velocities may be calculated everywhere on the

34

surface, not just at control points, which, in turn, allows more accurate calculation of forces. Note that the use of superimposed source and doublet networks in the third model is only modestly more expensive than the use of a doublet network alone since source strength is prescribed and terms common to both the source and doublet influence coefficients need be computed only once.

Efficiency of analysis networks.- Figure 9 is an illustration of wing body surface paneling with results computed from the present method and from the method of reference 9. Figure 9(a) shows the surface paneling used by the present method. A total of 160 curved, linear-strength source/analysis panels were used for the half airplane, 96 on the body and 64 on the upper and lower wing surfaces. An additional 32 doublet/analysis panels were placed on the wing camber surface and 13 wake panels were also used (some of which extended the wing doublet panels to the centerline, i.e., $y = 0$).

Results from the method of reference 9 were obtained using 936 flat, constant-strength source panels and 12 lifting elements. This is typical of the number of panels required by this method for wing-body applications.

Upper and lower wing surface pressures predicted by the two methods are shown in figure 9(b) for two span stations. The agreement is excellent at $y/(b/2) = 0.68$ and at two additional inboard stations which are not shown. The discrepancy at $y/(b/2) = 0.90$ is possibly due to the fact that the method of reference 9 underestimates spanwise velocities near wing tips, and may also be partly caused by the large width used for the outboard panels in the present method. The table in figure 9 shows that the lift and pitching moment coefficients are also in close agreement.

The table in figure 9 also gives the CPU times for the two methods. The present method enjoys a better than 20-to-1 advantage over the method of reference 9 due to the large reduction in the number of panels required.

Even on a panel-by-panel basis, the higher order singularity panels of the present method are competitive with the constant strength panels of reference 9. Figure 10 gives an estimate of CPU time comparisons between the pilot code of the present method and the highly optimized TEA230 program of reference 9. The CPU time represents time for setting up panel geometry, singularity strength and control point quantities, calculation of influence coefficients, and equation solving. The range of CPU times for a given number of panels reflects differences between sources and doublets and between near-field and far-field calculation times.

Wing design in presence of fixed fuselage geometry.- Figure 11 illustrates the three-dimensional design capability of the method.[6] This example shows how design-type panel networks are able to reproduce an original geometry from a modified geometry, using the pressure distribution of the original geometry as boundary conditions.[7] The pressure distributions

---

[6]Another application of the design networks is given in reference 10, which treats separated leading edge vortex flow.

[7]In an actual application, the desired geometry corresponding to a specified pressure distribution would of course not be known a priori.

calculated from the original geometry are shown by the solid curves in figure 11(b). A modified geometry and the corresponding pressures are shown by the dashed curves in figures 11(c) and 11(b), respectively. By replacing the analysis network in the modified geometry region with a design network, the desired geometry corresponding to the specified pressure distribution was then computed. After two iterations, the designed geometry and corresponding pressures are nearly identical to the originals, as shown by the circles in figures 11(b) and 11(c).

Supersonic Flow

Flow over spindles.- Figures 12 through 16 show results for flow over axisymmetric spindles and illustrate several features of the linear source panels.

Figure 12 shows a 0.1 fineness ratio spindle with a random paneling arrangement. Because of this extreme panel layout, and the use of only flat panels, the resultant surface is somewhat distorted. For example, surface indentations can be seen in the front view. Even so, the predicted pressures at panel control points, given by the dots in figure 12, are in remarkably good agreement with the exact method of characteristics solution.

Figure 13 is for the same spindle as in figure 12 but the paneling is laid out in a regular fashion. This paneling was used to compute source panel solutions for both a constant strength and the linearly varying strength distribution of the present method. These solutions are shown in figure 13, along with an axisymmetric line source solution. For this particular configuration, the results from all three methods are in good agreement with the exact solution.

Figure 14 is for the same configuration as figure 13, except that the fineness ratio has been halved. In this case the present linear source panels and the axisymmetric line source give the same results, but the constant-strength source panels show considerable differences, indicating a loss of accuracy.

Another indication that the linear source panels are more reliable than constant strength panels is provided by figures 15 and 16. Here, the 0.05 fineness ratio spindle of figure 14 is at $\alpha = 5°$ and pressures are given at three circumferential angles. Figure 15 is for constant-strength source panels, while figure 16 is for the linearly varying source panels of the present method (both cases are for the paneling shown in figure 13). The oscillations that occur in the constant-strength source panel solution are a clear indication of numerical stability problems. Note that the linear source panel solutions do not exhibit this oscillatory behavior.

Wing with subsonic and supersonic leading edges.- Figure 17 shows results for a wing having both a subsonic and a supersonic leading edge. Results predicted by a single network of planar doublet/analysis panels are in good agreement with the exact linearized theory solution in reference 11. By using two networks, with the special Mach line on the left as a network boundary,

the discontinuity in pressure at the Mach line can be represented even more accurately. For this case (not shown), the pressure remains exactly constant in the region between the supersonic leading edge and the special Mach line.

It should also be noted that the present method does not require artificial "diaphragm" panels between the subsonic leading edge and the right-hand side special Mach line.

Upper and lower surface paneling of thin wing.- Figure 18 shows the upper and lower surface paneling used on a 3% thick arrow wing (wing number 2 of refs. 12 and 13). This is a particularly severe test of the method due to the presence of internal waves, which for a source-paneled wing can repeatedly reflect from the closely spaced upper and lower wing surfaces with increasing intensity. To suppress these internal waves, separate source and doublet networks having identical paneling were superimposed, that is, each panel shown in figure 18 represents both a source and a superimposed doublet. Boundary conditions of the type shown in figure 2(b) were employed so that the modeling was the same as for the third model of the $\mathcal{R} = 2$, 12%-thick rectangular wing of figure 8.

Predicted and experimental upper and lower surface pressure distributions are shown in figure 19 for four spanwise stations. The predicted pressure distribution is smooth and compares well with the experimental data except in the tip region. The oscillations at the tip are thought to be caused by the combined effect of the discontinuous doublet strength (at panel edges) and the special Mach line emanating inboard from the leading edge of the wing tip. The discontinuity in doublet strength is equivalent to a concentrated line vortex, which produces infinite singularities propagating along Mach cones. This is perhaps causing the oscillations in the predicted wing tip flow field. It is anticipated that this problem will be overcome by the implementation of a new doublet network currently under development. This doublet network achieves exact continuity of doublet strength across panel edges by splitting each (quadrilateral) panel into four triangles via the panel diagonals. A different quadratic doublet distribution is defined on each triangle with the provision that doublet strength and gradient must be continuous across triangle edges within the panel. This leads to a doublet distribution on each quadrilateral panel with eight degrees of freedom versus the original six — enough to produce continuity of doublet strength (and in most cases gradient) across panel edges. Such a formulation would seemingly increase the number of influence coefficient computations for each panel by a factor of 3 (the increase in the number of edges). In fact this is not the case because the enhanced continuity properties of the new doublet distribution allow one to neglect terms that would cancel analytically. (With the present network, the lack of strict continuity requires the terms to be retained.) Such terms account for approximately 70% of the influence coefficient operation count.

Also, a more efficient version of the two separate but superimposed source and doublet panel networks is being developed. This will result in a single "composite" panel network for which certain terms in the influence coefficients will only have to be computed once, instead of twice as is done in the superimposed case.

37

Forebody pressures on B-1.- Figure 20 shows the paneling used on the forebody section of the B-1 bomber. The modeling technique was the same as in the preceding example. Pressure coefficient results at $M = 1.6$ are shown in figure 21 along the upper and lower fuselage lines. Also shown are the experimental data and finite difference results reported in reference 14. The panel method results are in good agreement along the lower fuselage line and along the upper fuselage line up to the canopy region. In the region aft of the canopy, the comparison is poorer; this again may be due to the discontinuity in doublet strength across panel edges discussed in the previous example.

The CPU time for the finite difference calculations on the forebody took about 55 min on a CDC 7600 (ref. 14). The panel method results took about 1 min, also on a CDC 7600.

Superinclined panel.- The current source and doublet panels must be inclined at angles less than that of the Mach cone. Currently under development is a "superinclined" panel that can be inclined ahead of the Mach angle. With this capability it will be possible to place panels at nacelle inlets and exhausts for:

1.   closing the nacelle volume so that potential-type boundary conditions can be specified in the interior.

2.   sealing off inlets to prevent the propagation of waves into the interior (which can degrade numerical accuracy).

3.   specifying exhaust mass flows.

These features are illustrated in figure 22.

The superinclined panels represent an initial value problem type of behavior and require two boundary conditions on the downstream panel side. Although these panels look like blunt surfaces, they do not influence the upstream flow.

CONCLUDING REMARKS

A higher order panel method for linearized subsonic and supersonic flow has been described. Numerical results illustrate the following features:

1.   The paneling can be applied to the true surface geometry of arbitrarily shaped aerodynamic configurations.

2.   Both supersonic and subsonic analysis, and subsonic design problems can be solved. In the design mode, the geometry required to produce a specified pressure distribution is determined. One or more components of a configuration can be designed in the presence of other components whose geometrical shapes are fixed.

3. The method offers the user a variety of modeling options. For example, with wing-like components, all the usual thin surface approximations are available. For more accurate results, the paneling and boundary conditions can be applied to the wing upper and lower surfaces. For closed bodies, either velocity or potential-type boundary conditions can be imposed.

4. For subsonic flow, the method is both stable and accurate. Unlike many other methods, the numerical results display a marked insensitivity to the size, shape, and arrangement of panels. Good accuracy is obtained with relatively sparse panel densities; convergence to highly accurate results occurs at moderate panel densities. For supersonic flow, spurious oscillations in pressure sometimes occur. It is anticipated that this problem can be solved by eliminating the discontinuity in doublet strength at panel edges.

5. The method is efficient. Individual panel influence coefficient calculation times are competitive with existing body surface paneling methods that use lower order singularities, and overall matrix sizes are much smaller because of the reduced number of panels required. In addition, the influence coefficient integrals are all evaluated in closed form.

REFERENCES

1. Perkin, B. R.; and Erickson, L. L.: FLEXSTAB — A Computer Program for the Prediction of Loads and Stability and Control of Flexible Aircraft. Proceedings of the SCAR Conference, NASA CP-001, 1977. (Paper no. 12 of this compilation.)

2. Johnson, F. T.; and Rubbert, P. E.: Advanced Panel-Type Influence Coefficient Methods Applied to Subsonic Flows. AIAA Paper 75-50, Jan. 1975.

3. Ehlers, F. E.; Johnson, F. T.; and Rubbert, P. E.: A Higher Order Panel Method for Linearized Supersonic Flow. AIAA Paper 76-381, July 1976.

4. Kellog, O. D.: Foundations of Potential Theory, Dover Publishing Co., 1953.

5. Ashley, H.: Engineering Analysis of Flight Vehicles. Addison-Wesley Publishing Co., 1974.

6. Rowe, W. S.: Collocation Method for Calculating the Aerodynamic Pressure Distributions on a Lifting Surface Oscillating in Subsonic Compressible Flow. AIAA Symposium on Structural Dynamics and Aeroelasticity, Boston, Mass., Aug. 1965.

7. Mercer, J. E.; Weber, J. A.; and Lesferd, E. P.: Aerodynamic Influence Coefficient Method Using Singularity Splines. NASA CR-2423, 1974.

8. Morino, L.; and Kuo, C. C.: Subsonic Potential Aerodynamics for Complex Configurations: A General Theory. AIAA J., vol. 12, no. 2, Feb. 1974, pp. 191-197.

9. Rubbert, P. E.; and Saaris, G. R.: Review and Evaluation of a Three Dimensional Lifting Potential Flow Analysis Method for Arbitrary Configurations. AIAA Paper 72-188, Jan. 1972.

10. Gloss, B. B.: Development of an Aerodynamic Theory Capable of Predicting Surface Loads on Slender Wings with Vortex Flow. Proceedings of the SCAR Conference, NASA CP-001, 1977. (Paper no. 3 of this compilation.)

11. Jones, R. T.; and Cohen, D.: High Speed Wing Theory. Princeton University Press, 1960, p. 158.

12. Carlson, H. W.: Aerodynamic Characteristics at Mach Number 2.05 of a Series of Highly Swept Arrow Wings Employing Various Degrees of Twist and Camber. NASA TM X-332, 1960.

13. Carlson, H. W.: Pressure Distributions at Mach Number 2.05 on a Series of Highly Swept Arrow Wings Employing Various Degrees of Twist and Camber. NASA TN D-1264, 1962.

14. D'Attorre, L.; Bilyk, M. A.; and Sergeant, R. J.: Three Dimensional Supersonic Flow Field Analysis of the B-1 Airplane by a Finite Difference Technique and Comparison with Experimental Data. AIAA Paper 74-189, 1974.

(a) INTERFERENCE   (b) ARBITRARY SURFACE PANELING
    SHELL MODEL   MODEL OF PRESENT METHOD
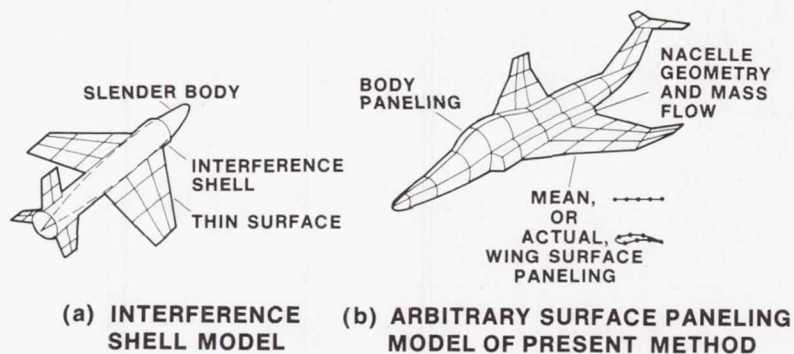
Figure 1.- Different levels of aerodynamic
geometry modeling.

(a) VELOCITY OR MASS FLUX BOUNDARY CONDITIONS

(b) POTENTIAL TYPE BOUNDARY CONDITIONS FOR
CLOSED BODIES (σ = SOURCE STRENGTH)
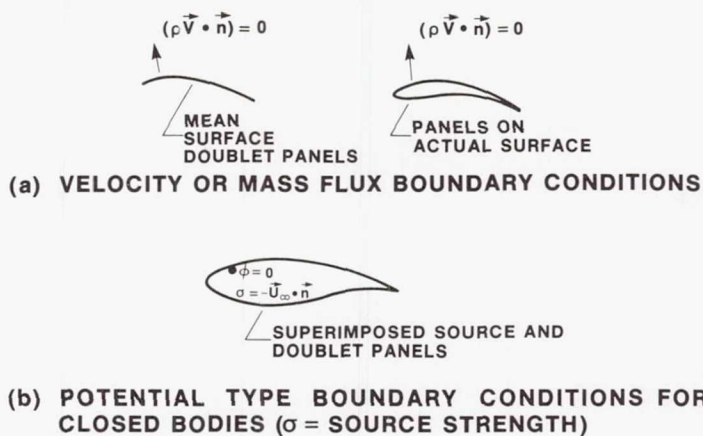
Figure 2.- Alternative forms for expressing
boundary conditions.
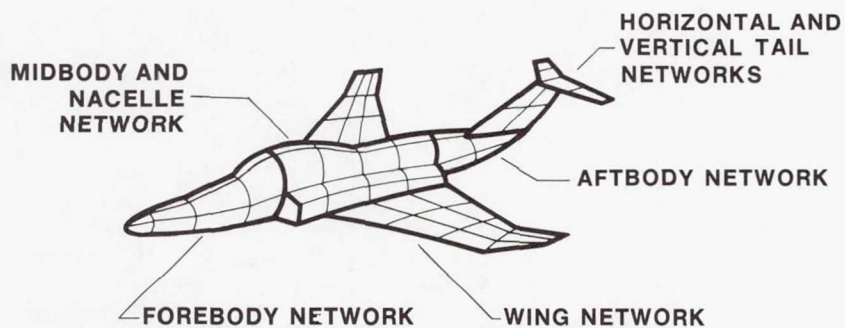
Figure 3.- Illustration of body surface broken into
independently defined networks of panels.

(a) NETWORK PANELS AND THE
SINGULARITY PARAMETER POINTS P_j

(b) LOCAL COORDINATE SYSTEM AND
REFERENCE PLANE FOR PANEL 13

$\mu^{13}(\xi,\eta)$ IS LEAST SQUARE FITTED TO μ_{25} AND
TO THE μ_j OF THE 8 ADJACENT PANELS

μ_{24} μ_{25} μ_{26} ← UNKNOWN SINGULARITY PARAMETERS

PANEL 13

(c) WEIGHTED LEAST SQUARES FIT OF PANEL
DOUBLET STRENGTH DISTRIBUTION $\mu^{13}(\xi,\eta)$
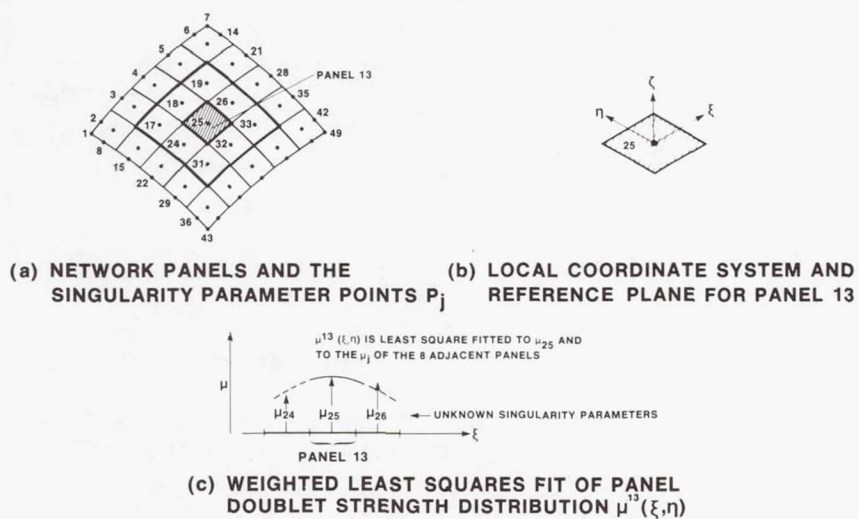
Figure 4.- Illustration of doublet/analysis network comprised
of 25 panels and 49 singularity parameters.

C_L 1 N = 2   N = 3   N = 4   N = 6   N = 12

WAKE NETWORK

$C_{L\alpha} = 2.44$ $C_{L\alpha} = 2.44$ $C_{L\alpha} = 2.45$ $C_{L\alpha} = 2.45$ $C_{L\alpha} = 2.45$ (PER RADIAN)
$N_O = .207$ $N_O = .210$ $N_O = .209$ $N_O = .210$ $N_O = .209$

- REGIONS I, II, III, IV, V ARE DISTINCT NETWORKS
- "EXACT SOLUTION OF $C_{L\alpha} = 2.47$, $N_O = 0.209$ IS OBTAINED BY INCREASING PANEL DENSITY AT LEADING EDGE.
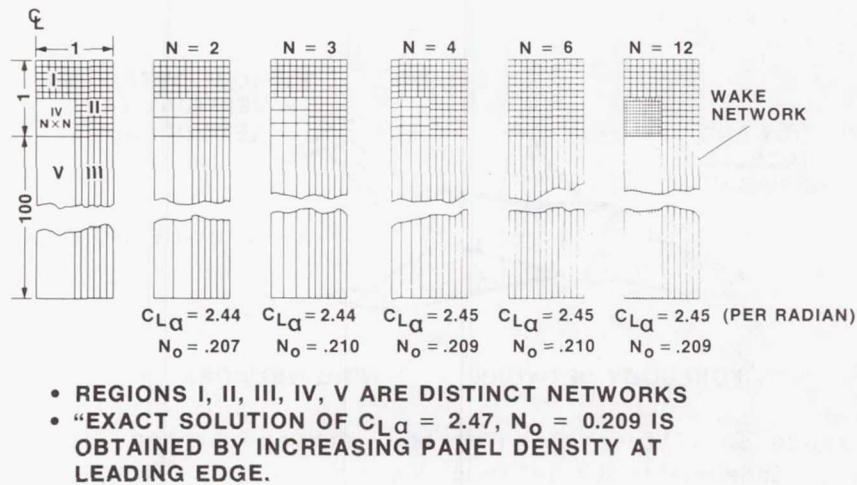
Figure 5.- Localized changes in panel density; AR = 2, M = 0.

UNIFORM COSINE U_∞

WING

WAKE

C_L

COSINE SPACING
ROWE (2.474)
UNIFORM SPACING

NUMBER OF PANELS

(a) UNIFORM AND COSINE PANEL SPACING

(b) LIFT COEFFICIENT AS FUNCTION OF NUMBER OF PANELS USED
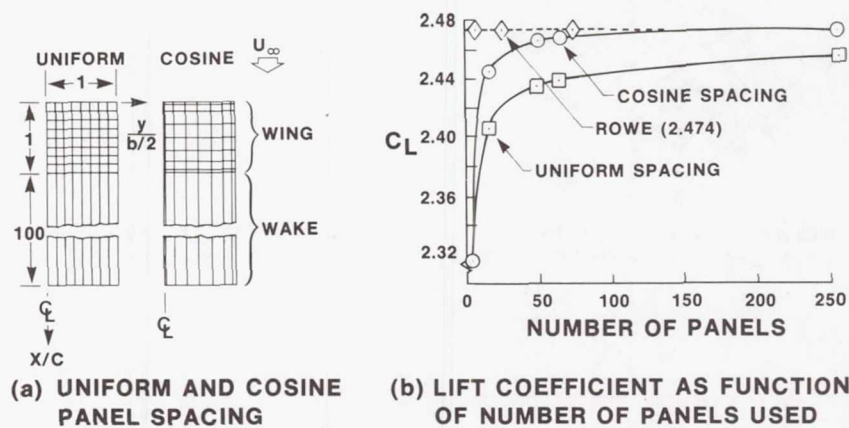
Figure 6.- Convergence behavior of doublet/analysis panels; results scaled to α = 1 rad, M = 0. (The diamonds for the Rowe solution denote number of pressure modes, rather than number of panels.)

44
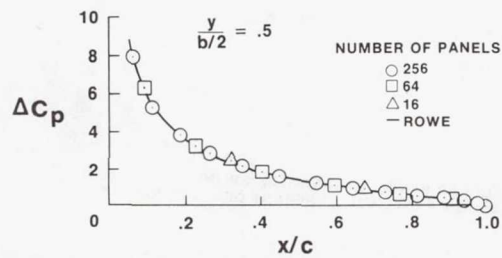
(c) CHORDWISE PRESSURE FOR COSINE SPACING
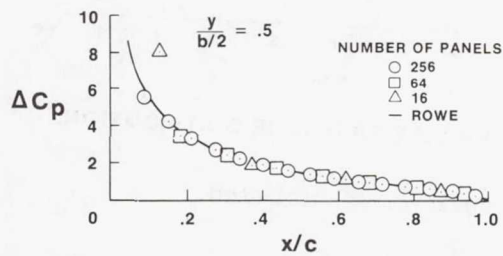
(d) CHORDWISE PRESSURE FOR UNIFORM SPACING

Figure 6.- Concluded.
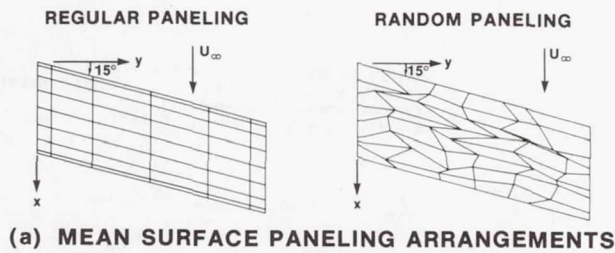
(a) MEAN SURFACE PANELING ARRANGEMENTS
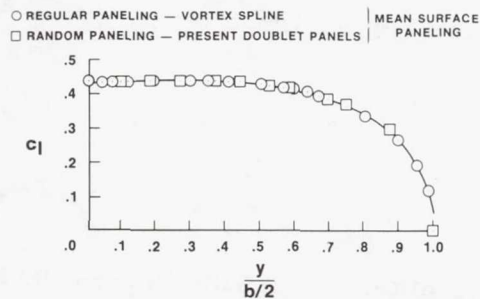
(b) SPANWISE LIFT DISTRIBUTION

Figure 7.- Insensitivity to panel arrangement;
$\alpha = 5.7^{\circ}$, $M = 0$.

45
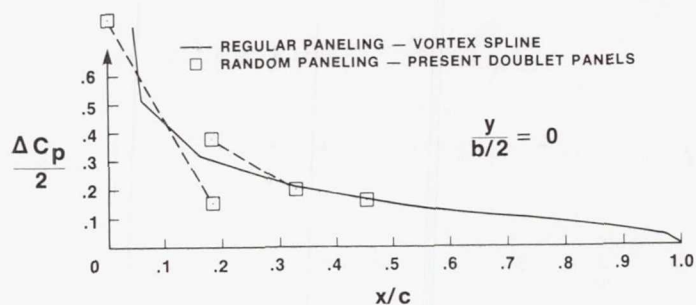
(c) CHORDWISE PRESSURE DISTRIBUTION;

Figure 7.- Concluded.

(a) WING SECTION & PANELING

(b) SPANWISE CIRCULATION

(c) SECTION PRESSURES
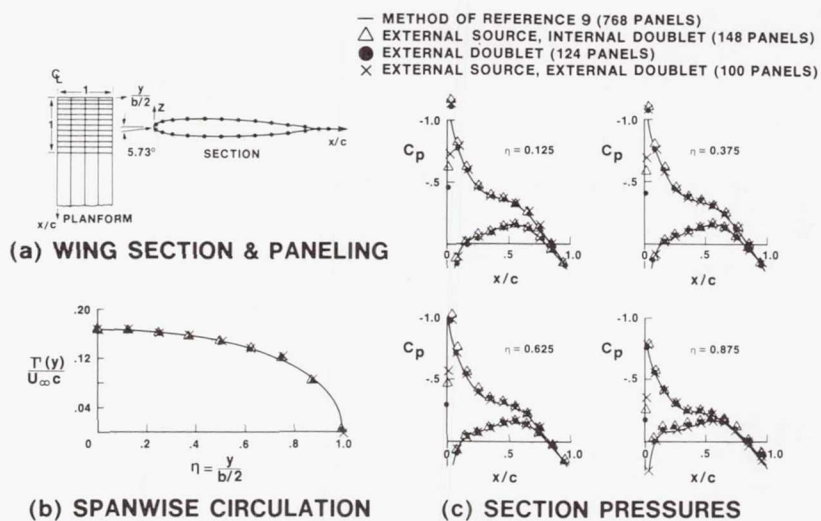
Figure 8.- Alternate surface paneling models.

ORIGIN FOR MOMENT
CALCULATION

WING-BODY CONFIGURATION	PRESENT METHOD	METHOD OF REF. 9
SOURCE DISTRIB.	LINEAR	CONSTANT
PANEL GEOMETRY	CURVED	FLAT
NO. SOURCE PANELS	160	936
CPU TIME, sec.*	150	3300
c_L	.689	.697
c_m	.00345	−.00325

*CDC 6600
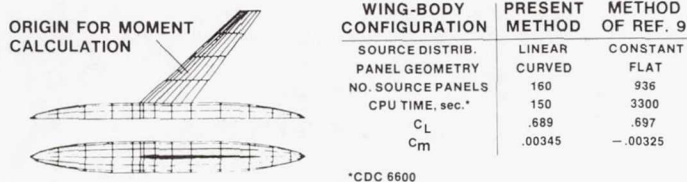
(a) SURFACE PANELING FOR PRESENT METHOD

$\frac{y}{b/2} = .68$
PRESENT METHOD
REF. 9

$\frac{y}{b/2} = .90$

c_p

x/c

c_p

x/c
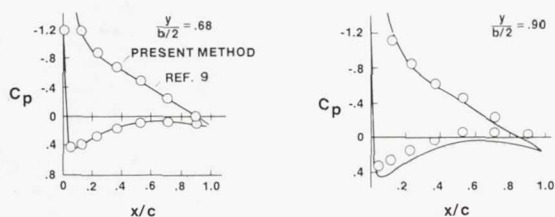
(b) CHORDWISE PRESSURE DISTRIBUTIONS

Figure 9.- Increased efficiency of current method
over method using flat, constant strength
sources; $\alpha = 10^o$, $M = 0$.

PRESENT METHOD
(PILOT PROGRAM)

METHOD OF REFERENCE 9
(TEA 230)

SECONDS
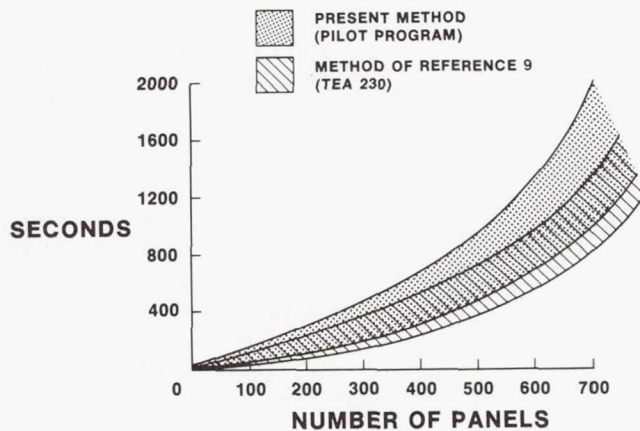
NUMBER OF PANELS

Figure 10.- Variation in CPU time with number
of panels.

(a) PANELING OF DESIGN MODEL

(b) WING-PRESSURE PROFILES
— ANALYSIS MODE
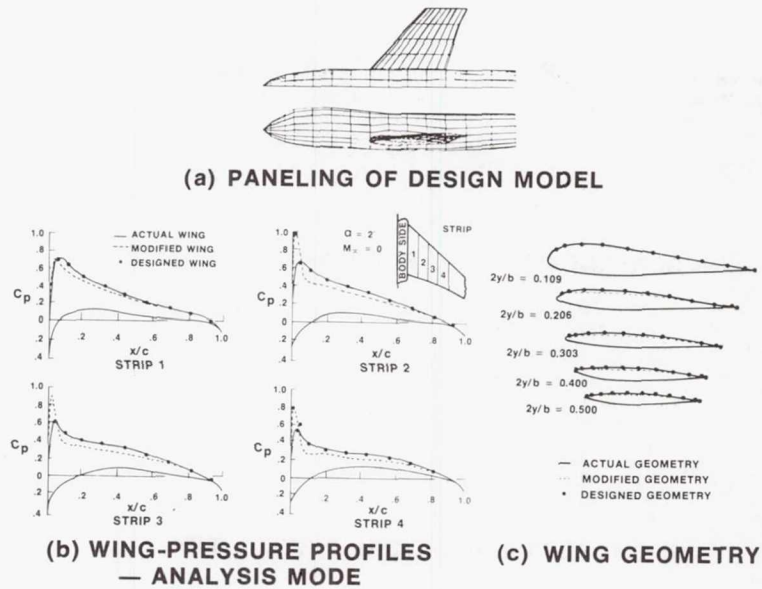
(c) WING GEOMETRY

Figure 11.- Wing design in presence of fixed
fuselage geometry.
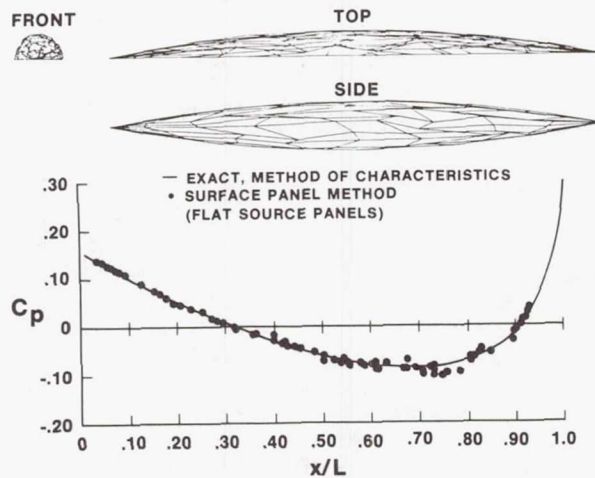
Figure 12.- Random source paneling on spindle,
$\alpha = 0$; $M = \sqrt{2}$, fineness ratio = 0.1.

α = 0°, __FINENESS RATIO = .1__

— EXACT, METHOD OF CHARACTERISTICS
○ AXISYMMETRIC SOURCE
□ CONSTANT STRENGTH SOURCE PANELS ⎰ FLAT SURFACE PANELS
△ LINEARLY VARYING SOURCE PANELS ⎱

$r/L = (1/5)\,(x/L)\,(1-x/L)$
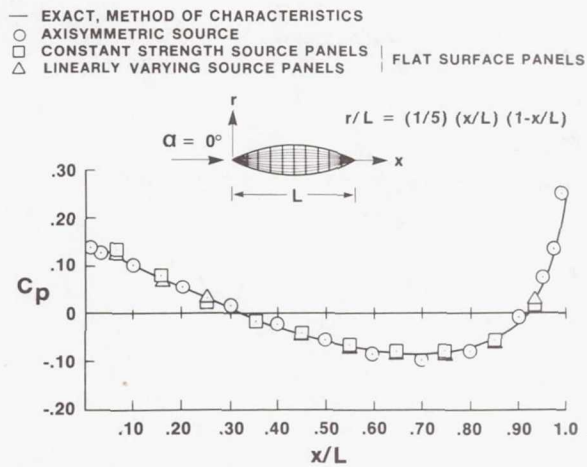
Figure 13.- Regular paneling for spindle
of figure 12; $M = \sqrt{2}$.

α = 0°, __FINENESS RATIO = .05__

○ AXISYMMETRIC SOURCE
□ CONSTANT STRENGTH SOURCE PANELS ⎰ FLAT SURFACE PANELS
△ LINEARLY VARYING SOURCE PANELS ⎱

$r/L = (1/10)\,(x/L)\,(1-x/L)$
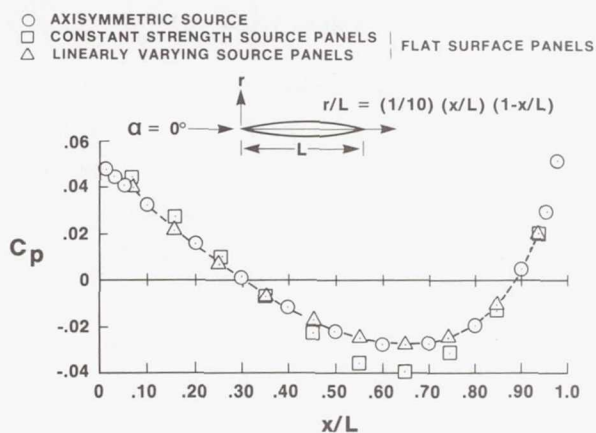
Figure 14.- Loss of accuracy for constant
strength panel as fineness ratio is
halved from that of figure 13; $M = \sqrt{2}$.
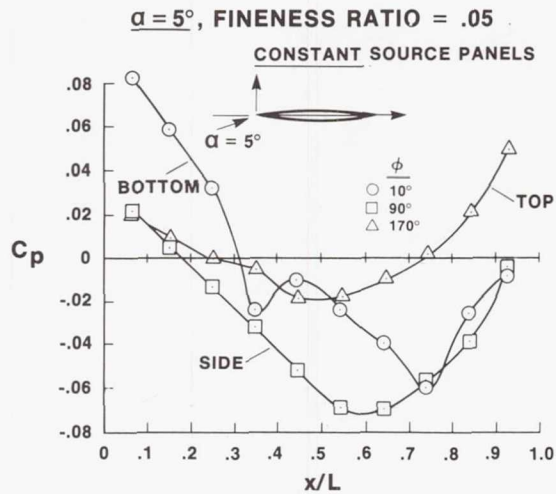
Figure 15.- Oscillatory solution produced
by constant strength panels for spindle
at angle of attack; $M = \sqrt{2}$.
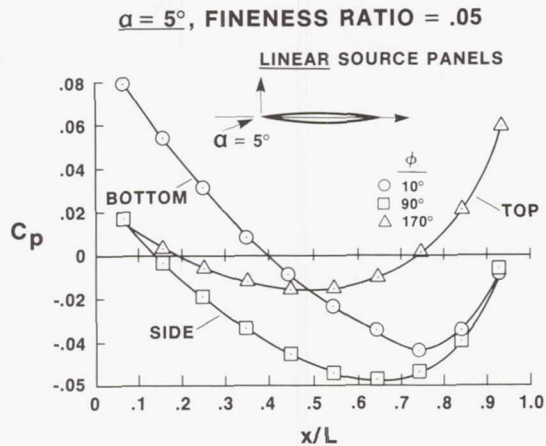
Figure 16.- Nonoscillatory solution produced
by linear strength panels for configuration
of figure 15; $M = \sqrt{2}$.
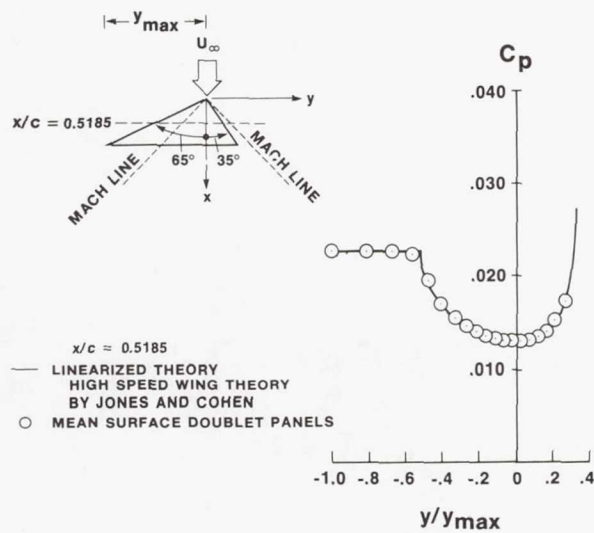
Figure 17.- Wing with subsonic and supersonic
leading edges; $\alpha = 0.01$ rad, $M = \sqrt{2}$.
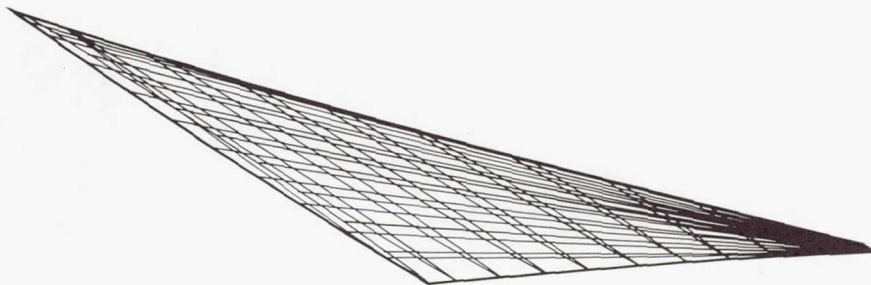
Figure 18.- Upper and lower surface paneling of 3% thick
arrow wing.
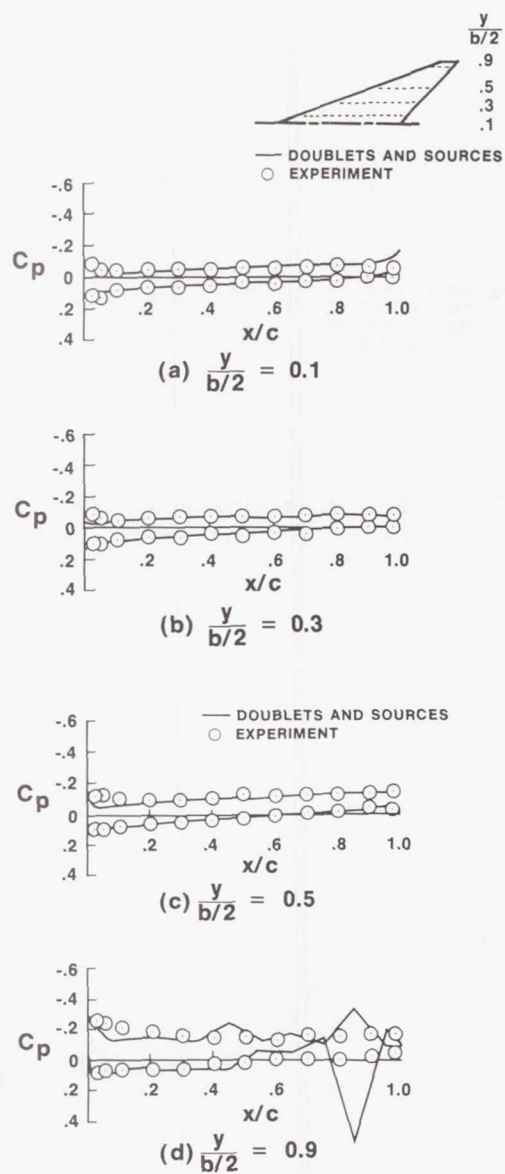
Figure 19.- Upper and lower surface
pressures on 3% thick arrow wing;
$\alpha = 2^o$, $M = 2.05$.

Figure 20.- Paneling on forebody of B-1
bomber.

UPPER FUSELAGE LINE
LOWER FUSELAGE LINE

UPPER FUSELAGE LINE

C_p

○ EXPERIMENT
● SOURCE & DOUBLET PANELS
···· SUPERSONIC FINITE
     DIFFERENCE METHOD

LOWER FUSELAGE LINE

C_p

BODY STATION, METERS

Figure 21.- Centerline pressures on forebody
of B-1 bomber; $\alpha = 2^o$, $M = 1.6$.

COMPOSITE PANELS ON ALL SURFACES
INCLINED BEHIND MACH ANGLE

UNIFORM FLOW
EVERYWHERE INSIDE

$\phi = 0$

$\sigma = -\vec{U}_\infty \cdot \vec{n}$

$\dfrac{\partial \phi}{\partial n} = 0$

$\dfrac{\partial \phi}{\partial n}$ SPECIFIED

$\phi = 0$

$\phi = 0$

SUPERINCLINED PANELS
AT INLET AND EXHAUST

Figure 22.- Combined use of composite panels and superinclined panels.

54

DEVELOPMENT OF AN AERODYNAMIC THEORY CAPABLE OF PREDICTING

SURFACE LOADS ON SLENDER WINGS WITH VORTEX FLOW

Blair B. Gloss
NASA Langley Research Center

Forrester T. Johnson
Boeing Commercial Airplane Company

SUMMARY

With advent of supersonic cruise aircraft that utilize vortex lift at
some point in their flight envelope, the need for an analytical method capable
of accurately predicting loads on wings with leading-edge separation has be-
come evident. The Boeing Commercial Airplane Company, under contract to
NASA Langley Research Center, has developed an inviscid three-dimensional
lifting surface method that shows promise in being able to accurately predict
loads, subsonic and supersonic, on wings with leading-edge separation and
reattachment.

INTRODUCTION

For the thin, relatively sharp edge, highly swept-back wings of interest
for supersonic cruise aircraft, the leading-edge vortex type of flow and
resulting vortex lift characteristics are important design considerations. In
addition to its well known high lift capability, this flow phenomena provides
a highly stable and consistent flow pattern over a wide range of flight condi-
tions, and for several modern supersonic aircraft, this type of flow is basic
to the aerodynamic design concept. In addition, the critical wing structural
loads for a wide variety of high speed aircraft are generated in angle-of-
attack ranges where this type of flow tends to predominate. As part of its
research program directed towards developing theoretical methods for the
design and analysis of wings for advanced high speed aircraft, the Langley
Research Center has contracted with the Boeing Commercial Airplane Company
for the development of a method for the prediction of aerodynamic load distri-
butions of wings with nonconical leading-edge vortex flow. This paper is
presented as a progress report on this work, bringing forward the motivation
for this research program, the objectives of the work, and some selected
results.

SYMBOLS

b	model span
c	local chord
C_L	lift coefficient, $\dfrac{\text{lift}}{qS}$
C_p	pressure coefficient, $\dfrac{p-p_{ref}}{q}$
ΔC_p	lower surface C_p minus upper surface C_p
M	free-stream Mach number
n	unit normal vector
p	local static pressure
p_{ref}	reference pressure
q	free-stream dynamic pressure
S	reference area
U_∞	free-stream velocity
V	local velocity vector
x	chordwise coordinate
y	spanwise coordinate
α	angle of attack, deg
ρ	density of air
ε_{tip}	Twist angle of wing tip, positive leading edge up

SOME APPLICATIONS OF VORTEX FLOW

Figure 1 shows a slender wing at angle of attack with associated leading-edge vortex. Shown on the right hand side of the figure is a plot of lift coefficient versus angle of attack illustrating the large amount of vortex lift developed. Presently, analytical techniques are available for computing the total lift versus angle of attack for wings having leading-edge vortices at subsonic and supersonic speeds (references 1 and 2). There are, however, no methods available that accurately predict the load distribution on wings with leading-edge vortices nor are there any design methods that will allow the

56

optimization of vortex flow. The prediction of loads on wings due to leading-edge vortex separation is an important problem to the structural designer and aeroelastician, since supersonic cruise vehicles either depend on or encounter vortex lift at many points in their flight envelope. Figure 2 presents some examples of aircraft that utilize vortex lift in their design.

Supersonic Cruise Transports

The wing geometry, thin and highly swept, for this type of aircraft is conducive to forming leading-edge vortices. For current supersonic cruise transports vortex lift is used as a simple, lightweight, high-lift system employed at take-off and landing, and because of the highly stable nature of the flow, it is utilized throughout a large part of the flight envelope. Even if the design concept called for suppression of the vortex at several points in the envelope by means of variable geometry devices, many conditions would be expected to exist where vortex flow still predominates. This is due to the differences in attached flow geometry requirements through the speed range and the large variations in lift relative to the design point. The large lift variations are illustrated in figure 3 for a typical slender wing transport where both the level flight and the 2.5 g structural load requirement is shown. It is apparent that both the structural loads and the design of any flow control devices will require the prediction of vortex flow characteristics even if this flow is not basic to the design concept.

Strategic Reconnaissance Aircraft

For this particular supersonic cruise aircraft, vortex lift is used to produce low-speed high lift, aerodynamic center control throughout the Mach number range and for improved directional stability characteristics.

Supersonic Cruise Fighters

Many of the implications regarding vortex flow discussed relative to the supersonic cruise transport would be expected to hold true for supersonic cruise fighters. In addition, vortex lift generated by the slender wing would, in all probability, be utilized for transonic maneuvering just as vortex lift strakes are basic to the design of current lightweight fighters.

It becomes apparent that a knowledge of the load distribution associated with the leading-edge vortex is needed early enough in the design of these supersonic cruise aircraft so that the aircraft will not be penalized with a structural weight penalty and that the most efficient trades between the aerodynamic and structural design can be made.

ANALYTICAL TOOLS CURRENTLY AVAILABLE

Although attached flow theory would not be expected to predict load distribution on wings with leading-edge vortex flow, current computer aided design and analysis methods are limited to attached flow theories. The data in figures 4(a) and (b) are presented to show the magnitude of the errors involved in using these methods. (These data in figure 4 are obtained from references 3 and 4.) The data in figures 4(a) and (b) are for Mach numbers 0.85 and 1.70; the theories shown are the Boeing TEA-230 program and FLEXSTAB. As was expected, the agreement between theory and experiment is poor and points up the magnitude of the problem. Since aeroelastic prediction techniques are also based on attached flow theories, the aeroelastic predictions on wings having leading-edge vortex flow also is poor. The data in figure 5 shows a comparison of aeroelastic prediction and experimental data for a highly swept wing at a Mach number of 0.85 (ref. 3). The triangular symbols are experimental data for a flat wing and the circular symbols are experimental data for a wing with the same geometric characteristics except it has a twist distribution. Using attached flow theory, the flat wing experimental data are corrected to represent data for a wing with the same twist distribution as that of the second wing. As can be seen, the agreement between experiment and theory is quite poor. It should be noted here that the agreement between experiment and theory for supersonic Mach numbers is also poor (ref. 4).

Until fairly recently, attempts to account for the vortex flow effects on wing load distributions have been based on conical flow assumptions in order to make the difficult mathematical modeling problem more tractable. While important contributions have been made by these conical flow studies, the improvements over attached flow theories are insufficient to satisfy the needs of the designer. As a short review, figure 6 shows a comparison of experiment and Smith's conical flow method (ref. 5). At the particular x/c station chosen, the agreement between experiment and Smith's theory is poor and, in fact, since the conical flow method does not satisfy the Kutta condition at the trailing-edge, it should be expected that the agreement between experiment and theory would worsen as the trailing-edge is approached. Linear attached flow lifting surface theory results are presented on figure 6 simply as a reference.

OBJECTIVES OF RESEARCH PROGRAM

The NASA Langley Research Center, realizing the potential benefits of having an analytical method of computing load distributions on wings with vortex flows, embarked on a research program with the objectives discussed below. The Boeing Commercial Airplane Company was awarded a contract to develop a 3-D lifting surface theory for analysis of aerodynamic characteristics and structural loads for configurations having free vortex flows at subsonic and supersonic speeds with arbitrary wing geometry. Having developed the theory, it would be evaluated by numerical and wind tunnel experimental studies. The final goal of this research program is to develop design modules

needed for computer aided design methods for application to supersonic and hypersonic cruise vehicles.

PANEL SCHEME

Figure 7 shows a typical panel arrangement for the wing and its vortex sheets. The wing is paneled with quadraticly varying strength doublet panels and linearly varying source panels. The boundary conditions on the wing are no flow through the wing and the Kutta condition at all edges is satisfied if the wing is thin; however, if the wing has thickness, the vortex sheet separation point can be moved aft of the leading edge to study the effect of moving the separation point.

All the vortex sheets are paneled with quadraticly varying doublet panels. The boundary conditions on the free-vortex sheet are no flow through the vortex sheet and that the vortex sheet be locally force free.

The fed sheet is a simplified model of the physical vortex core region. For the results presented in this paper, the fed sheet is a kinematic extension of the free sheet. The assumption in this model is that the boundary conditions applied to the free sheet are adequate to position the fed sheet. Current work is on going to improve the fed sheet model.

The trailing wake shape is frozen from the trailing edge to infinity. However, with the trailing-edge swept (arrow wing or cropped arrow wing), it has been found that the wing loadings in the vicinity of the trailing edge are highly sensitive to the trailing-edge sweep. As a temporary fix to this problem, the near wake region has an additional boundary condition, $\Delta C_p = 0$.

This seemed to improve the loadings on the wing, but caused serious problems with convergence. It is presently planned for future work to allow the wake to roll up rather than freezing the wake shape at the trailing edge. For further details, the reader is referred to references 6 and 7.

RESULTS AND DISCUSSION

Figure 8 presents results from the Boeing nonconical theory for an aspect ratio 2 delta wing. Since it has been shown in reference 1 that the suction analogy agrees well with experimental data, the suction analogy is used here as a bench mark. The attached flow theory and Smith conical flow theory (ref. 5) are presented as references. The symbols are results for the Boeing nonconical flow theory; it can be seen that the present theory agrees well with the suction analogy. On the plot of ΔC_p versus semispan station, it is observed that the present theory appears to be correctly handling the Kutta condition at the trailing edge, since the pressure levels decreased as the trailing edge is approached.

59

The comparison of theroetical and experimental (ref. 8) load distributions are presented in figure 9. These results are for an aspect ratio 1.46 delta wing at 14 degrees angle of attack at incompressible speeds. It is seen that the present theory agrees very well with experiment. Again, attached flow and conical flow theories are shown as references.

Figure 10 shows results for a thick wing with a swept trailing edge. This is a plot of ΔC_p versus x and the wing is at an angle of attack of 11.9^o. The leading-edge vortex sheet is assumed to be shed from the wing leading edge. Because of the near wake problem discussed earlier, the solution for this problem is not converged; however, the results do look very promising.

CONCLUDING REMARKS

Langley Research Center and the Boeing Commercial Airplane Company are engaged in a joint research program to develop and evaluate an analytical method capable of computing load distributions on swept wings with leading-edge vortices. Boeing, having developed the method, is working to improve the fed sheet model, to improve the computational efficiency, to increase the number of panels that may be used, and to add compressibility and general configuration capability (fuselage and thickness). In the near future, the Boeing Commercial Airplane Company will start developing a supersonic theory for the method, add wake roll up, and carry out an extensive evaluation of the existing method.

Langley Research Center will evaluate the method by numerical and wind-tunnel experiments. The design capability will be exercised to optimize vortex lift characteristics for supersonic cruise and maneuvering aircraft by combining vortex flow with thickness, camber, and twist distributions. Finally, the design capability will be evaluated by wind-tunnel tests.

The preliminary results are very promising and it appears that the approach will eventually provide the capability needed for optimizing and controlling vortex lift and for predicting the wing aerodynamic loads at the critical structural design conditions for slender wing aircraft.

REFERENCES

1. Polhamus, E. C.: A Concept of the Vortex Lift of Sharp-Edge Delta Wings Based on a Leading-Edge-Suction Analogy. NASA TN D-3767, 1966.

2. Lamar, J. E.: Prediction of Vortex Flow Characteristics of Wings at Subsonic and Supersonic Speeds. Journal of Aircraft, vol. 13, no. 7, July 1976, pp. 490-494.

3. Manro, M. E.; Manning, K. J. R.; Hallstaff, T. H.; and Rogers, J. T.: Transonic Pressure Measurements and Comparison of Theory to Experiment for an Arrow-Wing Configuration. NASA CR-2610, 1975.

4. Manro, M. E.: Supersonic Pressure Measurements In Comparison of Theory to Experiment for an Arrow-Wing Configuration. NASA CR-145046, 1976.

5. Smith, J. H. B.: Improved Calculation of Leading-Edge Separation From Slender Delta Wings. RAE Technical Report 66070, 1966.

6. Brune, G. W.; Weber, J. A.; Johnson, F. T.; Lu, P.: and Rubbert, P. E.: A Three-Dimensional Solution of Flows Over Wings with Leading-Edge Vortex Separation. NASA CR-132709, 1975.

7. Johnson, F. T.; Lu P.; Brunne, G. W.; Weber, J. A.; and Rubbert, P. E.: An Improved Method for the Prediction of Completely Three-Dimensional Aerodynamic Load Distributions of Configurations with Leading Edge Vortex Separation. AIAA 9th Fluid and Plasma Dynamics Conference, AIAA Paper No. 76-417, 1976.

8. Marsden, D. J.; et al: Investigation into the Flow-Over Delta Wings at Low Speeds with Leading-Edge Separation. Rep. 114, ARC 20409, College of Aeronautics, Cranfield, Feb. 1958.

SPIRAL VORTEX
SHEET

NONLINEAR
VORTEX LIFT

C_L

ATTACHED
FLOW LIFT

α
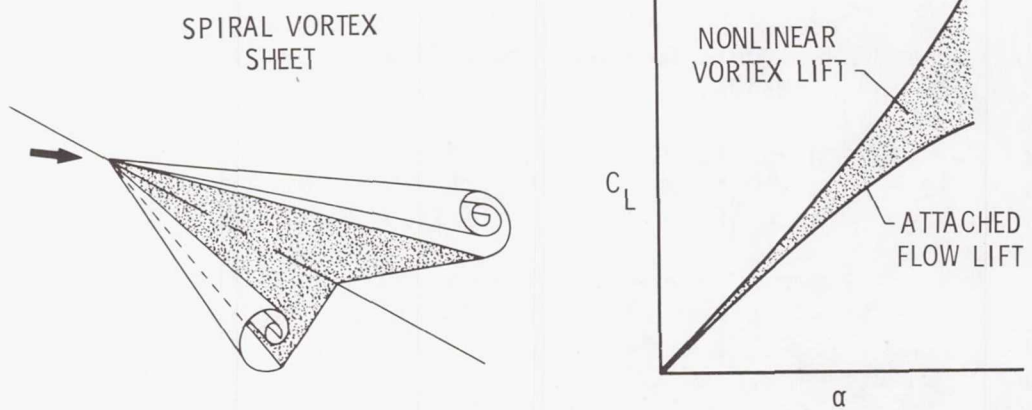
Figure 1.– Leading-edge vortex flow.

CONCORDE

BASIC WING DESIGN
SIMPLE HIGH-LIFT SYSTEM
WING STRUCTURAL LOADS

STRATEGIC RECONNAISSANCE AIRCRAFT

LOW-SPEED HIGH LIFT
A.C. CONTROL
DIRECTIONAL STABILITY

SUPERCRUISE FIGHTERS

LOW-SPEED HIGH LIFT
TRANSONIC MANEUVER LIFT
WING STRUCTURAL LOADS
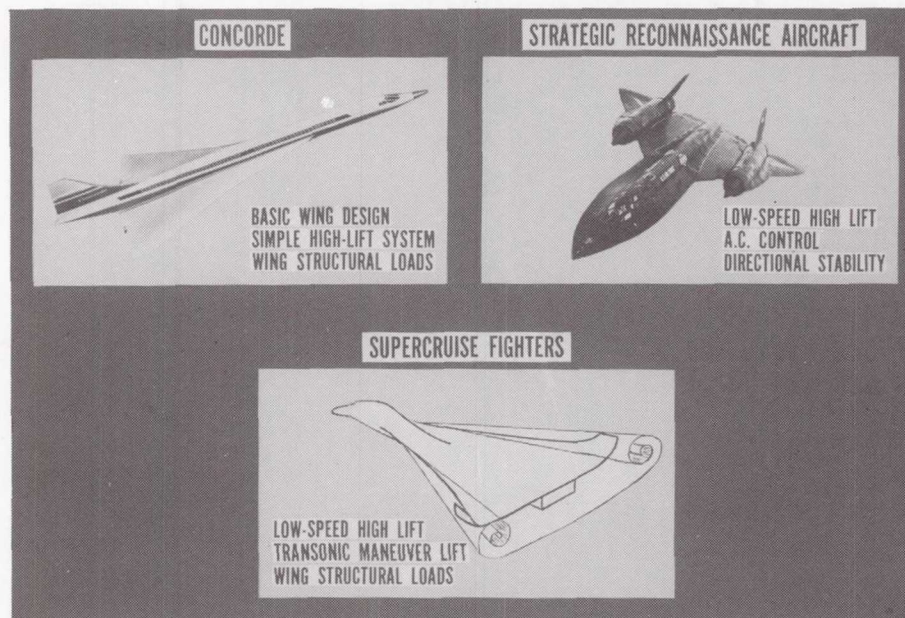
Figure 2.– Examples of aircraft that utilize vortex lift.
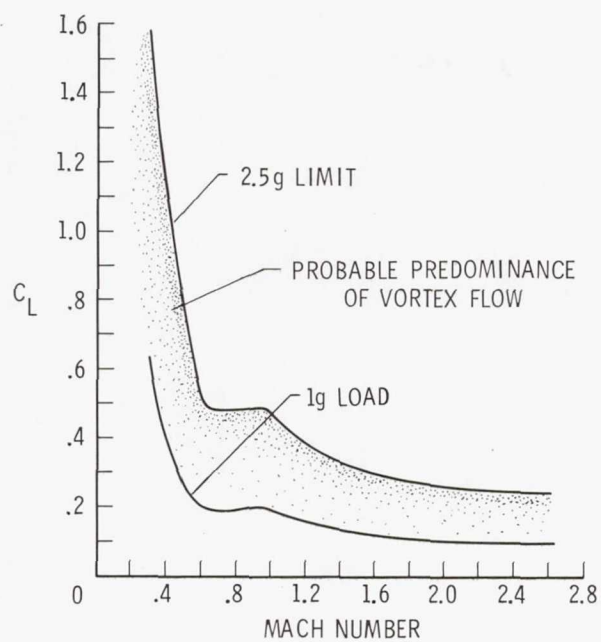
Figure 3.- Operating C_L for typical supersonic cruise aircraft.
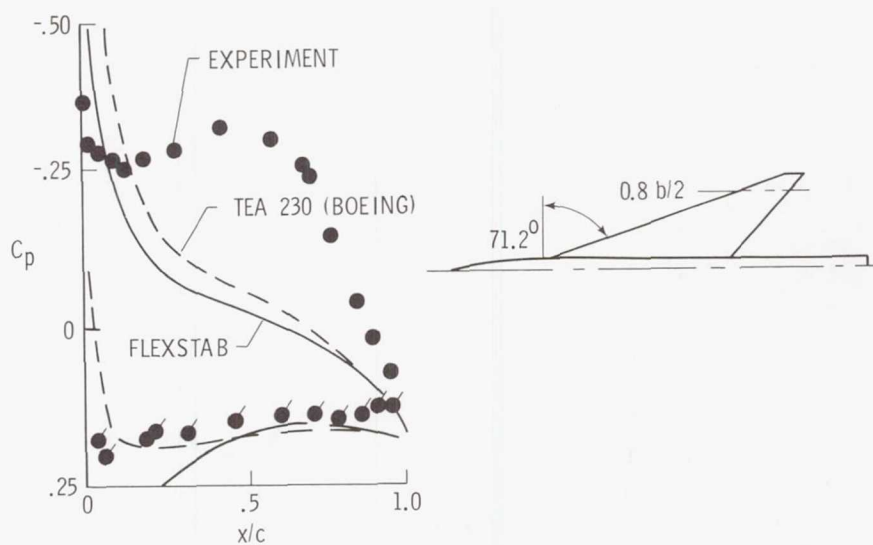
(a) M = 0.85; C_L = 0.2.
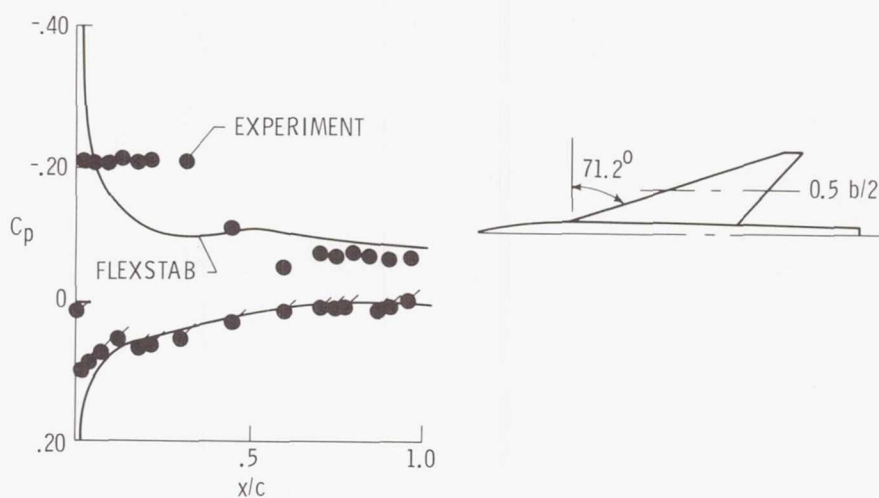
(b) M = 1.70; C_L = 0.15.

Figure 4.- Effect of vortex flow on pressure distribution
for structural design loads.

64
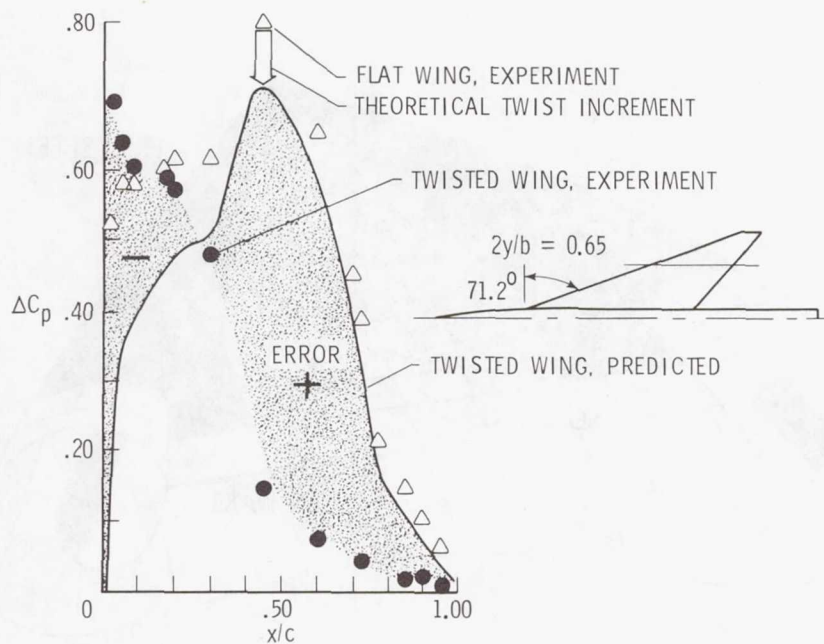
Figure 5.- Comparison of experiment and prediction for twist effects.   M = 0.85; $\alpha = 8^o$; $\varepsilon_{tip} = -4.5^o$.
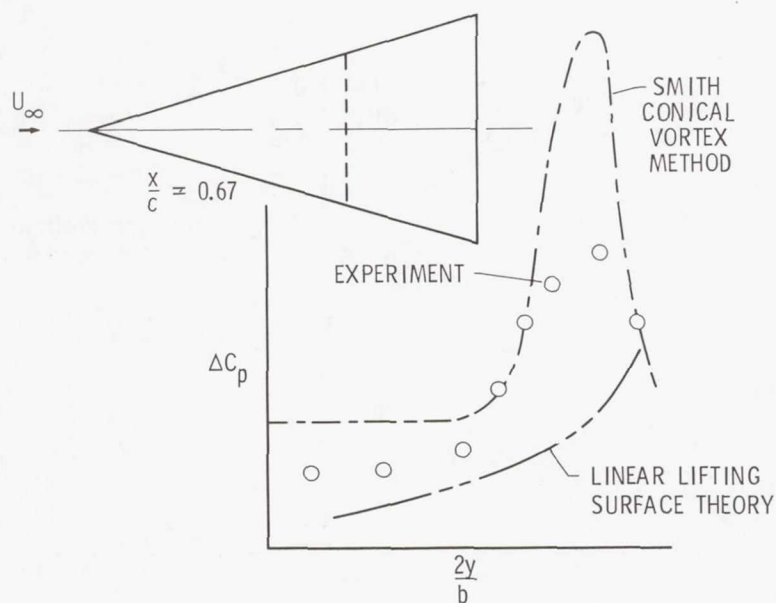
Figure 6.- Load distribution on delta wing given by earlier theories.
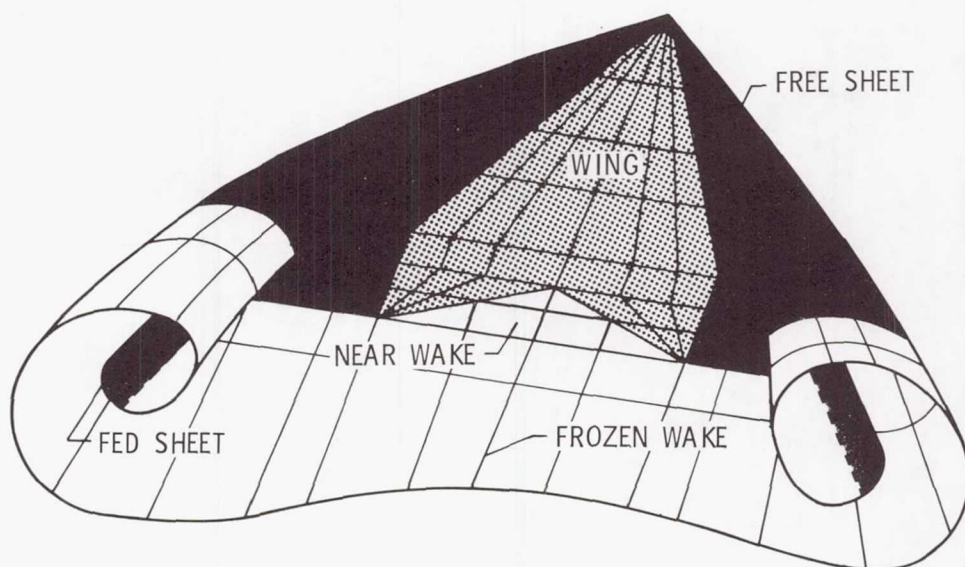
Figure 7.- Typical panel arrangement.
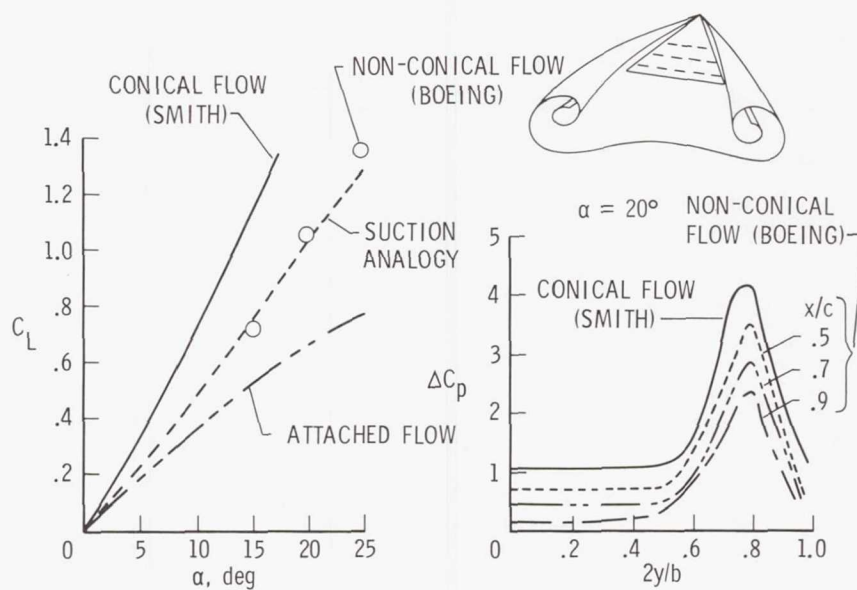
Figure 8.- Application of free vortex sheet method to slender wings. Aspect ratio of 2.
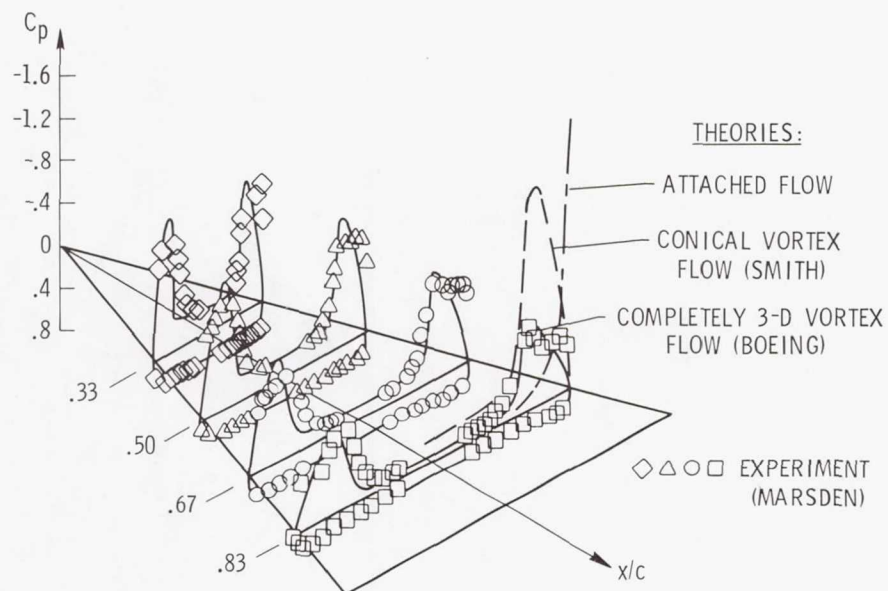
Figure 9.- Comparison of experimental (ref. 8) and
theoretical surface loadings for a delta wing.
Aspect ratio of 1.46; $\alpha = 14^{\circ}$; $M = 0$.
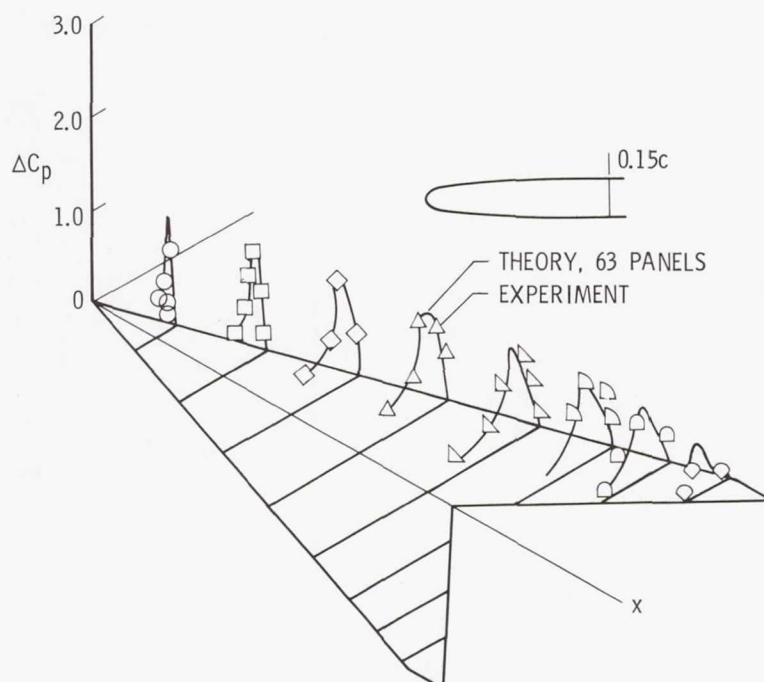
Figure 10.- Comparison of experimental (ref. 3) and
theoretical surface loadings for an arrow wing
with round leading edge. $\alpha = 11.9^{\circ}$; $M = 0.40$.

Page intentionally left blank

THE ROLE OF FINITE-DIFFERENCE METHODS IN DESIGN AND
ANALYSIS FOR SUPERSONIC CRUISE

James C. Townsend
NASA Langley Research Center

SUMMARY

Finite-difference methods for analysis of steady, inviscid supersonic flows are described, and their present state of development is assessed with particular attention to their applicability to vehicles designed for efficient cruise flight. As an illustration, calculations of the supersonic flows over delta wings are compared with experimental pressure distributions. The overall agreement with experiment is very good even well beyond the angles of attack where linearized theory methods are applicable. Current work is described which will allow greater geometric latitude, improve treatment of embedded shock waves, and relax the requirement that the axial velocity must be supersonic. The evolved finite-difference methods are expected to complement the design capability of linearized theory methods by identification of circumstances (the presence of shocks and critical pressures) which will impose constraints on linearized theory solutions. Thus they will allow refinement of designs before models are constructed, eliminating unnecessary wind tunnel tests of unsuitable designs. Further, they will accurately predict loadings required for structural design.

INTRODUCTION

Linearized theory methods are very familiar to those involved in supersonic cruise aircraft design and analysis. Over a period of 20 years or so these methods (such as refs. 1 and 2) have been developed into extremely useful tools for the aerodynamicist; and, as other papers in this conference show, they still have great potential for further development. However, because these methods are linearized, they have inherent limitations: They cannot account for the nonlinear effects of shock waves or of large flow angles, effects which can be important in aircraft design. Thus, there is a need to supplement the linearized theory methods with methods which do not have these limitations.

As part of the effort to meet this need, the study reported herein was initiated to assess the current status of finite-difference methods for computation of steady, inviscid, supersonic flows, to identify their present limitations, and to explore their potential role in aircraft design. This paper reports some of the study results obtained up to this time. Specifically, it will address four topics: (1) Distinguishing features of finite-difference

methods, (2) some past applications of these methods, (3) current developments aimed at overcoming limitations and (4) some applications in the design process to which these methods are ideally suited.

<div align="center">SYMBOLS</div>

b	span
c	local chord
$\bar{c}$	mean geometric chord
c_n	section normal force coefficient, $\dfrac{1}{S} \displaystyle\int_0^1 \dfrac{c}{\bar{c}}\, \Delta C_p \; d\!\left(\dfrac{x}{c}\right)$
C_p	pressure coefficient, $(p - p_\infty)/q_\infty$
ΔC_p	lifting pressure coefficient, $C_{p,\,lower} - C_{p,\,upper}$
M	Mach number
M_A	Mach number of velocity component along x axis
p	local static pressure
p_∞	free-stream static pressure
q_∞	free-stream dynamic pressure
S	wing reference area
x	longitudinal distance from model apex
y	spanwise distance from model centerline
α	angle of attack, deg
Λ	leading-edge sweep angle, deg

GENERAL DESCRIPTION OF FINITE-DIFFERENCE METHODS

The finite-difference approach to solving the flow equations is very different from that of linearized theory. Linearized theory methods solve a simplified set of flow equations in which all nonlinear terms are neglected. The overall solution to a given problem is built up by superposing the independent solutions for the complete flow field about each of the elementary panels composing the aircraft. Finite-difference methods, on the other hand, solve the complete equations for steady, inviscid flow. Since these equations are nonlinear, superposition of elementary solutions does not apply; instead, the overall solution is found by numerical integration over an extensive grid to obtain the complete solution at one point at a time. In supersonic flow, the points influencing the solution at a given point all lie upstream of that point, and this fact is the basis of the marching technique used in supersonic finite-difference methods to achieve greater computational efficiency.

The familiar method of characteristics can be used to illustrate the idea of point-by-point solution of the flow equations, for although it is usually classified separately, it employs basic finite-difference concepts (ref. 3). A two-dimensional characteristics network is shown schematically on the left in figure 1. The network is constructed a point at a time by following the Mach lines (characteristics) from each pair of neighboring points having known flow conditions (on the left in the figure) to their intersections. The flow conditions at the intersection point are determined by applying a local solution to the flow equations, which shows that certain quantities are invariant along the characteristics. This construction process is repeated, working back along the model using the new points for initial conditions. The intersection of two characteristics of the same family indicates that a shock wave is beginning to form; it must be inserted into the mesh with its strength determined by the Rankine-Hugoniot relation.

Because the characteristics network is determined as part of the solution, the user has no direct control over the size or direction of the multitude of individual steps that make up a complete flow field solution. For complex three-dimensional flows this lack of control can lead to a chaotic situation which makes the method of characteristics ill-suited to computer implementation. Thus, although there is some continuing interest in methods using characteristics (ref. 4), most research has turned to the development of the methods conventionally classified as finite-difference methods.

The two main classes of finite-difference methods are shown at the center and right in figure 1. These methods, like the method of characteristics, use a step-by-step computation of flow conditions starting from conditions known in an initial data plane. However, for the finite-difference methods each step is of uniform size so that each new set of points lies in a plane parallel to the initial plane. In addition, the computation is made by direct integration of the flow equations in such a way that each new point corresponds to a single initial point. The following paragraphs discuss the distinguishing features of the finite-difference methods without going into the mathematical detail. For a general treatment of the mathematics involved, see reference 5.

71

The shock-capturing technique, illustrated in the center of figure 1, uses the flow equations in their conservation form (refs. 6 to 8). The equations in this form apply across shock waves, so the integration can proceed right on through all shock waves which occur in the flow. These captured shocks have large gradients, which can introduce numerical oscillations into the solution, and it is customary to add an artifical viscosity term in the equations in order to dampen these oscillations. (See ref. 9, for example.) Since the equations are written in terms of the conserved quantities (e.g. momenta), an additional calculation is needed in order to recover the physical flow variables (e.g. pressure, velocity).

In the earliest applications of this method, a complete rectangular grid was entirely preset before the computation was begun. In more recent applications, the grid has usually been fitted between the body and the bow shock, with the latter computed as a discrete shock rather than being captured in the mesh. This technique effects a savings by avoiding the repetitive calculations of free-stream conditions at mesh points outside the bow shock. Since captured shocks are distributed over a number of mesh points, a fine grid is required for satisfactory resolution. Grid enrichment, in which extra grid points are introduced in the vicinity of shock waves, is a way of providing the fine mesh only where required and of retaining a coarser mesh where lower resolution is sufficient. This adaptive mesh is illustrated in the figure.

The shock-fitting finite-difference method forms the other major class (ref. 10). It is illustrated schematically on the right side of figure 1. Its principal difference from the shock-capturing class is in the treatment of shock waves. In the shock-fitting method each shock is treated discretely, with the flow through it computed to satisfy the Rankine-Hugoniot relation explicitly. In the implementation shown in the figure, the mesh is adjusted so that the shock lies along mesh lines. Program logic is required to readjust the mesh when appropriate. Since the flow equations are not integrated through the shock waves, the equations can be in terms of the physical variables and no artificial viscosity is needed. Also, a coarser mesh can be used with good results.

To achieve good resolution with a relatively coarse mesh, the mesh points need to be concentrated in high gradient regions but can be more spread out in regions of nearly uniform flow. One way to achieve this favorable distribution of mesh points is through the use of conformal mapping techniques. If, for example, a body-wing cross section is mapped to a near circle and the circle divided evenly into mesh points, the corresponding points in the physical plane tend to cluster toward the wing tip, a high gradient region. Thus conformal mapping can provide a measure of automatic mesh control.

PAST AND PRESENT APPLICATIONS

Figure 2 shows a few representative configurations of the many for which finite-difference calculations of flow fields have been made. The first is a real tour-de-force application which attempted to calculate the entire flow

field around a complete B-1 bomber under an Air Force contract (reference 11). The calculation, which used shock-capturing even for the bow shock, was made in an entirely preset square grid, graduated in spacing from 0.0007 of the (full scale) length at the nose to six times that in the far field. While the method used for this long-term demonstration project did not incorporate recently developed features which improve computational efficiency and provide ease of use, its results demonstrate the potential of more developed finite-difference methods.

The second part of the figure shows an early U.S. shuttle orbiter configuration for which the flow field was computed by a Russian shock-capturing method (ref. 12). In the reference, good agreement is shown with the results from the method of characteristics and from a shock-capturing finite-difference method given by Rakich and Kutler (ref. 13).

The last part of figure 2 shows results on a fighter-type configuration computed by a shock-fitting finite-difference method (ref. 10). Like some of the shock-capturing methods, this method was originally developed with emphasis on flow-field calculations about shuttle orbiter configurations. Consequently, while it has some advanced capabilities, such as real gas effect calculations, it has only limited capability to perform calculations about the complex geometries typical of supersonic cruise aircraft. Its application to a fighter forward fuselage section (as shown in the figure) is part of the subsequent effort to extend the method to more general configurations.

As part of the study of the possibilities of finite-difference methods for aircraft design, this same shock-fitting finite-difference method has been applied to one of a series of delta wings for which an extensive set of experimental data and results computed by other theories are available (refs. 14 and 15). The following three figures describe this delta wing and a few of the results obtained.

Figure 3 shows the $\Lambda = 76°$ uncambered, clipped-delta wing studied. It had a 4-percent-thick circular-arc airfoil section with sharp leading and and trailing edges. A faired body of circular cross section was added to provide a sting attachment for the experimental model. As shown in the figure, two modifications were made in the numerical model in order to meet geometric limitations imposed by the method. First, the forward 1 1/2-percent of the total length was replaced by a 24° half-angle cone faired to the original body and wing. This modification was necessary in order to obtain cone-flow starting solutions at angles of attack near 20°. The second, and more significant, modification was the replacement of the outer half of the wing by a thicker section providing an elliptical cross section. This was necessary since at the Mach numbers of interest, the flow normal to a leading edge swept 76° is subsonic; in this case, the computational method used requires the leading edge to be blunt.

It should be noted that several nose shape variations were tried unsuccessfully before this one was found for which complete runs could be made routinely. Each complete run at a single Mach number and angle of attack used less than 30 minutes of control processor time on a CDC6600 computer.

Figure 4 shows comparisons of computed centerline pressure coefficients with wind-tunnel measurements at Mach 3.5 and 4.6 and angles of attack typical of cruise conditions. The shock-fitting finite-difference method results (solid line) agree well with the experimental pressure distributions and span loadings. Also shown in the figure are curves (dashed lines) from a linearized-theory calculation (Woodward method, refs. 15 and 2). These curves also agree fairly well with the experimental results; this fair agreement at Mach numbers above the usual range of validity for linearized theory can be attributed to the extreme slenderness of the configuration.

Figure 5 shows a more complete comparison at a Mach number of 3.5 at an angle of attack near 20°. At this high angle, the agreement between the shock-fitting finite-difference and experimental results is still good. (The poor agreement at the wing tip is in a region dominated by the added leading-edge bluntness.) However, the linearized theory does not give useful estimates at this condition. From these two figures, then, it is seen that, although both the finite-difference method and the linearized theory can give good results at cruise conditions, only the finite-difference method can give usable loading estimates at high angles of attack, which are likely to produce critical design conditions.

CURRENT DEVELOPMENTAL AREAS

Since finite-difference methods show promise of being able to compute loadings at critical design conditions, work is progressing on improving their efficiency, range of applicability, and ease of use. The next three figures show three areas of current work on the shock-fitting finite-difference method used to obtain the preceding results.

Figure 6 indicates the proposed generalized conformal mapping currently being developed by Moretti (ref. 16). As mentioned previously, mapping is used to transform each cross section of the aircraft into a near circle about which a regular rectangular grid can be generated to form the computational mesh. The present mapping was set up to work well for shuttle orbiter cross sections but will not work for some typical cruise-aircraft cross sections. In partic- ular the mapping relations require that the cross section be single-valued in polar coordinates, a requirement which makes the highly cambered midsection and the detached aft section unmappable for configurations like that shown in the figure. The new mapping, by careful placement of singularities, will open up a cross section such as that shown at the bottom of the figure into the desired near circle. The open section between the wing and the body will form parts of the boundary (BC and EF), for which a special flow-through boundary condition is required in order to provide for the correct flow in that region.

Figure 7 illustrates a new method for handling embedded shock waves in the shock-fitting finite-difference method. In the present method (shown on the left) the mesh is adjusted so that the shock lies along mesh lines. The mesh points on the shock are actually double points, with the quantities on

each side of the shock calculated to satisfy the Rankine-Hugoniot relation explicitly. As the shock moves through the flow, the mesh must be readjusted as shown in the figure. Unfortunately, the mesh distortions and the partitioning of the flow field can sometimes lead to difficulties, particularly in three-dimensional flows. In the new method, shown on the right and called floating shock fitting, the shock is not required to be a boundary of the flow. It is still treated as a discontinuity satisfying the Rankine-Hugoniot relation, but it can move freely, or float, through the undisturbed mesh. In order to provide this capability, the relations required for evaluating the derivatives are modified for mesh points near the shock.

The floating shock-fitting finite-difference method has been developed for the two-dimensional case (ref. 17) and has shown good results for complex flows involving multiple shock interactions. Its extension to three-dimensional flows is currently underway.

Figure 8 shows a third area of improvement, development of a method for continuing the calculation through regions in which the Mach number of the flow component in the marching direction is subsonic even though the total velocity remains supersonic (ref. 18). This condition arises fairly frequently in the vicinity of canopies and blunt-leading-edge wings, which turn the flow strongly away from the marching direction. In the general flow calculation method illustrated at the left of the figure, flow conditions at point B' are calculated using the conditions at points A, B, and C, known for the previous step. For numerical stability, the step must be small enough so that the characteristics through B' (shown as dashed lines) pass between A and C. This condition, which is essentially the Courant-Friedricks-Levy (CFL) condition for an explicit marching scheme, can always be met if the axial Mach number M_A is greater than 1. However, if the flow is at a high angle, the axial Mach number may become subsonic. As shown in the middle of the figure, a characteristic is then swept forward relative to the marching direction, and it is impossible to meet the CFL criterion, so the marching stops. The method proposed for continuing the computation in this case makes use of the fact that the flow deflection to a high angle is caused by a boundary, as shown on the right in the figure. Thus, although the conditions at B' cannot be computed directly (because of the forward-inclined characteristic), the condition at A' can be computed from the known conditions at A and B plus the boundary conditions at A'. However, even with the conditions at A' known, the CFL criterion cannot be met for B' since the characteristic falls outside of A'ABC. The conditions at A" are also needed, but getting them directly would require knowing the conditions at B' first. Fortunately, the conditions at A" and B' can both be obtained through a simultaneous solution of the relations for both points and the boundary conditions at A". Thus, the CFL criterion can be met for both B' and A" and the computation can continue. This procedure can be extended to include in the simultaneous solution as many points along the oblique front as fall within the region of subsonic axial Mach number. In reference 18, Marconi and Moretti have successfully applied this method in conjunction with the shock-fitting finite-difference method to the three-dimensional flow over an aircraft with a region of subsonic axial Mach number embedded at the front of the canopy.

When these three improvements have been incorporated into the shock-fitting finite-difference method, it will be able to compute the steady inviscid supersonic flow about a very general class of aircraft configurations. Shock-capturing finite-difference methods are undergoing similar improvements. For example, this method also has been extended to the case of supersonic flow with subsonic axial Mach number (ref. 19). Thus, finite-difference methods are new tools which are now becoming available to aid aircraft designers in their work.

APPLICATION TO DESIGN

In order to use this new tool effectively and efficiently, it is necessary to understand its capabilities relative to those of linearized theory, the basis of so many of the present methods for aerodynamic analysis and design. Figure 9 indicates how the capabilities of the two kinds of methods complement one another. The most important asset of the linearized theory is its capability for direct design; for example, linearized theory methods are able to determine directly the camber surface required to produce a given aerodynamic pressure distribution on a wing. This capability is the result of reducing the problem of finding the flow over an aircraft to one of solving a large number of simultaneous linear algebraic equations. Since digital computers are able to solve such systems of equations quickly and efficiently, linearized theory methods are quick enough and inexpensive enough to allow the evaluation of a large number of design variations. With further increases in computational speed, linearized methods will make true interactive man-in-the-loop aerodynamic design a practical reality.

However, linearized theory has the inherent limitation of not being able to predict or analyze nonlinear effects. Thus finite-difference methods also have a role in the design process. Their most important asset is their accurate representation of the flow, through solution of the complete equations for inviscid, steady flow. The practical limit to this accuracy for inviscid flows comes only through the limitation of resources committed to it. That is, the limit is related to the number of mesh points used, and more points require more computer storage and more time.

The accurate analysis afforded by finite-difference methods makes them ideal for use in design critique. After a good design candidate has been found through use of the linearized theory methods, analysis of a finite-difference method will allow the detection of such potential problem areas as shock waves occurring in unfavorable locations or pressures reaching critical values. With this kind of information in hand the aerodynamicist can refine the design to alleviate the problems. For example, the configuration may have to be changed to avoid shock impingement on an inlet. As suggested by the figure, the avoidance of a critical condition revealed by the finite-difference calculation may impose new design restraints. Then the design procedure by linearized theory can be reinstituted using the new restraints to provide a refined candidate design. Use of this linearized-theory design and finite-difference critique iteration procedure will provide an aerodynamically efficient and practical design while avoiding the costly and time-consuming building and testing of

wind-tunnel models in the early design stages. Thus many more candidate con-
figurations may be considered in choosing the best overall design for confir-
mation by wind-tunnel tests. Refinement through the detail design of fillets,
inlets, etc. can then take place with each change checked using the accurate
analysis afforded by the finite-difference method (fig. 10). The result of
designing by this process will be a better aerodynamic design in less time and
at lower cost.

But this may not be the most important role of finite-difference methods
in the design process. Because of their accuracy, they are ideally suited for
rapidly obtaining the detailed loadings which now can be acquired only by an
extremely lengthy experimental process. This is particularly the case at off-
cruise-point conditions such as high angles of attack, which cannot be properly
treated by linearized theory, but which often form the critical loading condi-
tions for the structural design cycle.

CONCLUDING REMARKS

It has been shown that finite-difference methods for computing steady,
inviscid, supersonic flows are becoming developed to the point where they
form useful additional tools for the aircraft designer. For example, with
the incorporation of new features now under development, the shock-fitting
finite-difference method will be able to accurately analyze complex flows
over general aircraft configurations, including critical off-cruise-point
conditions. The detailed, accurate analysis afforded by finite-difference
methods suits them particularly well for a role complementary to the rapid
design capabilities of linearized theory methods. Finite-difference methods
are also well suited for determining critical loads for structural design
purposes.

REFERENCES

1. Middleton, W. D., Jr.; and Lundry J.: Aerodynamic Design and Analysis
   System for Supersonic Aircraft. NASA CR-2520, 1975.

2. Woodward, F. A.: An Improved Method for the Aerodynamic Analysis of
   Wind-Body-Tail Configurations in Subsonic and Supersonic Flow.
   NASA CR-2228, 1973.

3. Liepman, H. W.; and Roshko, A.: Elements of Gasdynamics. John Wiley
   and Sons, Inc., 1957.

4. Cameraro, R.: A Reference-Plane Method for the Solution of Three-Dimensional
   Supersonic Flows. Aero. Quart., Vol. 27, February 1976, pp. 75-86.

5. MacCormack, R. W.; and Warming, R. K.: Survey of Computational Methods for Three-Dimensional Supersonic Inviscid Flows With Shocks. Paper No. 5 of AGARD-LS-64, 1973.

6. Kutler, P.; Lomax, H.; and Warming, R. F.: Computation of Space Shuttle Flow Fields Using Noncentered Finite-Difference Schemes. AIAA Paper 72-193, 1972.

7. Walkden, F.; and Caine, P.: A Shock-Capturing Method for Calculating Supersonic Flow Fields. C.P. No. 1290, British A.R.C., 1972.

8. Sanders, B. R.; and Dwyer, H. A.: Analysis of Three-Dimensional Inviscid Flow Fields by Application of Shock Capturing Techniques. SAND 74-8666, Sandia Labs., 1974.

9. Thommen, H. U.; and D'Attorre, L.: Calculation of Steady, Three-Dimensional Supersonic Flow-Field by a Finite Difference Method. GDC-Err-AN718, General Dynamics Astronautics, 1965.

10. Marconi, Frank; Salas, Manuel; and Yaeger, Larry: Development of a Computer Code for Calculating the Steady, Super/Hypersonic Inviscid Flow Around Real Configurations. Volume I - Computational Technique. NASA CR-2675, 1976.

11. D'Attore, L.; Bilyk, M. A.; and Sergeant, R. J.: Three Dimensional Supersonic Flow Field Analysis of the B-1 Airplane by a Finite Difference Technique and Comparison With Experimental Data. AIAA Paper No. 74-189, 1974.

12. Ivanov, M. Ya.; and Nikitina, T. W.: Calculation of Three-Dimensional Supersonic Flows Past Bodies of Complex Configuration. NASA TT F-16192, 1975.

13. Rakich, J. V.; and Kutler, P.: Comparison of Characteristics and Shock-Capturing Methods With Application to the Space Shuttle Vehicle. AIAA Paper No. 72-191, 1972.

14. Sorrells, Russell B., III; and Landrum, Emma Jean: Theoretical and Experimental Study of Twisted and Cambered Delta Wings Designed for a Mach Number of 3.5. NASA TN D-8247, 1976.

15. Landrum, Emma Jean; and Townsend, James C.: Assessment of Existing Analytical Methods for Prediction of High Angle-of-Attack Loads on Delta Wings at Supersonic Speeds. AGARD Symposium on Prediction of Aerodynamic Loading, Paper No. 15, September 1976.

16. Moretti, Gino: Calculation of the Three-Dimensional, Supersonic Inviscid, Steady Flow Past an Arrow-Winged Airframe. NASA CR-147230.

17. Salas, Manuel D.: Shock Fitting Method for Complicated Two-Dimensional Supersonic Flows. AIAA Jour., Vol. 14, No. 5, 1976, pp. 583-588.

18. Marconi, Frank; and Moretti, Gino: Three-Dimensional Supersonic Flows With Subsonic Axial Mach Numbers. AIAA Paper No. 76-383, 1976.

19. Rizzi, A. W.; Klavins, A.; and MacCormick, R. W.: A Generalized Hyperbolic Marching Technique for Three-Dimensional Supersonic Flow With Shocks. Proceedings of 4th International Conference on Numerical Methods in Fluid Dynamics, June 1974, pp. 341-346.
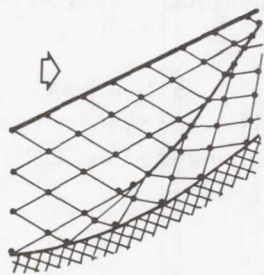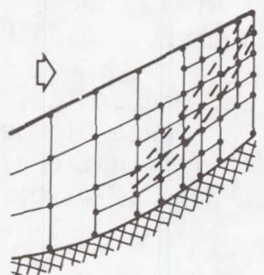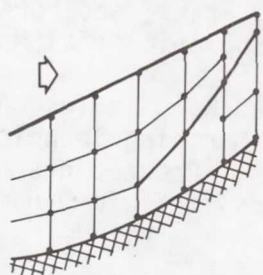
METHOD OF
CHARACTERISTICS

SHOCK-CAPTURING
FINITE DIFFERENCE

SHOCK-FITTING
FINITE DIFFERENCE

- EQUATIONS IN TERMS
  OF INVARIANTS

- EQUATIONS IN
  CONSERVATION FORM

- EQUATIONS IN
  PHYSICAL VARIABLES

- SHOCK INSERTED IF
  CHARACTERISTICS MEET

- SHOCK DISTRIBUTED
  OVER MESH POINTS

- SHOCK DISCRETELY
  FITTED IN MESH

- MESH CONTROLLED
  BY SOLUTION

- MESH PRESET
  OR ADAPTIVE

- MESH CONTROL BY
  CONFORMAL MAPPING

Figure 1.- Comparison of features of method of characteristics
and steady, inviscid, finite-difference methods.

- SHOCK-CAPTURING

  B-1 BOMBER

  (D'ATTORE, BILYK,
  AND SERGEANT)

C_p $M = 2.2$ $\alpha = 3°$

  SHUTTLE ORBITER

  (IVANOV AND NIKITINA)

C_p $M = 5.0$ $\alpha = 5°$

UPPER CENTERLINE
PRESSURE DISTRIBUTIONS

- SHOCK-FITTING

  GENERAL FIGHTER

  (MARCONI, SALAS,
  AND YAEGER)

○ EXPERIMENT
— FINITE DIFFERENCE

C_p $M = 2.2$ $\alpha = 5°$
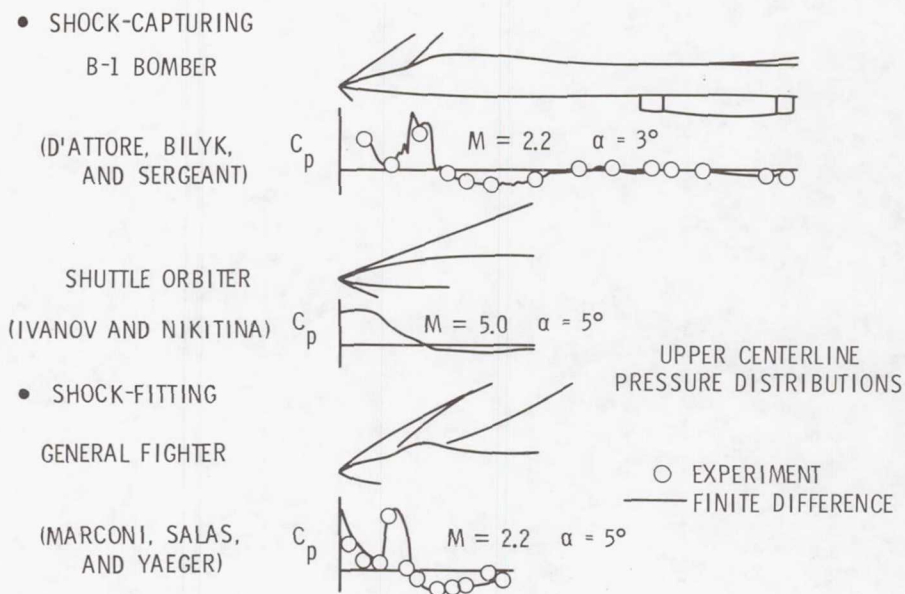
Figure 2.- Examples of past applications of finite-difference
methods.
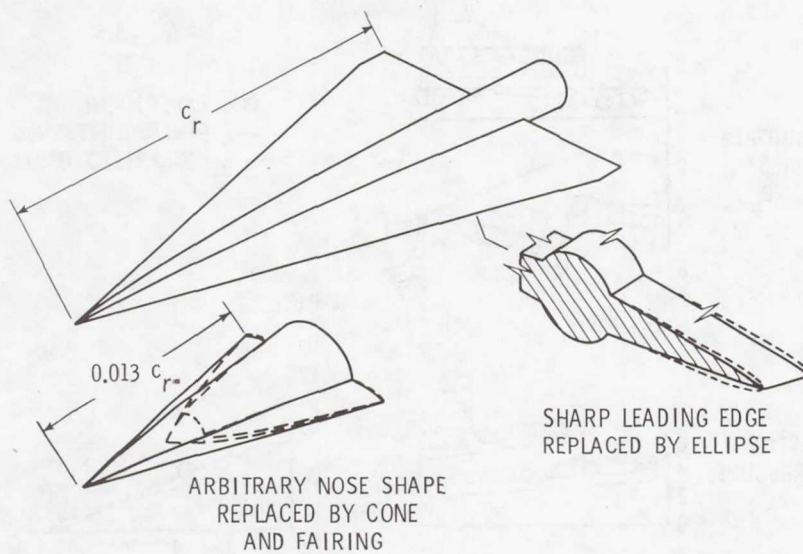
Figure 3.- Delta wing used for experimental comparisons
and modifications made for numerical model. Leading-
edge sweep angle, $\Lambda = 76^o$.
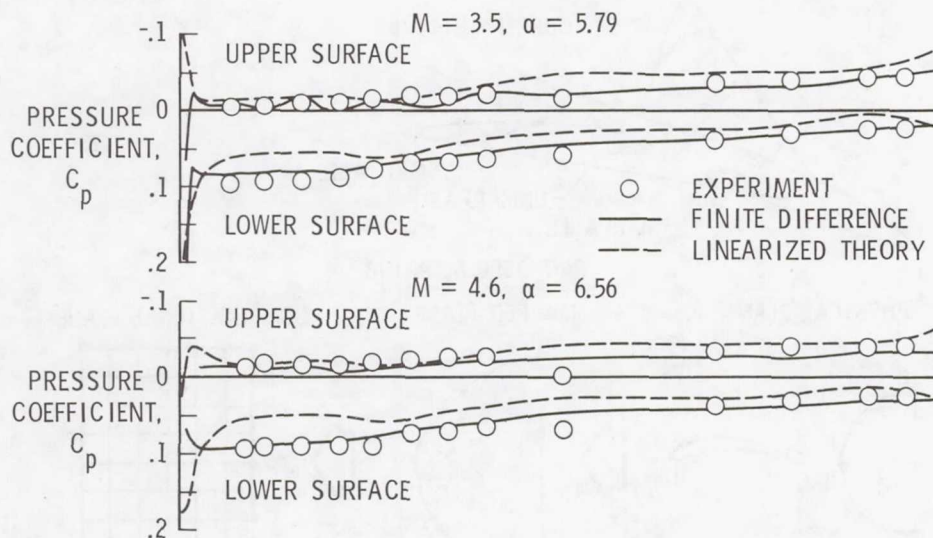
Figure 4.- Centerline pressure distributions for 76° delta
wing at low angles of attack. Experiment from reference 14;
linearized theory by Woodward method (ref. 2).
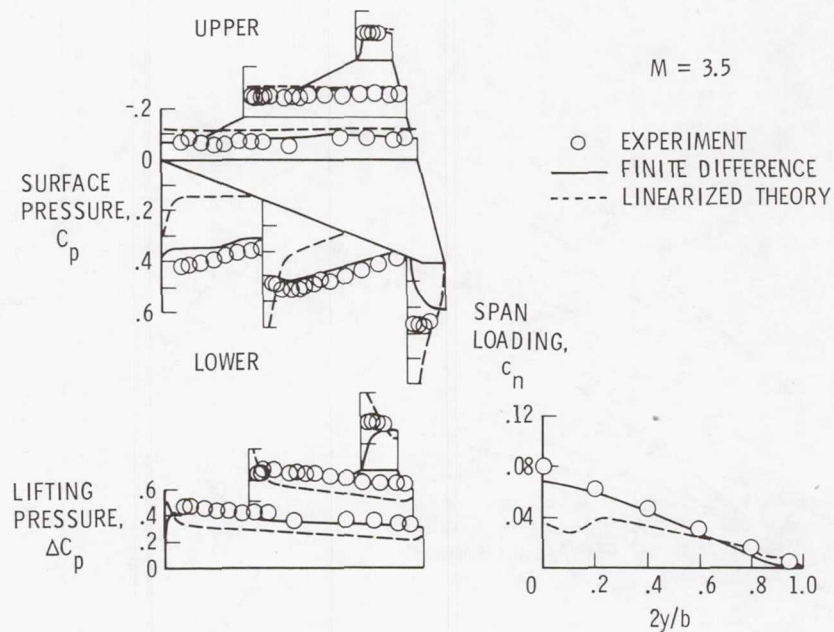
Figure 5.- Pressure distribution and span loading for 76° delta wing at 19.7° angle of attack (ref. 15).
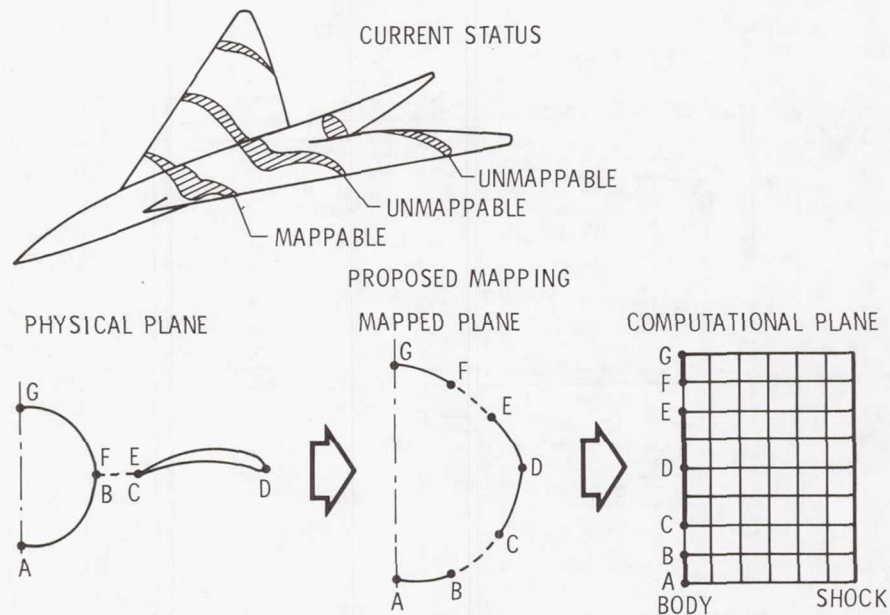
Figure 6.- Current work on generalizing conformal mapping technique used with shock-fitting finite-difference method by Moretti (ref. 16).

82

PRESENT METHOD:

MESH LINES FITTED
TO EMBEDDED SHOCK

PROPOSED METHOD:

SHOCK FLOATS WITHIN
UNDISTURBED MESH
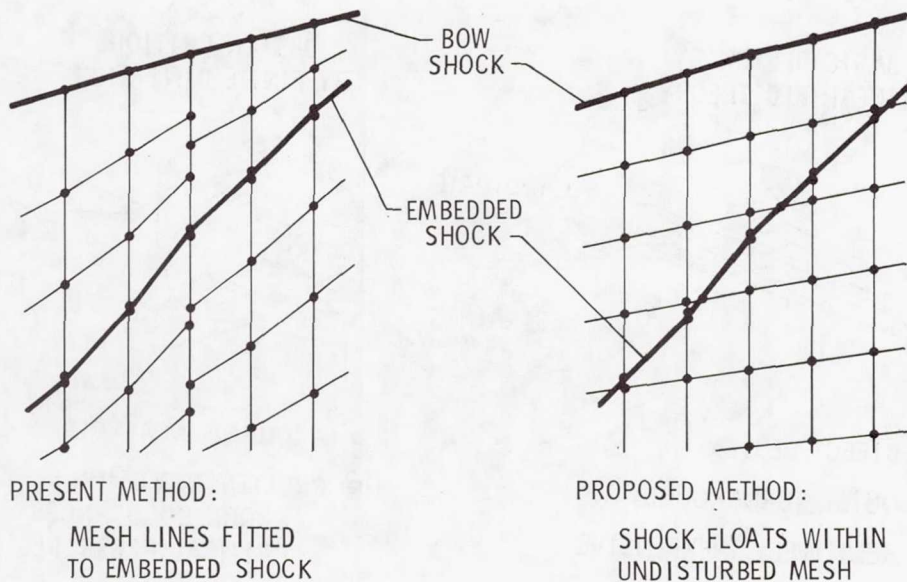
Figure 7.- Current work on improving treatment of embedded
shock waves in shock-fitting finite-difference method by
Salas (ref. 17).

CURRENT METHOD

STEP SIZE SET BY
CFL STABILITY
CRITERION

CFL CRITERION
CANNOT BE MET
FOR ANY STEP SIZE

PROPOSED METHOD

CFL CRITERION MET THROUGH
USE OF BOUNDARY CONDITIONS
AND SIMULTANEOUS SOLUTION
(FOR B' AND A'')
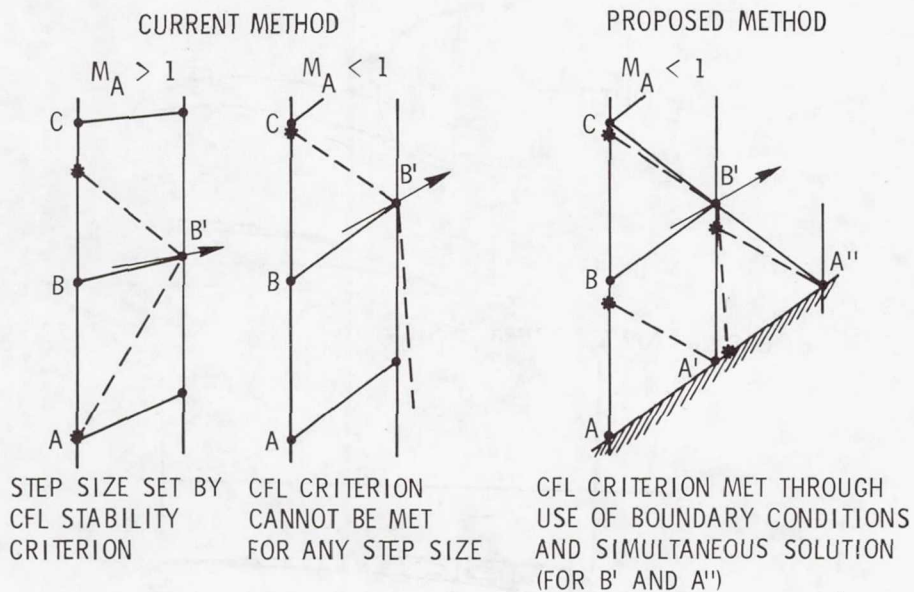
Figure 8.- Current work on extending shock-fitting finite-
difference method to include regions of supersonic flow
with subsonic axial Mach number by Marconi and Moretti
(ref. 18).

BASIC DESIGN BY
LINEARIZED THEORY

DESIGN CRITIQUE
BY FINITE DIFFERENCE

CANDIDATE

RESTRAINTS

- DIRECT DESIGN
- QUICK TURNAROUND
- RELATIVELY INEXPENSIVE

- ACCURATE ANALYSIS
- PROBLEM DETECTION
  SHOCK OCCURANCES
  CRITICAL PRESSURES

Figure 9.- Application of finite-difference methods in design
process.

- ITERATIVE DESIGN

  - FILLETS

  - INLETS

- LOADINGS FOR STRUCTURAL DESIGN
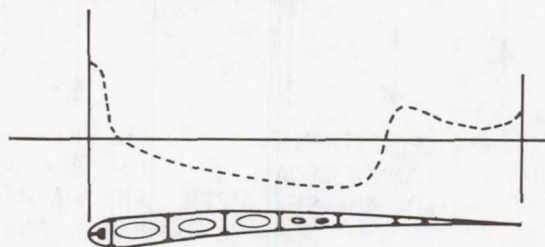
Figure 10.- Additional design application of finite-difference
methods made practical by their detailed accuracy.

THEORETICAL AND EXPERIMENTAL PRESSURE DISTRIBUTIONS

FOR A 71.2° SWEPT ARROW-WING CONFIGURATION AT

SUBSONIC, TRANSONIC, AND SUPERSONIC SPEEDS

Percy J. Bobbitt
NASA Langley Research Center

Marjorie E. Manro
Boeing Commercial Airplane Company

SUMMARY

A wind-tunnel test of an arrow-wing body configuration consisting of flat and twisted wings, as well as a variety of leading- and trailing-edge control-surface deflections, has been conducted at Mach numbers from 0.40 to 2.50 to provide an experimental data base for comparison with theoretical methods. Theory-to-experiment comparisons of detailed pressure distributions have been made using current state-of-the-art and newly developed attached- and separated-flow methods. The purpose of these comparisons was to delineate conditions under which these theories can provide accurate basic and incremental aeroelastic loads predictions. It was determined that current state-of-the-art linear and nonlinear attached-flow methods were adequate only at small-angle-of-attack cruise conditions. Of the several "separated-vortex" methods evaluated only the one utilizing a combination of linear source and quadratically varying doublet panels showed promise of yielding accurate loads distributions at moderate to large angles of attack. Force and moment predictions using the Polhamus suction analogy agreed well with experiments for both flat and twisted wings.
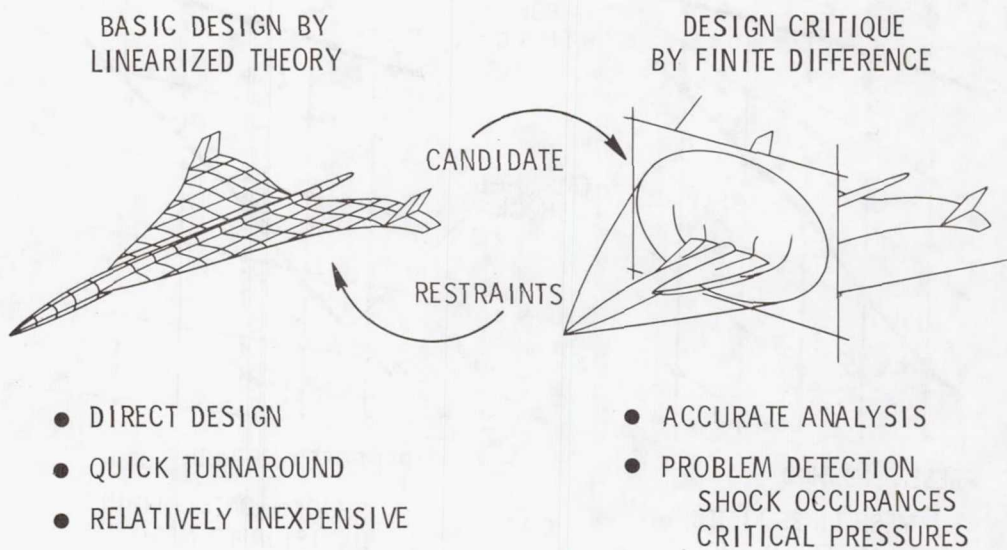
INTRODUCTION

The determination of critical design loads for various structural components of aircraft employing highly swept wings requires an examination of the loads at flight conditions involving moderate to high angles of attack. Moderate and high angles of attack in turn give rise to a flow-separation vortex at the wing leading edge. When one has to rely on theory for these loads, as is usually the case in parametric studies or for incremental aeroelastic effects, the lack of a validated analytical technique presents quite a dilemma. Inaccuracies in the predicted pressure distribution and related loads may result in an erroneous evaluation of aeroelastic effects, leading to understrength or overweight designs, performance panalties and reduced fatigue life. Aircraft stability and control estimates and control-surface-effectiveness calculations will also suffer from inaccurate loads information.

85

The problem of predicting aerodynamic pressure distributions on highly swept wings at moderate to high angles of attack is by no means a new one. It has received the attention of a number of theoreticians both here and abroad over the past 25 years (e.g., refs. 1 to 5) but, unfortunately, their attempts have met with only marginal success. Some relief may be forthcoming, however, in the form of methods now being developed by Boeing under contract to the Langley Research Center (ref. 6) and at Virginia Polytechnic Institute and State University (ref. 7).

At low-incidence cruise conditions the situation is much better. Attached-flow linear theories of both the lifting surface and discrete singularity type have been found to be generally adequate for aerodynamic calculations for highly swept wings. Uncertainty, however, as to the angle of attack (for a given wing geometry) at which one should cease to rely on these methods has limited their utility. In addition, the scarcity of detailed pressure data on a given configuration at both subsonic and supersonic speeds has prevented a comprehensive assessment of the unified subsonic-supersonic panel methods.

Of course, analytical methods are not the only predictive weapons aerodynamicists have at their disposal. Wind-tunnel pressure tests on a specific wing shape may be extrapolated by means of an aeroelastic solution to obtain the load distributions for other elastically deformed shapes of that wing. Methods for doing this for subsonic-transport-type wings are well developed and substantiated by flight tests. However, for highly swept wings and/or transonic flight conditions where various nonlinear phenomena become important, no satisfactory methods are available. Unless we develop reliable empirical techniques or analytical methods, such as discussed earlier, for these types of wings, the choice between extensive tunnel tests simulating a variety of flight conditions and a nonoptimum design will remain.

The primary purpose of this paper is to report on the results of a study carried out to define the ability of state-of-the-art as well as newly developed techniques to predict detailed pressures over configurations with highly swept wings. A second purpose is to describe the scope of the experimental program carried out on an arrow-wing configuration to make the present theory/experiment comparisons more comprehensive. The variety of configurational effects examined and the wide Mach number range of the tests conducted make the data obtained especially valuable for determining the efficacy of predictive techniques, present and future. Two wings were tested in the experimental program; each had the same planform and airfoil section but one was flat and the other twisted. Both were equipped with trailing-edge controls while the flat wing had leading-edge controls as well. In addition, the "basic" rounded leading edge on the flat wing could be replaced with a sharp one.

Theories evaluated in the present paper with the aid of the "arrow-wing" pressure and force data obtained in the experimental program include linear and nonlinear attached-flow methods and several separated-flow techniques. Results of calculations made using the Polhamus suction analogy (ref. 8) will also be shown even though this technique does not provide detailed pressure distributions. They are included because the method is particularly effective in predicting forces and moments and because the longitudinal load distributions

determined by this method have been used in conjunction with the Smith separated-flow method (ref. 3) in an effort to provide a better overall detailed pressure/force predictive capability.

Attempts have been made to predict not only the basic pressure distributions on a representative sample of configurations and free-stream conditions but also the incremental pressure changes due to twist. The latter is of interest since this calculation is similar to that often made to correct basic, rigid-model, wind-tunnel data for aeroleastic effects on the full-scale airplane. Incremental pressures have been evaluated by both attached- and separated-flow theories.

Results of the subsonic and transonic phase of the present program are summarized in NASA SP-347 (ref. 9) and discussed in more detail in reference 10. Some preliminary results of the supersonic phase are given in reference 11; complete results are contained in reference 12.

SYMBOLS AND ABBREVIATIONS

b	wingspan
BL	buttock line
c	local chord
$\bar{c}$	mean aerodynamic chord
c_r	root chord
C_m	pitching moment coefficient (moments about $0.25\bar{c}$)
C_N	normal force coefficient
C_n	section normal force coefficient
C_p	pressure coefficient
ΔC_p	lifting pressure coefficient
C_s	suction force coefficient
L.E.	leading edge
M	Mach number
MS	model station
s	local wing semispan

T.E.   trailing edge

x,y,z   orthogonal coordinates

α angle of attack

γ semiapex angle of wing

$\delta_{T.E.}$ trailing-edge control-surface deflection

ϕ velocity potential

Subscripts x, y, and z denote differentiation.

MODELS

The wind-tunnel-model configuration chosen for the present study is shown in figure 1. It is comprised of a highly swept (71.2°) wing of aspect ratio 1.65 mounted on the bottom side of a slender body. Actually two separate wings were constructed with the planform and airfoil section shown in figures 1 and 2. The only difference between the two was that one was flat, i.e., with no camber or twist, and the other was twisted (no camber). The twist distribution, which is plotted in figure 1, was taken from a super-sonic cruise transport concept and modified over the inboard third to facilitate model construction.

Both wings were equipped with 25-percent-chord trailing-edge control surfaces which were split at the 57-percent semispan station to permit partial as well as full span streamwise deflections of 0°, ±4.1°, ±8.3°, ±17.7°, and ±30.2°. In addition, the flat wing was provided with removable leading-edge segments that extended over 15 percent of the streamwise chord. These segments permitted testing of the leading-edge segment in two drooped positions, 5.1° and 12.8°, as well as undeflected. In order to investigate the effect of leading-edge shape, a second segment was constructed with a sharp leading edge. A sketch of the basic rounded leading edge with the sharp leading edge superimposed is given in figure 1.

The 217 pressure orifices on the wing were equally divided into 7 stream-wise sections on the left wing. Pressure taps were located on both the top and bottom surfaces at the chordwise locations shown in figure 2. The body orifices were arranged in 5 streamwise rows of 15 orifices each. An additional 8 orifices in the area of the wing-body junction made a total of 83 orifices on the left side of the body.

The model was constructed of steel to minimize aeroelastic deflections. To ensure close control of the model dimensions, a computerized lofting program was used to provide data for machining the model components using numerically controlled operations.

88

WIND-TUNNEL TESTS

The model was tested in the Boeing Transonic Wind Tunnel (BTWT) and in the supersonic 9- by 7-foot leg of the NASA Ames Unitary Wind Tunnel. The former is a continuous-flow, closed-circuit, atmospheric facility with a 12.5-percent porosity test section measuring 8 by 12 by 14.5 feet; the latter is a continuous-flow, closed-circuit, variable-density facility with a test section measuring 7 by 9 by 18 feet. Photographs of the model in the Boeing and NASA Ames tunnels are given in figures 3 and 4. Seven Mach numbers from 0.40 to 1.11 were tested in the BTWT, with angle of attack varying from -8° to $+16^o$. In the Ames facility, data were obtained primarily at Mach numbers of 1.7, 2.1, and 2.5. A few selected tests were run at a Mach number of 1.5 to provide better continuity of pressure as a function of Mach number. However, at this Mach number the shock from the nose of the model reflected off the wall back across the wing tip and only those pressures forward of the shock are valid. The major configurations tested are shown in tables I and II.

THEORETICAL METHODS

Theoretical calculations utilized in this paper are based on inviscid theories for both attached and detached flows. Results from three attached-flow theories are discussed: one uses the linear, subsonic/supersonic, constant-pressure-panel formulation, the second uses a panel solution of the exact incompressible-flow equation satisfying the exact boundary condition on the configuration surface, and the third solves the exact, nonlinear, full-potential equation using a finite difference technique.

Four separated-flow methods are examined; the first is the conical flow method of J. H. B. Smith outlined in reference 3. The second method is due to E. C. Polhamus and is widely known as the leading-edge suction analogy. The third method (more aptly termed a technique) is one which combines the Polhamus suction analogy with the Smith method. The last method to be examined is based on distributions of quadratically varying doublet and linearly varying source panels. Since this approach is still under development and only preliminary results are available, a final judgment on the accuracy of the method is not possible. However, it does have the ability to treat a wide variety of wing-body configurations while the older separated-flow methods can handle only simple wing geometries.

Because of the strong influence of the leading-edge vortex for angles of attack greater than a few degrees, attached-flow theories can be expected to yield good agreement only at low angles of attack. Detached-flow theories, on the other hand, should be able to do a good job of predicting loading trends at high angles of attack although they cannot now handle as geometrically complex configurations as the more mature attached-flow methods. Additional details of the analytical methods are discussed briefly in the next section.

Attached-Flow Theories

One of the most popular linear panel techniques in use today is the unified, subsonic/supersonic constant-pressure-panel method developed by Woodward (refs. 13 and 14). In the present study a slightly improved version of the original Woodward program contained in the FLEXSTAB system of programs (see refs. 15 to 17) has been chosen for evaluation. It should be noted that the FLEXSTAB aerodynamic module has been employed as the basic loads tool for another SCAR study (ref. 18) and is utilized in the FLEXSTAB system to evaluate the static and dynamic stability, the inertial and aero-dynamic loading, and the resulting aeroelastic deformations of aircraft configurations.

The paneling scheme utilized for the research arrow wing of the present study is depicted in figure 5. Note that the panels are of nearly equal width, their leading and trailing edges are at constant percent chord, and they are more concentrated near the wing leading edge and at the flap hingelines. In addition, the edges of the panels were chosen to coincide with the control-surface hingelines and breaklines.

In the Woodward/FLEXSTAB panel method, line sources and doublets are distributed along the longitudinal axis of the body to simulate its thick-ness and lifting effects. Similarly, source and vortex panels are placed in the plane of the wing to simulate its thickness and lifting effects. To account for the interference effects between the wing and body, constant-pressure vortex panels are placed on a shell around the body. This "interference" shell serves to cancel the normal velocity components on the body induced by the wing. At subsonic Mach numbers and the high super-sonic Mach numbers, 50 line singularities, 168 interference panels, and 160 wing panels were used to represent the configuration. For the very low supersonic Mach numbers (1.05 and 1.11), the number of interference panels had to be greatly increased (to 330) to overcome instabilities associated with the solution.

The second attached-flow method to be evaluated is that of Rubbert and Saaris (refs. 19 and 20) for the numerical solution of the exact incompress-ible potential-flow equation (Laplace's equation), with compressibility effects incorporated via the Gothert rule. In contrast to FLEXSTAB, the Rubbert-Saaris (hereafter referred to as TEA-230) solution satisfies the exact boundary conditions rather than approximate linear ones.

Figure 6 shows a typical paneling scheme used for the TEA-230 repre-sentation of the arrow-wing body model. The source panels are placed on the configuration surface; consequently, new paneling was required for each configuration. Linearly varying internal and trailing vortex panel networks are also used but not shown. (See ref. 10.) The number of source and vortex panels was different for each configuration but in every case more than 800 source and 280 vortex panels were used.

The third attached-flow method whose ability to predict arrow-wing pressures is to be determined is that of A. Jameson and D. A. Caughey.

90

This method, which is still under development, employs a finite difference technique to solve the full nonlinear potential equation for three-dimensional flow. Satisfaction of the exact boundary conditions is facilitated by the use of a sheared parabolic coordinate system in which the airfoil surface is coincident with a coordinate line. (See fig. 7.) The grid is stretched in all three coordinate directions to minimize the number of total grid points. In the calculations presented in the present paper approximately 60 grid points are employed on the top and bottom of the airfoil section at the wing root (total of 120) and 15 on the top and bottom of the tip section. With longitudinal grid networks located at each of 21 spanwise stations on the wing, the resolution obtained is more than twice that of the TEA-230 method. While the method has only been applied to plain wings (no body), there is almost no limit to the type of wing geometries that it can treat.

Detached-Flow Theories

A number of methods are available which have the capability of accounting for the leading-edge separated vortex. Many of these make the assumption that the flow is conical and, as a consequence, are able to reduce the three-dimensional problem to a two-dimensional one. Wing planforms that conical methods are able to treat are generally limited to deltas though an extension to cranked deltas has been effected (ref. 5). The trailing-edge Kutta condition is not satisfied in these programs.

One of the best known of the "conical" separated-flow programs is that developed by J. H. B. Smith of the RAE (ref. 3). This approach was published in 1966 and is an improved version of the well-known Mangler-Smith method of 1957. Solutions obtained with this method satisfy the leading-edge Kutta condition and that of pressure continuity across the vortex sheet. In addition, the vortex sheet is constrained to be a stream surface of the three-dimensional flow. The solution technique utilizes a conformal transformation which in effect opens the wing (positioned on the horizontal axis) into a circle and then squeezes it into a vertical slit. The wing tips map onto the origin of the transformed plane and the midpoints of the upper and lower surfaces are located on the vertical axis equidistant from the origin. The outer vortex sheet in the transformed plane is approximated by a series of linear segments, typically 20 to 40 in number, which are joined by a cut to a potential vortex core. An iterative technique is used to determine the shape of the vortex sheet, the strength of the sheet segments, and the vortex core.

As noted in the Introduction, results from the Polhamus suction analogy would be presented even though it does not produce detailed pressures. It does, however, predict longitudinal load distributions and it is capable of doing an excellent job on the lift and pitching moment of arbitrary wing geometries. Details of this method were first published in 1966 in reference 8; improvements in the "analogy" since that time have greatly increased its capabilities. (See ref. 21.) In a subsequent paragraph, two simple procedures for using the suction analogy longitudinal load distribution along

with the Smith separated-vortex method to obtain "improved" pressure distributions will be described.

The basic features of the suction analogy are depicted in figure 8. The bottom left-hand side of the figure depicts the attached-flow situation where linear theory predicts a square singularity in the pressure at the leading edge. This singularity in turn produces a suction force in the plane of the wing. In practice the flow at moderate angles of attack becomes like that depicted on the right-hand panel of the wing in figure 8. The flow separates off the leading edge, a vortex forms above the wing, and the flow reattaches inboard of the leading edge. The suction analogy assumes that the force required to make the flow over the vortex attach on the upper surface is the same as the leading-edge suction force which was lost when the flow separated.

Suction force calculations carried out for the present paper were determined using pressure distributions calculated by the FLEXSTAB aerodynamic module discussed earlier. These were added to the potential-flow lift modified for large angles of attack to obtain the total lift.

Since the suction analogy is known to provide good estimates of the force and moment of slender wings one would expect that the longitudinal load distributions determined by the method would also be in good agreement with experiment. One advantage that the suction analogy has over conical separated-vortex methods in producing accurate longitudinal load distributions is that it is based on potential-flow methods which satisfy the trailing-edge Kutta condition where appropriate. While the suction analogy can produce reasonably accurate longitudinal load distributions it is incapable of predicting detailed pressures. On the other hand, the conical separated-flow methods yield pressure distributions with the right character but not always the right magnitude. These two facts suggest the possibility that a semi-empirical method combining both of these approaches would do a better overall job. Two ways of expediting this marriage have been investigated. The first would simply take the local Smith spanwise pressure distributions and multiply them by the ratio of the local normal force obtained from the suction analogy by that obtained by the Smith method; i.e., the integration of the spanwise pressure distribution. The second empiricism would be to calculate the local spanwise pressure distributions with the Smith method using values of the parameter "a" = $(\tan \alpha / \tan \gamma)$ which produces the same local normal force as the suction analogy. This can be done rather easily by working backward from the empirical equation given in reference 3 for the total normal force coefficient.

A new method for the prediction of wing pressures including the effect of the leading-edge spiral vortex is now being developed under contract to NASA Langley Research Center (refs. 6 and 22). This method is capable of predicting forces, moments, and detailed surface pressures on wings of arbitrary planform, thickness, camber, and twist distributions mounted on a fuselage. The wing geometry is arbitrary in the sense that leading and trailing edges may be swept as well as curved or kinked.

The governing equation is the linear potential flow equation with nonlinear boundary conditions which require that the flow be parallel to the wing surface and that the free vortex sheet, springing from the leading and trailing edges, be alined with the local flow and support no pressure jump. The Kutta condition is imposed and satisfied along all wing edges. This problem is solved numerically by an aerodynamic panel method. The configuration is represented by quadrilateral panels on all surfaces with quadratically varying doublet and linear source singularities distributed on them. The vortex core is modeled as a simple line vortex that receives vorticity from the free sheet through a connecting kinematic sheet. The set of nonlinear equations is solved by an iterative procedure, starting with an assumed initial geometry.

Figure 9 shows the type of paneling arrangement used on the wing. Note that the leading and trailing edges are extended for the sake of simplicity to a point rather than chopped off to form a finite tip. This should have only a trivial effect on the answers obtained. The fuselage was not a part of the current model; instead, the wing external to the body was moved inboard to obtain a more realistic model of the wing alone. Results from two different paneling densities are used in the present paper. For the detailed comparison of the basic flat wing, pressure distribution a total of 212 panels was used: 63 panels to describe the wing, 108 panels to describe the rolled-up vortex, and 41 panels to describe the wake. In making a prediction of the incremental load due to twist a total of 142 panels was used with 49 on the wing.

LEADING-EDGE VORTEX CHARACTERISTICS

The large effect of the separated vortex on the flow field above the wing has been mentioned previously but only in general terms. It is helpful in trying to evaluate theory/experiment comparisons to have in mind a good picture of how the vortex develops and how it is affected by changes in the free-stream conditions or wing geometry. Some of this knowledge can be obtained by looking at upper-surface isobar plots. A large number of these plots has been generated; only a representative few will be shown here to emphasize the major effects.

Figure 10 shows formation and development of the leading-edge vortex on the basic rounded-leading-edge, flat wing at a Mach number of 0.40. At 2° angle of attack the isobars have the configuration typical of attached flow. Even at 4° the isobars have a "potential" look except perhaps near the tip where there is some evidence of vortex formation. The isobar plot for 8° angle of attack shows a well-developed vortex that dominates the flow over the outboard third of the wing. For the $\alpha = 16^o$ case the vortex is clearly affecting the flow over the entire wing.

The development of the leading-edge vortex with increasing angle of attack is influenced by the sharpness of the leading edge, wing twist, and wing camber for a given wing planform. Tests on a cambered arrow wing have

not yet been carried out but data are available to yield some idea of the effect of leading-edge radius and wing twist. The first of these influences can be seen by comparing the isobars of figure 10 with those of figure 11, which are for the sharp-leading-edge flat wing. It is evident from figure 11 that the vortex develops much more rapidly for the sharp leading-edge wing than for the round. The sharp-leading-edge vortex for 4° angle of attack is almost as well developed as the round-leading-edge one is at 8°. This contrast tends to diminish as Mach number and angle of attack are increased. For instance, at 16° angle of attack the difference between the sharp- and rounded-leading-edge isobar configurations is negligible.

A comparison of figure 12 with figure 10 gives one a good idea of the effect of twist on vortex formation. An angle of attack of nearly 8° is required to produce the same kind of isobar configuration as was evident at 4° on the flat wing. Since the local angles of attack for the twisted wing are less than those of the flat wing this type of behavior is not surprising.

Finally, the effect of Mach number on vortex movement can be seen by comparing the isobar plots of figure 13 for an $M = 2.5$ with those of figure 10 which were for $M = 0.40$. At $M = 2.5$ the vortex appears to form at only a few degrees angle of attack but is not as concentrated as at the subsonic Mach number. For $\alpha = 8^O$ the vortex appears to be fairly well formed and much further inboard than it was at $M = 0.40$. Not noted on the isobar plots, but significant, is the fact that the increment in pressure between isobars on the $M = 2.5$ plot is a factor of 5 to 10 less than on the $M = 0.40$ plot. While there is clearly a vortex type flow at $M = 2.5$, it is very much weaker than that at $M = 0.40$.

TEST-THEORY COMPARISONS

The real value of any aerodynamic theory lies in its ability to accurately predict flight or wind-tunnel results. Consequently, the predictive methods that designers normally use, or that the theoreticians have just developed and hope will find acceptance, must be evaluated through comparisons with experiment. Of course the configurations and free-stream conditions used for the comparisons should be as similar as possible to those which one eventually expects to apply the theory. With this in mind, and recognizing the limited amount of detailed pressure data available for arrow-wing configurations which spans both subsonic and supersonic speed regimes, the present experimental program and associated theoretical-methods evaluation were undertaken. Subsequent sections will describe a number of theory/experiment comparisons made in effecting an evaluation of some of our state-of-the-art and newly developed methods.

Attached-Flow Methods

Before examining theory/experiment pressure-distributions correlation it is instructive to take a look at the ability of the linear attached theories

to predict gross aerodynamic quantities. A comparison is shown in figures 14 and 15 of experimental and theoretical normal force and pitching moment coefficients over the complete Mach number range for the FLEXSTAB program and at subsonic speeds for the TEA-230 method. The calculations are in good agreement with experiment for all Mach numbers at low angles of attack. However, at moderate angles the TEA-230 method underpredicts the data; the FLEXSTAB methods continue to agree quite well. This agreement is fortuitous, as will be seen in the subsequent discussion, and points up once again the well-known fact that detailed pressure distributions are required to determine the adequacy of theoretical methods for predicting load distributions on wings.

Chordwise distributions of experimental and theoretical surface pressure on the flat-wing configuration are shown in figures 16 to 23 for four Mach numbers. Data are presented for three spanwise stations, 20, 50, and 80 percent of the semispan, and at angles of attack of 4^0 and 12^0. At the low angle of attack, generally good agreement with experimental results was obtained by the use of either attached-flow theory. However, the lack of agreement of the upper-surface pressures at the most outboard station at Mach numbers of 0.85 and 1.05 is due to the start of vortex formation. At M = 1.7 the midspan and outboard sections are affected by the vortex. No significant degradation of the agreement due to separation is evident for a Mach number of 2.5. The TEA-230 predictions are somewhat better near the leading edge than the FLEXSTAB results, which exhibit the typical linear theory leading-edge singularity.

At 12^0 angle of attack good agreement of the predictions with the experimental data is obtained only at the most inboard wing section (2y/b = 0.20) for M = 0.85 and 1.05. (See figs. 17 and 19.) At the two outboard stations, neither the FLEXSTAB nor the TEA-230 results compare well with experimental data. The distributions for M = 1.7 (fig. 21) indicate a substantial effect of the vortex at the midspan station, but because the vortex crosses the trailing edge just beyond this station the theory/experiment agreement is much better in the outboard region of the wing. Isobar plots indicate that at M = 2.50 the vortex crosses the trailing edge inboard of the midspan station; consequently, the theory in figure 23 does a better job at the outboard stations than it did at lower Mach numbers. One final point of interest with respect to these chordwise pressure distributions is the diminishing effect of the leading-edge vortex as Mach number increases from 1.05 to 2.50.

The spanwise load distributions shown in figure 24 demonstrate the same points made earlier with respect to the chord load distributions. The agreement is best at small angles of attack and near the wing root. At high angles of attack, the theory generally underpredicts the load level over the inboard half of the wing and overpredicts it outboard. For M = 2.5 the lack of agreement near the wing tip for high angles cannot be attributed to the close proximity of a spiral vortex. The flow is either separated over the whole chord, giving rise to the near constant pressure, or, because the pressures are approaching the vacuum level, they cannot go any lower.

Application of the Jameson-Caughey transonic wing code to the research arrow wing yields the results depicted on figures 25 to 27. Calculations are

shown for Mach numbers of 0.85, 0.95, and 1.05 at three spanwise stations and for 4^0 angle of attack. The Mach 1.05 calculation is particularly noteworthy since most transonic wing codes are limited to subsonic speeds ($M < 1$) by virtue of the type of differencing schemes used. The Jameson-Caughey method is able to obtain accurate theoretical results because it employs the so-called Jameson "rotated" difference scheme which takes proper account of the zone of dependence in the supersonic regions of the flow. (See ref. 23.)

Comparisons of theory and experiment at $M = 0.85$, figure 25, show excellent agreement everywhere except close to the leading edge on the upper side of the most outboard station. This discrepancy, as noted earlier, is caused by the formation of the leading-edge vortex. Numerical results obtained using the Jameson-Caughey program are very similar to those obtained using the TEA-230. (See fig. 16.) Correlations at $M = 0.95$, shown in figure 26, are also quite good but the vortex formation at the tip has a larger effect on the pressure distribution at this Mach number and the upper surface agreement is correspondingly degraded.

Finally at $M = 1.05$ (see fig. 27) there seems to be an upward shift of the experimental data relative to the theory. This is particularly noticeable over the rear half of the distributions for $2y/b = 0.2$ and 0.5. It is not clear whether this is due to the effect of the body (not accounted for in the theory), the effect of a reflected shock from the wall, or a viscous effect.

Detached-Flow Theories

As indicated in the section on theoretical methods the leading-edge suction analogy was adapted for use with the FLEXSTAB aerodynamic module for the calculation of lift, pitching moment, and longitudinal load distribution. Four arrow-wing configurations were analyzed - the flat wing, the twisted wing, and the flat wing with 5.1^0 and 12.8^0 leading-edge control-surface deflection. (See ref. 10.) Only results from the first two of these configurations will be discussed here.

Comparisons of the calculated total lift, pitching moment, and longitudinal load distribution for the flat and twisted wings at a Mach number of 0.85 are given in figures 28 to 31. The potential solution by itself underpredicts the experimental results; adding the vortex lift yields a total which overpredicts experiment. The fact that the theory assumes a flat sharp-edged wing would lead one to expect better agreement with the sharp-leading-edge data in figure 28 than with the round edge. This seems to be the case, at least for the lift.

A recent improvement to the suction analogy method, termed the augmented vortex-lift concept, when applied to wings with swept-back trailing edges results in a negative lift and moment increment. Calculations for the arrow-wing increments were made by John E. Lamar of NASA Langley Research Center and are labeled on figure 28 as the augmented vortex lift and augmented vortex increment. The prediction of total lift is clearly improved. To obtain the effect on pitching moment, the augmented vortex lift is placed at

96

the two-thirds semispan station on the trailing edge. As in the lift case the pitching moment prediction is improved by the augmented vortex increment.

Whereas the augmented vortex concept does not provide for a method of predicting the associated reductions in the longitudinal load distribution, it does indicate that the loss would occur in the region aft of the apex of the trailing edge. This seems to be confirmed by the overprediction of the experimental load aft of the trailing edge shown in figure 30.

Lift and moment curves for the twisted wing are plotted in figure 29. The agreement of the vortex plus potential lift and moment with experiment are about the same as for the flat wing. Indeed the curves are almost identical; twist primarily causes a shift of two to three degrees in the zero-lift and zero-moment angles of attack. On this basis, the augmented vortex increments for the twisted wing should be nearly the same as for the flat wing; they would just be added to the lift and moment at an angle of attack 2° greater.

Theoretical predictions of the longitudinal load distributions for the flat and twisted wing exceed the experimental values over the whole length of the wing. Generally the differences are not large so the agreement may be termed fair to good.

The next detached-flow method to be compared with experiment is that due to J. H. B. Smith of the Royal Aircraft Establishment. This method yields detailed pressures but only for incompressible flow. Another limitation to the application of the Smith method derives from the assumption of conical flow; i.e., the pressures beyond the trailing-edge apex cannot be determined. Consequently, comparisons of the theoretical and experimental spanwise variations of the lifting pressure have been made only for longitudinal locations up to 93 percent of the root chord.

Figure 32 shows results from the Smith method compared to interpolated sharp-edged wing experimental data (M = 0.40) for x/c_r values of 0.55, 0.74, and 0.93 and an angle of attack of 12°. At x/c_r = 0.55, the Smith method agrees fairly well inboard but peaks at a value almost twice that of the experimental maximum. As one moves toward the trailing edge, the agreement inboard deteriorates to where at x/c_r = 0.93 the theoretical level is almost twice the experimental. This is probably due to the fact that the Smith method does not satisfy the Kutta condition.

The large differences in the peak pressures outboard indicate that the theoretical vortex strength is too large or the vortex is too close to the surface. Experimental data summarized in reference 3 indicate that, for a tan α/tan γ ratio less than 1.0 (the arrow wing for α = 12° yields a value for tan α/tan γ of approximately 0.6), the vortex will generally be higher and further inboard than the theoretical location. Reference 3 also indicates that for tan α/tan γ ratio on the order of 1.0 or larger the position of the vortex is better predicted and the maximum pressures are in much better agreement with experiment.

A second calculation has been made using the Smith method by constraining the spanwise integration of pressure distribution; i.e., the local value of the longitudinal load, to have the same value as that given by the suction analogy. As noted in the section on theoretical methods there are two ways of doing this. The calculations shown on figure 32 (modified Smith method) are for the technique wherein the value of $\tan \alpha / \tan \gamma$ is used which gives the same value of the longitudinal load as the suction analogy. A comparison of this modified Smith method with experiment and the original Smith method shows some improvement inboard of the midspan stations but no significant improvement outboard. The second empiricism suggested for the Smith method, whereby the pressures are simply multiplied by the ratio of the suction analogy and Smith method longitudinal loads, provided no better agreement than that shown in figure 32.

The last detached-flow method to be evaluated with the aid of arrow-wing pressure data is an improved version of the panel method detailed by Weber et al. in reference 6. (See ref. 22.) A brief description of its features, including the paneling arrangement, was given in the theoretical methods section. Panel-method calculations for $M = 0$ have been made for the same longitudinal location and angle of attack as those shown in figure 32 for the "Smith" method. Figure 33 compares these results with the sharp-edged wing data for $M = 0.40$. (Note the ordinate scale in fig. 33 is one-half that of fig. 32.) It is quite clear from figure 33 that the separated-flow panel method correlates with experiment much better than the Smith method, doing a good job on the level of the inboard pressures as well as the outboard pressure peak. Spanwise distributions of pressure for locations aft of the trailing-edge apex (not shown in fig. 33) remain quite good although the theoretical pressure peaks exceed the experimental ones. (See ref. 11.)

SIMULATED AEROELASTIC CALCULATIONS

Aside from parametric studies, theoretical methods are used mainly to correct experimental data from a rigid wind-tunnel model for the effects of the elastic deformation of the aircraft structure under load. Examples of this procedure are shown in figures 34 and 35 for Mach 0.85 and 2.1 at an angle of attack of 8°. Here experimental data for the flat wing are taken as representative of a typical rigid-model tunnel test. A theoretical increment calculated for the known twist of the model (supposed elastic deformation) using the FLEXSTAB program is added to obtain the predicted distribution. This result is compared with the twisted-wing data at the same angle of attack (deformed airframe). Three spanwise locations are shown; the section at $2y/b = 0.35$ is typical of the other inboard stations. The error in predicting the pressure distribution is small at the inboard stations, primarily because the relative twist in this region is small. However, there are significant differences at the midspan and outboard stations between the experimental flat-wing data theoretically corrected for twist and the experimental twisted-wing data. This is because the linear FLEXSTAB program does not account for the nonlinear vortex effects.

Since the linear attached-flow methods do not do an adequate job of providing aeroelastic corrections of highly swept wings, at least for the effect of twist, it is of interest to determine if the separated-flow panel program of reference 22 can do any better. Figure 36 shows the results of a crude first attempt. Spanwise rather than chordwise variations of pressure are presented due to the paneling arrangement. (See fig. 7.) It should also be noted that wing thickness and the fuselage were not accounted for in the panel model used and only 49 panels were employed on the wing (7 rows of panels with 7 panels each).

Calculations have been carried out for the flat and twisted wing at $M = 0.40$ and an angle of attack of 12^0. As in the calculations for figures 34 and 35 the increment between these two theoretical results has been added to the flat-plate experimental data. The simulated aeroelastic prediction for the twisted wing is the solid line and should be judged by the square symbols for the twisted-wing experimental results. In the outboard region at the $x/c_r = 0.435$ station, where the experimental differences are large, the simulated aeroelastic prediction does not agree with the twisted wing data. At $x/c_r = 0.91$ the agreement is quite good with the largest discrepancy occurring around the 75-percent semispan station. Agreement between the prediction and the twisted-wing data deteriorates considerably in moving from the $x/c_r = 0.91$ station to $x/c_r = 1.26$. Theory says that the increment is negative everywhere, whereas experimentally there are both positive and negative increments. Overall one would have to say that the separated-vortex panel program did not do much better than the linear attached-flow panel method in predicting the "aeroelastic" increment. However, it should be remembered that the paneling scheme was very crude (49 panels on the wing) and the fuselage and wing thickness were not accounted for. Certainly the 63-panel calculation for the flat wing shown in figure 33 offers some hope that when the full capability of the program now being developed can be utilized more accurate incremental predictions will result.

CONTROL SURFACE EFFECTS

The experimental program carried out on the arrow-wing model included a number of tests with the leading and trailing edges deflected. (See Tables I and II.) As in the case of the basic flat and twisted wings, theoretical calculations were carried out for the deflected-control configurations using the FLEXSTAB and TEA-230 programs. A sample of these calculations is shown in figure 37 which depicts the change with Mach number of the chordwise distribution of pressure for a trailing-edge, control-surface deflection of 8.3^0 and the wing at zero angle of attack. The station $2y/b = 0.65$ is used in this figure since the agreement between theory and experiment is typical of that obtained at other spanwise stations. It is apparent from figure 37 that the prediction of the pressures at the leading edge and at the hingeline are much better with the TEA-230 method (only $M = 0.40$ calculation shown) than with FLEXSTAB. FLEXSTAB overpredicts the pressures on the control surface at all Mach numbers shown, although at this angle of attack the distribution

forward of the hingeline is quite good except at the leading edge. For higher deflection angles, i.e., 17.7 and 30.2^o, the flow separates on the bottom side of the flap and the agreement becomes worse. Also as the flap angle is increased at subsonic speeds the circulation induced by the flap causes a leading-edge vortex to form, further impairing the agreement of theory and experiment near the tip. Similarly, when the wing is at an angle of attack sufficient to cause the formation of a leading-edge vortex the effectiveness of the outboard part of the trailing-edge control is greatly reduced. (See ref. 11.)

CONCLUDING REMARKS

It has been shown that the attached-potential-flow methods can yield good agreement with experimental data for a highly swept, arrow-wing configuration only at low angles of attack such as one encounters at cruise conditions (load factor one). At critical structural and control design conditions, which usually involve moderate to large angles of attack and/or large control-surface deflections, the attached-flow theories are inadequate. Attempts to introduce empirical corrections using attached- and detached-flow methods have been unsatisfactory.

Calculations for four separated-flow methods were compared to theory. The Polhamus suction analogy, which does not provide predictions of the detailed pressures, showed generally good agreement for the lift, moment and longitudinal load predictions for both flat and twisted wings. Detailed pressure distributions calculated using the Smith conical flow method and two slightly modified versions of the Smith method did not agree well with experiment particularly in the vicinity of the vortex. A new detached-flow method which uses linearly varying source and quadratically varying doublet panels showed the best agreement with experimental pressure data for the basic flat-wing configuration. Further development of this type of analysis technique is mandatory if we are to be successful in predicting the pressures on wings with a separated leading-edge vortex.

The prediction of control-surface-induced and direct loads was more accurately done by the TEA-230 program which satisfies the exact boundary conditions of the wing and control surface than by the FLEXSTAB program which uses only planar boundary conditions. For high flap deflections separated flow at the hinge line degraded the theory/experiment correlation. At large flap deflections and/or angles of attack greater than 4° a leading-edge vortex existed which greatly reduced the effectiveness of the outboard half of the trailing-edge vortex.

100

REFERENCES

1. Brown, Clinton E.; and Michael, William H., Jr.: On Slender Delta Wings
With Leading-Edge Separation. NACA TN 3430, 1955.

2. Mangler, K. W.; and Smith, J. H. B.: A Theory of Flow Past a Slender
Delta Wing With Leading Edge Separation. Proc. Roy. Soc. (London),
ser. A. vol. 251, no. 1265, May 26, 1959, pp. 200-217.

3. Smith, J. H. B.: Improved Calculations of Leading-Edge Separation From
Slender Delta Wings. Tech. Rep. No. 66070, Brit. R.A.E., Mar. 1966.

4. Legendre, R.: Nappes de tourbillons deferlant des bords d'attaque des
ailes en delta (in English). Presented to I.U.T.A.M. Symposium on
Concentrated Vortex Motions, Ann Arbor, July 1964. Prog. in Aeron.
Sci. (ed Kuchemann et al.) 7, Pergamon Press, Oxford, 1966.

5. Wei, M. H. Y.; Levinsky, E. S.; and Su, F. Y.: Nonconical Theory of Flow
Past Slender Wing-Bodies With Leading-Edge Separation. NASA CR 73446,
1969.

6. Weber, James A.; Brune, Guenter W.; Johnson, Forrester T.; Lu, Paul; and
Rubbert, Paul E.: Three-Dimensional Solution of Flows Over Wings With
Leading Edge Vortex Separation. Printed in Aerodynamic Analyses
Requiring Advanced Computers. NASA SP-347, pp. 1013-1032, 1975.

7. Kandil, O. A.; Mook, D. T.; and Nayfeh, A. H.: Nonlinear Prediction of
the Aerodynamic Loads on Lifting Surfaces. AIAA Paper No. 74-503,
June 1974. Also J. of Airc., vol. 13, no. 1, Jan 1976, pp. 22-28.

8. Polhamus, E. C.: A Concept of the Vortex Lift of Sharp-Edge Delta Wings
Based on a Leading-Edge-Suction Analogy. NASA TN D-3767, 1966.

9. Manro, Majorie E.; Tinco, Edward N.; Bobbitt, Percy J.; and Rogers,
John T.: Comparison of Theoretical and Experimental Pressure
Distributions on an Arrow-Wing Configuration at Transonic Speed.
Printed in Aerodynamic Analyses Requiring Advanced Computers.
NASA SP-347, pp. 1141-1188, 1975.

10. Manro, Marjorie E.; Manning, Kenneth J. R.; Hallstaff, Thomas H.; and
Rogers, John T.: Transonic Pressure Measurements and Comparison of
Theory to Experiment for an Arrow-Wing Configuration. Summary Report,
NASA CR-2610, 1975.

11. Manro, M. E.; Bobbitt, P. J.; and Rogers, J. T.: Comparisons of
Theoretical and Experimental Pressure Distributions on an Arrow-Wing
Configuration at Subsonic, Transonic and Supersonic Speeds. AGARD
Conference Preprint No. 204 on Prediction of Aerodynamic Loading,
Sept. 1976.

12. Manro, M. E.: Supersonic Pressure Measurements and Comparison of Theory to Experiment for an Arrow-Wing Configuration. NASA CR-145046, 1976.

13. Woodward, F. A.; Tinoco, E. N.; and Larsen, J. W.: Analysis and Design of Supersonic Wing-Body Combinations, Including Flow Properties in the Near Field. Part 1 - Theory and Application. NASA CR-73106, 1967.

14. Woodward, F. A.: Analysis and Design of Wing-Body Combinations at Subsonic and Supersonic Speeds. J. of Airc., vol. 5, no. 6, Nov.-Dec. 1968, pp. 528-534.

15. Tinoco, E. N.; and Mercer, J. E.: FLEXSTAB - A Summary of the Functions and Capabilities of the NASA Flexible Airplane Analysis Computer System. NASA CR-2564, Oct. 1974.

16. Dusto, A. R., et al.: A Method for Predicting the Stability Characteristics of an Elastic Airplane. Volume 1, FLEXSTAB Theoretical Manual. NASA CR-114712, 1974.

17. Perkin, Brian R.; and Erickson, Larry L.: FLEXSTAB - A Computer Program for the Prediction of Loads and Stability and Control of Flexible Aircraft. Proceedings of the SCAR Conference, NASA CP-001, 1977. (Paper no. 12 of this compilation.)

18. Turner, M. J.; and Hoy, J. M.: Titanium and Advanced Composite Structures for a Supersonic Cruise Arrow Wing Configuration. Proceedings of the SCAR Conference, NASA CP-001, 1977. (Paper no. 28 of this compilation.)

19. Rubbert, P. E.; Saaris, G. R.; Scholey, M. B.; Standen, N. M.; and Wallace, R. E.: A General Method for Determining the Aerodynamic Characteristics of Fan-in-Wing Configurations. Volume I, Theory and Application. USAAVLABS Technical Report 67-61A, 1967.

20. Rubbert, P. E.; and Saaris, G. R.: Review and Evaluation of a Three-Dimensional Lifting Potential Flow Analysis Method for Arbitrary Configurations. AIAA Paper No. 72-188, 1972.

21. Lamar, John E.: Some Recent Applications of the Suction Analogy to Vortex-Lift Estimates. Printed in Aerodynamic Analyses Requiring Advanced Computers. NASA SP-347, pp. 985-1912, 1975.

22. Gloss, Blair B.; and Johnson, Forrester, T.: Development of an Aerodynamic Theory Capable of Predicting Surface Loads on Slender Wings With Vortex Flow. Proceedings of the SCAR Conference, NASA CP-001, 1977. (Paper no. 3 of this compilation.)

23. South, Jerry C., Jr.; and Jameson, Antony: Relaxation Solutions for Inviscid Axisymmetric Transonic Flow Over Blunt or Pointed Bodies. AIAA Computational Fluid Dynamics Conference. Palm Springs, Calif., July 1973, pp. 8-17.

TABLE I.– SUMMARY OF CONDITIONS TESTED IN BOEING TRANSONIC WIND TUNNEL

WING	TRAILING EDGE	LEADING-EDGE DEFLECTION, degrees	TRAILING-EDGE DEFLECTION, degrees
ROUNDED-LEADING-EDGE FLAT WING	FLAT	0	0, $\pm$ 4.1, $\pm$ 8.3, $\pm$ 17.7, $\pm$ 30.2
			PARTIAL SPAN $\pm$ 8.3, + 17.7
		PARTIAL SPAN 5.1	PARTIAL SPAN $\pm$ 8.3, + 17.7
		5.1, 12.8	0, + 4.1, $\pm$ 8.3, + 17.7
	TWISTED	0	0, + 4.1, $\pm$ 8.3, + 17.7
SHARP-LEADING-EDGE FLAT WING	FLAT	0	0
ROUNDED-LEADING-EDGE TWISTED WING	TWISTED	0	0, + 4.1, $\pm$ 8.3, + 17.7, + 30.2

MACH NUMBERS : 0.40, 0.70, 0.85, 0.95, 1.00, 1.05, 1.11
ANGLE OF ATTACK : -8° TO $+16^{\circ}$ (2° INCREMENTS)

TABLE II.– SUMMARY OF CONDITIONS TESTED IN NASA AMES UNITARY WIND TUNNEL

WING	TRAILING EDGE	LEADING-EDGE DEFLECTION, degrees	TRAILING-EDGE DEFLECTION, degrees
ROUNDED-LEADING-EDGE FLAT WING	FLAT	0	0, $\pm$ 4.1, + 8.3
			PARTIAL SPAN + 4.1, + 8.3
		5.1	0
SHARP-LEADING-EDGE FLAT WING	FLAT	0	0
		5.1	0
ROUNDED-LEADING-EDGE TWISTED WING	TWISTED	0	0, + 8.3

MACH NUMBERS : 1.70, 2.10, 2.50
ANGLE OF ATTACK : -8° TO $+14^{\circ}$ (2° INCREMENTS) $+ 15^{\circ}$
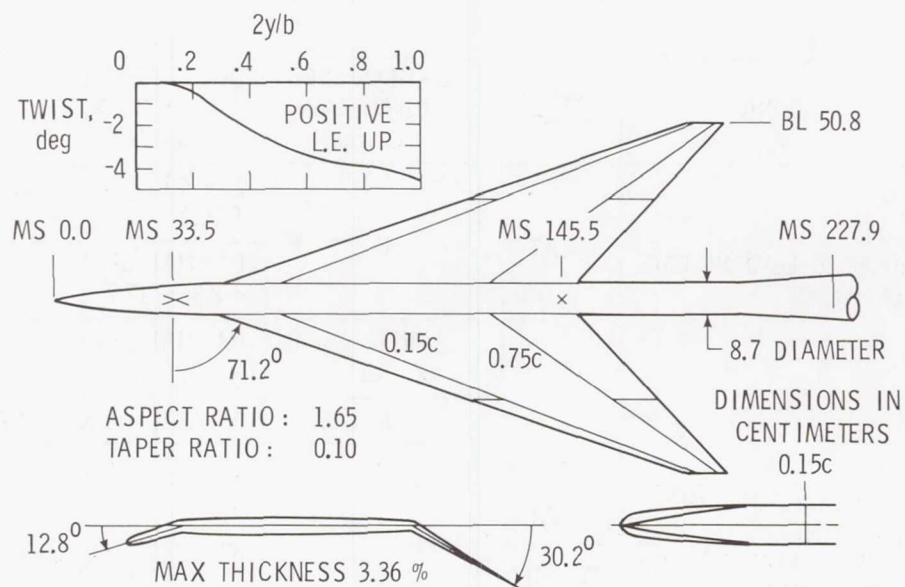
Figure 1.- General arrangement and characteristics
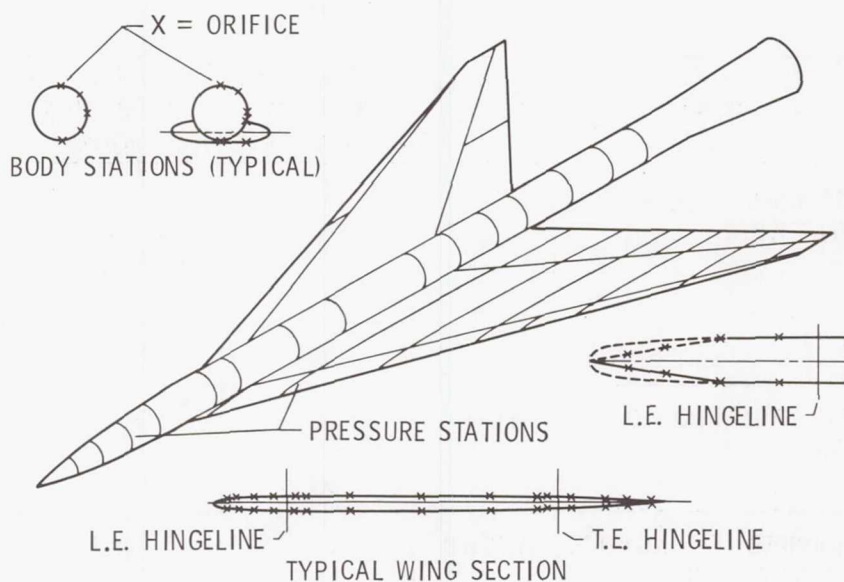of arrow-wing wind-tunnel-model configuration.

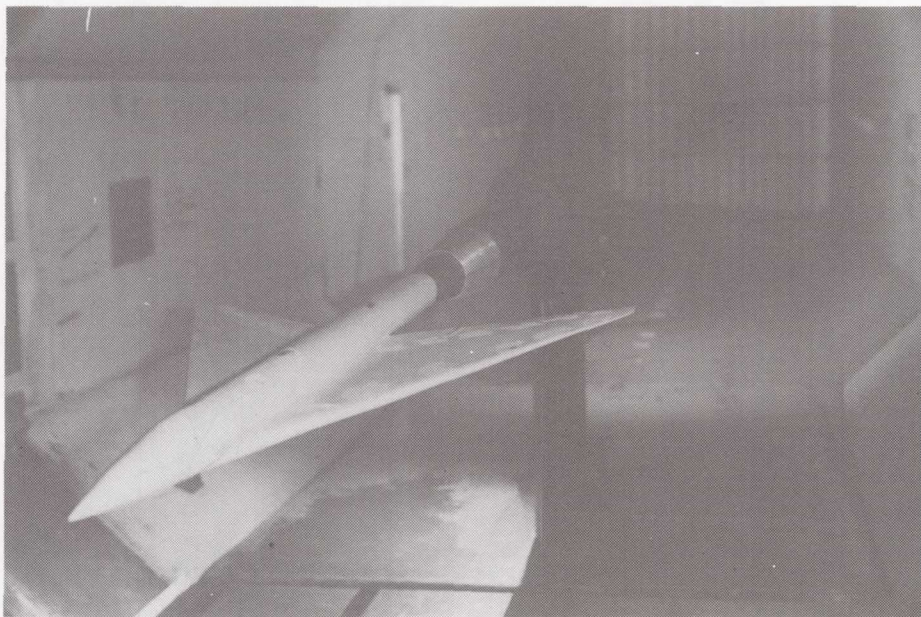Figure 2.- Pressure orifice locations on wind-tunnel model.

Figure 3.- Flat arrow-wing model mounted in
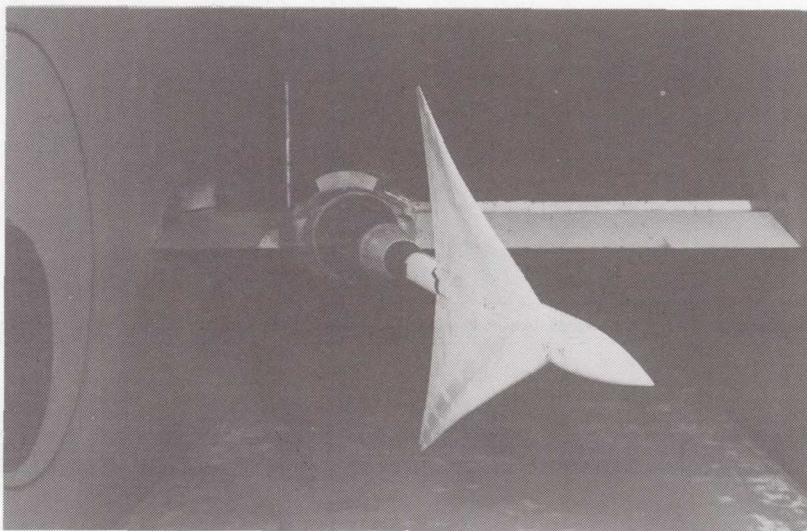Boeing 8 × 12 ft Transonic Wind Tunnel.

Figure 4.- Twisted arrow-wing model mounted
in Ames 9 × 7 ft Unitary Wind Tunnel.

105

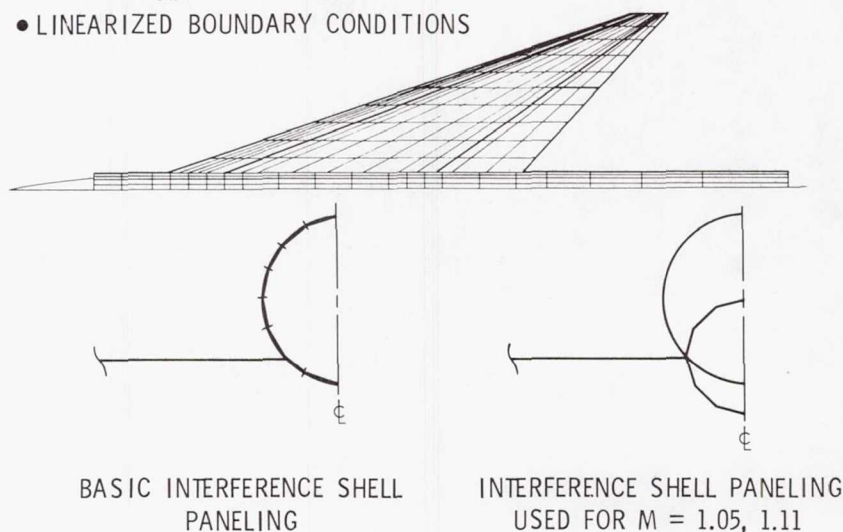- $(1 - M^2)\, \Phi_{XX} + \Phi_{YY} + \Phi_{ZZ} = 0$
- LINEARIZED BOUNDARY CONDITIONS

BASIC INTERFERENCE SHELL
PANELING

INTERFERENCE SHELL PANELING
USED FOR M = 1.05, 1.11

Figure 5.- FLEXSTAB paneling scheme for present arrow wing.

- $\Phi_{XX} + \Phi_{YY} + \Phi_{ZZ} = 0$
- EXACT BOUNDARY CONDITIONS
- GOTHERT COMPRESSIBILITY RULE

DEFLECTED FLAP
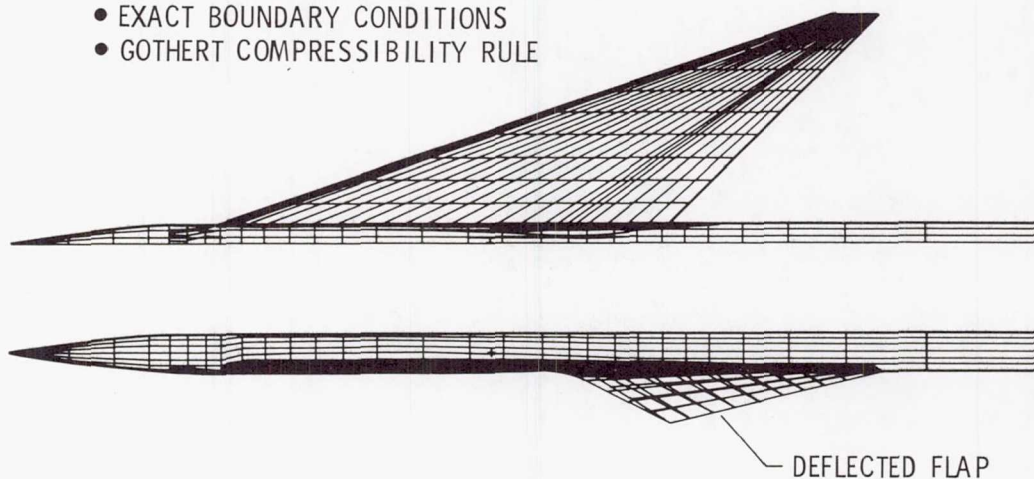
Figure 6.- TEA-230 paneling scheme for present arrow wing.

SHEARED PARABOLIC
COORDINATES
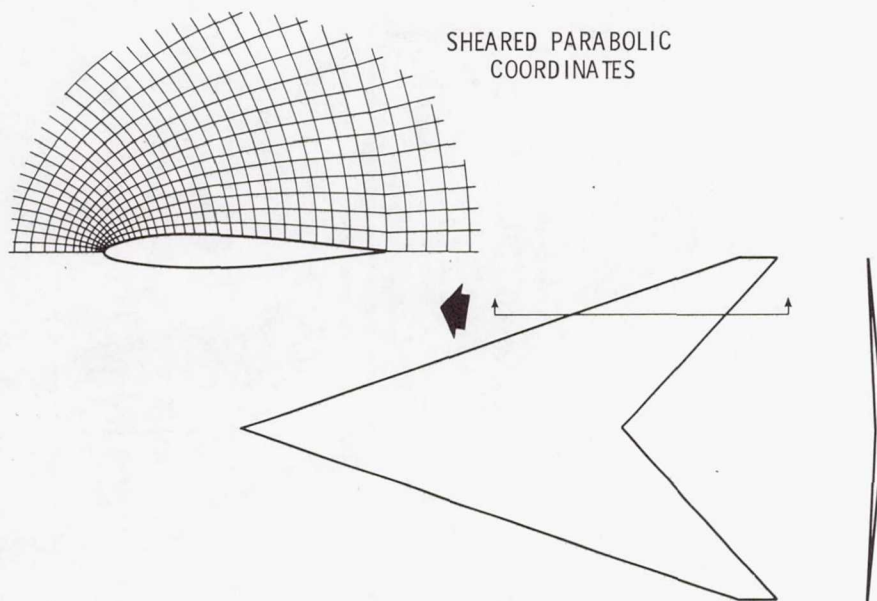
Figure 7.- Sketch showing coordinate scheme used in Jameson-
Caughey full-potential-equation numerical method.

- POTENTIAL LIFT DISTRIBUTION - FLEXSTAB
- SUCTION FORCE CALCULATED FROM PRESSURE DISTRIBUTION
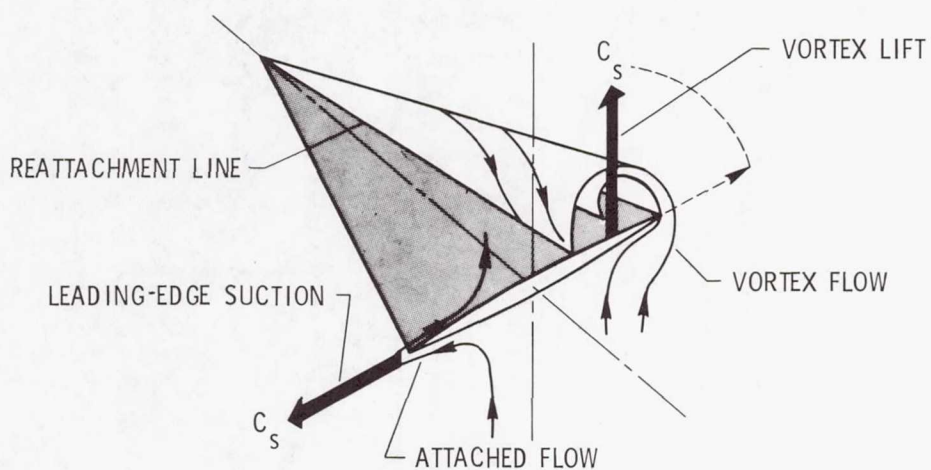- VORTEX LIFT OBTAINED BY ROTATING LEADING EDGE-SUCTION FORCE

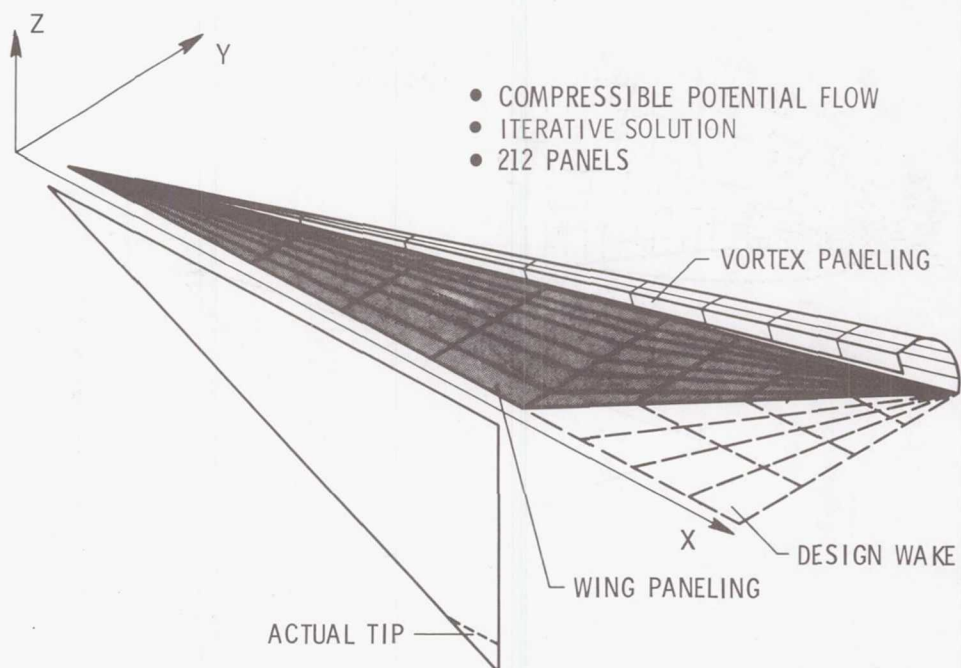Figure 8.- Basic features of leading-edge suction analogy.

- COMPRESSIBLE POTENTIAL FLOW
- ITERATIVE SOLUTION
- 212 PANELS

Figure 9.- Three-dimensional vortex program paneling scheme.

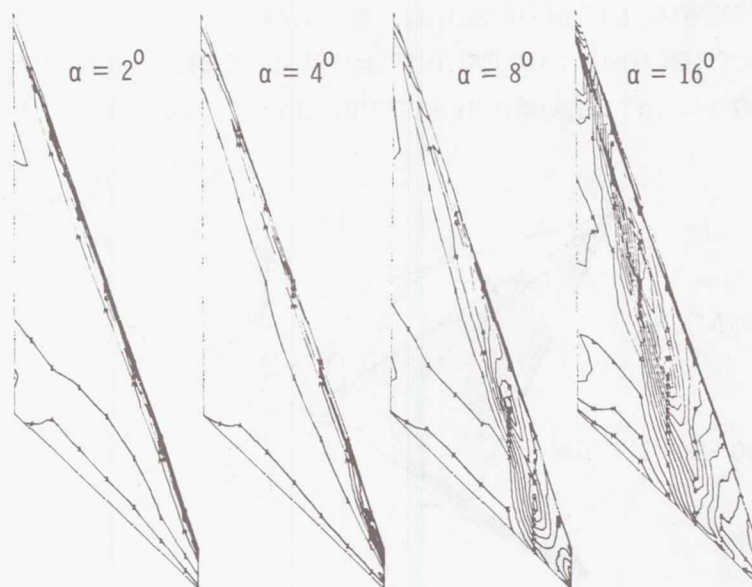$\alpha = 2^0$ $\alpha = 4^0$ $\alpha = 8^0$ $\alpha = 16^0$

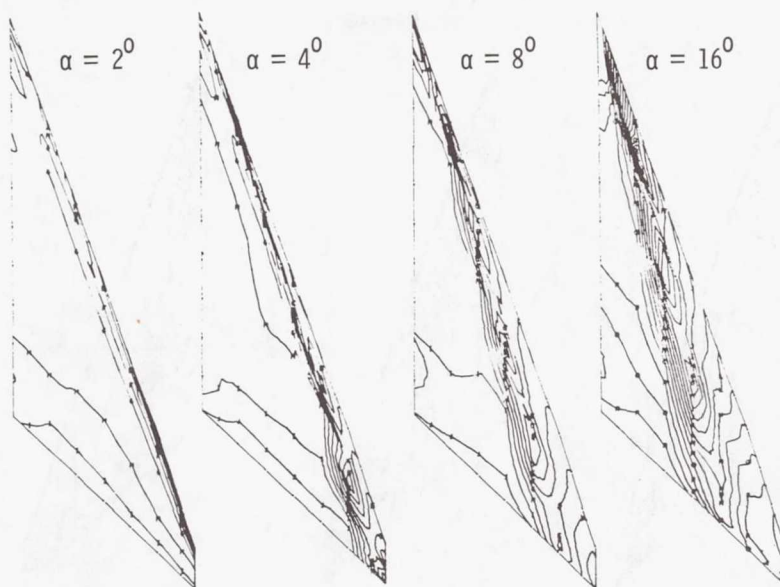Figure 10.- Upper-surface isobars on rounded-leading-edge flat wing.
M = 0.40.

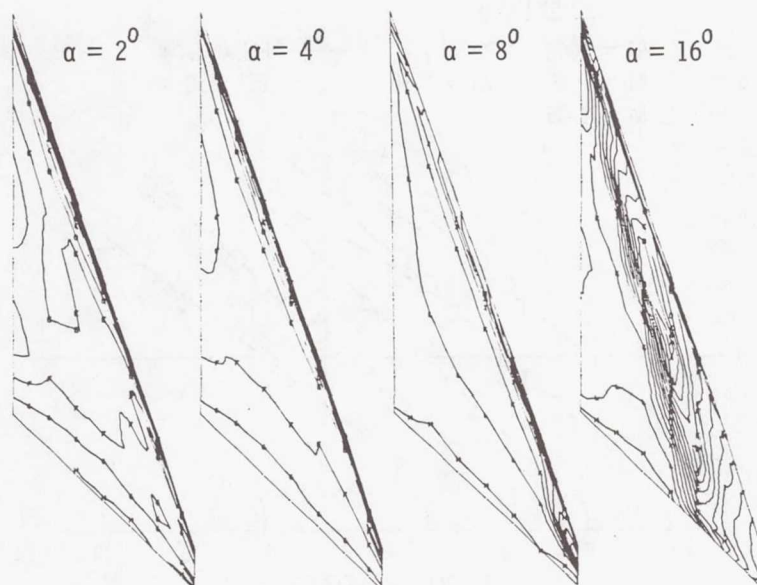Figure 11.- Upper-surface isobars on sharp-leading-edge flat wing.
M = 0.40.

Figure 12.- Upper-surface isobars on rounded-leading-edge twisted wing.
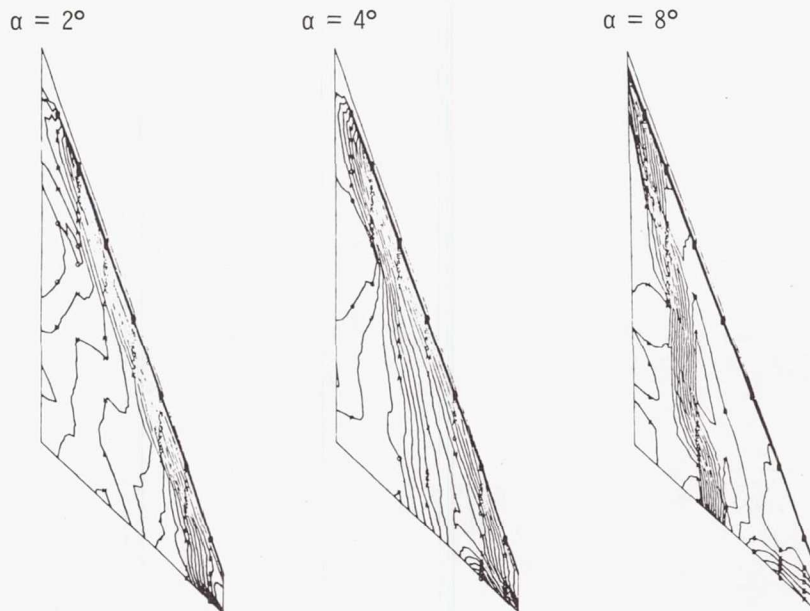M = 0.40.

α = 2°   α = 4°   α = 8°

Figure 13.- Upper-surface isobars on rounded-leading-edge flat wing.
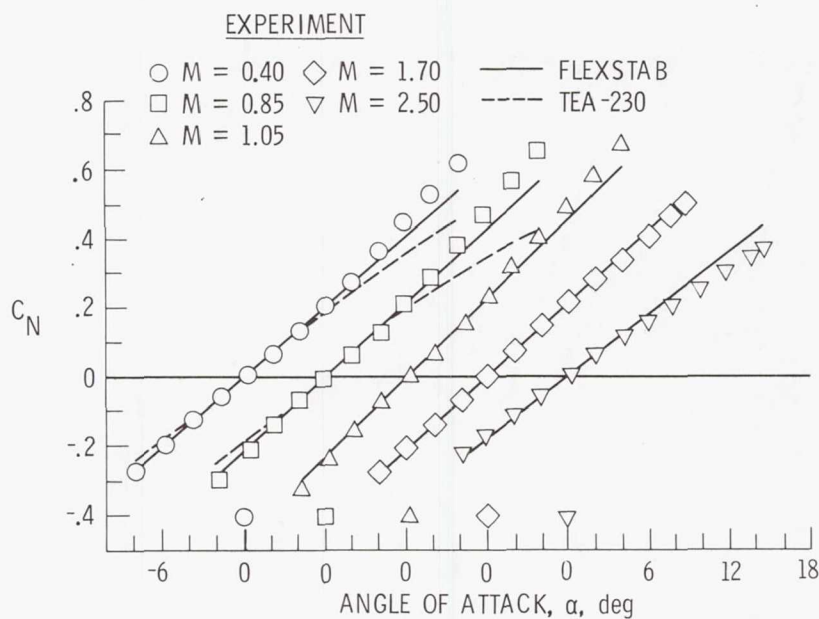M = 2.50.

Figure 14.- Total normal force coefficient as a function
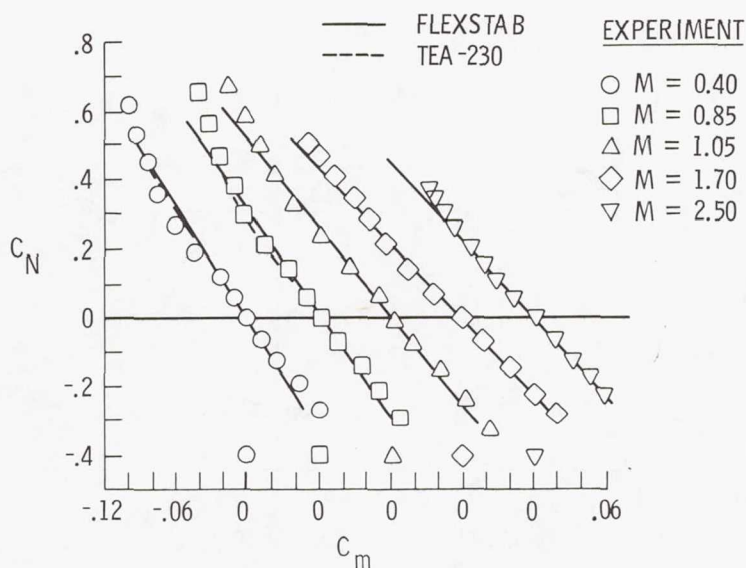of angle of attack for flat wing.

Figure 15.- Total normal force as a function of pitching moment coefficients for flat wing.

Figure 16.- Surface pressure distributions at three spanwise locations on flat wing. M = 0.85; $\alpha = 4^{\circ}$.

Figure 17.- Surface pressure distributions at three spanwise locations on flat wing. M = 0.85; α = 12°.

Figure 18.- Surface pressure distributions at three spanwise locations on flat wing. M = 1.05; α = 4°.
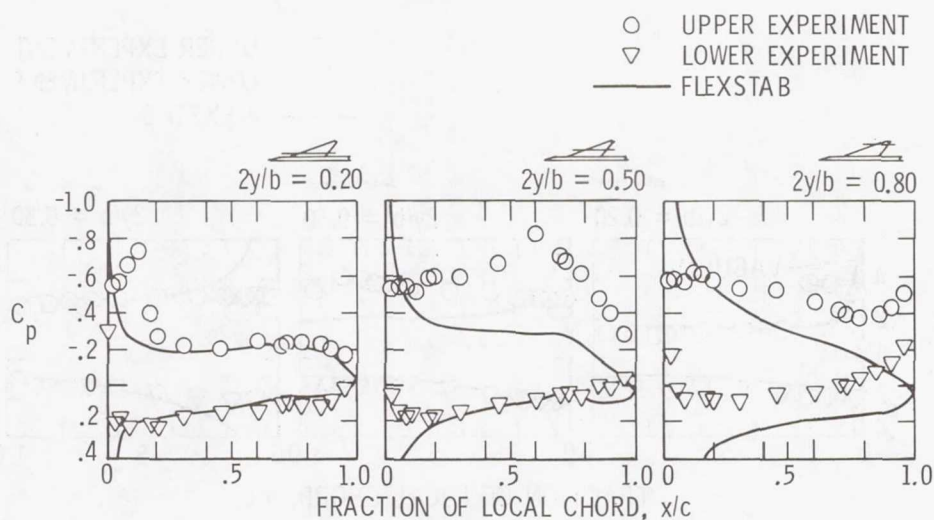
Figure 19.- Surface pressure distributions at three spanwise locations on flat wing. M = 1.05; $\alpha = 12^{\circ}$.
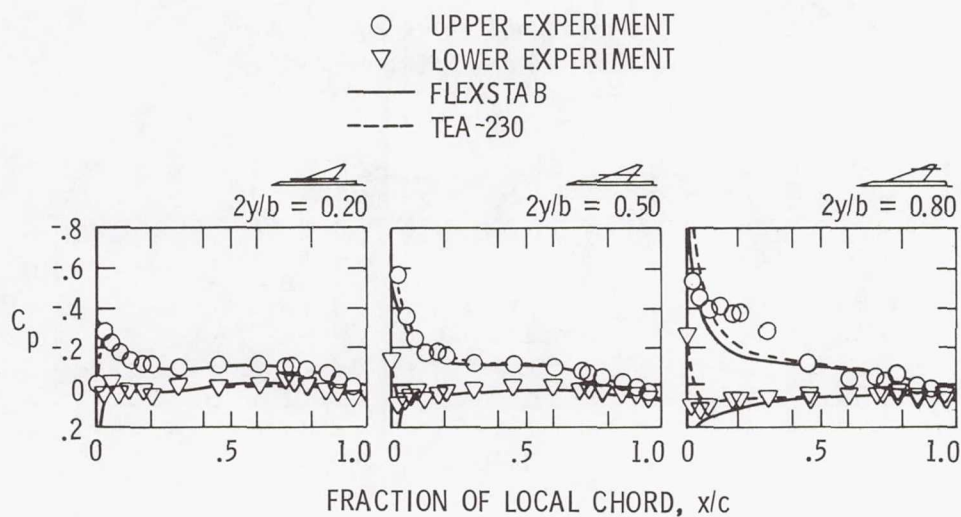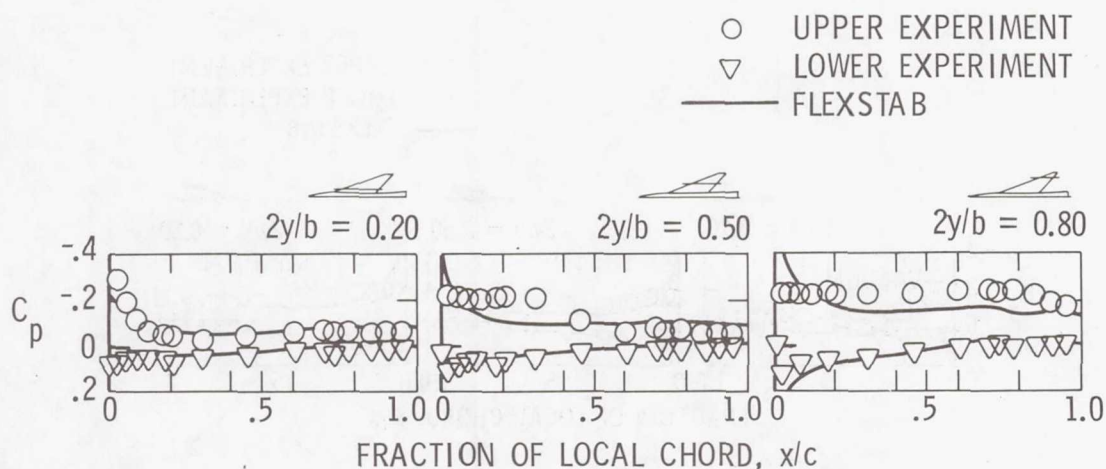
Figure 20.- Surface pressure distributions at three spanwise locations on flat wing. M = 1.70; $\alpha = 4^{\circ}$.
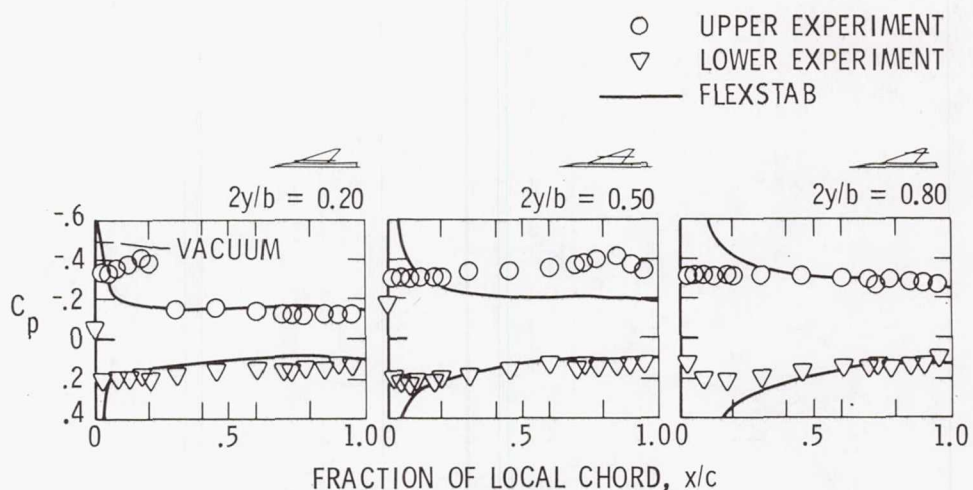
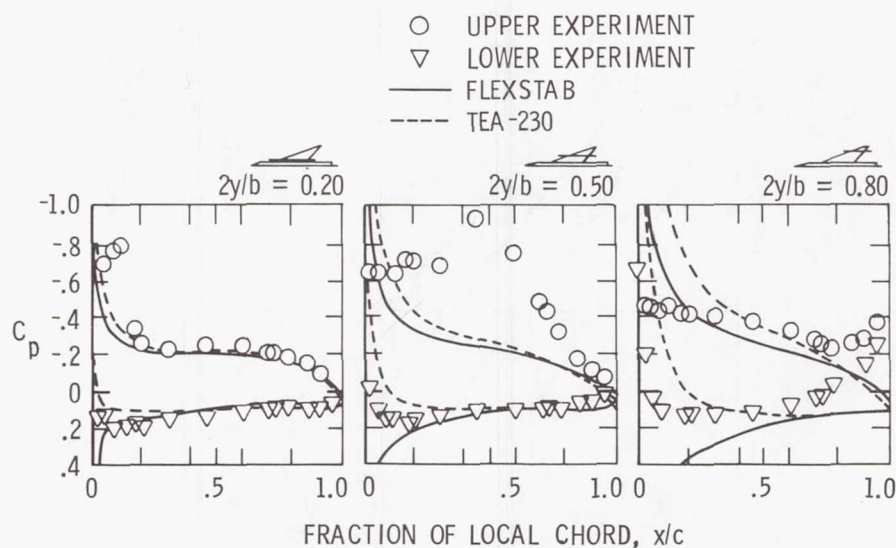Figure 21.- Surface pressure distributions at three spanwise locations on flat wing. $M = 1.70$; $\alpha = 12°$.

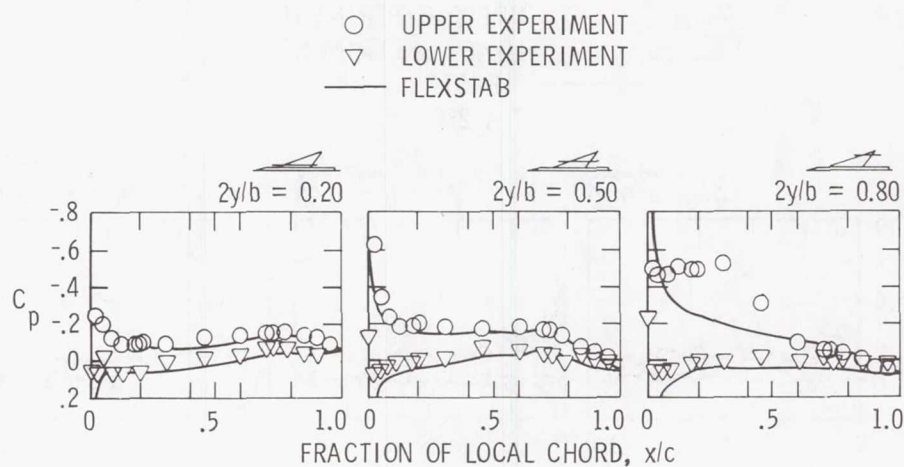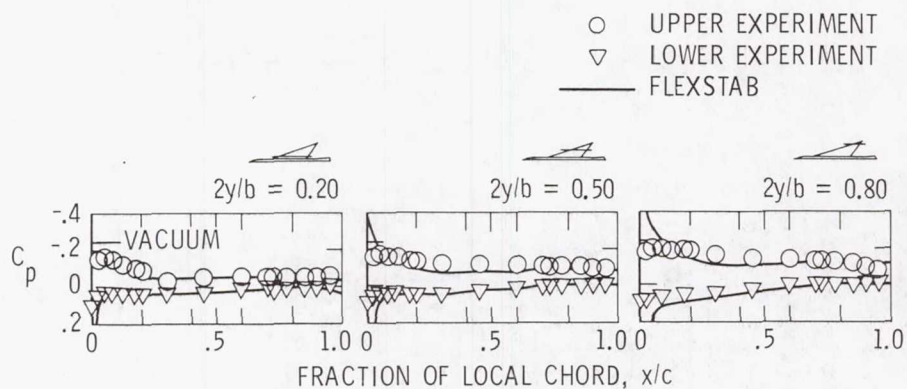
Figure 22.- Surface pressure distributions at three spanwise locations on flat wing. $M = 2.50$; $\alpha = 4°$.
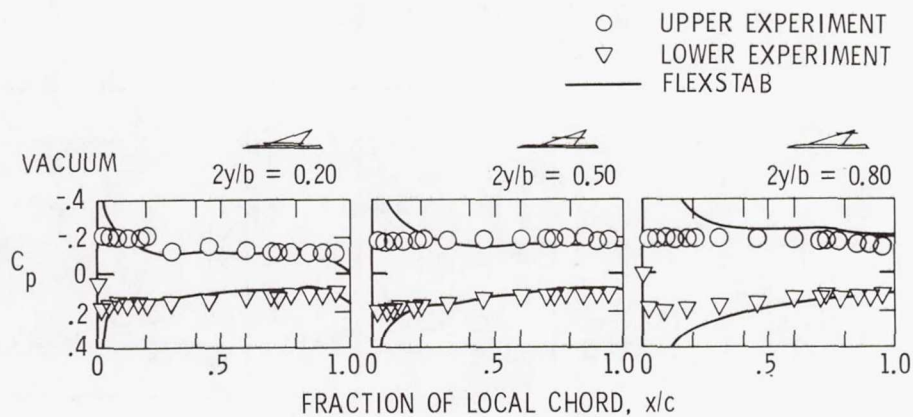
Figure 23.- Surface pressure distribution at three spanwise locations on flat wing. M = 2.50; $\alpha = 12^{\circ}$.
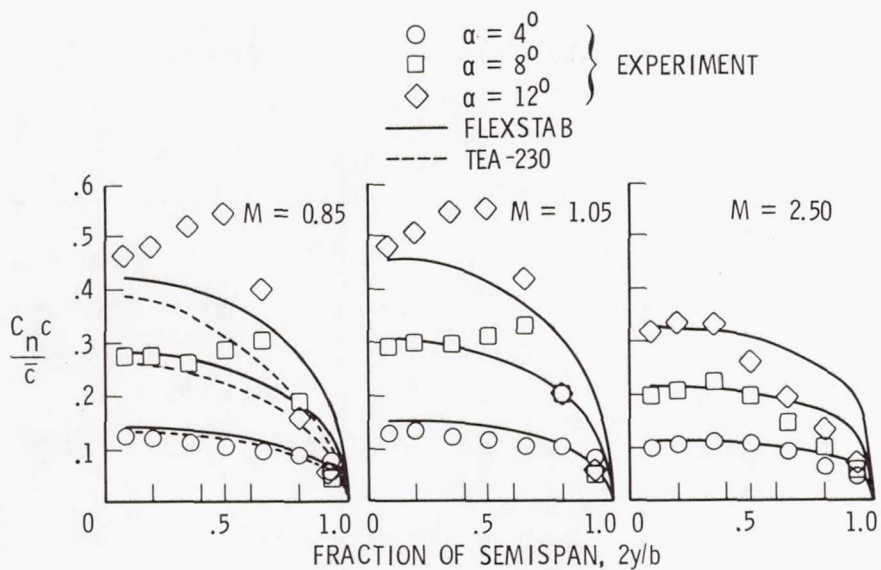
Figure 24.- Spanwise load distributions on flat wing at three Mach numbers and three angles of attack.
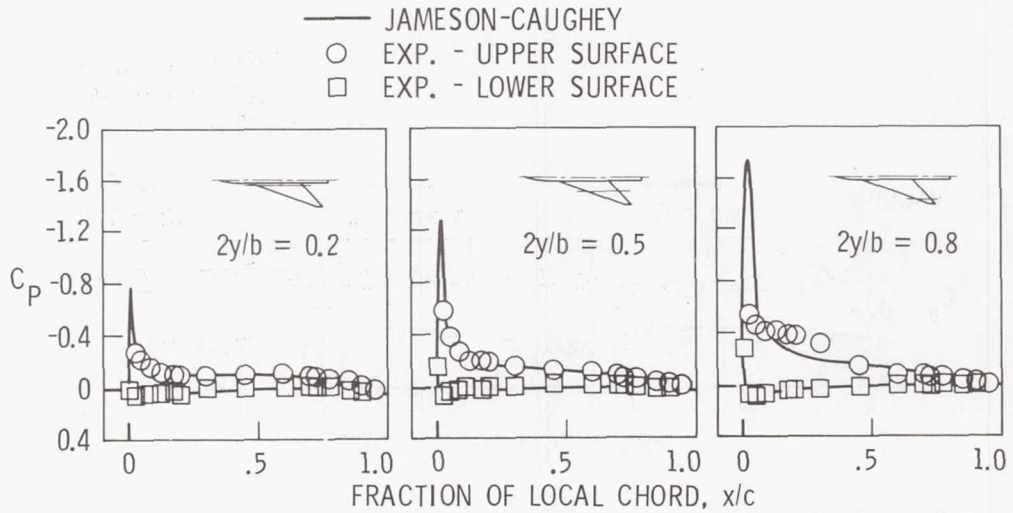
Figure 25.- Comparison of experiment with Jameson-Caughey transonic method. Flat wing; M = 0.85; α = 4°.
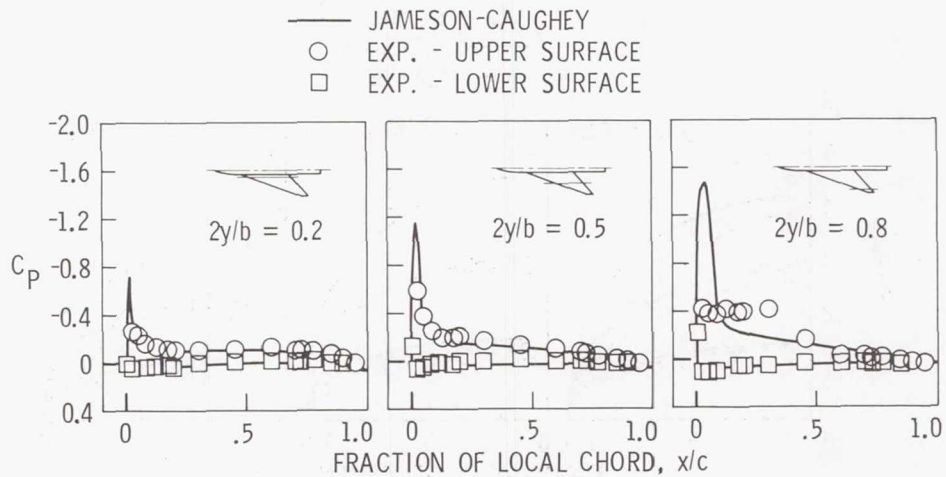
Figure 26.- Comparison of experiment with Jameson-Caughey transonic method. Flat wing; M = 0.95; α = 4°.
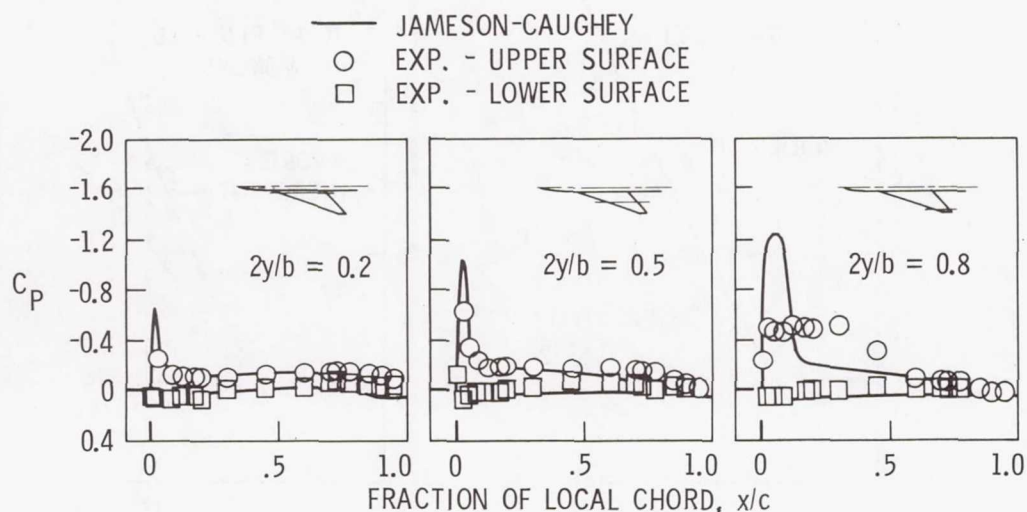
Figure 27.- Comparison of experiment with Jameson-Caughey transonic
method. Flat wing; M = 1.05; $\alpha = 4^\circ$.
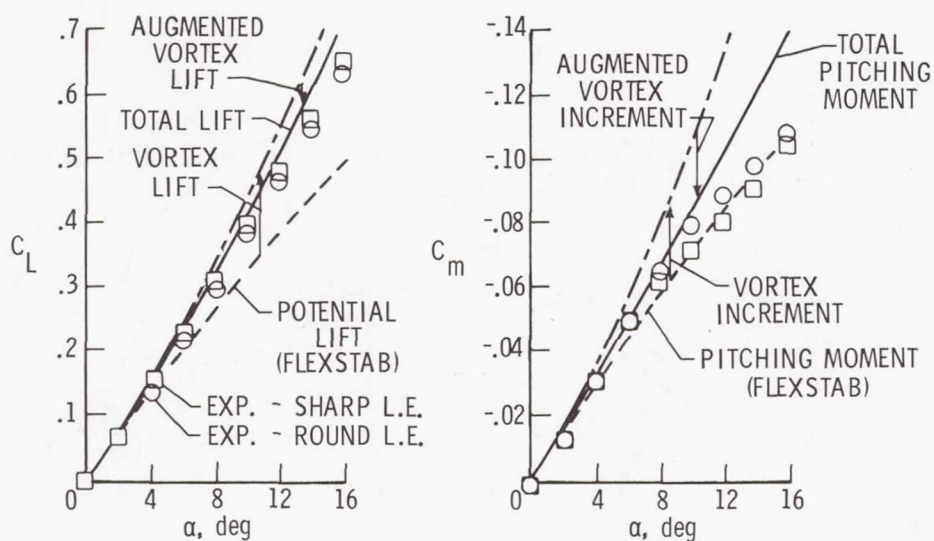
Figure 28.- Comparison of experiment with leading edge suction calculations
of lift and pitching moment for flat wing. M = 0.85.

117
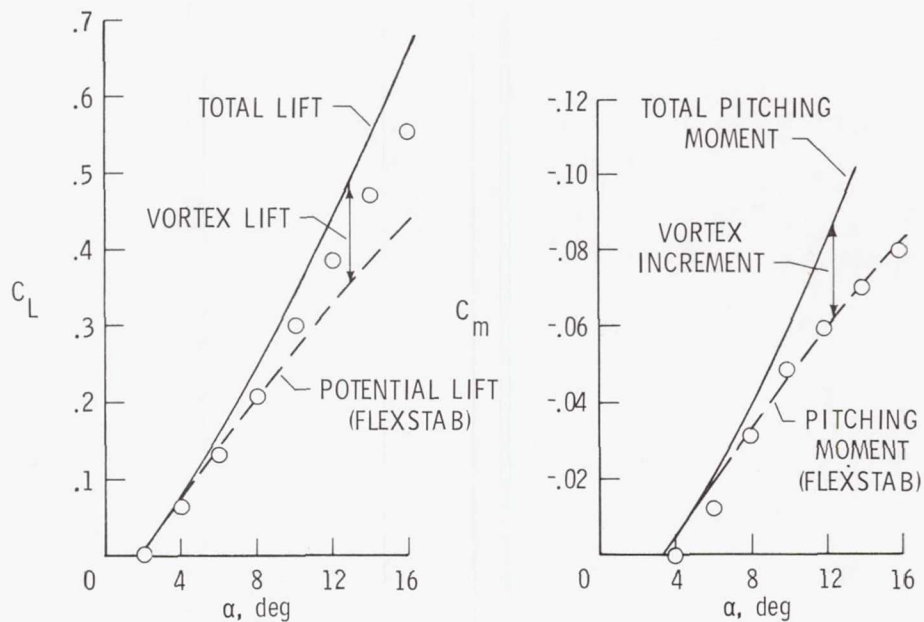
Figure 29.- Comparison of experiment with leading edge suction calculations of lift and pitching moment for twisted wing. M = 0.85.
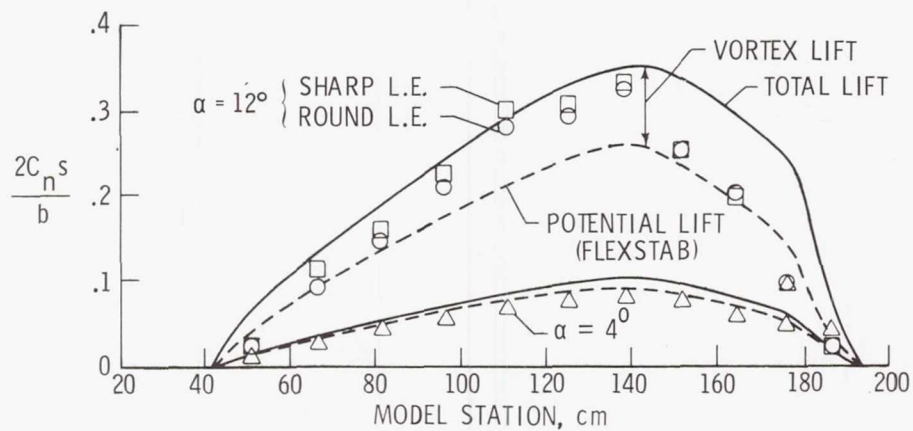
Figure 30.- Comparison of experiment with leading edge suction calculations of longitudinal load distribution for flat wing. M = 0.85.
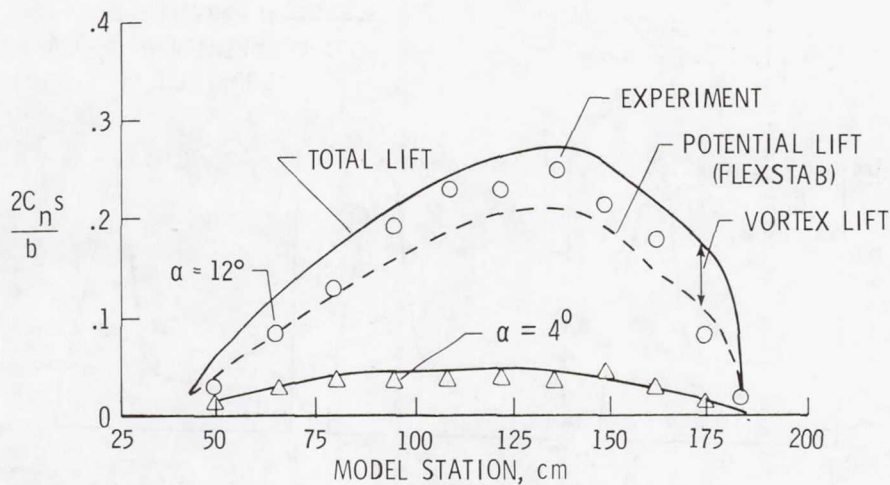
Figure 31.- Comparison of experiment with leading edge suction calculations of longitudinal load distribution for twisted wing. M = 0.85.
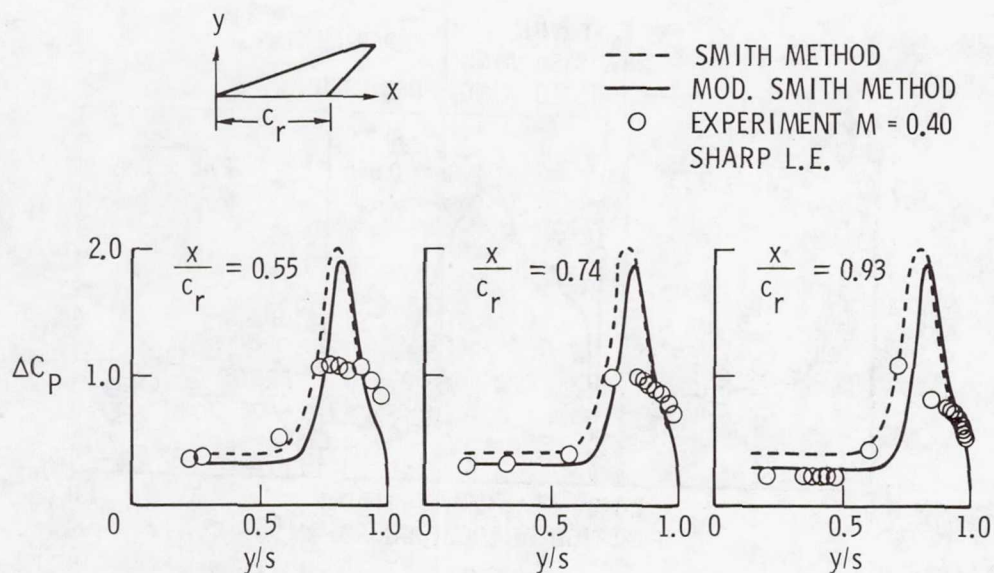
Figure 32.- Theory/experiment comparison of spanwise pressure distributions. Smith and modified Smith methods; $\alpha = 12^{\circ}$.
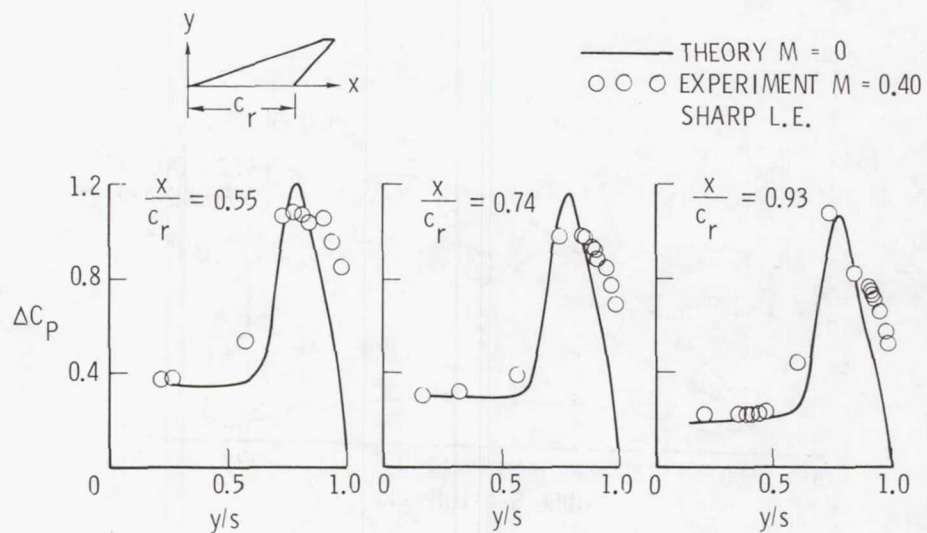
Figure 33.- Theory/experiment comparison of spanwise pressure distributions. Separated-flow panel method; $\alpha = 12^{\circ}$.
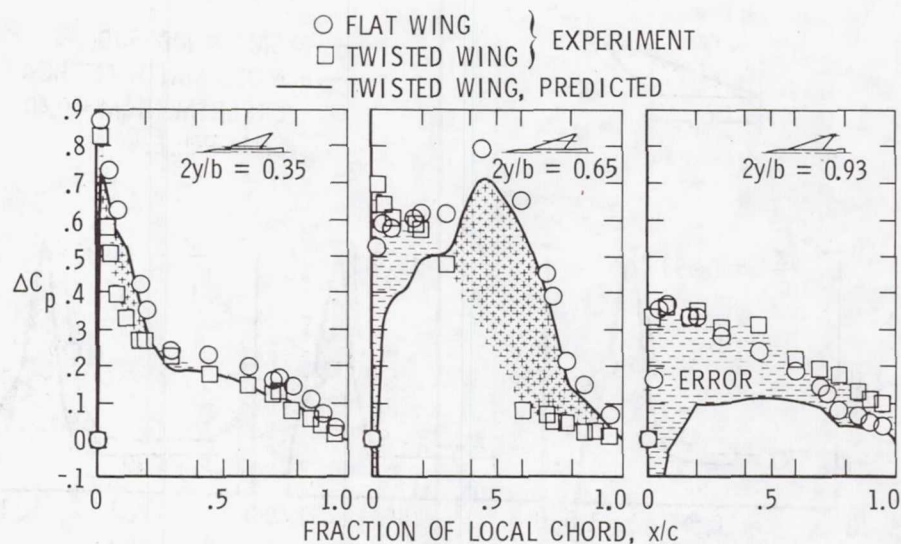
Figure 34.- Pseudo-aeroelastic predictions using linear FLEXSTAB program. $M = 0.85$; $\alpha = 8^{\circ}$.
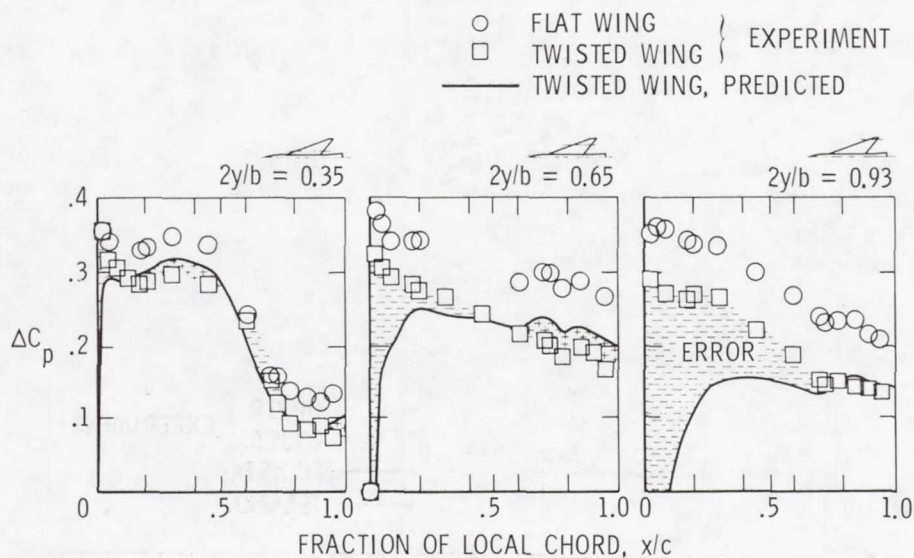
Figure 35.- Psuedo-aeroelastic predictions using linear FLEXSTAB program. M = 2.10; $\alpha = 8^o$.
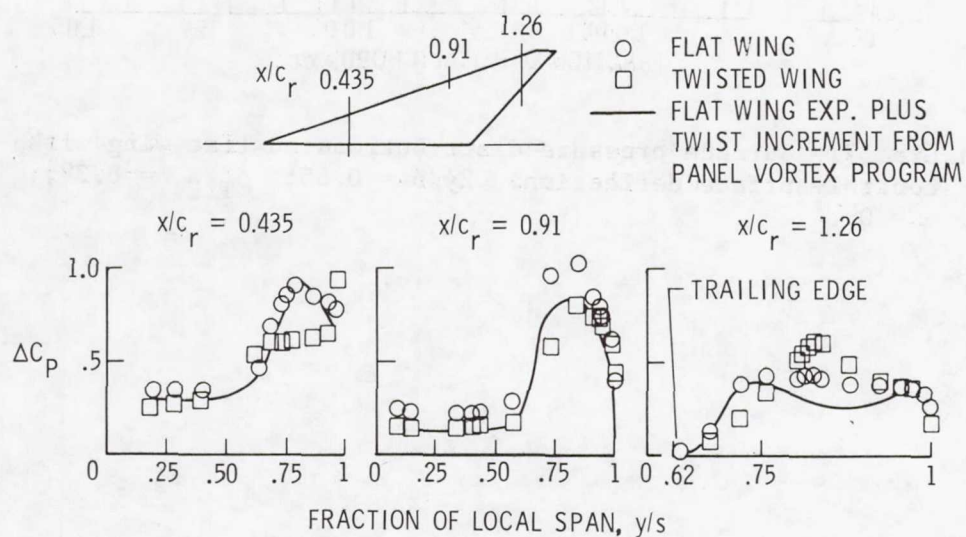
Figure 36.- Pseudo-aerolastic prediction using separated-flow panel program. M = 0.40; $\alpha = 12^o$.
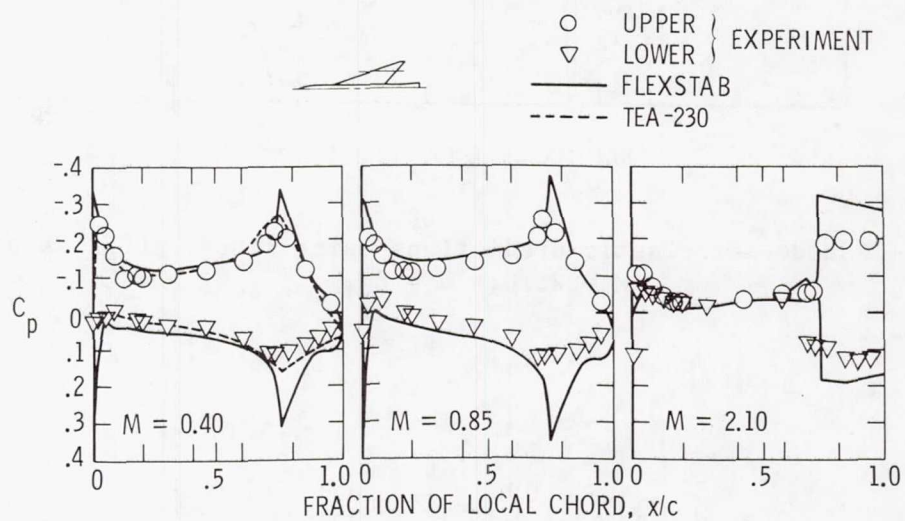
Figure 37.– Surface pressure distributions on flat wing with control-surface deflection. $2y/b = 0.65$; $\delta_{T.E.} = 8.3^o$; $\alpha = 0^o$.

RESULTS OF RECENT NASA RESEARCH ON LOW-SPEED AERODYNAMIC

CHARACTERISTICS OF SUPERSONIC CRUISE AIRCRAFT

Paul L. Coe, Jr.
NASA Langley Research Center

A. B. Graham
Old Dominion University

SUMMARY

The present paper summarizes the results of recent NASA research on the low-speed aerodynamic characteristics of supersonic cruise aircraft. The results indicate that the relatively low values of lift-curve slope produced by highly swept arrow wings, coupled with the low scrape angle of the fuselage, result in relatively low values of take-off and approach lift coefficients. Although acceptable low-speed performance is obtainable for the configurations currently under study, the low-speed deficiencies dictate a design compromise which prohibits such configurations from achieving maximum range potential. However, through the use of more efficient high-lift systems and the application of propulsive-lift concepts, it is possible to optimize the engine-airframe design for maximum range potential and also to provide good low-speed performance. The results also indicate that nose strakes provide significant improvements in directional stability characteristics and that the use of a propulsive lateral control system may provide a solution to problems associated with inherently low levels of lateral control.

INTRODUCTION

The NASA Langley Research Center has initiated a broad research program for the development of a technology base for aircraft capable of cruising efficiently at supersonic speeds. Such configurations typically incorporate a low-aspect-ratio, highly swept arrow wing which has been found to exhibit high levels of aerodynamic efficiency at design Mach numbers of 2.7. (See refs. 1 and 2.) However, these configurations have generally exhibited relatively poor low-speed performance and stability and control characteristics. (See refs. 3 and 4.) The present paper summarizes the results of recent studies conducted to explore means for providing supersonic cruise aircraft with improved low-speed aerodynamic characteristics in the areas of performance, longitudinal stability, lateral-directional stability, and lateral control.

C_L lift coefficient

C_l rolling-moment coefficient

C_{l_β} effective dihedral derivative

C_m pitching-moment coefficient

C_n yawing-moment coefficient

C_{n_β} static directional stability derivative

S   wing area

T   engine thrust

W   airplane weight

α angle of attack

β angle of sideslip

BLC   boundary-layer control

PLC   propulsive lateral control

LOW-SPEED PERFORMANCE

One of the fundamental considerations in the design of an efficient supersonic cruise vehicle is the sizing of the configuration with regard to wing area and installed thrust requirements. It is recognized that the sizing process involves considerable compromise and that low-speed performance plays a key part in the trade-off.

Presented in figure 1 is an illustration of the classical "thumb print" plot which shows the variation of range with installed thrust-weight ratio (T/W) and wing loading (W/S). From figure 1 it is seen that increased range can generally be obtained by reducing T/W and increasing W/S. However, as shown in figure 2, low-speed operational constraints related to approach speed and take-off field length requirements prohibit the attainment of the maximum range potential. Therefore, improvements in the low-speed performance, which allow the operational requirements to be satisfied with reduced values of T/W and increased values of W/S, will result in increases in range. Figure 3 illustrates the increase in range which has been provided by improved low-speed performance for a configuration currently under study. The NASA generated baseline Advanced Supersonic Technology Concept (designated the AST-100) is predicted to have a range of approximately 7413 km (4000 n. mi.). Improvements in the low-speed performance of this configuration have permitted the low-speed

124

operational requirements to be met with an increased wing loading and a reduced thrust-weight ratio. The resized vehicle (designated the AST-102) is predicted to have a range of approximately 8154 km (4400 n. mi.), which represents an increase of over 10 percent in vehicle range. From figure 3 it is seen that, based on the engine-airframe sizing studies, an additional increase in range of approximately 371 km (200 n. mi.) may be achieved — provided that further improvements in the low-speed performance (which offset the operation constraints) can be obtained. It is, of course, recognized that noise constraints are of critical importance and must also be considered in the final analysis of the engine-airframe sizing studies.

Figure 4 shows the variation of lift coefficient with respect to angle of attack for the baseline configuration in the approach condition. As would be expected, the low-aspect-ratio highly swept arrow wing results in a relatively low value of lift-curve slope, and the low fuselage scrape angle constrains the approach lift coefficient to values of only about 0.6. Furthermore, the relatively high attitude of the configuration, required to obtain the lift coefficient of 0.6, requires the use of a Concorde-type visor nose for improved pilot visibility and also requires an elongated landing-gear installation which results in a weight and volume penalty.

Langley Research Center is currently engaged in research studies intended to evaluate means for providing increased low-speed lift characteristics and thereby minimize or eliminate the low-speed deficiencies. These studies have included the use of propulsive-lift concepts as shown in figure 5. A photograph of a large-scale model of an advanced supersonic technology configuration, which was used to evaluate the propulsive-lift concepts, is shown mounted for tests in the Langley full-scale tunnel in figure 5. The propulsive-lift concepts investigated for improved high-lift performance include (1) the use of boundary-layer control for enhanced flap effectiveness and prevention of flow separation at high flap deflections, (2) the use of upper-surface blowing (USB) for additional circulation lift (this concept also has another advantage in that the trailing-edge flap system may be continuous, rather than the segmented system necessitated by the use of conventional underslung engines), and (3) the use of simple thrust vectoring schemes.

The potential benefits of the propulsive-lift concepts investigated are illustrated in figure 6, which shows the variation of lift coefficient with angle of attack for the concepts studied. The data for the baseline configuration are replotted from figure 4 for comparison. From these data it can be seen that both the thrust vectoring and upper-surface-blowing concepts can provide substantial increases in the low-speed lift capability. For example, both the thrust vectoring and USB concepts are seen to permit a lift coefficient of 0.7 to be obtained at a reduced angle of attack. The increase in lift coefficient (from 0.6 to 0.7) will permit the wing size to be reduced and allow the low-speed operational constraints to be met with an increase in wing loading. This, in turn, may allow the maximum range potential to be realized. Furthermore, the reduced attitude of the configuration may allow for a reduction in landing-gear length and may also eliminate the visor nose requirement, which represents a significant weight savings.

125

LONGITUDINAL STABILITY

The variation of pitching-moment coefficient with respect to angle of attack for the baseline AST configuration is presented in figure 7. As can be seen from figure 7, the configuration is intended to be flown with a slightly negative static margin (i.e., $\partial C_m / \partial C_L = 0.03$) during the low-speed phases of flight. The impact of the longitudinal instability on the handling qualities of the configuration and the requirements for stability augmentation are discussed in detail in reference 5. The primary concern, however, in the area of longitudinal stability is the nonlinear variation of C_m with α. As shown in figure 7, the basic airframe exhibits a marked nonlinear pitching-moment characteristic for angles of attack greater than about 6°. Results of flow visualization studies have indicated that this nonlinearity is associated with the formation of wing-apex vortices and also with the premature stall of the outboard wing panels. Previous studies of similar configurations have shown that deflection of wing-apex flaps is an effective means of delaying the angle of attack at which these vortices occur. Furthermore, these studies have shown that the use of a Krueger flap on the outboard wing panel is an effective means for providing well attached flow to substantially higher angles of attack. As can be seen from figure 7, when these surfaces are deployed on the current AST concept, the resulting variation of C_m with respect to α is essentially linear. It should be noted that the nonlinearity has a negligible impact on the configuration during normal approach conditions; however, in the gust upset condition, the nonlinearity of the pitching moment would require the longitudinal control surfaces to be sized to provide pitch trim for approximately a 30-percent increase in pitching moment. This would, of course, require a significantly larger control surface, which would penalize the supersonic cruise performance.

LATERAL-DIRECTIONAL STABILITY

Figure 8 presents the variation of the static directional stability derivative C_{n_β} and the effective dihedral derivative C_{l_β} with angle of attack. These data show that in the normal operational angle-of-attack range, the configuration exhibits relatively low values of C_{n_β} and high values of $-C_{l_\beta}$. As discussed in reference 5, this combination of low C_{n_β} and high $-C_{l_\beta}$ results in relatively poor lateral-directional handling qualities. Furthermore, the high level of $-C_{l_\beta}$ is found to require excessive lateral-control capabilities in order to meet established crosswind landing criteria. Therefore, research is currently being conducted in order to obtain increased levels of C_{n_β} and reduced levels of $-C_{l_\beta}$.

It is, of course, recognized that increased directional stability could be provided by increasing the size of the vertical tail; however, this modification would penalize the supersonic cruise performance. Therefore, the use of nose strakes (currently in use on the Concorde) has been investigated. Figure 9 shows the favorable effect of the nose strakes on C_{n_β}. The data indicate large increases in directional stability due to the strakes. For example, at the approach angle of attack of 8°, the strakes approximately double the value of C_{n_β}. It should be noted that the particular nose strakes investigated were

126

simply intended to determine if increased levels of C_{n_β} could be obtained; unfortunately, these strakes also produced a slight pitchup tendency. However, it is considered that with careful attention to strake detail, increased levels of C_{n_β} can be provided without the attendant pitchup characteristics.

In addition to relatively low levels of C_{n_β}, the configuration may also be subject to large out-of-trim moments. Figure 10 shows that the baseline configuration exhibited large asymmetric yawing-moment coefficients at high angles of attack during wind-tunnel tests of several models. Previous studies conducted at Langley (see, for example, ref. 6) have shown that these asymmetric yawing moments are due to the formation of asymmetrically disposed vortices on long slender fuselage forebodies. For the present configuration the significance of these asymmetries is particularly critical in that at high angles of attack, the magnitude of the yawing moment produced at $\beta = 0^\circ$ is found to be in excess of the directional control power. (See fig. 10.) Such asymmetries are probably sensitive to Reynolds number; however, reference 7 indicates that this phenomenon may persist at Reynolds numbers corresponding to those of the full-scale aircraft. As shown in figure 10, the use of the previously discussed nose strakes is an effective means for eliminating these asymmetric yawing moments.

Previous investigations (see ref. 8) have indicated that reductions in $-C_{l_\beta}$ may be obtained by increasing the load on the inboard portion of the wing. Figure 11 shows the variation of C_L with α and the corresponding variation of C_{l_β} with C_L for two trailing-edge flap deflections. As expected, increasing the trailing-edge flap deflection from 0° provides an increase in lift coefficient at a given angle of attack and also provides a substantial reduction in $-C_{l_\beta}$ at a given lift coefficient. Additional results obtained for this configuration indicate that the reduction in $-C_{l_\beta}$ is primarily associated with the reduction in angle of attack at which the given lift coefficient was obtained and that the level of C_{l_β} appears to be essentially independent of the spanwise variation of the deflection of the trailing-edge flap segments. Although further study is required to validate this conclusion, the data of figure 11 indicate that if further reductions in the operational angle of attack can be obtained (for example with the use of propulsive-lift concepts), it may be possible to provide further reductions in $-C_{l_\beta}$.

LATERAL CONTROL

As mentioned previously, the high levels of effective dihedral produced by highly swept arrow wings require an excessive amount of lateral control power in order to satisfy established crosswind landing criteria. Figure 12 illustrates the severity of the problem for the baseline configuration. The solid curve presented in figure 12 is the amount of lateral control required in order to obtain lateral trim with 10° of sideslip. The dashed curve of figure 12 is the amount of lateral control currently available for the configuration. The significant point brought out by the data of figure 12 is that at the normal approach condition the amount of lateral control required for the NASA baseline configuration is significantly in excess of the control currently available.

In light of these considerations Langley is exploring means for providing increased lateral control capabilities. One promising concept employs propulsive lateral control (PLC) nozzles as shown in figure 13. With the propulsive lateral control system, a portion of the nozzle exhaust flow is vented over the trailing-edge flap during the low-speed phases of flight. Recent studies have shown that this arrangement provides levels of additional circulation lift which are comparable with the USB concept. In addition, the arrangement allows increased lateral control to be obtained by management of the additional circulation lift. This increase in control is accomplished by rotating the slider block system shown in the sketch of figure 13. With the slider block in the closed position, the exhaust flow is prevented from flowing over the trailing-edge flap segments, and hence, additional circulation lift is not generated on the appropriate wing panels. Recent studies indicate that this arrangement will provide approximately a 25-percent increase in roll control. It should be noted that even greater increases in roll control can be provided by combining differential thrust vectoring with the PLC concept.

The impact of the increased lift and increased roll control capability provided by the propulsive lateral control nozzle concept is illustrated in figure 14. As can be seen in figure 14, the increase in lift from this concept permits a reduction in angle of attack for the approach condition, which, when coupled with the increase in lateral control, provides the configuration with sufficient lateral control to meet the crosswind landing criteria at the design approach lift coefficient.

CONCLUDING REMARKS

The results of recent research on the low-speed aerodynamic characteristics of supersonic cruise aircraft indicate that improved low-speed performance can be achieved with more efficient high-lift systems and the application of propulsive-lift concepts. The improved low-speed performance allows the configuration to be configured so as to achieve its maximum range potential. The results also indicate that significant improvements can be obtained in the lateral-directional characteristics with the use of nose strakes and by the introduction of propulsive lateral control concepts.

REFERENCES

1. Morris, Odell A.; and Fournier, Roger H.: Aerodynamic Characteristics at
   Mach Numbers 2.30, 2.60 and 2.96 of a Supersonic Transport Model Having A
   Fixed, Warped Wing. NASA TM X-1115, 1965.

2. Morris, Odell A.; and Patterson, James C., Jr.: Transonic Aerodynamic
   Characteristics of a Supersonic Transport Model With A Fixed, Warped Wing
   Having 74° Sweep. NASA TM X-1167, 1965.

3. Shivers, James P.; McLemore, H. Clyde; and Coe, Paul L., Jr.: Low-Speed
   Wind Tunnel Investigation of a Large-Scale Advanced Arrow Wing Supersonic
   Transport Configuration with Engines Mounted Above the Wing for Upper-
   Surface Blowing. NASA TM X-72761, 1975.

4. Coe, Paul L., Jr.; McLemore, H. Clyde; and Shivers, James P.: Effects of
   Upper-Surface Blowing and Thrust Vectoring on Low-Speed Aerodynamic
   Characteristics of a Large-Scale Supersonic Transport Model. NASA
   TM X-72792, 1975.

5. Grantham, William D.; Nguyen, Luat T.; Neubauer, M. J., Jr.; and Smith,
   Paul M.: Simulator Study of the Low-Speed Handling Qualities of a Super-
   sonic Cruise Arrow-Wing Configuration During Approach and Landing. SCAR
   Conference, Hampton, VA, Nov. 1976, pp. 100-120. (Paper no. 11 of this
   compilation.)

6. Coe, Paul L., Jr.; Chambers, Joseph R.; and Letko, William: Asymmetric
   Lateral-Directional Characteristics of Pointed Bodies of Revolution at
   High Angles of Attack. NASA TN D-7095, 1972.

7. Chapman, Gary T.; Keener, Earl R.; and Malcolm, Gerald N.: Asymmetric
   Aerodynamic Forces on Aircraft Forebodies at High Angles of Attack — Some
   Design Guides. Stall/Spin Problems of Military Aircraft, AGARD-CP-199,
   June 1976, paper no. 12.

8. Lockwood, Vernard E.: Effect of Trailing Edge Flap Deflection on the
   Lateral and Longitudinal-Stability Characteristics of a Supersonic
   Transport Model Having a Highly-Swept Arrow Wing. NASA TM X-71936, 1974.
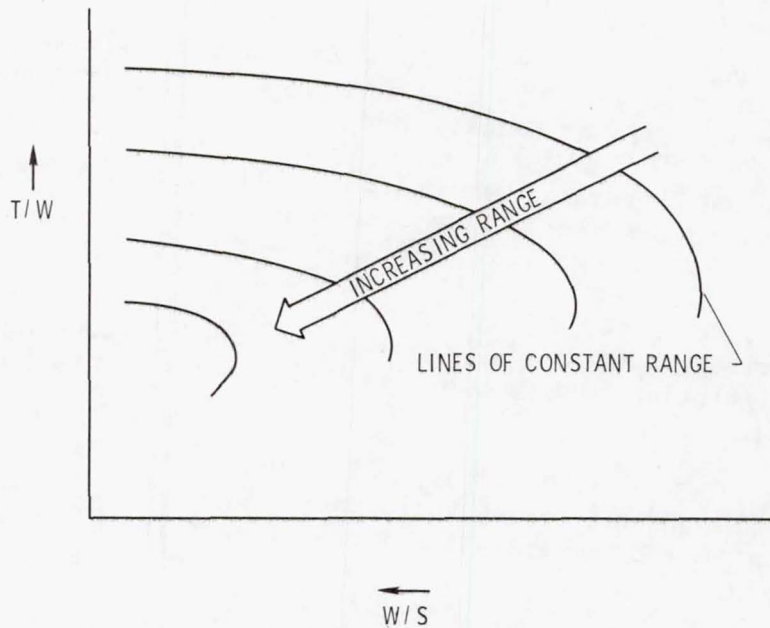
Figure 1.- Variation of range with T/W and W/S.
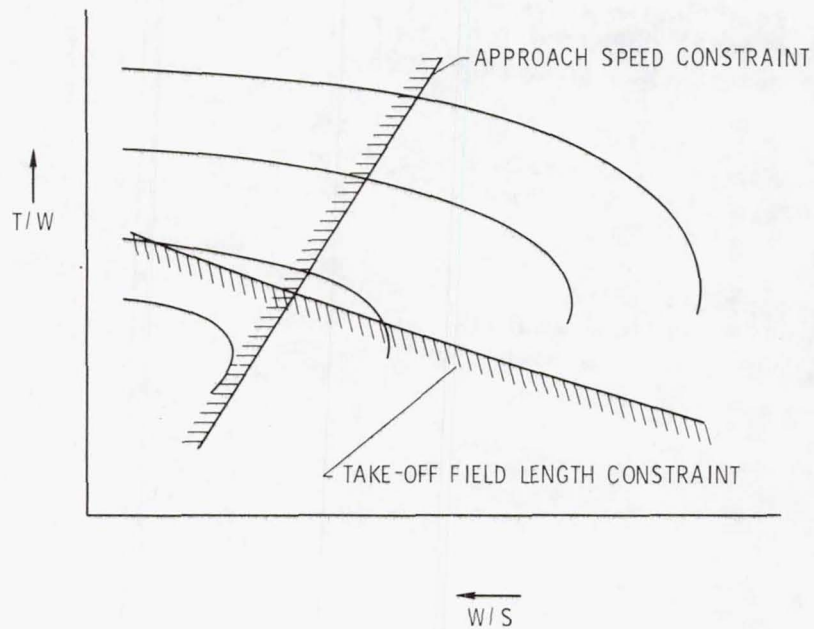
Figure 2.- Low-speed operational constraints.
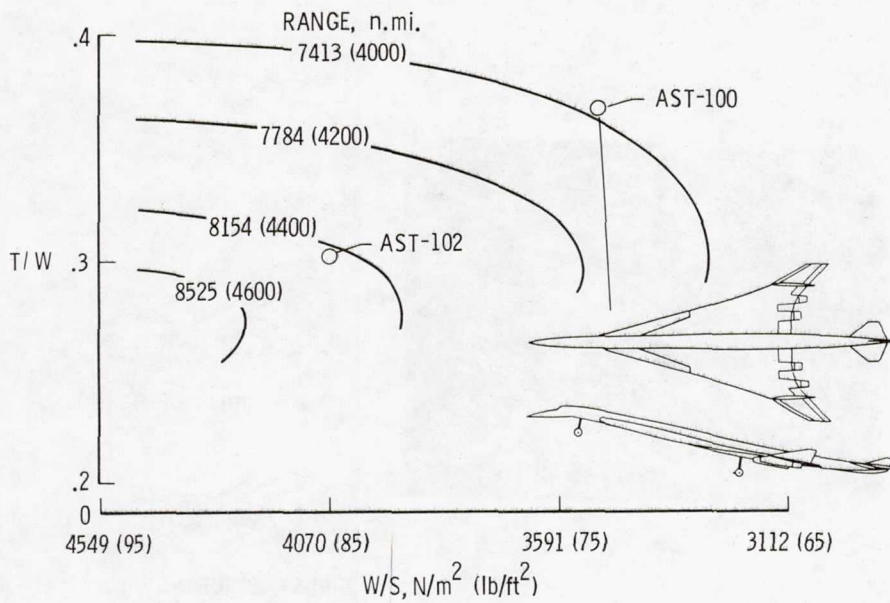
Figure 3.- Increased range provided by
improved low-speed performance.
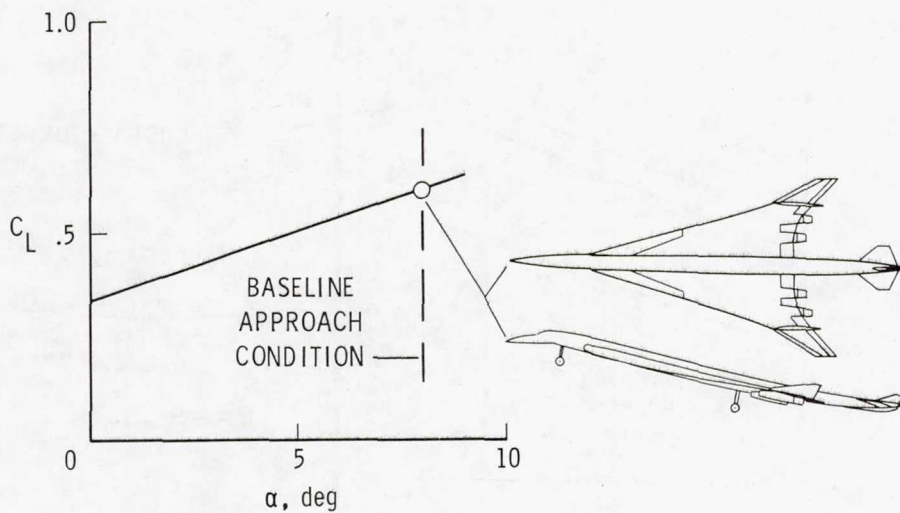
Figure 4.- Variation of C_L with α.

131
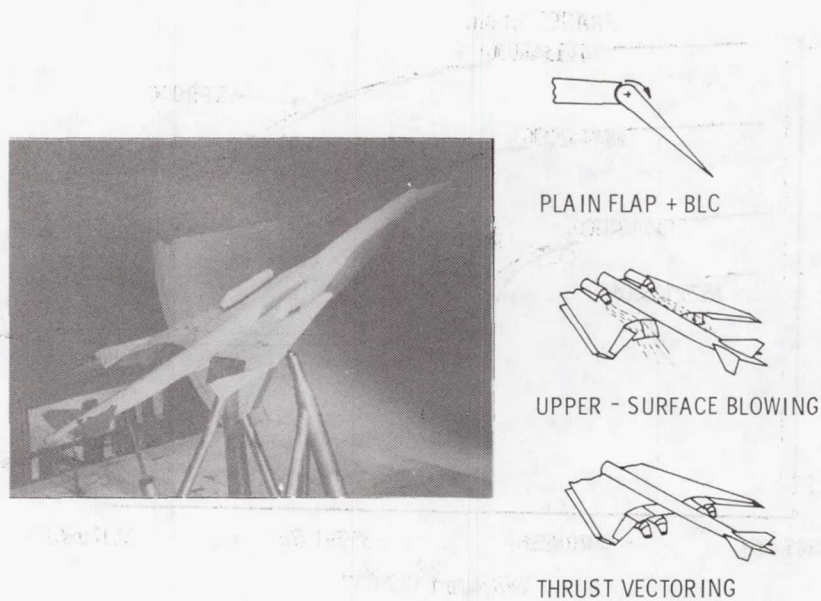
Figure 5.- Propulsive-lift concepts investigated.
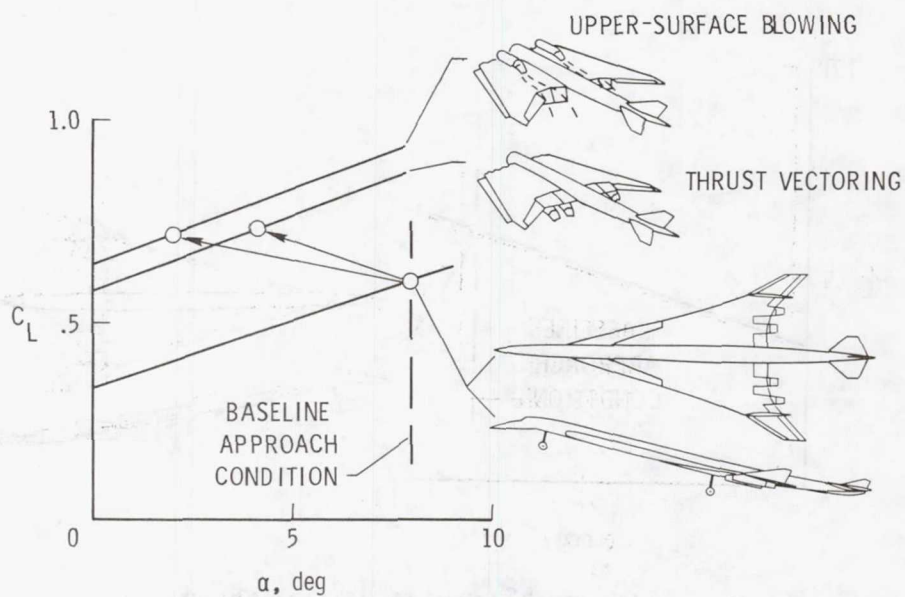
Figure 6.- Potential benefits of propulsive-lift concepts.
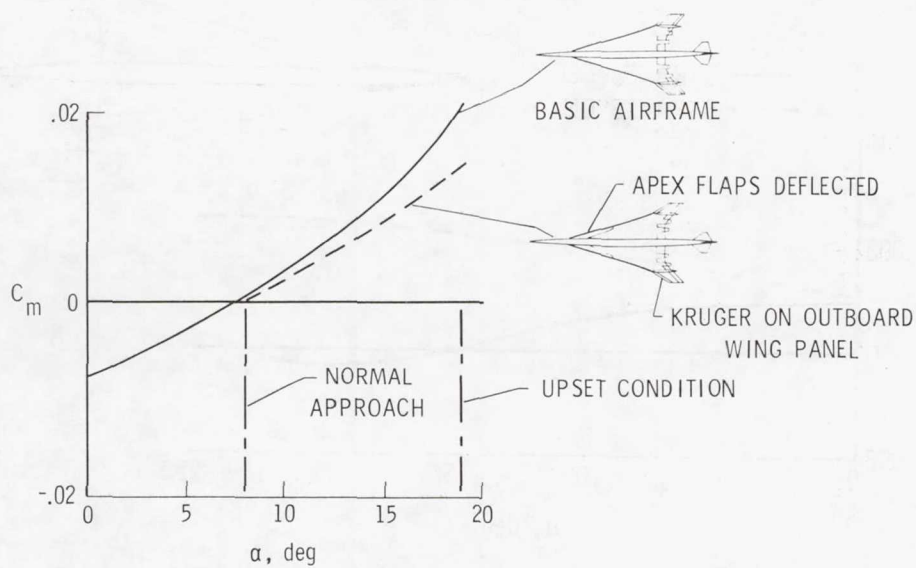
Figure 7.- Variation of C_m with α.
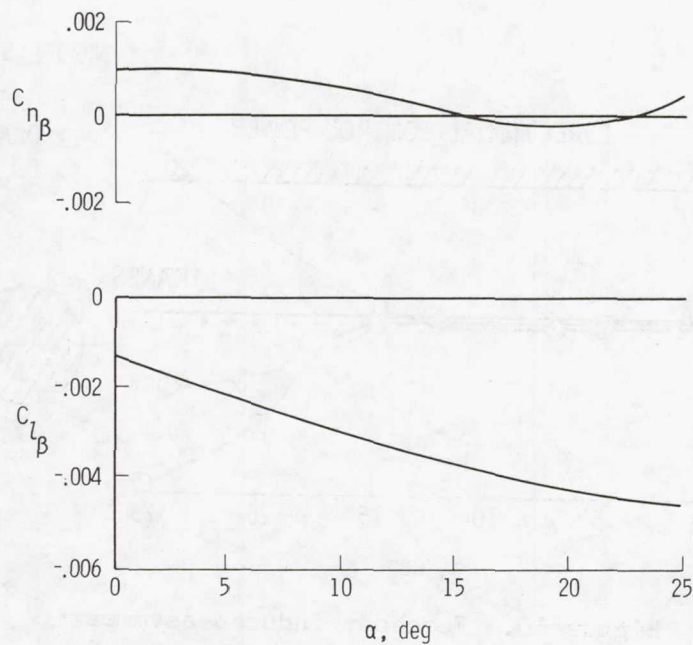
Figure 8.- Static lateral-directional
stability characteristics.

133
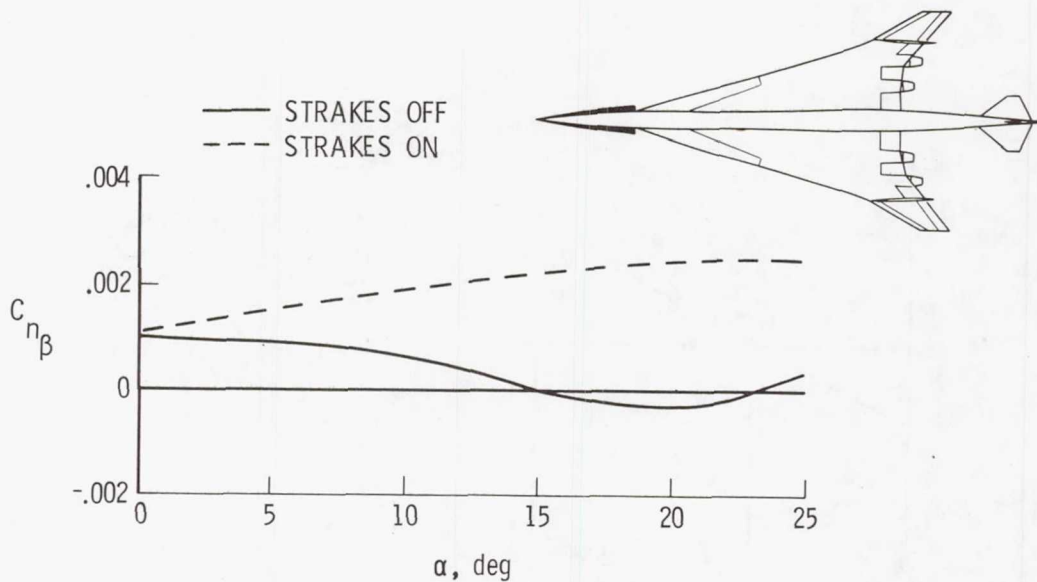
Figure 9.- Effect of nose strakes on C_{n_β}.
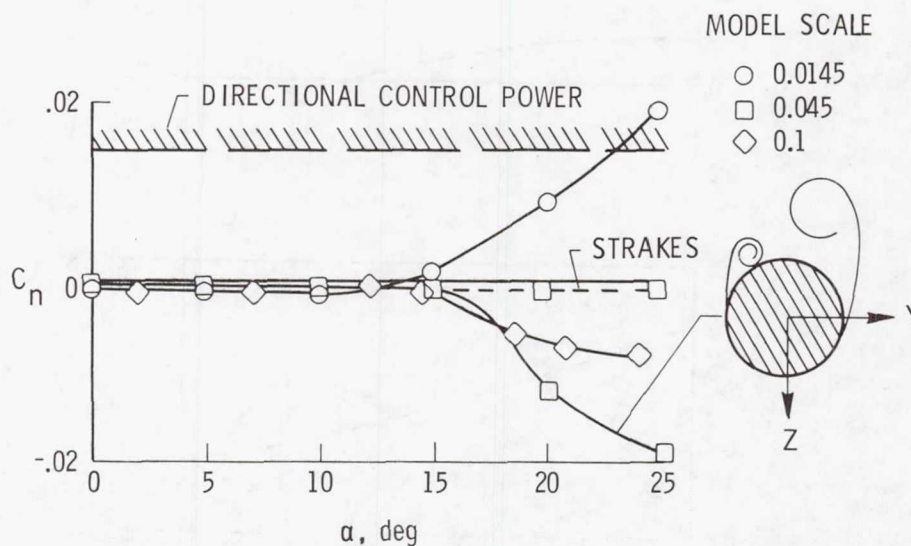
Figure 10.- Forebody-induced asymmetric
yawing-moment coefficient. $\beta = 0^o$.
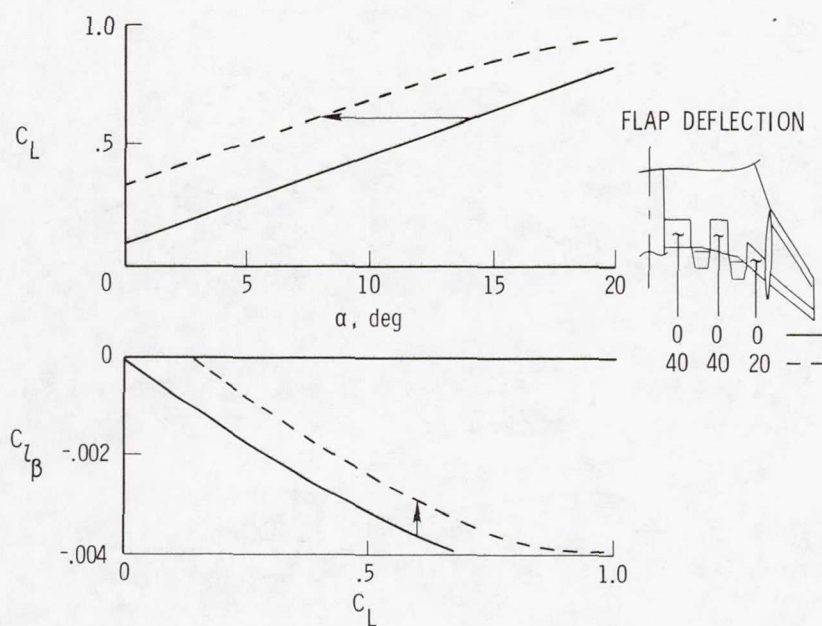
Figure 11.- Variation of C_{l_β} with C_L.
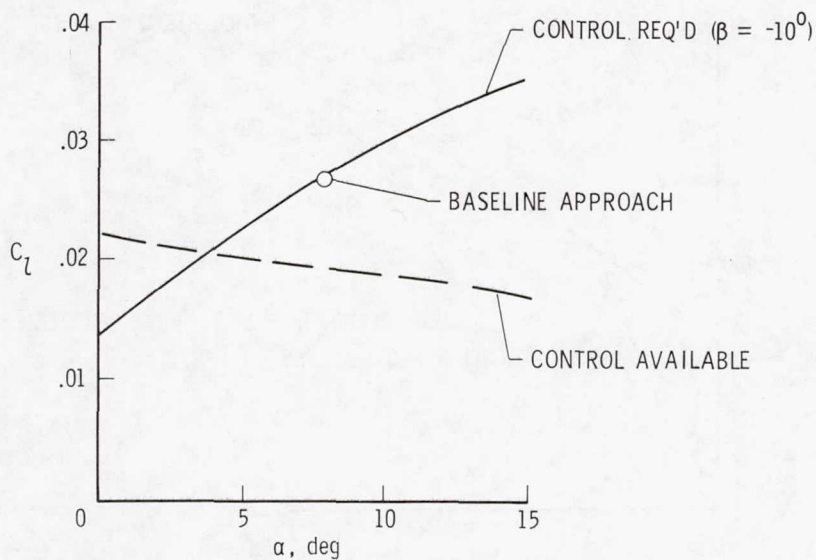
Figure 12.- Lateral control requirements for crosswind landing.

135
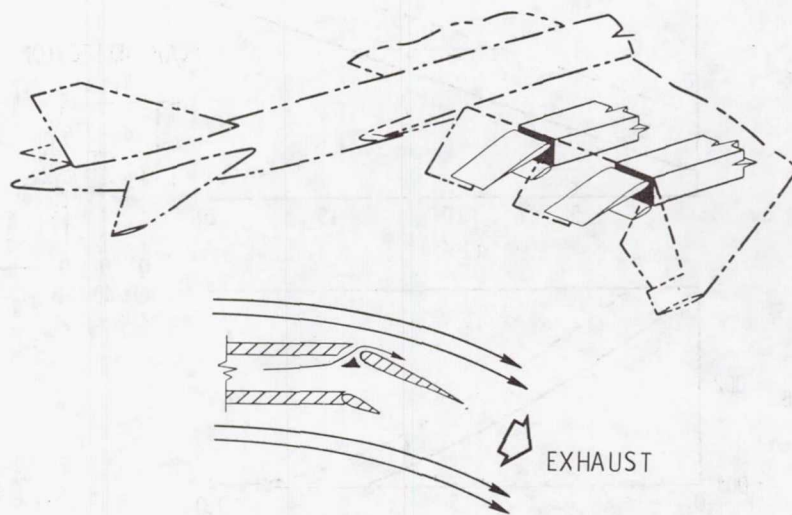
Figure 13.- Sketch of propulsive lateral control nozzle.
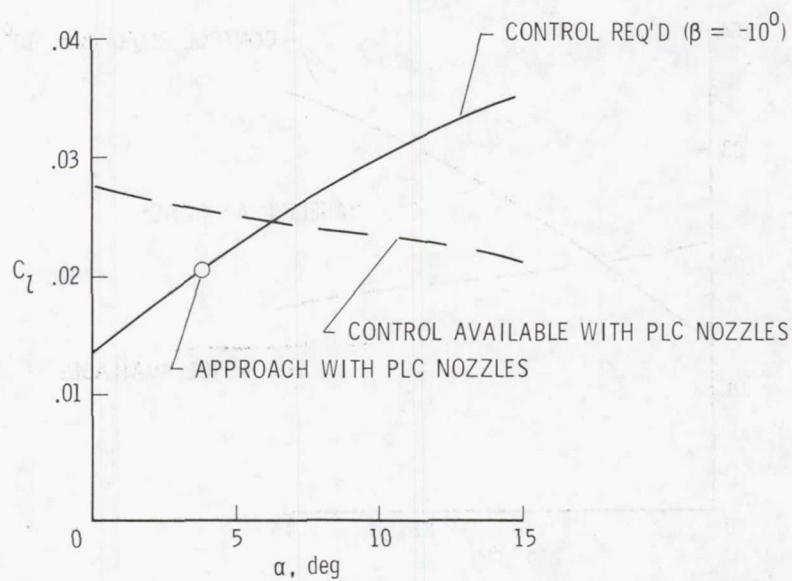
Figure 14.- Lateral control requirements
for configuration with propulsive
lateral control nozzles.

UPPER SURFACE NACELLE INFLUENCE ON SCAR AERODYNAMIC

CHARACTERISTICS AT TRANSONIC SPEEDS

Charles E. Mercer and George T. Carson, Jr.
NASA Langley Research Center

SUMMARY

An investigation has been conducted in the Langley 16-foot transonic tunnel to determine the influence of upper surface nacelles on the aerodynamic characteristics of a SCAR configuration at Mach numbers from 0.6 to 1.2. The arrow-wing transport configuration with detached engines located over the wing to produce upper surface exhaust flow effects was tested at angles of attack from $-4°$ to $8°$ and jet total-pressure ratios from 1 (jet off) to approximately 10. Wing tip leading edge flap deflections of $-10°$ to $10°$ were tested with the wing-body configuration only (no nacelles). Tests were made with various nacelle chordwise, spanwise, and vertical height locations over the Mach number, angle of attack, and jet total-pressure ratio ranges. The results show that deflecting the wing tip leading edge flap from $0°$ to $-10°$ increased maximum lift to drag ratio by 1.0 at subsonic speeds. Installation of upper surface nacelles (no wing/nacelle pylons) increased the wing-body pitching moment at all Mach numbers and decreased the drag of the wing-body configuration at subsonic Mach numbers. Jet exhaust interference effects were negligible.

INTRODUCTION

Extensive research programs have been conducted to define and meet the design requirements of a commercially acceptable supersonic cruise transport aircraft. The highly swept arrow-wing supersonic transport configuration with engine nacelles mounted under the wing has been shown to be aero-dynamically efficient at transonic and supersonic speeds. However, this type configuration exhibits poor takeoff and landing performance (refs. 1-4). Tests conducted in low speed wind tunnels have shown that blowing the jet exhaust over the upper surface of the wing provides an effective means for providing the high lift required for improved takeoff and landing performance (ref. 5).

The purpose of the present investigation was to determine the influence of upper surface nacelle exhaust flow on the longitudinal aerodynamic characteristics of a SCAR configuration at transonic speeds. The tests were conducted in the Langley 16-foot transonic tunnel at Mach numbers up to 1.2 and angles of attack from $-4°$ to $8°$. Jet total-pressure ratio was varied from 1 (jet off) to approximately 10. Three different chordwise, spanwise, and vertical height locations of the nacelles were investigated.

SYMBOLS

b	wing span
C_D	drag coefficient, Drag/qS
C_L	lift coefficient, Lift/qS
C_m	pitching-moment coefficient, Pitching moment/$qS\bar{c}$
C_p	pressure coefficient, $\dfrac{\Delta p}{q}$
c	local geometric chord of wing at any given spanwise location
$\bar{c}$	mean geometric chord of reference wing
D_e	nozzle exit diameter
L/D	lift to drag ratio
M	free-stream Mach number
NPR	nozzle pressure ratio
p	local static pressure
q	free-stream dynamic pressure
S	reference wing area
x	axial distance from wing leading edge to nacelle exit at any given spanwise station
y	lateral distance from body center plane to nacelle center plane perpendicular to body center plane
z	vertical height of nacelle centerline relative to wing leading edge at given spanwise station
α	angle of attack of model reference line
δ_F	wing-tip flap deflection angle relative to model reference line (positive leading edge up)
Δp	local static pressure minus free-stream static pressure

138

APPARATUS AND METHODS

Wind Tunnel

The 16-foot transonic tunnel, which has an octagonal test section with eight longitudinal slots, is an atmospheric wind tunnel with continuous air exchange for cooling. It has a remotely controlled Mach number range from 0 to 1.3. The average Reynolds number per meter varies from 9.71×10^6 at $M = 0.5$ to 12.6×10^6 at $M = 1.3$.

Model Description

A photograph of the model installed in the tunnel test section is shown in figure 1. A sketch of the SCAR model and air-powered sting system is presented in figure 2(a). A three-view computerized sketch showing nacelle reference planes is shown in figure 2(b). The model consisted of an arrow-wing-body combination having an overall length of 141.61 cm and a wing span of 84.66 cm. The fixed wing was highly swept back, twisted, and cambered with reflexed trailing edge. The main wing section has a leading edge sweep of 75° and the wing tips were swept 60°. The wing tips were detachable from the main wing. Wing tips were available with both positive and negative leading edge flap deflections. Twin vertical tails were located near the main wing/wing-tip juncture. Two engine nacelles were pylon-mounted over the wing as shown in figure 2(a). The engine nacelles were not attached to the wing-body configuration and no wing/nacelle pylon was provided to simulate this attachment. The nacelle geometry was configured to simulate a turbofan-jet engine operating in an afterburning-power mode. The nacelle support was designed to independently support the two nacelles above the wing-body configuration while providing the capability to vary the location of each nacelle relative to the configuration. The support system also provided the means for supplying high-pressure air to each engine nacelle.

Instrumentation and Data Reduction

Aerodynamic forces and moments on the wing-body configuration were measured with a six-component internal strain gage balance. Forces and moments on the nacelles were not measured for these tests. The upper surface of the left wing and lower surface of the right wing were pressure-instrumented with static pressure orifices. To insure a turbulent boundary layer over the wing-body configuration and nacelles, transition trips were applied to each of these components.

This investigation generally covered a Mach number range from 0.6 to 1.2. Angle of attack was varied from -4° to 8° and jet total-pressure ratio was varied from 1 (jet off) to approximately 10 depending on Mach number.

RESULTS

Wing-Tip Leading Edge Flap Effects

Presented in figure 3 are the effects of deflection of wing tip leading edge flaps on lift to drag ratio. These effects are for the wing-body configuration only without the influence of the nacelles. Lift to drag ratio as a function of lift coefficient is shown only for Mach 0.9. Similar results were obtained for other Mach numbers. Maximum lift to drag ratio occurs at a lift coefficient of 0.15 at all Mach numbers. Also shown in figure 3 is the variation of maximum lift to drag ratio as a function of flap angle for M = 0.6, 0.9, and 1.2. Leading edge flap deployment from 0° to -10° (leading edge down) increased maximum L/D by 1.0 at subsonic Mach numbers and by 0.5 at M = 1.2. This increase in $(L/D)_{max}$ is primarily a result of increased lift on the wing tips since other data, which are not presented in this report, show no significant effect on drag or pitching moment due to flap deflection.

Nacelle Installation Interference Effects

Aerodynamic force and moment characteristics of the wing-body configuration with and without interference effects due to nacelle installation (jet off) are presented in figure 4. Data are presented for Mach numbers of 0.9 and 1.2 which represent subsonic cruise and low supersonic flight conditions; data at M = 0.9 are typical of other subsonic Mach numbers. The unstable pitching moment coefficient, shown in figure 4, results from the model not having the horizontal and vertical tails which are required to balance the longitudinal loads of the aircraft (reference 1). Nacelle installation effects increased the wing-body pitching moment at all Mach numbers investigated. Installation of the over-the-wing nacelles reduced wing-body drag at subsonic speeds, but increased drag at M = 1.2. Little effect of nacelle installation was observed on airplane lift.

Figure 5 presents typical wing pressure distributions with and without the presence of the nacelles (jet off). Pressure coefficients are presented for Mach numbers of 0.9 and 1.2 and angles of attack of 0 and 4 degrees. Wing pressures in the proximity of the jet nacelles appear to be more positive over both the upper and lower surfaces of the wing at M = 0.9. Although the nacelle/support installation influenced the upper and lower wing surfaces at subsonic speeds, little effect due to the nacelle/support installation was observed on the wing lower surface pressure at M = 1.2.

The effect of jet operation on the SCAR aerodynamic characteristics is presented in figure 6 for M = 0.9 and M = 1.2. Jet exhaust flow was varied from jet off conditions (NPR ≈ 1) up to a jet total-pressure ratio of about 10. Jet interference effects on the wing appear to be negligible at all Mach numbers and nacelle locations investigated. This result indicates that the jet plume did not wash the wing upper surface and that there was no overall alteration of the wing flow field due to jet operation. Pressure distributions, shown in figure 7, show pronounced local effects from jet

operation (see $y/(b/2) = 0.450$ and 0.555 in figure 7(a) for example). These pressure perturbations appear to be self-compensating, however, such that little effect of jet operation occurs in the total wing-body forces and moments as shown in figure 6.

Nacelle Chordwise Location

The effect on the longitudinal aerodynamic coefficients due to chordwise movement of the nacelles (along the wing semispan station $y/(b/2) = 0.46$) is presented in figure 8. A chordwise nacelle location near the wing leading edge ($x/c = -0.17$ and 0.10) had little or no effect on the wing-body force and moment coefficients. However, as the jet nacelle approaches the wing trailing edge ($x/c = 0.82$), an increase in lift and a corresponding stabilizing effect on pitching moment are seen to occur at subsonic speeds. This indicates that a nacelle location near the wing trailing edge results in a beneficial influence on the wing flow field. However, as a result of increased drag, maximum lift to drag ratio was decreased by 1.0 at subsonic speeds when the nacelle was located near the wing trailing edge. At $M = 1.2$, nacelle chordwise location had generally smaller effects on wing-body forces and moments and has a negligible effect on lift to drag ratio.

Nacelle Spanwise and Vertical Location Effects

Shown in figures 9 and 10 are the effects of nacelle spanwise and vertical height locations on the wing-body longitudinal aerodynamic characteristics for Mach numbers of 0.9 and 1.2. Neither lateral or vertical movement of the jet nacelles had any significant influence on the wing-body force or moment coefficients. Examination of wing pressure distributions (not shown herein) indicates that either lateral or vertical movement of the jet nacelles resulted in localized pressure gradients with self-compensating effects on forces and moments.

Comparison With Theory

Comparisons between the experimental pressure coefficients on the wing and those predicted by the method of Woodward (reference 6) are shown on figure 11 for a Mach number of 0.9. Comparison appears to be poor mainly due to theory not accounting for vortex flow which apparently is forming on wing leading edge.

The predicted lift curve slope is similar to the measured values but at a slightly higher level as shown by figure 12.

141

CONCLUDING REMARKS

An investigation has been conducted in the Langley 16-foot transonic tunnel to determine the influence of upper surface nacelles on a supersonic cruise aircraft at Mach numbers up to 1.2. Results from this study indicate the following:

1. Wing tip leading edge flap deployment of -10° increased maximum lift to drag ratio by 1.0 at subsonic speeds.

2. Upper surface nacelle installation effects increased the wing-body pitching moment at all Mach numbers and decreased drag at subsonic Mach numbers. Jet exhaust interference effects were negligible at all conditions tested.

3. At subsonic speeds, chordwise movement of the over-the-wing nacelles, from a forward to an aft location, resulted in increased lift but a reduction of lift to drag ratio as a result of increased drag.

4. Spanwise and vertical nacelle position had negligible effects on wing-body aerodynamic characteristics.

142

REFERENCES

1. Morris, Odell P.; and Fournier, Roger H.: Aerodynamic Characteristics at
   Mach Numbers 2.30, 2.60, and 2.96 of a Supersonic Transport Model
   Having a Fixed, Wrapped Wing. NASA TM X-1115, 1976.

2. Harris, Roy V., Jr.; and Corlett, William A.: Transonic Aerodynamic
   Characteristics of a Supersonic Transport Model with Variable-Sweep
   Auxiliary Wing Panels, Outboard Tail Surfaces, and a Design Mach Number
   of 2.6. NASA TM X-1075, 1976.

3. Henderson, William P.: Low-Speed Aerodynamic Characteristics of a
   Supersonic Transport Model with a Highly Swept, Twisted and Cambered,
   Fixed Wing. NASA TM X-1249. 1966.

4. Henderson, William P.: A Low-Speed Longitudinal Stability Improvement
   Study on a Highly Swept Supersonic Transport Configuration. NASA TM X-
   1071, 1965.

5. Shivers, James P.; McLemore, H. Clyde; and Coe, Paul L., Jr.: Low-Speed
   Wind-Tunnel Investigation of a Large-Scale Advanced Arrow Wing
   Supersonic Transport Configuration With Engines Mounted Above the Wing
   for Upper-Surface Blowing. NASA TN D-8350, 1976.

6. Woodward, F. A.: An Improved Method for the Aerodynamic Analysis of
   Wing-Body-Tail Configuration in Subsonic and Supersonic Flow.
   NASA CR-2228, May 1973.
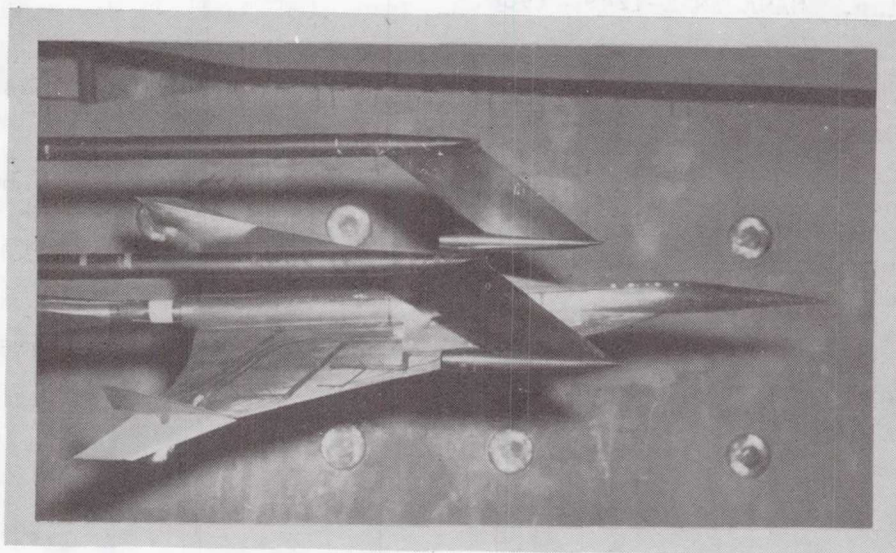
Figure 1.- Model in Langley 16-foot transonic tunnel.

(a) SCAR model and air-powered sting system.

JET NACELLE LOCATIONS

x/c	$y/(b/2)$	z/D_e
-0.170	0.462	2.04
.102	.462	2.04
.820	.462	2.04
.308	.249	2.04
-0.170	.462	2.04
-0.686	.580	2.04
-0.170	.462	2.25
-0.170	.462	2.04
0.170	.462	1.59

FRONT VIEW

TOP VIEW

LEFT SIDE VIEW
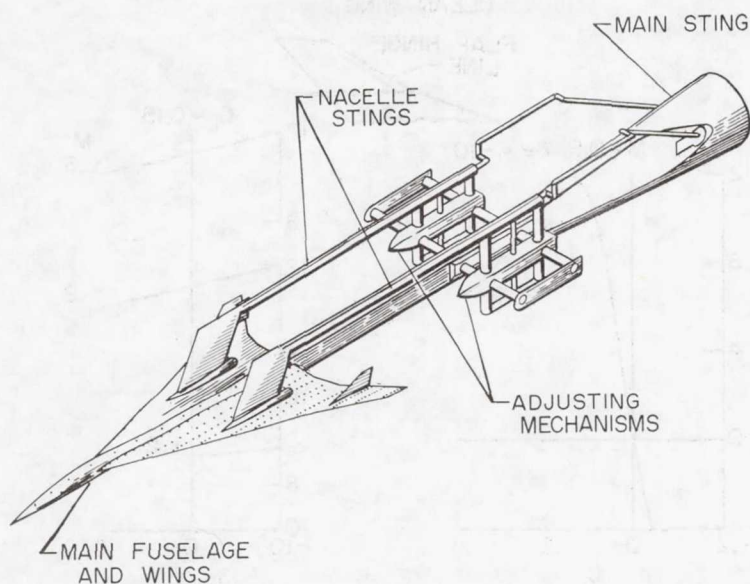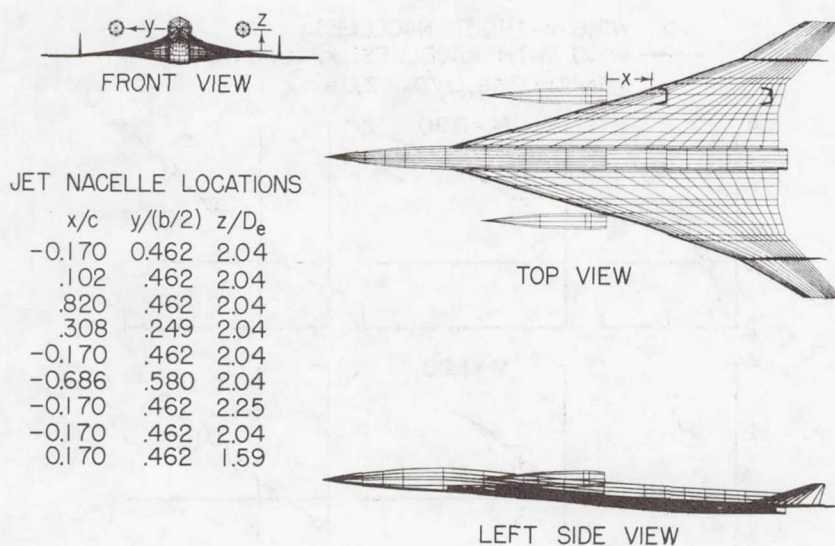
(b) Computerized three-view sketch of model with jet nacelle locations.

Figure 2.- Sketches of model.

145
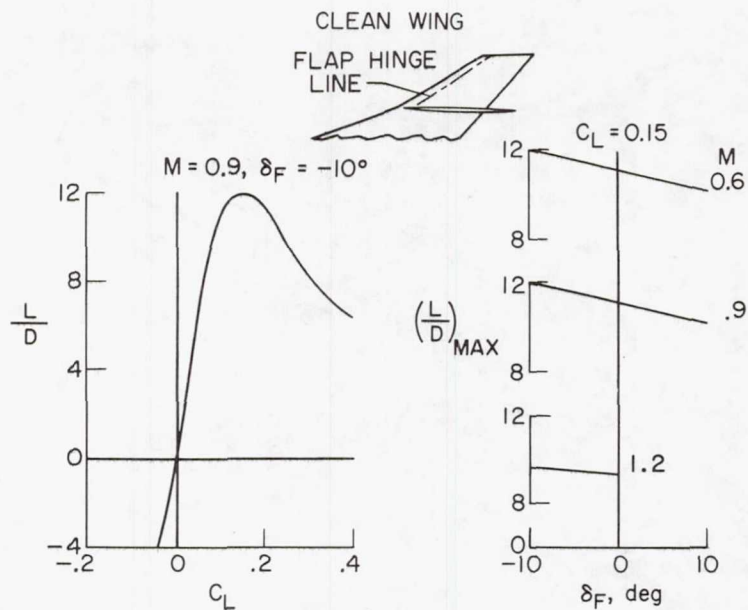
Figure 3.- Effects of deflection of wing tip
leading edge flaps on lift to drag ratio.
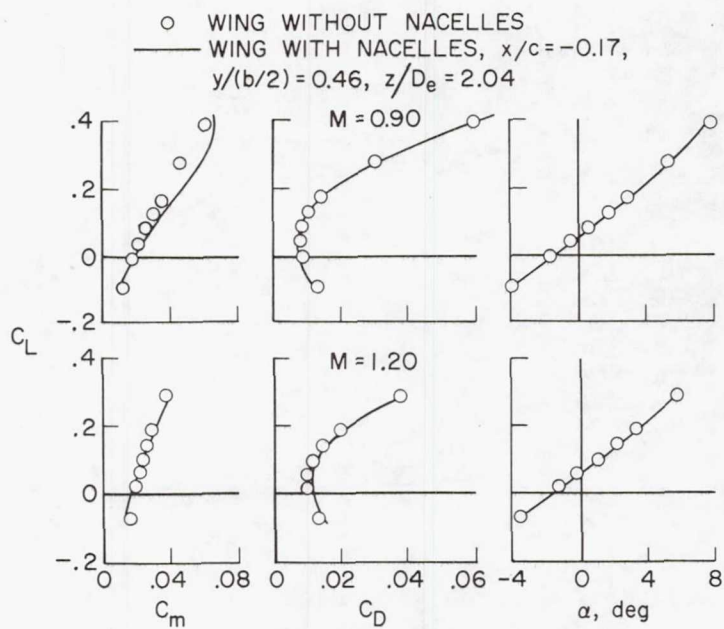
Figure 4.- Nacelle installation interference
effects.

146
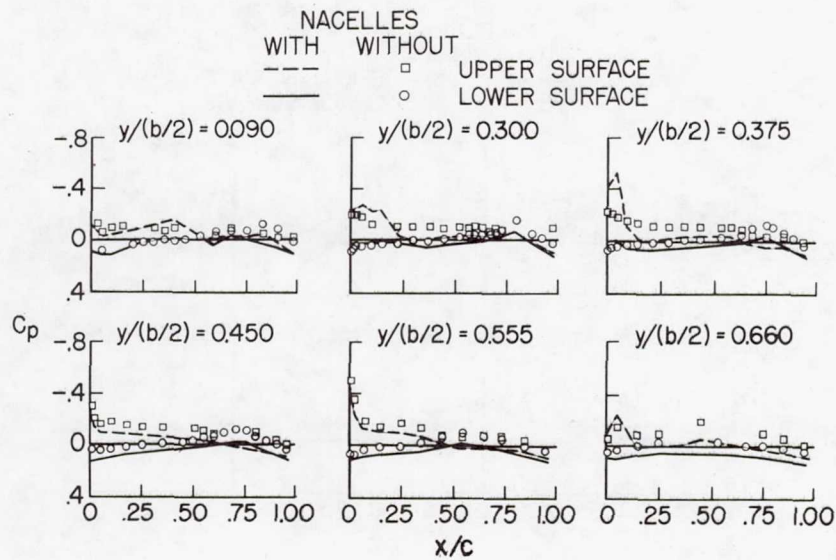
(a) M = 0.9; $\alpha = 0°$.
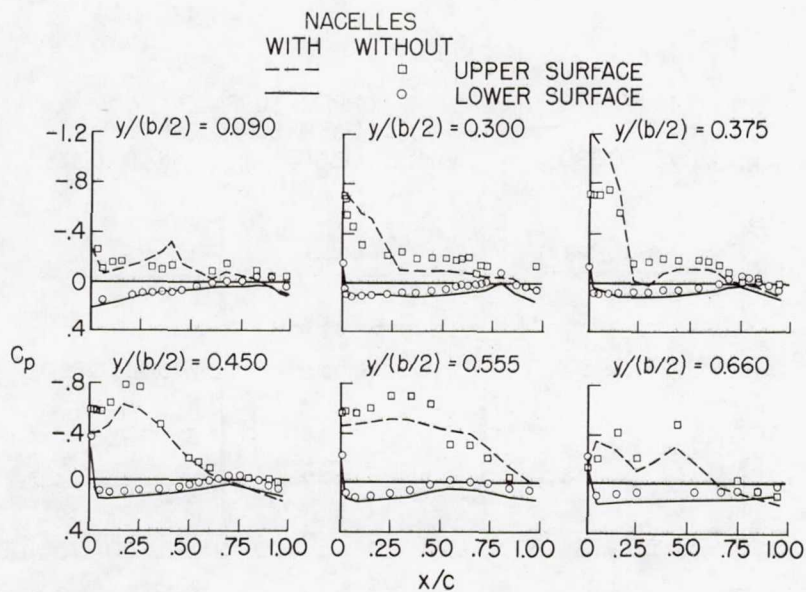
(b) M = 0.9; $\alpha = 4°$.

Figure 5.- Typical wing pressure distributions with
   and without jet nacelles. $x/c = -0.17$;
   $y/(b/2) = 0.46$; $z/D_e = 2.04$.

147
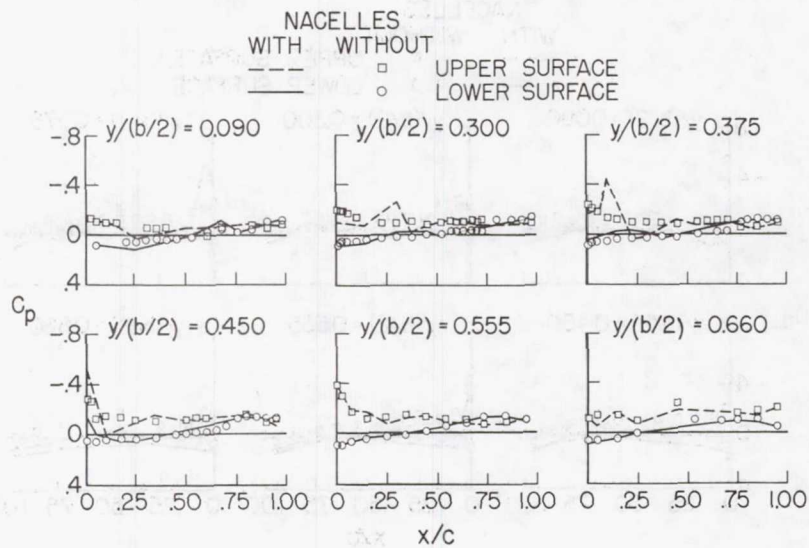
(c) M = 1.2; $\alpha = 0°$.
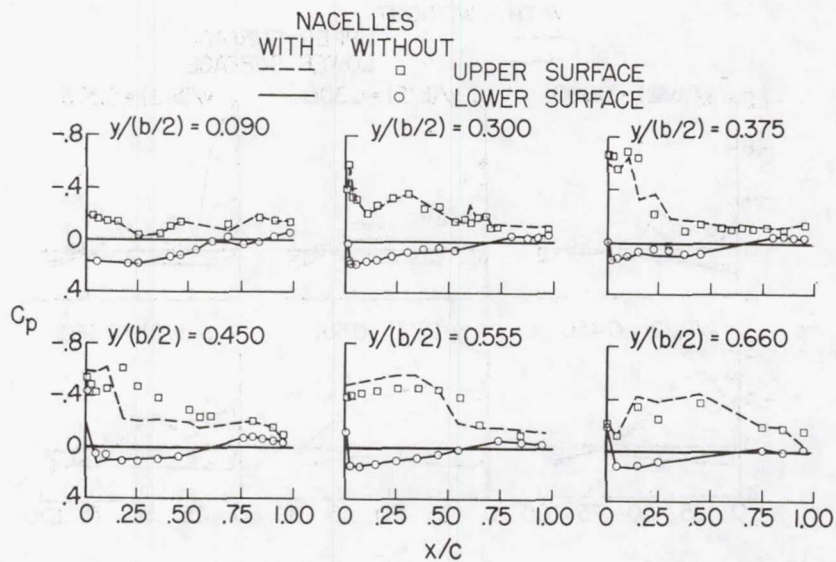
(d) M = 1.2; $\alpha = 4°$.

Figure 5.- Concluded.
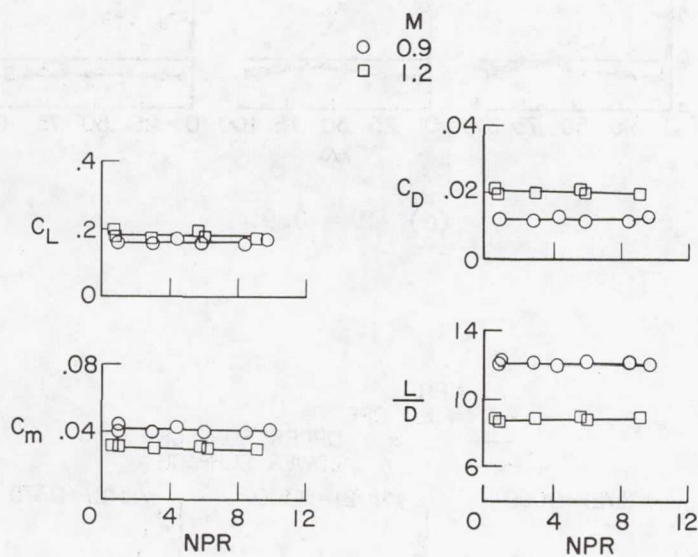
Figure 6.- Effect of jet exhaust flow variation
on aerodynamic forces and moments. $\alpha \approx 3^\circ$;
$x/c = -0.17$; $y/(b/2) = 0.46$; $z/D_e = 2.04$.
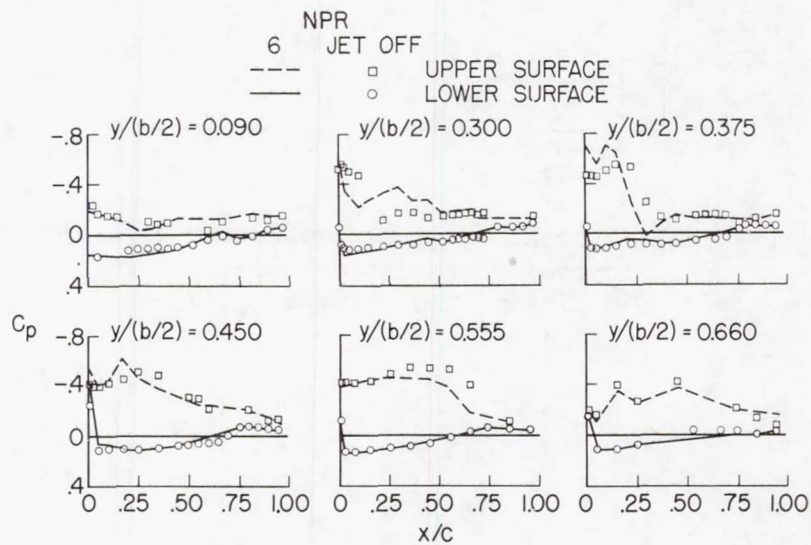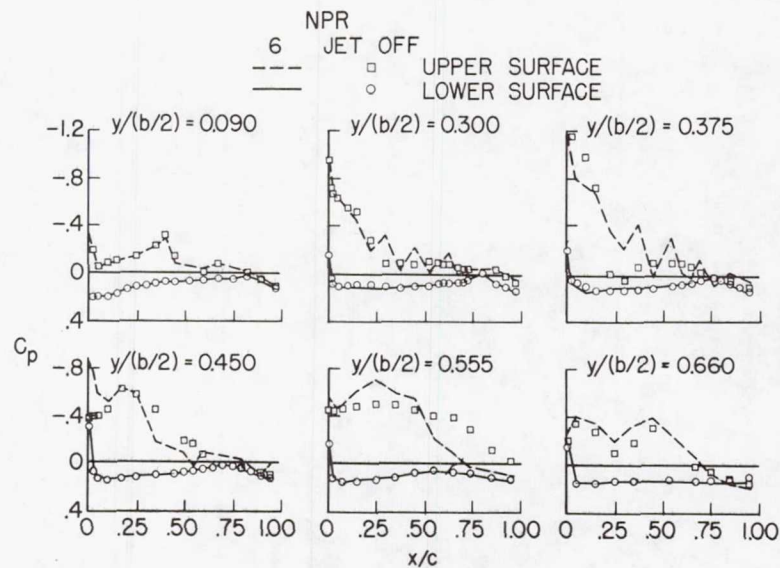
(a) M = 0.9.

(b) M = 1.2.

Figure 7.- Effect of jet exhaust flow on wing
   pressure distributions. $\alpha = 4°$; $x/c = -0.17$;
   $y/(b/2) = 0.46$; $z/D_e = 2.04$.
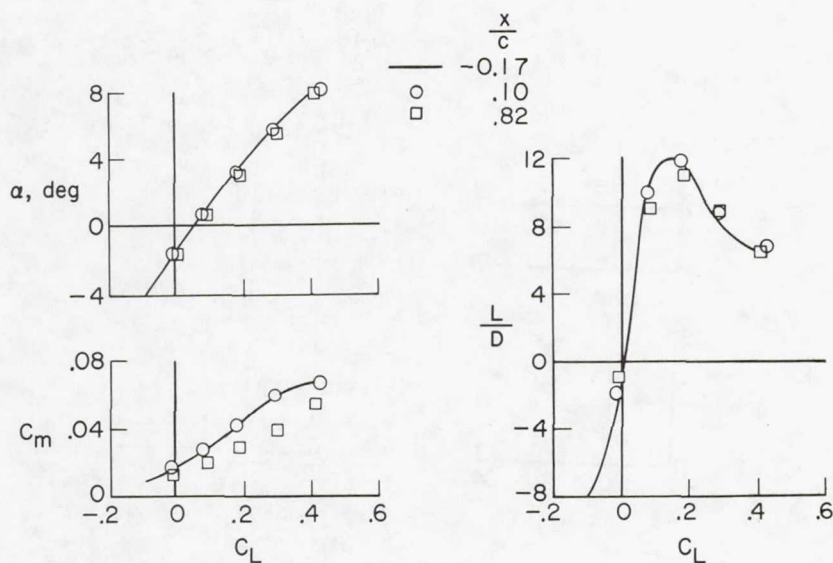
(a) M = 0.9; NPR = 4.6.
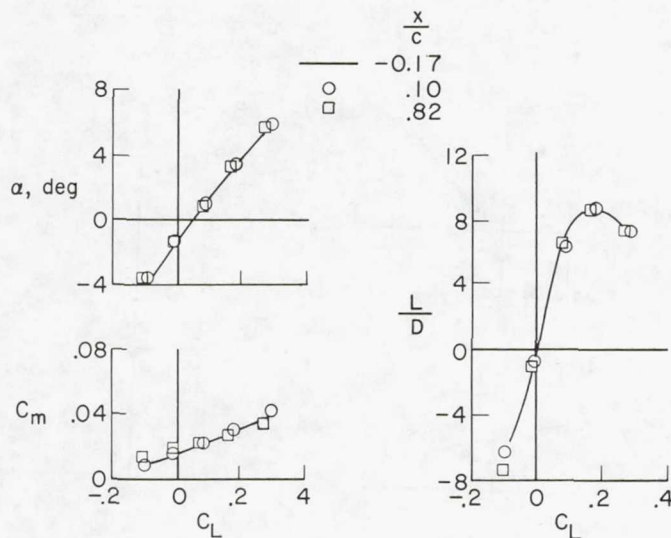
(b) M = 1.2; NPR = 8.0.

Figure 8.- Effect of nacelle chordwise location on
  longitudinal aerodynamic forces and moments.
  $y/(b/2) = 0.46$; $z/D_e = 2.04$.
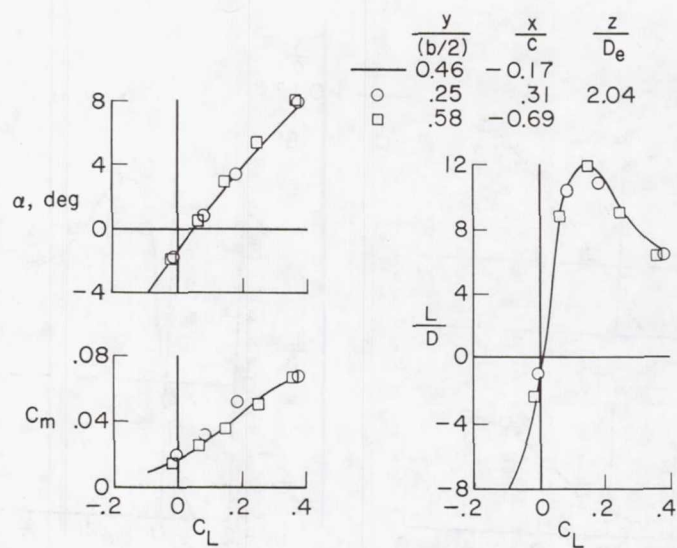
(a) M = 0.90; NPR = 4.6.
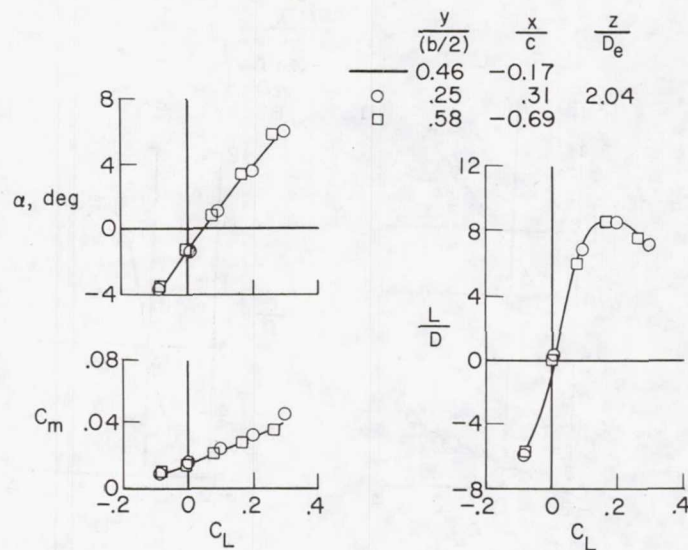
(b) M = 1.2; NPR = 8.0.

Figure. 9- Effect of nacelle spanwise position
on aerodynamic forces and moments.
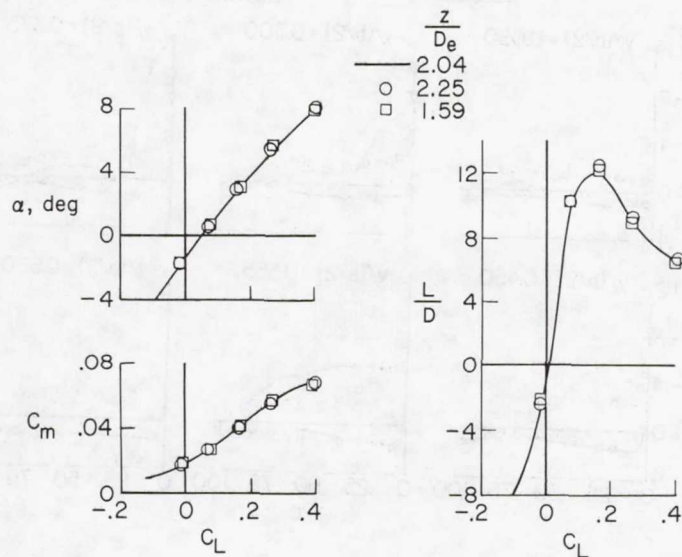
(a) M = 0.9; NPR = 4.6.
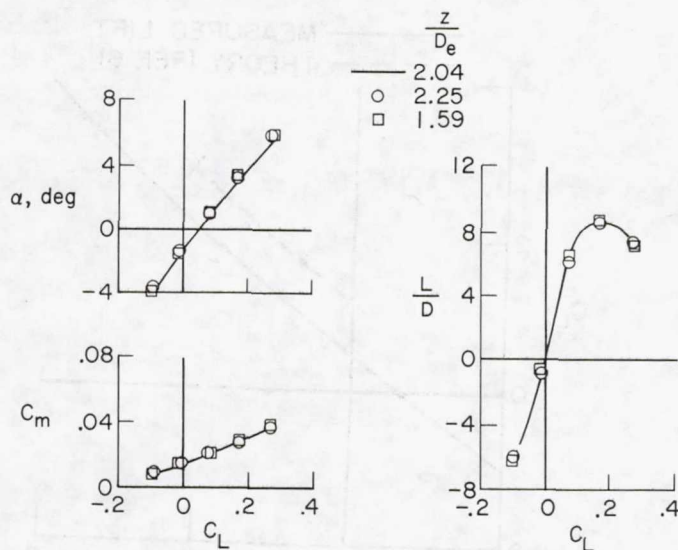
(b) M = 1.2; NPR = 8.0.

Figure 10.- Effect of vertical nacelle height
variation on aerodynamic forces and moments.
x/c = -0.17; y/(b/2) = 0.46.
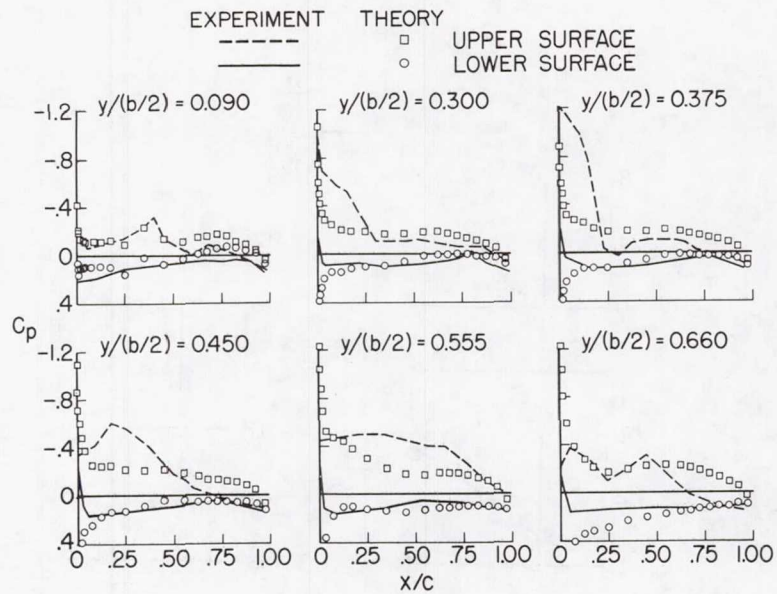
Figure 11.- Comparison between experimental pressure coefficients and theory of reference 6. $M = 0.9$; $\alpha = 4^\circ$; jet off; $x/c = -0.17$; $z/D_e = 2.04$.
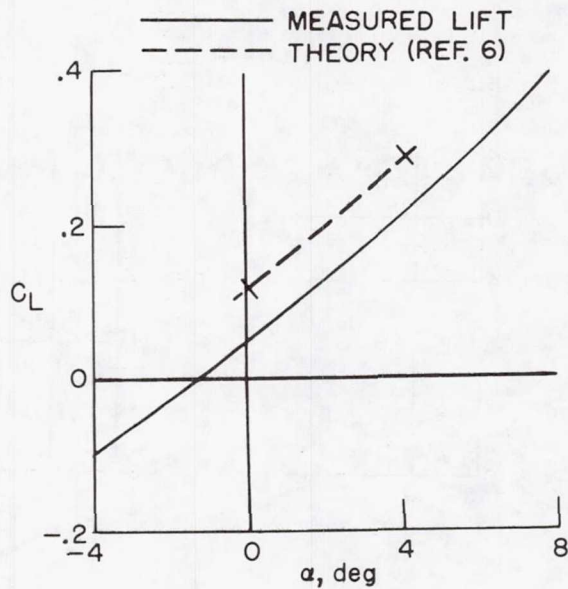
Figure 12.- Measured and predicted (ref. 6) wing-body lift coefficients. $M = 0.9$; $x/c = -0.17$; $y/(b/2) = 0.46$; $z/D_e = 2.04$.

154

AERODYNAMIC VALIDATION OF A SCAR DESIGN

Robert L. Roensch
McDonnell Douglas Corporation

SUMMARY

The results of a wind tunnel test of a model of the McDonnell Douglas Supersonic Cruise Aircraft justify the design procedures used to develop the configuration. The data obtained with a baseline and improved performance wing support the analysis and design methods. The minimum drag is almost exactly as predicted. Despite small discrepancies in the predicted level of drag-due-to-lift, the increments between configurations are as predicted and can be used to identify further improvements in performance. The results also verified the aerodynamic efficiency of the configuration with a demonstrated trimmed L/D_{max} of 9.1. It should be noted that this configuration was not optimized solely for aerodynamics, but was tailored to provide a good match between structural and aerodynamic performance.

There is demonstrable evidence that known refinements are possible to raise the L/D_{max} to 9.6, and a goal of 10.3 has been set for technology research as a realistic target for an arrow wing design at a Mach number of 2.2.

INTRODUCTION

A wind tunnel test[*] of the McDonnell Douglas Supersonic Cruise Aircraft, designed for a cruise Mach number of 2.2, was conducted in the NASA Ames Unitary Plan Wind Tunnels. Extensive force, pressure, and flow visualization data were obtained over a Mach number range from 0.5 to 2.4. Comparisons between theory and measurements of both forces and pressures presented in this paper concentrate on the results obtained in the 9-Foot by 7-Foot Supersonic tunnel. Schlieren and tuft pictures are presented to help provide an understanding of the nonlinearities observed at off-design conditions.

SYMBOLS

Values are given in both SI and U.S. Customary Units. The measurements and calculations were made in U.S. Customary Units.

α angle of attack, deg.

B_1 fuselage

C_D drag coefficient

C_L lift coefficient

C_m pitching moment coefficient about 1/4 MAC

C_{n_β} variation of yawing moment coefficient with sideslip angle, 1/rad (1/deg.)

CG,cg   center of gravity

C_P pressure coefficient

ΔC_D increment in drag coefficient

L/D_{max} maximum lift-to-drag ratio

M   Mach number

MAC   mean aerodynamic chord of the trapezoidal wing formed by extending the leading and trailing edges of the outer panel to the aircraft centerline

Y/(b/2)   spanwise location in fraction of semi-span

W_1, W_2, W_3 wings

N_1, N_2 nacelles

CONFIGURATION

A three view of the MDC Supersonic Cruise Aircraft is shown in figure 1. This 273-passenger aircraft is designed for ranges in excess of 8300 km (4500 n.mi) at a takeoff gross weight of 340,194 kg (750,000 lb). It features a 929 m^2 (10,000 ft^2) arrow-type wing designed for a cruise Mach number of 2.2 with the planform based on the NASA SCAT-15F concept, a conventional horizontal tail, a single fuselage-mounted vertical tail, and four engines mounted in axisymmetric nacelles. The inboard leading edge of the wing has a sweep of 71 degrees with the sweep reduced to 57 degrees outboard of the leading edge break. The average thickness ratio of the wing is slightly less than three percent. The thickness ratio is equal to 2.25 percent of the chord at the wing root and

156

is constant at three percent of the chord from the trailing edge break to the wing tip. The development of this configuration has been described in some detail in references 1, 2, and 3.

WIND TUNNEL TEST

A cooperative MDC-NASA wind tunnel test program using a 1.5-percent scale model of this configuration was conducted in the NASA Ames Unitary Plan Wind Tunnels in the latter part of 1975. Data were obtained at Mach numbers from 0.5 to 1.3 in the 11-Foot Transonic tunnel and at Mach numbers from 1.6 to 2.4 in the 9-Foot x 7-Foot Supersonic tunnel. All the data were obtained at a Reynolds number of slightly less than four million based on the model MAC. The aft portion of the fuselage of the model departed somewhat from the aircraft in order to accommodate the balance and sting as can be seen in the photographs of the model installed in the Supersonic tunnel (fig. 2) and the Transonic tunnel (fig. 3). Extensive pressure data were obtained along with the force data, as well as tuft and schlieren flow visualization photographs.

Three different wings were tested during the program along with two different nacelle inlet designs. The following pertinent model designations were used for the test:

B_1 baseline model fuselage.

W_1 wing optimized at a C_L of 0.1 without regard to trim drag.

W_2 improved performance wing optimized at a C_L of 0.1 with a pitching moment constraint to reduce the trim drag.

W_3 wing W_1 with a fairly sophisticated reflex in the region of the nacelles to relieve the nose down pitching moments generated by the nacelle flow field.

N_1 external compression inlet with a cowl lip angle of 24 degrees.

N_2 mixed compression inlet with a cowl lip angle of 6 degrees.

The results of the nacelle and wing reflex test are presented fairly completely in reference 4 and are only summarized here. The wing reflex tested was not totally successful since it cancelled only about 75 percent of the nacelle induced pitching moment. A simpler reflex concept may well be adequate for this task. Further wind tunnel tests are necessary to develop the optimum geometry. The wave drag with the external compression inlet was approximately five drag counts $(\Delta C_D = 0.0005)$ higher than with the mixed compression inlet. This is the magnitude of the difference predicted by the method of characteristics analysis (ref. 5).

157

TEST RESULTS

The majority of the presentation deals with the results obtained with wing W_2. Comparisons of the wind tunnel data for the wing-body configuration with theory are shown in figures 4, 5, and 6. The wind tunnel data have been corrected to full scale aircraft conditions. In addition to the skin friction correction for the difference between flight Reynolds number and the wind tunnel test Reynolds number, the measured drag has been increased to account for the estimated difference between the wave drag of the open afterbody of the model and the closed aft fuselage of the aircraft. The drag-due-to-lift, the lift, and the pitching moment have also been corrected for the estimated difference in each of these parameters due to the afterbody shapes of the model and the aircraft.

The zero-lift wave drag of the configuration was estimated using the MDC-developed Arbitrary Body Wave Drag program (ref. 6) which calculates, based on the area rule theory (ref. 7 and 8), the wave drag of completely arbitrary configurations. All analyses were performed with the full geometry of the configuration at the cruise attitude. Drag-due-to-lift, lift, and wing-body pitching moments were calculated with the MDC version of the Woodward program (ref. 9) by a direct analysis of the wing-body configuration including wing thickness and body camber effects. Since the Woodward program, when run with wing and body thickness, includes a zero-lift wave drag, an uncambered version of the configuration was analyzed with the Woodward program to obtain a Woodward wave drag. This was subtracted from the cambered configuration Woodward drag analysis and the remainder is considered to be the drag-due-to-lift including the twist drag.

As can be seen by the drag polars shown in figure 4, the agreement between the estimated and measured minimum drag of the configuration across the Mach number spectrum is excellent. The calculated drag-due-to-lift, however, shows a trend of overprediction at the lower supersonic Mach numbers and underprediction at the higher Mach numbers. Almost perfect agreement is obtained at Mach 2.0, 0.2 below the design Mach number. This would suggest that perhaps the configuration should be designed for a Mach number 0.2 higher than the desired cruise Mach number. Earlier NASA SCAT wind tunnel tests found a similar phenomenon to exist.

The agreement of the data with the calculated lift curves shown in figure 5 is reasonably good, though there is a slight overprediction of the lift which increases as the Mach number increases.

The pitching moment characteristics shown in figure 6 show fairly good agreement between the data and the estimate near the cruise C_L, which is approximately 0.11. At the Mach 2.2 design condition the measured aerodynamic center is approximately 2.5 percent of MAC ahead of the estimated value. At higher C_L's the data show evidence of a mild pitchup. The magnitude is not considered to be a significant problem because the horizontal tail has sufficient control authority to compensate for this deviation from linear pitching moments using only a fraction of the available tail effectiveness, even at the design load

factor. The tail-on data show the same trends, with the horizontal tail effectiveness relatively insensitive to angle of attack.

The pressure data obtained during this test help explain the nonlinear behavior of the pitching moments. Shown in figure 7 are the estimated and measured pressures at Mach 2.2 on the upper and lower surface of the wing at an angle of attack of 2.5 degrees, which is near the cruise angle of attack. The agreement between the Woodward program predictions and the data is fairly good. However, there is a lack of agreement at high angles of attack as shown in figure 8, which is not unexpected. The linear theory pressure coefficients are predicted to exceed the vacuum limited C_p which is approximately equal to $1/M^2$ (about -0.2 at Mach 2.2) over much of the upper surface of the wing, particularly on the outer wing panel. The measured lower surface pressures are in reasonably good agreement with the linear theory on the inboard portion of the wing, but there is a significant deviation on the outer panel. These two effects, limiting C_p's on the upper surface and less than predicted positive pressures on the lower surface, contribute to a loss in outer panel loading at high angles of attack which results in the mild pitchup observed.

Small mini-tufts were attached to the wing to learn how the flow field varies as the upper surface reaches the limiting C_p. The results are shown in figure 9. At the lower angle of attack the flow is very well behaved. At the high angle of attack, it can be seen that the flow has changed character considerably but there is no evidence of any flow separation. The tufts on the lower surface showed no significant variation over this range of angle of attack. Schlieren photographs taken from the top of the model over the same angle of attack range show that the shock wave which is created at the leading edge break sweeps forward as the angle of attack is increased (fig. 10).

The pressure, flow visualization, and force data obtained during this test clearly identify the cause of the nonlinear behavior of the pitching moments. The arrow-wing concept is characterized by fairly high loading of the outer panel which will cause the upper surface to reach limiting C_p's at moderate C_L's. While this does result in a mild pitchup, there are some favorable side benefits in the structural area. The structural loads that the outer panel must carry at supersonic speeds do not grow as rapidly with load factor as the linear theory would predict. This may result in a reduction in the wing weight from that estimated using linear theory loads.

Yawed polars and a limited number of constant angle of attack yaw sweeps were obtained to evaluate the lateral-directional characteristics of the configuration. Of interest was whether a single fuselage mounted vertical tail would provide adequate directional stability throughout the flight envelope of the aircraft. This can be particularly significant at low speeds and high angles of attack.

The tail-on and tail-off directional stability characteristics (C_{n_β}) of the model are shown in figure 11. In the subsonic range, no significant deterioration of the vertical tail effectiveness occurred within the angle of attack range for which data were obtained. It is anticipated that the tail effectiveness will be reduced at higher angles of attack. This will require

the use of strakes on the nose similar to those used on the Concorde and the DC-9-50 to provide satisfactory directional stability characteristics at high sideslip angles at high angles of attack in the low speed flight regime. The supersonic data show that from Mach 1.6 to 2.4 there is a gradual degradation in vertical tail effectiveness as the angle of attack is increased. But, at conditions corresponding to the design load factor $(C_L \cong 0.27)$ the configuration shows positive directional stability.

VALIDATION OF DESIGN PROCEDURES

The extent to which the wind tunnel test provides validation of the design procedures used for developing this configuration is shown by comparing the wing-body characteristics of the baseline wing and the improved performance wing at Mach 2.2. As shown in figure 12, the incremental differences in all the coefficients are nearly as predicted. The change in the pitching moment observed between W_1 and W_2 is of special interest because the design of W_2 was predicated on making the wing-body pitching moments positive, requiring an up-tail load to trim the aircraft.

The value of this concept is shown in figure 13. The trimmed L/D_{max} shown as a function of cg location includes the skin friction and wave drag of the horizontal and vertical tails as well as the trim drag due to the horizontal tail lift and drag-due-to-lift. While the level of experimental L/D_{max} is slightly less than predicted, the experimental increments between W_1 and W_2 are almost as predicted. This figure also points out the real benefit obtained by optimizing the wing for a desired pitching moment. The highest achievable L/D_{max} can be obtained within desired cg limits. The cg limits shown were chosen so that the aft supersonic limit corresponds to the subsonic neutral point, an MDC design requirement for this configuration.

CONCLUSIONS

The results of a wind tunnel test of a model of the McDonnell Douglas Supersonic Cruise Aircraft justify the design procedures used to develop the configuration. The data obtained with a baseline and improved performance wing support the analysis and design methods, with the possible exception of some discrepancy in the prediction of the drag-due-to-lift. However, even with discrepancies in the predicted level of drag-due-to-lift, the increments between configurations are as predicted and can be used to identify further improvements in performance. The results also verified the good aerodynamic efficiency of the configuration with a demonstrated trimmed L/D_{max} of 9.1. It should be noted that this configuration was not optimized solely for aerodynamics, but was tailored to provide a good match between structural and aerodynamic performance.

There is demonstrable evidence that known refinements are possible to raise the L/D_{max} to 9.6, and a goal of 10.3 has been set for technology

research as a realistic target for an arrow wing design at a Mach number of 2.2.

The value of obtaining wing pressure distributions as well as force and flow visualization data, even during the early stages of the development of a configuration, was amply demonstrated. With this degree of detailed data it is possible to determine the true limitations of the linear theory used in the aircraft design process.

REFERENCES

1. FitzSimmons, R. D. and Hoover, W. C.: AST-A Fifth Engine for Environmental Consideration. SAE Paper 730899, 1973.

2. FitzSimmons, R. D. and Roensch, R. L.: Advanced Supersonic Transport. SAE Paper 750617, 1975.

3. Radkey, R. L., Welge, H. R., and Roensch, R. L.: Aerodynamic Design of a Mach 2.2 Supersonic Cruise Aircraft. AIAA Paper No. 76-955, 1976.

4. Welge, H. R., Radkey, R. L., and Henne, P. A.: Nacelle Aerodynamic Design and Integration on a Mach 2.2 Supersonic Cruise Aircraft. AIAA Paper No. 76-757, 1976.

5. Henne, P. A.: Unique Application of the Method of Characteristics to Inlet and Nozzle Design Problems. AIAA Paper No. 75-1185, 1975.

6. Gentry, A. E., Smyth, D. N., and Oliver, W. R.: The Mark IV Supersonic-Hypersonic Arbitrary-Body Program. AFFDL-TR-73-159, 1973.

7. Jones, R. T.: Theory of Wing-Body Drag at Supersonic Speeds. NACA Report 1284, 1956. (Supersedes NACA RM A53H18a, 1953.)

8. Whitcomb, R. T.: A Study of the Zero-Lift Drag Rise Characteristics of Wing-Body Combinations Near the Speed of Sound. NACA Report 1273, 1956. (Supersedes NACA RM L52H08, 1952.)

9. Woodward, F. A., Tinoco, E. N., and Larson, J. W.: Analysis and Design of Supersonic Wing-Body Combinations, Including Flow Properties in the Near Field. NASA CR-73106, 1967.
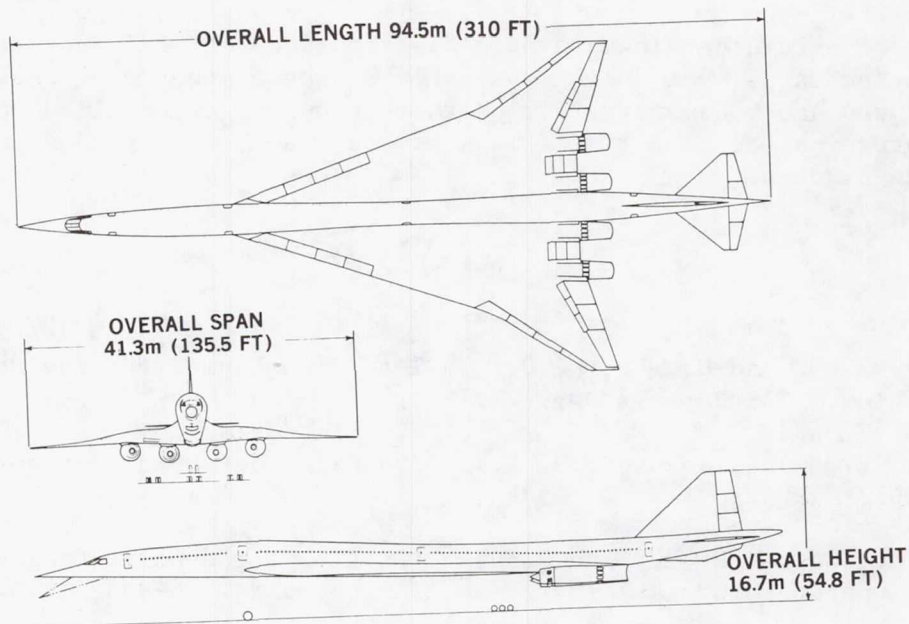
Figure 1.- MDC baseline supersonic cruise aircraft.
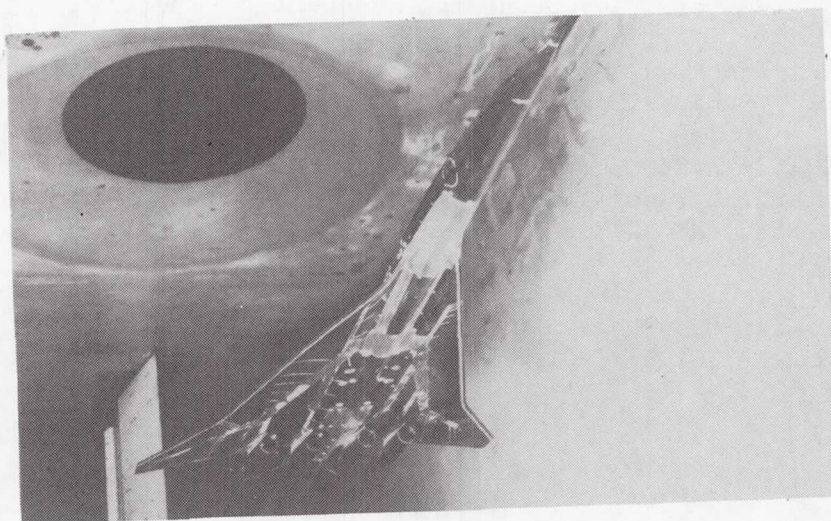
Figure 2.- Model in Ames 9-foot by 7-foot tunnel.
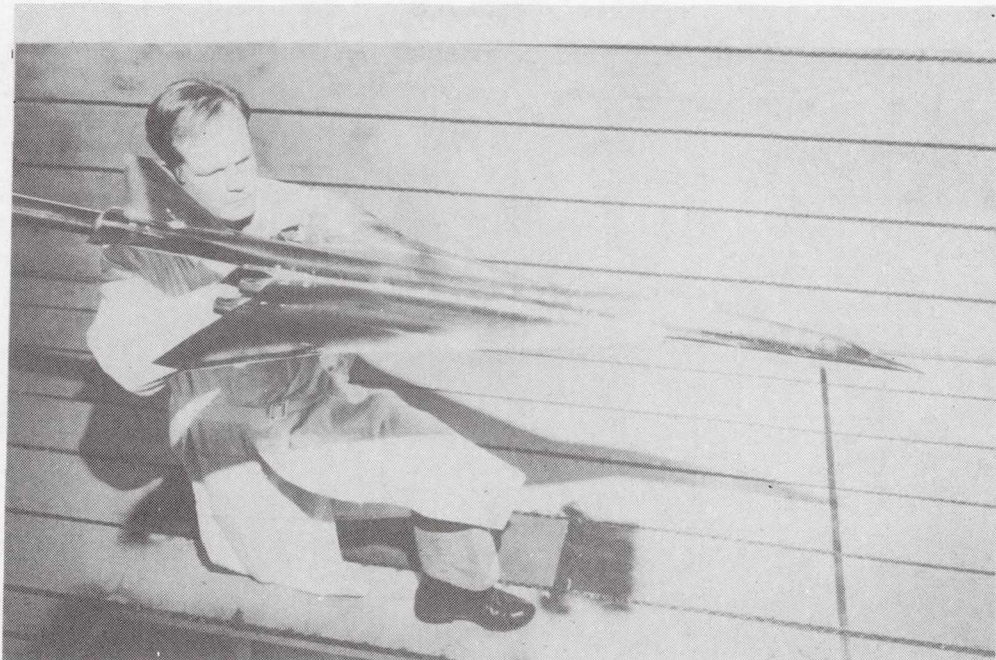
Figure 3.- Model in Ames 11-foot tunnel.
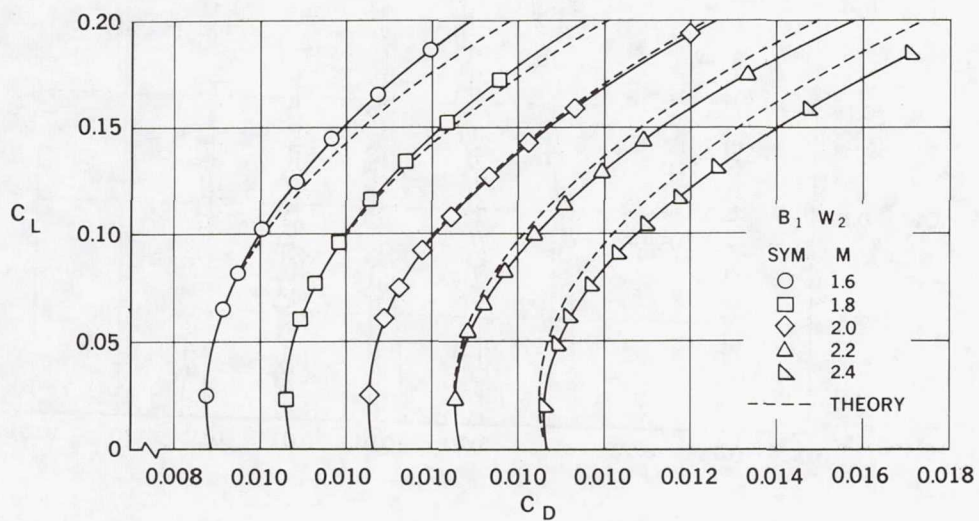
Figure 4.- Wing-body drag polars.

163
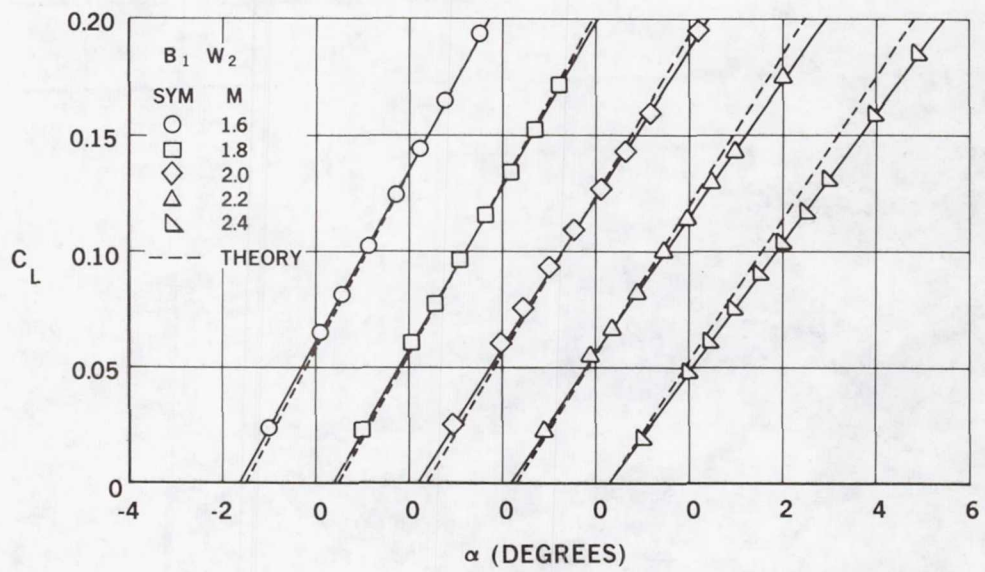
Figure 5.- Wing-body lift curves.
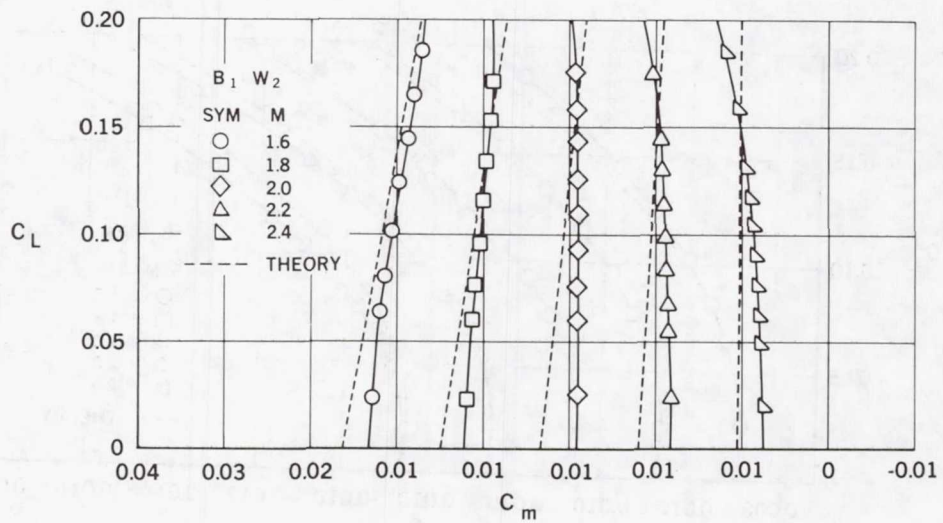
Figure 6.- Tail-off pitching moment characteristics.

164
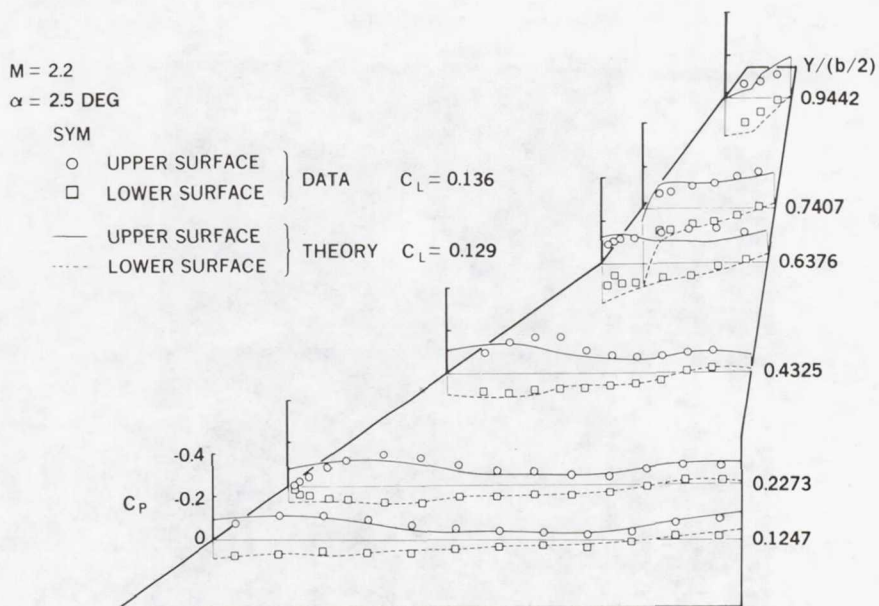
Figure 7.- Low angle of attack calculated and
experimental pressure distributions on B_1W_2.
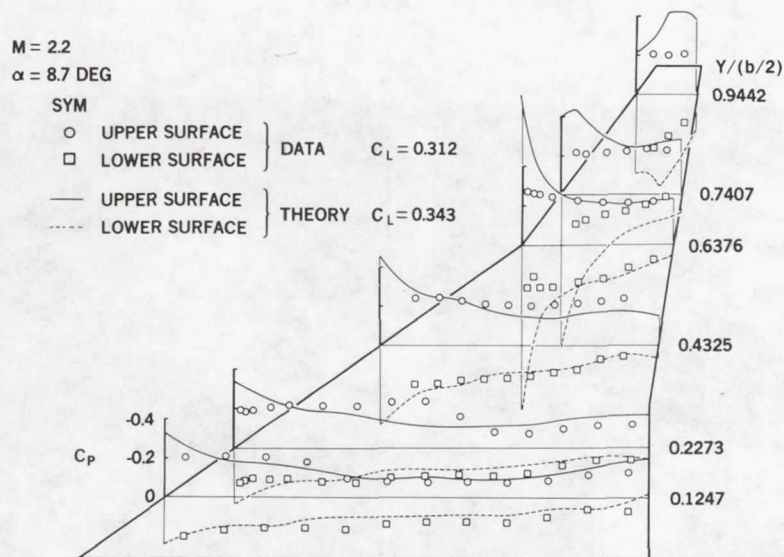
Figure 8.- High angle of attack calculated and
experimental pressure distributions on B_1W_2.

165
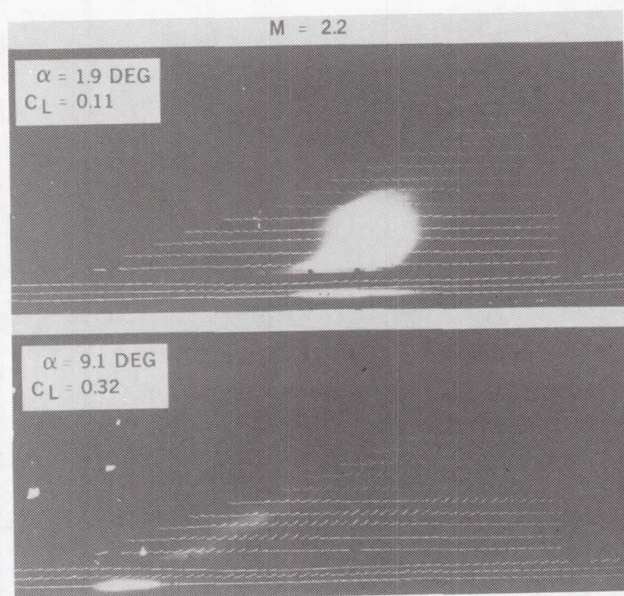
Figure 9.- Upper surface tufts.
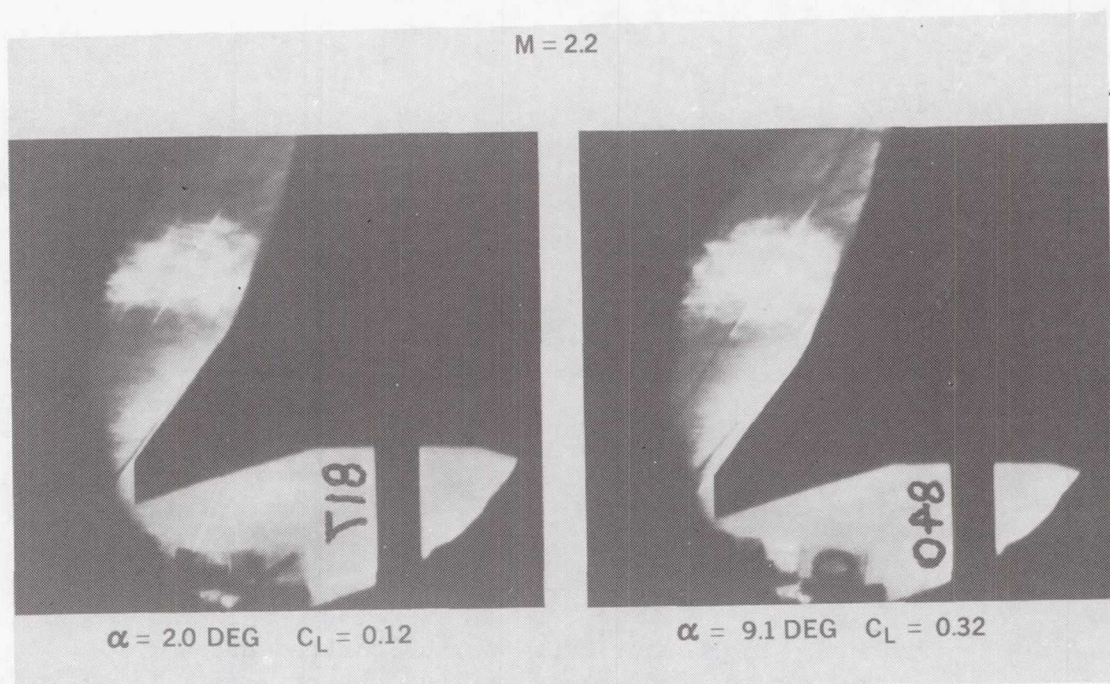
Figure 10.- Schlieren photographs.
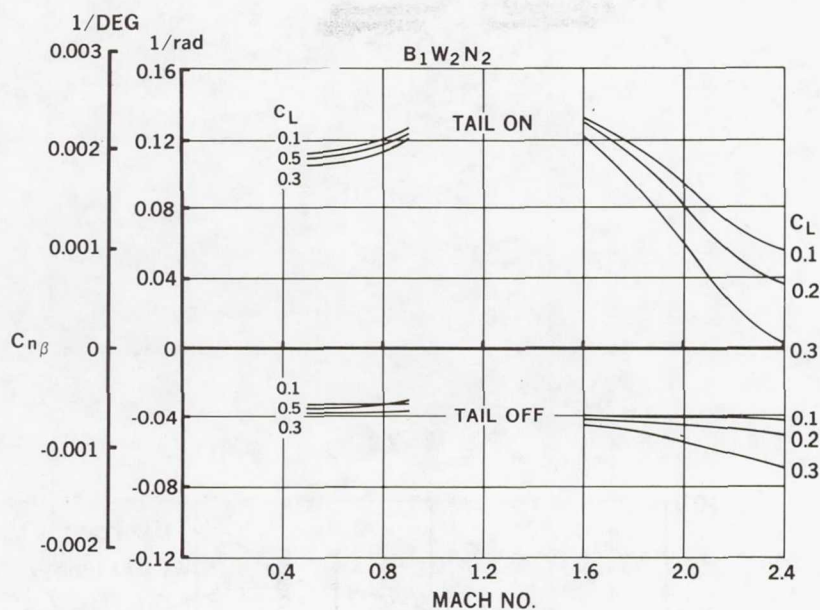
Figure 11.— Measured directional stability characteristics.
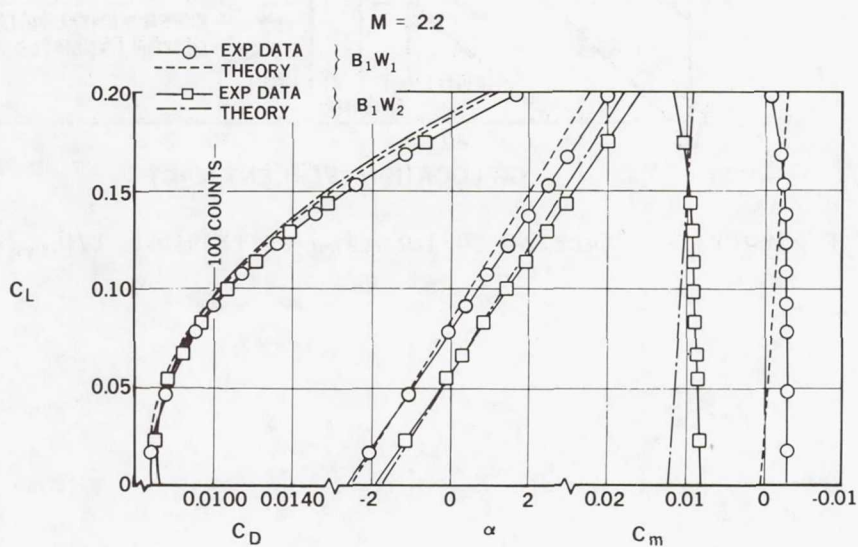
Figure 12.— Comparison of wing-body characteristics
for two wing designs.

167

M = 2.2
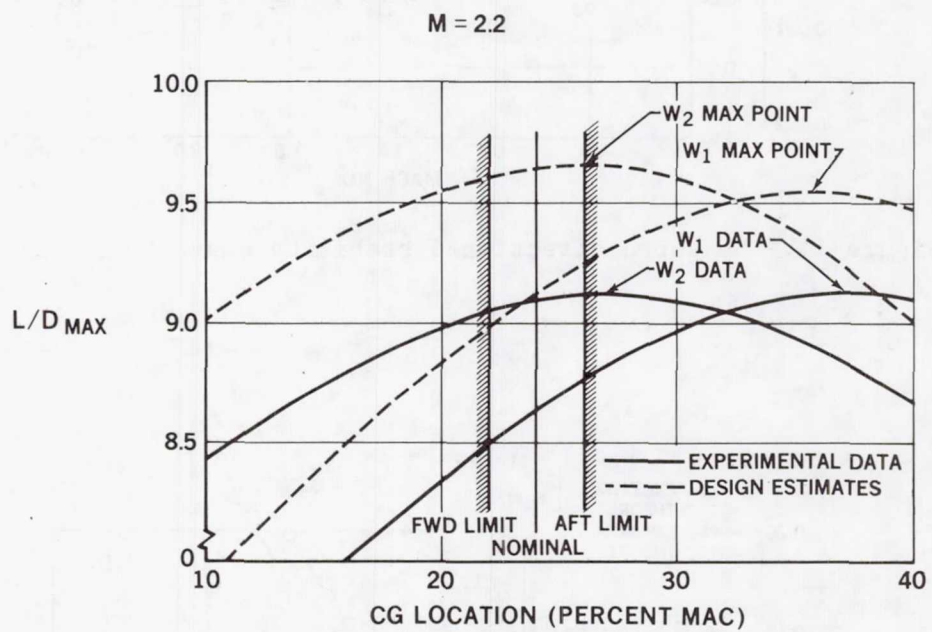
Figure 13.- Effect of CG location on trimmed L/D_{max}.

SESSION II - STABILITY AND CONTROL

Page intentionally left blank

DEVELOPMENT OF LONGITUDINAL HANDLING QUALITIES CRITERIA FOR

LARGE ADVANCED SUPERSONIC AIRCRAFT*

Robert W. Sudderth
Boeing Commercial Airplane Company

Walter E. McNeill
Ames Research Center

SUMMARY

A piloted simulation study was conducted with the aim of advancing the development of longitudinal handling qualities criteria for large supersonic cruise aircraft. The areas of study investigated, using the NASA Ames Flight Simulator for Advanced Aircraft, included high-speed cruise maneuvering, stall-recovery control power, and landing approach for normal and minimum-safe operation. Only the first two areas are discussed in this paper. Comparisons were made with existing criteria and, for the cruise condition, a time response criterion was developed which correlated well with pilot ratings and comments. For low-speed stall recovery a new criterion was developed in terms of nose-down angular acceleration capability. The results of the study were reported in reference 1.

INTRODUCTION

Developmental research conducted during the National SST Program showed the important benefits in aircraft economics that could be gained through advancements in flight control system design. For example, a sophisticated stability and control augmentation system can provide satisfactory handling qualities in an airplane after the low-speed static stability of the bare airframe has been sacrificed to minimize supersonic trim drag.

These highly-augmented control systems characteristically generate airplane dynamic responses that are more complex than ordinarily observed, and which are not adequately specified by existing handling qualities criteria (refs. 2 and 3). The simulation study described herein was conducted to improve the data base for establishing generalized handling qualities criteria for large supersonic cruise aircraft with these advanced flight control systems, thus allowing definition of control system design requirements for normal operation, and establishment of factors contributing to minimum stability levels for minimum-safe operation.

*Performed under contract NAS2-7966

171

SYMBOLS AND ABBREVIATIONS

CAS   calibrated airspeed (knots)

cg   center of gravity (% C_R)

C_L lift coefficient

cm   centimeters

C_R root chord

deg   degree

EADI   electronic attitude director indicator

F_{col} column force (N, lb)

fpm   feet per minute

fps   feet per second

ft   feet

g   gravity (m/sec^2, ft/sec^2)

in   inches

L_α normalized lift per angle of attack ($1/_{sec}$)

lb   pounds

max   maximum

NASA   National Aeronautics and Space Administration

n_α normalized load factor per angle of attack (g's/rad)

N   newton

n_Z normal load factor (g's)

$n_{Z_{ss}}$ steady state normal load factor (g's)

PR   pilot rating

PT   prototype

$\dot{q}$ pitch angular acceleration (deg/sec^2)

172

rad	radian
rms	root mean square
sec	seconds (time)
SST	supersonic transport
T	time (seconds)
$T_{2\theta}$	time-to-double pitch attitude (seconds)
$T_{\dot{\theta}_{max}}$	time-to-maximum pitch rate (seconds)
ξ	damping ratio
θ	pitch attitude (deg)
$\dot{\theta}$	pitch rate (deg/sec)
$\dot{\theta}_{max}$	maximum pitch rate (deg/sec)
$\dot{\theta}_{ss}$	steady state pitch rate (deg/sec)
σ_w	vertical turbulence component, rms (m/sec, fps)
ω_n	natural frequency (rad/sec)

SIMULATION FACILITY

The pilot evaluations were performed using the NASA-Ames Flight Simulator for Advanced Aircraft (Fig. 1). The cockpit is outfitted with two crew stations and is mounted on a large-motion system having six degrees of freedom. In addition to conventional cockpit control and instrument arrangements, the simulator incorporates a visual display generated by a closed-circuit color television system with visual models for high-altitude cruise or landing approach. All control forces were simulated by means of hydraulic control loaders with adjustable force gradients. Real-time computations necessary for the simulation were performed by a large capacity digital computer. A complete mathematical model of the Boeing 2707-300 PT (Fig. 2) served as the baseline aircraft for this study.

The cockpit instrument panel configuration used for the portions of the study discussed herein is shown in Figure 3. Dominating the center of the panel was an electronic attitude director indicator, or EADI, with which it was possible to vary the pitch attitude display sensitivity from 0.41 cm/deg. to 0.76 cm/deg. (0.16 in/deg to 0.30 in/deg) for the high-speed cruise maneuvering case.

173

HIGH-SPEED CRUISE MANEUVERING

The handling qualities criteria data base for high speed cruise maneuvering was to be based on aircraft response characteristics and parameters related to longitudinal handling qualities. Response parameters were selected that describe the airplane's short period mode characteristics. These parameters were derived from a series of airplane pitch response characteristics resulting from a given input command. Selected as an input command, representative of a typical pilot input, was a column step input. The response parameters were pitch rate overshoot ratio ($\dot{\theta}_{max}/\dot{\theta}_{ss}$), time-to-peak pitch rate ($T_{\dot{\theta}_{max}}$), and damping constant ($\xi\omega_n$). Response parameters were selected as a criteria data base in order to allow evaluation of airplane handling qualities with airplanes that have non-linear longitudinal characteristics, airplanes that cannot be represented by a simple second order system. Such criteria would be more generally applicable to large supersonic aircraft, the subject of this study.

Other parameters that relate to longitudinal handling qualities that were evaluated in this study were the column force gradient and the sensitivity of the pitch attitude display indicator, in this case an EADI. These parameters were considered relevant since they are parameters in the pilot-airplane control loop, and conceivably would impact the handling qualities perceived by the pilot.

A complete list of all parameters evaluated along with parameter values is presented in Table I. Each parameter was varied by the magnitudes indicated, and evaluated independently with the other parameters set at the nominal values as indicated by the arrow in the Table.

To be consistent through the evaluation a set of defined pilot tasks was established for each area studied. The pilot tasks defined for the high speed maneuvering study area discussed here are presented in Table II. All pilot evaluations were rated using the Cooper-Harper pilot rating scale reproduced in Figure 4.

The flight condition selected for the high-speed evaluations was the condition occurring at the end of supersonic climb for the 2707-300PT airplane, identified as follows:

o   Mach 2.7

o   18,288 meters (60,000 feet) altitude

o   567 knots CAS

o   Gross weight 251,744 kilograms (555,000 pounds)

174

o   62% C_R center of gravity (aft limit)

Results of the high-speed maneuvering evaluations can be summarized as follows:

o   Most sensitive EADI scale available was found most desirable.

o   Short period response parameters could be categorized in terms of a time response envelope criterion.

o   Column force gradient was insensitive within the range evaluated.

The evaluation sequence was to first determine the desired sensitivity of the attitude display indicator which for these tests was an electronic attitude director indicator (EADI) and is described in Figure 5. Then the desired EADI sensitivity was used for all of the remaining high speed evaluations. Detailed results of these evaluations will be presented in the following paragraphs.

Pitch Attitude Display Sensitivity

For all testing at high speed cruise the EADI was used. Variation of the pitch attitude scale was desired as part of the high-speed evaluation since a greater sensitivity is required at high supersonic cruise speeds than at subsonic cruise speeds. The pitch attitude scale sensitivity requirement should be roughly proportional to the magnitude of the true velocity vector which defines the relationship between a change in vertical velocity and a change in pitch attitude. For example, one degree of pitch attitude at Mach 2.7 results in 853 m/min (2800 feet per minute) vertical velocity, while at Mach .8 one degree of pitch change results in approximately 244 m/min (800 feet per minute) vertical velocity. With the requirement established for a greater pitch attitude sensitivity, the objective was to first define the optimum pitch attitude sensitivity and then conduct all other evaluations at that scale sensitivity value.

Three pitch scale values were evaluated as seen in Table I. The results of this study are presented in Figure 6. Both pilots conducting this evaluation preferred the .762 cm/deg (.30 in/deg) sensitivity according to the ratings given and according to their comments. They were both given their choice of any of the three settings for the remainder of the high-speed evaluation, and both selected this setting, the most sensitive. Also, it should be pointed out that this was the most sensitive setting possible with the EADI system available. This was due to the spacing of the pitch bars approaching the limit of the screen size available. Pilot comments were received during the evaluation of other parameters indicating a more sensitive pitch scale would be desirable.

175

Pitch Response Parameters

Results of the evaluation of the three pitch response parameters (pitch rate overshoot ratio, time-to-peak pitch rate, and pitch damping constant) are presented in Figures 7, 8, and 9. The overshoot ratio parameter indicates an upper limit at 7.1 but no lower limit. That is, the smaller overshoot ratio the better. Also, the time-to-peak pitch rate results show an upper limit of 1.2 seconds but no lower limit. The quicker responding the better as long as that is combined with good overshoot characteristics and good damping. Results of pitch damping evaluation show a lower limit of $\xi\omega_n$ = .55 with no upper limit; the more damping the better as long as good quick response exists.

These results just described say that pilots like an airplane that responds precisely and quickly and has high damping. Such results are logical and to be expected, which tend to lend confidence in these test results.

The problem now becomes one of summarizing these results in an analytical manner to form the basis for longitudinal handling qualities criteria.

Criteria Development

Previously established criteria were investigated to determine if any were adequate and complete for this area of study. These criteria were:

Mil F-8785B

C* Longitudinal Handling Qualities Criterion

National SST Time Response Criteria (Based on the Shomber-Gertsen Criteria)

Both the Mil F-8785 (Reference 1) short period response criteria and the C* Longitudinal Handling Qualities Criterion (Reference 4) were found to be unsatisfactory in a significant number of cases. The SST time response criteria (reference 5) were found to correlate very favorably with the results of this evaluation; and with a slight modification they are believed to be satisfactory criteria by which to judge high-speed longitudinal handling qualities.

As mentioned previously, the SST time response criteria are based on the Shomber-Gertsen Criteria (Reference 6) which are defined in Figure 10. The problem with using the Shomber-Gertsen Criteria directly is that they are based on a simple second order system and direct comparison with higher order systems and non-linear systems would be inappropriate. However, such a

176

comparison is possible by comparing the time history response to a common input command, such as a column step, of the second order system to the higher order system. This was the approach taken during the National SST Program in developing the longitudinal response time history criteria which will be referred to as the SST Time Response Criteria in this paper.

The SST Time Response Criteria were developed from the Shomber-Gertsen Criteria by selecting points around the boundary and determining the response to a step input for each point. All responses for all points selected were then normalized based on the steady state value following the input and overlaid on top of each other. A boundary was then drawn that enclosed the overlaid normalized responses and this boundary then established the time response criteria. Boundaries can be developed using either pitch rate or normal load factor as presented in Figure 11. The boundaries for high-speed cruise must be based on the Shomber-Gertsen boundary for high n_α values ($n_\alpha \geqslant 15$) since the math model being evaluated had n_α = 16.535 g/rad.

The SST Time Response Criteria in terms of pitch rate and load factor were both compared with the results of the piloted evaluation discussed previously. However, the load factor envelope was not as consistent with the results as the pitch rate envelope was. Therefore, only comparisons with the pitch rate boundary will be made in this paper.

Comparison of the pitch response characteristics of the three response parameters and the SST Time Response Criterion are presented in Figures 12, 13, and 14. In Figure 12 the pitch rate overshoot ratio comparison is made. As seen in this figure, the comparison is quite good. Those responses that are within or on the envelope boundary are rated satisfactory or better. The only serious exception is at the lower boundary where the criterion calls for at least an overshoot ratio of 2.65. As seen, the response with an overshoot ratio of 1.94, which has the best pilot rating of 2.3, violates the boundary. No justification is apparent for requiring a minimum overshoot ratio value as the criterion presently does. At these low pitch rate values associated with Mach 2.7, for a given load factor, the pitch rate overshoot ratio becomes less important to the pilot at the lower overshoot ratio. Therefore, a boundary modification is recommended to this criterion consisting of truncating the lower boundary at an overshoot ratio of 1.0.

Figure 13 presents the comparison of the time-to-peak pitch rate responses with the time response criterion envelope. These responses and corresponding average pilot ratings compare well with the envelope boundaries. The time-to-peak of 1.4 seconds is just outside of the pitch rate time history boundary and is rated slightly unsatisfactory. The time-to-peak of 2.0 seconds is considerably outside the boundary and the pilot ratings definitely reflect this. The only area of any slight disagreement exists with the time-to-peak of .45 seconds. This does slightly violate the boundary on the low side. However, it should be remembered that this portion of the boundary is definitely in disagreement with the overshoot ratio test results, and should be modified as recommended in the discussion of those

test results. With this recommended modification to the boundary, the response for the time-to-peak of .45 seconds will then not violate the criterion envelope.

Comparison of the pitch responses based on damping constant ($\xi\omega_n$) with the criterion envelope is very straightforward as seen in Figure 14. All responses that were rated satisfactory are well within the envelope and the one response that was unsatisfactory (pilot rating = 4.5) violates the boundary.

The conclusion is that the SST Time Response Criterion with the recommended boundary modification presented in Figure 15 does provide an adequate and complete method for verifying satisfactory high-speed longitudinal handling qualities for the parameters investigated.

Column Force Gradient

Results of the evaluation of column force gradient are presented in Figure 16. As seen, these results did not establish any preferred boundary over the range tested. No real conclusions were drawn from these data.

STALL RECOVERY CONTROL POWER

The purpose of evaluating stall recovery control power was to develop a criterion that defines the magnitude of elevator control power needed for safe, positive recovery from this high angle of attack, minimum speed condition.

Normal stall is associated with a sudden loss of lift and a nose-down pitch reaction which results in a stable stall recovery with minimum reaction required from the pilot. Delta wing and arrow wing configurations do not exhibit the normal stall characteristic, that is, there is normally not a sudden loss of lift nor a nose-down moment. With such configurations the stall speed is a defined speed known as the minimum demonstrated speed, or in more general terms, the speed associated with the maximum demonstrated lift coefficient. Establishment of the defined stall speed is based on restricting the aircraft to avoid encountering undesirable high angle of attack characteristics such as a loss of directional stability, pitch up, etc. Also, one of the items that might be limiting at the defined stall speed is the amount of elevator control power available in the nose-down direction, since the pilot must recover the aircraft from the defined stall speed manually. Defining a criterion covering elevator control power for stall recovery was the purpose of this simulator evaluation.

The stall recovery control power evaluation was conducted by varying the magnitude of the elevator control power and having the pilot fly a series

of typical stall approaches terminated with manual stall recovery. A detailed description of the pilot task is presented in Table III.

Longitudinal stability from this evaluation was near neutral as seen in Figure 17, which is typical for an airplane of this type. Variations of the elevator control power were made in such a manner as to not affect the longitudinal stability.

In addition to evaluating the variation in elevator control power the effect of atmospheric turbulence was also determined. Atmospheric turbulence was varied from zero to 2.13 m/sec (7.0 ft/sec) root mean square vertical gusts.

Results of this study are presented in Figure 18 as a function of nose-down angular acceleration rather than elevator control power to make the results generally applicable. Nose-down angular acceleration was based on full nose-down elevator at the defined stall speed from a trimmed flight condition. Corrections to the data were applied for any out of trim condition at initiation of stall recovery.

Some data scatter does result as can be seen in Figure 18, but satisfactory fairings have been generated. Also, a boundary is shown corresponding to a pilot rating of 3.5. The pilot rating of 3.5 was selected as the boundary for required stall recovery control power since that is the dividing line between a configuration needing improvement and one not needing improvement. Stall recovery is an emergency maneuver for commercial airplanes and airplanes must be judged satisfactory with no improvement needed for this maneuver to insure positive recovery.

The effect of turbulence was to require an increased nose-down angular acceleration with increased turbulence levels. In order to generalize the criterion the data were cross plotted to provide angular acceleration required as a function of turbulence level for a pilot rating of 3.5. This criterion is presented in Figure 19.

This generalized criterion then gives the designer the option of establishing the required nose-down angular acceleration based on his particular probable maximum turbulence level associated with stall. As long as stall recovery is not coupled with some other stability or control problem, this criterion is satisfactory.

CONCLUDING REMARKS

Results of this study have shown a requirement for increased sensitivity of the pitch attitude display at high-speed cruise. The desired sensitivity established for this evaluation was .762 cm/deg (.3 in/deg).

Short period longitudinal response parameters have been shown to correlate with the previously defined SST Time Response Criterion. This criterion with a recommended modification will define satisfactory handling qualities considering the type of response characteristics evaluated in this study.

A minimum level of longitudinal control power was defined for stall recovery for aircraft that exhibit the delta wing or arrow wing stall characteristics. The control power was found to be affected by atmospheric turbulence. Correlation of longitudinal control power with atmospheric turbulence as a general criterion was accomplished.

REFERENCES

1. Sudderth, R. W., Bohn, J. G., Caniff, M.A., Bennett, G. A., "Development of Longitudinal Handling Qualities Criteria for Large Advanced Supersonic Aircraft," NASA CR-137635, March, 1975.

2. Anon: Military Specification, Flying Qualities of Piloted Aircraft, MIL-F-8785 (ASG), United States Air Force, August 7, 1969.

3. Anon: Federal Aviation Regulations, Part 25, "Airworthiness Standards: Transport Category Airplanes. Code of Federal Regulations, Federal Aviation Administration. Revised January 1, 1973.

4. Malcom, L. G. and Tobie, H. N., "New Short Period Handling Quality Criteria for Fighter Aircraft," Boeing Document No. D6-17841-T/N, September, 1965.

5. SST Engineering Staff, "Stability and Control, Flight Control, and Hydraulic Systems Design Criteria," Boeing Document No. D6-6800-5, 1970.

6. Shomber, H. A. and Gertsen, W. M., "Longitudinal Handling Qualities Criteria," AIAA Paper No. 65-780, November, 1965.

TABLE I.- HIGH-SPEED CRUISE MANEUVERING TEST CONDITIONS

VARIED PARAMETERS		RANGE
EADI PITCH SCALE SENSITIVITY		.41 cm / deg (.16 in/deg) .58 (.23) .76◊ (.30) ◊
PITCH RESPONSE TO A COLUMN STEP INPUT	PITCH RATE OVERSHOOT RATIO, $\dot{\theta}_{max} / \dot{\theta}_{ss}$	1.94 4.10 ◊ 6.10 8.20
	TIME-TO-PEAK PITCH RATE, $T\dot{\theta}_{max}$	.45 sec .90 ◊ 1.40 2.00
	DAMPING CONSTANT, $\xi\omega_n$	.36 1/sec .90 ◊ 2.42
COLUMN FORCE GRADIENT, F_{col}/g		45 N/g (10 lb/g) 111 (25) 200◊ (45)◊ 285 (64)

◊ NOMINAL VALUES

TABLE II.- HIGH-SPEED CRUISE MANEUVERING PILOT TASK

ALTITUDE CHANGES (HOLDING MACH NO. CONSTANT):

1. CLIMB 76M @ 152M/MINUTE (250 FT @ 500 FPM) AND STABILIZE
2. DESCEND 229M @ 305M/MINUTE (750 FT @ 1000 FPM) AND STABILIZE
3. CLIMB 305M @ 610M/MINUTE (1000 FT @ 2000 FPM) AND STABILIZE
4. DESCEND 152M @ 152M/MINUTE (500 FT @ 500 FPM) AND STABILIZE

AIRSPEED CHANGES (HOLDING ALTITUDE CONSTANT):

1. INCREASE SPEED 20 KNOTS AND STABILIZE
2. DECREASE SPEED 40 KNOTS AND STABILIZE
3. INCREASE SPEED 20 KNOTS AND STABILIZE

HEADING CHANGES (HOLDING ALTITUDE AND AIRSPEED CONSTANT):

1. TURN 15° LEFT IN 15° BANK AND LEVEL OFF
2. TURN 20° RIGHT IN 30° BANK AND LEVEL OFF

TABLE III.- STALL RECOVERY PILOT TASK

1. TRIMMED AT MINIMUM OPERATION SPEED (145 KNOTS CAS)

2. REDUCE THRUST TO ESTABLISH DECELERATION RATE

3. AT MINIMUM DEMONSTRATED SPEED (118 KNOTS CAS) INITIATE MAXIMUM EFFORT STALL RECOVERY

4. USE THRUST AS NECESSARY TO MINIMIZE ALTITUDE LOSS

5. CONDUCT TEST THREE TIMES VARYING AIRCRAFT DECELERATION RATE WITH 1 KNOT/SEC AS NOMINAL
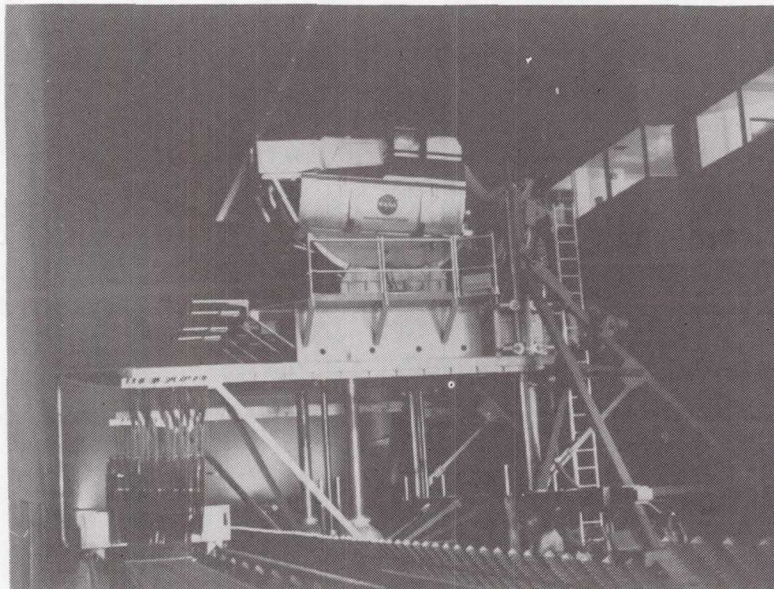
Figure 1.- Flight simulator for advanced aircraft.

WING AREA = 715. 3 m^2 (7700 ft^2)
WING SPAN = 30. 9 m (101. 5 ft)
REF CHORD = 43. 18 m (141. 67 ft)
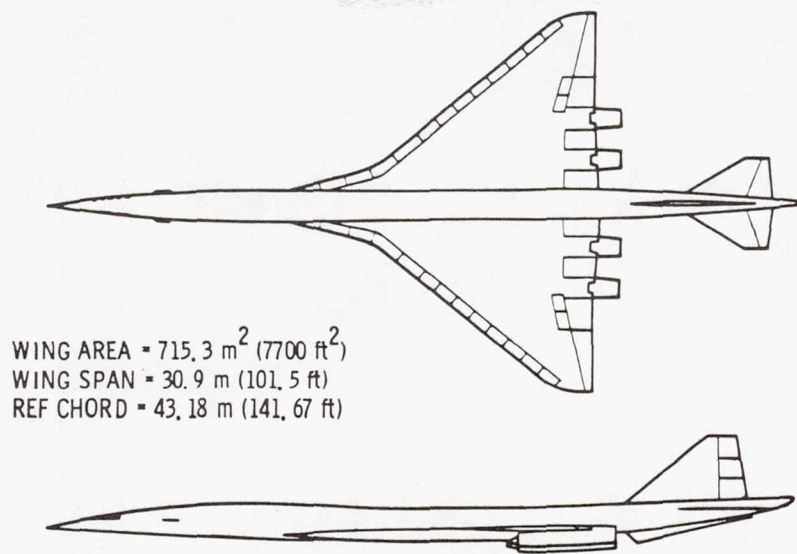
Figure 2.- Baseline configuration (2707-300 PT).

Figure 3.- Simulator cockpit.

ADEQUACY FOR SELECTED TASK OR REQUIRED OPERATION*	AIRCRAFT CHARACTERISTICS	DEMANDS ON THE PILOT IN SELECTED TASK OR REQUIRED OPERATION*	PILOT RATING
	Excellent Highly desirable	Pilot compensation not a factor for desired performance	1
	Good Negligible deficiencies	Pilot compensation not a factor for desired performance	2
	Fair — Some mildly unpleasant deficiencies	Minimal pilot compensation required for desired performance	3
Is it satisfactory without improvement? — Yes / No → Deficiencies warrant improvement	Minor but annoying deficiencies	Desired performance requires moderate pilot compensation	4
	Moderately objectionable deficiencies	Adequate performance requires considerable pilot compensation	5
	Very objectionable but tolerable deficiencies	Adequate performance requires extensive pilot compensation	6
Is adequate performance attainable with a tolerable pilot workload? — Yes / No → Deficiencies require improvement	Major deficiencies	Adequate performance not attainable with maximum tolerable pilot compensation. Controllability not in question	7
	Major deficiencies	Considerable pilot compensation is required for control	8
	Major deficiencies	Intense pilot compensation is required to retain control	9
Is it controllable? — Yes / No → Improvement mandatory	Major deficiencies	Control will be lost during some portion of required operation	10

Pilot decisions

* Definition of required operation involves designation of flight phase and/or subphases with accompanying conditions.

Figure 4.- Handling qualities rating scale.
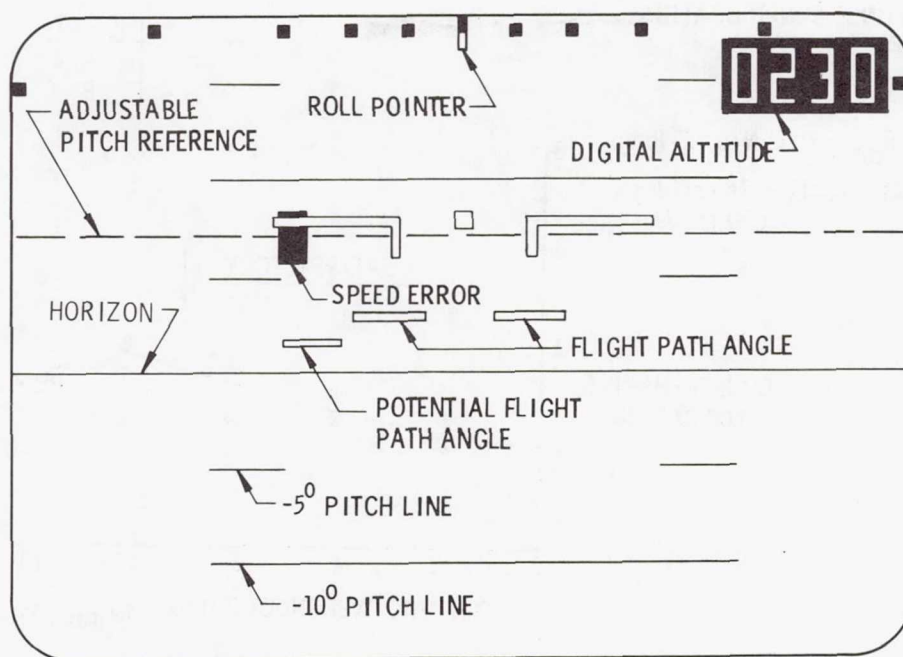
Figure 5.- Electronic attitude director indicator.
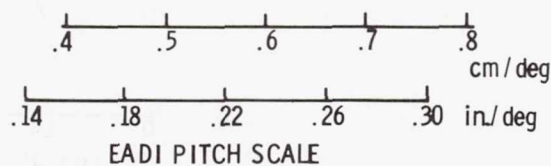
Figure 6.- High-speed cruise evaluation of EADI pitch scale sensitivity.

RESPONSE CONFIGURATION
$T\dot{\theta}_{max}$ = 0.9 sec
$\xi\omega_n$ = 0.9 1/sec
F_{col}/g = 111 N/g (25 lb/g)
EADI SCALE = .76 cm/deg
(.30 in./deg)

SYM	PILOT
O	A
△	B

COOPER-HARPER
PILOT RATING

SATISFACTORY

PR = 3.5

PITCH RATE OVERSHOOT RATIO, $\dot{\theta}_{max}/\dot{\theta}_{ss}$
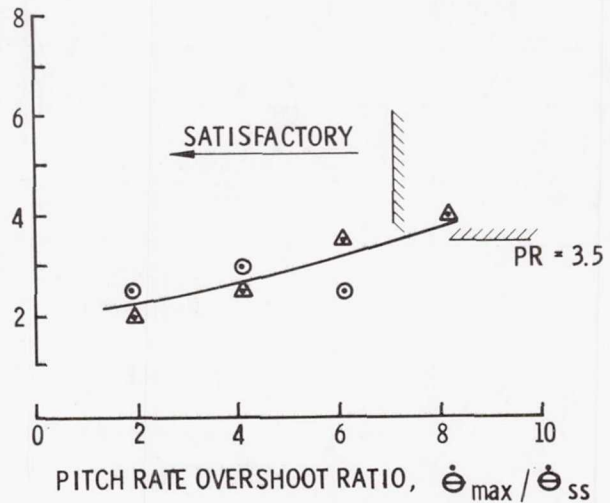
Figure 7.- High-speed cruise evaluation of
pitch rate overshoot ratio.

RESPONSE CONFIGURATION
$\dot{\theta}_{max}/\dot{\theta}_{ss}$ = 4
$\xi\omega_n$ = 0.9 1/sec
F_{col}/g = 111 N/g (25 lb/g)
EADI SCALE =
.76 cm/deg
(.30 in./deg)

SYM	PILOT
O	A
△	B

COOPER-HARPER
PILOT RATING

SATISFACTORY

PR = 3.5

TIME-TO-PEAK PITCH RATE, $T\dot{\theta}_{max}$, sec
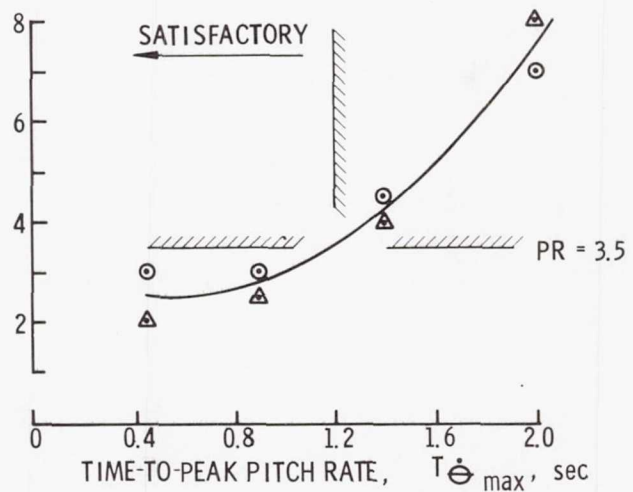
Figure 8.- High-speed cruise evaluation of
time-to-peak pitch rate.

RESPONSE CONFIGURATION

$\dot{\Theta}_{max}/\dot{\Theta}_{ss}$ = 5.3 TO 3.8

$T\dot{\Theta}_{max}$ = .7 TO .95 sec

F_{col}/g = 111 N/g (25 lb/g)

EADI SCALE =
.76 cm/deg
(.30 in./deg)

SYM	PILOT
O	A
△	B

COOPER-HARPER
PILOT RATING

SATISFACTORY

PR = 3.5

LONGITUDINAL DAMPING CONSTANT, $\xi\omega_{n'}$ 1/sec
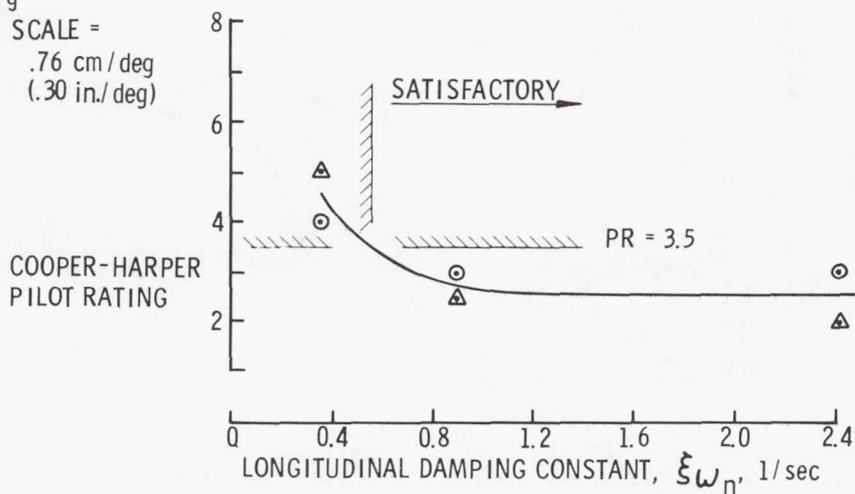
Figure 9.- High-speed cruise evaluation of
longitudinal damping.

NORMAL OPERATION
PR = 3.5

L_α/ω_n CRITERION

n_α/ω_n CRITERION

FOR LOW n_α
($n_\alpha < 15$)

$\frac{L_\alpha}{\omega_n}$

DAMPING RATIO ξ

FOR HIGH n_α
($n_\alpha \geq 15$)

$\frac{n_\alpha}{\omega_n}$
(sec)

DAMPING RATIO ξ
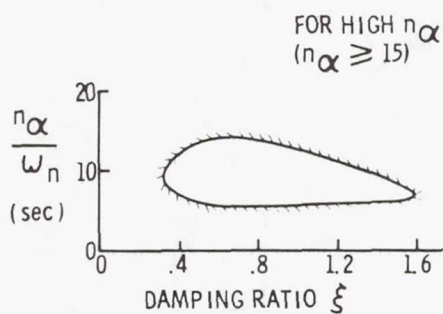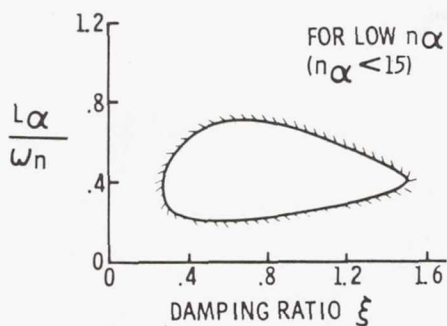
REFERENCE: AIAA PAPER 65-780

Figure 10.- Shomber-Gertsen longitudinal
handling qualities criteria.

187

RESPONSE TO STEP INPUT

n_α = 16.535 g/rad

NORMAL OPERATION

PR = 3.5

$\dfrac{\dot{\theta}}{\dot{\theta}_{ss}}$

TIME , sec

$\dfrac{\Delta n_z}{\Delta n_{z_{ss}}}$

TIME , sec
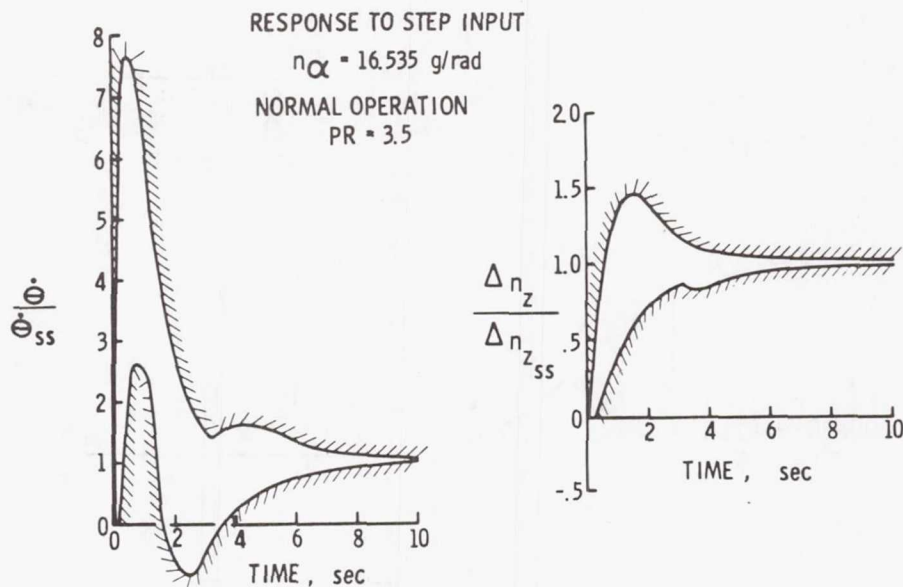
Figure 11.- SST time response criteria (derived from Shomber-Gertsen criteria).

$\dot{\theta}_{max}/\dot{\theta}_{ss}$

8.20 (PR = 3.8)

6.10 (PR = 3.2)

4.10 (PR = 2.6)

1.94 (PR = 2.3)

RESPONSE TO STEP INPUT

n_α = 16.535 g/rad

NORMALIZED PITCH RATE

$\dot{\theta}/\dot{\theta}_{ss}$

TIME , sec
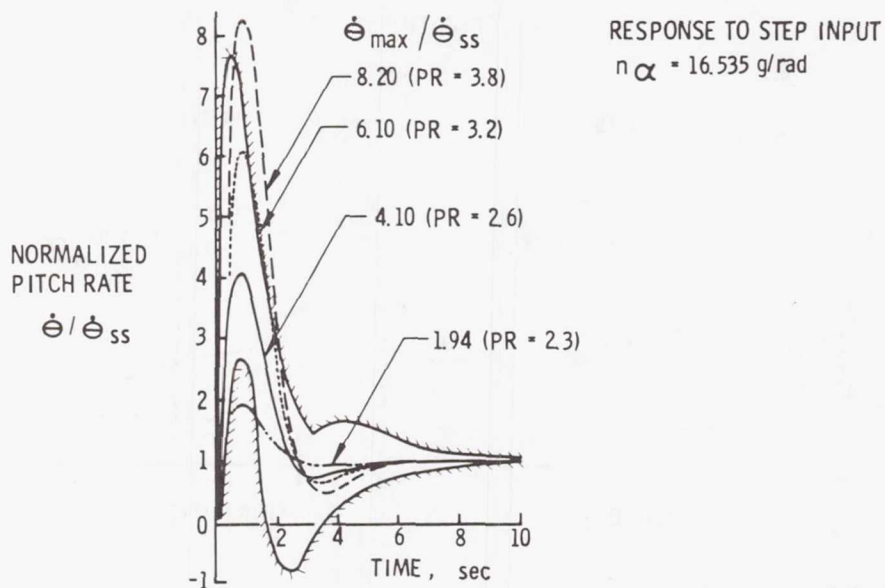
Figure 12.- Pitch rate overshoot comparison with criterion.
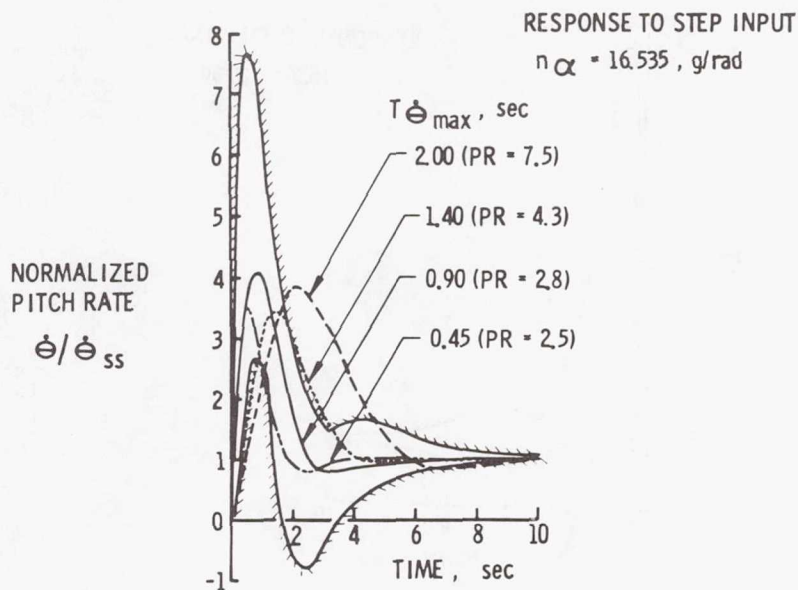
Figure 13.- Time-to-peak pitch rate comparison
with criterion.
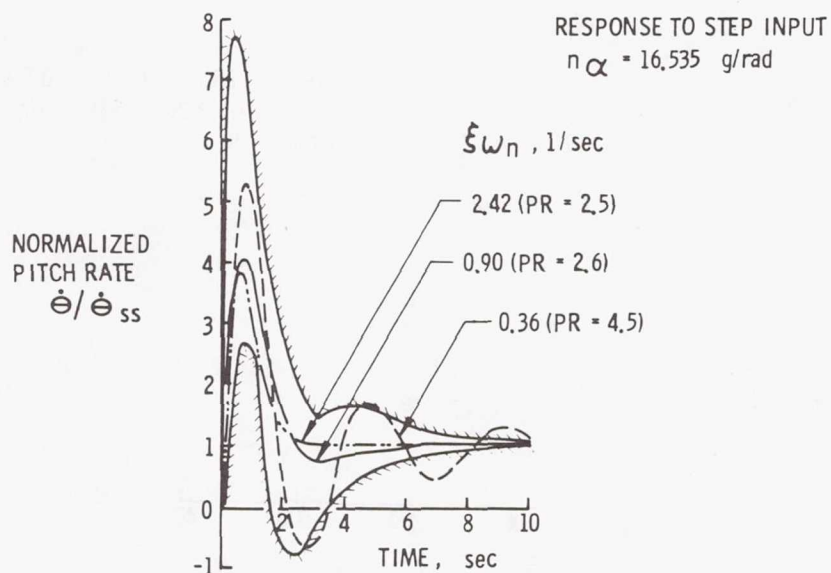
Figure 14.- Pitch damping comparison with criterion.

RESPONSE TO STEP INPUT
$n_\alpha = 16.535$ g/rad

$\dfrac{\dot{\theta}}{\dot{\theta}_{ss}}$

TIME , sec
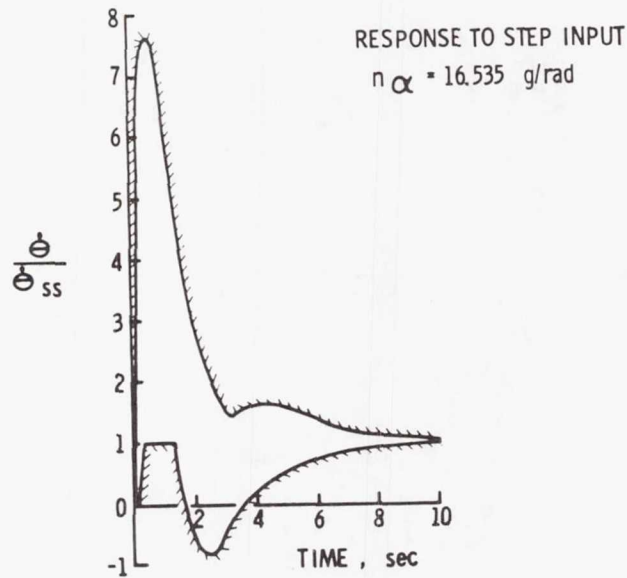
Figure 15.- Modified SST high-speed pitch rate
response criterion.

RESPONSE CONFIGURATION
$\dot{\theta}_{max}/\dot{\theta}_{ss} = 4$
$T\dot{\theta}_{max} = 0.9$
$\xi \omega_n = 0.9$ 1/sec
EADI SCALE =
7.6 cm/deg
(.30 in./deg)

SYM	PILOT
Δ	B

MIL-F-8785 LIMITS BASED ON
A LOAD FACTOR DESIGN LIMIT
OF 2.5 g'S

COOPER-HARPER
PILOT RATING

N/g

lb/g

COLUMN FORCE GRADIENT
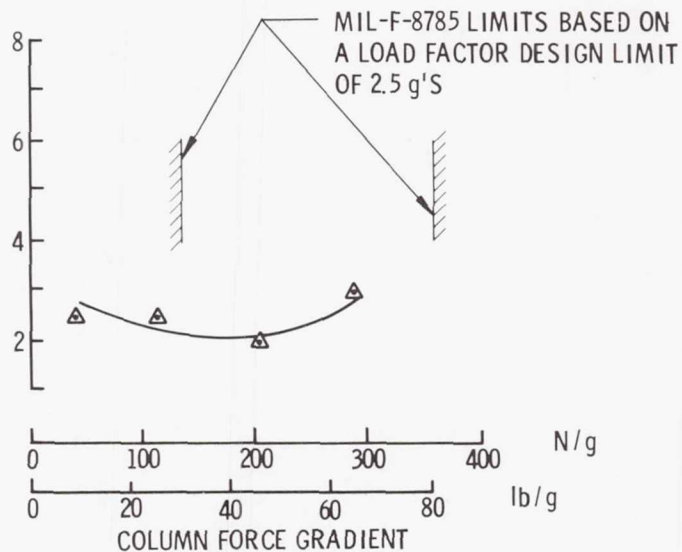
Figure 16.- High-speed cruise evaluation of
column force gradient.
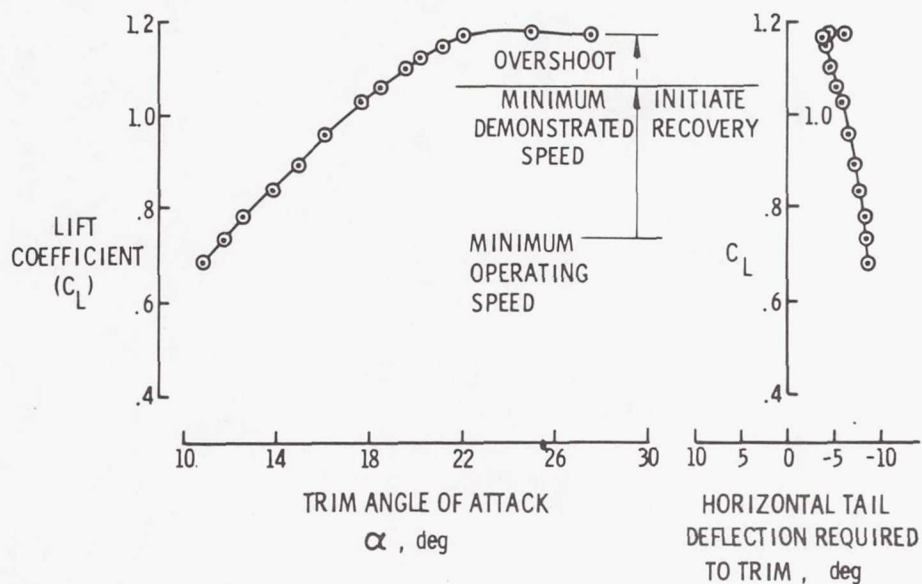
Figure 17.- Longitudinal stability — stall recovery evaluation.
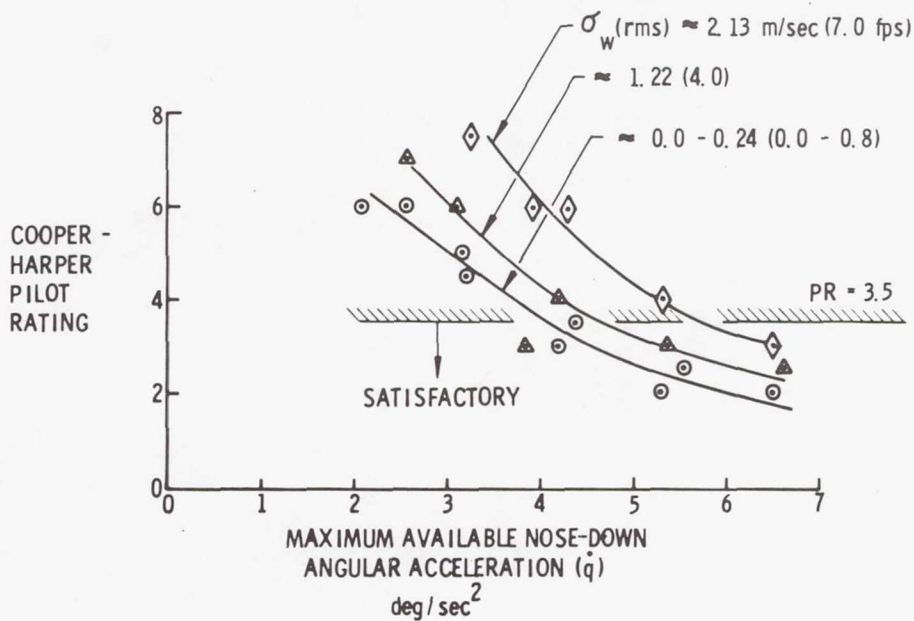
Figure 18.- Stall recovery control power evaluation.

NORMAL OPERATION
PILOT RATING = 3.5

SATISFACTORY

MAXIMUM AVAILABLE
NOSE-DOWN ANGULAR
ACCELERATION
$\dot{q}$, deg/sec^2
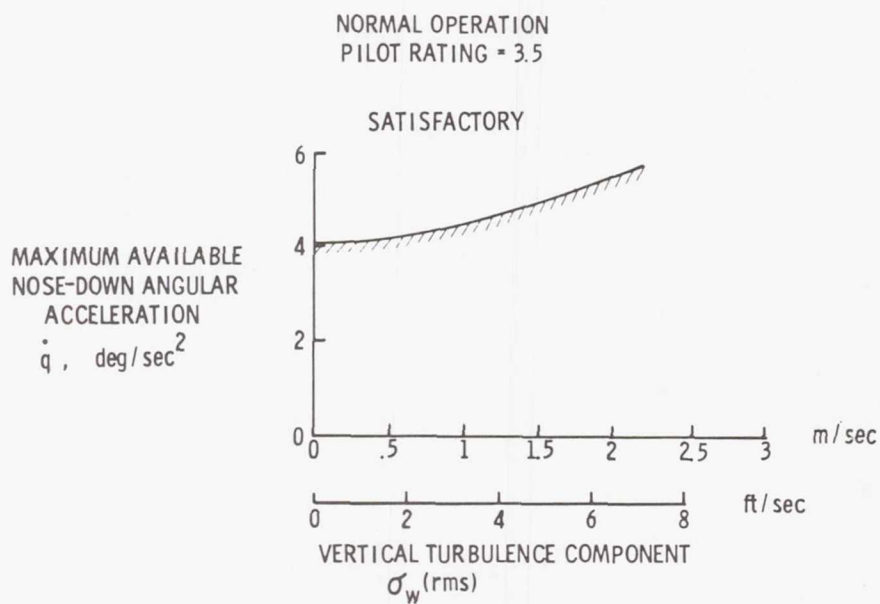
Figure 19.- Effect of turbulence on stall recovery
control power.

192

HANDLING QUALITIES ASPECTS OF

NASA YF-12 FLIGHT EXPERIENCE

Donald T. Berry, Donald L. Mallick,
and Glenn B. Gilyard
NASA Dryden Flight Research Center

SUMMARY

This paper reviews the handling qualities of the YF-12 airplane as observed during NASA research flights over the past five years. Aircraft behavior during takeoff, acceleration, climb, cruise, descent, and landing are discussed. Pilot comments on the various flight phases and tasks are presented. Handling qualities parameters such as period, damping, amplitude ratios, roll-yaw coupling, and flight path response sensitivity are compared to existing and proposed handling qualities criteria. The influence of the propulsion systems, stability augmentation, autopilot systems, atmospheric gusts, and temperature changes are also discussed. The results indicate that YF-12 experience correlates well with flying qualities criteria, except for longitudinal short period damping, where existing and proposed criteria appear to be more stringent than necessary. Problems with long period flight path control and inlet unstarts are generic to supersonic cruise vehicles, and criteria for these characteristics do not exist. The influence of the propulsion system must be considered when evaluating vehicle stability and control.

INTRODUCTION

The YF-12 airplane is the only true Mach 3 cruise aircraft in the free world, and, as the record books attest, aircraft of the YF-12 series are the fastest in the world. Although designated a fighter, the aircraft was designed for missile-launching interceptor and high-altitude reconnaissance roles. Consequently, its design emphasizes range and speed, rather than maneuverability. Flight research programs with this aircraft have offered NASA a unique opportunity to observe the handling qualities of a supersonic cruise vehicle in an actual flight environment.

This paper discusses aspects of YF-12 handling qualities that appear to have general applicability to supersonic cruise vehicles, with particular emphasis on operating problems and handling qualities criteria. A qualitative description of the aircraft's flying qualities throughout the flight envelope is presented in terms of pilot comments. Since the aircraft is normally operated with a full-time stability augmentation system (SAS), this paper primarily discusses the augmented aircraft. However, some SAS-off cases of special interest are also covered. The latter part

of the paper presents a detailed and quantitative description of certain selected characteristics. Correlations with handling qualities criteria are made where applicable. Finally, the implications of this experience are discussed in terms of potential requirements for future supersonic cruise vehicles.

SYMBOLS

Physical quantities are given in the International System of Units (SI) and parenthetically in U.S. Customary Units. All measurements were taken in Customary Units.

a_t lateral acceleration at aircraft center of gravity, g

a_x longitudinal acceleration at aircraft center of gravity, g

Δh incremental altitude, m (ft)

M Mach number

n/α change in normal acceleration per unit change in angle of attack, g/rad

p roll rate, deg/sec

r yaw rate, deg/sec

β angle of sideslip, deg

δ_a differential elevon deflection, percent of maximum

δ_r rudder deflection, percent of maximum

ζ_{DR} Dutch roll damping ratio

ζ_{SP} longitudinal short period damping ratio

$\dfrac{\dot{\theta}}{\dot{\theta}_{ss}}$ ratio of peak pitch rate to steady state pitch rate

τ_r roll mode time constant, sec

τ_s spiral mode time constant, sec

194

φ bank angle, deg

$\omega_{n_{DR}}$ Dutch roll undamped natural frequency, rad/sec

$\omega_{n_{SP}}$ longitudinal short period undamped natural frequency, rad/sec

ω_{φ} frequency term of bank angle-to-aileron transfer function numerator, rad/sec

AIRPLANE DESCRIPTION

The YF-12 airplane is an advanced, twin-engined, delta-winged interceptor designed for long-range cruise at speeds greater than Mach 3 and at altitudes above 24,384 meters (80,000 feet). A photograph and a three-view drawing of the airplane are shown in figures 1 and 2, respectively. The airplane has two axisymmetric, variable-geometry, mixed-compression inlets, which supply air to two J58 engines. Each inlet has a translating compression spike and forward bypass doors to control the position of the normal shock in the inlet. An automatic inlet control system varies the spike and bypass door positions to maintain the normal shock in the optimum position. Manual control of the spike and bypass doors is also available, which enables the pilot to fix the spike and bypass doors at a desired position.

Two nacelle-mounted, all-movable vertical tails provide directional stability and control. Additional directional stability is provided by ventral fins on the nacelles and fuselage. Each vertical tail is canted inward and pivots on a small stub section attached directly to the top of each nacelle. Two elevons on each wing, one inboard and one outboard of each nacelle, perform the combined functions of ailerons and elevators.

The airplane is normally operated with a stability augmentation system (SAS) engaged to provide artificial stability in pitch and yaw, and damping in pitch, yaw, and roll. An autopilot with pitch attitude, knots equivalent airspeed (KEAS), Mach, and altitude hold modes is also available. Additional details on the flight and propulsion controls can be found in references 1 to 3.

QUALITATIVE DESCRIPTION OF AIRCRAFT FLYING QUALITIES

When test pilots discuss aircraft handling qualities, they are more likely to concentrate on the poor characteristics and not mention the good points. In this paper both the desirable and undesirable handling qualities of the YF-12 aircraft are discussed to give a complete picture of a very impressive high-speed,

high-altitude aircraft. In addition to the basic handling qualities, such as damping, force gradients, and control responses, other important areas, such as pilot visibility, structural modes, inertias, and aircraft systems, are discussed.

The pilot commentary presented here is a product of five years of flight experience during the NASA YF-12 flight research program. In this program, the U.S. Air Force YF-12A and YF-12C aircraft are used as test vehicles to gather flight data on aerodynamic loads, propulsion system characteristics, and other areas unique to the environment at speeds in excess of Mach 3.0 and altitudes above 24,384 meters (80,000 feet). The sequence followed in the discussion is that of a normal test flight from takeoff to landing.

Takeoff and Initial Climb

Takeoff is begun with afterburner power and takeoff acceleration is normally good. Back stick force is applied at approximately 160 knots indicated airspeed (KIAS) and the nose wheel lifts off at approximately 180 KIAS. The aircraft is then rotated and held at a 10° pitch attitude while it accelerates to approximately 200 KIAS where lift-off occurs. The longitudinal control response and damping are good and there is no tendency to overrotate or hunt for the 10° takeoff attitude. However, the aircraft's ride and its response to a rough runway make it difficult at times to smoothly rotate to and hold a given takeoff attitude. At Edwards Air Force Base, both rough and smooth runways are available to help evaluate these characteristics. On a rough runway, the flexible fuselage of the YF-12 aircraft gives the pilot a very bumpy ride in the vertical axis. This physical input to the pilot, in addition to the motion of the aircraft's nose, makes it difficult to hold a precise takeoff attitude. The problem involves a very uncomfortable ride and the possibility of skipping or touching down after initial lift-off. For the pilot, the problem is not considered dangerous, but rather a nuisance; for revenue passengers, the ride may be objectionable.

Gear retraction results in a moderate nose-up trim change that is easily controlled. The pilot must compensate for the trim change to avoid an excessive nose-high attitude after takeoff. Acceleration to 400 KEAS is rapid and the normal procedure is to reduce power to military for the initial climb. Some concentration on speed control is required during the climb. This may be partly due to the loss of the visual horizon as a result of the nose-high climb attitude. In addition, the aircraft's speed stability seems low. Roll and pitch control forces are harmonized and reasonable; responses in these axes are quite adequate. All three axes are well damped with SAS on. Very little rudder activity is required except for trim.

Acceleration and Climb

The subsonic climb is made to approximately 10,700 meters (35,000 feet). Minimum afterburner is selected at 6100 meters (20,000 feet) and maximum afterburner at 7600 meters (25,000 feet). When a speed of Mach 0.9 and an altitude of 10,700 meters (35,000 feet) are attained, a pushover-type acceleration is used to

reach supersonic speed. The pushover acceleration is used rather than a level acceleration to expedite the aircraft through the transonic range of high drag into the low supersonic range where more excess thrust is available for the continued acceleration and climb to cruise conditions.

When the supersonic climb KEAS is reached, a constant KEAS (constant dynamic pressure) acceleration climb is made to cruise conditions. Little trim change is required for this particular phase of flight. The aircraft's longitudinal and speed stability is such that the pilot must pay attention to KEAS to avoid overshoots or undershoots in speed. A lack of care with pitch control inputs may result in the pilot's chasing airspeed (making continual corrections to attain the desired air-speed). The autopilot relieves the pilot of the airspeed control task. However, if only the attitude command feature is used on the autopilot, the pilot may still be chasing airspeed through the pitch command wheel. The autopilot KEAS hold mode resolves the problem of airspeed control during the acceleration climb.

A problem that contributes to the pilot's task of maneuvering the aircraft is the delay due to inertia, or the time required to alter the aircraft's vector. Because of this delay, the pilot must anticipate changes and lead the aircraft to arrive at a new speed or altitude without an overshoot. This delay is especially obvious in the establishment of a stabilized point in cruise.

Cruise Flight

As the aircraft approaches the point to level off for cruise, it is operating at design conditions and has excess thrust available. Approximately 1000 meters (3000 feet) below the desired cruise altitude, the pilot must reduce throttle and start the noseover maneuver. Even with anticipation and experience, it is difficult to maneuver precisely to the desired conditions and sometimes several secondary adjustments in speed and altitude are required.

One problem that was discovered early in the program was the excessive lag in the pressure rate of climb indicator. The lag was such that the pilot would often be chasing the pressure rate of climb. This problem was present not only while leveling off, but also during cruise. The addition of an inertial rate of climb display for the pilot's panel greatly improved this situation. The inertial rate of climb display enabled the pilot to control altitude so well that he then became more aware of the inertia in speed response that is associated with the engines, inlets, airspeed, and, in some cases, atmospheric temperature changes. In other words, once the altitude was stabilized by means of the inertial rate of climb information, the pilot noticed it was difficult to set a throttle position that would hold constant speed. This problem was essentially solved by providing the pilot with an inertial longitudinal acceleration display. The addition of an inertial rate of climb display and an inertial longitudinal acceleration display greatly aided the research pilot in setting up the numerous stabilized test points required in the program.

Stability

Stability augmentation system on.—As noted earlier, the longitudinal (speed) stability is such that much effort is required to set up a trim or cruise condition. Once the condition is established, the aircraft with the SAS on will hold speed and altitude well if not disturbed. Unfortunately, small pitch attitude changes not immediately apparent to the pilot occur, and by the time the pilot notices it, a moderate altitude change is underway. In addition, atmospheric changes can cause Mach number changes of ±0.05 without pilot inputs. Therefore, the pilot's constant scanning and full attention are required to hold a precise test condition. The lateral stability appears to be neutral with no tendency for the aircraft to roll off. It is difficult, however, to trim the aircraft with wings exactly level and it is not unusual to have a degree or two of undesired bank angle. Throughout the flight envelope, the directional stability and damping are very high. The aircraft tends to change slightly in directional trim with Mach number change, which may be due to slight differences in engine-inlet performance. Short period damping in all axes is high with the SAS on.

Stability augmentation system off.—Extended flight tests have been conducted with pitch SAS off and with roll and yaw SAS off, but never with pitch and yaw SAS off at the same time. With pitch SAS off, the short period is not as well damped, but the decrease in damping is not immediately apparent to the pilot during cruise conditions with pulse-type inputs. With the yaw and roll SAS off, the reduction in directional damping with increasing Mach number can be observed by the pilot. This reduction is apparent in the case of a rudder-induced sideslip and the slow tendency of the nose to return when the controls are neutralized. In addition, another phenomenon related to the engine-inlet system will actually drive the aircraft into a slowly divergent yaw oscillation with the yaw and roll SAS off. This is caused by the phasing of the automatic inlet response to the sensed sideslip.

Inlet Unstart

The unstart condition of the engine inlets introduces strong pitch, yaw, and roll moments to the aircraft. Depending on the aircraft's attitude at the time of unstart, these inputs can be of some concern to the pilot. The aircraft's response to an unsymmetrical unstart is to roll toward the unstarted inlet and to pitch upward. In level flight with a normal center of gravity and SAS on, the unstart is not of great concern to the pilot; however, the sharp cracking noise, the vibration in the aircraft, and the loss of speed and altitude are disconcerting. The SAS input, in addition to the pilot's natural reaction of forward stick and roll control, normally results in a minimal attitude change. However, if the unstart occurs on the inside engine during a turn or a pullup maneuver, the pilot must respond positively to prevent the divergence of the aircraft's attitude.

The unstart converts a smoothly running, steady aircraft into a noisy, vibrating machine that is rapidly losing altitude and speed. Planned and uplanned unstarts have been experienced with SAS on and SAS off and the pilot's opinion is that it is a much nicer condition with inlets started and SAS on.

Descent

Normal descents are made with inlets started and military power, which results in a long distance being required for descent. No unique handling qualities are present; aircraft handling is similar to that in acceleration and cruise. In an emergency, a more rapid descent can be made by setting the inlets to restart (a high drag condition) to expedite the letdown. Because of the rapid rate of engine cooling, some engine damage could occur in the rapid descent.

Landing

The handling qualities in the landing pattern are very good. The aircraft is well damped and control response is positive. Throttle and thrust response at landing weights is rapid. There is some tendency for the approach speed to vary, which could be due to the high sensitivity of thrust change with throttle movement. The aircraft has a positive ground effect and flare to touchdown is comfortable, usually resulting in smooth landings. A large drag parachute provides braking and nose steering is available for directional control. The military have reported that landings on wet runways with high crosswinds are a problem, but the operation at Edwards has not provided an opportunity to evaluate this condition.

Pilot's Summary

I have had the opportunity to fly a number of high-speed, high-altitude aircraft and, although they all have been fine aircraft, I have been most impressed with the YF-12 aircraft. It is a sophisticated, advanced aircraft that flies in an environment unmatched by other aircraft and does it well. I know that the manufacturer has been lauded numerous times for its accomplishments, but this pilot adds his congratulations for a job well done and still impressive—even today, years after its conception.

QUANTITATIVE DESCRIPTION OF AIRCRAFT HANDLING QUALITIES

The pilot comments in the preceding section are summarized in table I to provide a convenient cross-reference for the more quantitative information contained in this section.

General Characteristics

The pilot comments in the takeoff and landing phase (table I) include a reference to the rough ride on rougher portions of the runway. Figure 3 shows a typical YF-12 response to runway roughness. Peak-to-peak normal accelerations of over 1.0g are

experienced. Revenue passengers may object to such a ride, but for military missions it is acceptable.

In the high-speed flight phase, the pilot describes inlet unstarts as a disconcerting experience. An example of the aircraft's response to a typical unstart is given in figure 4 (ref. 4). These time histories illustrate an unstart that occurred at approximately Mach 2.7 with the SAS on and the inlets operating automatically. Within the first second after the unstart, the airplane decelerates 0.2g and experiences a peak lateral acceleration of 0.3g. Obviously, these accelerations would be disturbing to a passenger, and even hazardous if he were not belted in his seat. In addition, the roll rate exceeds 10° per second, and a structural vibration is evident in the directional mode. Although these motions could disturb a passenger, the airplane is considered to be well controlled from the pilot's point of view. However, this control was achieved with the aid of lateral acceleration feedback loops in the SAS and a crosstie system between the inlets, and by limiting the aft center-of-gravity position to maintain relatively high stability levels. Nevertheless, approximately 60 percent of rudder and of aileron was used to control the unstart reactions. No criteria presently exist to evaluate this situation.

Longitudinal Characteristics

Figure 5 summarizes typical YF-12 longitudinal characteristics on the military specification Mil-F-8785B format (ref. 5) for short period natural frequency, $\omega_{n_{SP}}$, and normal acceleration change per unit change in angle of attack, n/α. For the acceleration, climb, and cruise flight phases, n/α varies from 17g to 32g per radian and $\omega_{n_{SP}}$ varies from 2.0 radians per second to 4.6 radians per second with SAS on. With SAS off, the $\omega_{n_{SP}}$ for a high-speed cruise case decreases to 1.6 radians per second. These characteristics are well within the level one boundaries (satisfactory for normal operation), which correlates well with the pilot comments on good longitudinal response, even for the cruise case with SAS off.

Figure 6 summarizes longitudinal short period damping as a function of flight phases with the military specification level one requirements superimposed. SAS-on damping dips below the requirements during the climb, but the pilots still consider the aircraft well damped. Even the SAS-off damping is considered satisfactory by the pilots. This indicates that the military specification requirement may be too stringent for high-altitude climb and cruise flight.

Another criterion of interest is the modified supersonic transport (SST) pitch rate response criterion proposed in reference 6. This criterion is in terms of the time history of the aircraft's response to a step control input. Pure step responses from flight are not available from YF-12 flights, so step responses have been computed using flight verified data for the aerodynamics and control system. In figure 7,

typical responses for high-speed cruise are compared to the pitch rate response criterion. The SAS-on case (fig. 7 (a)) meets the criterion fairly well, but the SAS-off cruise case (fig. 7(b)) does not. The pilot comments indicate that this SAS-off cruise case is satisfactory. Although SAS-off experience with the aircraft is quite limited as compared to SAS-on experience, there seems to be a tendency for the pilots to be more tolerant of low damping for high-speed cruise than the criterion would indicate. This SAS-off case also did not correlate with the military specification requirements for damping; however, the military specification is based on a very limited data base (ref. 7).

The pilot comments and aircraft parameters discussed so far are concerned with short term control response, and in general, theses characteristcs are good. However, as table I indicates, Mach and altitude control can be very demanding. This behavior is related to the phugoid and long term control response of the aircraft. Many factors are involved, such as an unfavorable balance of kinetic to potential energy, atmospheric disturbances, low levels of speed stability, low aircraft drag, changes of thrust with Mach number, cockpit displays, and autopilot behavior. It is beyond the scope of this paper to consider these factors in depth, but the following discussion will attempt to provide an appreciation of these various influences.

Because kinetic energy increases with the square of velocity whereas potential energy increases directly with height, large altitude changes at high speed are equivalent to small Mach number changes. As a consequence, if Mach number is to be closely controlled, large altitude changes may be required to maintain flight at a constant energy level. Supersonic cruise aircraft must fly near their limit Mach numbers for maximum efficiency, and therefore very little Mach number change can be tolerated. When Mach number disturbances that can be induced by atmospheric temperature changes are considered, the scope of the problem becomes more apparent. Figure 8 shows the theoretical altitude change required to compensate for a 10° C (18° F) change in atmospheric temperature while maintaining cruise Mach number. The calculation assumes constant energy flight, which implies that Mach number is controlled with the elevons, and the throttles are fixed. The required altitude excursion increases parabolically with cruise Mach number. Consequently, a Concorde aircraft requires almost ten times the altitude change of a B-52 aircraft and a YF-12 aircraft requires twice that of a Concorde aircraft. This situation can be alleviated somewhat by the use of throttle control, but as the pilot comments indicate, throttle response at cruise speeds is sluggish (due to low thrust to weight ratios at cruise). This sluggish response makes it difficult for the pilot to anticipate the results of his control inputs. In addition, excess thrust tends to increase with Mach number for efficient supersonic cruise aircraft, which destabilizes the aircraft's long period modes of motion. When the inlets are fixed, the propulsion system is less efficient and the long period modes are slightly stable or neutral. With the inlets operating automatically, however, the long period motion is divergent. The time history in figure 9 illustrates this effect.

Improved displays, such as the inertial rate of climb and longitudinal acceleration displays, help the pilot cope with these problems. However, an autopilot is still considered necessary to reduce pilot workload for long flights typical of a cruise vehicle. An autopilot using conventional control laws (that is, controlling Mach number with elevons) will induce large altitude excursions, just as a human pilot

does. However, studies on the YF-12 simulator have shown that if elevons are used to control altitude and an autothrottle is used to control Mach number, good flight path control can be achieved, even in the presence of atmospheric temperature changes. This is illustrated in figure 10. Concorde experience (ref. 8) has also shown the need for a supersonic cruise autothrottle. Additional information on YF-12 flight research on autopilots for supersonic cruise vehicles can be found in reference 2.

Lateral-Directional Characteristics

Table II summarizes typical YF-12 lateral-directional characteristics throughout the flight envelope. The military specification (ref. 5) requires a minimum Dutch roll frequency of 0.4 radians per second and a minimum Dutch roll damping ratio of 0.15 for level one (satisfactory, normal operation) for takeoff, landing, climb, and cruise for a YF-12-class (class II-L) aircraft. The YF-12 aircraft with SAS on is well within these requirements. The military specification requirement of a maximum roll mode constant, τ_r, of 1.4 seconds is also met. The slightly positive spiral stability is well within the military specification requirement of a time to double of no less than 20 seconds.

Note that the Dutch roll-aileron coupling parameter, $\dfrac{\omega_\varphi}{\omega_{n_{DR}}}$, is close to 1.0, indicating little or no Dutch roll excitation due to aileron control inputs, throughout the flight envelope. This was achieved without interconnects or special turn coordination channels in the SAS system, which is unusual for an aircraft with a flight envelope as large as that of the YF-12 aircraft. In general, the SAS-on lateral-directional behavior of the aircraft is very good, as the pilot comments indicate.

An interesting aspect of lateral-directional behavior occurs with SAS off above Mach 2.5. Automatic inlet operation causes significant changes in the aircraft's lateral-directional characteristics as compared to the aircraft with inlets fixed. This is illustrated in figure 11, which shows flight data of the aircraft's response to a rudder pulse with the inlets fixed and with the inlets operating automatically. When the inlets are fixed, the Dutch roll oscillations converge, but when the inlets operate automatically, the Dutch roll motions diverge. For a SAS-failed case, the Dutch roll damping meets the military specification requirements with inlets fixed, but with inlets automatic it does not. However, because of the long period of the motion, the aircraft can be safely controlled until SAS is brought back on line or the aircraft decelerates to a lower Mach number. Although complete loss of SAS is a rare occurrence because of the high reliability of the triply redundant system, the YF-12 experience illustrates the need to consider propulsion system effects when evaluating the stability and control characteristics of a supersonic cruise vehicle. It is also interesting to note in table II that automatic inlet operation increases the Dutch roll frequency and changes the phase of w/b. A detailed analysis of these phenomena is contained in reference 9.

CONCLUDING REMARKS

In general, the YF-12 aircraft has very good handling qualities, considering the large flight envelope of the aircraft. Longitudinal and lateral-directional characteristics agree well with existing short period criteria, except for longitudinal damping where both the military specification and the supersonic transport pitch rate response criteria appear to be more stringent than necessary for climb and cruise at higher altitudes.

Pilot comments indicate difficulties with inlet unstarts and long period flight path control. These problems are generic to supersonic cruise vehicles and good criteria for these characteristics do not exist. Improved displays and autopilot functions are needed to provide satisfactory flight path controls. The occurrence of inlet unstarts must be rare and automatic controls may be required to minimize their effects if they do occur.

The influence of the propulsion system on the aircraft's stability and control must be considered when evaluating the aircraft's handling qualities.

Inertial rate of climb and longitudinal acceleration displays in the cockpit help the pilot to establish stabilized conditions.

REFERENCES

1. McMaster, John R.; and Schenk, Frederick L.: The Development of the F-12 Series Aircraft Manual and Automatic Flight Control System. AIAA Paper 73-822, Aug. 1973.

2. Gilyard, G. B.; Smith, J. W.; and Falkner, V.L.: Flight Evaluation of a Mach 3 Cruise Longitudinal Autopilot. AIAA Paper 74-910, Aug. 1974.

3. Burcham, Frank W., Jr.; Holzman, Jon K.; and Reukauf, Paul J.: Preliminary Results of Flight Tests of the Propulsion System of a YF-12 Airplane at Mach Numbers to 3.0. AIAA Paper 73-1314, Nov. 1973.

4. Berry, Donald T.; and Gilyard, Glenn B.: Airframe/Propulsion System Interactions—An Important Factor in Supersonic Aircraft Flight Control. AIAA Paper 73-831, Aug. 1973.

5. Flying Qualities of Piloted Airplanes. Mil. Spec. MIL-F-8785B(ASG), Aug. 7, 1969. (Supersedes MIL-F-008785A(USAF), Oct. 31, 1968, and MIL-F-8785(ASG), Sept. 1, 1954).

6. Sudderth, Robert W.; Bohn, Jeff G.; Caniff, Martin A.; and Bennett, Gregory R.: Development of Longitudinal Handling Qualities Criteria for Large Advanced Supersonic Aircraft. NASA CR-137635, 1975.

7. Chalk, C. R.; Neal, T. P.; Harris, T. M.; Pritchard, F. E.; and Woodcock, R. J.: Background Information and User Guide for MIL-F-8785B(ASG), "Military Specification—Flying Qualities of Piloted Airplanes". AFFDL-TR-69-72, Air Force Flight Dynamics Lab., Wright-Patterson Air Force Base, Aug. 1969.

8. World News. FLIGHT International, Oct. 9, 1975, pp. 512-514.

9. Gilyard, Glenn B.; Berry, Donald T.; and Belte, Daumants: Analysis of a Lateral-Directional Airframe/Propulsion System Interaction of a Mach 3 Cruise Aircraft. AIAA Paper 72-961, Sept. 1972.

TABLE I. —SUMMARY OF PILOT COMMENTS

Takeoff and Landing

Poor ride on rough runway
Very good handling qualities
Good longitudinal control
Good SAS-on damping
Speed stability low
Sensitive throttle

Acceleration and Climb

Speed stability low
Autopilot speed control desired

High-Speed Flight and Cruise

SAS-on longitudinal damping high
SAS-off longitudinal damping low but satisfactory
Speed stability low
High workload to control Mach and altitude
Standard flight path displays inadequate
Inertial displays great improvement
SAS-on lateral-directional damping high
SAS-off lateral-directional damping divergent but
    controllable
Unstarts disconcerting

TABLE II.—TYPICAL YF-12 LATERAL-DIRECTIONAL CHARACTERISTICS

Flight phase	$\omega_{n_{DR}}$	ζ_{DR}	$\dfrac{\omega_\varphi}{\omega_{n_{DR}}}$	φ/β		τ_r, sec	τ_s, sec	SAS	Inlet
				Magnitude	Phase, deg				
Takeoff, landing	0.81	0.43	0.96	3.7	52	0.27	190	On	Automatic
[a]Acceleration and climb									
Minimum	1.30	0.36	0.94	1.5	50	0.25	254	On	Automatic
Maximum	2.00	0.61	0.97	2.5	0	0.90	523	On	Automatic
Cruise	1.36	0.43	1.00	0.4	-64	1.20	$>10^6$	On	Automatic
	1.20	-0.01	1.00	0.4	-176	3.50	$>10^6$	Off	Automatic
	1.00	0.06	1.10	0.6	40	4.50	$>10^6$	Off	Fixed

[a]Minimum and maximum values are given because of the wide range of flight conditions in this phase.

Figure 1.- Test airplane.

FORWARD BYPASS DOOR EXIT LOUVERS

CENTERBODY SPIKE

17 m
(56 ft)

31 m
(102 ft)
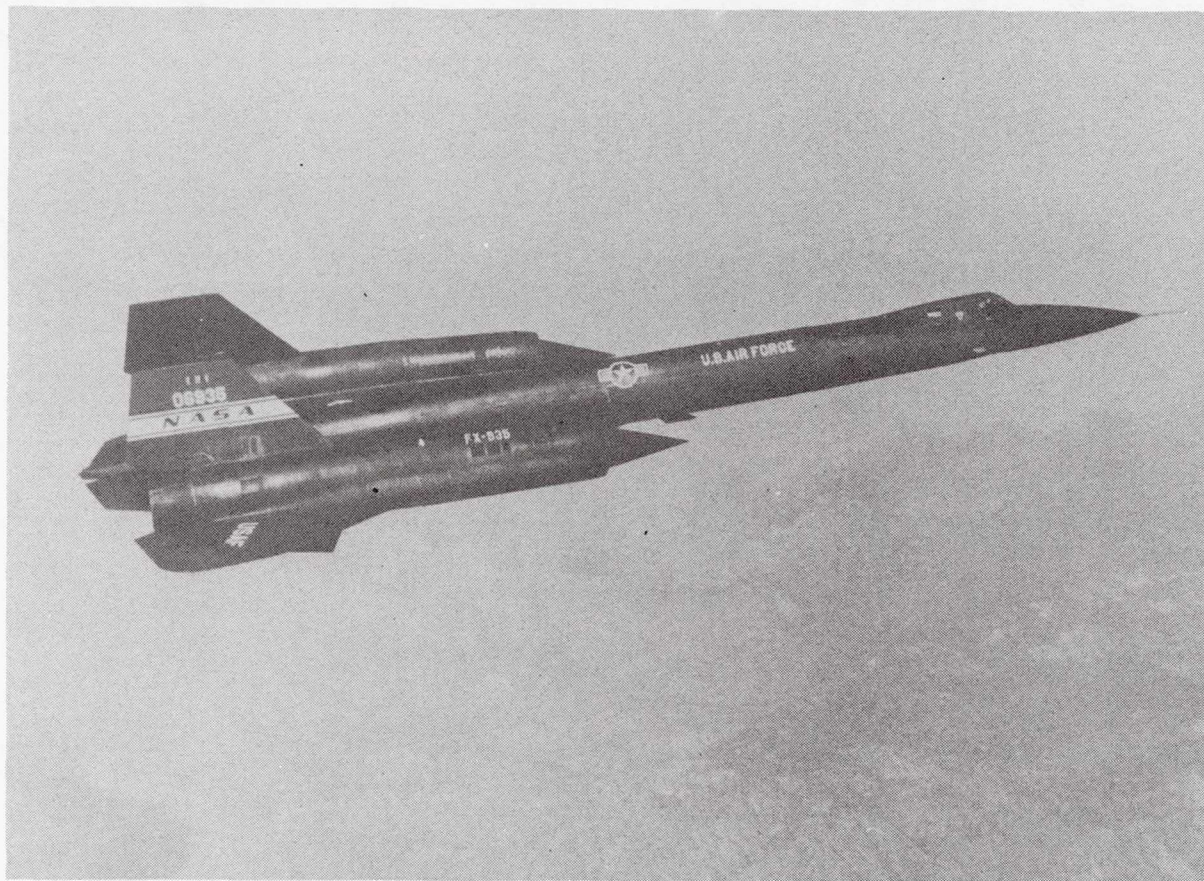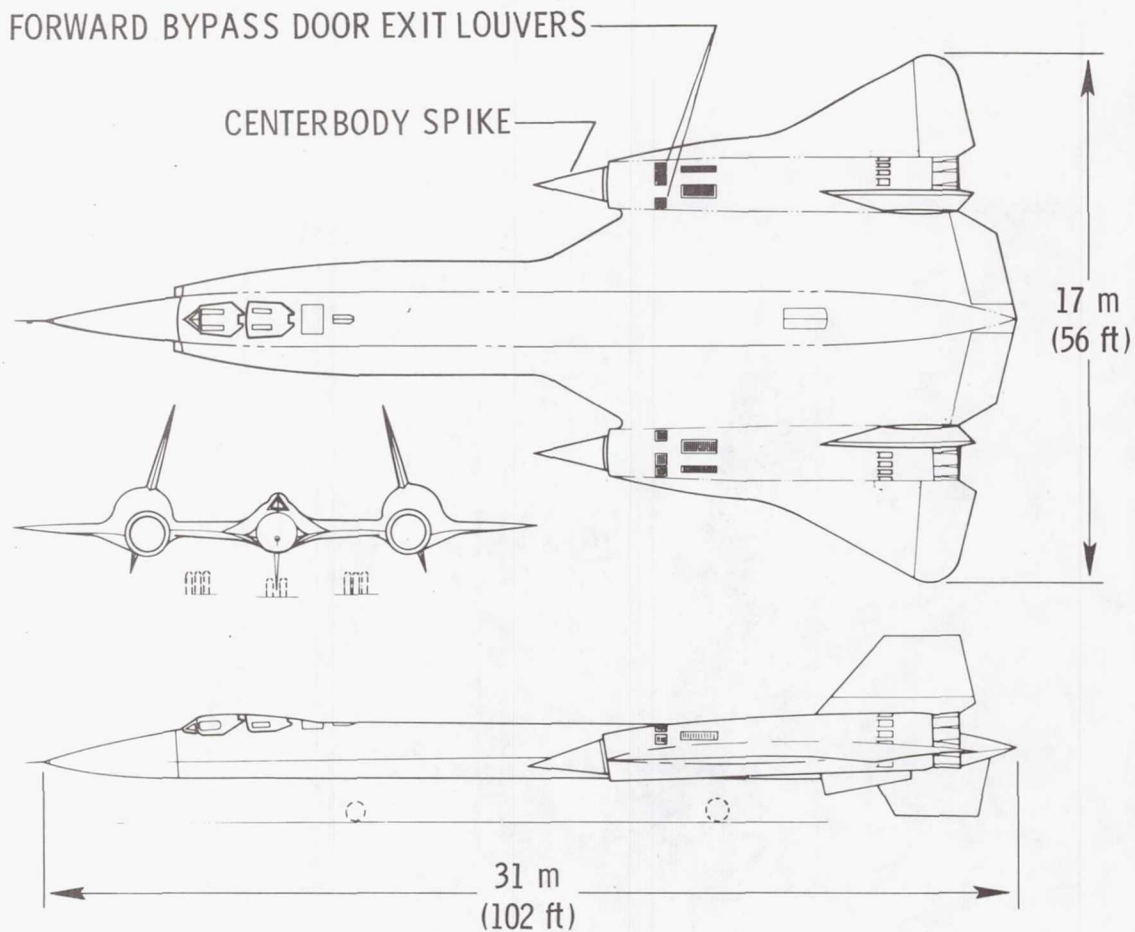
Figure 2.- Three-view drawing of test airplane.

COCKPIT NORMAL
ACCELERATION, g

TIME, sec
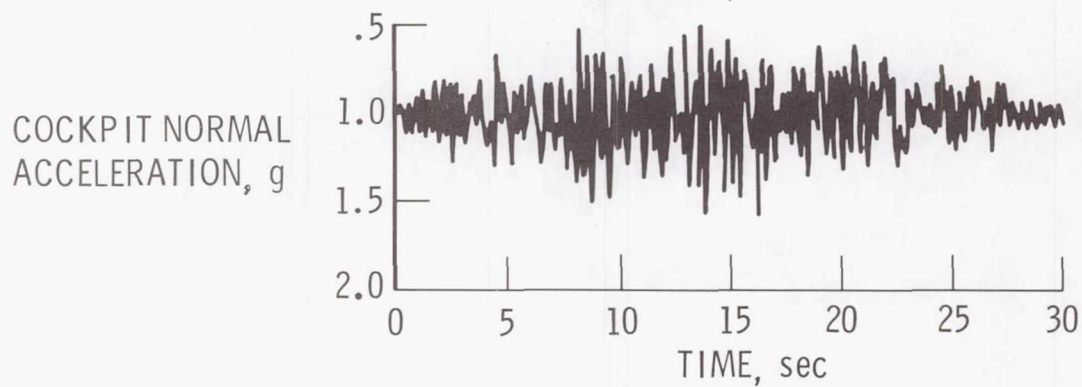
Figure 3.- YF-12 response to runway roughness during takeoff.

208

(a) a_x, a_t, δ_a, δ_r.
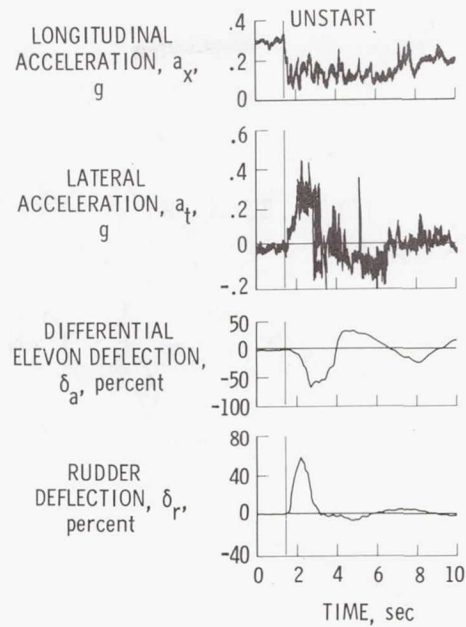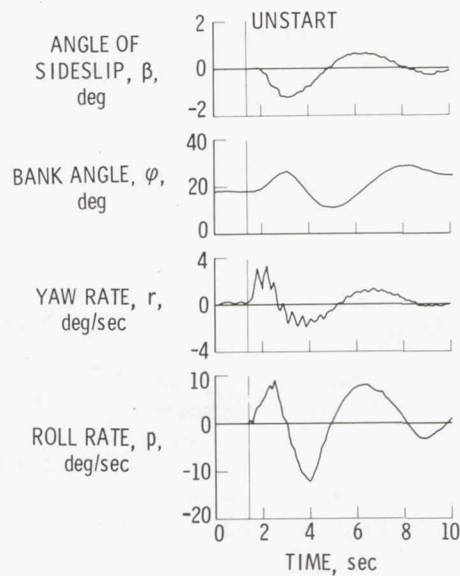
(b) β, φ, r, p.

Figure 4.- Time history of typical unstart. SAS on;
inlets automatic. $M \approx 2.7$.
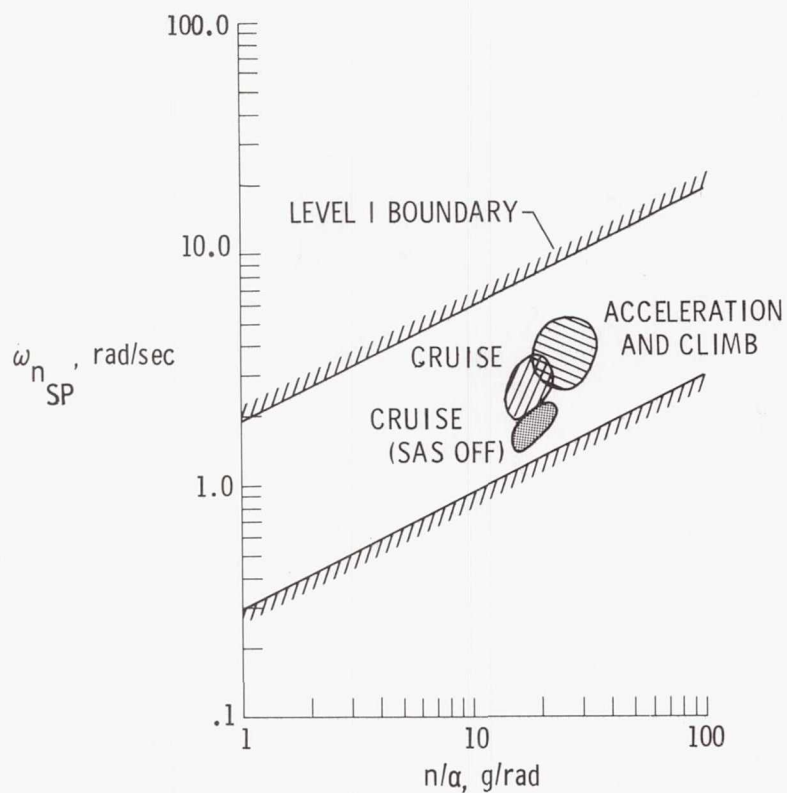
Figure 5.- Typical YF-12 longitudinal characteristics and MIL-F-8785B requirements for acceleration, climb, and cruise.
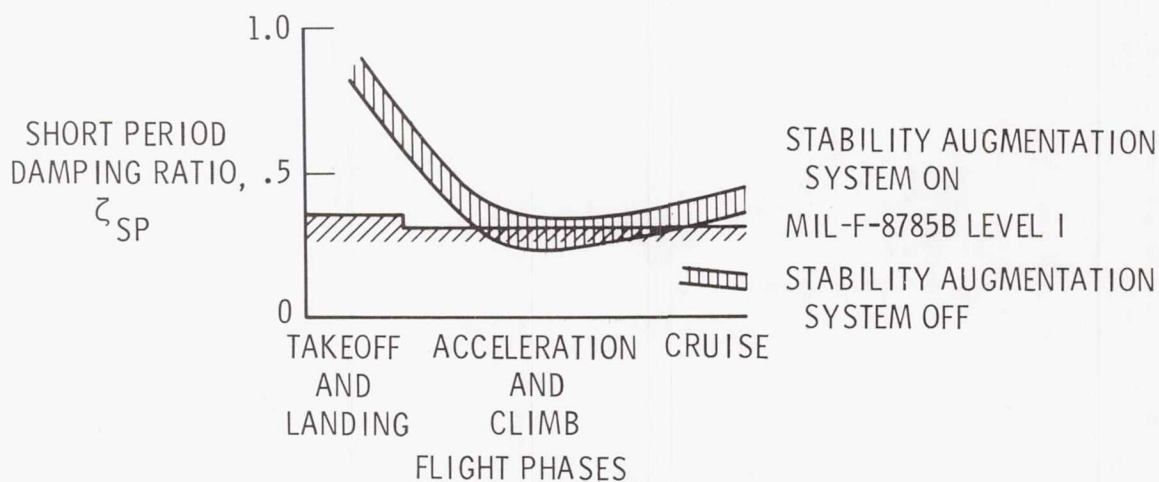
Figure 6.- Typical YF-12 longitudinal short period damping ratios.
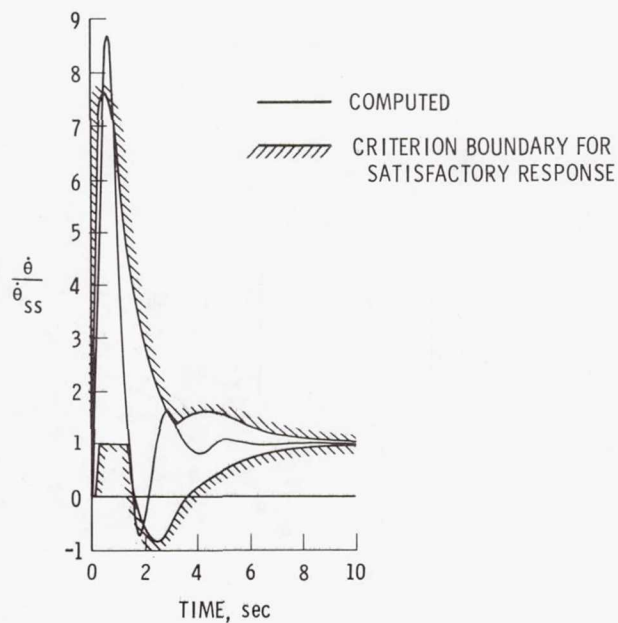
(a) Stability augmentation system on.
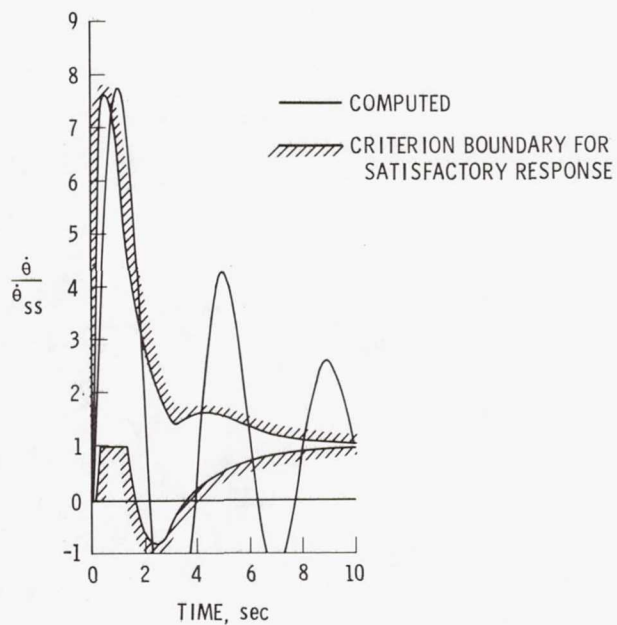
(b) Stability augmentation system off.

Figure 7.- Comparison of computed YF-12 step responses with modified supersonic transport high-speed pitch rate response criterion.
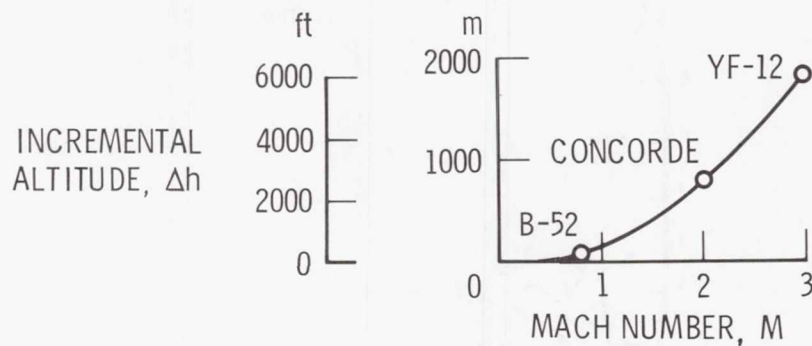
Figure 8.- Altitude change required to compensate for a 10° C (18° F) atmospheric temperature change and maintain Mach number; constant energy flight.
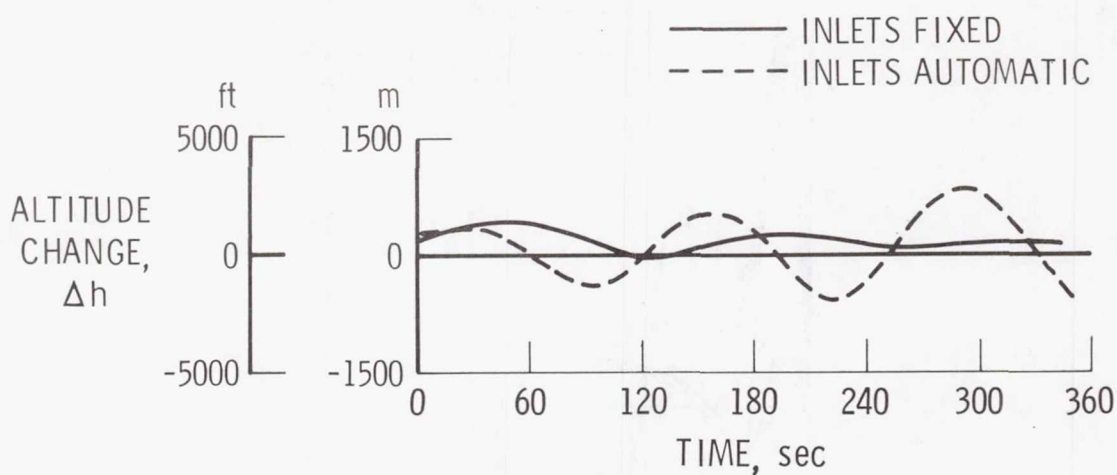
Figure 9.- YF-12 long period response to drag pulse. M ≈ 3.0.
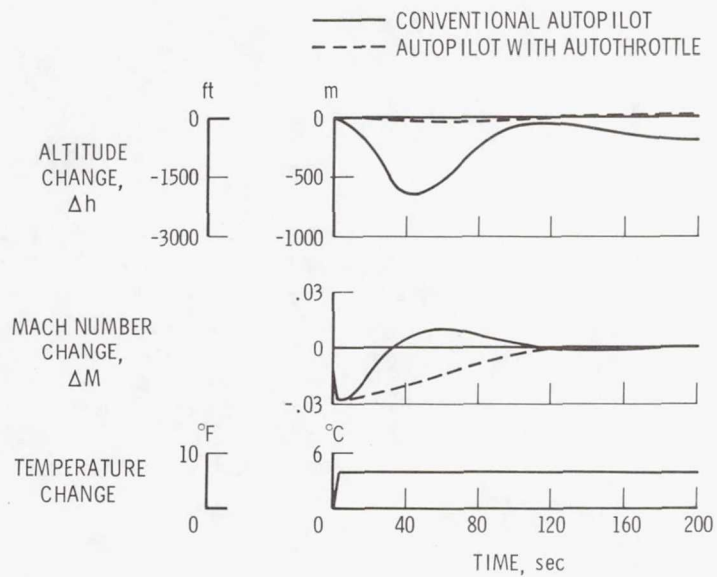
Figure 10.- Mach hold autopilot response. YF-12 simulator; Mach 3.
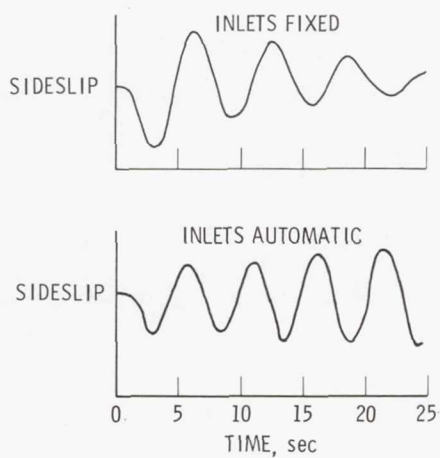
Figure 11.- Dutch roll response. Yaw SAS off; $M \approx 3.0$.

Page intentionally left blank

SIMULATOR STUDY OF THE LOW-SPEED HANDLING QUALITIES

OF A SUPERSONIC CRUISE ARROW-WING TRANSPORT

CONFIGURATION DURING APPROACH AND LANDING

William D. Grantham, Luat T. Nguyen, M. J. Neubauer, Jr.
NASA Langley Research Center

Paul M. Smith
Vought Corporation Hampton Technical Center

SUMMARY

A fixed-based simulator study was conducted to determine the low-speed flight characteristics of an advanced supersonic cruise transport having an arrow wing, a horizontal tail, and four dry turbojets with variable geometry turbines. The primary piloting task was the approach and landing.

The results of the study indicated that the statically unstable (longitudinally) subject configuration has unacceptable low-speed handling qualities with no augmentation. Therefore a hardened stability augmentation system (HSAS) will be required to achieve "acceptable" handling qualities should the normal operational stability and control augmentation system (SCAS) fail. In order to achieve "satisfactory" handling qualities, considerable augmentation was required. Although the SCAS developed in this study to achieve satisfactory handling qualities was complex, it is within current technology.

It was concluded from the results of this study that additional research is required to achieve improved lateral-directional static stability and satisfactory control power on the subject supersonic cruise transport configuration - particularly roll control power and reduced dihedral effect.

INTRODUCTION

During the National Supersonic Transport (SST) Program of the early 1960's, various aerodynamic research studies conducted at NASA Langley to develop an efficient supersonic cruise transport airplane resulted in the highly-swept, arrow-wing configuration designated the SCAT-15F. The SCAT-15F offered considerable promise for superior supersonic cruise performance; but unfortunately, such configurations designed for high-speed flight do not usually possess good low-speed handling characteristics. Some early wind-tunnel and piloted simulation studies (for examples see refs. 1 and 2) identified some of the low-speed handling problems of the SCAT-15F. Also, in 1968, the Boeing Company made an in-depth study of a supersonic cruise transport concept which

was based on the NASA arrow-wing SCAT-15F configuration (see fig. 1), and the results are reported in reference 3. That airplane configuration promised good take-off and landing performance by utilizing a lifting canard and a small horizontal tail; the primary purpose of the canard was to trim the pitching moments due to the wing trailing-edge flap deflections. Although the use of a canard improved the trimmed lift-to-drag ratios, there was an associated reduction in airplane stability for similar center-of-gravity positions.

Since the early 1970's, the Langley Research Center has been conducting extensive wind-tunnel tests in support of the Supersonic Cruise Aircraft Research (SCAR) Program to improve the stability characteristics of the arrow-wing configuration at high angles of attack (low speeds) without a canard and with an aft mounted horizontal tail. The resulting improvements in longitudinal stability were achieved by careful attention to wing planform, leading-edge radius, leading-edge high-lift devices and locations, and trailing-edge flap location, size, and deflection. Utilizing these improved aerodynamic characteristics, performance calculations have shown that with 2 to 3 percent negative static margin, this configuration should produce lift-to-drag ratios as good as those of the stable concept with a forebody canard. However, the results of lateral-directional stability and control analyses in reference 4 indicated that the arrow-wing concept had several inherent deficiencies - especially in the high-lift landing approach configuration. Specifically, these were sluggish roll response and inadequate wings-level sideslip capability.

Since the aforementioned studies were made without a pilot in the loop and since the analyses of those studies compared the calculated dynamic stability characteristics of an advanced supersonic cruise airplane design with criteria developed for conventional airplanes, the subject simulation study was undertaken to investigate the low-speed, pilot-in-the-loop flight characteristics of an advanced, arrow-wing supersonic cruise transport airplane performing representative approach and landing tasks. The primary objective of this simulation study was to obtain sufficient information to provide guidance for future low-speed research requirements. Other major objectives of the present study were:

1. Evaluate the general handling qualities of the unaugmented airplane in the approach configuration and at the approach speed.

2. Develop the stability augmentation and flight control systems required to achieve satisfactory handling qualities (Normal Operational Augmentation) as well as acceptable handling qualities (Hard Augmentation).

3. Determine the control power required to meet the established criteria.

4. Evaluate the effects of various atmospheric conditions, including heavy turbulence, steady winds, and wind shear on the ability of the pilot to make a satisfactory approach and landing.

5. Attempt to determine if existing handling qualities criteria can be applied to statically unstable supersonic cruise transport airplanes.

216

Values are given in both SI and U.S. Customary Units. The measurements and calculations were made in U.S. Customary Units.

$\bar{c}_{ref}$ reference mean aerodynamic chord, m (ft)

g acceleration due to gravity, meters/sec^2 (ft/sec^2)

I_X, I_Y, I_Z moments of inertia about X, Y, and Z body axes, respectively, kilogram-meters^2 (slug-ft^2)

I_{XZ} product of inertia, kilogram-meters^2 (slug-ft^2)

P_{SP} period of longitudinal short period oscillation, sec

P_d period of Dutch roll oscillation, sec

p, q rolling and pitching angular velocities, respectively, deg/sec or rad/sec

S wing area, meters^2 (ft^2)

S_{a_n} static normal acceleration gust sensitivity, g/(m/sec) (g/(ft/sec))

s Laplace operator

T thrust, newtons (pounds force)

$t_{1/2}$ time to damp to one-half amplitude, sec

t_2 time to double amplitude, sec

V airspeed, knots (ft/sec)

W airplane weight, newtons (pounds force)

α angle of attack, deg

β angle of sideslip, deg

θ pitch angle, deg

ϕ roll angle, deg

ψ heading angle, deg

δ_c control-column deflection, positive for pull force, deg

δ_f flap deflection, deg

δ_p pedal travel, centimeters (inches)

δ_r rudder deflection, deg

δ_a aileron deflection, positive for right roll command, deg

δ_{af} flaperon deflection, positive for right roll command, deg

δ_s asymmetric deflection of spoilers for roll control, positive for right roll command, deg

δ_t horizontal-tail deflection, positive when trailing edge is deflected down, deg

δ_w wheel deflection, deg

ζ_d Dutch roll damping ratio

ζ_{SP} short period damping ratio

ζ_ϕ damping ratio of numerator quadratic of ϕ/δ_a transfer function

ρ air density, kilograms/meter^3 (slugs/ft^3)

τ_R time constant of roll mode, sec

ω_d undamped natural frequency of Dutch roll mode, rad/sec

ω_{SP} longitudinal short-period undamped natural frequency, rad/sec

ω_ϕ undamped natural frequency appearing in numerator quadratic of ϕ/δ_a transfer function, rad/sec

L_α lift per unit angle of attack per unit of momentum, per second

C_{L_α} lift coefficient curve slope per unit angle of attack, per radian

n/α steady-state normal acceleration change per unit change in angle of attack for an incremental horizontal-tail deflection at constant airspeed, g units/radian

ψ_β phase angle expressed as a lag for a cosine representation of the Dutch roll oscillation in sideslip, deg

$t_{\phi=30^\circ}$ time required to roll 30°, sec

p_1, p_2 rolling angular velocities at the first and second peaks of a roll rate oscillation, deg/sec or rad/sec

Subscripts:

c   commanded

ss   steady state

osc   oscillation

ave   average

Abbreviations:

HSAS   hardened stability augmentation system

IFR   instrument flight rules

ILS   instrument landing system

PR   pilot rating

SCAS   stability and control augmentation system

DESCRIPTION OF SIMULATED AIRPLANE

The airplane concept studied is a resized version of the configuration described in reference 4. It is a conventional fossil-fueled supersonic cruise transport incorporating four under-the-wing, single-spool, dry turbojets with variable geometry turbines. A three-view sketch of the simulated airplane is presented in figure 2; its geometric characteristics are given in table I; and the engine response characteristics used in the simulation are presented in figure 3.

The static aerodynamic data were estimated based on various low-speed wind-tunnel test results, e.g. references 5 and 6, and corrected for configuration differences. The control surfaces used for low-speed lateral control consisted of outboard ailerons, outboard spoiler slot and inverted spoiler slot deflectors, and inboard flaperons. The rigid lateral control data were estimated based on unpublished aileron control tests, and the flaperon, spoiler slot and inverted spoiler slot deflector data were taken from reference 3, and modified to account for the size and location of the subject airplane's control surfaces. A 40-percent chord, full-span rudder was used for low-speed directional control. The rigid rudder effectiveness data were estimated by using the method presented in reference 4. The reduction of lateral control effectiveness due to wing flexibility was estimated based on the data presented in reference 3; and the reduction of directional control effectiveness due to fuselage side-bending was based on unpublished data. The methods presented in reference 7 were used to estimate the aerodynamic effects of ground proximity.

The dynamic stability derivatives were estimated using a combination of the forced oscillation test data of reference 1 and the estimation techniques of reference 8.

The mass and dimensional characteristics, and the control-surface deflection and deflection rate limits are presented in table I.

DESCRIPTION OF SIMULATION EQUIPMENT

The fixed-base simulator had a transport-type cockpit which was equipped with conventional flight and engine-thrust controls and with a flight-instrument display representative of those found in current transport airplanes. (See fig. 4.) Instruments indicating angle of attack, sideslip, and flap angle were also provided. A conventional cross-pointer-type flight director instrument was used, but the command bars (cross pointers) were driven by the main computer program.

The simulator control forces were provided by a hydraulic servosystem and were functions of control displacement and rate. The control characteristics of the simulator are defined in table II. Real-time digital simulation techniques were used wherein a digital computer was programed with equations of motion for six degrees of freedom. The simulator did not incorporate cockpit motion.

A visual display of a hypothetical airport (fig. 5) was used in order to provide visual cues for the flare and landing. The display consisted of a closed-circuit television presentation, viewed through a collimating lens in the pilot's windshield, of the simulated approach to a 3505-meter (11,500 ft) runway. (See fig. 6.) Each flight was terminated at touchdown; the roll-out was not simulated.

TESTS AND PROCEDURES

The low-speed flight characteristics of the subject supersonic cruise transport airplane are presented and discussed in relation to pilot opinions and ratings (see table III for pilot rating system). Three research pilots participated in the simulation program and used standard flight-test procedures in the evaluation of the handling qualities. The primary piloting task was the approach and landing.

The ILS approach was initiated with the airplane in the power-approach condition (power for level flight) with a lateral offset from the localizer and at an altitude below the glideslope. The pilot's task was to capture the localizer and glideslope and to maintain them as closely as possible while under IFR conditions. At an altitude of 61 meters (200 ft) a visual display of the runway and surrounding area was displayed to the pilot, and from that altitude the pilot attempted to land the airplane visually (with limited reference to the flight director).

220

The various atmospheric conditions simulated included calm air, heavy turbulence, steady crosswinds, and various wind shears.

RESULTS AND DISCUSSION

The results of this study are discussed in terms of the previously stated objectives. Also, throughout the discussion, the pilot ratings listed for the various conditions will be an average of the ratings from all pilots who "flew" that particular condition.

The dynamic stability and response characteristics of the simulated supersonic cruise transport airplane for various levels of stability augmentation are presented in tables IV and V.

Basic Airplane (No Augmentation)

The pilot rating assigned to the longitudinal handling qualities of the unaugmented airplane was seven. As can be seen from table IV, the time to double amplitude (t_2) of the longitudinal aperiodic mode is 4.6 seconds, which might be expected to be unacceptable since the landing approach minimum-safe (PR = 6.5) criterion of reference 9 stated that a $t_2 < 6$ seconds would be unacceptable. A comparison of the pitch rate response of the unaugmented airplane to the desired response is presented in figure 7, and shows that the response to a column step input appears as an acceleration command instead of the desired rate command. Table V indicates that the airplane also has less than satisfactory pitch control power.

A pilot rating of seven was assigned to the unaugmented lateral-directional handling qualities. The major objections were: (1) unacceptably large adverse sideslip excursions in turns; (2) easily excited, lightly damped Dutch roll mode; (3) poor roll and heading control; and (4) sluggish roll response with low roll damping. The dynamic parameters shown in table IV indicate acceptable roll ($\tau_R < 3.0$) and Dutch roll characteristics ($\zeta_d\omega_d > 0.05$) according to reference 10. However, the pilots commented that more roll damping and Dutch roll damping were desirable. The primary factor that contributed to the poor pilot rating for the lateral-directional characteristics was the large adverse sideslip excursions experienced during rolling maneuvers. This characteristic is indicated in figure 8, and compared with the desired response for a lateral control step input. For a step input it is desirable to have: (1) a fast roll rate response that reaches a reasonably steady state value with a minimum of oscillations; (2) essentially zero sideslip produced by the roll control input; and (3) an immediate response in heading. However, it is obvious from figure 8 that for a lateral control step input on this unaugmented configuration, a large amount of adverse sideslip is experienced that washes out the roll rate ($\dot{\phi}$) in a short period of time and also causes an undesirable lag in the initiation of turn rate (ψ). This large adverse sideslip characteristic, in combination with the low roll damping, required constant attention and considerable effort on the part of the pilot; even then, the lateral-directional control remained very poor.

221

It must be noted that although the longitudinal and lateral-directional handling qualities of this unaugmented supersonic cruise transport airplane were assigned a pilot rating of seven when evaluated individually, the combination of these resulted in a PR = 10 for all aspects of the airplane. Therefore, it is apparent that considerable stability and control augmentation will be required to achieve satisfactory handling qualities for the landing approach piloting task.

<div align="center">

Normal Operational Stability and Control
Augmentation System (SCAS)

</div>

Based on the results obtained for the unaugmented configuration the approach selected for design of the SCAS was that the system should provide satisfactory handling qualities (PR $\leq$ 3.5) at all flight conditions evaluated during the study. A block diagram of the SCAS design obtained with this approach is shown in figure 9.

Longitudinally, a high gain pitch rate command/attitude hold system was chosen because: (1) stabilization of the unstable mode was achieved with the pitch attitude feedback; (2) the system provided good short-period characteristics and fast response to pilot inputs; and (3) the attitude hold feature minimized disturbances due to engine coupling effects and turbulence.

Laterally, a roll rate command/attitude hold system was employed to provide a fast roll mode and quick, uniform response to pilot inputs; the attitude hold feature resulted in a neutrally stable spiral mode while counteracting disturbances due to turbulence. Directionally, roll rate and roll attitude feedbacks were used to provide turn coordination and improved Dutch roll characteristics. A roll control to rudder interconnect was also included to reduce adverse sideslip and therefore minimize Dutch roll coupling during roll maneuvers (obtained $\omega_\phi/\omega_d \approx 1$).

An autothrottle was also used as part of the normal operational augmentation that maintained the selected airspeed during the approach and landing. Since the simulated engine dynamics produced very quick thrust response, the autothrottle generally maintained the desired airspeed within ± 2 knots, and therefore reduced the pilot workload on the landing approach. Although this airplane is flown well up the "backside" of the thrust required curve at the approach speed of 153 knots $\frac{\partial T/W}{\partial V} \approx -0.0023/\text{knot}$, where normally the pilot would primarily use pitch attitude for airspeed control and thrust for glidepath control, the simulated quick, engine-thrust response allowed the use of thrust (manually or automatically) for airspeed control and thus enabled the pilot to use pitch attitude for glidepath control - which is a very natural, simple technique.

The longitudinal SCAS (fig. 9) provided pitch rate proportional to column deflection, and produced the desired characteristics of rapid, well-damped responses to pilot inputs as well as inherent attitude stability. Figure 10

shows the improvement in pitch rate response provided by the SCAS, and it can be seen from table IV that the time to double amplitude (t_2) of the longitudinal aperiodic mode increased from 4.6 seconds with no augmentation to infinity with the SCAS configuration. With this augmentation system operative, the average pilot rating for the longitudinal handling qualities on the ILS approach was improved from seven with no augmentation to two.

Also shown in figure 9 is a block diagram of the lateral-directional SCAS. Laterally, a rate command system provided roll rate proportional to wheel position, and the directional system consisted of several turn coordination features. Table IV shows that the Dutch roll characteristics were improved considerably; (ω_ϕ/ω_d) was increased from 0.565 to 1.03, which indicates that the Dutch roll oscillation should be much less easily excited for roll-control inputs, and the damping parameter ($\zeta_d\omega_d$) was increased from 0.066 rad/sec to 0.182 rad/sec. The improvement in the roll response and damping are indicated by the reduction of τ_R from 1.6 sec to 0.38 sec (table IV).

Figure 11 shows the improvement in the roll rate response provided by the SCAS; by elimination of the large adverse sideslip, the roll-rate reversal was eliminated and the heading response was immediate (no lag). The lateral SCAS also provided a desirable roll-attitude-hold feature which proved to be very beneficial, particularly during landing approaches made in simulated heavy turbulence. With this augmentation system operative, the average pilot rating for the lateral-directional handling qualities on the ILS approach was improved from seven with no augmentation to two with augmentation.

With the SCAS operative, the overall pilot rating of this simulated supersonic cruise transport airplane for the landing approach piloting task was two.

Hardened Stability Augmentation System (HSAS)

As discussed previously, the configuration had unacceptable low-speed handling qualities with no augmentation. Therefore, a hardened stability augmentation system (HSAS) will be required to achieve acceptable handling qualities should the normal operational augmentation (SCAS) fail. (The term "hardened" SAS implies sufficient redundancy to negate loss of this system.)

The HSAS design objective was to provide improved handling qualities so that acceptable pilot ratings (PR $\leq$ 6.5) could be obtained for the approach and landing task, and that the system be kept as simple as possible to maximize reliability and ease of implementation. The HSAS design obtained using this approach is shown in figure 12. Longitudinally, a filtered pitch rate feedback signal acting through a relatively high gain was used to reduce the instability of the unstable mode and to enhance the short period characteristics. Laterally, a simple roll damper provided a faster roll mode and increased Dutch roll damping. Directionally, roll rate feedback was used to provide: (1) improved turn-entry coordination; (2) reduced Dutch roll coupling during roll maneuvers (increased (ω_ϕ/ω_d)); and (3) further enhancement of the Dutch roll damping. Note that only two angular rate signals (pitch rate and roll

rate) were required for the HSAS implementation so that sensor reliability problems and mechanization complexity would be minimized. The autothrottle was also considered to be part of the HSAS.

The average pilot rating assigned to the longitudinal handling qualities when the HSAS was operative was four. The primary objection was the less than desired pitch damping. Table IV shows that the short-period damping ratio (ζ_{SP}) for this configuration is 0.693, which would normally indicate adequate damping; however, the slowly divergent aperiodic mode (t_2 = 25.3 sec) superimposed on the short-period response caused the motions to appear to the pilot as being inadequately damped. It should be noted that reference 9 also indicated acceptable pilot ratings (PR $\leq$ 6.5) when t_2 was greater than 6 seconds. Figure 10 compares the pitch response to a column step for the unaugmented airplane, with SCAS operative, and with HSAS operative. The reason a higher gain was not implemented for the pitch rate damper, in order to satisfy the pilot's objection of low pitch damping, was that more damping would make the pitch axis unacceptably sluggish. It is obvious from figure 10 that the HSAS configuration is already very sluggish in pitch, compared to the SCAS configuration.

The average pilot rating assigned to the lateral-directional handling qualities with the HSAS operative was four. The primary objections were sluggish roll response and less than desired roll damping. Figure 11 shows a comparison of the roll response to a lateral control step input for the HSAS, SCAS, and unaugmented configurations.

Effects of Turbulence on Landing Apporach

Flight in rough air was evaluated by using a turbulence model based on the Dryden spectral form. The root-mean-square value of the longitudinal, lateral, and vertical gust-velocity components was 2.7 m/sec (9 ft/sec) and these values were described by the pilots as being representative of heavy turbulence.

Static normal acceleration gust sensitivity can be defined as $S_{a_n} = \dfrac{C_{L_\alpha}\rho V}{2W/S}$; that is, the vertical response of an airplane to turbulence is directly proportional to the product of lift-curve slope and velocity, and is inversely proportional to the wing loading. Table VI presents a comparison of S_{a_n} for the subject supersonic cruise transport and a typical present-day subsonic jet transport during the landing approach. Note that the lower value of C_{L_α} for the subject supersonic transport is offset by the lower wing loading and slightly higher airspeed. Therefore, the two S_{a_n} values are nearly equal; the supersonic cruise transport actually showing a slightly lower value. From consideration of these points, the response of the subject supersonic cruise airplane to atmospheric turbulence would not be expected to be any worse than the response of present-day subsonic transport airplanes - neglecting flexibility differences.

The pilots commented that the pilot rating for the approach task on the subject supersonic cruise transport airplane was degraded by one rating when the landing approach was made in the simulated heavy turbulence since the ILS glideslope tracking task required considerable pilot effort - added pilot workload.

Crosswind Landings

Both steady crosswinds (up to 20 knots) and crosswinds with horizontal shear were simulated. The piloting technique used for making the approach and landing was the same for all crosswind conditions flown. The technique consisted of - crabbed approach, and at some nominal altitude, usually about 15 meters (50 ft), changing to a sideslipping, wing-down condition.

The requirements of reference 10 are that transport airplanes without crosswind landing gear be capable of landing in 90° crosswinds up to 30 knots, and that the lateral control used shall not exceed 75 percent of the control power available. Figure 13 indicates the amount of steady-state sideslip, bank angle, rudder deflection, and lateral control deflection required for side-slipping crosswind approaches at an airspeed of 153 knots (the nominal approach speed). It can be seen that 75 percent of available lateral control was required for a crosswind component of approximately 21 knots. It is, therefore, obvious that this supersonic cruise transport airplane could not be landed (with an adequate lateral control margin) in 90° crosswinds higher than approximately 20 knots. Also, from a piloting standpoint, the lateral-directional control coordination required for the transition from a crabbed-approach condition to a sideslipping, wing-down condition becomes increasingly difficult as the 90° crosswind increases above approximately 15 knots. It is, therefore, concluded from these ground-based, fixed-cockpit simulator results that the subject supersonic cruise transport airplane should be equipped with crosswind gear and/or provided with additional roll control power.

It should be mentioned that although the accuracy of the control coordination was the prime factor that affected the pilot's ability to make "precise" landings in high crosswinds, deficiencies of the visual presentation (lack of peripheral vision and adequate height cues) and possibly the lack of cockpit motion also affected the pilot's ability to make satisfactory landings in large crosswinds.

Dynamic Stability Requirements and Criteria

For several years the aircraft industry has been aware that many of the existing stability requirements of aircraft have become outdated because of the expansion of flight envelopes and the increases in airplane size. Although research is presently being conducted in an effort to remedy this situation, to date essentially no clearly defined stability requirements and criteria have been established for aircraft similar to that for the supersonic cruise transport. Therefore, in an effort to aid in the establishment of new stability

requirements, the low-speed handling qualities parameters of the subject supersonic transport are compared with existing handling qualities criteria.

Two of the most widely used longitudinal handling qualities criteria are presented in figure 14. Figure 14(a) shows the short-period frequency requirements of reference 10, and as can be seen, this criterion agrees with the results obtained during the present simulation study. Figure 14(b) shows the Shomber-Gertsen longitudinal handling qualities criterion of reference 11. This criterion relates the ability of the pilot to change flight path with normal acceleration to the factor L_α. By using this parameter, and by recognizing that the pilot's mode of control is not constant for all flight regimes, a criterion for satisfactory short-period characteristics was developed that correlates well with current airplane experience, and reasonably well with the results obtained during the present low-speed supersonic cruise transport simulation program. The low-speed pitch rate response criterion shown in figure 15, and reported in reference 12, was based on the Shomber-Gertsen criteria. As can be seen, there is excellent agreement of the results obtained during the present study and this low-speed pitch response criterion when the normal operational augmentation (SCAS) was operative. The constraints imposed upon the use of this criterion, however, negates its use for any of the other configurations evaluated during the present study. The pitch divergence criterion of reference 9, with a time-to-double pitch attitude of 6 seconds or greater for the most unstable root, was considered when the HSAS and unaugmented configurations were evaluated, and the subject simulation results agreed very well with the criterion.

The roll rate and bank angle oscillation limitations criteria of reference 10 are presented in figure 16. Figure 16(a) relates the phase angle of the Dutch roll component of sideslip (ψ_β) to the measure of the ratio of the oscillatory component of roll rate to the average component of roll rate $\dfrac{p_{osc}}{p_{ave}}$, and figure 16(b) relates the measure of the ratio of the oscillatory component of bank angle to the average component of bank angle $\dfrac{\phi_{osc}}{\phi_{ave}}$ with ψ_β. The conditions evaluated during the present simulation study are indicated in these plots, and it can be seen that these simulated characteristics agree, reasonably well, with the aforementioned criteria - particularly the fully augmented (SCAS) and unaugmented conditions.

Figure 17 presents a criterion for satisfactory roll-sideslip coupling characteristics. This criterion relates pilot rating to the roll coupling parameter ω_ϕ/ω_d, as presented in reference 13, and the conditions flown during the present simulation are indicated. It is seen that the results of this study agree very well with this criterion.

In general, it is concluded that the results of the present simulation study agree with the established handling qualities criteria used for comparison in this paper.

SUMMARY OF RESULTS

A fixed-base simulator program was conducted to determine the low-speed flight characteristics of an advanced supersonic cruise transport having an arrow wing, an aft mounted horizontal tail, and four dry turbojets with variable geometry turbines. The primary piloting task was the approach and landing. The results may be summarized as follows:

1. This statically unstable (longitudinally) supersonic cruise transport configuration has unacceptable low-speed handling qualities with no augmentation. Therefore, a hardened stability augmentation system (HSAS) will be required to achieve acceptable handling qualities should the normal operational stability and control augmentation system (SCAS) fail.

2. The longitudinal normal operational stability and control augmentation system, consisting of a high-gain pitch rate command/attitude hold system and an autothrottle, essentially eliminated the longitudinal control problems. The lateral-directional SCAS, consisting of a roll rate command/attitude hold system, and of roll rate (p), roll angle (ϕ), and roll control deflection (δ_w) feedback signals to the rudder, made the lateral-directional handling characteristics satisfactory. With these augmentation systems operative, the average pilot rating for the instrument approach task was 2.

3. The hardened stability augmentation system (HSAS), designed to provide "acceptable" handling qualities with maximum simplicity (for reliability and ease of implementation), consisted of a filtered pitch rate feedback signal to the longitudinal control surface for additional pitch damping, and a roll rate feedback signal to the roll control surfaces as well as to the rudder for additional roll damping and improved turn-entry coordination. With this HSAS operative, the average pilot rating for the instrument approach task was 4.

4. The available control power for all axes (roll, pitch, and yaw) was determined to be inadequate to meet existing handling qualities and crosswind requirements.

5. The response of the subject supersonic cruise transport airplane to atmospheric turbulence would not be expected to be any worse than the response of present-day subsonic transport airplanes - neglecting flexibility differences. However, the pilots commented that the pilot rating for the approach task on the subject supersonic cruise airplane was degraded by one rating when the landing approach was made in the simulated heavy turbulence since the glideslope tracking task required higher pilot workload.

6. In general, it is concluded that the results of the subject simulation study agree with the established handling qualities criteria used for comparison in this paper.

7. It is concluded that additional low-speed research is required to achieve satisfactory control power on this supersonic cruise transport configuration - particularly, roll control power.

REFERENCES

1. Freeman, Delma C., Jr.: Low Subsonic Flight and Force Investigation of a Supersonic Transport Model With a Highly Swept Arrow Wing. NASA TN D-3887, 1967.

2. Grantham, William D.; and Deal, Perry L.: A Piloted Fixed-Base Simulator Study of Low-Speed Flight Characteristics of an Arrow-Wing Supersonic Transport Design. NASA TN D-4277, 1968.

3. The Boeing Company: Mach 2.7 Fixed Wing SST Model 939-336C (SCAT-15F), Document No. D6A-11666-1, November 1969.

4. Baber, H. T., Jr.; and Swanson, E. E.: Advanced Supersonic Technology Concept AST-100 Characteristics Developed in a Baseline-Update Study. NASA TM X-72815, January 16, 1976.

5. Lockwood, Vernard E.: Effect of Trailing-Edge Flap Deflection on the Lateral and Longitudinal Stability Characteristics of A Supersonic Transport Model Having A Highly-Swept Arrow Wing. NASA TM X-71936. March 19, 1974.

6. Coe, Paul L., Jr.; McLemore, H. Clyde; and Shivers, James P.: Effects of Upper-Surface Blowing and Thrust Vectoring on Low-Speed Aerodynamic Characteristics of A Large-Scale Supersonic Transport Model. NASA TM X-72792, November 1975.

7. LTV Aerospace Corporation, HTC: Advanced Supersonic Technology Concept Study, Reference Characteristics. NASA CR-132374, December 21, 1973.

8. Anon: U.S. Air Force Stability and Control DATCOM - Stability and Control Methods. Air Force Flight Dynamics Laboratory, Ohio, October 1973, Revised January 1975.

9. Lockheed-California Company: A Study of the Effects of Relaxed Static Stability on Stability Augmentation System Reliability Requirements. LR 26833, December 20, 1974.

10. Chalk, C. R.; Neal, T. P.; Harris, T. M.; and Pritchard, F. E.: Background Information and User Guide for MIL-F-8785B(ASG): Military Specification-Flying Qualities of Piloted Airplanes. AFFDL-TR-69-72, August 1969.

11. Shomber, H. A.; and Gertsen, W. M.: Longitudinal Handling Qualities Criteria: An Evaluation. AIAA Paper No. 65-780, November 1965.

12. Sudderth, Robert W.; Bohn, Jeff G.; Caniff, Martin A.; and Bennett, Gregory R.: Development of Longitudinal Handling Qualities Criteria for Large Advanced Supersonic Aircraft. NASA CR-137635, March 1975.

13. Ashkensas, I. L.: A Consolidation of Lateral-Directional Handling
    Qualities. AIAA Paper No. 65-314, July 1965.

14. Anon.: Aerospace Recommended Practice – Design Objectives for Flying
    Qualities of Civil Transport Aircraft. ARP 842, Society of Automotive
    Engineers, August 1964.

TABLE I.- MASS AND DIMENSIONAL CHARACTERISTICS OF SIMULATED SUPERSONIC CRUISE TRANSPORT AIRPLANE (LANDING WEIGHT)

Weight, N (lbf) 1,924,479 (432,640)

Reference wing area, m^2 (ft^2) 784.75 (8,447)

Wing span, m (ft) 38.66 (126.83)

Wing leading-edge sweep, deg 74.00/70.84/60.00

Reference mean aerodynamic chord, m (ft) 27.00 (88.59)

Center-of-gravity location, percent $\bar{c}_{ref}$ 56

Static margin, percent . . . . (-3.2)

I_X, $kg\text{-}m^2$ ($slug\text{-}ft^2$) 6,887,550 (5,080,000)

I_Y, $kg\text{-}m^2$ ($slug\text{-}ft^2$) 67,994,260 (50,150,000)

I_Z, $kg\text{-}m^2$ ($slug\text{-}ft^2$) 72,902,230 (53,770,000)

I_{XZ}, $kg\text{-}m^2$ ($slug\text{-}ft^2$) . . . . -2,833,660 (-2,090,000)

Maximum control-surface deflections:

δ_t, deg . . . . $\pm$ 20

δ_f, deg . . . . 0 to 40

δ_a, deg . . . . $\pm$ 30

δ_{af}, deg . . . . $\pm$ 22.5

δ_s, deg . . . . $\pm$ 50

δ_r, deg . . . . $\pm$ 35

Maximum control-surface deflection rates:

$\dot{\delta}_t$, deg/sec . . . . $\pm$ 50

$\dot{\delta}_f$, deg/sec . . . . $\pm$ 10

$\dot{\delta}_a$, deg/sec . . . . $\pm$ 70

$\dot{\delta}_{af}$, deg/sec . . . . $\pm$ 40

$\dot{\delta}_s$, deg/sec . . . . $\pm$ 50

$\dot{\delta}_r$, deg/sec . . . . $\pm$ 50

TABLE II.- SIMULATOR CONTROL CHARACTERISTICS

Control	Maximum Travel In			Breakout Force		Force Gradient	
	deg	cm	in.	N	lbf	N/cm	lbf/in.
Column:							
Forward	14.0	16.43	6.47	15.5	3.5	17.5	10.0
Aft	18.0	21.34	8.40				
Wheel	±55.0	±16.48	±6.48	13.3	3.0	3.8	2.2
Pedal		±8.89	±3.50	15.3	3.5	70.0	40.0

TABLE III.- PILOT RATING SYSTEM

ADEQUACY FOR SELECTED TASK OR REQUIRED OPERATION*		AIRCRAFT CHARACTERISTICS	DEMANDS ON THE PILOT IN SELECTED TASK OR REQUIRED OPERATION*	PILOT RATING
		Excellent Highly desirable	Pilot compensation not a factor for desired performance	1
		Good Negligible deficiencies	Pilot compensation not a factor for desired performance	2
		Fair – Some mildly unpleasant deficiencies	Minimal pilot compensation required for desired performance	3
Is it satisfactory without improvement? — Yes ↑ / No →	Deficiencies warrant improvement	Minor but annoying deficiencies	Desired performance requires moderate pilot compensation	4
		Moderately objectionable deficiencies	Adequate performance requires considerable pilot compensation	5
		Very objectionable but tolerable deficiencies	Adequate performance requires extensive pilot compensation	6
Is adequate performance attainable with a tolerable pilot workload? — Yes ↑ / No →	Deficiencies require improvement	Major deficiencies	Adequate performance not attainable with maximum tolerable pilot compensation. Controllability not in question	7
		Major deficiencies	Considerable pilot compensation is required for control	8
		Major deficiencies	Intense pilot compensation is required to retain control	9
Is it controllable? — Yes ↑ / No →	Improvement Mandatory	Major deficiencies	Control will be lost during some portion of required operation	10

Pilot decisions

*Definition of required operation involves designation of flight phase and/or subphases with accompanying conditions.
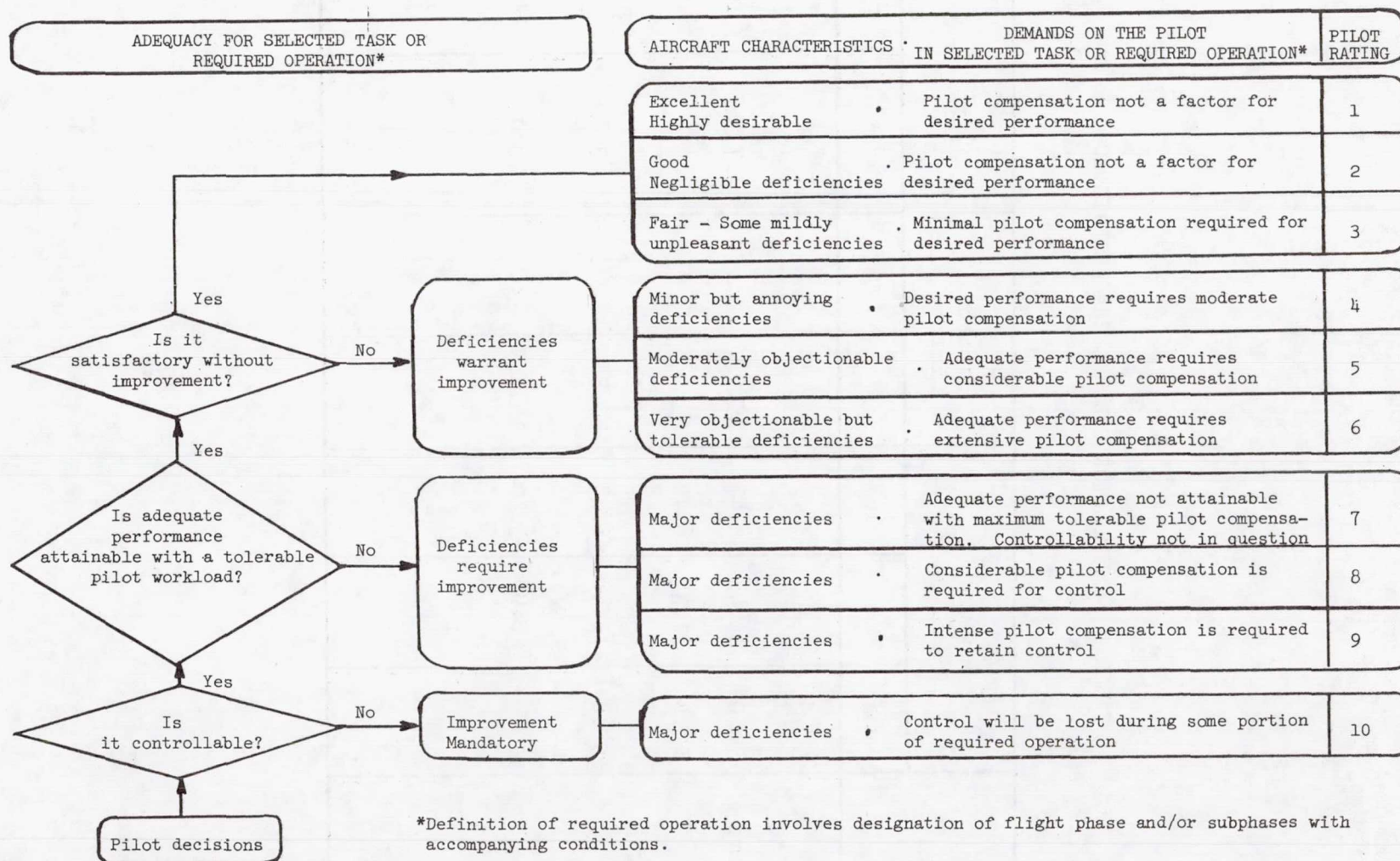
TABLE IV.- DYNAMIC STABILITY CHARACTERISTICS OF SIMULATED
SUPERSONIC CRUISE TRANSPORT AIRPLANE

Parameters / Augmentation	None	HSAS*	SCAS*	Satisfactory criterion	Acceptable criterion
Short-period mode					
ω_{SP}, rad/sec	.154	.714	1.249	See figure 14	See figure 14
P_{SP}, sec	50.90	12.21	11.03	–	–
ζ_{SP}	.598	.693	.890	.35 to 1.30	.25 to 2.00
L_α/ω_{SP}	2.490	.537	.307	See figure 14	See figure 14
n/α, g units/rad	3.13	3.13	3.13	–	–
Long-period (aperiodic) mode					
t_2, sec	4.6	25.3	∞	–	> 6
Roll mode					
τ_R, sec	1.656	.545	.380	≤ 1.4	≤ 3.0
Spiral mode					
$t_{1/2}$, sec	21.2	18.6	∞	–	–
Dutch roll mode					
ω_d, rad/sec	.811	.480	.991	> .4	> .4
ζ_d	.081	.419	.184	> .08	> .02
$\zeta_d\omega_d$, rad/sec	.066	.201	.182	> .15	> .05
P_d, sec	7.77	14.42	6.45	–	–
ϕ/β	2.71	2.55	.88	–	–
Roll-control parameters					
ω_ϕ/ω_d	.565	.956	1.03	See figure 17	See figure 17
ζ_ϕ/ζ_d	3.12	.630	1.42	–	–

*Autothrottle on.

TABLE V.– CONTROL RESPONSE CHARACTERISTICS OF SIMULATED SUPERSONIC
CRUISE TRANSPORT AIRPLANE

Augmentation \ Parameter	None	HSAS*	SCAS*	Satisfactory Criterion	Acceptable Criterion
Longitudinal					
$\ddot{\theta}_{max}$, rad/sec^2	$-.062^+$	$-.052^+$	$-.062^+$	$-.08$	–
$\dot{\theta}/\dot{\theta}_{ss}$	–	–	See fig. 15	See figure 15	–
Lateral					
$\ddot{\phi}_{max}$, rad/sec^2	.243	.203	.205	See figure 18	See figure 18
$\dot{\phi}_{max}$, deg/sec	16.84	9.54	20.86	–	See figure 18
p_2/p_1	$-.111$	.802	.896	$>.60$	$>.25$
p_{osc}/p_{ave}	1.299	.121	.007	See figure 16	See figure 16
ϕ_{osc}/ϕ_{ave}	1.042	.052	.052	See figure 16	See figure 16
$t_{\phi = 30°}$, sec	2.66	3.88	2.65	≤ 2.5	≤ 3.2

* Autothrottle on.

+ Minimum demonstrated speed of 125 knots. Note that at the design minimum demonstrated speed of 140 knots the criterion is satisfied.

TABLE VI.- COMPARISON OF SIMULATED SUPERSONIC CRUISE TRANSPORT AND
TYPICAL SUBSONIC JET TRANSPORT GUST
SENSITIVITY PARAMETERS

$$\left[S_{a_n} = \frac{C_{L_\alpha} \rho V}{2W/S} \right]$$

AIRPLANE	Weight, kN (lbf)	Wing Area, m^2 (ft^2)	W/S, kN/m^2 (lbf/ft^2)	C_{L_α}, RAD^{-1}	V, m/sec (ft/sec)	S_{a_n}, g/(m/sec) (g/(ft/sec))
Supersonic cruise transport	1924.5 (432640)	784.7 (8447)	2.5 (51.2)	2.06	78.8 (258.4)	0.056 (.017)
Subsonic jet transport	800.7 (180000)	256.2 (2758)	3.13 (65.3)	4.85	72.1 (236.5)	.069 (.021)
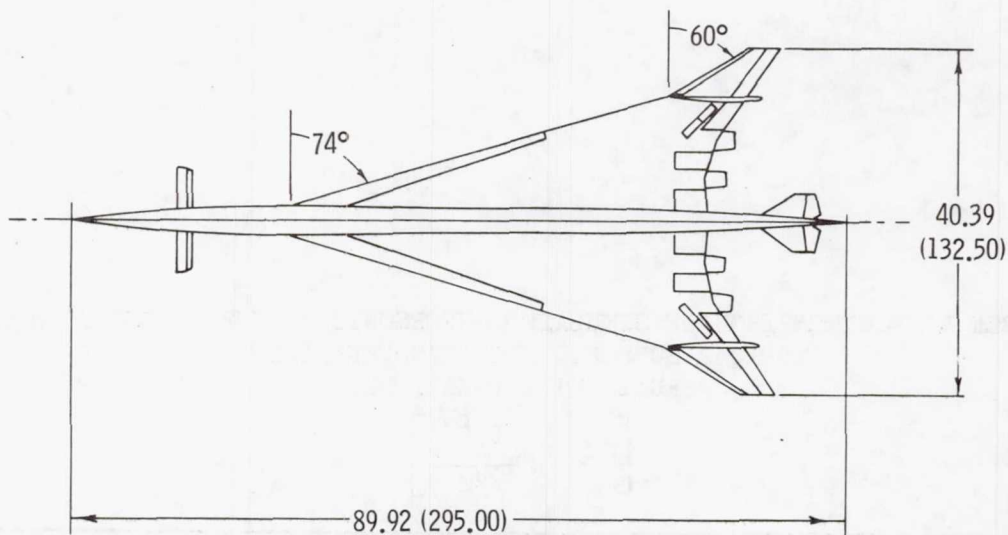
Figure 1.- Boeing model 969-336C based on NASA SCAT-15F configuration.
All linear dimensions are in meters (feet).
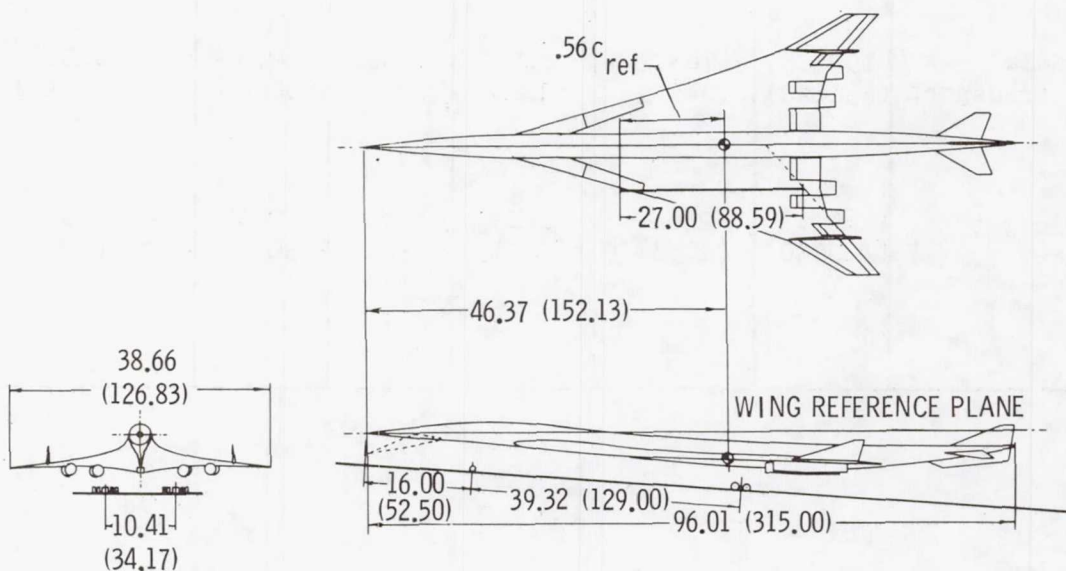
Figure 2.- Three-view sketch of simulated airplane.
All dimensions are in meters (feet).
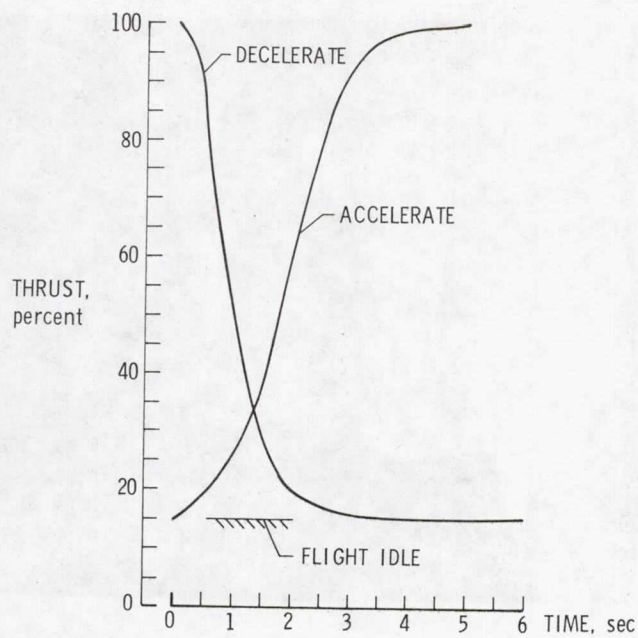
Figure 3.- Simulated engine response characteristics.
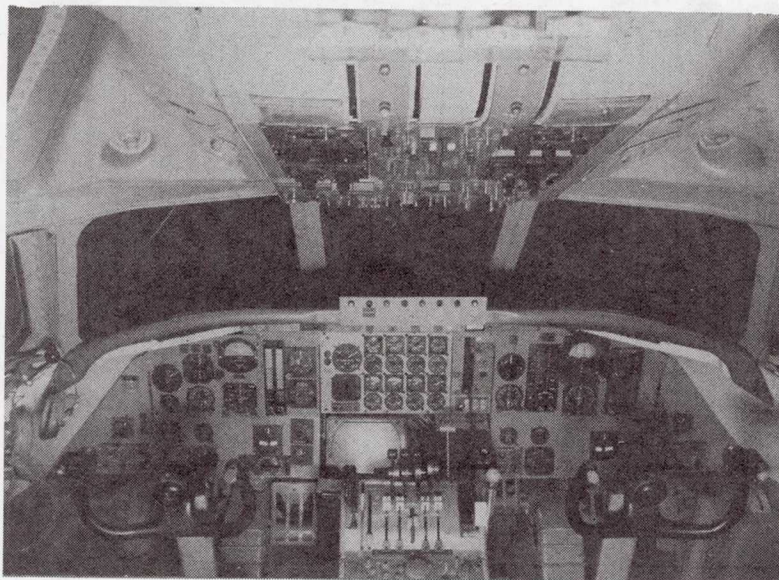
Figure 4.- Simulator cockpit and instrument display.

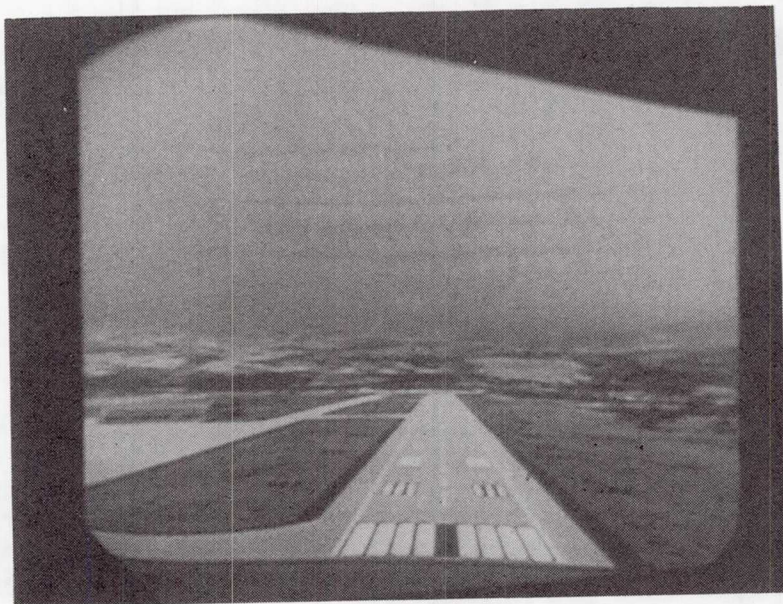Figure 5.- Photograph of landing scene
equipment and airport model.

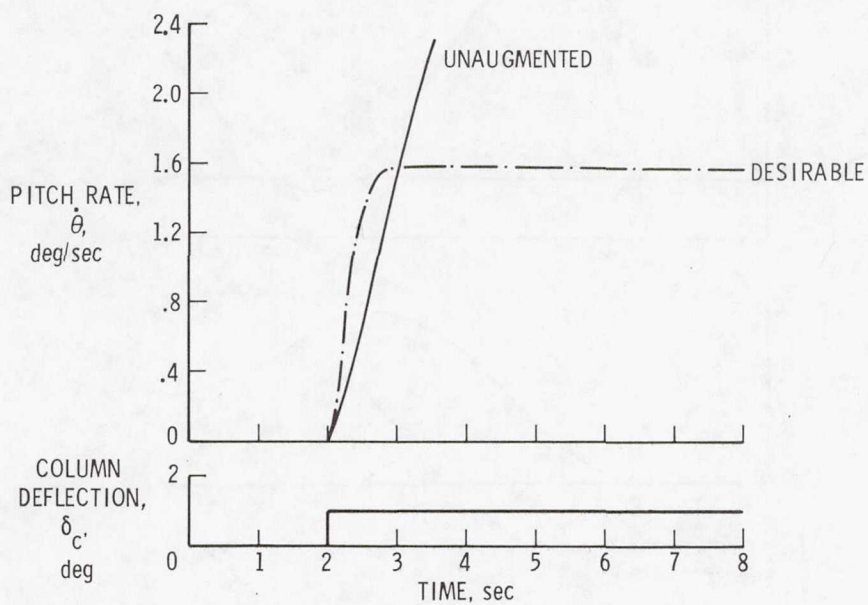Figure 6.- View of runway as seen by
pilot prior to touchdown.

Figure 7.- Comparison of desirable pitch rate
    response characteristics with those of
    unaugmented airplane.
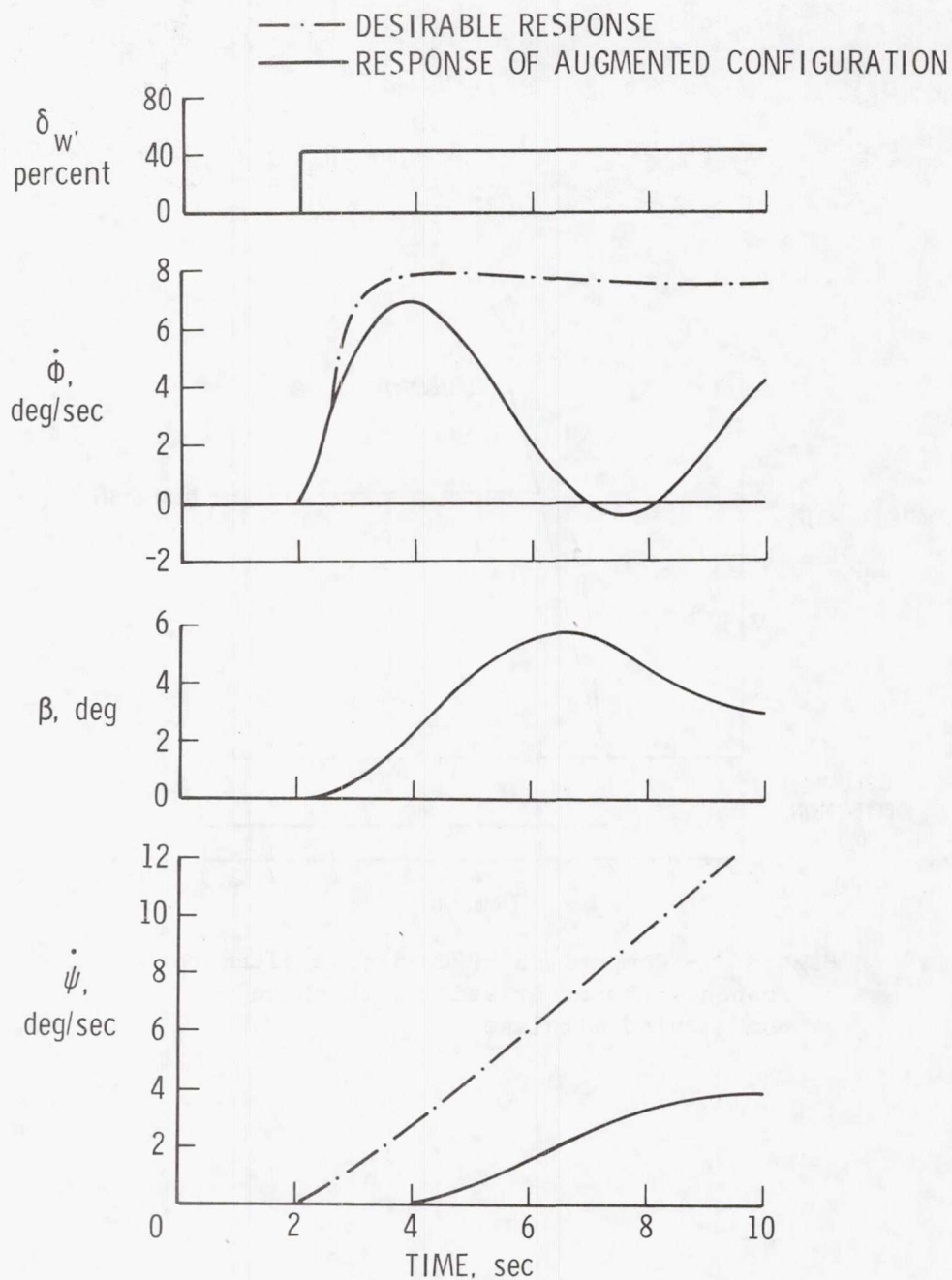
Figure 8.- Comparison of desirable lateral-directional response characteristics with those obtained for unaugmented configuration.
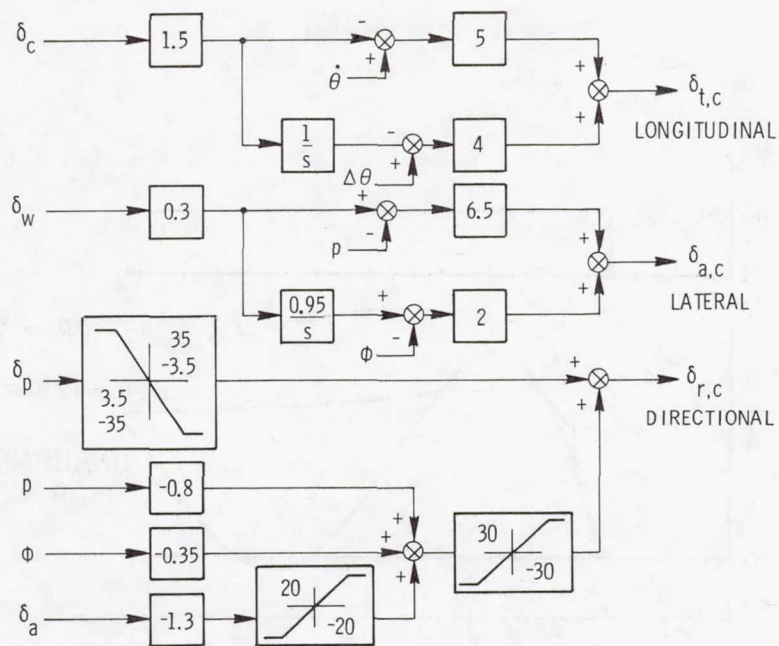
Figure 9.- Normal operating stability and control augmentation system (SCAS).
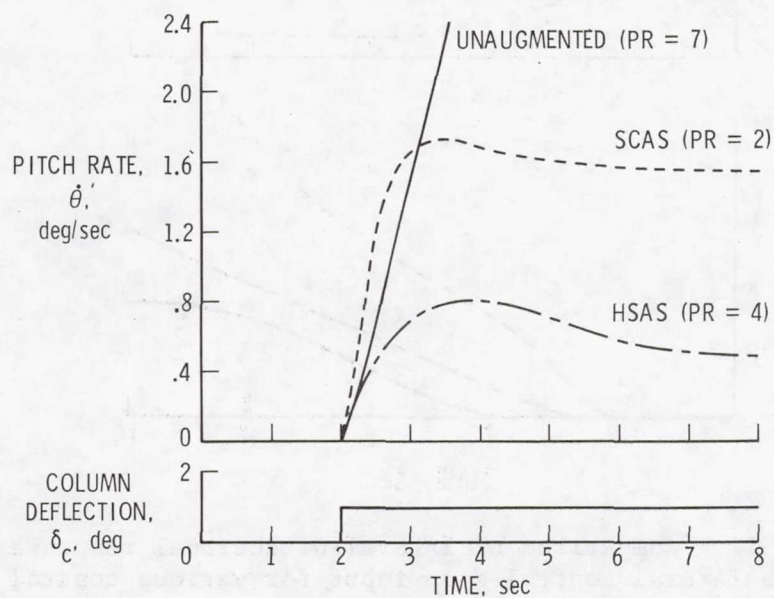

Figure 10.- Comparison of pitch rate response characteristics for various control systems.
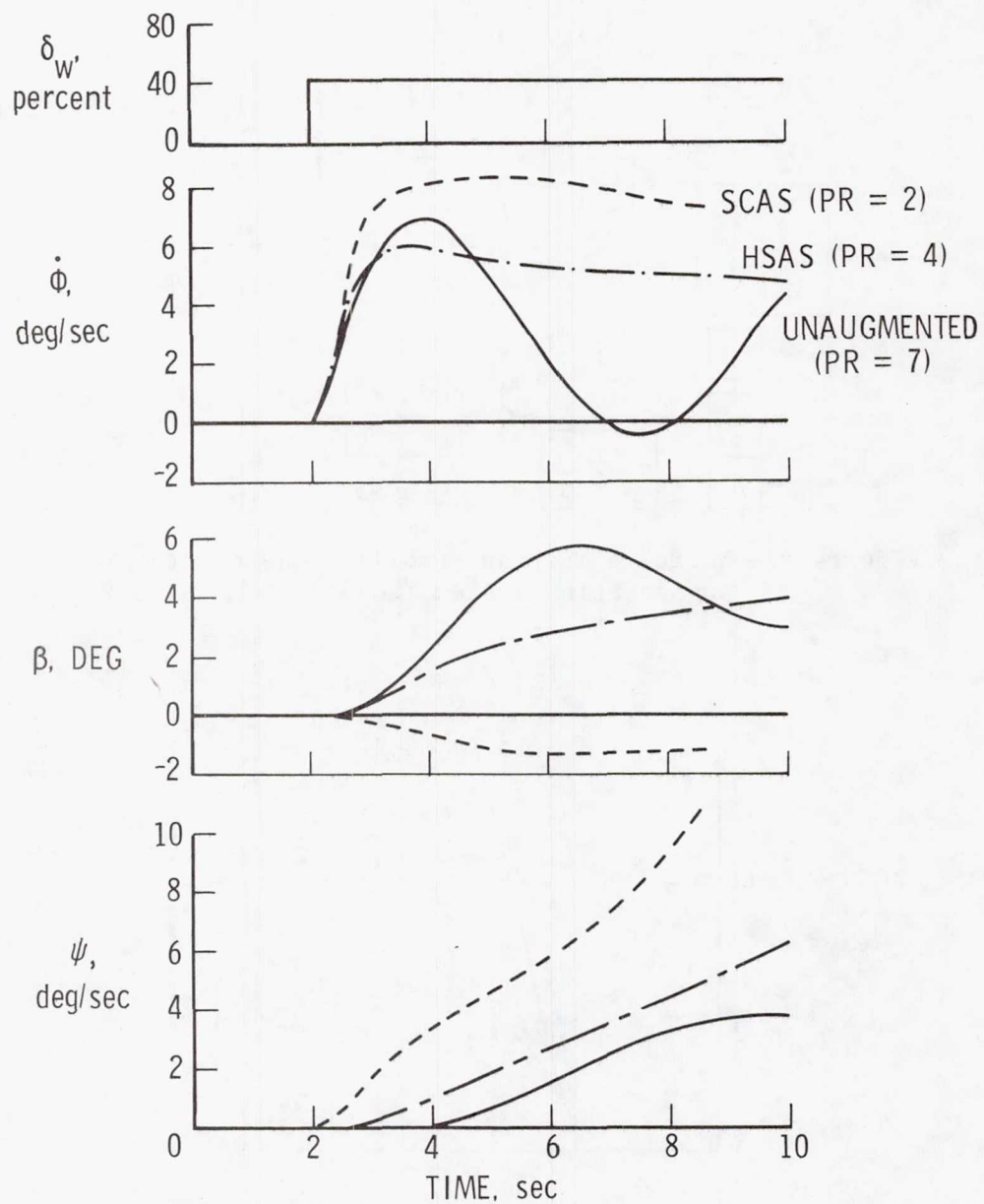
Figure 11.- Comparison of lateral-directional response to a lateral control step input for various control systems.
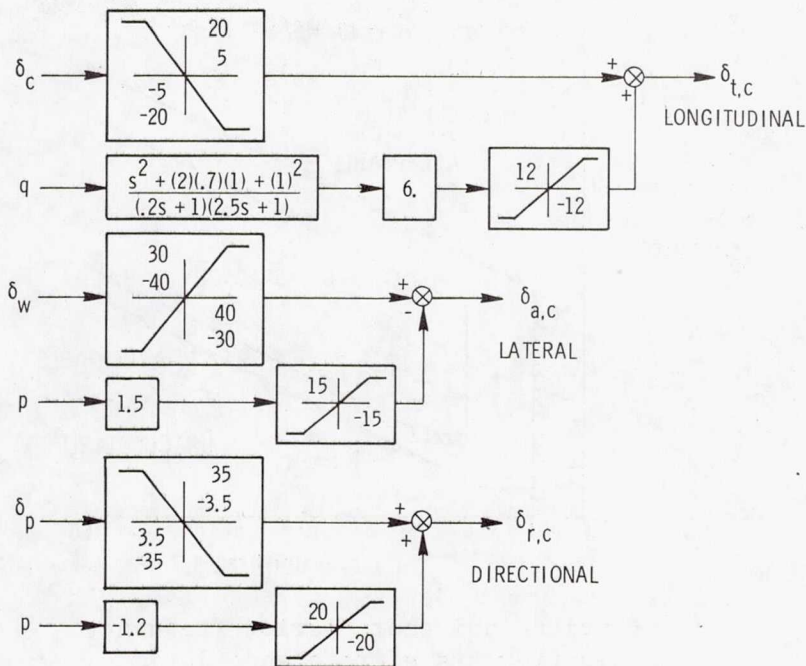
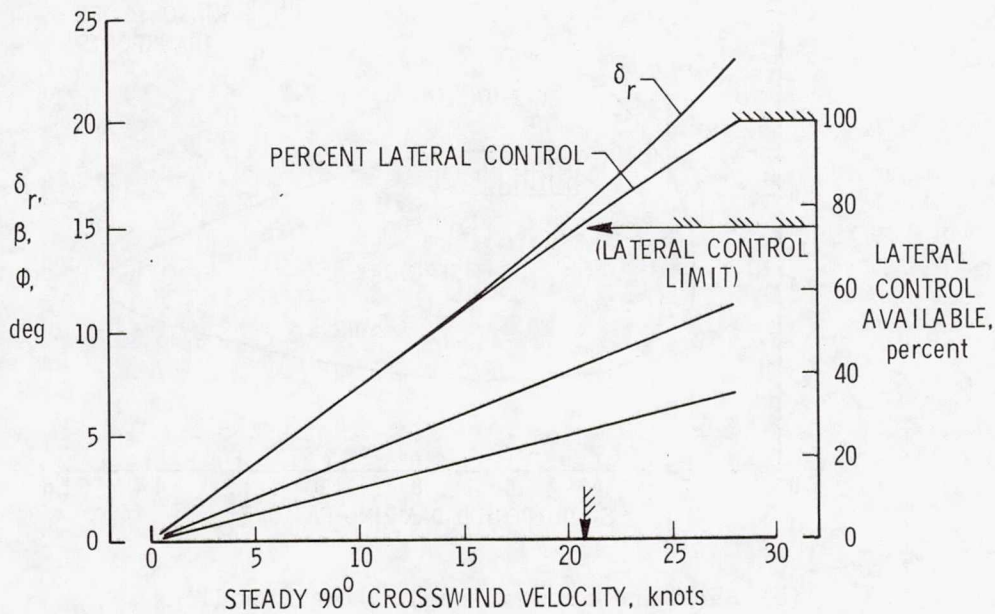Figure 12.- Hardened stability augmentation system (HSAS).
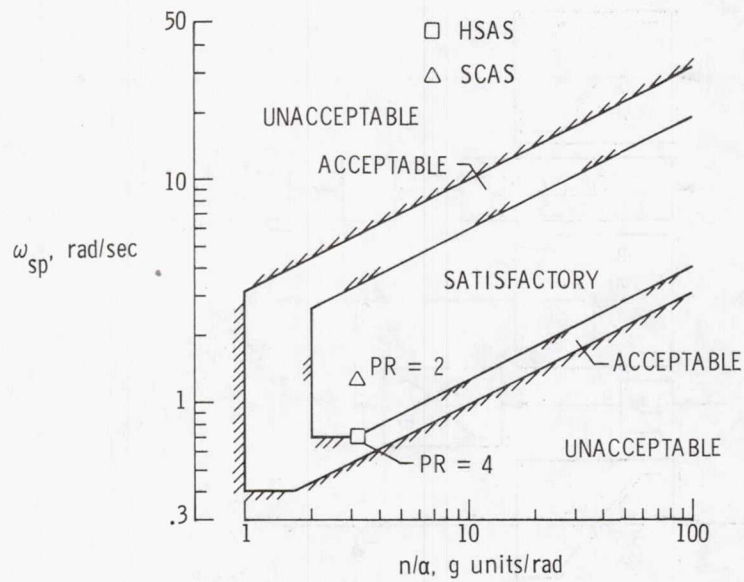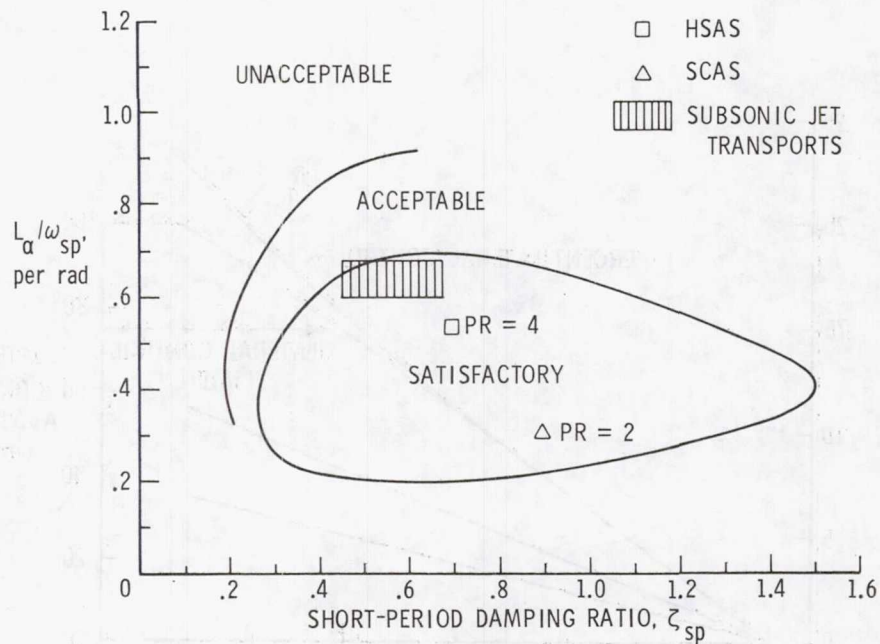

Figure 13.- Indication of crosswind trim capability ($\psi = 0^{\circ}$).

243

(a) Longitudinal short-period frequency
requirements of reference 10.

(b) Shomber-Gertsen longitudinal handling
qualities of reference 11.

Figure 14.- Longitudinal handling qualities criteria.
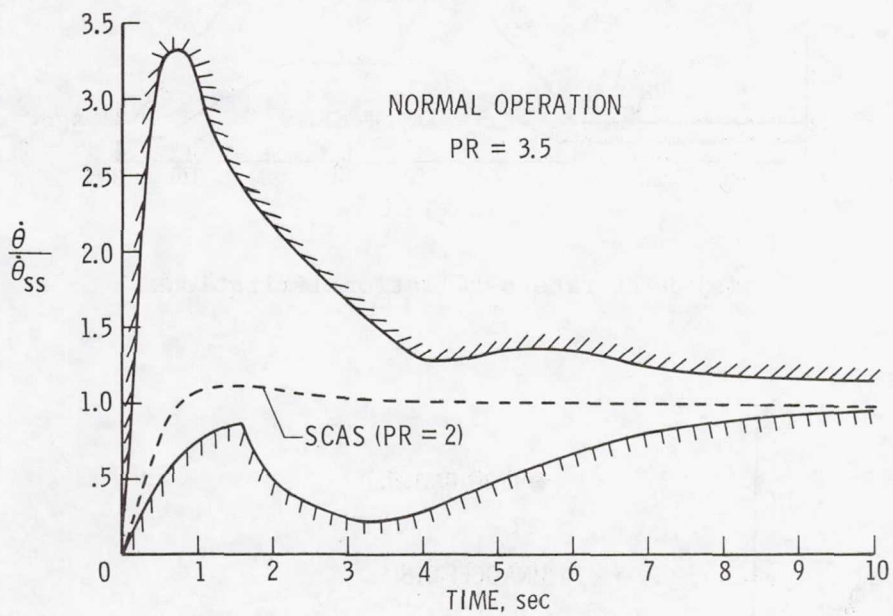
Figure 15.- Low-speed rate response
criterion of reference 12.
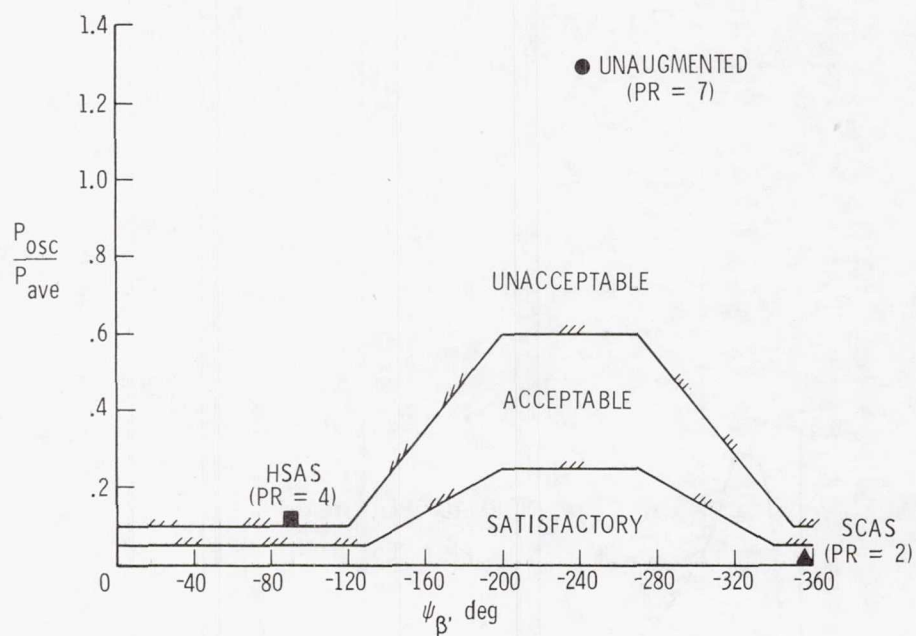
(a) Roll rate oscillation limitations.
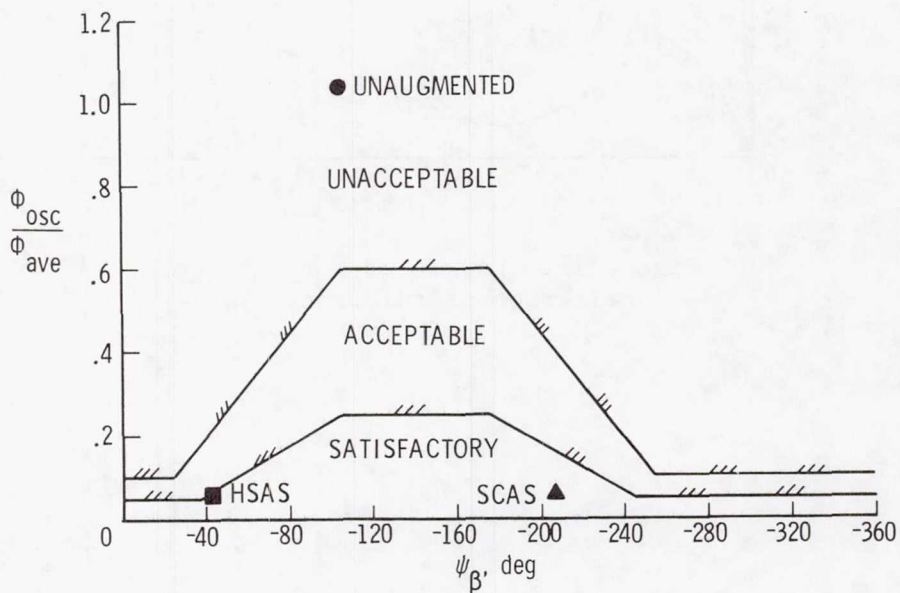
(b) Bank angle oscillation limitations.

Figure 16.- Lateral-directional handling qualities
criteria of reference 10.

Figure 17.- Variation of pilot rating with roll
coupling parameter. (Shaded area presented
in ref. 13.)

(a) Roll acceleration response boundaries
    for large aircraft. Boundaries from
    reference 10.

(b) Roll rate response criterion for
    transport aircraft. Boundaries
    from reference 14.

Figure 18.- Lateral response criteria.

FLEXSTAB - A COMPUTER PROGRAM FOR THE PREDICTION OF LOADS AND
STABILITY AND CONTROL OF FLEXIBLE AIRCRAFT

Brian R. Perkin
Boeing Aerospace Company

Larry L. Erickson
NASA Ames Research Center

SUMMARY

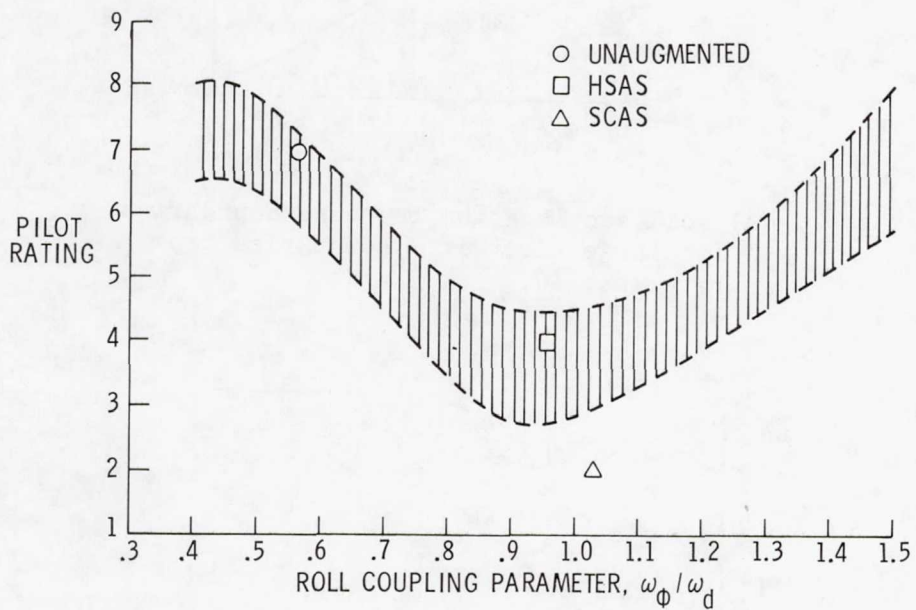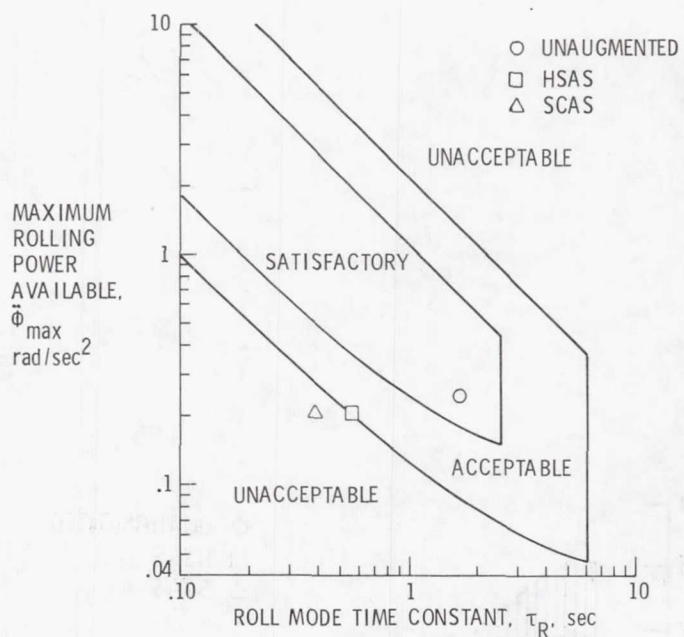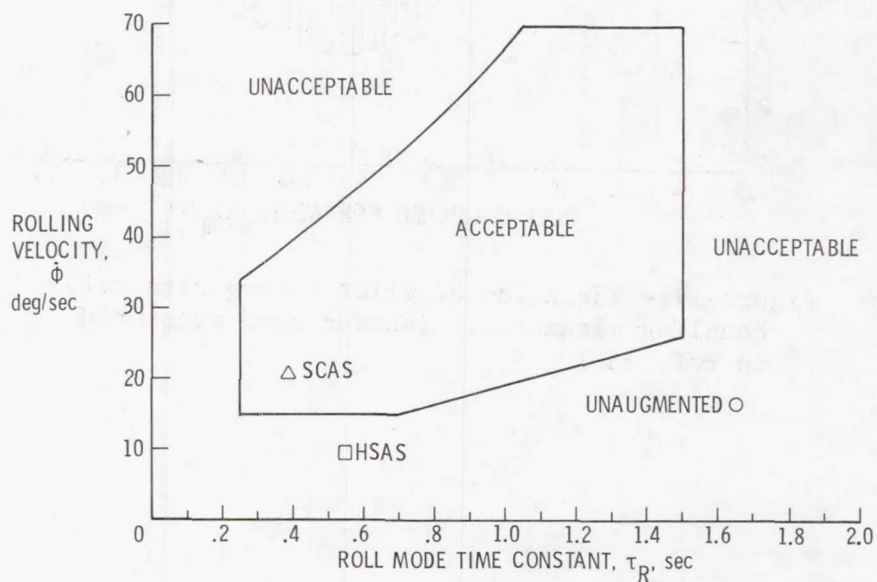This paper describes and illustrates capabilities of the FLEXSTAB Computer Program System. FLEXSTAB is a system of computer programs for performing aeroelastic analysis of a wide variety of current and future aircraft configurations. There are two versions of FLEXSTAB: a NASA controls-fixed version* identified as Level 1 FLEXSTAB; and an Air Force version,** identified as Level 2 FLEXSTAB, which provides for active controls analysis at low frequencies. The aerodynamic theory used in FLEXSTAB is applicable to both steady and unsteady, subsonic and supersonic flow for multiple wing-body-tail-nacelle configurations with a plane of symmetry. For unsteady flow calculations, an unsteady aerodynamic theory is used which is appropriate for the low reduced frequencies associated with aircraft flight dynamics. The aircraft may be modeled as either a rigid or flexible structure. FLEXSTAB will trim the aircraft in steady reference flight and compute both static and dynamic stability and control derivatives and the stability behavior about the trim condition. The airplane lifting pressure distribution, aerodynamic and inertia loads and deflected shape are also computed.

INTRODUCTION

FLEXSTAB is a system of computer programs for performing aeroelastic analysis of a wide variety of current and future aircraft configurations. There are two versions of FLEXSTAB: a NASA, controls-fixed version, identified as Level 1 FLEXSTAB (ref. 1 and 2); and an Air Force version, identified as Level 2 FLEXSTAB (ref. 3), which provides for active controls analysis at low frequencies. Effort is currently underway to consolidate these two versions into a Level 3 FLEXSTAB program. This paper describes the NASA version of FLEXSTAB in some detail with a brief description of the Air Force version.

The degree to which aeroelasticity influences aircraft flight behavior, such as stability or controllability and structural loads, varies greatly from aircraft to aircraft, depending upon configuration and performance requirements. Obviously the aeroelastic effects become more significant with the trend to lighter weight, more flexible aircraft structures. The low aspect ratio, thin wing, slender body configurations of large supersonic aircraft are a prime example. The aeroelastic effects for this class of aircraft arise from complex structural deformation shapes (relative to higher aspect ratio configurations) affecting both the loads and the stability. Further, because some of their structural motions may have characteristic frequencies approaching those of their rigid body motions, dynamic stability may be significantly affected by the dynamics of the structure through aerodynamic coupling between the rigid body and structural motions.

In recognition of these needs, NASA, and later the U.S. Air Force, sponsored the development of the FLEXSTAB computer programs. These are regarded as first generation programs which partially satisfy the need for an automated aeroelastic analysis tool.

This paper presents a brief introduction to the capabilities and limitations of the FLEXSTAB programs. Some of the capabilities are illustrated by results from application of FLEXSTAB to actual and proposed aircraft configurations including the YF-12A aircraft, the NASA Arrow-Wing Supersonic Cruise Aircraft, and the Boeing Fixed-Wing SST.

FLEXSTAB CAPABILITIES

The NASA Level 1 FLEXSTAB is a system of fourteen separate computer programs (totalling about 100 000 source statements) using linear theories to evaluate controls-fixed static and dynamic stability, trim state, inertial and aerodynamic loading, and elastic deformations of aircraft configurations at subsonic and supersonic speeds. The functional configuration of Level 1 FLEXSTAB is shown in figure 1. A wide range of analysis capability has been incorporated into the FLEXSTAB system as shown in table 1. A typical analysis sequence is shown in figure 2.

The aerodynamic theory is applicable to both steady and unsteady, subsonic and supersonic flow for multiple wing-body-tail-nacelle configurations with a plane of symmetry. The aerodynamic theory is a linearized potential flow theory and contains a low frequency approximation to unsteady flow. A single aerodynamic paneling scheme can be used for steady and unsteady, subsonic and supersonic flow. Structural flexibility and inertial properties are modeled using an elastic axis representation with beam finite elements (internal to FLEXSTAB). Also, structural properties generated externally by programs such as NASTRAN® or ATLAS can be interfaced with FLEXSTAB where a better structural definition is required, such as for low aspect ratio aircraft. Structural and aerodynamic properties are integrated using a mean-axis representation. The

250

dynamics of a flexible aircraft are resolved into structural dynamic free vibration modes superimposed on rigid body dynamics. The equations of motion are expressed for a steady, reference motion to determine trim and static stability, inertial and aerodynamic loading, and elastic deformations. They are also expressed in terms of unsteady perturbations about the reference motion to determine dynamic stability by characteristic roots or by time histories following an initial perturbation or following penetration of a discrete gust flow field. A brief description of these capabilities with corresponding limitations follows.

FLEXSTAB AERODYNAMIC MODELING

Geometry

The user inputs the aerodynamic geometry of a symmetric configuration as a series of slender bodies with interference surfaces and thin surfaces as shown in figure 3. A fuselage, a nacelle, or an external store is represented by a slender body of revolution. The body camber is defined as camber slopes with respect to a straight aerodynamic mean centerline, and the boundary conditions are set up on a cylindrical surface of revolution. This aerodynamic mean centerline also defines the elastic axis for the body. Interference effects on a slender body are accounted for by an interference shell which is a cylinder of constant polygonal cross section. A wing, horizontal tail, vertical tail, or any other lifting surface (including control surfaces) is represented by linearization of the boundary conditions about a mean plane.

Aerodynamics

The aerodynamic influence coefficient method used in FLEXSTAB to solve the linearized potential flow equations is an extension of the constant pressure paneling technique due to Woodward (ref. 4). For each of the components in the aerodynamic model, FLEXSTAB computes aerodynamic influence coefficient matrices which relate pressure at one aerodynamic panel to the flow incidence and incidence rates of another panel. Incidence angles are expressed in terms of the configuration geometry (involving camber, twist, thickness, dihedral, control surface deflection), aircraft attitude and motion, and elastic deformations. The flow boundary conditions are the flow incidences. Interference effects between thin bodies and slender bodies are approximately accounted for by vortex panels on the thin bodies and by interference surfaces (shells) enclosing each slender body.

For unsteady flow calculations, an unsteady aerodynamic theory is used which is appropriate for the low reduced frequencies associated with aircraft flight dynamics. The theory is not intended to deal with high frequency motion such as encountered in flutter or dynamic loads due to atmospheric turbulence (fig. 4). The unsteady flow model is unique in that it has the same three-dimensional capability as the steady flow model at both supersonic and subsonic speeds ... a feature not found in other unsteady formulations.

Also, unlike other supersonic schemes such as the Mach Box method, the FLEXSTAB aerodynamic model does not require the introduction of "diaphragm regions" for wings with subsonic edges.

Nonlinear and viscous effects are not accounted for analytically since the aerodynamic formulation is based on linearized potential flow theory. The severity of these limitations is a function of the configuration and flight condition. To partially alleviate this limitation, provision has been made for incorporating user specified changes to the aerodynamic matrices, flow incidence vectors, aerodynamic force and moment coefficients, and lifting pressure distributions.

FLEXSTAB STRUCTURAL MODELING

The user can model the aircraft either as a rigid or flexible structure. For a flexible structure, two modeling options are available (see fig. 5). If the structure is amenable to an elastic axis idealization, an internal structures program using beam type finite-elements is provided. In this case, the user supplies FLEXSTAB with the elastic axis geometry, and stiffness (EI, GJ) and mass information.

For elastic modeling of complex structures, FLEXSTAB will accept the structural output of external finite element programs such as NASTRAN® or ATLAS (fig. 6). In this case, a general three-dimensional model must be "reduced" to an equivalent representation consistent with the FLEXSTAB aerodynamic model. That is, the flexibility and inertia definitions are reduced to structural nodes located on the mean aerodynamic plane of thin bodies and on the mean aerodynamic centerlines of slender bodies (fig. 5).

A flexible structure can be represented in either of two ways.

1. Static-Elastic - The structural deformations are assumed to occur statically, and all effects due to structural vibration are ignored. Using this assumption, the structural deformations are related to the applied loads by the flexibility matrix of the unrestrained vehicle and are in phase with the rigid body motion.

2. Residual-Elastic - The structural dynamic motion is accounted for by using the free-vibration-mode shape amplitudes as structural degrees of freedom. FLEXSTAB uses the "residual flexibility" technique, whereby the dynamic effects of just the lower frequency modes (which are most likely to couple with the rigid body motion) are retained. The dynamic effects of the higher frequency modes are neglected, but their static flexibility effects are retained (hence the name residual flexibility). The frequencies of the retained modes must not violate the low frequency approximation of the unsteady aerodynamics.

In both cases the inertial relief is included in the flexibility matrix which is then transformed to the mean-axis system. The static-elastic approach is used for the trim and static stability problems; also, it is usually quite adequate for dynamic stability cases in which the lowest structural vibration frequency is relatively far removed from the frequency of the aircraft short-period motion. The residual flexibility technique is provided for analyzing dynamic stability problems in which the lower structural frequencies and the short-period aircraft motion may be close enough together to significantly couple the aircraft "rigid" body and structural dynamic motion.

In general, the present FLEXSTAB versions are not applicable to dynamic loads analysis. This is because of the low reduced frequency approximation used for the unsteady aerodynamics and the simplifications made in the structural dynamic model. The structural simplifications define the fuselage mass and stiffness along a straight line elastic axis and neglect all rotary inertia terms, (fig. 7). For a wing surface, a dumbbell mass representation is used to represent the wing panel inertial properties.

PROBLEM ANALYSIS

The aerodynamic and structural representations are combined into an aeroelastic set of equations which govern the aircraft loads and flight behavior. Except for the time histories response and the postprocessing of the loads, solutions to these equations are computed in the Stability Derivatives and Static Stability (SD&SS) program. Figure 8 presents a schematic of the SD&SS program illustrating the user input including the empirical data and the program output. The basic calculations for the trim solution and stability and control are further described below.

Trim Solution

From user specified values of steady reference flight conditions (load factor or pitch rate, flightpath angle or thrust, yaw and roll rates, bank angle, and altitude or speed and dynamic pressure), FLEXSTAB computes the trim parameters and trimmed force coefficients shown in table 2. Three solution options are available:

1. Trim solution with constant coefficients: Here, all the aerodynamic force coefficients are computed analytically by FLEXSTAB, and the trim parameters are obtained directly from the linearized equations of motion.

2. Iterative trim solution: In this case the user can supply a table of nonlinear force and moment coefficients to replace all or a portion of the FLEXSTAB computed rigid aerodynamic coefficients; aeroelastic increments to these coefficients are computed on the basis of linear theory.

3. User specified trim parameters: This option allows the user to specify values for the trim parameters, thus, in general leaving the aircraft in an unbalanced load condition. This option is useful for calculating loads per unit control surface deflection, for specifying untrimmed flight maneuvers, or for matching rigid model wind tunnel test conditions.

After the trim variables are obtained (or specified), FLEXSTAB computes lifting pressure distributions, aerodynamic and inertial loads at aerodynamic centroids, and elastic deflections due to these loads. In addition, for steady symmetric flight, the aerodynamic pressures can be integrated over user specified portions of the aircraft to obtain shear, bending, and torque reactions to the applied airloads (ALOADS program) when the structural model originates from an external finite element program.

Stability and Control Calculations

The FLEXSTAB analysis proceeds by perturbing the aircraft motion variables (both rigid and elastic) about their values for the reference flight condition. This results in explicit matrix equations from which the static and dynamic stability and control derivatives are computed. These derivatives, listed in tables 3 and 4, are computed for both longitudinal and lateral directional motions. The linearized flow equations used in FLEXSTAB govern first order aerodynamic effects; second-order nonlinear terms, such as the product of angle of attack with angle of sideslip, are neglected. For small dihedral configurations these second-order terms can significantly affect the yaw rate and sideslip stability derivatives (ref. 5).

The stability characteristics about the reference condition are computed for two cases, 1. static (steady state flight), and 2. dynamic, (time varying motion of the aircraft). For the static case, the static stability parameters listed in table 2 are computed. For the dynamic case, the aircraft stability behavior is determined with controls fixed. (In the Air Force version of FLEXSTAB, reference 3, the low frequency dynamics of vehicles with feedback controls and sensors can be evaluated). Using the linearized equations of motion, the roots of the corresponding characteristic equation are computed. These roots in turn supply the dynamic modes of motion together with the associated frequencies and damping coefficients. Each real root and each oscillatory pair of roots are described individually. For each mode the following is printed:

.   Times and number of cycles to one-half (or double) and one-tenth amplitude

.   Frequency and period

.   Logarithmic decrement and ratio of successive maximum displacement

254

- Undamped natural frequency

- Damping ratio

- Phase and amplitudes of modal coupling terms

Time Histories Response

The nonlinear perturbation equations of motion are numerically integrated using a Runge-Kutta procedure to determine the time histories response. The time histories response is required when the user wants to investigate the dynamic stability due to; (a) the large perturbations to motion variables, and (b) a discrete gust. Three types of discrete gust inputs may be specified, these are sine, 1-cosine, and modified square wave. Nonlinear aerodynamic data may be input as a tabular series for calculating the response. Specification of the discrete gust must be consistent with the limitation of the low frequency approximation.

APPLICATIONS OF LEVEL 1 FLEXSTAB

Some of the capabilities of FLEXSTAB are illustrated by the results from application to different airplane configurations. The NASA Arrow-Wing Supersonic Cruise Aircraft has been used to illustrate the prediction of stability and control parameters for the rigid and flexible airplane. Also, comparisons between FLEXSTAB results and results from other analysis tools, wind tunnel tests, and flight data are presented for the YF-12A, an Arrow-Wing— Body configuration, the Boeing Fixed-Wing SST, and the Space Shuttle Orbiter. The YF-12A results are for a flexible aircraft and the other three for rigid aircraft.

NASA Arrow-Wing Supersonic Cruise Aircraft

This configuration was used by Boeing in support of the NASA SCAR program (ref. 6). In that program FLEXSTAB was used to determine the aeroelastic loads using elastic properties supplied by the ATLAS finite-element structural analysis program. FLEXSTAB has also been used to predict the stability and control parameters for the configuration. Figure 9 shows the aerodynamic paneling used in the analysis. Tables 5-8 list the stability and control parameters for both the rigid and elastic airplane as output by FLEXSTAB. The elastic airplane parameters are shown for both the "free-free structure" and the "fixed-free structure". The free-free airplane analysis is programmed in the FLEXSTAB code. The elastic displacements and rotations in the free-free analysis are with respect to a mean axis system with the origin selected at the aircraft mass center. The elastic distortions relative to a mean-axis system correspond to those of the actual unrestrained flight vehicle and do not contribute to the linear and angular momenta of the relative motion with

respect to the body axes. Hence, the origin of the body axes remains at the aircraft mass center at every instant and reduces the inertial coupling between the overall and relative deformation motions. The fixed-free airplane analysis consists of using a cantilevered (clamped) flexibility matrix which contains implicitly the inertial relief effects. The fixed-free airplane analysis was patched into the FLEXSTAB code for this example to illustrate the significance of the mean-axis formulation. The fixed-free type of solution is sometimes used in present aircraft design, but the free-free solution is more representative of the airplane in flight. Tables 5-8 show the effects of using the free-free analysis. The difference between the free-free and fixed-free analyses for the trim α ($\Delta\alpha = 0.800^o$) represents the angle through which the mean axis rotates relative to the clamped axis. The effect of this rotation can be significant for the stability derivatives as presented in tables 6 and 7.

YF-12A

A comparison between the FLEXSTAB predicted and flight measured deformed shape of the YF-12A is shown in figure 10. These results are for a load factor of 1 at a Mach number of 2.8. For this flight condition the agreement is generally good. At subsonic Mach numbers there is not such good agreement. This is probably due to the chine induced vortex flows which FLEXSTAB cannot model.

Arrow-Wing-Body Configuration

Reference 7 presents comparisons of theoretical and experimental transonic pressure distributions for an arrow-wing—body configuration. Example results at M=0.85 for α = 2.1^o and 7.9^o are given in figure 11 for 2 spanwise locations. In addition to wind tunnel results, 2 sets of analytic potential flow results are shown; one of these is from FLEXSTAB and the other is from Boeing program TEA-230. The FLEXSTAB results for the individual upper and lower surface pressures were computed from a Boeing modified version of FLEXSTAB. The released version of FLEXSTAB computes only the pressure difference between the lower and upper surfaces (lifting pressure).

At α = 2.1^o both FLEXSTAB and TEA-230 predict pressure distributions which compare well with the experimental results. In contrast to the mean surface paneling method used in FLEXSTAB, the TEA-230 model employs on-the-surface paneling and boundary conditions. This feature enables the actual wing leading-edge pressures to be more closely predicted by TEA-230 than by FLEXSTAB.

At α = 7.9^o the presence of a vortex spiraling off the wing leading edge alters the pressure distribution over a major portion of the wing. As seen in figure 11 the analytic results still agree with experiment at the inboard station but not at the outboard station. This is because neither of the two analytic methods can model the leading-edge vortex flow.

Boeing Fixed-Wing SST

FLEXSTAB and wind tunnel comparisons for the Boeing Fixed-Wing Supersonic Transport (B2707-300) are shown in figure 12. These analytic results were computed from an early version of FLEXSTAB. The figure shows the variation in lift-curve slope and aerodynamic center with Mach number. Agreement between the measured and FLEXSTAB predicted results is good. For supersonic Mach numbers the aerodynamic center predicted by FLEXSTAB tends to be slightly aft of the measured locations, and the lift curve slope tends to be slightly high.

Space Shuttle Orbiter

Figures 13 and 14 show comparisons of pitching moment coefficients due to pitch rate $c_{m\hat{q}}$ (table 3) and due to rate of change of angle of attack $c_{m\hat{\alpha}}$ (table 4) for the Space Shuttle Orbiter. Wind tunnel values for the sum $(c_{m\hat{q}} + c_{m\hat{\alpha}})$ are compared to FLEXSTAB computed values in figure 13. The agreement is remarkably good considering the unstreamlined shape of the Orbiter. In contrast to wind tunnel measurements in which only the sum $c_{m\hat{q}} + c_{m\hat{\alpha}}$ is generally measured, FLEXSTAB computes each derivative separately. These are shown in figure 14 where it is seen that $c_{m\hat{\alpha}}$ is destabilizing at the supersonic Mach number.

LEVEL 1   FLEXSTAB DOCUMENTATION, AVAILABILITY AND IMPLEMENTATION

The documentation for Level 1 FLEXSTAB is listed under references 1 and 2.

Both a CDC and an IBM version of the NASA FLEXSTAB Program are available from COSMIC through a lease arrangement. Inquiries concerning the lease should be made to:

> Computer Software Management and Information Center
> Barrow Hall
> University of Georgia
> Athens, Georgia   30601

The CDC version has been executed on the following computers, using FORTRAN Extended compilers:

1.   CYBER 70, Model 73, SCOPE 3.4 Operating System

2.   CDC 6600, KRONOS 2.1 and SCOPE 3.4 Operating Systems

3.   CDC 7600, SCOPE 2.1.3 Operating System

The IBM version requires both the G and H compilers and has been executed on the following computers:

1. IBM 360-91/OS

2. IBM 360-67/OS

Additional information on the program implementation requirements is summarized in reference 1.

LEVEL 2   FLEXSTAB CAPABILITIES

The Air Force has developed additional capabilities for FLEXSTAB for the evaluation of the low frequency dynamics of control configured vehicles (ref. 3). These capabilities are subject to the same limitations as Level 1 FLEXSTAB imposed by the structural modeling and the low frequency aerodynamic approximation. The additional capabilities can be summarized as:

- Active Controls Capability
- User Specification of Linear Control System
- Sensor Simulations
- Time Histories of Controlled Airplane
- RMS Aircraft Motion Due to Turbulence PSD
- Frequency Response Calculations
- Structural Damping
- Modal Truncation Formulation for the Structural Dynamic Model
- Plotting of Dynamic Analysis Data
- Data Interface For Flight Simulators
- Fore and Aft Gust Capability
- Aerodynamic Hinge Moments

This extended capability of FLEXSTAB allows the analytical representation of arbitrary combinations of active control systems and linear systems analysis of the response to turbulence and control commands. Nonlinear response to discrete gusts and control commands may also be evaluated by time histories generated by the system.

The functional configuration of the Level 2 FLEXSTAB system is shown in figure 15. The program system totals twelve separate programs with about 140 000 source statements. Five of the programs remain the same as for Level 1 FLEXSTAB, six have been modified, mainly to allow definition of motions at the sensor locations used by the flight control system, and one program, the linear system analysis, is new.

The program has been used by the Air Force for research on the following aircraft; YF-16, B-1, C-5A, and the F-111 TACT. Also the program is being used in a preliminary design mode of operation for system integration in support of fire control systems on the airborne laser weapons program.

Figure 16 shows a typical result from Level 2 FLEXSTAB for the B-52E aircraft response to a lateral gust with and without a yaw stability augmentation system (yaw SAS).

LEVEL 2   FLEXSTAB DOCUMENTATION, AVAILABILITY AND IMPLEMENTATION

The documentation for Level 2 FLEXSTAB is listed under reference 3. The program is available only for application to Department of Defense problems from the Air Force by sending a request to:

AFFDL
Flight Control Division
Wright-Patterson Air Force Base
Ohio   45433

The Level 2 version has been executed on the CYBER 74 and CDC 6600 under the KRONOS 2.0 and 2.1, SCOPE 3.4 and NOS/BE Operating Systems.

CONCLUDING REMARKS

The development of the Level 1 FLEXSTAB computer program system provides a first generation program to partially satisfy the requirement for an automated aeroelastic analysis tool. The system is based on integrated aerodynamic, structural, and dynamic analytical methods applicable to aircraft configurations having a plane of symmetry. The aerodynamic analysis may be supplemented or modified with empirical data. Also the system includes the low frequency aerodynamic effects appropriate for evaluating the stability of large aircraft.

Through application to several different aircraft configurations it has been shown that the linearized theory employed is capable of providing aeroelastic analysis of complex configurations. The linearized theory provides good correlation with experiment as long as the flow over the configuration remains attached, although in some cases it may also provide useful data for separated flow conditions. Further work is required to develop methods of representing leading-edge vortex flow.

The Level 2 system integrates the aerodynamic and structural methods used in Level 1 with control system dynamics. The resulting system is capable of analyzing the static and low frequency dynamic characteristics of control configured vehicles.

By refining the structural modeling and providing full unsteady aerodynamic capability, the FLEXSTAB system could be applied to prediction of dynamic loads at higher structural frequencies.

REFERENCES

1. Tinoco, E. N.; and Mercer, J. E.: FLEXSTAB - A Summary of the Functions and Capabilities of the NASA Flexible Airplane Analysis Computer System. NASA CR-2564, 1975.

2. Boeing Commer. Airplane Co.: A Method for Predicting the Stability Characteristics of an Elastic Airplane.

   a. Vol. I   - FLEXSTAB Theoretical Description, NASA CR-114712, 1974
   b. Vol. II - FLEXSTAB 1.02.00 User's Manual, NASA CR-114713, 1974
   c. Vol. III - FLEXSTAB 1.02.00 Program Description, NASA CR-114714, 1974
   d. Vol. IV* - FLEXSTAB 1.02.00 Demonstration Cases and Results,
               NASA CR-114715, 1974.

3. Boeing Commer. Airplane Co.: A Method for Predicting the Stability Characteristics of Control Configured Vehicles. AFFDL-TR-74-91, 1974.

   a. Vol. I   - FLEXSTAB 2.01.00 Theoretical Description
   b. Vol. II - FLEXSTAB 2.01.00 User's Manual
   c. Vol. III - FLEXSTAB 2.01.00 Programmer's Manual
   d. Vol. IV - FLEXSTAB 2.01.00 B-52E LAMS Demonstration Case and Results

4. Woodward, F. A.: Analysis and Design of Wing-Body Combinations at Subsonic and Supersonic Speeds. Journal of Aircraft, Vol. 5, No. 6, November-December, 1968, pp 528-534.

5. Rubbert, P. E., "Sideslip of Wing-Body Combinations", NASA CR-114716, 1975.

6. Preliminary Design Dep., Boeing Commer. Airplane Co.: Study of Structural Design Concepts for an Arrow Wing Supersonic Transport Configuration. Vols. 1 and 2. NASA CR-132576, 1976.

7. Manro, M. E., Manning, K.J.R., Hallstaff, T. H., Rogers, J. T., Transonic Pressure Measurements and Comparison of Theory to Experiment for an Arrow-Wing Configuration. Vol. III: Data Report — Comparison of Attached Flow Theories to Experiment. NASA CR-132729, 1975.

---

* Not yet released. Preliminary copies available from NASA Ames Research Center.

EI   beam flexural rigidity

GJ   beam torsional rigidity

[LSC]   steady lifting aerodynamic influence coefficient matrix

P, Q, R   components of angular velocity, ω

u, v, w   perturbation components of velocity

ρ density of air

θ, ϕ, ψ Euler angles

Subscripts:

1   reference state

Superscripts:

• (dot)   first derivative with respect to time

TABLE 1.– PROGRAMS OF THE LEVEL 1 FLEXSTAB SYSTEM

No.	Program Title	Program Name	Purpose	Data Flow	
				Input	Output
AIRPLANE MODELING SECTION					
1	Geometry definition program	GD	To geometrically construct an airplane configuration that complies with the requirements of the aerodynamic and structural theories	• Basic geometric description of the airplane (wing plan-form, airfoil shapes, wing twist, body radius distribution, body camber, etc.) in its cruise or unload condition	• Geometric defining quantities required for a linearized aerodynamic and structural representation (such as panel corner points and location of line doublet segments) CalComp plots of the airplane's configuration
2	Aerodynamic influence coefficient program	AIC	To produce matrices that relate the change in pressure on a panel to the change in flow incidence at another panel $$A_{ij} = \frac{\partial P_i}{\partial \psi_j}$$ and to produce matrices that relate the change in pressure on a panel to the rate of change in flow incidence at another panel $$\delta A_{ij} = \frac{\partial P_i}{\partial \dot{\psi}_i}$$	• Mach number • Geometric defining quantities produced by the GD program	• Aerodynamic influence coefficient (AIC) matrices
3	AIC matric correction program	CAIC	To correct the [LSC] AIC matrix using (a) a correction matrix $[C_2]$ based on wind tunnel or flight-test data (b) a replacement technique in which the user specifies elements of the matrix	• The [LSC] AIC matrix	• A corrected [LSC] matrix

TABLE 1.- CONTINUED

No.	Program Title	Program Name	Purpose	Data Flow	
				Input	Output
STRUCTURAL MODELING SECTION					
4	Internal structural influence coefficient program	ISIC	To produce flexibility matrices based on beam theory and consistent with paneling used for computing the AIC matrices	•Geometric defining quantities produced by the GD program •Elastic axis geometric description •EIs and GJs of beam segments •Mass distribution	•Flexibility matrices (Static-elastic) •Mass matrix
5	Elastic axis plot program	EAPLOT	To plot the structural elastic axes	•Elastic axis data	•CalComp plots of the airplane's elastic axis
6	Normal modes program	NM	To calculate the free-vibration normal mode shapes and then to construct normal mode matrices	•Number of normal modes requested •Structural (ISIC) flexibility matrices	•Mode shape matrices •Residual flexibility matrices
7	Normal modes plot program	NMPLOT	To plot the normal mode shapes	•Normal mode shapes	•CalComp plots of the mode shapes
8	External structural influence coefficient program	ESIC	To accept a flexibility matrix from a source external to the FLEXSTAB system and by interpolation produce a new flexibility matrix consistent with paneling used for computing the AIC matrices	•Geometric defining quantities produced by the GD program •Structural mode shapes •External flexibility matrix	•New flexibility matrices •Mass matrix •Normal mode matrices

TABLE 1.- CONCLUDED

No.	Program Title	Program Name	Purpose	Data Flow	
				Input	Output
PROBLEM ANALYSIS SECTION					
9	Stability derivatives and static stability program	SD&SS	To calculate the static and dynamic stability characteristics of the airplane	•Geometric defining quantities produced by the GD program •AIC matrices •Flexibility matrices •Normal mode matrices •Flight condition (altitude, ρ, P_1, R_1, Q_1, ϕ, γ_1, T_1) •Wind tunnel data •Exterior downwash data	•Trim parameters (α_1, δ_{e_1}, T_1, β_1, δ_{a_1}, and δ_{r_1} •Deformed shape •Steady and unsteady pressure distribution •Static and dynamic stability derivatives •Static stability parameters (static margin, neutral point, etc.) •Control effectiveness
10	Pressure distribution plot program	PDPLOT	To plot the steady and unsteady pressure distributions	•Steady or unsteady pressure distribution	•CalComp plots of the pressure distribution
11	Time histories program	TH	To help the user evaluate the stability of an airplane using large-disturbance theory (nonlinear equations)	•Geometric data •Dynamic stability derivatives •Stability data (α_1, β_1, ϕ_1, γ_1, etc.) •Wind tunnel data	•Values of motion variables versus time of flight (u, v, w, $\dot{u}$, $\dot{v}$, $\dot{w}$, θ, ϕ, ψ, $\dot{\theta}$, $\dot{\phi}$, $\dot{\psi}$, etc.)
12	Time histories plot program	THPLOT	To plot the time histories (motion variables versus time) of the flight	•Motion variables versus time	•CalComp plots of the time histories
13	Structural loads program	SLOADS	To print the structural elastic axis loads	•Structural load matrices	•Structural loads on elastic axis
14	Aerodynamic loads	ALOADS	To calculate air loads	•Air load matrices	•Air loads

TABLE 2.- STATIC STABILITY AND TRIM PARAMETERS

TRIM PARAMETERS	
α	angle of attack
β	angle of sideslip
δ_e	elevator deflection angle
δ_a	aileron deflection angle
δ_r	rudder deflection angle
T	thrust
γ	flightpath angle
TRIMMED FORCE COEFFICIENTS	
C_L	lift coefficient
C_D	drag coefficient
C_m	pitching moment coefficient
C_y	sideforce coefficient
C_ℓ	rolling moment coefficient
C_n	yawing moment coefficient
STATIC STABILITY PARAMETERS	
h_n-h	static margin
h_n	neutral point
h_m-h	maneuver margin
$\partial\delta_e/\partial n \left(=\dfrac{\Delta\delta_e}{n-1}\right)$	elevator angle per g (turn, pullup)
$\partial\delta_e/\partial V$	speed stick stability

TABLE 3.— STATIC STABILITY DERIVATIVES AND CONTROL EFFECTIVENESS COEFFICIENTS

C_{Lo}	lift coefficient at $\alpha = \delta_e = 0$	$C_{n_{\hat{p}}}$	yawing moment coefficient due to roll rate
C_{Do}	drag coefficient at $\alpha = \delta_e = 0$	$C_{y_{\hat{r}}}$	sideforce coefficient due to yaw rate
C_{mo}	pitching moment coefficient at $\alpha = \delta_e = 0$	$C_{\ell_{\hat{r}}}$	rolling moment coefficient due to yaw rate
C_{L_α}	lift coefficient due to angle of attack	$C_{n_{\hat{r}}}$	yawing moment coefficient due to yaw rate
C_{D_α}	drag coefficient due to angle of attack	C_{y_β}	sideforce coefficient due to sideslip
C_{m_α}	pitching moment coefficient due to angle of attack	C_{ℓ_β}	rolling moment coefficient due to sideslip
$C_{L_{\hat{q}}}$	lift coefficient due to pitch rate	C_{n_β}	yawing moment coefficient due to sideslip
$C_{D_{\hat{q}}}$	drag coefficient due to pitch rate	$C_{y_{\delta_a}}$	sideforce coefficient due to aileron deflection (antisymmetrically deflected)
$C_{m_{\hat{q}}}$	pitching moment coefficient due to pitch rate	$C_{\ell_{\delta_a}}$	rolling moment coefficient due to aileron deflection (antisymmetrically deflected)
$C_{L_{\delta_e}}$	lift coefficient due to elevator deflection		
$C_{D_{\delta_e}}$	drag coefficient due to elevator deflection	$C_{n_{\delta_a}}$	yawing moment coefficient due to aileron deflection (antisymmetrically deflected)
$C_{m_{\delta_e}}$	pitching moment coefficient due to elevator deflection	$C_{y_{\delta_r}}$	sideforce coefficient due to rudder deflection
$C_{y_{\hat{p}}}$	sideforce coefficient due to roll rate	$C_{\ell_{\delta_r}}$	rolling moment coefficient due to rudder deflection
$C_{\ell_{\hat{p}}}$	rolling moment coefficient due to roll rate	$C_{n_{\delta_r}}$	yawing moment coefficient due to rudder deflection

TABLE 4.– DYNAMIC STABILITY DERIVATIVES AND CONTROL EFFECTIVENESS COEFFICIENTS

$C_{L_{\hat{\alpha}}}$	lift coefficient due to angle-of-attack rate	$C_{y_{\hat{\beta}}}$	sideforce coefficient due to sideslip rate
$C_{D_{\hat{\alpha}}}$	drag coefficient due to angle-of-attack rate	$C_{\ell_{\hat{\beta}}}$	rolling moment coefficient due to sideslip rate
$C_{m_{\hat{\alpha}}}$	pitching moment coefficient due to angle-of-attack rate	$C_{n_{\hat{\beta}}}$	yawing moment coefficient due to sideslip rate
$C_{L_{\hat{u}}}$	lift coefficient due to speed change	$C_{L_{\dot{\delta}_e}}$	lift coefficient due to elevator deflection rate
$C_{D_{\hat{u}}}$	drag coefficient due to speed change	$C_{D_{\dot{\delta}_e}}$	drag coefficient due to elevator deflection rate
$C_{m_{\hat{u}}}$	pitching moment coefficient due to speed change	$C_{m_{\dot{\delta}_e}}$	pitching moment coefficient due to elevator deflection rate
$C_{L_{\hat{q}}}$	lift coefficient due to pitch acceleration	$C_{y_{\dot{\delta}_a}}$	sideforce coefficient due to aileron deflection rate (antisymmetric deflection)
$C_{D_{\hat{q}}}$	drag coefficient due to pitch acceleration	$C_{\ell_{\dot{\delta}_a}}$	rolling moment coefficient due to aileron deflection rate (antisymmetric deflection)
$C_{m_{\hat{q}}}$	pitching moment coefficient due to pitch acceleration	$C_{n_{\dot{\delta}_a}}$	yawing moment coefficient due to aileron deflection rate (antisymmetric deflection)
$C_{y_{\hat{p}}}$	sideforce coefficient due to roll acceleration	$C_{y_{\dot{\delta}_r}}$	sideforce coefficient due to rudder deflection rate
$C_{\ell_{\hat{p}}}$	rolling moment coefficient due to roll acceleration	$C_{\ell_{\dot{\delta}_r}}$	rolling moment coefficient due to rudder deflection rate
$C_{n_{\hat{p}}}$	yawing moment coefficient due to roll acceleration	$C_{n_{\dot{\delta}_r}}$	yawing moment coefficient due to rudder deflection rate
$C_{y_{\hat{r}}}$	sideforce coefficient due to yaw acceleration		
$C_{\ell_{\hat{r}}}$	rolling moment coefficient due to yaw acceleration		
$C_{n_{\hat{r}}}$	yawing moment coefficient due to yaw acceleration		

TABLE 5.– NASA ARROW–WING SUPERSONIC CRUISE AIRCRAFT STATIC STABILITY
AND TRIM PARAMETERS

	Free-Free Airplane		Fixed-Free Airplane
	Rigid	Static-Elastic	Static-Elastic
Trim parameters			
α_1 deg.	5.318	5.441	6.241
β_1 deg.	0	0	0
δ_{e_1} deg.	2.298	14.156	14.156
δ_{a_1} deg.	0	0	0
δ_{r_1} deg.	0	0	0
T_1 lb.	144 000	144 000	144 000
γ_1 deg.	7.319	7.349	6.549
Static stability parameters			
h_n-h	0.0983	0.0183	0.0183
h_n	0.6213	0.5413	0.5413
h_m-h	0.1010	0,0205	0.0205
$\partial\delta_e/\partial n \left(=\dfrac{\Delta\delta_e}{n\text{-}1}\right)$ deg./g	-8.000	-2.416	-2.421
$\partial\delta_e/\partial v$ deg./ft/sec.	0.0070	0.0010	0.0010

Weight = 298 636 Kg C_L = 0.0666 C.G = 0.523 $\bar{c}$
(657 000 lb) M = 2.9 h = 17 435 m
(57 200 ft)

TABLE 6.– NASA ARROW–WING SUPERSONIC CRUISE AIRCRAFT STATIC STABILITY
DERIVATIVES AND CONTROL EFFECTIVENESS COEFFICIENTS

	Free-Free Airplane		Fixed-Free Airplane
	Rigid	Static-Elastic	Static-Elastic
C_{L_o}	-0.090394	-0.087729	-0.093639
C_{D_o}	0.004326	0.004246	0.004306
C_{m_o}	0.016662	0.010725	0.010831
C_{L_α}/deg.	0.029008	0.026645	0.023918
C_{D_α}/deg.	0.003038	0.002916	0.002955
C_{m_α}/deg.	-0.002851	-0.000486	-0.000438
$C_{L_{\hat{q}}}$/rad.	0.636205	0.345434	0.500099
$C_{D_{\hat{q}}}$/rad.	0.068107	0.047567	0.072209
$C_{m_{\hat{q}}}$/rad.	-0.881881	-0.727361	-0.730188
$C_{L_{\delta_e}}$/deg.	0.000939	0.000568	0.000804
$C_{D_{\delta_e}}$/deg.	0.000059	0.000046	0.000780
$C_{m_{\delta_e}}$/deg.	-0.000918	-0.000566	-0.000570
$C_{y_{\hat{p}}}$/rad.	-0.002286	-0.001445	0.006297
$C_{\ell_{\hat{p}}}$/rad.	-0.133523	-0.099685	-0.100626
$C_{n_{\hat{p}}}$/rad.	0.006054	0.005165	0.004863
$C_{y_{\hat{r}}}$/rad.	0.219438	0.128576	0.172671
$C_{\ell_{\hat{r}}}$/rad.	-0.007389	-0.018225	-0.025462
$C_{n_{\hat{r}}}$/rad.	-0.167888	-0.114434	-0.122142
C_{y_β}/deg.	-0.003305	-0.001722	-0.002574
C_{ℓ_β}/deg.	0.000038	0.000214	0.000327
C_{n_β}/deg.	0.001279	0.000292	0.000443
$C_{y_{\delta_a}}$/deg.	-0.0	0.000010	0.000013
$C_{\ell_{\delta_a}}$/deg.	-0.000115	-0.000057	-0.000057
$C_{n_{\delta_a}}$/deg.	0.000011	0.000003	0.000004
$C_{y_{\delta_r}}$/deg.	0.000228	0.000071	0.000163
$C_{\ell_{\delta_r}}$/deg.	-0.000002	0.000015	0.000003
$C_{n_{\delta_r}}$/deg.	-0.000172	-0.000069	-0.000086

TABLE 7.- NASA ARROW–WING SUPERSONIC CRUISE AIRCRAFT DYNAMIC
STABILITY DERIVATIVES

	Free-Free Airplane		Fixed-Free Airplane
	Rigid	Static-Elastic	Static-Elastic
$C_{L_{\hat{\alpha}}}/\text{rad}$	-0.048826	0.064902	0.244706
$C_{D_{\hat{\alpha}}}/\text{rad}$	-0.006662	0.004098	0.024072
$C_{m_{\hat{\alpha}}}/\text{rad}$	0.058374	-0.021734	-0.024995
$C_{L_{\hat{u}}}$	0.064077	0.068511	0.045412
$C_{D_{\hat{u}}}$	0.005153	0.059110	0.004428
$C_{m_{\hat{u}}}$	0.008657	0.007856	0.008273
$C_{L_{\hat{q}}}/\text{rad}$	-0.280092	0.345434	0.500099
$C_{D_{\hat{q}}}/\text{rad}$	-0.015575	0.047567	0.072209
$C_{m_{\hat{q}}}/\text{rad}$	-0.062581	-0.727361	-0.730188
$C_{y_{\hat{p}}}/\text{rad}$	-0.021108	-0.011722	-0.020624
$C_{\ell_{\hat{p}}}/\text{rad}$	0.009710	-0.003486	-0.002221
$C_{n_{\hat{p}}}/\text{rad}$	0.014685	0.008969	0.010627
$C_{y_{\hat{r}}}/\text{rad}$	-0.043381	-0.031054	-0.040741
$C_{\ell_{\hat{r}}}/\text{rad}$	-0.043000	-0.009016	-0.008496
$C_{n_{\hat{r}}}/\text{rad}$	-0.043619	-0.051572	-0.049689
$C_{y_{\hat{\beta}}}/\text{rad}$	-0.059523	-0.058859	-0.059655
$C_{\ell_{\hat{\beta}}}/\text{rad}$	-0.002412	-0.001590	-0.001705
$C_{n_{\hat{\beta}}}/\text{rad}$	-0.015210	-0.015543	-0.015375

TABLE 8.− NASA ARROW−WING SUPERSONIC CRUISE AIRCRAFT LONGITUDINAL AND LATERAL DIRECTIONAL

DYNAMIC CHARACTERISTICS

M_1 = 2.9, h_1 = 17 435 m , γ_1 = 7.3°, cg = 0.523$\bar{c}$, wt = 298 636 Kg
　　　　　　　(57 200 ft)　　　　　　　　　　　　　　　(657 000 lb)

V = 1015 km/hr
(548 keas)

		Short Period			Phugoid		
		Period (sec)	$T_{1/2}$ or T_2* (sec)	$C_{1/2}$ or C_2* (cycles)	Period (sec)	$T_{1/2}$ or T_2* (sec)	$C_{1/2}$ or C_2* (cycles)
Free-Free Airplane	Rigid	3.55	$T_{1/2}$ = 2.44	$C_{1/2}$ = 0.687	368.3	T_2 = 28 904	C_2 = 78.5
	Static-elastic	8.54	$T_{1/2}$ = 2.69	$C_{1/2}$ = 0.316	214.9	$T_{1/2}$ = 267.8	$C_{1/2}$ = 1.25
Fixed-Free Airplane	Static-elastic	8.99	$T_{1/2}$ = 2.84	$C_{1/2}$ = 0.316	215.9	$T_{1/2}$ = 225.7	$C_{1/2}$ = 1.05

		Dutch roll					Roll convergence	Spiral mode
		Period (sec)	$T_{1/2}$ or T_2* (sec)	$C_{1/2}$ or C_2* (cycles)	$|\phi/\beta|$	Phase angle (deg.)	$T_{1/2}$ (sec)	$T_{1/2}$ or T_2 (sec)
Free-Free Airplane	Rigid	4.83	$T_{1/2}$ = 10.7	$C_{1/2}$ = 2.21	0.22	41.45	$T_{1/2}$ = 1.36	T_2 = 308.0
	Static-elastic	12.15	$T_{1/2}$ = 241.3	$C_{1/2}$ = 19.85	5.56	-144.43	$T_{1/2}$ = 1.49	T_2 = 60.7
Fixed-Free Airplane	Static-elastic	10.23	T_2 = 107.93	C_2 = 10.5	6.17	-146.74	$T_{1/2}$ = 1.39	T_2 = 61.2

*Time or cycles to half or twice amplitude.
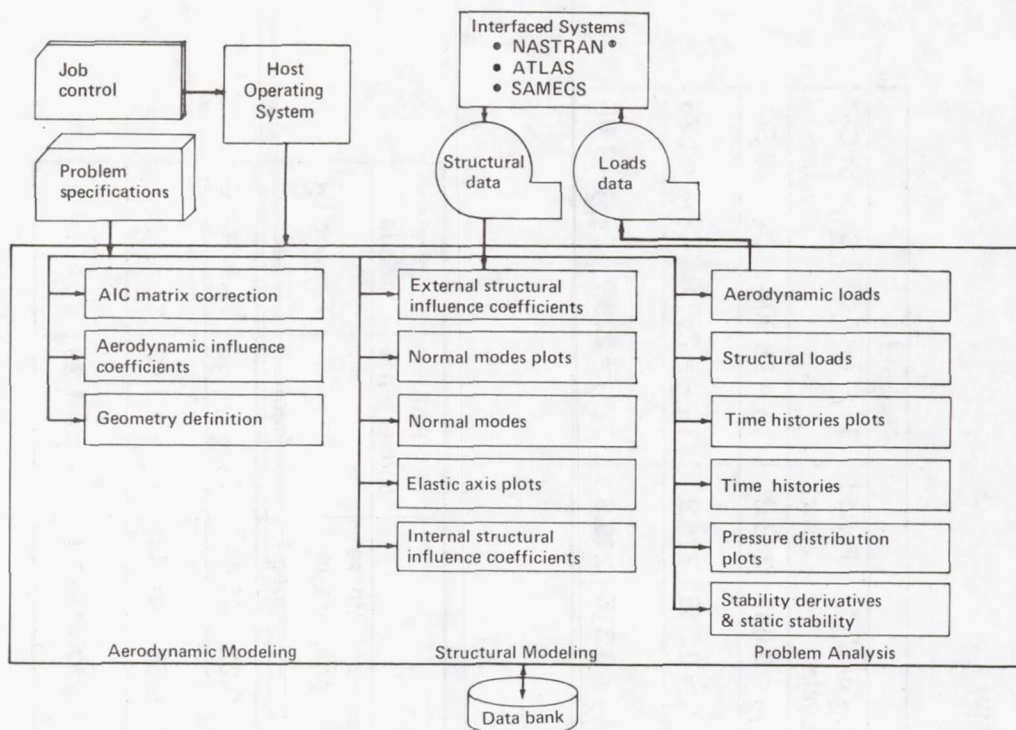
Figure 1.- Level 1 FLEXSTAB functional configuration.
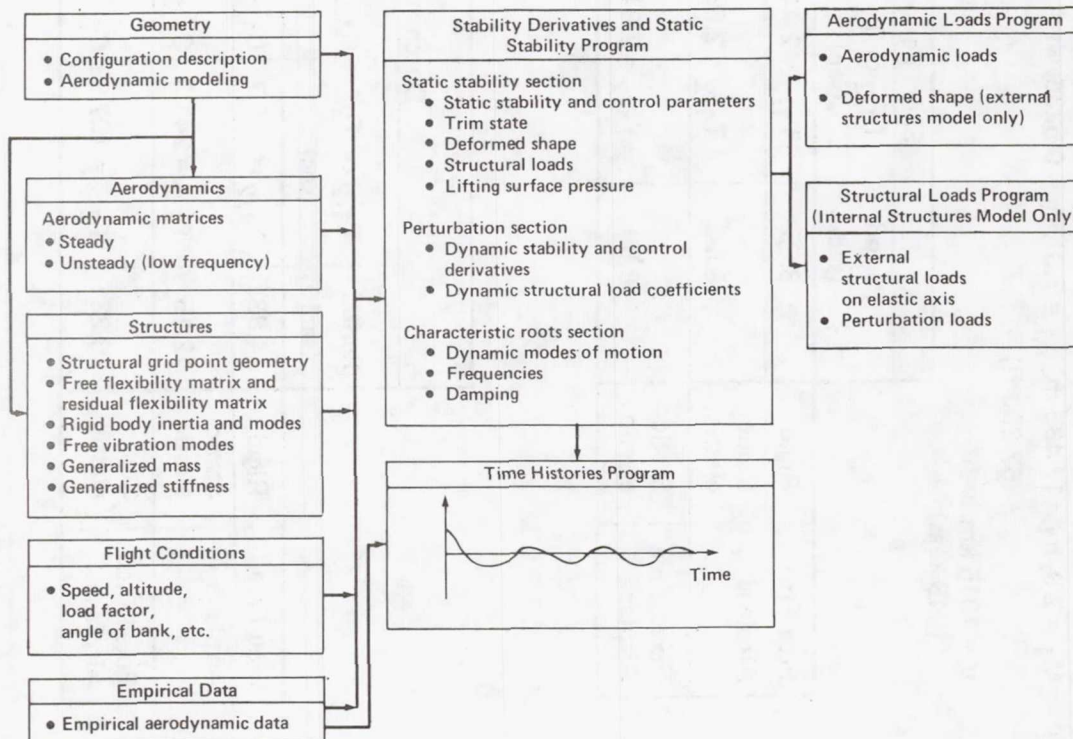
Figure 2.- FLEXSTAB analysis sequence.
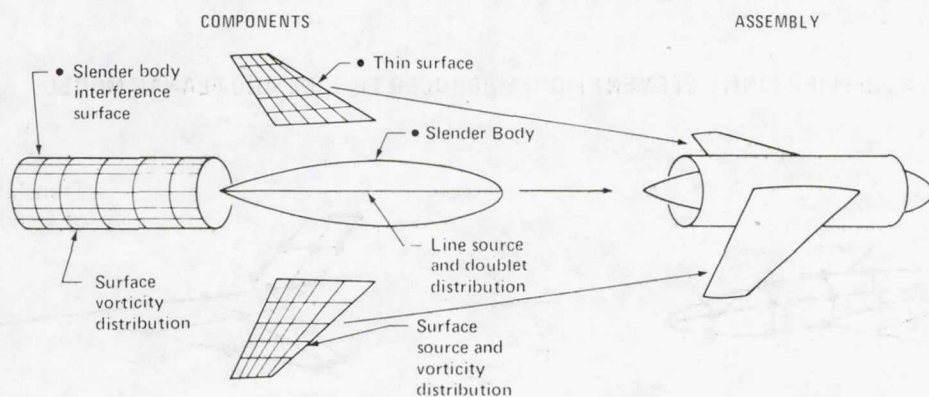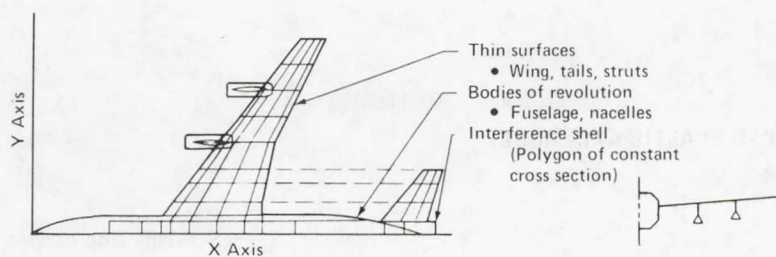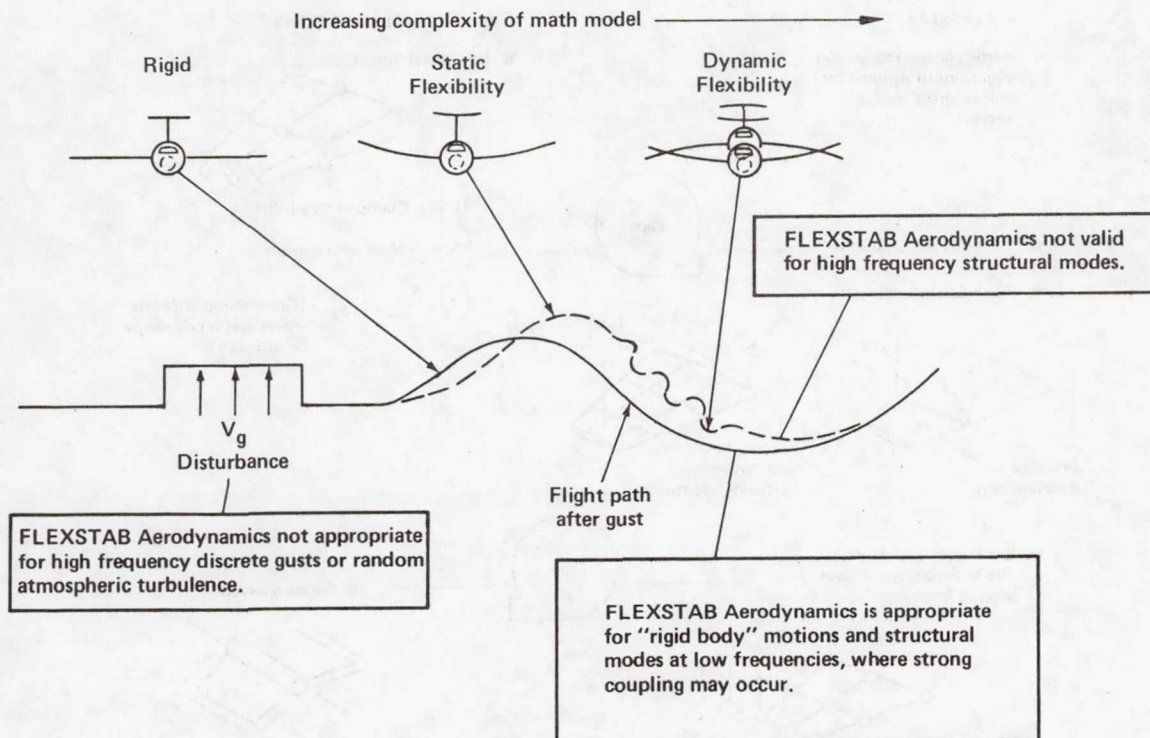
Figure 3.- FLEXSTAB aerodynamic geometry modeling.

Figure 4.- Limitations on low frequency aerodynamic approximation.

273

Straight line elastic axis
for fuselage

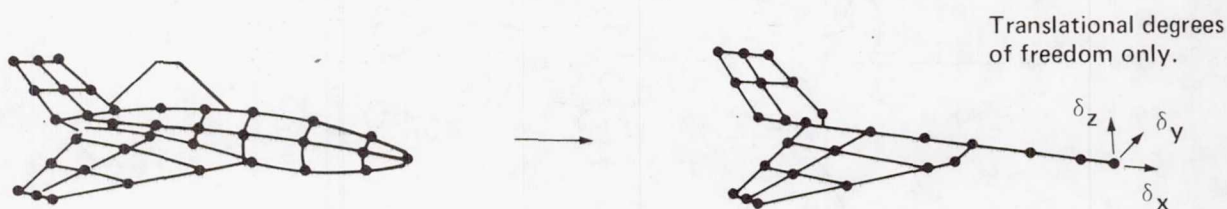● EXTERNALLY SUPPLIED FINITE ELEMENT MODEL REDUCED TO LINE AND PLANAR MODEL

Translational degrees
of freedom only.

Figure 5.- FLEXSTAB structural modeling.

FLEXSTAB

● Aerodynamic model and
equations of motion for
unrestrained elastic
aircraft

● $[\tilde{c}]$ — Free flexibility

● Aeroelastic loads

ATLAS, NASTRAN ●

● Structural model

$[c]$ — Clamped flexibility

$[m_\delta]$ — Mass distribution

$[k]$, $[m_\delta]$, $[\phi_\delta]$ — Generalized stiffness
mass and mode shape
matrices

Tape

Δp

Pressure
distributions

$\{fA\}$

Forces at
aerodynamic
centroids; reactions

● Equivalent nodal forces
due to aerodynamic and
inertial forces

Tape

● Stress analysis

$\{Q\}$

σ

τ

Figure 6.- FLEXSTAB/ATLAS, NASTRAN® interface.

TRUE AERODYNAMIC GEOMETRY
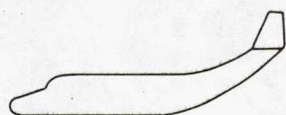
Upswept aft fuselage

FLEXSTAB AERODYNAMIC GEOMETRY

Fin placed at edge
of interference shell

Fuselage is a body of revolution plus
camber slopes defined along straight
aerodynamic mean centerline.

FLEXSTAB ELASTIC AXIS
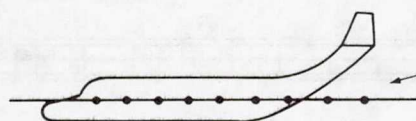
Mass and stiffness properties
Defined along aerodynamic
mean centerline.
(No rotary inertia)

Figure 7.- FLEXSTAB modeling limitations.

SD&SS data deck
• Altitude
• Rotational velocities; P_1, Q_1, R_1
• Load factor n_{z_1} instead of Q_1
• Roll angle; ϕ_1
• Wing geometry; S_w, $\bar{c}$, b
• Flightpath angle, γ_1, or thrust, T_1
• Rigid, static-elastic, or
  residual-elastic
• Type of reference motion
• Number of engines and location
• Engine angular momentum
• Control surface data
• Panel area ratios
• External pressure distribution
• Recycle data

Reference
equations
of
motion

Nonlinear wind
tunnel data

Airplane trim parameters

α_1, angle of attack for trim
δ_{e_1}, elevator trim setting
T_1 (or θ_1), thrust (or pitch attitude)
β_1, sideslip angle for trim
δ_{a_1}, aileron trim setting
δ_{r_1}, rudder trim setting

Static results

• Deformed shape   • Static stability parameters
• Reference structural loads   Static margin
• Steady pressure distribution   Neutral point
• Static stability derivatives   Maneuver margin
• Speed stability derivatives   Elevator angle per g
                                   Stick speed stability

From GD

GDTAPE

From AIC

AICTAP

From ISIC/NM
or ESIC

SICTP3

Dynamic results

• Unsteady pressure distribution
• Dynamic stability derivatives
• Airplane control derivatives
• Dynamic elastic axis loads
• Generalized aerodynamic modal forces
  due to control surfaces
• Characteristic equation rooting
• FLEXSTAB summary

Input option

Rigid wind tunnel
dynamic stability
derivatives

Static and
dynamic
stability
results

To
TH
SLOADS
ALOADS

SDSSTP

• Deform
shape

To SD&SS
(future run)

• Pressure
distribution

To
PDPLOT

Figure 8.- Schematic of the SD&SS program.

275
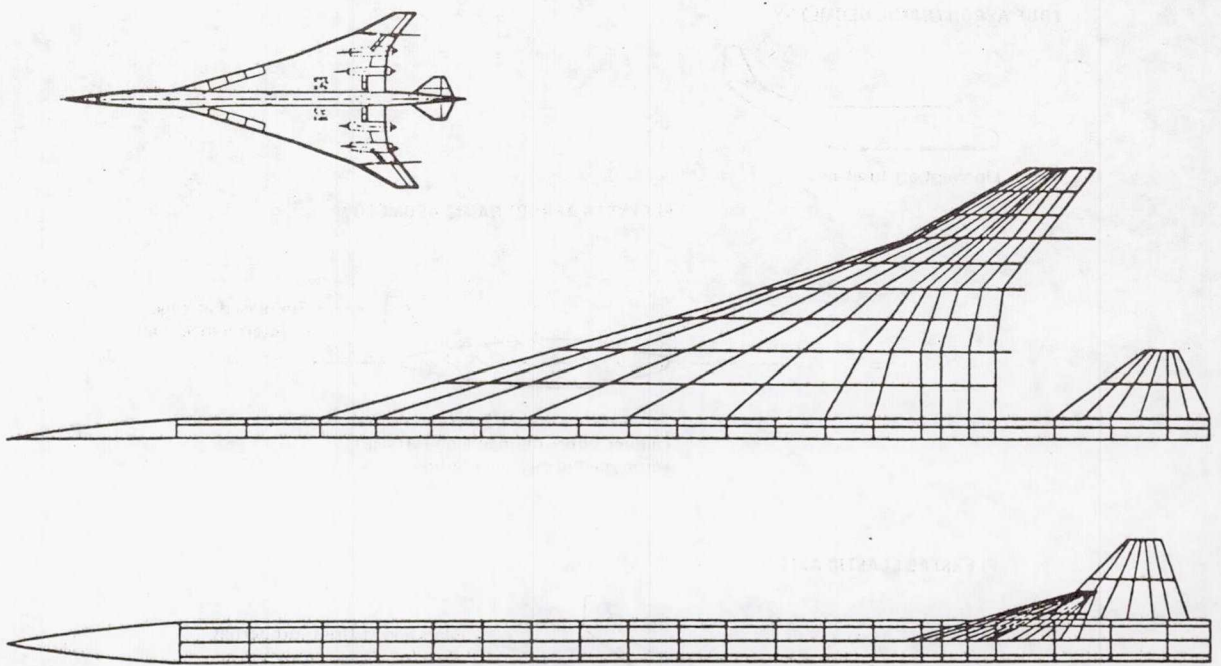
Figure 9.- NASA Arrow-Wing supersonic cruise aircraft aerodynamic peneling.
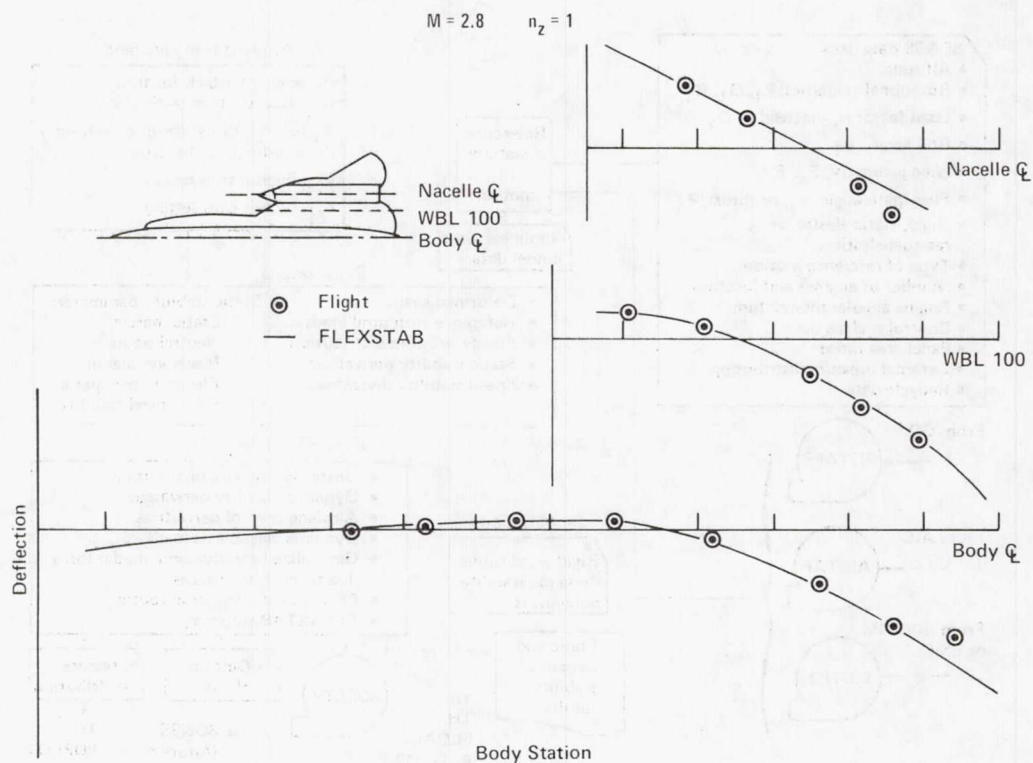
Figure 10.- FLEXSTAB/flight deformed shape of YF-12A.
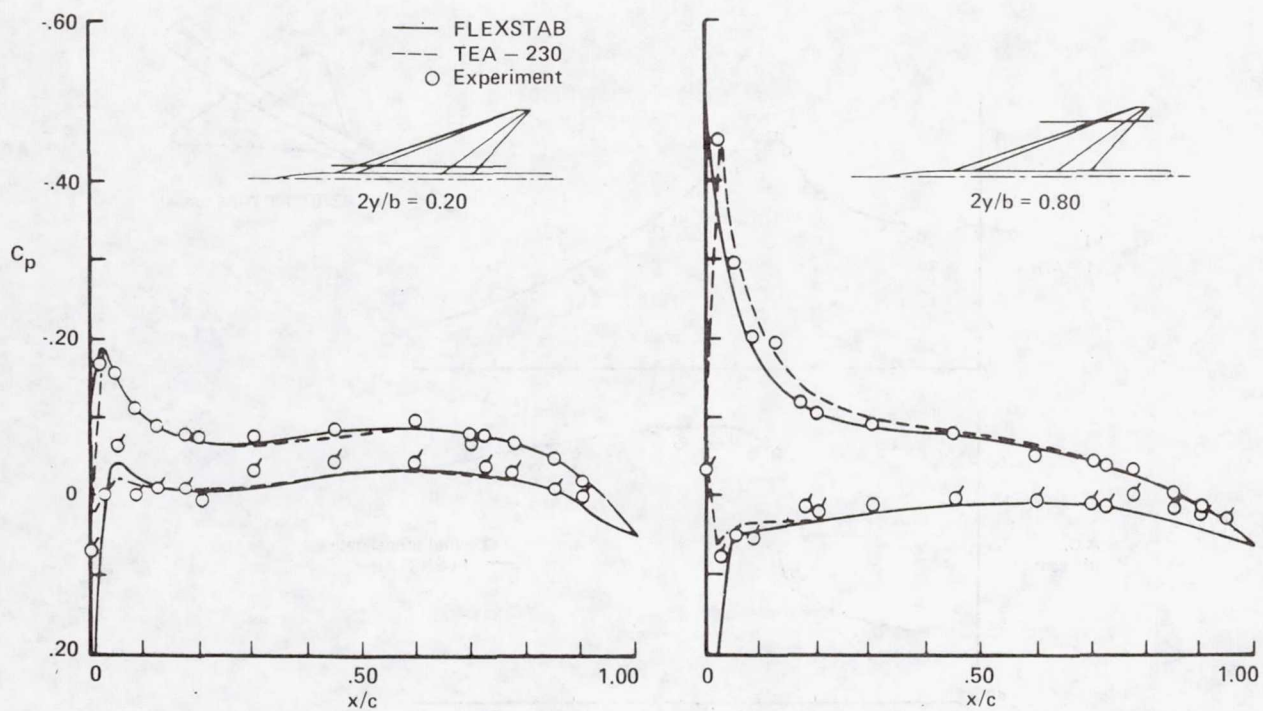
(a) M = 0.85 and α = 2.1°.
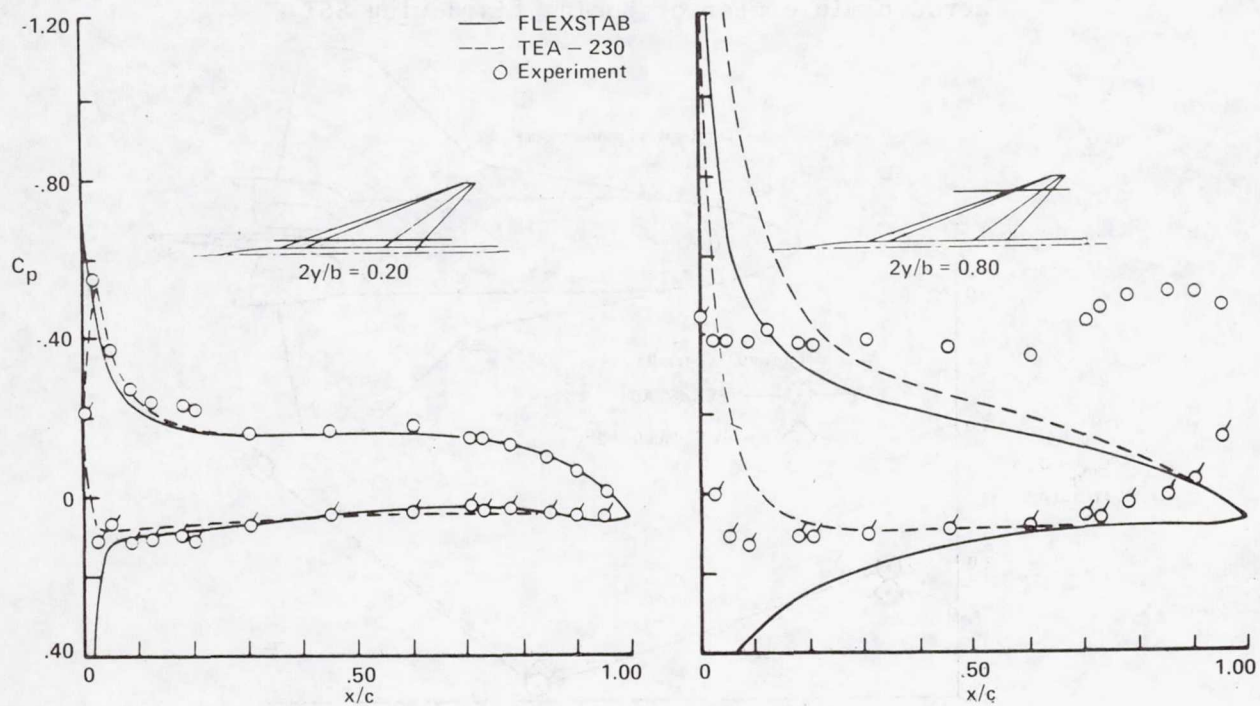
(b) M = 0.85 and α = 7.9°.

Figure 11.- Flat wing pressure distribution of Arrow-Wing — body.
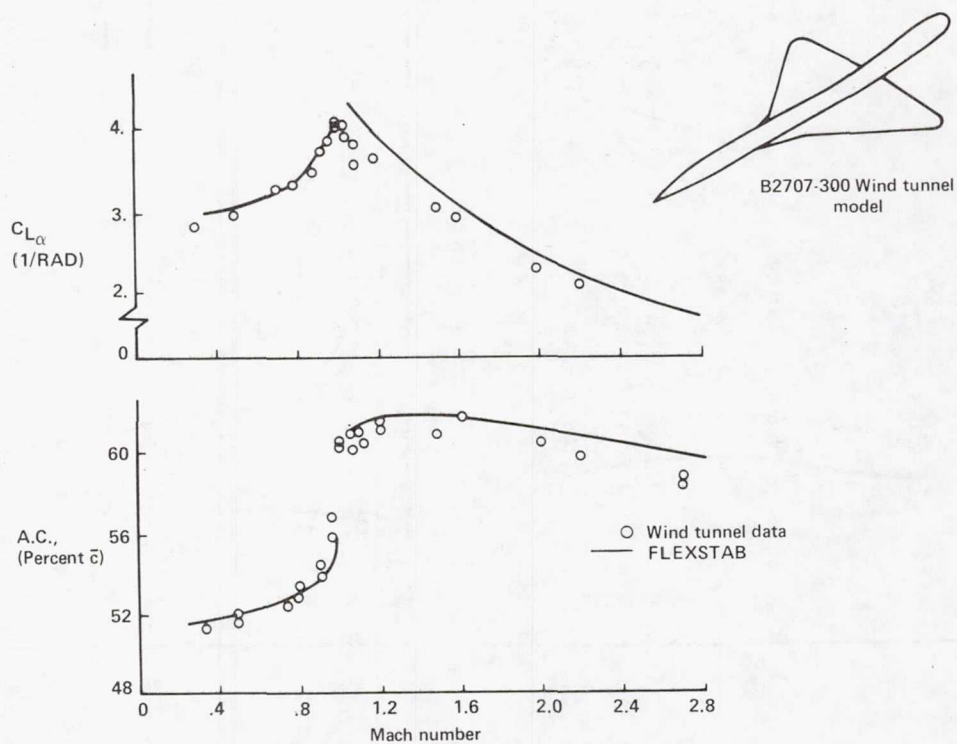
Figure 12.- Effect of Mach number on lift-curve slope and aerodynamic center of Boeing fixed-wing SST.
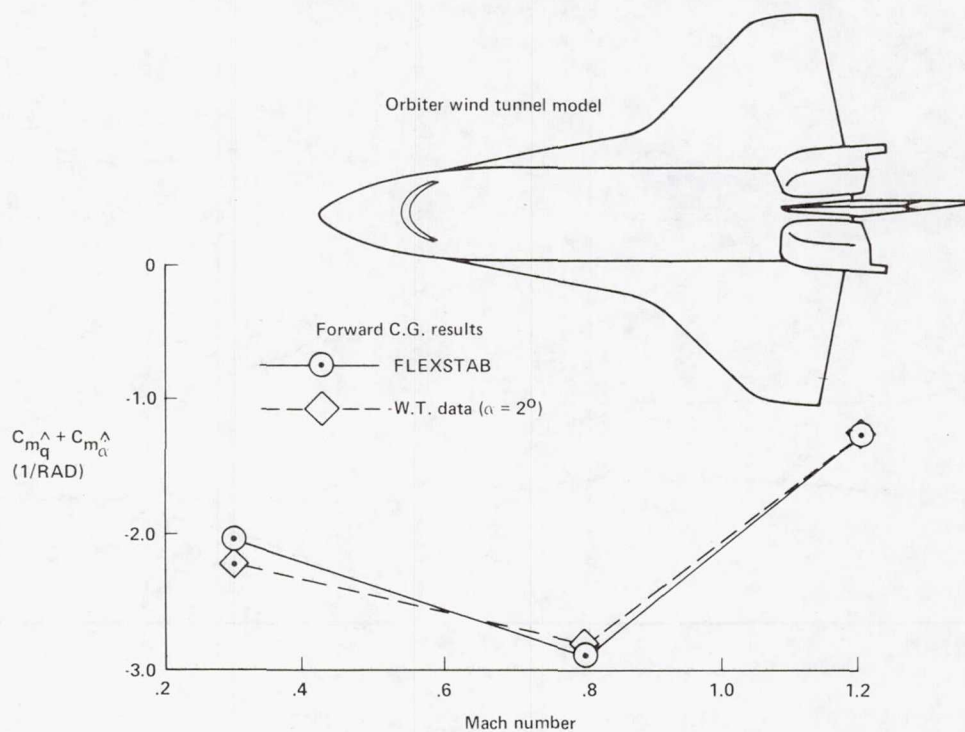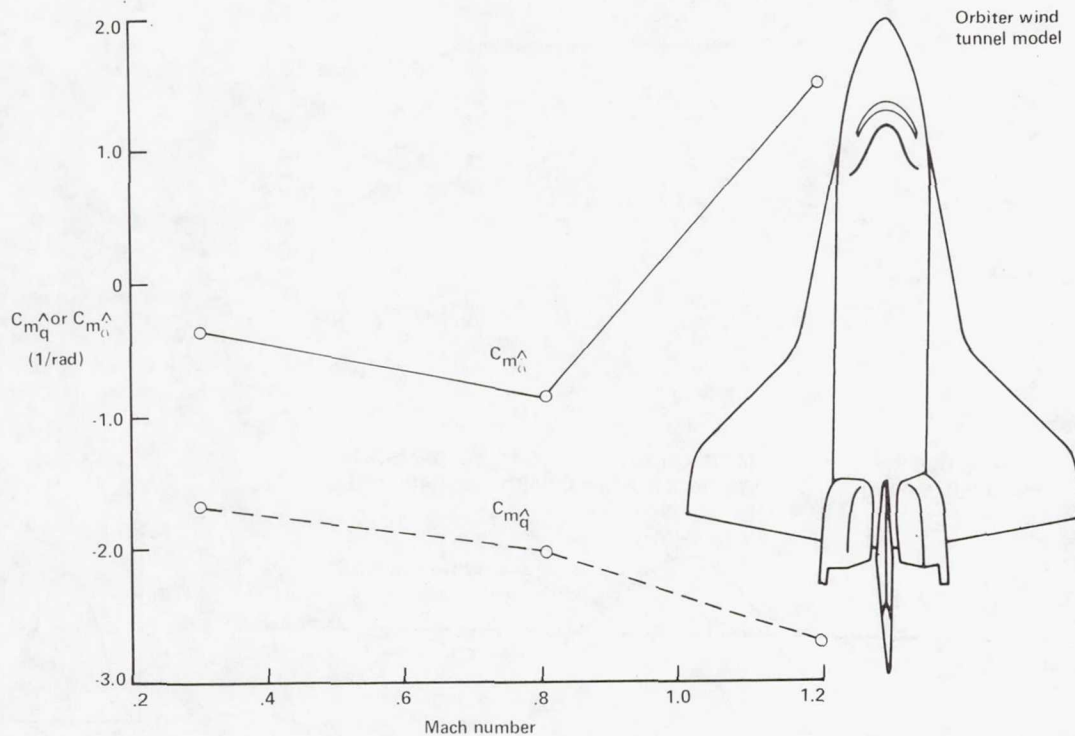

Figure 13.- Space shuttle orbiter values of $C_{m_{\hat{q}}} + C_{m_{\hat{\alpha}}}$.

2.0

1.0

0

$C_{m_{\hat{q}}} \text{ or } C_{m_{\hat{\alpha}}}$
(1/rad)

-1.0

-2.0

-3.0

$C_{m_{\hat{\alpha}}}$

$C_{m_{\hat{q}}}$

.2   .4   .6   .8   1.0   1.2

Mach number

Orbiter wind tunnel model

Figure 14.- FLEXSTAB values of $C_{m_{\hat{q}}}$ and $C_{m_{\hat{\alpha}}}$.

Job control

Host Operating System

Problem specifications

Interfaced Systems
• NASTRAN •   • KONPACT
• ATLAS
• SAMECS

Structural data

Equations of motion

AIC matrix correction

Aerodynamic influence coefficients

Geometry definition

External structural influence coefficients *

Normal modes plots

Normal modes *

Elastic axis plots

Internal structural influence coefficients *

Linear systems analysis **

Time histories *

Pressure distribution * plots

Stability derivatives * & static stability

Aerodynamic Modeling

Structural Modeling

Problem Analysis

Data bank

*Modified for level 2
**Level 2 addition

Figure 15.- Level 2 FLEXSTAB functional configuration.

279

159 090 Kg   648.6 Km/Hr   1219.2 m
(350 000 lbs)   (350 kn EAS, M = 0.569)   (4000 ft)
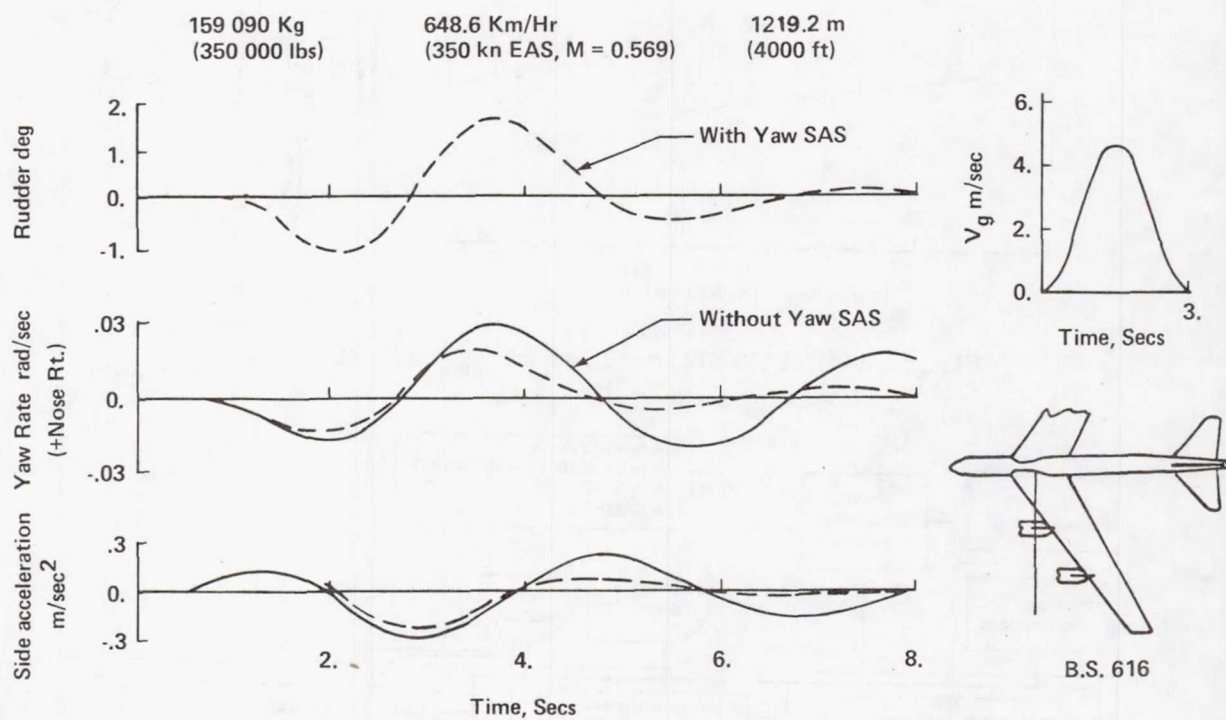
Figure 16.- B-52 response to lateral gust at B.S.616.

PROPULSION SYSTEM/FLIGHT CONTROL INTEGRATION

FOR SUPERSONIC AIRCRAFT

Paul J. Reukauf and Frank W. Burcham, Jr.
NASA Dryden Flight Research Center

SUMMARY

The NASA Dryden Flight Research Center is engaged in several programs to study digital integrated control systems. Such systems allow minimization of undesirable interactions while maximizing performance at all flight conditions. One such program is the YF-12 cooperative control program. In this program, the existing analog air-data computer, autothrottle, autopilot, and inlet control systems are to be converted to digital systems by using a general purpose airborne computer and interface unit. First, the existing control laws are to be programed and tested in flight. Then, integrated control laws, derived using accurate mathematical models of the airplane and propulsion system in conjunction with modern control techniques, are to be tested in flight. Analysis indicates that an integrated autothrottle-autopilot gives good flight path control and that observers can be used to replace failed sensors.

INTRODUCTION

Supersonic airplanes, such as the XB-70, YF-12, F-111, and F-15 airplanes, exhibit strong interactions between the engine and the inlet or between the propulsion system and the airframe (refs. 1 and 2). Taking advantage of possible favorable interactions and eliminating or minimizing unfavorable interactions is a challenging control problem with the potential for significant improvements in fuel consumption, range, and performance.

In the past, engine, inlet, and flight control systems were usually developed separately, with a minimum of integration. It has often been possible to optimize the controls for a single design point, but off-design control performance usually suffered. The evolution of propulsion and flight controls is depicted in figure 1. Early aircraft had totally separate propulsion and flight control systems. Because these systems were manually controlled by the pilot, they were low response systems. With the advent of jet engines and supersonic aircraft, more complex control systems were required. In the flight control area, stability augmentation systems were used to compensate for unstable or high rate conditions and autopilots were used to reduce pilot workload. In the propulsion control area, active controls were devised to control engine nozzles and supersonic air inlet systems. However, even at this stage of complexity, the propulsion and flight control systems had a minimum of integration. Recently, the first step toward integration has been taken

by mechanizing autothrottles. When used in conjunction with an autopilot, an auto-throttle allows precise altitude and Mach number control. For efficient flight of future multimission aircraft, total integration of the propulsion and flight control systems will be necessary to minimize undesirable interactions and to optimize air-craft performance across the full flight envelope.

Because of the size and complexity of the controls integration problem, digital control is considered necessary. Digital control systems provide the logic necessary to handle the many variables and offer advantages in terms of speed, accuracy, and flexibility. The recent development of flight-qualified digital computers has made it attractive to investigate the use of digital integrated systems. In addition, analytical methods for analysis of large-scale, multivariable control problems are now in common use.

The NASA Dryden Flight Research Center (DFRC) has begun to investigate and evaluate advanced control concepts that show potential for improved aircraft perform-ance. The investigations include the evaluation of new controls hardware in flight, the application of modern system analysis techniques to existing systems, and studies in the area of propulsion system/airframe interactions. Figure 1 shows three programs undertaken at DFRC to investigate digital control techniques and integrated control laws. The F-111 integrated propulsion control system (IPCS) program studied interactions between the inlet and the engine (ref. 3). The YF-12 coopera-tive airframe/propulsion control system program is directed toward the control of adverse interactions between the inlet and airframe, which can be severe for high speed cruise airplanes. For example, reference 4 indicates that the inlet bypass doors can generate as great a yawing moment as the rudders and in certain cases can cause the aircraft's Dutch roll mode to become unstable. The F-8 digital fly-by-wire program has already shown that digital control systems can be used in flight-critical applications (ref. 5). During a future program, such as the F-15 program, a totally integrated engine, inlet, and airframe control system will be designed.

This paper describes the YF-12 cooperative airframe/propulsion control system program: the program guidelines, the systems to be controlled, the selection of the digital system, and the advanced control laws presently being considered.

SYMBOLS

Physical quantities are given in the International System of Units (SI). Measure-ments were taken in U.S. Customary Units.

a_n	normal acceleration
$PpLM$	inlet total pressure used for calculation of duct pressure ratio
$PsD8$	inlet static pressure used for calculation of duct pressure ratio
p_s	static pressure measured at the nose boom

p_t total pressure measured at the nose boom

Δp_α nose boom differential pressure measured in the pitch plane

Δp_β nose boom differential pressure measured in the yaw plane

α angle of attack

β angle of sideslip

Δ change from initial conditions

PROGRAM GUIDELINES

The primary purpose of the YF-12 cooperative airframe/propulsion control system program is to evaluate the benefits in aircraft performance derived from the systems integration concept. The program has two phases (fig. 2). In the first phase (fig. 2(a)), the existing analog air-data computer, autopilot, inlet control, and autothrottle systems are converted to digital systems. Each of these analog systems has a suitable backup mode of operation, so redundancy is unnecessary for flight safety. This digital system will be flight tested to validate the hardware and software.

In the second phase (fig. 2(b)), the systems are integrated by using control laws developed from models of the propulsion system and the airplane's aerodynamics. Optimal control methods as well as classical methods will be used to derive the new control laws.

During the program, the existing system's hardware is to be used: that is, the actuators, transducers, and fuel controls are to remain unchanged. The primary emphasis of the propulsion system control study is on the inlet. Engine control changes will be limited to throttle inputs and possibly trim functions for some engine parameters. Engine control was studied in detail during the F-111 IPCS program (ref. 3).

AIRPLANE DESCRIPTION

The two-place, twin-engined YF-12 airplane (fig. 3) is capable of extended flight at Mach numbers greater than 3.0 and at altitudes above 24,380 meters. The airplane has a delta wing planform and a long, slender fuselage with prominent chines. A nacelle is mounted approximately halfway out on each wing. An all-movable vertical fin is mounted on top of each nacelle to provide directional control and stability. Longitudinal and roll control is provided by elevons located inboard and outboard of each nacelle. The propulsion system of the airplane consists of an

283

axisymmetric mixed-compression inlet and a J58 afterburning turbojet engine. The airplane has an air-data system which determines such parameters as Mach number, altitude, angle of attack, and angle of sideslip. An autopilot, inlet computers, and autothrottles provide automatic control for the airplane and inlets. A block diagram of the existing analog control system is shown in figure 4.

AIR-DATA SYSTEM

The air-data system (ref. 6) is composed of a nose boom and an air-data computer. The nose boom of the YF-12 airplane (fig. 5) features a compensated pitot-static probe and an offset hemispherical head flow-direction sensor. The compensated pitot-static probe senses impact pressure, p_t, at the probe tip and static pressure, p_s, at two sets of orifices. These orifices provide the pressure measurements for the airplane's air-data computer, inlet computers, and pilot instruments. Measurements of angle of attack and angle of sideslip are obtained from the hemispherical head flow-direction sensor. Flow angularity in the pitch and yaw planes is determined from the four surface pressures on the hemispherical head. A computer uses the differential pressures Δp_α and Δp_β to compute angle of attack and angle of sideslip.

The air-data computer (fig. 5) converts pitot-static pressures into proportional rotary shaft positions, which are equivalent to static pressure and dynamic pressure. Total temperature, used in the calculation of true airspeed, is converted to a shaft position. By means of analog computation, which uses cams, gears, and gear differentials, these shaft rotations are transposed into data outputs and the terms necessary for further internal computation. The outputs include true airspeed, pressure altitude, Mach number, knots equivalent airspeed (KEAS), Mach number and altitude rates of change, and logarithmic representations of static pressure and compressible dynamic pressure. Also calculated are differences between Mach number and a Mach number schedule, differences between KEAS and a KEAS schedule, and a KEAS bleed schedule as a function of Mach number.

AUTOPILOT SYSTEM

The autopilot subsystem provides a way to achieve hold modes in the roll and pitch axes during flight. The autopilot performs best at the design flight conditions. The use of the autopilot is optional and often depends upon the mission requirements. The autopilot uses outputs from the air-data computer, the automatic navigation system, and the flight reference system to maintain its modes of operation. The autopilot outputs are summed with stability augmentation system (SAS) outputs and applied to the flight control surface actuators.

Roll Axis

The roll autopilot (fig. 6) provides three modes of control: attitude hold, heading hold, and automatic navigation. In the attitude hold mode, a roll rate gyro input and an attitude hold reference signal from the flight reference system are used. In the automatic navigation mode, automatic navigation system outputs are used. In the heading hold mode, outputs from the flight reference system are used. Roll axis autopilot outputs are combined with roll SAS outputs, and the resulting signals are supplied to the elevon actuators.

Pitch Axis

The autopilot pitch axis provides five modes of control: attitude hold, Mach hold, KEAS hold, altitude hold, and Mach trim. An automatic trim circuit functions during all of these modes. A block diagram showing inputs to the pitch autopilot is shown in figure 7. The attitude hold mode uses the pitch attitude reference, logarithmic static pressure, and pitch rate gyro inputs. A pitch wheel on the pilot's panel allows minor corrections to the reference attitude. The Mach hold mode uses signals of Mach number error and Mach number rate of change from the air-data computer. The KEAS hold mode is similar to the Mach hold mode except that KEAS rate of change and KEAS error inputs are used. The KEAS hold mode is capable of maintaining a specified KEAS bleed line. The altitude hold mode uses signals of altitude and altitude rate of change from the air-data computer to keep pressure altitude constant. Modifications to the altitude hold mode are discussed in reference 7. The pitch axis autopilot outputs are combined with the pitch SAS outputs and fed to the elevon actuators.

The Mach number trim system provides artificial speed stability during aircraft accelerations or decelerations in the Mach number range from 0.2 to 1.5 whenever the pitch autopilot is disengaged. The system uses Mach number inputs from the air-data computer, which, after processing, are fed to the pitch trim actuator.

AUTOTHROTTLE SYSTEM

The autothrottle system has two control modes: Mach number hold and KEAS hold. The purpose of the system is to allow these modes of operation without changing the longitudinal flight path of the airplane. Mach number error, KEAS error, and pitch attitude inputs go to the system from the air-data computer and the flight reference system (fig. 8). The autothrottle computer processes the inputs and produces a command signal which goes to the autothrottle servos. Both engines are controlled symmetrically. Autothrottle authority is limited to the afterburning range.

INLET SYSTEM

The inlet (fig. 9) is of the translating spike type, with approximately 40 percent of the compression occurring externally and 60 percent internally. Boundary layer air is removed through a slotted surface on the spike and a ram scoop or shock trap on the cowl. Forward bypass doors of the rotary type are used to match engine airflow to inlet airflow and to control the position of the terminal shock wave. Aft bypass doors just in front of the compressor face provide additional bypass capacity for intermediate Mach numbers. Aft bypass airflow and shock trap bleed air are ducted rearward to the ejector of the J58 engine. Spike bleed and forward bypass flow are dumped overboard through louvered exits. A more detailed description of the inlet is given in reference 8.

INLET CONTROL SYSTEM

In the automatic inlet control system, normal acceleration from a transducer near the aircraft center of gravity as well as Δp_α, Δp_β, p_s, and p_t from the nose boom are fed into the inlet computer. Each inlet has a separate control system, one of which is shown in figure 10. The outputs of each computer are commanded spike position and commanded duct pressure ratio.

Spike Position Loop

The spike position loop is used to control the inlet's throat area and contraction ratio. The schedule is primarily a function of airplane Mach number, which is derived from p_s and p_t in much the same manner as in the air-data computer. The nominal spike schedule is biased to more forward positions when deviations from nominal values of angle of attack, angle of sideslip, or normal acceleration occur.

Duct Pressure Ratio Loop

The duct pressure ratio loop is used to control the position of the terminal shock wave in the inlet. The duct pressure ratio is the ratio of a static pressure in the inlet throat, *PsD8*, to an impact pressure on the outer surface of the cowl, *PpLM*. The throat static pressure varies as a function of the terminal shock wave position. The forward bypass doors are used to move the terminal shock wave until the duct pressure ratio measured by the system matches the duct pressure ratio commanded by the inlet computer. There is a nominal duct pressure ratio schedule which varies with airplane Mach number. This schedule was derived from wind tunnel and flight tests and is intended to result in the desired shock position. The schedule is biased to a lower duct pressure ratio for deviations from nominal values of angle of attack, angle of sideslip, and normal acceleration. At a given flight condition, this lower duct pressure ratio command increases the opening of the forward bypass doors and moves the terminal shock wave farther downstream.

286

Restart Mode

The automatic inlet control system is equipped with an inlet unstart sensor to detect when the normal shock moves outside the inlet. When an unstart occurs, the unstarted inlet is switched to an open loop restart mode. The forward bypass doors open at maximum rate to the full open position, and the spike moves 0.381 meter forward or full forward if it is retracted less than 0.381 meter. The spike then returns slowly to the scheduled position and the bypass doors slowly close to return the duct pressure ratio to the scheduled command.

The airplane rolling and yawing motions associated with an inlet unstart can be severe (ref. 2). To reduce the severity of the unstart transient, the opposite inlet switches automatically into the restart mode at the same time as the affected inlet. This mode, which is called a crosstie, is so effective that sometimes the pilot cannot tell which inlet unstarted.

Aft Bypass Door Control System

The aft bypass doors on the YF-12 airplane are positioned by the pilot. The system consists of a commanded voltage which is nulled by position feedback from the actuator.

Manual Inlet Control System

The pilot can position the spike and forward bypass doors of each inlet manually. The primary parameter used for manual inlet control is the cockpit display of Mach number.

DIGITAL CONTROL SYSTEM

In the digital control system (fig. 11), the analog air-data computer, autopilot, autothrottle, and inlet control systems are replaced by a digital computer and an interface unit. All the signals are available for calculations, making signal integration easy. The digital system also makes it relatively easy to modify the individual systems with software changes.

At first, the existing control laws are to be programed and the systems kept separate. This will not make use of the full capability of the digital computer. The development of the advanced control laws necessary for the complete integration of the various systems is expected to be quite complex. Therefore, a large capacity, high speed computer is considered necessary for real-time computations.

CRITERIA FOR COMPUTER SELECTION

Because the primary purpose of the program is research and the objective of the research is the total integration of the systems described, the computer had to meet several criteria to insure that its capabilities were not a limiting factor in the realization of the project's goals. The computer had to have the following features: performance comparable to the state of the art in computer technology; a central processing unit with a word length of at least 16 bits; a memory capacity of 32,000 words, expandable to 65,000 words; floating point arithmetic hardware; rapid input-output processing capability; basic operational software, including an assembler, FORTRAN compiler, utility routines, diagnostics, loader, and software debugging aids; compatibility with commercial grade peripheral equipment (fig. 12); compliance with military standard MIL-E-5400 (the airborne avionics specification); go/no go selftestability; microprogramability; and compatibility with a hardware bootstrap loader.

The computer selected on the basis of these criteria is a general purpose, 16-bit digital computer with 32,000 words of memory and built-in trigonometric and hyperbolic functions. Its execution times are 1 microsecond for an addition, 6.4 microseconds for a multiplication, and 10 microseconds for a division. The interrupt scheme has three levels with 13 interrupts. There are eight independently accessible input-output channels.

INTERFACE UNIT

The interface unit is required to communicate with the digital computer through a memory interface from a dedicated block of computer-addressable memory. It must also convert aircraft signals into twos complement binary representations and convert digital computer parameters into correct aircraft representations. The interface must provide status information to the digital computer and the aircraft. The input and output signal transfers are handled by a block of computer-addressable memory in the interface unit. The signal conditioning, demodulation, multiplexing, and conversion should not introduce errors in excess of 2 percent of full scale.

Table 1 lists the input and output signals the interface must process. Spare channels not used for the conversion of the aforementioned systems are to be used later. The unit should be capable of converting all the signals shown in table 1 at a rate of 200 samples per second. Even though a high sample rate capability is not necessary for all parameters, there are some parameters with bandwidths of 20 hertz in the inlet system. In addition, the Tustin transform technique is being used where possible and a rate of 200 samples per second may be necessary for an accurate representation. Other transform techniques will be used if computer speed becomes a limiting factor. Once a parameter has been sampled it is stored in the random access memory for use by the computer. The ac signals are sampled at the peak of their respective references.

FLIGHT SYSTEM SIMULATION

Before being installed on the airplane, the digital system (hardware and software) must be verified. A complete digital system, identical to the flight system, has been interfaced with a fixed-base hybrid simulator. The hybrid simulator is programed to reproduce the aircraft and propulsion system dynamics in real time across the full flight envelope. All signals input to the digital control system are in the same form as they would appear on the airplane. This closed loop simulator is the basis for all software design and verification during the program.

The software has been programed in modular form, with each module corresponding to an analog system on the airplane. Each of the modules is checked out on the closed loop simulator and compared to its analog counterpart. Each module checked so far has exactly reproduced the performance of the analog system it replaced when run at an adequate sample rate. The closed loop simulator is also used to determine the sample rate necessary for proper operation of the digital module. As an example, figure 13 shows time histories of various parameters in the closed loop simulation with the digital air-data system in the loop. The basic conditions are a speed of Mach 3 and an altitude of 22,100 meters, with the altitude hold mode engaged. The parameters are compared for sample rates of 3 samples per second and 15 samples per second with a static pressure fluctuation input. The figure shows a definite stepping action in the elevon and autopilot elevon command signal traces at 3 samples per second. Therefore, a sample rate greater than three was selected for air-data parameters.

INTEGRATED CONTROL LAWS

Plans for the last part of the program include the derivation and flight testing of some integrated control laws. Modern system analysis techniques are to be used for the derivation because these techniques are suited to large multivariable problems. An additional goal of the program is to evaluate the performance of reduced-state feedback controllers as compared to full-state feedback controllers, which are generally unobtainable in actual applications.

Mathematical models are necessary for the derivation of optimal control laws. Two nonlinear mathematical models—one of the propulsion system and one of the airplane's aerodynamics—have been created. These models have been verified with comparisons to flight test data (ref. 9) and are the basis for all other mathematical models to be used during the program.

Several interesting performance criteria have been proposed for development of integrated control laws. One of these criteria is the minimization of flight path and Mach number deviations during the cruise portion of the flight. A study of the longitudinal control problem by other investigators used linear quadratic regulator theory to derive the control laws. The results indicated that an autothrottle-autopilot combination was effective in maintaining Mach number and altitude simultaneously.

An example of the aircraft's response (as predicted by a mathematical model) to a step increase in temperature is shown in figure 14. The solid lines indicate the response with the presently mechanized altitude hold control laws and the dashed lines indicate the response with a partial-state feedback controller which was derived using linear quadratic regulator theory. The air-data system interprets the step increase in temperature as a step decrease in Mach number of approximately 0.03 and a step increase in pressure altitude. In the altitude hold case, the aircraft immediately dives and then goes into a lightly damped altitude oscillation. By the end of the time history the Mach number has decreased by approximately 0.45. In comparison, the partial-state feedback controller does a much better job: it uses the autothrottle to compensate for the Mach number loss and thus controls Mach number and altitude simultaneously. Upon sensing the Mach number decrease, the power lever angle is commanded to +10°, which is its full authority, thus compensating for the loss in thrust. Very little elevon is commanded as compared to the -3° commanded in the altitude hold case. The airplane's Mach number and altitude show only small deviations from their original values. Toward the end of the trace, the power lever angle is commanded to -10° to compensate for the slight overshoot in Mach number.

Because the digitized systems are single channel, a study of fail operational techniques for nonredundant sensors is of interest. A technique which uses observers to reconstruct the unavailable states is discussed in reference 10. Figure 15 shows the reconstruction of yaw rate, roll rate, bank angle, and angle of sideslip using the technique and assuming information only from roll attitude, rudder deflection, and aileron deflection signals. For this time history, the model used by the observer was not a perfect model of the actual system: some of the model coefficients were 100 percent in error. The figure indicates that it is feasible to use reconstructed signals for control purposes in the case of sensor failures. Further work is necessary to explore the use of these techniques for the stochastic case.

Two additional areas of interest are also being considered: a controller to maximize range during cruise and a controller to minimize deviations from optimal climb profiles which have been calculated *a priori*.

CONCLUDING REMARKS

Airframe/propulsion system interactions can be severe for high speed cruise airplanes. To achieve the efficiency required for future multimission aircraft, a totally integrated propulsion/flight control system will be necessary. Because of the size and complexity of the controls integration problem, digital control systems are considered necessary. Digital systems allow the flexibility and logic to minimize undesirable interactions while optimizing aircraft performance across the full flight envelope.

The NASA Dryden Flight Research Center is engaged in several programs to study digital integrated control systems. The YF-12 cooperative control program is using this technology to digitally mechanize the inlet control system, autopilot,

autothrottle, and air-data computer. This digital system will allow mechanization of advanced integrated control laws for investigation of their benefits for high speed aircraft. Preliminary analytical studies indicate that an autothrottle-autopilot combination can achieve simultaneous Mach number and altitude control. These studies also indicate that observers can be used to effectively reconstruct failed sensor signals.

REFERENCES

1. Burcham, Frank W., Jr.; Hughes, Donald L.; and Holzman, Jon K.: Steady-State and Dynamic Pressure Phenomena in the Propulsion System of an F-111A Airplane. NASA TN D-7328, 1973.

2. Schweikhard, William G.; and Berry, Donald T.: Cooperative Airframe/Propulsion Control for Supersonic Cruise Aircraft. SAE Paper 740478, Apr. 1974.

3. Bentz, Charles E.; and Zeller, John R.: Integrated Propulsion Control System Program. SAE Paper 730359, Apr. 1973.

4. Berry, Donald T.; and Gilyard, Glenn B.: A Review of Supersonic Cruise Flight Path Control Experience With the YF-12 Aircraft. Aircraft Safety and Operating Problems, NASA SP-416, 1976, pp. 147-163.

5. Advanced Control Technology and its Potential for Future Transport Aircraft. NASA TM X-3409, 1976.

6. Larson, Terry J.: Compensated and Uncompensated Nose Boom Static Pressures Measured From Two Air Data Systems on a Supersonic Airplane. NASA TM X-3132, 1974.

7. Gilyard, G. B.; Smith, J. W.; and Falkner, V. L.: Flight Evaluation of a Mach 3 Cruise Longitudinal Autopilot. AIAA Paper 74-910, Aug. 1974.

8. Burcham, Frank W., Jr.; Montoya, Earl J.; and Lutschg, Phillip J.: Description of YF-12C Airplane, Propulsion System, and Instrumentation for Propulsion Research Flight Tests. NASA TM X-3099, 1974.

9. Reukauf, Paul J.; Burcham, Frank W., Jr.; and Holzman, Jon K.: Status of a Digital Integrated Propulsion/Flight Control System for the YF-12 Airplane. AIAA Paper 75-1180, Sept. 1975.

10. Shapiro, E. Y.: Software Techniques for Redundancy Management of Flight Control Systems. AIAA Paper 76-1934, Aug. 1976.

TABLE 1.- INTERFACE UNIT SIGNAL REQUIREMENTS

(a) Inputs

Signal	Number
Autopilot synchros	5
Inlet synchros	2
Autopilot transducers (ac)	13
Inlet transducers (ac)	14
Autothrottle transducers (ac)	3
Autopilot transducers (dc)	5
Autothrottle transducers (dc)	1
Air-data transducers (dc)	3
Spare dc channels	8
Digital air-data transducers	2
Instrumentation (digital)	2
Control switches (discrete)	22
Spare discretes	16
28-volt dc power	3
	Total: 99

(b) Outputs

Signal	Number
Autopilot (ac)	4
Inlet (ac)	2
Autothrottle (ac)	2
Inlet (dc)	6
Inlet (discrete)	6
Autothrottle (discrete)	2
Mach trim (discrete)	1
Failure master (discrete)	1
Air data (digital)	3
Instrumentation (digital)	1
Synchro test	1
Spare discretes	16
	Total: 45
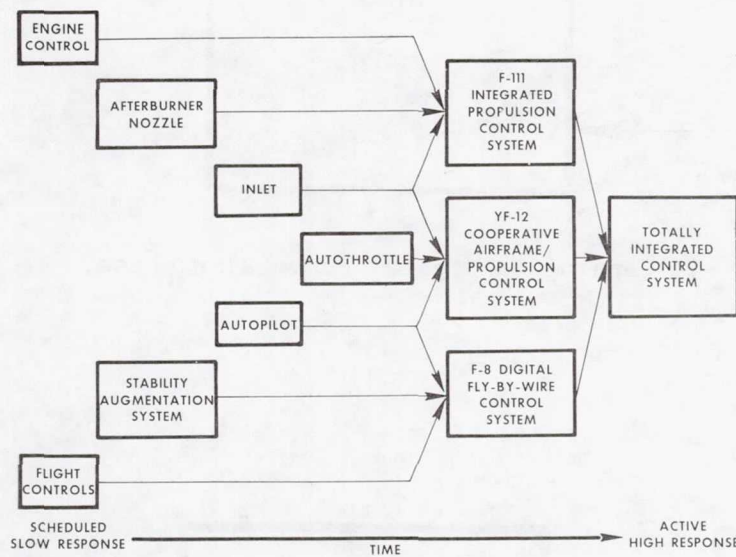
Figure 1.- Evolution of propulsion and flight controls.
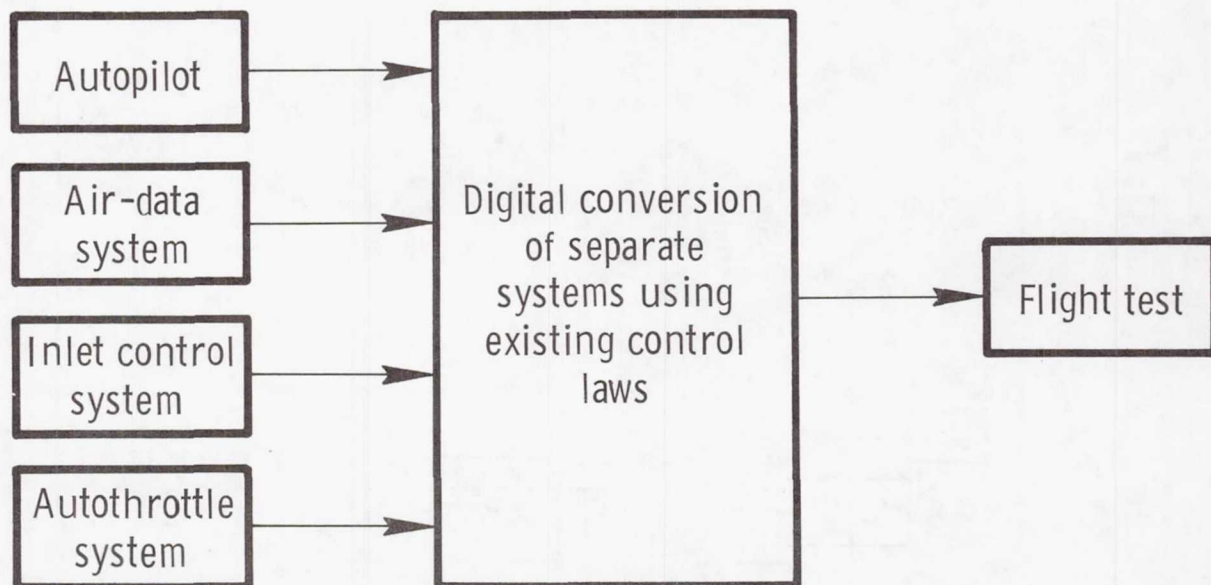
(a) Analog to digital conversion phase.
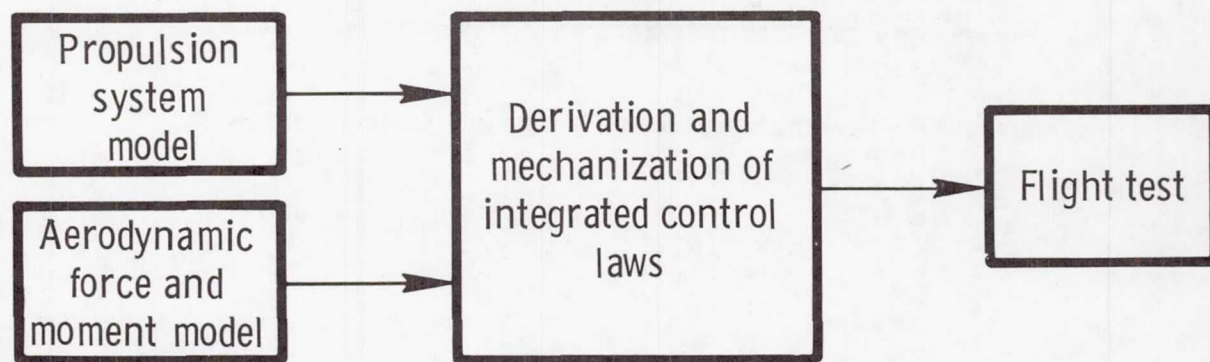
(b) Integrated control law phase.

Figure 2.- Digital integrated airframe/propulsion control program.

294
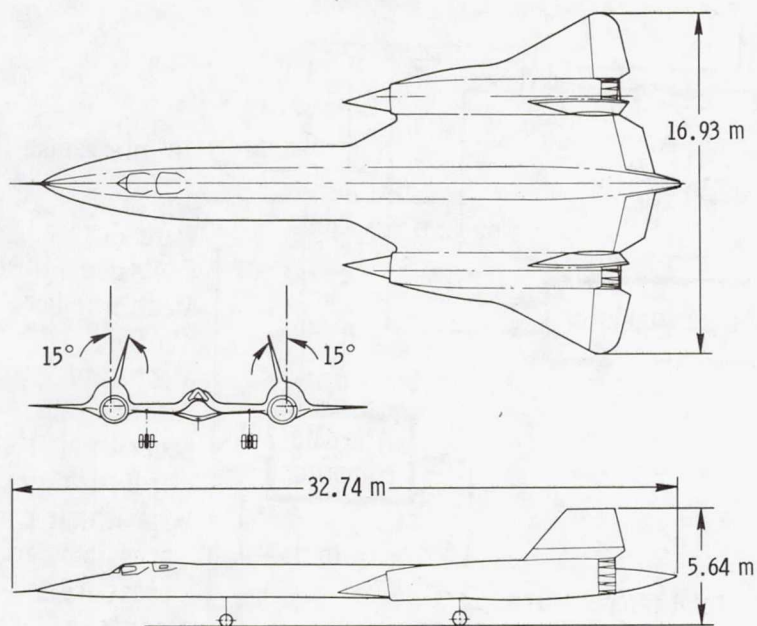
Figure 3.- Three-view drawing of YF-12 airplane.
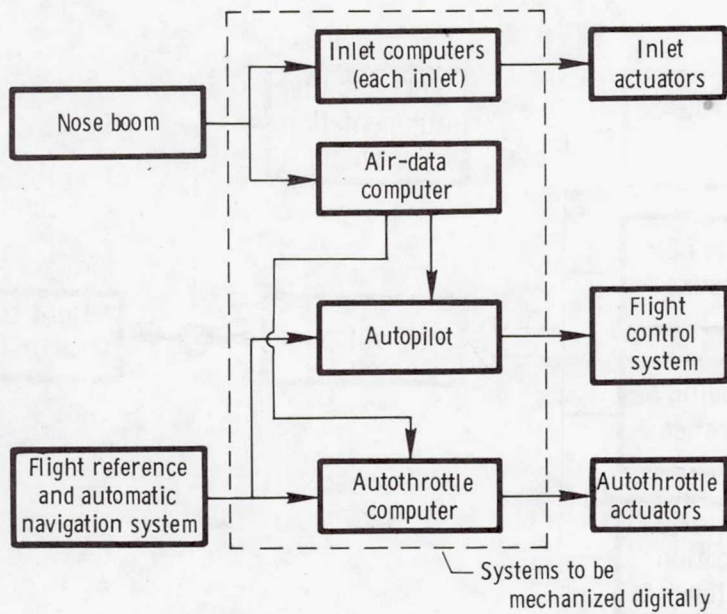
Figure 4.- Existing analog control systems.
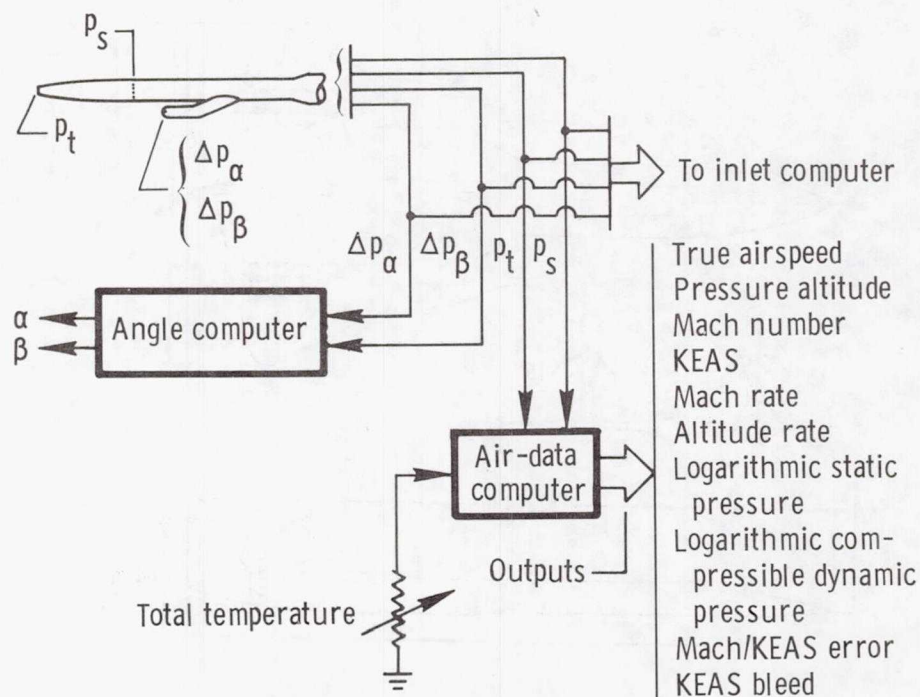
Figure 5.- Air-data system.
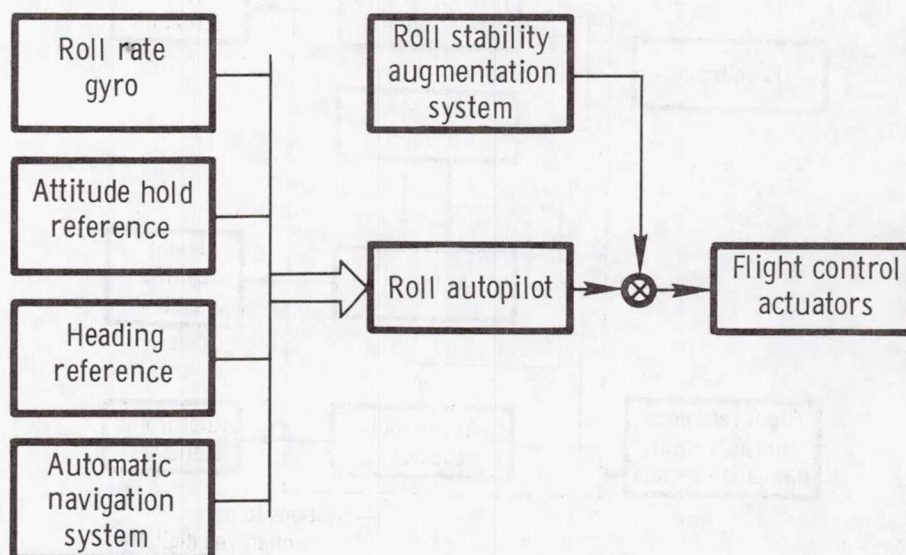
Figure 6.- Roll autopilot schematic.
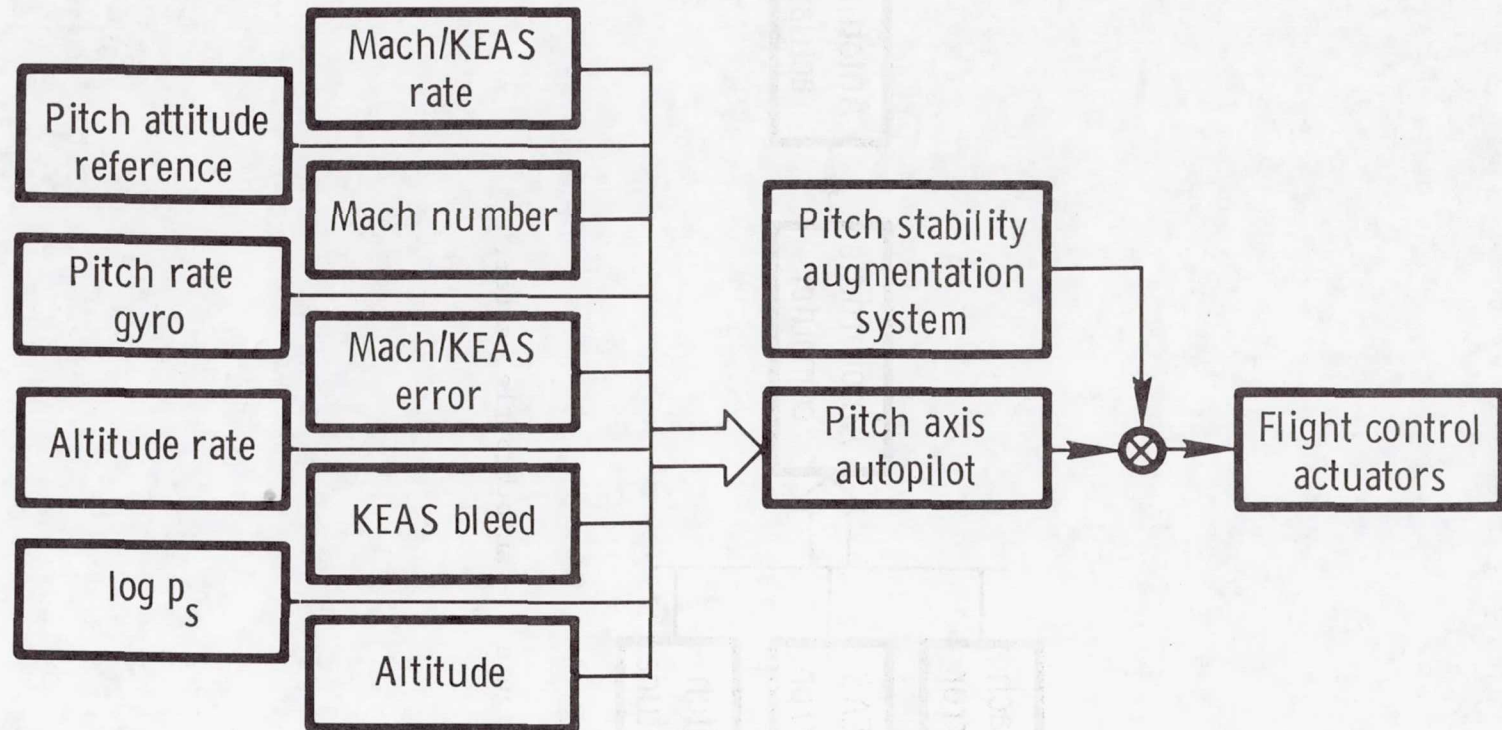
Figure 7.- Pitch axis autopilot schematic.
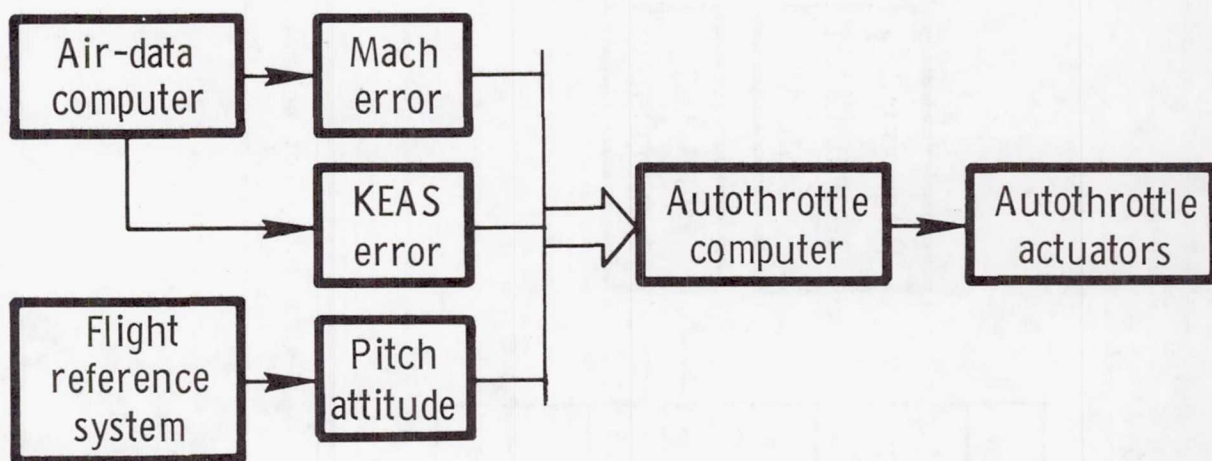
Figure 8.- Autothrottle system.
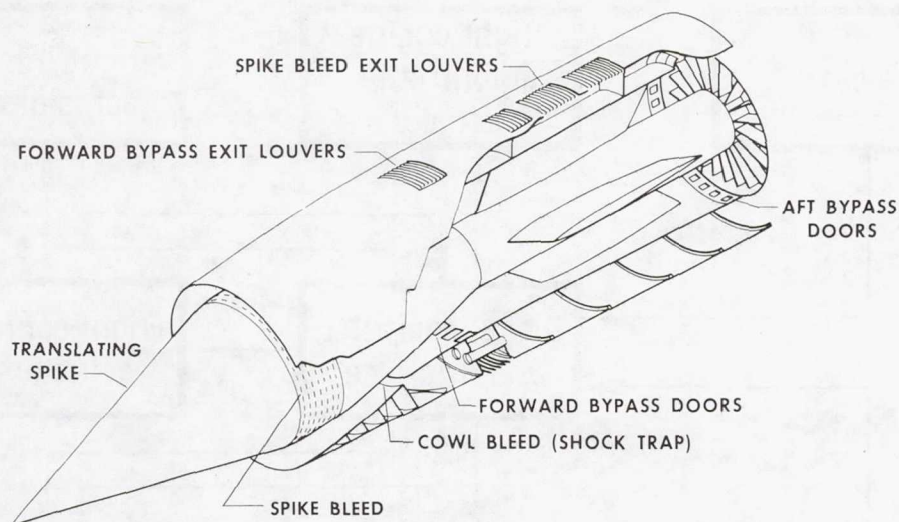
Figure 9.- Inlet system.
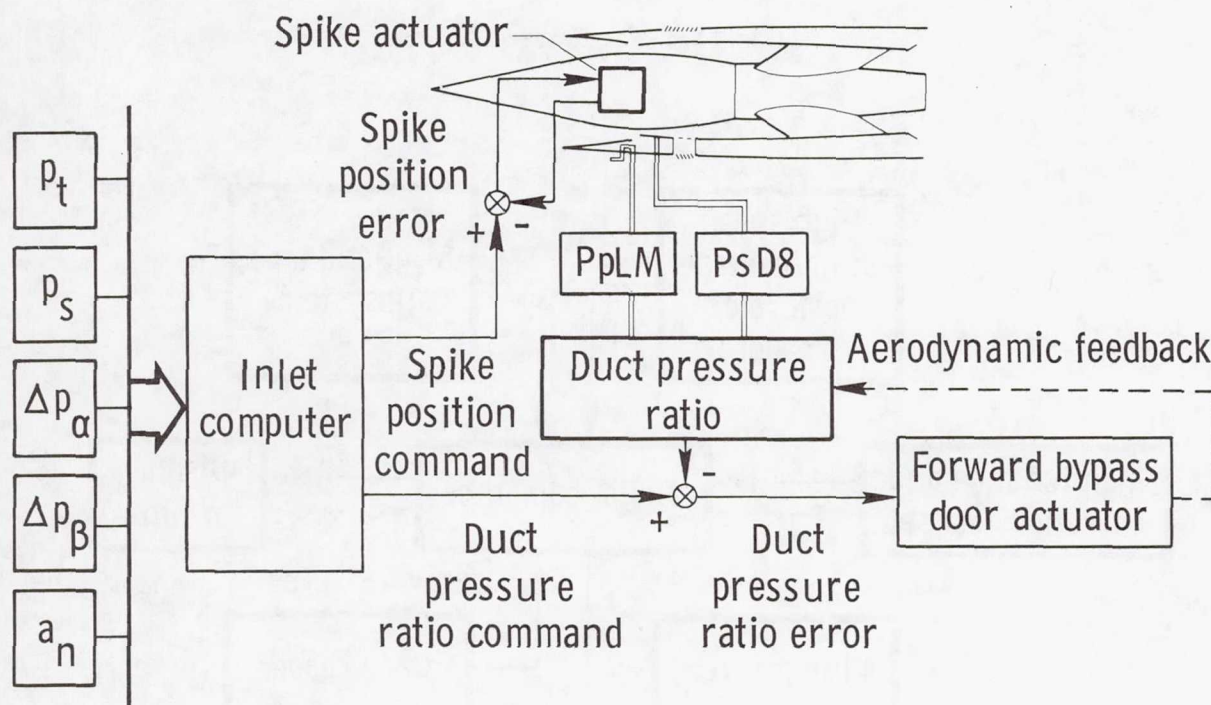
Figure 10.- Inlet control system.
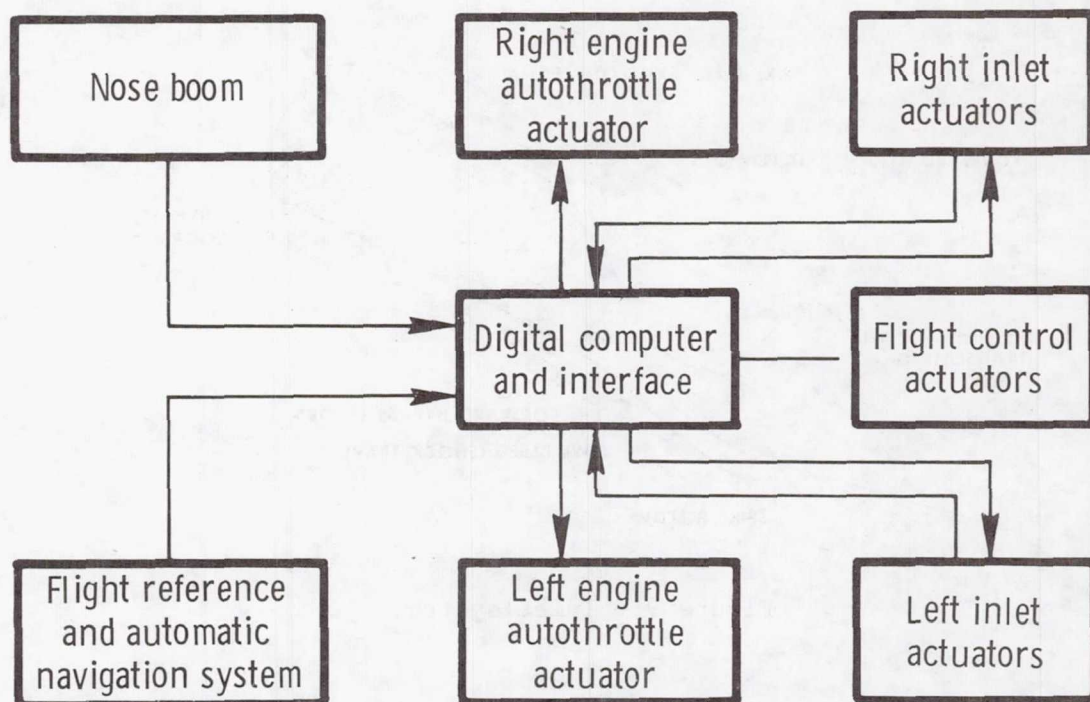
Figure 11.- Digital control system.
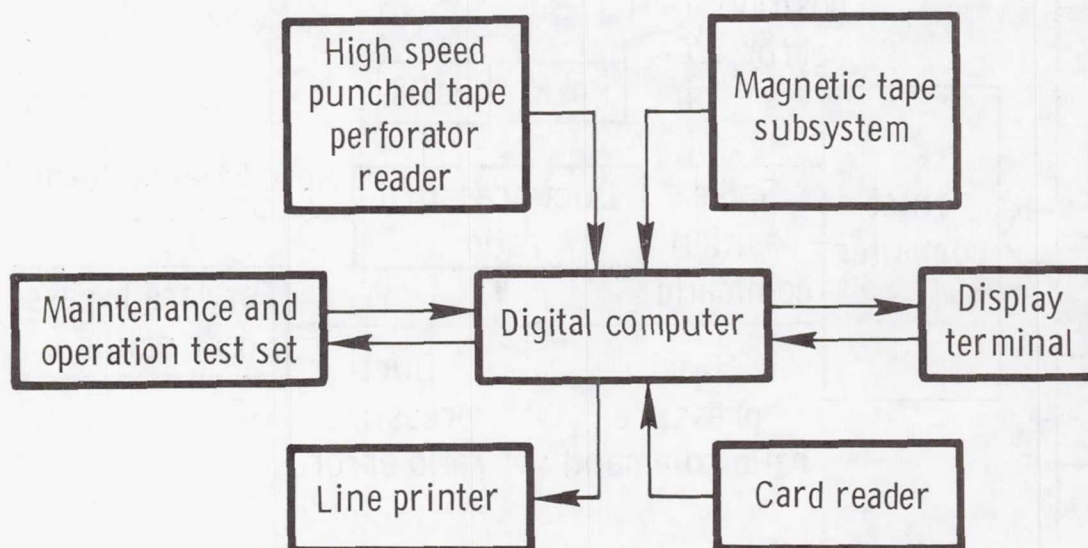
Figure 12.- Computer and peripheral equipment.
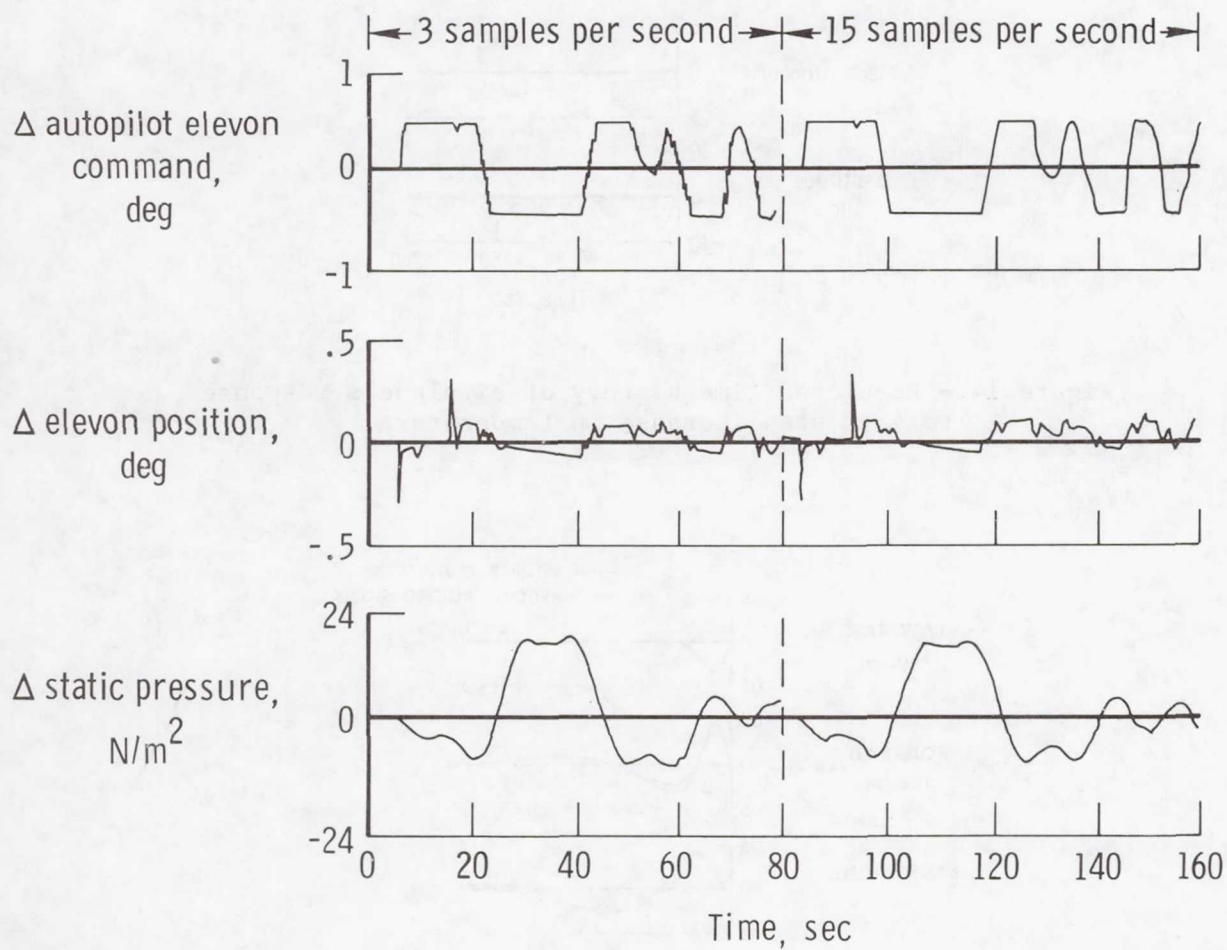
Figure 13.- Effect of sample rate on digital system response.
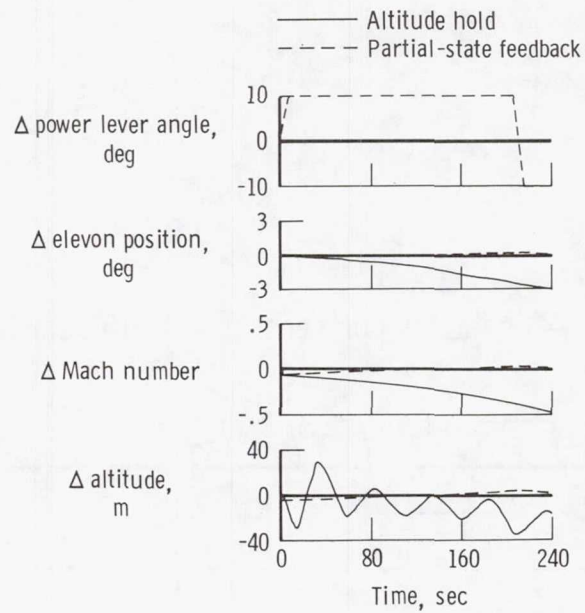
Figure 14.- Predicted time history of airplane's response
to 4° C step increase in temperature.
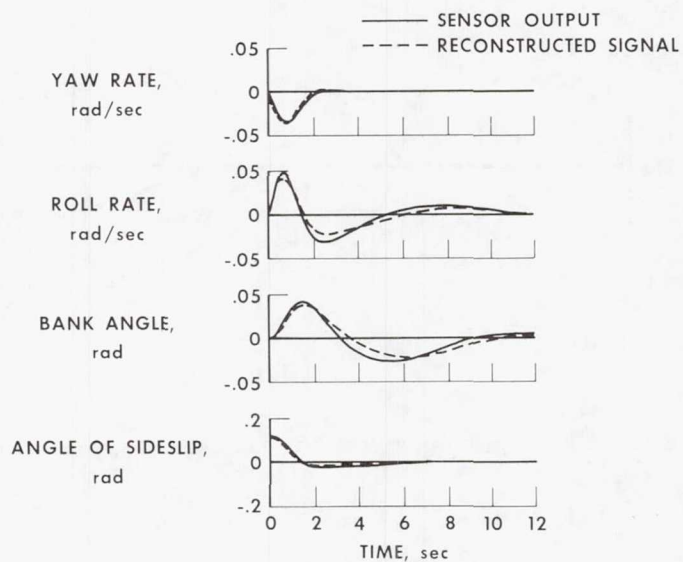
Figure 15.- Comparison of reconstructed signals and
actual sensor outputs.

FLUTTER SUPPRESSION BY ACTIVE CONTROL AND ITS BENEFITS

Robert V. Doggett, Jr.
NASA Langley Research Center

and

James L. Townsend
The Boeing Company

SUMMARY

A general discussion of the airplane applications of active flutter sup-
pression systems is presented with focus on supersonic cruise aircraft configu-
rations. Topics addressed include a brief historical review; benefits, risks,
and concerns; methods of application; and applicable configurations. Highlight
results are presented from previous analytical and wind-tunnel model studies
for supersonic cruise aircraft configurations. These results show that signifi-
cant increases in flutter speed (or flutter dynamic pressure) can be accom-
plished by using active flutter suppression.

Results of a study are presented where the direct operating costs and
performance benefits of an arrow-wing supersonic cruise vehicle equipped with
an active flutter suppression system are compared with corresponding costs and
performance of the same baseline airplane where the flutter deficiency was
corrected by passive methods (increases in structural stiffness). The design,
synthesis, and conceptual mechanization of the active flutter suppression sys-
tem are discussed. The results show that a substantial weight savings can be
accomplished by using the active system. For the same payload and range, air-
plane direct operating costs are reduced by using the active system. The
results also indicate that the weight savings can be translated into increased
range or payload.

INTRODUCTION

Commercial airplane designers are constantly striving to improve airplane
performance. One technique currently being considered is the increased use of
active controls. An active control application that is receiving more and more
attention is active flutter suppression. The subject of this paper is the
application of active flutter suppression to supersonic cruise aircraft.

This paper is divided into four major sections. In the first section,
entitled "Background," active flutter suppression is described in general terms,
a brief historical review is presented, and reasons for the interest in using
an active system for supersonic cruise aircraft are pointed out. In the second
section, entitled "General Discussion of Active Flutter Suppression," such topics
as benefits, risks, and concerns; methods of application; and applicable con-
figurations are addressed. In the third section, entitled "Past Supersonic

Cruise Airplane Flutter Suppression Studies," highlight results from analytical studies and wind-tunnel model investigations for supersonic cruise airplane configurations are presented. In the fourth section, entitled "Arrow-Wing Active Flutter Suppression System Design and Benefits," results are presented from a study that examines the potential direct-operating-cost (DOC) benefits of an active flutter suppression system for an arrow-wing configuration that required a substantial increase in structural weight to provide sufficient stiffness for satisfactory flutter margins. Direct comparisons are made between the airplane with the active flutter suppression system and the same baseline airplane with a passive flutter solution (increases in structural stiffness). In addition, the design, synthesis, and conceptual mechanization of the active flutter suppression system are described.

BACKGROUND

Supersonic Cruise Airplane Flutter Characteristics

Flutter is an oscillatory instability that must be properly accounted for in aircraft design. In fact, Federal Aviation Administration (FAA) regulations require a commercial transport to be flutter free at speeds 20 percent greater than the design dive speed V_D. Although flutter has caused problems in present-day subsonic jet transport design, and in some instances has impacted engine locations on the wing, satisfactory flutter-free configurations have been realized usually without requiring significant increases in structural stiffness and resulting increases in structural weight. That is, a strength-design structure had sufficient or very nearly adequate stiffness to satisfy flutter requirements. However, studies have shown that if wing aspect ratios for this type of airplane increase to values above about 10, substantial stiffness increases for flutter avoidance may be required.

Although no actual supersonic cruise airplane has been built in the United States, several designs have been taken to sufficient depth to indicate that the flutter deficiency of a strength-design structure may be rather large. This is illustrated in figures 1 and 2, where the flutter boundary relative to the operating boundary is shown for two strength-design supersonic-cruise vehicles, namely, the national program configuration and a version of the NASA arrow-wing configuration. More information on the flutter characteristics of these two configurations is presented in references 1 and 2, respectively. The application of passive flutter solutions (increases in structural stiffness, mass balance, etc.) to increase the flutter speeds to an acceptable level required the addition of over 4536 kg (10 000 lbm) of structural weight in both cases. (Other strength-design arrow-wing configurations, although flutter deficient, have flutter characteristics different from those shown in fig. 2 and consequently required different amounts of increased structural weight. (See refs. 3 and 4.)) Such weight additions, of course, penalize the aircraft by increasing the initial costs, reducing payload and range, and increasing direct operating costs throughout the operational life. Consequently, there is considerable interest in developing better methods of increasing flutter speed which can be used in place of, or in combination with, the traditional passive methods.

304

Active Flutter Suppression

Active flutter suppression is an alternative to passive flutter solution. An active system offers a means of artificially stiffening and damping the aircraft structure to increase the flutter speed by using aerodynamic control surfaces which are activated by control surface actuators through a feedback system control law (feedback gains) which receives structural motion information from dynamic motion sensors. Although active flutter suppression may eliminate the requirement for added structural weight that just goes along for the ride, so to speak, it may also increase airplane complexity and system maintenance costs. That is, there are both advantages and disadvantages to the use of an active system. The relative margin that the advantages outweigh the disadvantages is undoubtedly a governing factor in whether an active flutter suppression system is considered for implementation in any new airplane design.

Other Active Control Concepts

Active flutter suppression is only one of many active control concepts that are currently being considered to improve the performance of new technology airplanes. (See refs. 5 and 6.) Other concepts are relaxed static stability, gust load alleviation, ride quality control, and maneuver load control. In fact, during the past decade, some of these concepts have already begun to appear in production aircraft although, in most cases, they have been add-on systems that were not included in the preliminary design. A good illustration is the ride quality improvement system that was developed and certified for the Boeing 747 subsonic transport airplane (ref. 7).

Historical Review of Active Flutter Suppression

Active flutter suppression is not a new idea. The concept is suggested in a 1955 classic textbook (ref. 8), and it is a natural outgrowth of a flight flutter testing technique proposed a year earlier (ref. 9). In the late 1950's to mid-1960's very little research was done on active flutter suppression as is evidenced by the lack of published papers for this time period. In the mid to late 1960's, some interest in the subject developed. For example, at Lockheed-Georgia, some analyses and experiments were conducted to demonstrate the use of servo-control to delay flutter onset (ref. 10); Boeing conducted analytical studies of possible flutter suppression systems for the national supersonic transport (SST) configuration (ref. 11); and the NASA initiated some combined analytical and wind-tunnel model studies (ref. 12). In the 1970's interest

continued to increase as is evidenced by the increasing number of published papers which describe a variety of analytical and experimental studies (refs. 13 to 39).[1]

A significant development during the early 1970's was the inclusion of active flutter suppression as one of the active control concepts to be demonstrated during the B-52 control configured vehicle (CCV) program (refs. 18, 34, 38, and 40). The successful flight demonstration beyond the basic airplane flutter speed by using the B-52 CCV airplane gave an affirmative answer to the question whether an active flutter suppression system can be designed, built, and demonstrated in flight. Of course, the B-52 system was developed to meet research program objectives and was not designed to meet the requirements of a commercial airplane system. Some wind-tunnel model studies were conducted in conjunction with the flight tests (refs. 28 and 31). Because the model results correlated well with flight-test results, it was confirmed that models can be used to predict accurately flight flutter suppression results. This accomplishment is important because uncertainties in present-day flutter analysis techniques require extensive use of wind-tunnel model testing in developing and validating active flutter suppression systems for commercial transport aircraft.

GENERAL DISCUSSION OF ACTIVE FLUTTER SUPPRESSION

Although other topics are mentioned, the discussion in this section focuses on the benefits, risks, and concerns associated with active flutter suppression. In preparing this section, the authors found very useful the information in two excellent papers (refs. 5 and 6) that describe the prospects for many active control applications including flutter suppression.

The implementation of an active flutter suppression system on a commercial transport airplane will depend on the tip of the scales shown in figure 3 where the potential benefits are shown balanced against the risks. The most often stated benefit is that for an airplane with a flutter deficiency, an active system may require a smaller increase in aircraft weight than that weight increase required by a passive flutter solution. However, this smaller weight increase is only the apparent benefit. A true benefit will only exist if this weight reduction can be translated into a performance, or economic, benefit. It is this performance benefit that must be balanced against the risks. The term "performance benefit" as used herein is consistent with that of reference 6

---

[1] Although the reference list in this paper contains numerous papers on active flutter suppression, the list is certainly not all inclusive. It is intended to be only a representative sampling of the many papers available, and with one exception (ref. 27) is limited to papers that are available without restriction. Permission to cite reference 27 and to include material therefrom in this paper was granted by the Department of Transportation, Federal Aviation Administration. Their cooperation in this regard is hereby acknowledged.

where performance was defined as "a productivity increase of sufficient magnitude to provide a reasonable return on investment." This definition is rather broad and is not limited to the usual items such as increased speed and longer range.

Many of the risks and concerns relative to the use of active flutter suppression are because it is a new technology. The manufacturer has little past experience on which to base the certification of such systems. The manufacturer also is concerned about the apparent weaknesses in analytical methods in accurately predicting system performance. The users, primarily the airlines, are concerned about such items as maintenance costs and reliability. Here again lack of previous experience is the key ingredient. Because maintenance costs are a large fraction of the total DOC of commercial transport airplanes, any appreciable growth in these costs could more than offset other economic advantages of using an active flutter suppression system.

Design Cycle Integration

The benefits of active flutter suppression will undoubtedly be a function of when the decision is made to consider its use. If it is considered as an option in the preliminary design stage, the potential benefit may be considerably larger than it would be if it is initially considered after the preliminary design is complete. In the first case, the active system is an integral part of the airplane design, and its requirements for such things as hydraulic system capacity, control surface size and location, and actuator power and frequency response are considered at the outset. In the second case, the active system is a substitute for a passive system. At this stage, the introduction of the active system may require changes in already designed systems such as hydraulic power and control surface actuators. Furthermore, at this stage the active system design will probably be constrained to use existing control surfaces whose size and location were selected without any consideration of active flutter suppression.

Although the potential benefits may be larger the sooner the decision is made, it can be argued that the earlier the decision, the greater the potential technical risk. This is because a major unforeseen problem may arise after the commitment to active flutter suppression has been made and considerable money and time have been expended. Analytical uncertainties in accurately predicting active system performance may be a critical factor in not identifying a major problem early in the design cycle. Perhaps some reduction in this technical risk can be accomplished by judicious use of wind-tunnel model tests to validate analytical methods as early in the design cycle as possible. Candidate tests would include the measurement of control surface aerodynamic characteristics because, in many instances, existing aerodynamic theories do not predict control surface characteristics to the required accuracy.

Limited Application System

One primary concern about active flutter suppression is that it would be a flight critical system and would have to be as reliable as the passive flutter

solution structure that it replaces. This concern is certainly justified in light of the current state of the art if the active system is required to increase the flutter speed from below the design dive speed V_D to the flutter margin requirement 1.2 V_D. Presently, it appears that only limited applications of active flutter suppression should be considered. By limited applications is meant that the active system provides only the required flutter margin, V_D to 1.2 V_D (or a portion of the margin). The idea of limited application is illustrated schematically in figure 4. Any flutter deficiency below V_D is corrected by a passive flutter solution. Consequently, the airplane would be flutter free throughout its normal flight envelope and the flutter suppression system would provide the required 20-percent margin of safety.

Considerable precedent exists today for using mode damping systems in commercial airplane operations. Some commercial transports operate with yaw dampers that are flight safety critical. For example, one highly successful subsonic jet transport airplane uses a dual yaw damper system. Although only one system is required to be functional for dispatch, both systems must be working for the airplane to operate throughout its full flight envelope. If one system fails during flight, the airplane operational altitude is restricted to below about 9250 m (30 000 ft). At this altitude and below, the unaugmented Dutch roll characteristics are considered acceptable for commercial airplane operations.

A limited application active flutter suppression system relies on a similar operating restriction (speed reduction rather than altitude reduction) and a fail-operational mechanization. Of course, there are presently no FAA regulations on active flutter suppression. The lack of a specific FAA policy is naturally a concern because the certification requirements and costs represent an unknown risk.

Applicable Configurations

In reference 6, some qualitative indication of the relative benefits of active flutter suppression are presented for several different airplane variables. Some of these results are repeated in figure 5 for speed range, gross weight, and wing aspect ratio. Note that the relative benefits for the ranges of these parameters which are applicable to supersonic cruise airplanes (large speed range, heavy gross weight, and low to moderate aspect ratio) are considered to be moderate to major. It should be recognized that active flutter suppression will not be beneficial for all configurations, and, in some instances, the airplane actually may be penalized if an active system is chosen over a passive system. A case in point is one of the designs generated during the NASA-sponsored Advanced Transport Technology (ATT) Program (see ref. 41) where it was concluded for one of the designs studied that the benefits of an active system would be more than offset by the complexity of such a system.

Interrelation With Other Active Control Concepts

In a new airplane design where the designers attempt to take advantage of
as many active control applications as practicable, it may not be possible to
make the decision to implement an active flutter suppression system independent
of the decision to implement other concepts. For example, a flutter suppres-
sion system may be required in order to achieve maximum benefits from a load
alleviation system. The interrelation of various active control concepts for
supersonic cruise aircraft is discussed in reference 42. If more than one
concept is implemented, there may be advantages in common system components.
For example, flutter suppression and gust load alleviation systems may use
some of the same control surfaces and actuators.

PAST SUPERSONIC CRUISE AIRPLANE SUPPRESSION STUDIES

In this section, highlight results from some flutter suppression studies
that have been conducted for supersonic cruise airplane configurations are
presented. Remember that flutter suppression studies for other configurations
may be applicable to supersonic cruise aircraft. For example, from the results
of the B-52 CCV model/airplane studies mentioned previously, it can be con-
cluded that full-scale supersonic cruise aircraft flutter suppression system
performance can be accurately simulated by using appropriately scaled wind-
tunnel models.

National Configuration Analytical Studies

During the latter stages of the National Program, some analytical studies
were made by The Boeing Company to determine whether an active flutter suppres-
sion system could be used effectively to increase the flutter speed of the
national configuration. As pointed out previously, the strength-design con-
figuration was rather flutter deficient (see fig. 1), and a substantial increase
in structural weight was required for a passive flutter solution. During these
studies, it was assumed that satisfactory flutter margins would be achieved by
a combination of passive and active flutter solutions (the limited application
concept mentioned previously). Although the complete results of these studies
are not generally available in the literature, some information is contained
in reference 11. Various combinations of aerodynamic control surfaces, types
and locations of motion sensors, and feedback control laws (feedback gains)
were investigated. One combination of control surfaces and motion sensors
that yielded a substantial increase in airplane flutter speed is shown in
figure 6. Some results obtained at a Mach number M of 0.90 by using this
combination are presented in figure 7 as the variation in damping with airspeed
for two of the important flutter critical modes, namely, a wing mode and a
wing-body mode. The effectiveness of this active system in substantially
increasing the flutter speed of the unaugmented basic airplane is readily
apparent. For the basic airplane, both modes flutter near the design dive
speed V_D. The active system increased the flutter speed for both modes to at
least the $1.2 V_D$ flutter margin requirement. Indeed, at this velocity, both
damping trends are toward increasing stability.

DOT Technology Follow-On Model Study

After the cancellation of the National Program, the Department of Transportation (DOT) sponsored a wind-tunnel model active flutter suppression study as part of the SST Technology Follow-On Program. The results of this study are given in reference 27, and only some of the highlights are presented here. The model was a 1/20-scale low-speed model of the national configuration that was modified to include active-control aerodynamic surfaces for flutter suppression and stability augmentation. A photograph of this model is presented in figure 8. During the wind-tunnel tests, the full-span model was mounted on a cable suspension system to simulate the free-flying condition. Three active flutter suppression systems were investigated. The first used the inboard ailerons; the second used the outboard ailerons; the third used both the inboard and outboard ailerons. The locations of these control surfaces are shown in figure 9. The experimental flutter results for all three systems are presented in figure 10. All three systems increased the flutter speed of the unaugmented aircraft. The inboard-outboard aileron system provided the largest increase, about 11 percent. A comparison of the experimental results with analytical results was somewhat contradictory. The analysis accurately predicted the inboard aileron system experimental results. However, the analysis for the outboard aileron system predicted about a 13-percent increase in flutter speed, about four times the experimental value. The reason for this discrepancy is unknown at present.

Incidentally, this model was damaged near the end of the wind-tunnel program. Since that time it has become the property of the NASA and has been repaired. Additional testing is planned in the Langley transonic dynamics tunnel to study different flutter suppression systems as well as other active control applications.

Delta-Wing Flutter Suppression Model Study

For a number of years the Langley Research Center has been sponsoring considerable research activity in active flutter suppression. Both in-house and contractor work have been involved. Much of this activity has utilized a cantilever delta-wing model that was equipped with hydraulically actuated leading-edge and trailing-edge control surfaces for active flutter suppression. Although this model does not scale dynamically any particular airplane configuration, it is representative of a contemporary supersonic cruise airplane design. A photograph of the model mounted in the Langley transonic dynamics tunnel is shown in figure 11. One of the purposes of this model study was to experimentally evaluate and validate the aerodynamic energy approach to active flutter suppression that was developed in reference 15. This goal was successfully accomplished, and the study is described in detail in reference 35.

Some analytical and experimental results from the delta-wing study are presented in figures 12 and 13. These data are presented in terms of dynamic pressure rather than velocity as was the case for the two previous examples. An important point can be made by referring to the calculated results shown in figure 12 for various locations of aerodynamic control surfaces and wing motion sensors — accelerometers in this case. Three possible locations of

the pair of leading-edge and trailing-edge control surfaces were investigated with three possible accelerometer locations for each control surface arrangement. The greatest increase in flutter dynamic pressure was obtained for the outboard control-surface location with the accelerometers alined with the outboard edges of the control surfaces. However, on this model the installation of the outboard control surface actuators was not practical without violating the external contour of the airfoil section. For this and other reasons, the control surface arrangement chosen was the midspan strip. The point to be made is that on this model, as undoubtedly will be the case in airplane applications, there were practical considerations that really had nothing to do with the flutter suppression system itself that played an important role in the choice of system that was actually implemented.

The delta-wing model was used over the Mach number range from 0.60 to 0.90 to demonstrate successfully the aerodynamic energy approach. Some experimental and analytical results obtained at a Mach number of 0.90 are shown in figure 13 for the three control laws studied, designated as control laws A, B, and C, respectively. Which control surfaces were used, and whether two-dimensional (2D) or three-dimensional (3D) unsteady aerodynamics were used in determining the feedback gains constituted the differences between the three control laws. These differences are indicated in figure 13. All three control laws were effective in increasing the flutter dynamic pressure of the unaugmented basic model. One word of caution — although the trailing-edge control (law C) indicated the largest increase in flutter dynamic pressure, this does not mean that a trailing-edge control system is better necessarily than a leading-edge trailing-edge control system. Analytical studies (not shown in the figure) indicated just the contrary. See reference 35 for details.

The only direct comparison that can be made between experiment and analysis is for control law A, since this is the only case where the model was actually taken to flutter with the flutter suppression system operational. For law A, the analysis and experiment are in good agreement. However, to obtain the analytical results shown, the theoretical unsteady aerodynamic characteristics of the control surfaces were adjusted by using measured hinge-moment data that had been determined previously for this model. If purely theoretical aerodynamics are used in the calculations, the predicted improvement in flutter dynamic pressure is considerably larger than that shown in the figure.

System and Technology Assessment Studies

The NASA has sponsored several system and technology assessment studies for advanced supersonic cruise aircraft. Both in-house and contractor activities have been included. (A bibliography of published reports from these studies is given in ref. 43.)

The system and technology studies, taken as a whole, indicate that a savings in structural weight can be accomplished by using an active flutter suppression system on an advanced supersonic cruise airplane and that this weight saving can be translated into economic benefits, such as a decrease in direct operating costs or an increase in range. The magnitude of the potential

311

benefit, although considerably smaller than that of some other active control applications such as relaxed static stability, will become larger as technology advances occur, will be a function of whether other active control systems are included in the preliminary design, and will be affected by the use of other advanced technologies such as composite structures.

ARROW-WING ACTIVE FLUTTER SUPPRESSION SYSTEM DESIGN AND BENEFITS

Presented in this section are the results obtained to date from a study that compares the relative structural weight, performance, and direct operating costs of an arrow-wing supersonic cruise aircraft configuration that had its flutter deficiency corrected by an active flutter suppression system with the corresponding weight, performance, and DOC of the same baseline airplane where the flutter deficiency was corrected by using a passive system (increased structural stiffness). The baseline airplane was the strength-design configuration developed by The Boeing Commercial Airplane Company during the NASA-sponsored arrow-wing structural design concepts studies. (See ref. 2.) The geometry of this configuration is shown in figure 14. The flutter deficiency of this airplane was large (see fig. 2), and 4627 kg (10 200 lbm) of structural weight was required to increase the flutter speed to the $1.2 V_D$ requirement. This airplane is referred to as the passive system airplane. The other airplane, referred to as the active system airplane, used the same baseline design, but the flutter deficiency was corrected by a combination of passive and active system applications. A passive solution was used to increase the minimum flutter speed to V_D, and an active flutter suppression system was used to further increase the flutter speed to $1.2 V_D$. This is the limited application concept described previously. In the following discussion, the design criteria, synthesis, and conceptual mechanization of the active flutter suppression system are described. Finally, the results of an economic analysis are presented where the DOC of the active system airplane are compared directly with the DOC of the passive system airplane. This comparison gives a direct indication of the benefits of using an active flutter suppression system for the arrow-wing configuration studied.

Design Criteria

Basically, the active flutter suppression system design criteria were based on contemporary industry design practices and existing FAA and military regulations and specifications.

Flutter criteria.- The basic flutter requirement, as shown in figure 15, was that the active flutter suppression system would provide a 20-percent increase in the flutter speed, V_D to $1.2 V_D$. A passive system was to be used to correct any deficiencies below V_D. At speeds less than V_D, the active system was required to provide the equivalent of 3 percent structural damping for all flutter critical modes. In addition, criteria were adopted which required that the damping of other modes could not be significantly reduced. For example, the ride quality of the active system airplane could not be significantly degraded by the active flutter suppression system. Handling

qualities were required to remain essentially unchanged, active flutter suppression system on or off. Furthermore, criteria governing repeated loads on the structure were adopted so that fatigue loading in turbulence would be no greater for the active system airplane than for the passive system airplane. Gain and phase margin requirements were adopted also. At V_D, the active system was required to have 6 dB gain and 45° phase margins.

Turbulence criteria.- A significant factor in the design of an active flutter suppression system is to account properly for atmospheric turbulence and gusts because structural responses resulting from turbulence can place additional demands on the flutter suppression system that can cause system saturation. The turbulence criteria are shown in figure 16. Turbulence effects were allowed to degrade system performance but not to levels below those required by the flutter criteria. That is, turbulence effects could produce reductions in the damping in a critical flutter mode to levels below those in smooth air, but not to levels below 3 percent equivalent structural damping.

Flight safety and reliability criteria.- The basic flight safety criteria was that the flutter suppression system remain completely operational following a first failure. That is, a fail-operational system was required. The system was not required to be functional for dispatch nor was it required that a mission be aborted following an in-flight failure. However, should a system failure occur, either on the ground or in flight, the airplane operational envelope would be placarded to insure the 20-percent flutter margin. For example, if an in-flight failure occurs when the airplane is flying at a speed greater than 80 percent of V_D, speed would be reduced to provide the required 20-percent flutter margin in velocity. If only a single failure occurs, the airplane is still flutter free to 1.2 V_D. Should a failure be detected on the ground prior to take-off, the airplane could still be dispatched, but its operating envelope would be restricted to provide the flutter margin, that is, lower speed climb and descent schedules. Recall that the passive system provides safety from flutter up to V_D.

In establishing the reliability requirements, the basic consideration was that the chances of a failure or other event occurring that would result in a catastrophe would be extremely remote. In this case, the catastrophic event would be encountering flutter. For flutter to occur, both of the following must occur: (1) the airplane must be at a speed greater than V_D and (2) there must be a total failure of the active flutter suppression system. For system design purposes, the probability of a total failure of the fail-operational system was chosen to be less than 1×10^{-4} which is a value consistent with the state of the art in fail-operational flight control systems, perhaps even on the conservative side. The same probability value was selected for being beyond V_D. Admittedly, this choice was somewhat arbitrary, but it is believed to be a realistic value. The two contributors to flutter were considered to be independent; therefore, the probability of flutter occurring is less than 1×10^{-8}. This value is consistent with values usually quoted for the chances of experiencing primary structural failure.

Analytical Development

In the analytical development of the active flutter suppression system, the airplane equations of motion were expressed in terms of generalized modal coordinates. These equations were transformed to Laplace variable space where the synthesis was accomplished by using root locus analysis methods.

Structural and aerodynamic modeling.- The airplane structure was modeled by a finite-element idealization developed for The Boeing Commercial Airplane Company's ATLAS integrated structural analysis and design system. Although the basic mathematical structural model was already available (see ref. 2), some modifications were necessary to meet the needs of the present study.

The aerodynamic model was developed by using a finite-element solution of the linear, unsteady, compressible flow equations that provide continuous solutions throughout the Mach number range, subsonic, transonic, and supersonic. The technique was developed by Kenneth L. Roger and his associates at Boeing-Wichita, and is currently unpublished. Unpublished results show that the method is as accurate as other similar existing methods, but is computationally more efficient. The technique requires the airplane to be subdivided into an arrangement of trapezoidal boxes, provides a very general modeling capability, and accounts for such things as intersecting surfaces, out-of-plane surfaces, and arbitrary arrangement of control surfaces. For the steady-state case, the method is similar to that described in reference 44; for the subsonic unsteady flow case, it shares certain similarities with the doublet-lattice method (ref. 45).

Since the airplane equations of motion were expressed in the Laplace domain, it was necessary to transform the frequency-dependent (actually reduced frequency) unsteady aerodynamic coefficients into functions of the Laplace variable. This transformation was accomplished by a least-squares curve-fitting procedure which used rational functions of the Laplace variable with fourth-order denominators. This technique has been used previously with good results. (See refs. 14 and 16.)

System synthesis.- During the initial synthesis studies, various combinations of aerodynamic control surfaces and accelerometer locations were investigated in combination with different feedback control laws. The control surfaces and accelerometer locations are shown in figure 17. The midspan control surface and accelerometer location chosen for the final synthesis are shown darkened in figure 17. The accelerometer location chosen was attractive for two reasons. First, because of local stiffening produced by the engine support beams, very little response of the wing is produced at this point by higher frequency modes which are not flutter critical. Second, studies indicated that the precise location of the accelerometer was not critical; thus the conceptual installation of the accelerometer was facilitated.

Although the chosen control surface, accelerometer location, and feedback control law were effective in providing the required flutter speed increase, a nonflutter-critical mode was adversely affected in that the gain and phase margin requirements were not satisfied. This effect was corrected by adding

314

an aft-fuselage accelerometer whose signal was added to the wing accelerometer signal, and by making a small adjustment in the feedback control law.

A block diagram of the final flutter suppression system is presented in figure 18. Note that gain scheduling is provided, both in terms of Mach number M and dynamic pressure q. Scheduling was used because the active flutter suppression system is only required to provide the flutter margin over a portion of the flight envelope, primarily in the transonic regime. At other flight conditions, the passive system provides sufficient stiffness to give the required 20-percent margin.

The calculated variation of damping in the critical flutter mode with equivalent airspeed is shown in figure 19 for the active system on and off. These data are for a Mach number of 0.90. The effectiveness of the active system in increasing the damping is obvious.

System Mechanization

No hardware items were built during this study, but the required hardware was defined in sufficient detail so that realistic estimates could be made of manufacturing costs and weight. Such information was required for the economic analysis. A simplified block diagram of the system mechanization is presented in figure 20. An important part of the mechanization was the modified nonlinear describing function analysis that accounted for such nonlinear effects as system saturation due to turbulence. This analysis determined the control surface physical size (the location was determined during the synthesis), and the position and rate limits. Control surface size and motion limits plus hinge-moment requirements dictated the control surface actuator selection which, in turn, defined the hydraulic system flow-rate requirements. The flow rate essentially specified the hydraulic system power and cooling requirements. In this application, the hydraulic and electrical power requirements of the flutter suppression system were easily handled by the existing baseline airplane hydraulic and electrical power systems. This situation may exist in other applications as well, since design of these systems is normally based on peak requirements which occur at lower speeds. At the higher speeds, where the active flutter suppression system has substantial power requirements, the baseline airplane had surplus hydraulic and electrical power available beyond expected airplane requirements.

Of course, during the conceptual mechanization the reliability requirements had to be taken into account. For example, triple tandem actuators were required for each control surface.

The estimated weight of the active flutter suppression system was 159 kg (350 lbm). This weight estimate includes all system components such as actuators and electronics. The weight of the passive system part of the limited application flutter suppression system was about 317 kg (700 lbm). Therefore, the total weight of the flutter suppression system for the active system airplane was 476 kg (1050 lbm). When compared with the 4627 kg (10 200 lbm) of structure that was needed for the passive system airplane, there is a net weight savings of about 4151 kg (9150 lbm).

Economic Evaluation

An economic evaluation study was made to obtain a direct comparison of
the DOC of the active system airplane with the DOC of the passive system air-
plane. Although this economic study has not been completed, it is believed
that the final results may indicate only changes in detail, but no changes in
substance.

The criteria used in the economic comparison are (1) direct comparison of
active system airplane with passive system airplane, (2) performance evaluated
at constant payload, and (3) cost analysis based on procurement and maintenance
costs of similar complex equipment. The basic criterion was that the comparison
would be made for the two airplanes where the only differences between them
would be in the type of flutter improvement system employed. Some airplane
characteristics used in the economic analyses are presented in table I. Of
course, for the same payload and fuel loading the take-off gross weights of the
two airplanes are different because of the 4151 kg (9150 lbm) weight saving
benefit realized by using the active flutter suppression system. The specific
methodology used in the economic analysis is described in reference 46. Crew
costs, fuel, depreciation, and insurance were calculated by the conventional
ATA formula, using 1976 coefficients. Procurement and maintenance costs of the
flutter control system were estimated separately based on a comparison with
contemporary complex systems of a similar nature.

Some DOC results for the two airplanes are presented in figure 23 as a
function of stage length. The DOC of the active system airplane are lower
throughout the range shown. For example, for a 3000-nautical-mile trip, the
reduction is about 2 percent, $9.54 per nautical mile (active) versus $9.73
per nautical mile (passive). These data were obtained by using the same pay-
load for both airplanes. The take-off gross weights were different. The fuel
cost used was 10.83 cents per liter (41 cents per U.S. gallon).

The items which contributed to the DOC savings are shown in figure 24.
The fuel, depreciation, and insurance costs were less whereas a slight increase
in airframe maintenance cost was indicated. DOC items such as crew costs and
engine maintenance were unchanged. About 71 percent of the DOC savings
obtained by using the active flutter suppression system were produced from
fuel savings, which correlate with the lower take-off gross weight. The other
major contributor was depreciation (about 25 percent of the total savings).
This was due primarily to the fact that the estimated purchase price of the
active system airplane was about 2-1/4 percent less than that of the passive
system airplane.

The net weight savings gained by using the active flutter suppression
system can be translated into an increase in range or payload. For example,
if both airplanes are assumed to have the same take-off gross weights and
equal payloads, the range of the active system airplane may be increased by
about 186 n. mi. This is accomplished by absorbing the weight savings as
additional fuel. For the same take-off gross weight and equal range, a payload
increase of several thousand pounds is another possible option. In this case,
additional payload is carried, instead of additional fuel.

CONCLUDING REMARKS

A general discussion of the application of active flutter suppression systems for increasing airplane flutter speeds has been presented. The discussion focused on applications to supersonic cruise aircraft. In addition to the presentation of some general background information concerning active flutter suppression, such topics as benefits, risks, and concerns; methods of application; and applicable configurations have been discussed.

Highlight results obtained during previous analytical and wind-tunnel model experimental studies made for supersonic cruise airplane configurations have been presented and discussed. These results show that substantial increases in flutter speed (or flutter dynamic pressure) can be obtained by using an active system for the configurations studied.

Results obtained to date in a study to determine the direct operating costs and performance benefits of applying an active flutter suppression system to an arrow-wing supersonic cruise vehicle have been presented. In this study, a direct comparison was made between a baseline airplane equipped with an active system to correct the flutter deficiency and the same baseline airplane with a passive system (increases in structural stiffness). The design, synthesis, and conceptual mechanization of the active system have been described. Results of this study indicate the following:

1. A substantial airplane weight saving can be accomplished by using the active flutter suppression system rather than the passive system. This weight saving is about 4151 kg (9150 lbm).

2. For the same payload and range, the use of the active flutter suppression system decreases the direct operating costs as compared with the passive system airplane. For a 3000-nautical-mile trip, this saving is about 2 percent. The major factors contributing to this reduction are lower fuel costs and depreciation.

3. For the same payload, the range of the active system airplane can be increased about 186 n. mi. over that of the passive system airplane by absorbing the weight savings as additional fuel.

4. For the same range, the payload of the active system airplane can be increased over that of the passive system airplane by absorbing the weight savings as additional payload.

317

REFERENCES

1. Turner, M. J.; and Bartley, J. B.: Flutter Prevention in Design of the
    SST. Symposium on Dynamic Response of Structures, Stanford University,
    Stanford, California, June 28-29, 1971.

2. Robinson, James C.; Yates, E. Carson, Jr.; Turner, M. Jonathan; and
    Grande, Donald L.: Application of an Advanced Computerized Structural
    Design System to an Arrow-Wing Supersonic Cruise Aircraft. AIAA Paper
    No. 75-1038, Aug. 1975.

3. Sakata, I. F.; and Davis, G. W.: Substantiating Data for Arrow-Wing
    Supersonic Cruise Aircraft Structural Design Concepts Evaluation.
    Volume 2. (Lockheed-California Co.; NASA Contract NAS1-12288) NASA
    CR-132575-2, 1976.

4. Sobieszczanski, Jaroslaw; McCullers, L. Arnold; Ricketts, Rodney H.;
    Santoro, Nick J.; Beskenis, Sharon D.; and Kurtze, William L.:
    Structural Design Studies of a Supersonic Cruise Arrow-Wing Configura-
    tion. Proceedings of the SCAR Conference, NASA CP-001, 1977.
    (Paper no. 31 of this compilation.)

5. Shomber, Henry A.; and Hollaway, Richard B.: Advanced Controls for
    Commercial Transport Aircraft. SAE Paper No. 740453, April-May 1974.

6. Schoenman, R. L.; and Shomber, H. A.: Impact of Active Controls on Future
    Transport Design, Performance, and Operation. SAE Paper No. 751051,
    Nov. 1975.

7. Cohen, Gerald C.; Cotter, Clifford J.; and Taylor, Donald L.: Use of
    Active Control Technology to Improve Ride Qualities of Large Transport
    Aircraft. Advanced Control Technology and Its Potential for Future
    Transport Aircraft. NASA TM X-3409, Aug. 1976, pp. 373-407.

8. Bisplinghoff, Raymond L.; Ashley, Holt; and Halfman, Robert L.: Aero-
    elasticity. Addison-Wesley Pub. Co., Inc., c. 1955.

9. Pepping, R. A.: A Theoretical Investigation of the Oscillating Control
    Surface Frequency Response Technique of Flight Flutter Testing.
    J. Aeronaut. Sci., Vol. 21, No. 8, Aug. 1954, pp. 533-542.

10. Theisen, J. G.; and Robinette, W. C.: Servo Control of Flutter. ASME/
    AIAA 10th Structures, Structural Dynamics, and Materials Conf.,
    New Orleans, Louisiana, April 1969.

11. Thompson, G. O.; and Kass, G. J.: Active Flutter Suppression — An Emerg-
    ing Technology. J. Aircraft, Vol. 9, No. 3, March 1972, pp. 230-235.

12. Rainey, A. Gerald; Ruhlin, Charles L.; and Sandford, Maynard C.: Active
    Control of Aeroelastic Response. Stability and Control, AGARD CP-119,
    1972, pp. 16-1 — 16-5.

318

13. Topp, L. J.: Potential Performance Gains by Use of a Flutter Suppression System. Paper No. 7-B3, 1971 Joint Automatic Control Conference, St. Louis, Missouri, Aug. 1971.

14. Sevart, Frank D.: Analysis of Aeroelastic Model Stability Augmentation Systems. Doc. D3-8390-4, Boeing Co., Mar. 1971. (Available as NASA CR-132354.)

15. Nissim, E.: Flutter Suppression Using Active Controls Based on the Concept of Aerodynamic Energy. NASA TN D-6199, 1971.

16. Sevart, F. D.; Patel, S. M.; and Wattman, W. J.: Analysis and Testing of Stability Augmentation Systems — Final Report. Doc. D3-8884, Boeing Co., June 1972. (Available as NASA CR-132349.)

17. Triplett, William E.: A Feasibility Study of Active Wing/Store Flutter Control. J. Aircraft, Vol. 9, No. 6, June 1972, pp. 438-444.

18. Hodges, Garold E.: Active Flutter Suppression — B-52 Controls Configured Vehicle. AIAA Paper No. 73-322, Mar. 1973.

19. Noll, Thomas E.; and Felt, Larry R.: Active Flutter Suppression — A Practical Application. Proceedings of National Aerospace Electronics Conference 1973, IEEE, May 1973, pp. 329-334.

20. Lyons, M. G.; Vepa, R.; McIntosh, S. C., Jr.; and DeBra, D. B.: Control Law Synthesis and Sensor Design for Active Flutter Suppression. AIAA Paper No. 73-832, Aug. 1973.

21. Sevart, Francis D.; and Patel, Suresh M.: Analysis and Testing of Aeroelastic Model Stability Augmentation Systems — Final Report. Doc. D3-9245, Boeing Co., Oct. 1973. (Available as NASA CR-132345.)

22. Triplett, W. E.; Kappus, H. P. F.; and Landy, R. J.: Active Flutter Control — An Adaptable Application to Wing/Store Flutter. J. Aircraft, Vol. 10, No. 11, Nov. 1973, pp. 669-678.

23. Abel, Irving; and Sandford, Maynard C.: Status of Two Studies on Active Control of Aeroelastic Response. NASA TM X-2909, 1973.

24. Buchek, Philip M.: Modern Control Techniques in Active Flutter Suppression Using a Control Moment Gyro. SUDAAR No. 474, Stanford Univ., Mar. 1974. (Available as NASA CR-138494.)

25. Cwach, Emil; and Stearman, Ronald O.: Suppression of Flutter on Interfering Lifting Surfaces by the Use of Active Controls. AIAA Paper No. 74-404, April 1974.

26. Roger, Kenneth L.; Hodges, Garold E.; and Felt, Larry.: Active Flutter Suppression — A Flight Test Demonstration. AIAA Paper No. 74-402, April 1974.

27. Gregory, R. A.; Ryneveld, A. D.; and Imes, R. S.: A Low Speed Model Analysis and Demonstration of Active Control Systems for Rigid-Body and Flexible Mode Stability. Fed. Aviation Adm. Report FAA-SS-73-18, June 1974.

28. Redd, L. T.; Gilman, J., Jr.; Cooley, D. E.; and Sevart, F. D.: Wind-Tunnel Investigation of a B-52 Model Flutter Suppression System. J. Aircraft, Vol. 11, No. 11, Nov. 1974, pp. 659-663.

29. Nissim, E.: Flutter Suppression and Gust Alleviation Using Active Controls. TAE Rep. No. 198, Technion-Israle Inst. Technol., 1974. (Available as NASA CR-138658.)

30. Turner, M. R.: Active Flutter Suppression. AGARD CP-175, April 1975, pp. 2-1 — 2-14.

31. Thompson, G. O.; and Sevart, F. D.: Wind Tunnel Investigation of Control Configured Vehicle Systems. Flutter Suppression and Structural Load Alleviation, AGARD CP-175, April 1975, pp. 4-1 — 4-8.

32. Destuynader, Roger: Essai en Soufflerie d'un Suppresseur de Flottement sur une Aile Droite Flutter Suppression and Structural Load Alleviation. AGARD CP-175, April 1975, pp. 6-1 — 6-3.

33. Nissim, E.: Active Flutter Suppression Using Trailing-Edge and Tab Control Surfaces. AIAA Paper No. 75-822, May 1975.

34. Roger, Kenneth L.; Hodges, Garold, E.; and Felt, Larry: Active Flutter Suppression — A Flight Test Demonstration. J. of Aircraft, Vol. 12, No.   , June 1975, pp. 551-556.

35. Sandford, Maynard C.; Abel, Irving; and Gray, David L.: Development and Demonstration of a Flutter-Suppression System Using Active Controls. NASA TR-450, 1975.

36. Noll, R. B.; and Marino, L.: Flutter and Gust Response Analysis of Flexible Aircraft With Active Control. Proceedings of AIAA/ASME/SAE 17th Structures, Structural Dynamics, and Materials Conference, King of Prussia, Pennsylvania, May 5-7, 1976, pp. 389-397.

37. Doggett, Robert V., Jr.; Abel, Irving; and Ruhlin, Charles L.: Some Experiences Using Wind-Tunnel Models in Active Control Studies. Advanced Control Technology and Its Potential for Future Transport Aircraft. NASA TM X-3409, Aug. 1976, pp. 831-892.

38. Arnold, James I.; and Murphy, Frank B.: B-52 Control Configured Vehicles: Flight Test Results. Advanced Control Technology and Its Potential for Future Transport Aircraft. NASA TM X-3409, Aug. 1976, pp. 75-89.

39. Nissim, E.; Caspi, A.; and Lottati, I.: Application of the Aerodynamic Energy Concept to Flutter Suppression and Gust Alleviation by Use of Active Controls. NASA TN D-8212, 1976.

40. Johannes, R. P.: Active Flutter Control — Flight Test System Synthesis. Paper No. 7-B1, 1971 Joint Automatic Control Conference, St. Louis, Missouri, Aug. 1971.

41. Hood, R. V.: A Summary of the Application of Active Controls Technology in the ATT System Studies. Advanced Control Technology and Its Potential for Future Transport Aircraft. NASA TM X-3409, Aug. 1976, pp. 603-637.

42. Pratt, Kermit G.: A Survey of Active Controls Benefits to Supersonic Transports. Advanced Control Technology and Its Potential for Future Transport Aircraft. NASA TM X-3409, Aug. 1976, pp. 639-659.

43. Hoffman, Sherwood: Supersonic Cruise Aircraft Research (SCAR) Program Bibliography. NASA TM X-73950, 1976.

44. Woodward, Frank A.: Analysis and Design of Wing-Body Combinations at Subsonic and Supersonic Speeds. J. Aircraft, Vol. 5, No. 6, Nov.-Dec. 1968, pp. 528-534.

45. Albano, E.; and Rodden, W. P.: A Doublet-Lattice Method for Calculating Lift Distributions on Oscillating Surfaces in Subsonic Flows. AIAA Journal, Vol. 7, No. 2, Feb. 1969, pp. 279-285. (Errata, Vol. 7, No. 11, Nov. 1969, p. 2192.)

46. Fuel Conservation Possibilities for Terminal Area Compatible Aircraft. (Boeing Commercial Airplane Company; NASA Contract NAS1-12018), NASA CR-132608, 1975.

TABLE I.- SOME CHARACTERISTICS OF ARROW-WING CONFIGURATION

CRUISE MACH NUMBER	2.7
NUMBER OF CREW MEMBERS	3
NUMBER OF ENGINES	4
THRUST PER ENGINE	235 756 N (53 000 lbf)
MAXIMUM TAKEOFF GROSS WEIGHT	339 287 kg (748 000 lbm)
NUMBER OF FIRST CLASS SEATS	0
NUMBER OF TOURIST SEATS	234
PAYLOAD	22 226 kg (49 000 lbm)
MAXIMUM LANDING WEIGHT	217 724 kg (480 000 lbm)
AIRFRAME STRUCTURAL WEIGHT	
PASSIVE SYSTEM AIRPLANE	101 605 kg (224 000 lbm)
ACTIVE SYSTEM AIRPLANE	97 454 kg (214 850 lbm)
DIFFERENCE	4 151 kg (9 150 lbm)
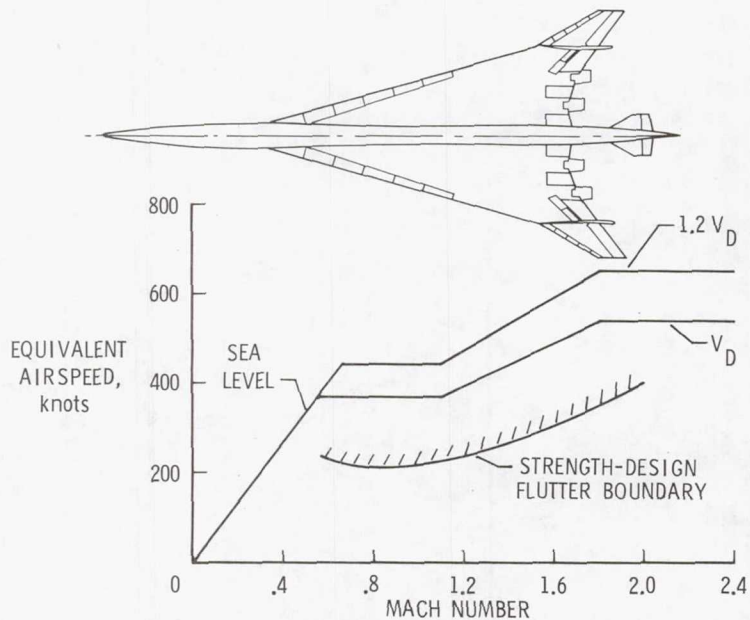
Figure 1.- Strength-design national configuration flutter boundary.
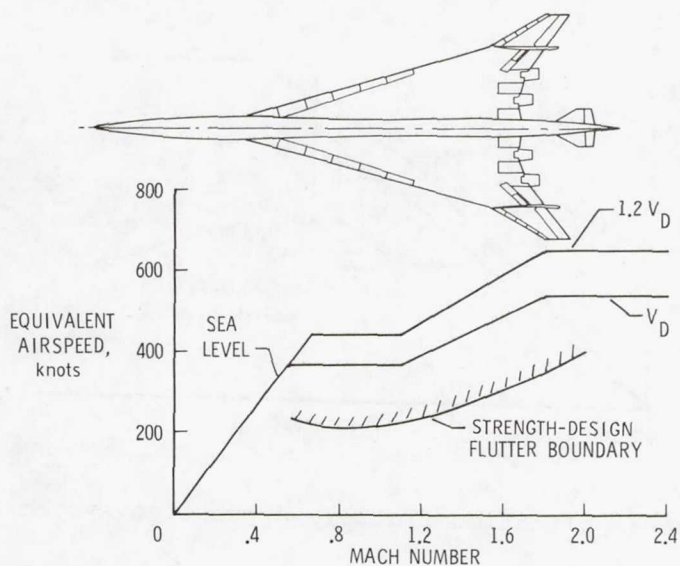
Figure 2.- Strength-design arrow-wing flutter boundary.
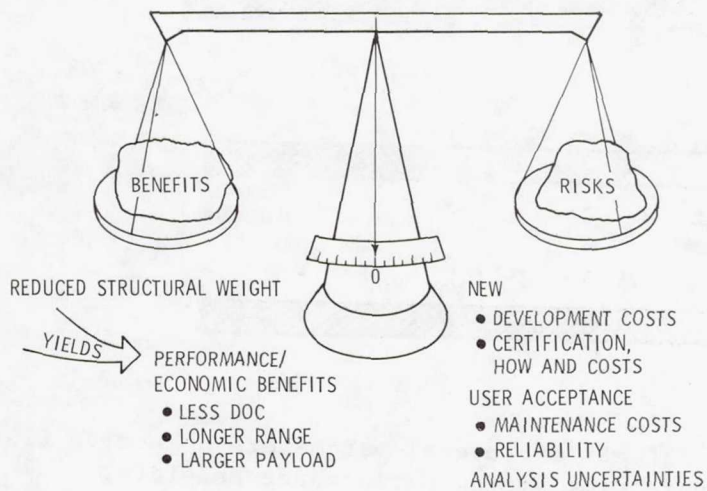
Figure 3.- Benefits and risks of active flutter suppression.
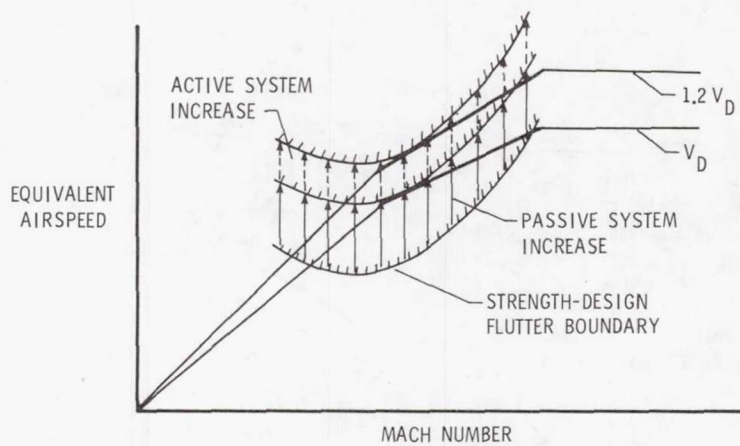
Figure 4.- Limited application flutter suppression system concept.
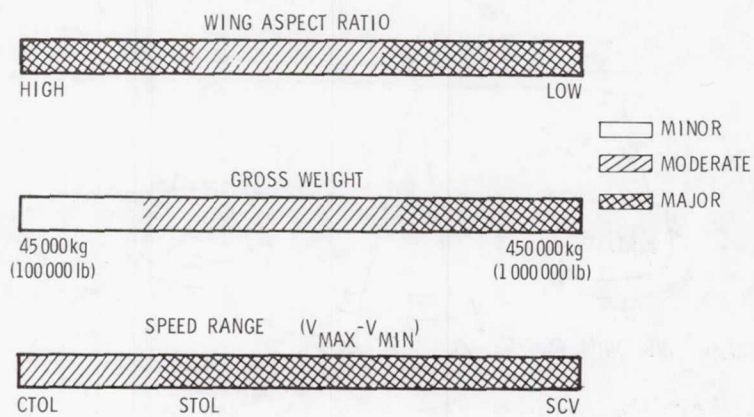
Figure 5.- Effects of several parameters on active flutter
suppression system performance benefits.

324
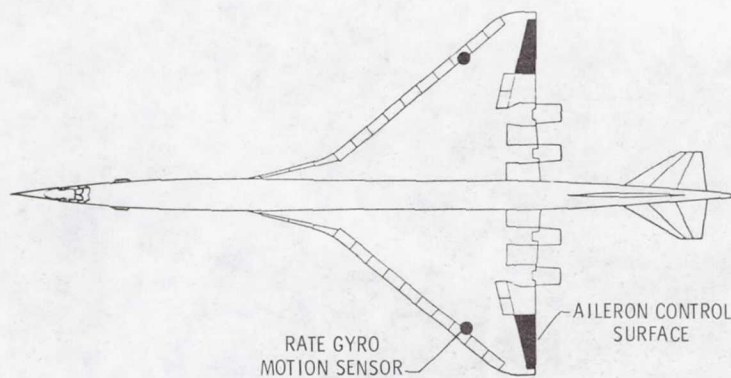
Figure 6.- National configuration active flutter suppression system.
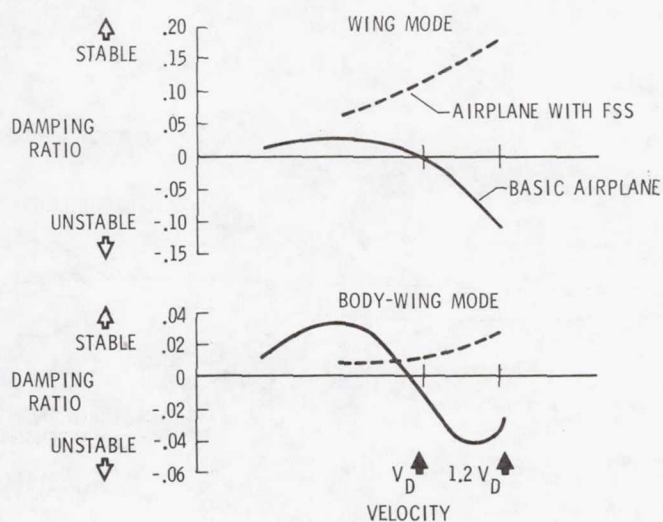
Figure 7.- Calculated active flutter suppression system results
for national configuration (M = 0.90).
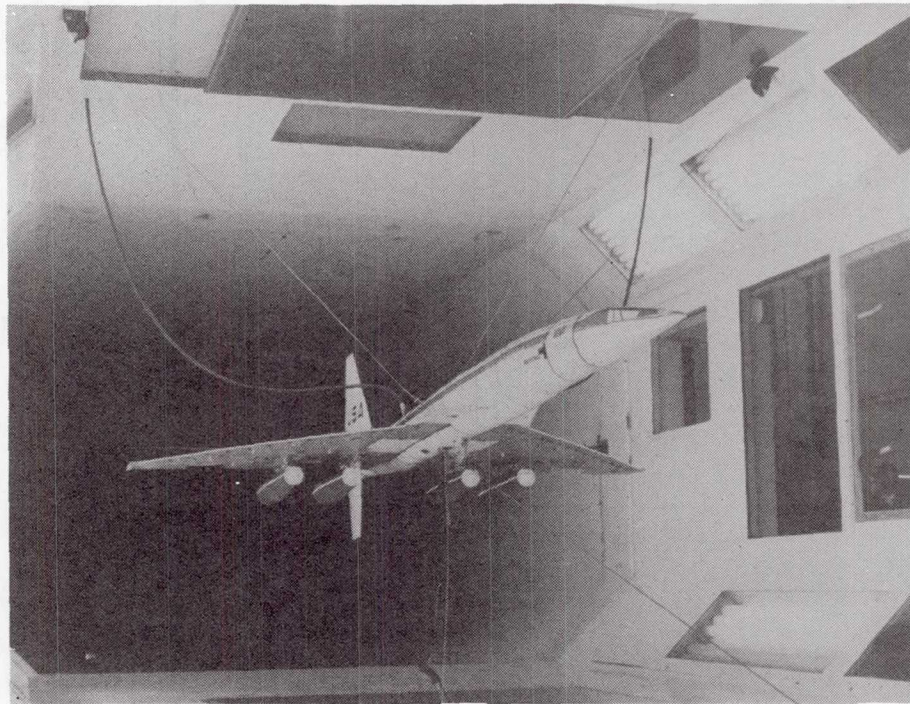
Figure 8.- Low-speed active flutter suppression model
mounted in wind tunnel.
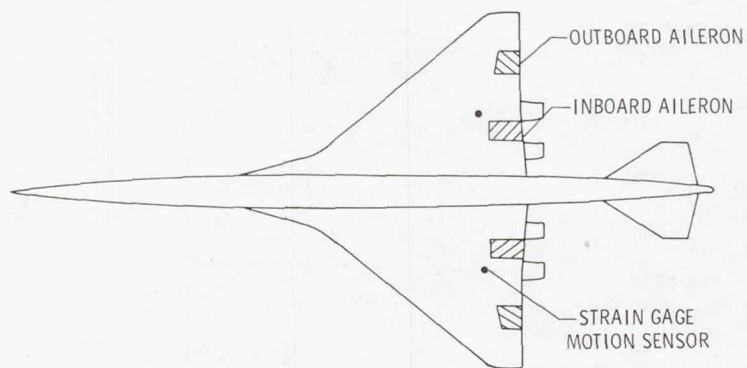
Figure 9.- Low-speed model active flutter suppression systems.

326
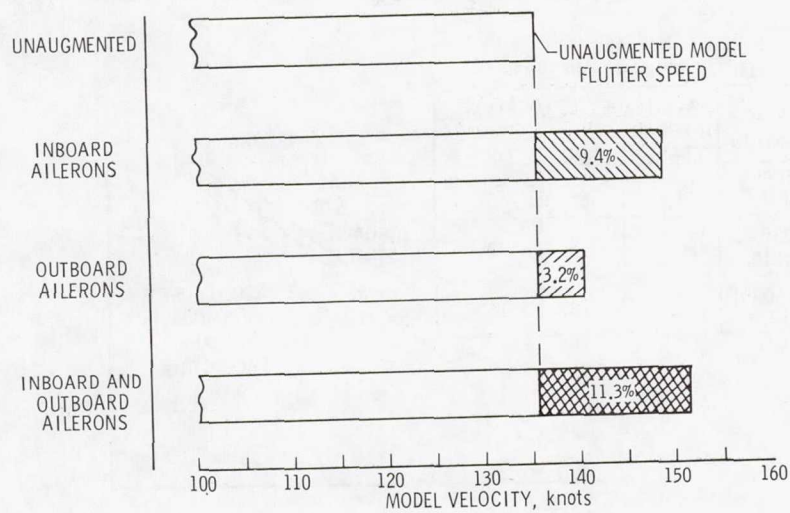
Figure 10.- Experimental results for low-speed active flutter suppression model.
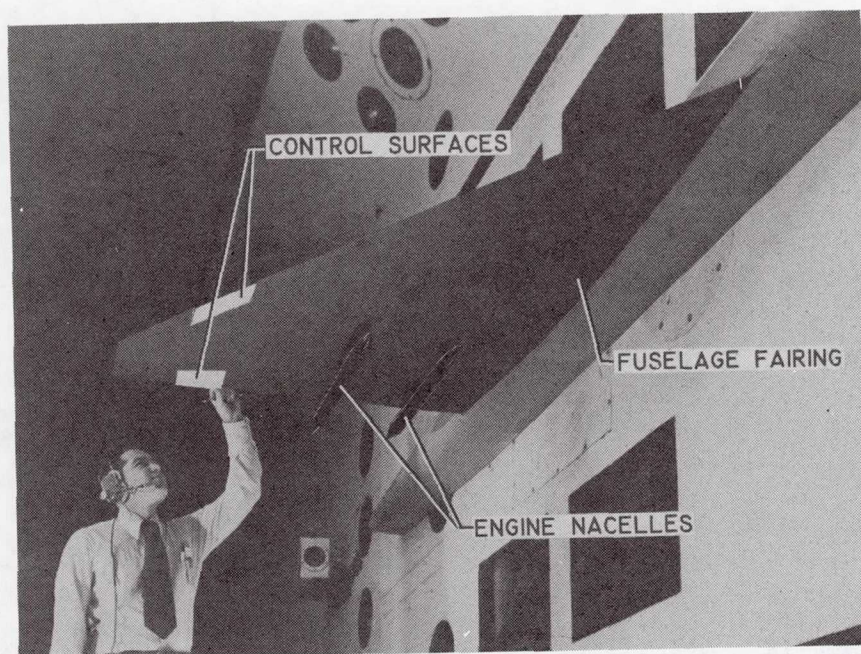
Figure 11.- Delta-wing active flutter suppression model mounted in wind tunnel.

327

PERCENT INCREASE IN
FLUTTER DYNAMIC PRESSURE

SURFACE LOCATION	ACCELEROMETER LOCATION		
	INBOARD EDGE	CENTER LINE	OUTBOARD EDGE
INBOARD STRIP	18	22	21
MIDSPAN STRIP	26	17	8
OUTBOARD STRIP	6	25	36
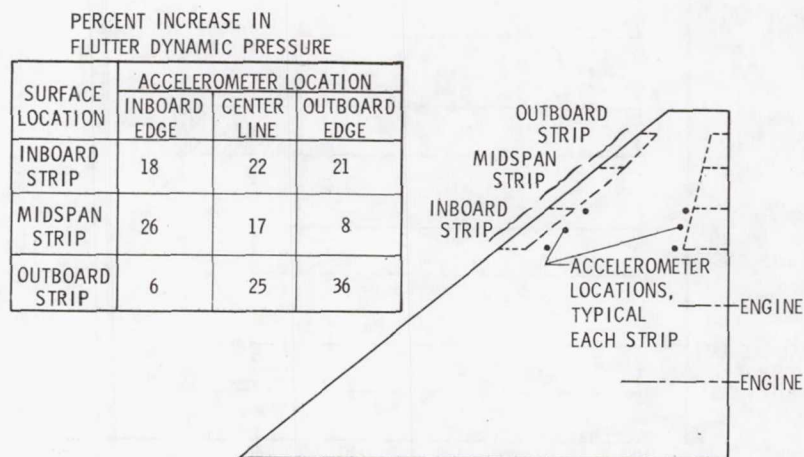
Figure 12.- Calculated effects of control surface and
accelerometer locations on delta-wing model flutter
dynamic pressure.
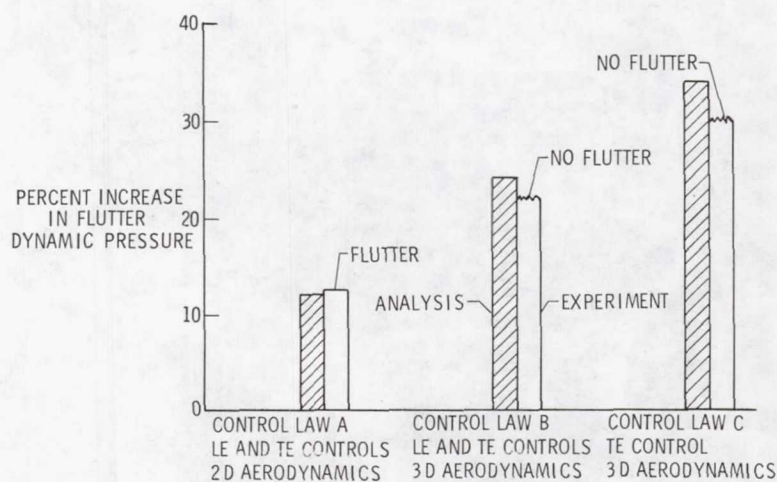
Figure 13.- Experimental and calculated active flutter
suppression results for delta-wing model (M = 0.90).
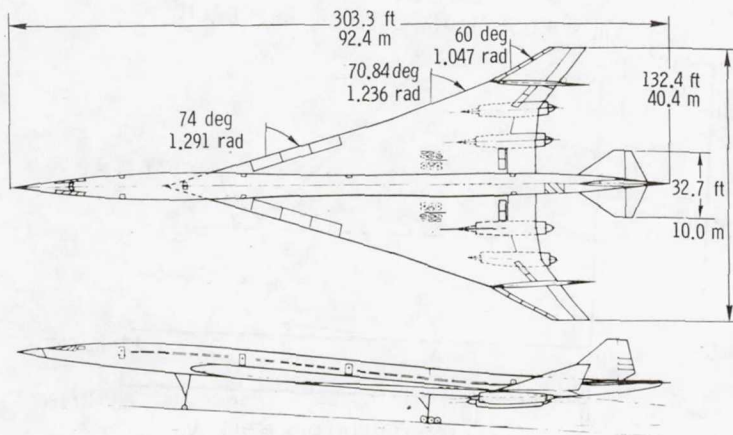
Figure 14.- Arrow-wing configuration.
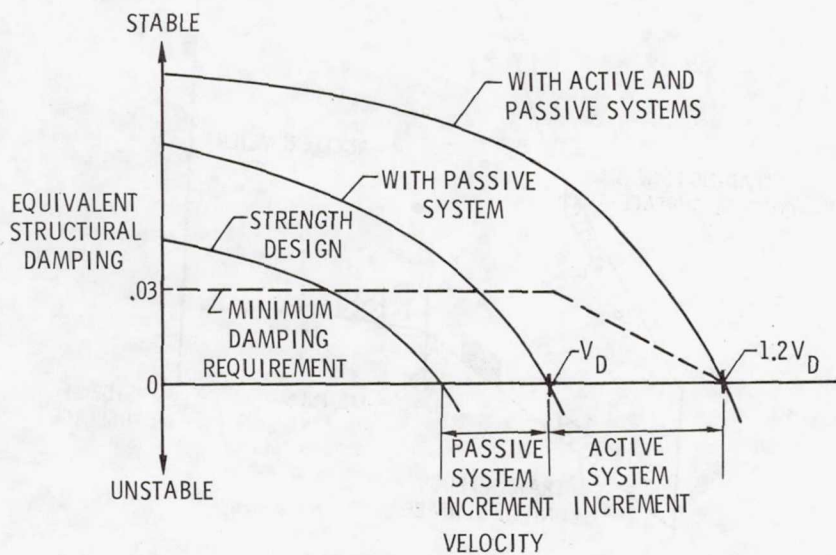
Figure 15.- Flutter design criteria for arrow-wing active
flutter suppression system.

● FUNCTION IN TURBULENCE USED FOR DESIGN LOADS
● IN DESIGN TURBULENCE AT V_D, MAINTAIN 3%
   EQUIVALENT STRUCTURAL DAMPING IN
   CRITICAL MODES
● USE DESIGN ENVELOPE APPROACH
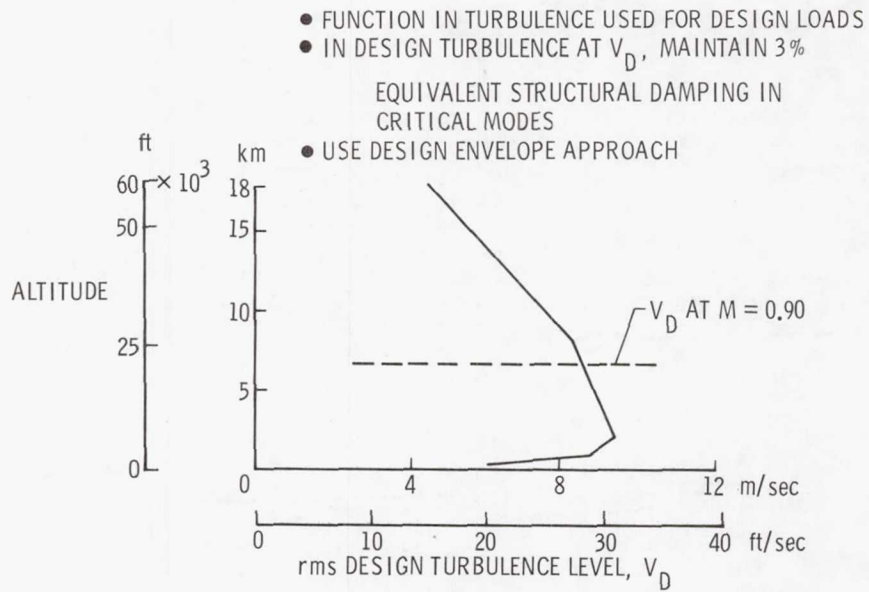
Figure 16.- Turbulence design criteria for arrow-wing active
flutter suppression system.
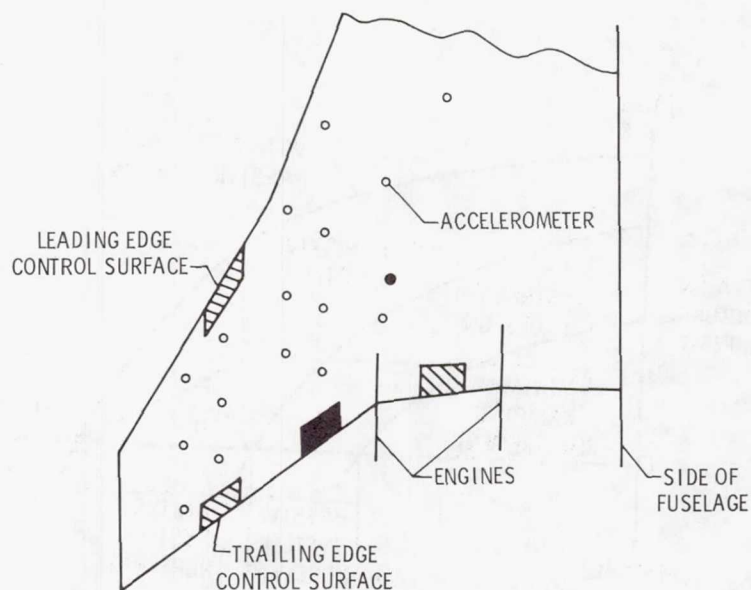
Figure 17.- Control surface and accelerometer locations
surveyed during synthesis of arrow-wing active flutter
suppression system.
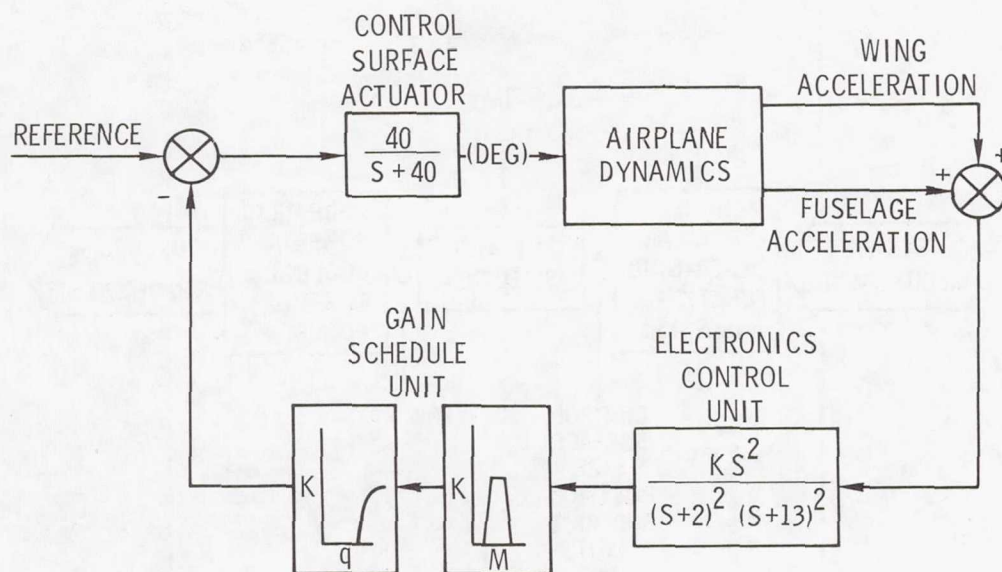
Figure 18.- Block diagram of arrow-wing active flutter
   suppression system. K denotes gain and S is the
   Laplace variable.
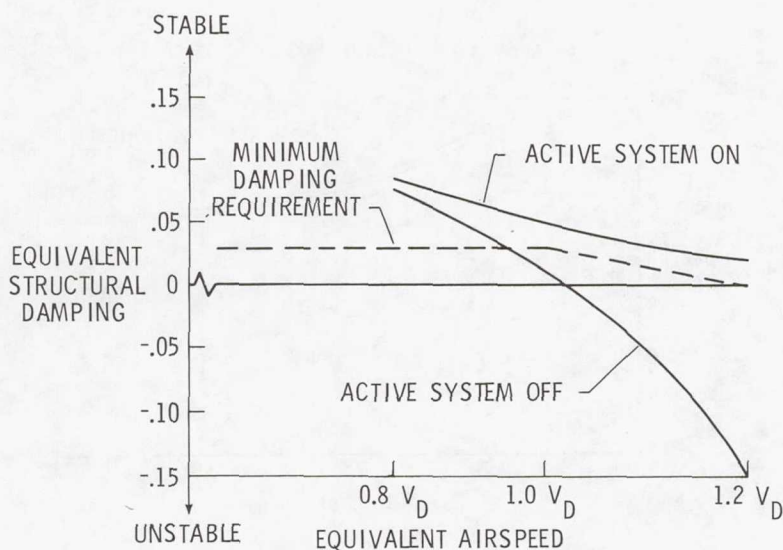
Figure 19.- Calculated variation of damping in critical
   flutter mode with equivalent airspeed for arrow-wing
   flutter suppression system on and off (M = 0.90).
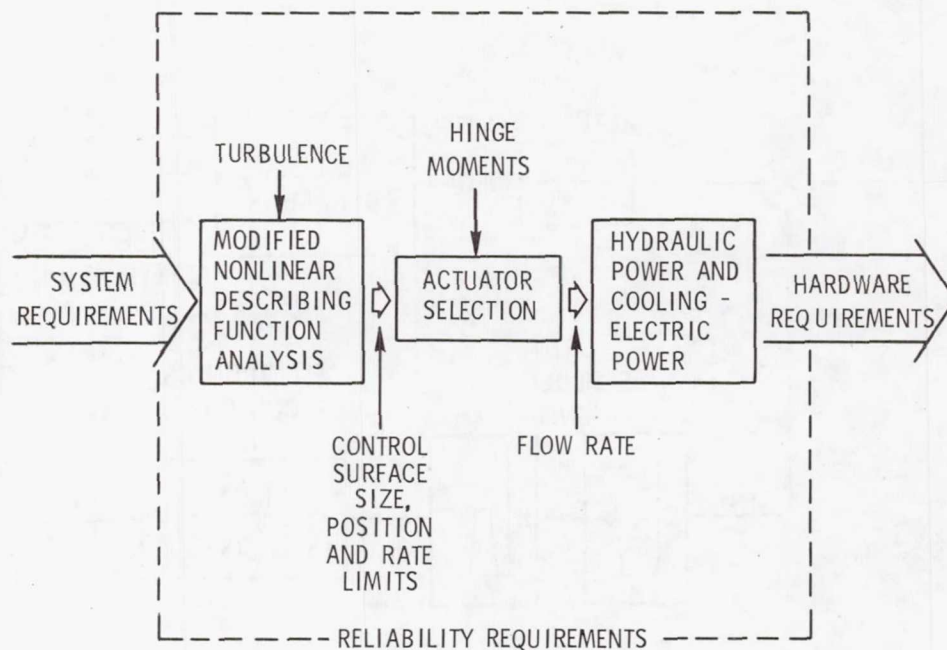
Figure 20.- Mechanization of arrow-wing active flutter
suppression system.
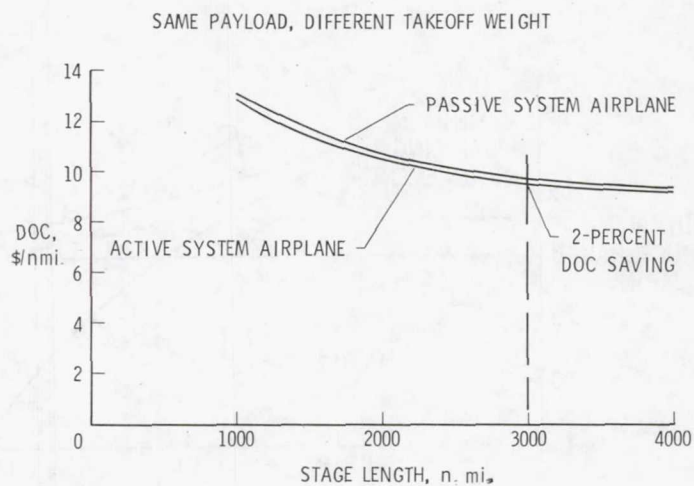
Figure 21.- Variation of direct operating costs (DOC) with
stage length for active system airplane and passive
system airplane.

3000 n.mi. TRIP
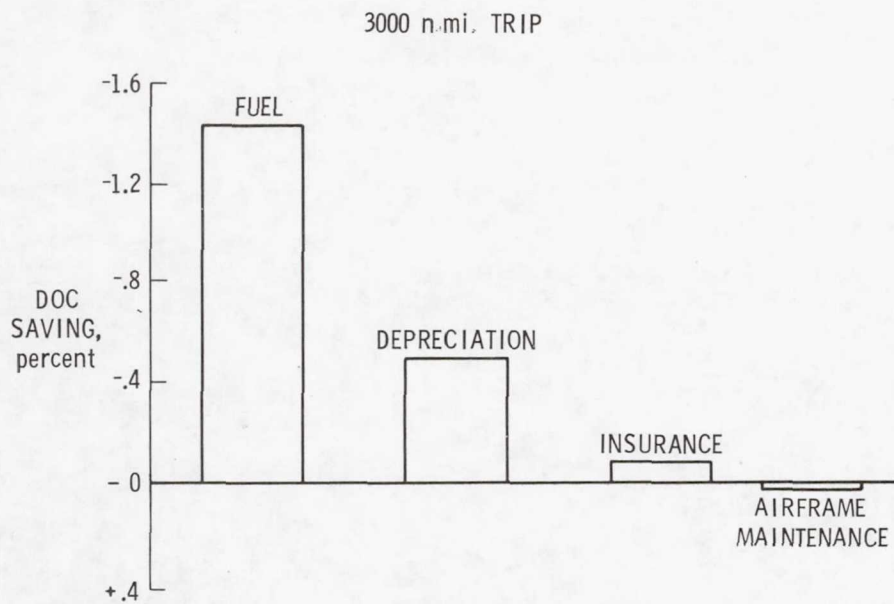
Figure 22.- Contributions of fuel, depreciation, insurance,
and airframe maintenance costs to change in direct
operating costs (DOC).

Page intentionally left blank

SESSION III - PROPULSION

Page intentionally left blank

INTRODUCTION

Warner L. Stewart
NASA Lewis Research Center

The major attributes of a commercial supersonic cruise aircraft are
closely related to the characteristics of the propulsion system. This is
obviously true of the environmental factors of noise and exhaust emissions,
which are direct products of the engines. Additionally, the propulsion
system weight (including fuel) constitutes the largest single fraction of
the airplane gross weight. As a result, the airplane size and operating
economics are critically dependent on such engine parameters as specific
fuel consumption and thrust-weight ratio.

The normal difficulties of selecting an optimum engine design are com-
pounded by the wide range of operating conditions for a supersonic airplane.
For example, if we trace through a typical mission (fig. 1), the engine must
provide adequate takeoff thrust with a minimum of weight and without exceeding
allowable noise and pollution limits; it must climb, accelerate, and possibly
cruise subsonically with good efficiency; it must cruise supersonically with
very good efficiency, again without exceeding pollution limits; hold and
other reserve requirements at the end of the flight again place a premium
on subsonic efficiency.

Some of the engine design conflicts that arise from such a mission are
indicated in figure 2. For good subsonic efficiency, we would desire a high-
bypass-ratio turbofan, such as is used in modern wide-body transports. But
for good supersonic efficiency, we prefer a low-bypass-ratio engine, approach-
ing a turbojet. Also, for low jet noise we would prefer an engine with low
jet velocity at takeoff; however, the turbojet-type engine tends to have high
jet velocity. Conflicts such as these have led to interest in the concept of
a variable-cycle engine, that is, an engine that can vary its mode of opera-
tion during flight in order to best suit the needs of each particular flight
segment.

Figure 3 outlines the structure of the NASA research program that is
aimed at providing the technology base that is needed for a successful propul-
sion system design. First, there is an ongoing baseline program in all the
various disciplines affecting engine design. Much of this baseline activity
is applicable to any engine type, subsonic or supersonic. Supplementing this
general research is the more focused work under SCAR, which is directed at
the unique problems of supersonic flight. Included here is research on noise
and pollution reduction (covered in detail in Session IV - Environmental
Factors), inlet stability, engine studies, and materials. On the basis of
the results of the baseline and SCAR research, we are now initiating the
Component Test Program, which will experimentally study some of the unique
components and/or operating conditions on a larger scale than was previously
accomplished. A possible follow-on to this phase would be an actual experi-
mental engine.

A major part of the SCAR program has been the engine studies. As shown in figure 4, these started in 1973 with a very broad examination of a large number of conventional and variable-cycle concepts. In the later years attention was focused in greater and greater detail on a smaller number of surviving concepts. The identification of favored concepts was accomplished with the assistance of the various airframe system study contractors. Also, the engine studies helped to identify the technology deficiencies that were addressed in the other SCAR research programs. And in turn, the results of those programs were incorporated in the studies as they became available.

The first two papers in this session summarize the engine studies that were performed by General Electric and Pratt & Whitney under contract to NASA. The next paper describes the Component Test Program that will experimentally investigate some key aspects of the engine concepts identified by the studies. The remaining four papers discuss in general terms progress in some of the major technologies that are relevant to supersonic propulsion system design.
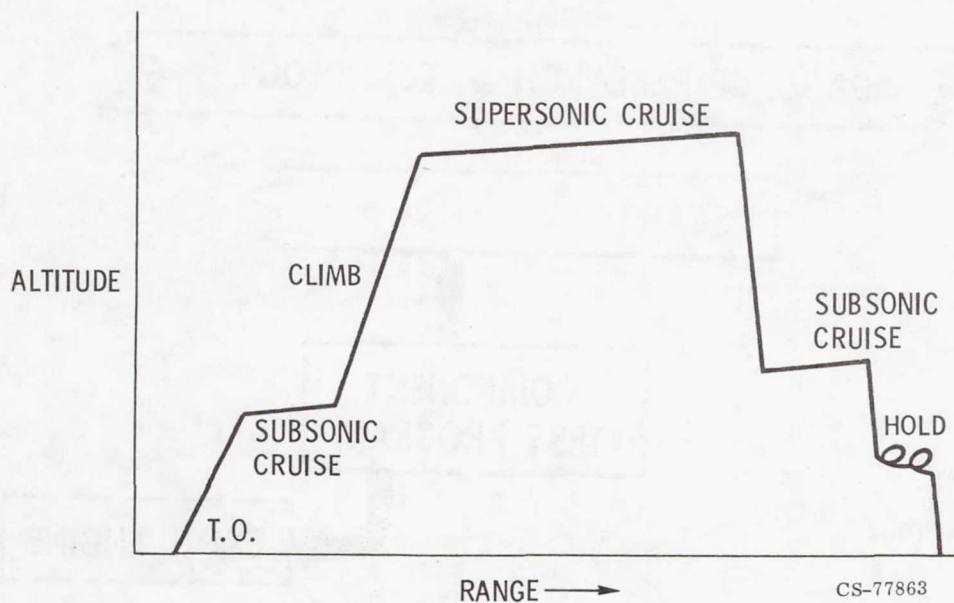
Figure 1.- Supersonic transport mission profile.
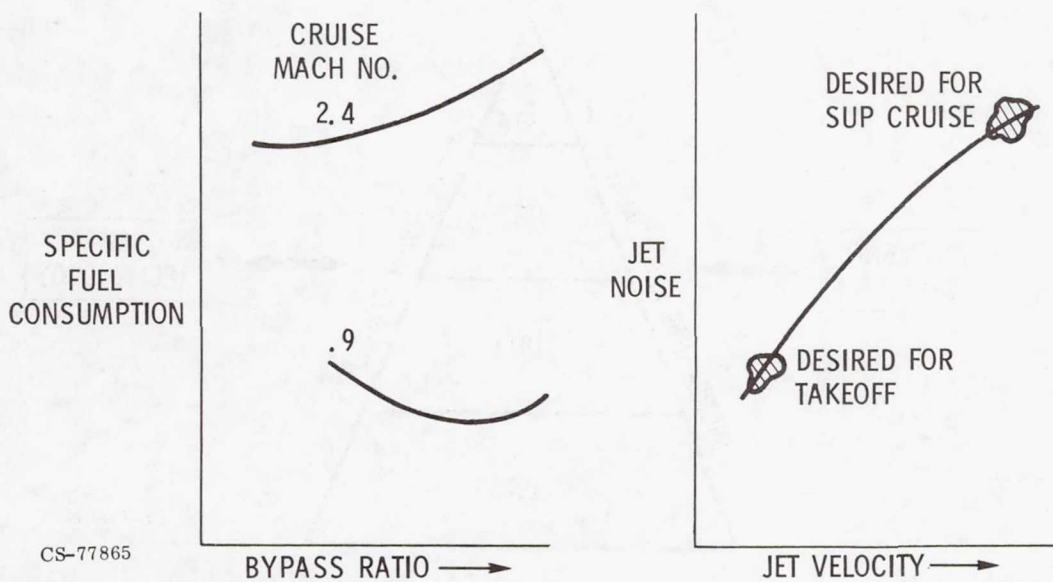
Figure 2.- Factors in engine design.
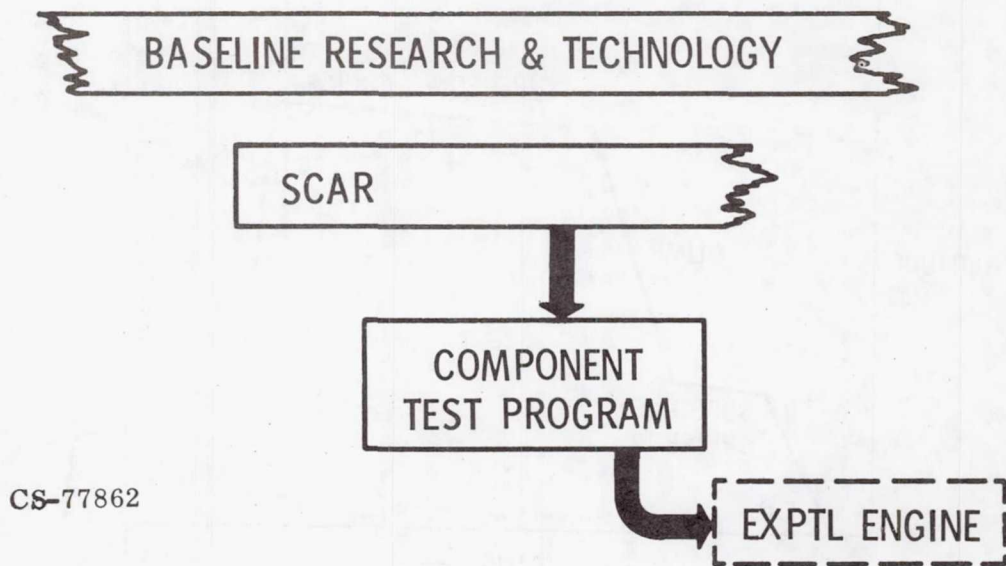
Figure 3.- Supersonic propulsion research program.
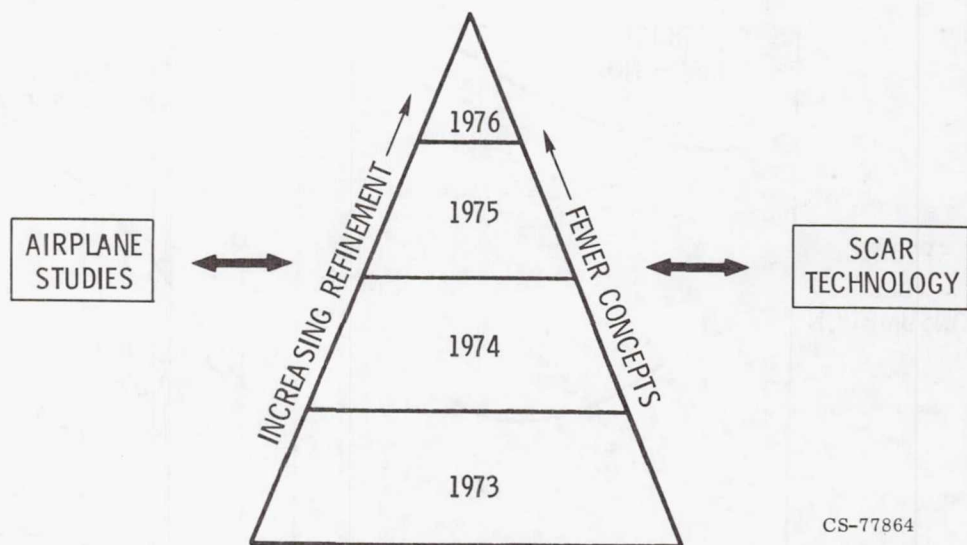
Figure 4.- Evolution of engine studies.

340

VARIABLE STREAM CONTROL ENGINE CONCEPT FOR ADVANCED

SUPERSONIC AIRCRAFT – FEATURES AND BENEFITS

Robert A. Howlett
Pratt & Whitney Aircraft Group

SUMMARY

The Variable Stream Control Engine being studied for advanced supersonic cruise aircraft shows potential for significant environmental and performance improvements relative to first-generation supersonic turbojet engines. This engine concept has two separate flow streams — each with independent burner and nozzle systems. By unique control of the exhaust temperatures and velocities in these two coannular streams, significant reduction in jet noise may be obtained. This engine has the potential for other major improvements, including matching the engine flow schedule with the inlet airflow at critical operating points, improved stability, and a less severe thermal environment for the thrust augmentor and nozzle/reverser systems. Technology programs are required to qualify and demonstrate these potential improvements. The most critical programs are: expanded configuration testing and large-scale noise tests of coannular nozzles, and experimental evaluation of advanced combustor concepts for the duct burner.

INTRODUCTION

The National Aeronautics and Space Administration (NASA) is engaged in studies of advanced technology for future supersonic commercial aircraft, with emphasis on improving environmental and economic characteristics. As part of this overall program, Pratt & Whitney Aircraft (P&WA) is conducting advanced propulsion studies which are directed toward three basic objectives:

- Evaluation of a variety of conventional and unconventional engine types, in terms of environmental and economic factors,

- Identification of engine concepts that warrant further study. These studies include engine/airframe integration evaluation, and an assessment of the impact of advanced technology,

- Direction of critical technology programs so that a data base can be established for guiding future supersonic engine design decisions.

The time frame for this study program is consistent with advanced technology projections that would provide the capability for a U.S. entry into the commercial supersonic aircraft market by the late 1980's or early 1990's. The engine definitions and related technology requirements described herein would, therefore, be applicable to second-generation supersonic cruise aircraft.

The approach for this on-going study program has been to conduct broad parametric studies of many types of conventional and unconventional engine concepts. These parametric engines were evaluated, compared, and screened on the basis of environmental and economic characteristics. The most promising concepts were then selected for further evaluation including refinement studies and preliminary design.

Over 100 different engine types and configurations have been studied and evaluated in this program. The broad scope of the study is indicated by the general types of configurations illustrated in figure 1. Shown are cross-sections (top half only) of some of the conventional and unconventional engines that were evaluated. Several of the variable cycle engine configurations have very significant improvements relative to first-generation supersonic engines. The advanced engine configuration identified as having the greatest potential is the Variable Stream Control Engine (VSCE).

The potential improvements provided by the advanced VSCE concept relative to first-generation supersonic engines are shown in table 1. The 8 dB reduction in take-off noise results from the use of a coannular nozzle with an inverted velocity profile. The 25 percent weight improvement results from the two-stream engine configuration, where as much airflow bypasses the engine core as passes through it, thereby reducing the size and weight of the engine core, and also from advanced technology components. The 20 percent lower fuel consumption at subsonic cruise is due to the VSCE engine operating as a conventional turbofan at these conditions. The improvement in subsonic fuel consumption provided by the VSCE is particularly important, since the VSCE-powered supersonic aircraft will be capable of cruising substantial distances over land, where supersonic operation may be prohibited by sonic boom noise constraints, without a loss in range capability. At supersonic cruise conditions, the VSCE fuel consumption is approximately three percent higher than that of the turbojet because of cycle differences.

The overall potential of the VSCE on advanced supersonic aircraft performance is very significant, as shown in figure 2. The VSCE offers both a 25 percent improvement in airplane range, and an 8 dB reduction in noise during take-off. Significant improvements in the enonomic characteristics of advanced supersonic aircraft will also be provided by the VSCE.

DESCRIPTION OF VARIABLE STREAM CONTROL ENGINE (VSCE)

The advanced VSCE concept employs variable geometry components and a unique throttle schedule for independent control of two flow streams to provide reduced jet noise at take-off and high performance at both subsonic and supersonic cruise. Figure 3 shows the basic arrangement of the major engine components. It has a twin spool configuration similar to a conventional turbofan engine. The low spool consists of an advanced technology, multi-stage, variable geometry fan and low pressure turbine. The high spool consists of a variable geometry compressor driven by an advanced single-stage high temperature turbine. The primary burner and the duct-burner require low emissions, high efficiency combustor concepts. The nozzle is a two stream, concentric, annular (coannular) design with variable throat areas in both streams and an ejector/reverser exhaust system.

The independent temperature and velocity control for both primary and bypass streams provides an inherent reduction in jet noise during take-off. This noise reduction characteristic is based on an inverse velocity profile, where the bypass stream jet velocity is 60 to 70 percent higher than the primary stream velocity. Results from a P&WA model nozzle test program sponsored by NASA indicate that noise levels measured for coannular nozzles with this inverted velocity profile are approximately 8 EPNdB (effective perceived noise level in dB) lower than a single-stream nozzle operating at the same airflow and thrust levels. These results are based on both static tests and wind-tunnel tests simulating take-off flight conditions. Based on these model tests, the coannular noise benefit represents a breakthrough in jet noise control. Further evaluation — a large-scale demonstration of this noise benefit — is in the planning stage.

CRITICAL OPERATING CONDITIONS

The variability of the VSCE concept to meet the diverse requirements of low jet noise and good fuel consumption at both supersonic and subsonic cruise, can be illustrated best by describing the three most critical operating conditions: take-off, supersonic cruise, and subsonic cruise.

Take-Off

Figure 4a depicts the unique inverted velocity profile for take-off operation. As indicated, the primary stream is throttled to an intermediate power setting so that the jet noise associated with the primary stream is low. To provide both the required take-off thrust, and the inverse velocity profile, the duct-burner is operated at its maximum design temperature of approximately $1430°C$ ($2600°F$). It is this condition that sets the cooling requirements for the duct-burner and nozzle system. Relative to military engine augmentor systems, which approach stoichiometric combustion, the peak duct-burner temperatures for the VSCE are relatively low, and will not compromise the life capability of this commercial engine.

Supersonic Cruise

For supersonic operation, the VSCE primary burner temperature is increased (relative to take-off), and the high spool speed and flow rate are matched to the higher primary burner temperature. This matching technique is referred to as the inverse throttle schedule (ITS) - inverse relative to conventional subsonic engines which cruise at much lower temperatures and spool speeds than they require for take-off conditions. This ITS feature enables matching the high spool to a higher flow rate at supersonic conditions relative to a conventional turbofan. In effect, this high-flow condition reduces the cycle bypass ratio. The level of thrust augmentation required for the duct-burner during supersonic operation can therefore be reduced. At this condition, the exhaust temperature from the coannular streams are almost equal and, as shown in Figure 4b, the velocity profile is flat, to provide optimum propulsive efficiency. The resulting VSCE fuel consumption characteristics approach those of a turbojet cycle designed exclusively for supersonic operation. The ITS feature enables sizing the VSCE propulsion system for optimum supersonic cruise performance, while also meeting FAR Part 36 noise levels at the other end of the operating spectrum, by means of the coannular noise benefit.

Subsonic Cruise

For subsonic cruise operation, the main burner is throttled to a low temperature ($<1090°C$ ($<2000°F$)), and the VSCE operates like a moderate bypass ratio turbofan. Exhaust conditions for this third critical operating point are shown in figure 4c. The variable geometry components are matched to "high-flow" the engine, so that the inlet airflow and the engine airflow can be matched almost exactly. This greatly reduces inlet spillage and bypass losses, and also improves nozzle performance by working with the ejector to fill the nozzle exhaust area at this part-power condition. This reduces boat-tail drag. In this subsonic mode of operation, the VSCE has low fuel consumption that approaches performance levels of turbofan engines designed strictly for subsonic operation.

INLET/ENGINE AIRFLOW MATCHING

A special feature of the VSCE concept is its capability to match inlet/engine airflow at critical operating points. Figure 5 shows the mass flow ratio for a representative, axisymmetric, mixed-compression inlet as a function of Mach number. Also shown is a band that represents various engine airflow schedules for the VSCE. These different schedules can be obtained with only minor changes to the engine design. This band of engine airflow schedules indicates the flexibility of the engine to match installations for the advanced airplane designs being evaluated in the SCAR program. The various engine schedules indicated by the band in figure 5 allow each installation to be optimized for the best balance between subsonic and supersonic characteristics. The bottom half of the band in figure 5 corresponds to engines with high ratios of supersonic/subsonic airflow. The top half corresponds to low ratios. Relative to an engine that is matched exactly to the inlet airflow schedule, the bottom of the band represents an engine match that reduces fuel consumption at supersonic cruise (more engine airflow - less augmentation). However, this improvement is gained at the expense of subsonic performance (larger inlet resulting in a small installation loss). The top half of the band represents an engine matched for a more efficient airplane design at supersonic cruise (higher lift-to-drag ratio — reduced thrust requirements), but with some additional complexity to the inlet (such as the requirement for more variable geometry) to accommodate the relative increase in engine flow requirements at subsonic cruise.

As an indication of the improvement in the inlet/engine flow-matching capability of the VSCE, the subsonic cruise airflow level for the first-generation supersonic turbojet engine is also shown in figure 5. The subsonic airflow schedule differences between these two engines is shown in figure 6 over a range of thrust levels. The VSCE schedule maintains higher levels of airflow as it is throttled back to part-power operation, such as for subsonic cruise. As indicated in figure 6, the VSCE can handle significantly higher airflow than the first-generation turbojet engine at subsonic cruise. This improves installed performance of the VSCE by essentially eliminating inlet spillage at subsonic cruise.

The high-flow capability shown in figure 6 is also beneficial during take-off when designing the system for low jet noise. By maintaining maximum engine airflow at part-power take-off operation, jet velocity (which is directly proportional to the ratio of thrust/airflow) can be minimized. In this manner, high flowing complements the coannular noise benefit during take-off.

VSCE STABILITY FEATURES

The VSCE concept includes design features which provide the potential for improved stability characteristics of the overall propulsion system.

The VSCE compression system incorporates variable fan and compressor stators for optimizing performance while maintaining stability margins over the entire flight envelope. Improved sensors and increased control accuracy and logic provide high performance for the fan and compressor, including surge line and operating line control, self-trim, and efficiency. A key stability and performance feature of the compressor is an active tip clearance control system.

The primary burner and duct-burner have two-zone fuel flow distribution systems. The fuel flow zone split varies with power setting to provide smooth lighting, continuous zone transfer, and low emissions. An augmentor light-off/flame-out detector in conjunction with integrated Mach number control of the augmentor fuel flow and duct nozzle provides improved stability during both augmented and non-augmented operation.

Continuously variable primary and duct nozzles provide improved stability, in addition to matching the engine with the inlet airflow, and controlling jet noise. This variable nozzle geometry, in conjunction with improved sensors, provides sufficient flexibility to tune the propulsion system for component variations associated with manufacturing tolerances or from deterioration and transient effects.

Because of the extensive use of variable geometry components, a full authority digital electronic control system is a critical requirement for the VSCE concept. Current technology hybrid hydromechanical/supervisory electronic control systems are not adequate for this engine. The advanced electronic control system provides computational capability, closed-loop feed-back safety and accuracy, and self trim/test capability.

This advanced electronic control will be integrated with the aircraft control system to realize total aircraft performance, stability, and safety advantages. Features of this integration will include performance-seeking control modes to minimize cruise fuel consumption, propulsion control resets for varying flight conditions to insure adequate stability margins, and automatic recovery from distrubances caused by transients or other operational problems.

CRITICAL TECHNOLOGY REQUIREMENTS AND PROGRAMS

To realize the potential benefits shown in figure 2 for the VSCE concept, the critical technologies listed in table 2 will be required. The programs needed to substantiate these technologies over the next ten years are shown in figure 7. There are five basic programs:

1. Feasibility demonstration of those components most critical to the success of the VSCE using small-scale rig tests. These components include the low-emissions duct burner, the main burner, and the coannular nozzle.

2. Evaluation of the critical technology duct burner and coannular nozzle in large-scale tests in an engine environment.

3. Substantiation testing of demonstrator engine components.

4. Substantiation of the VSCE concept by demonstrator engine testing.

5. Studies of the integrated propulsion system, involving both the airplane and engine manufacturers.

Programs 1 through 4 would be conducted sequentially, with the small rig tests preceding the large-scale component and engine tests. This is a low risk approach where the preliminary testing and screening is accomplished in relatively inexpensive component rigs. The integration study must be conducted by both the airplane and engine manufacturers concurrent with the engine technology programs. This is necessary to ensure that all of the interfaces are appropriately understood and resolved, and that the propulsion system design is tailored to give the best overall airplane performance and economics. These technology programs would bring us to the point where a full-scale supersonic engine development program could be initiated.

CONCLUSION

In conclusion, the advanced VSCE concept with its coannular nozzle has been identified as having the best combination of performance and noise characteristics. This engine has promise of making significant environmental and economic improvements to advanced supersonic aircraft. Establishing technology readiness for this engine is a formidable challange, both technically and financially, and NASA-sponsored programs will have a dominant effect on the eventual timing and success of advanced supersonic aircraft.

TABLE 1

IMPROVEMENT PROVIDED BY VARIABLE STREAM CONTROL ENGINE RELATIVE TO FIRST-GENERATION SUPERSONIC TURBOJET ENGINE

Take-off noise	8 dB reduction
Engine weight	25 percent reduction
Specific fuel consumption at	
Subsonic cruise	20 percent reduction
Supersonic cruise	3 percent increase

Note: Comparisons made by scaling first-generation turbojet engine to flow size of variable stream control engine

TABLE 2

CRITICAL TECHNOLOGY REQUIREMENTS FOR VSCE CONCEPT

- Low noise – high performance coannular nozzle

- Low-emissions – high efficiency burner systems

- Variable geometry components
  - Nozzle/ejector/reverser
  - Inlet
  - Fan
  - Compressor

- High temperature burners and turbines with commercial life

- Integrated propulsion system

- Electronic control system

FRONT-VALVE VCE

DUAL-VALVE VCE

REAR-VALVE VCE

LOW BYPASS ENGINES

TURBOFAN ENGINES

SEPARATE ENGINES
FOR TAKE-OFF
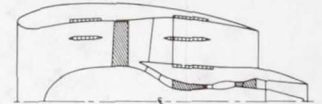
VARIABLE STREAM
CONTROL ENGINES

SUPERSONIC
FAN ENGINES

AUGMENTED WING
CONCEPT
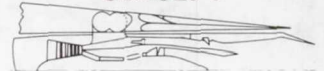
INTERCOOLING PLUS
REHEAT CYCLES
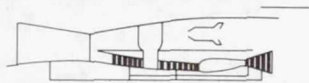
TURBOFAN RAMJET
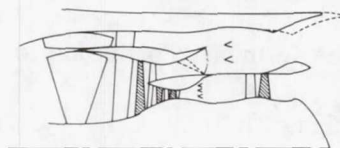
Figure 1.- Types of engines evaluated.

ADVANCED SUPERSONIC TRANSPORT TAKE-OFF
GROSS WEIGHT = 345,600 kg (762,000 lbm)
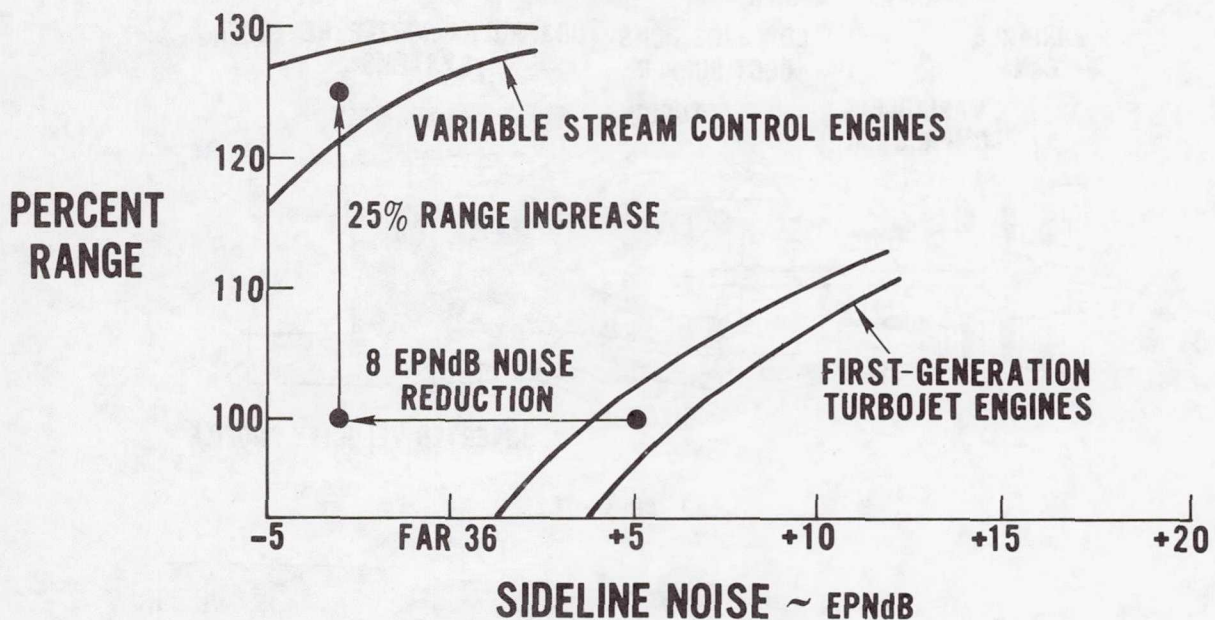
Figure 2.- Potential impact of advanced supersonic technology on
aircraft range and noise.
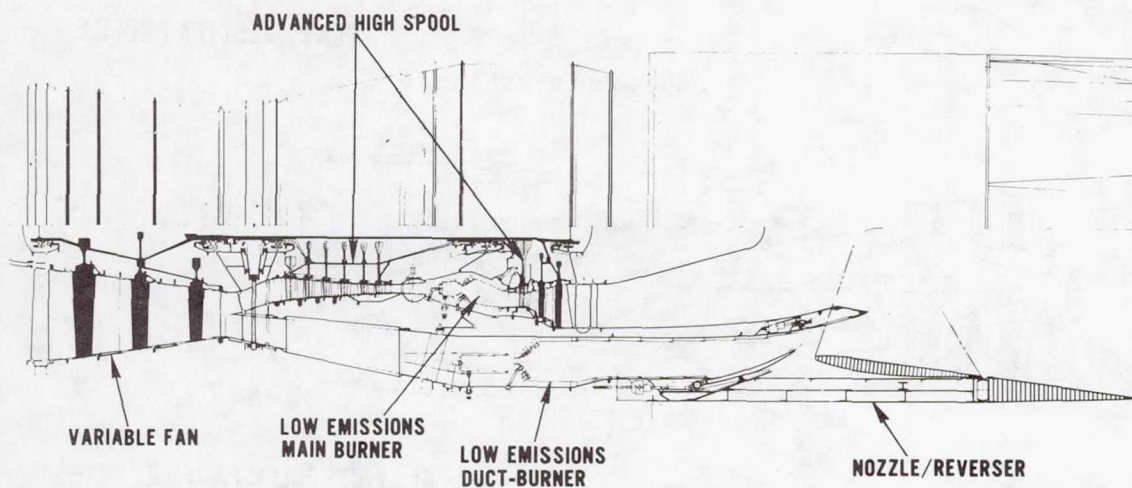
Figure 3.- Variable stream control engine cross-section.

LOW EMISSIONS
PRIMARY BURNER

VARIABLE   LOW EMISSIONS   COANNULAR NOZZLE/REVERSER
FAN   DUCT BURNER   SYSTEMS

VARIABLE   TURBINE
COMPRESSOR

EJECTOR   INVERTED VELOCITY PROFILE

(a) Take-off.

FLAT VELOCITY PROFILE

(b) Supersonic cruise.

EJECTOR
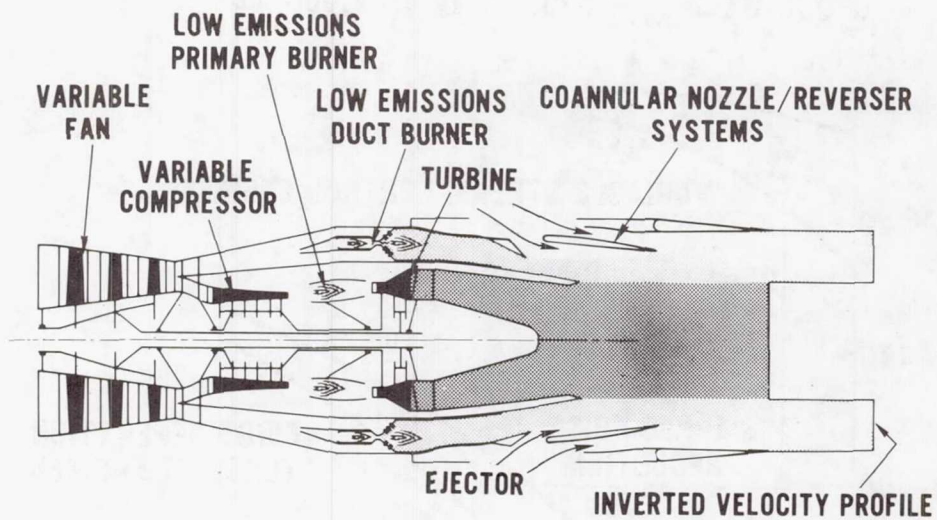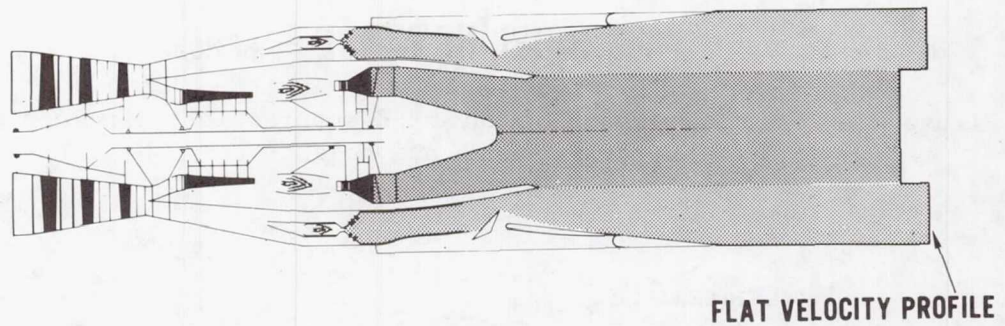
FLAT VELOCITY PROFILE
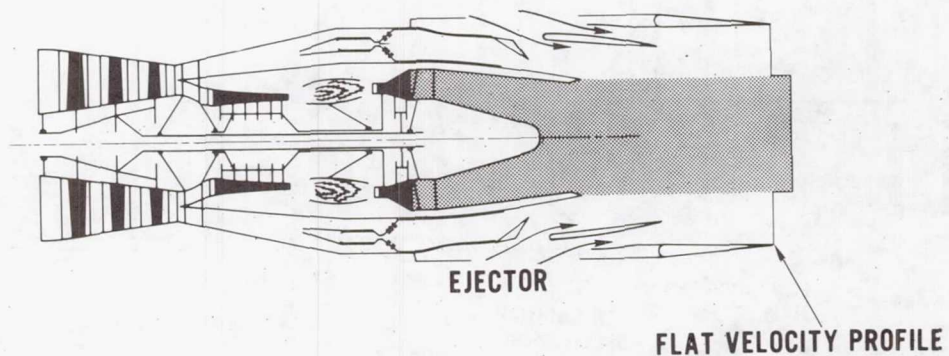
(c) Subsonic cruise.

Figure 4.- Variable stream control engine at critical operating conditions.

350
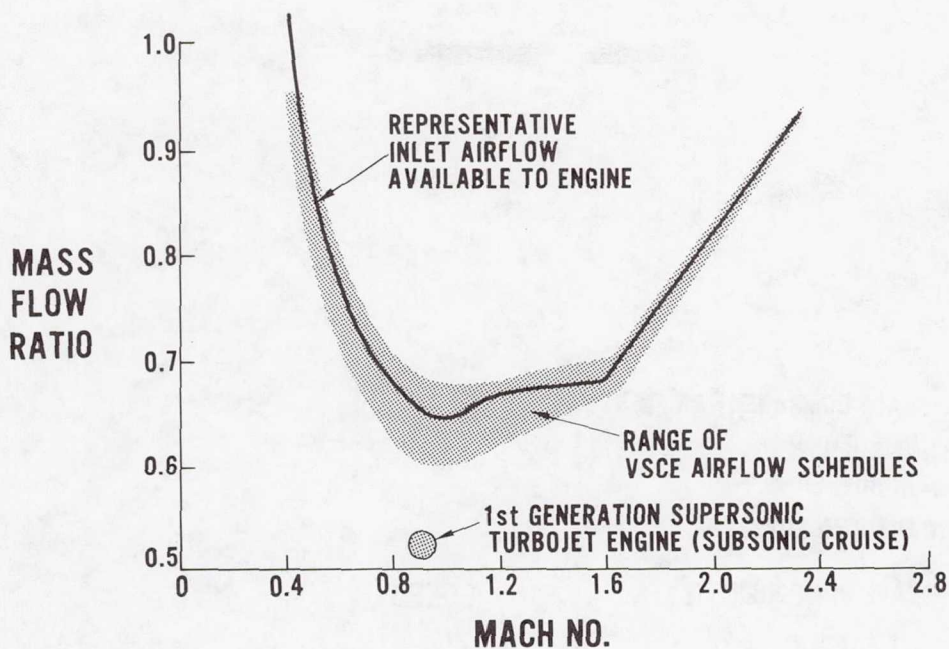
Figure 5.- Mass flow ratio versus Mach number for a representative supersonic inlet and for the VSCE.
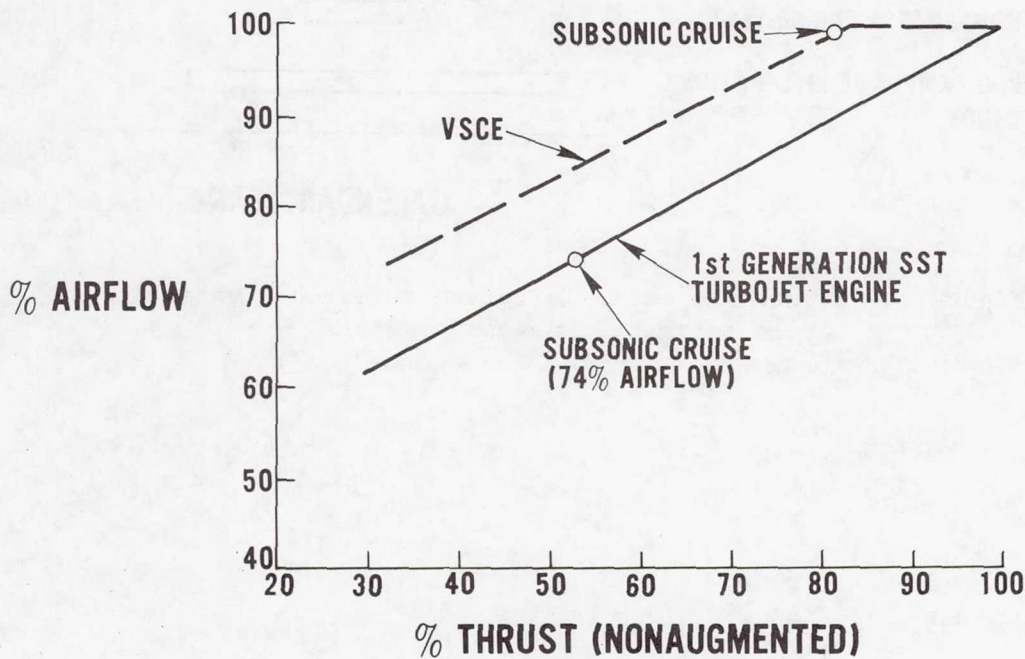
Figure 6.- High-flowing capability of VSCE relative to first-generation supersonic turbojet engine.

351

1. SMALL-SCALE COMPONENT RIG TESTS
   DUCT BURNER
   MAIN BURNER
   COANNULAR NOZZLE

2. LARGE-SCALE COMPONENT TESTS
   DUCT BURNER
   COANNULAR NOZZLE

3. DEMONSTRATOR ENGINE COMPONENT
   SUBSTANTIATION

4. DEMONSTRATOR ENGINE TEST

5. ENGINE/AIRFRAME INTEGRATION
   STUDY

75   80   85   90

CALENDAR YEAR
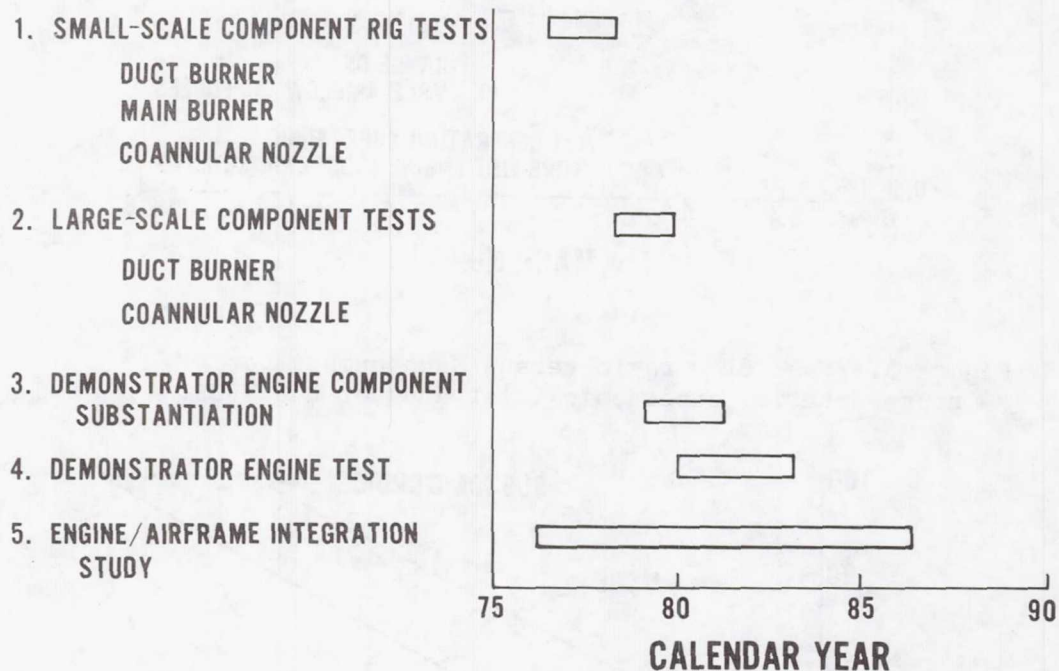
Figure 7.- Supersonic cruise airplane research - variable
cycle engine technology programs.

ADVANCED SUPERSONIC TECHNOLOGY STUDY

ENGINE PROGRAM SUMMARY

SUPERSONIC PROPULSION - 1971 to 1976

J. N. Krebs
General Electric Company

SUMMARY

Sustained supersonic rruise propulsion systems for military applications
have been developed by General Electric since the early 1950's. The J79-5 in
the Mach 2 B-58; YJ93 in the Mach 3.0 B-70 and the current F101 in the B-1,
are all examples of military propulsion systems and airplanes operated at sus-
tained supersonic cruise speeds.

The Mach 2.7 B2707 transport powered by GE4 turbojet engines was the only
non-military, sustained supersonic cruise vehicle intended for commercial pas-
senger service. The cancellation of the B2707 and GE4 programs in 1971 ended
hardware development effort.

In 1972 NASA initiated study programs to identify the required propulsion
system and airplane technology necessary for an environmentally acceptable
supersonic cruise vehicle. The Advanced Supersonic Propulsion System Tech-
nology Studies at General Electric screened conventional turbojets, mixed
flow and duct burning turbofans and variable cycle engines. This resulted in
the selection of a Variable Cycle Engine (VCE) concept that provides high air-
flow for low take off noise levels, using a coannular acoustic exhaust nozzle,
and a cruise airflow matched to the airplane inlet flow schedule. This VCE
has been refined and its mechanical design simplified to improve reliability
and maintainability. Technology predicted to be available for start of devel-
opment in 1985 is incorporated in the engine, as well as commercial life
requirements the same as used in the GE4 turbojets. The propulsion system
technology has improved to the point that definition of a second generation
supersonic cruise aircraft propulsion system much improved from the 1971 GE4
turbojet is now possible.

SYMBOLS

Values are given in both SI and U.S. Customary Units.

A/B   afterburner

M   flight Mach number

T/O	takeoff
VCE	variable cycle engine
SFC	specific fuel consumption
CO	oxides of carbon
HC	hydrocarbon
NO_X	oxides of nitrogen

DISCUSSION

The GE4 development program, up until its cancellation in 1971, had accumulated 1800 engine test hours on ten nameplate engines, with over 200 hours of simulated altitude operation at Mach 2.7 inlet conditions. Table I shows the GE4/J5 test engine cycle, and figures 1 and 2 show test engines prior to installation in the test cell and on test at the Peebles Test Center.

A cross section of the GE4/J5 engine is shown on figure 3. The engine is a single rotor afterburning turbojet with eleven turbomachinery stages, and uses a two stage ejector nozzle (TSEN) to pump secondary air for nacelle cooling. The GE4/J5 engine was designed for afterburning takeoff and supersonic cruise at Mach 2.7 using partial afterburning. The afterburning takeoff resulted in noise levels of approximately 120 EPNdb.

The environmental impact of the GE4/J5 afterburning turbojet in the B2707 airplane, noise levels, emissions, etc. became a major problem during the development program. Extensive studies resulted in the selection of the GE4/ J6H dry turbojet for the production engine configuration (see table II). The GE4/J6H was designed to come close to FAR 36 takeoff noise by providing a high takeoff airflow of 408 kg/sec (900 lbs/sec) at an exhaust velocity of 762 m/sec (2500 ft/sec) to meet the required takeoff thrust. Figure 4 shows a cross section of the GE4/J6H, which is similar to the GE4/J5P, that is, basic engine scaled up in airflow and increased turbine temperature, with a new annular plug exhaust system with a retractable 10 PNdb chute type mechanical jet noise suppressor, (see figure 5), and no afterburner system. The large airflow size provided the thrust required for dry power climb and acceleration and supersonic cruise, but the large engine size and weight reduced the range of the B2707 airplane.

At this point in the development of the engine and airplane, the program was cancelled.

In 1972, the National Aeronautics and Space Administration (NASA) sponsored study efforts by aircraft and engine manufacturers to identify needed technology for supersonic cruise vehicles aimed at the start of full scale development in the 1980-1985 time period. Under contracts from NASA Lewis

Research Center, General Electric has conducted Advanced Supersonic Propulsion System Technology Studies (AST). These studies have screened conventional and variable cycle concepts and combined features of both types into a variable cycle engine that has characteristics suited for sustained supersonic cruise, while also providing inlet flow matching capability over a wide range of airflows. The AST VCE is basically a low bypass ratio (0.35) dual rotor turbofan engine with a low temperature augmentor, designed for dry power supersonic cruise, using the afterburner for transonic climb and acceleration only. At takeoff conditions (see table III) the bypass ratio is almost twice the supersonic cruise level with airflow to provide acceptable FAR 36 noise levels and thrust. Figure 6 shows a schematic of the double bypass VCE concept. The basic differences between the VCE and a conventional turbofan engine are the separation of the fan into two blocks with an outer bypass duct between the fan blocks, and the normal bypass duct after the second fan block. For the low noise takeoff mode the front block of the fan is set at its maximum flow configuration. The second fan block is operated to tailor the jet exhaust velocity and flow to produce the desired thrust/noise relationships for takeoff. During subsonic cruise operation the front fan block is set to provide the best match between inlet spillage and internal performance. In this mode the second fan block is set to provide the proper cruise thrust. The inlet airflow can be maintained down to the required subsonic cruise thrust requirement, which practically eliminates inlet spillage drag, and because of the high flow also reduces the afterbody drag. The effect of the increased bypass ratio and reduction of installation drag decreases the installed specific fuel consumption (SFC) by about 15%.

In the climb/acceleration and supersonic cruise modes, the front block fan is set to meet the aircraft inlet flow supply, and the rear block fan and high pressure compressor are set to pass all of the front block fan flow, and the engine operates the same as the nominal 0.35 bypass ratio turbofan engine. An advantage of the split fan configuration, beyond its inlet matching capability, is that for high takeoff airflow, only the front block fan and low pressure turbine are affected, and a large weight saving is realized over the weight of a conventional turbofan engine sized for the same takeoff airflow and noise level.

A major effort has been made to simplify the engine and exhaust system to reduce cost and weight and increase reliability. The cycle was established for dry (non afterburning) takeoff and supersonic cruise, and to require only two turbine stages. The choice of mixed flow eliminates the need for a sophisticated high performance duct burner and requires only a very simple climb acceleration low temperature rise augmentor. The low bypass ratio mixed flow selection for supersonic operation also assures inlet compatibility. The introduction of the annular jet noise suppression concept on the VCE resulted in a simpler, lighter weight exhaust system with fewer movable parts and actuation systems. These and other improvements have resulted in a lighter, more reliable engine than the GE4 turbojets. A continuing effort on weight, cost reduction and increased reliability through simpler design will show further improvements in the future.

To compare the propulsion system advances from the GE4/J6H of 1971 to the

VCE of 1976, figure 7 compares the subsonic and supersonic fuel consumption and engine weight for the engines sized for the same takeoff noise level. The engines are installed in a Mach 2.4 cruise airplane of 1976 technology so that airplane characteristics are the same. The VCE has about 9% lower M2.4 fuel consumption than the GE4/J6H; about 22% lower subsonic (M0.95) cruise performance and a 25% lower weight. These differences can be attributed to:

Supersonic SFC

    Smaller VCE cruise airflow size - matched to aircraft
    Higher turbine temperature
    Improved component efficiencies and cooling technology

Subsonic SFC

    Cycle selection - higher bypass and cycle pressure
    ratio (M2.4 vs. M2.7)
    VCE features - minimum installation drag - inlet
    flow matching
    Smaller VCE cruise airflow size
    Improved component efficiencies

Engine Weight

    High flowed front block fan
    VCE bypass ratio
    Advanced nozzle concepts
    Advanced materials
    Higher turbine temperature

Figure 8 shows installation type outlines of the GE4/J5, GE4/J6H and the GE21/J11B3 VCE. It is apparent that the engine volume required to produce the required airflow has been greatly reduced. The reduction in cruise Mach number from M2.7 to M2.4 has eliminated the requirement to package the engine accessories for cooling. The smaller engine volume and the smaller advanced technology accessories should result in a smaller, lighter and lower drag nacelle.

The effect of the performance and weight advantages of the VCE can be seen in figure 9, which compares all supersonic cruise range at Mach 2.4 with engine takeoff airflow size. With both engines sized for FAR 36 noise levels, the VCE is much better matched to the airplane requirements, and operates at close to its optimum range. The GE4/J6H is not well matched, and its range is much lower than its optimum. Performance differences would account for about a 741 km (400 n.m.) range difference if both engines were sized to the optimum but the actual range difference is about 1296 km (700 n.m.) when sized at approximately the same takeoff airflow and FAR 36 noise level.

The VCE also offers even more advantages when subsonic cruise requirements are added, since the VCE reduces the subsonic installation drag and gives much better installed performance.

356

The VCE shows the potential of providing viable supersonic cruise range while also meeting takeoff and landing noise requirements with its high takeoff airflow capability and the annular acoustic plug nozzle. Another environmental consideration which had a major impact on the GE4/J6H and B2707 airplane is exhaust emissions around the airport and at high altitude supersonic cruise.

Figure 10 compares the emission levels of the 1971 GE4/J6H with the 1976 VCE. Major reductions in airport emission levels have been achieved; in fact, the VCE is predicted to meet the recently issued 1984 EPA Proposed Standards. Large reductions have been made in the altitude cruise NO_X emissions, but major combustor improvements must be made to approach the suggested Climatic Impact Assessment Program (CIAP) NO_X emission target of 3 g/kg fuel.

The double bypass VCE concept will require some real advancements over today's technology levels. Some of these are unique to the VCE, and others will apply to both military and commercial engines developed in the 1980-1990 time period.

The VCE concepts and features that provide performance advantages, such as inlet matching capability, reduction in installation drags, high takeoff airflow, can be demonstrated in a test bed engine program in the 1978-1980 time period. Other high payoff technology such as high turbine temperatures and improvements in component efficiencies must be demonstrated, and some programs are already underway which should contribute. A major technology item which impacts the VCE is the annular acoustic plug nozzle system. Static model testing has shown the potential for meeting noise requirements with the annular plug nozzle, but unknowns such as in flight effects, full scale test noise measurements, static and in flight at the high exhaust velocities required, may show the need for a back-up system with a 5-10 PNdb mechanical jet noise suppressor.

Commercial experience to date has shown the major impact of hot parts life on operating costs, and we are planning 100-200°C (200-400°F) higher turbine temperature than current commercial engines.

The cost of a supersonic propulsion system will be high. A major effort is required to reduce this cost by use of better, simpler designs, advanced materials and fewer parts.

The flexibility of the variable cycle engine introduces another dimension in engine control complexity. The number of control parameters is more than doubled over a conventional cycle engine. The use of a full authority digital electronic control (FADEC), integrated with the aircraft control system, will be a requirement. Programs are now underway on these types of engine control systems, but the AST VCE will have unique control requirements to fully exploit its flexibility of operation.

The current NASA Lewis Research Center Experimental Clean Combustor Program (ECCP) is showing the potential for solving the airport emission problem. The AST VCE uses the double annular combustor developed in this program and

meets the proposed 1984 EPA standards. The high altitude cruise NO_χ emissions require a new combustor technology to meet CIAP targets. These combustors will require major research and development effort to achieve a practical design which meets the engine operating requirements, and both airport and altitude cruise emission levels.

The major question, not yet answered is, if all of these technology goals are attained, can we have a commercial supersonic cruise vehicle which will make money for the airlines?

The answer to this question will require a continuing major effort to refine the variable cycle engine, and match the airplane and propulsion system in an integrated economically viable commercial transport.

358

TABLE I.- GE4/J5 M2.7 TURBOJET RESULTS

- **Thrust, N (lb)**   **311,360**   **(70,000)**

- **Airflow, kg/sec (lb/sec)**   **290**   **(640)**

- **Pressure Ratio**   **12.5**

- **Turbine Rotor-In Temp.,**   **1260**   **(2300)**
  °C (°F)

- **A/B Temperature, °C (°F)**   **1693**   **(3080)**

TABLE II.- GE4/J6H M2.7 TURBOJET

- **Thrust, N (lb)**   **328,722**   **(73,900)**

- **Airflow, kg/sec (lb/sec)**   **408**   **(900)**

- **Pressure Ratio**   **12.4**

- **Turbine Rotor-In Temp.,**   **1383**   **(2520)**
  °C (°F)

TABLE III.- AST-VCE M2.4

- **Airflow at T/O,** **380** **(840)**
  kg/sec (lb/sec)

- **Bypass at T/O** **0.8**

- **Pressure Ratio** **17.3**

- **Turbine Rotor-In Temp.,** **1538** **(2800)**
  °C (°F)

- **A/B Temperature, °C (°F)** **1038** **(1900)**
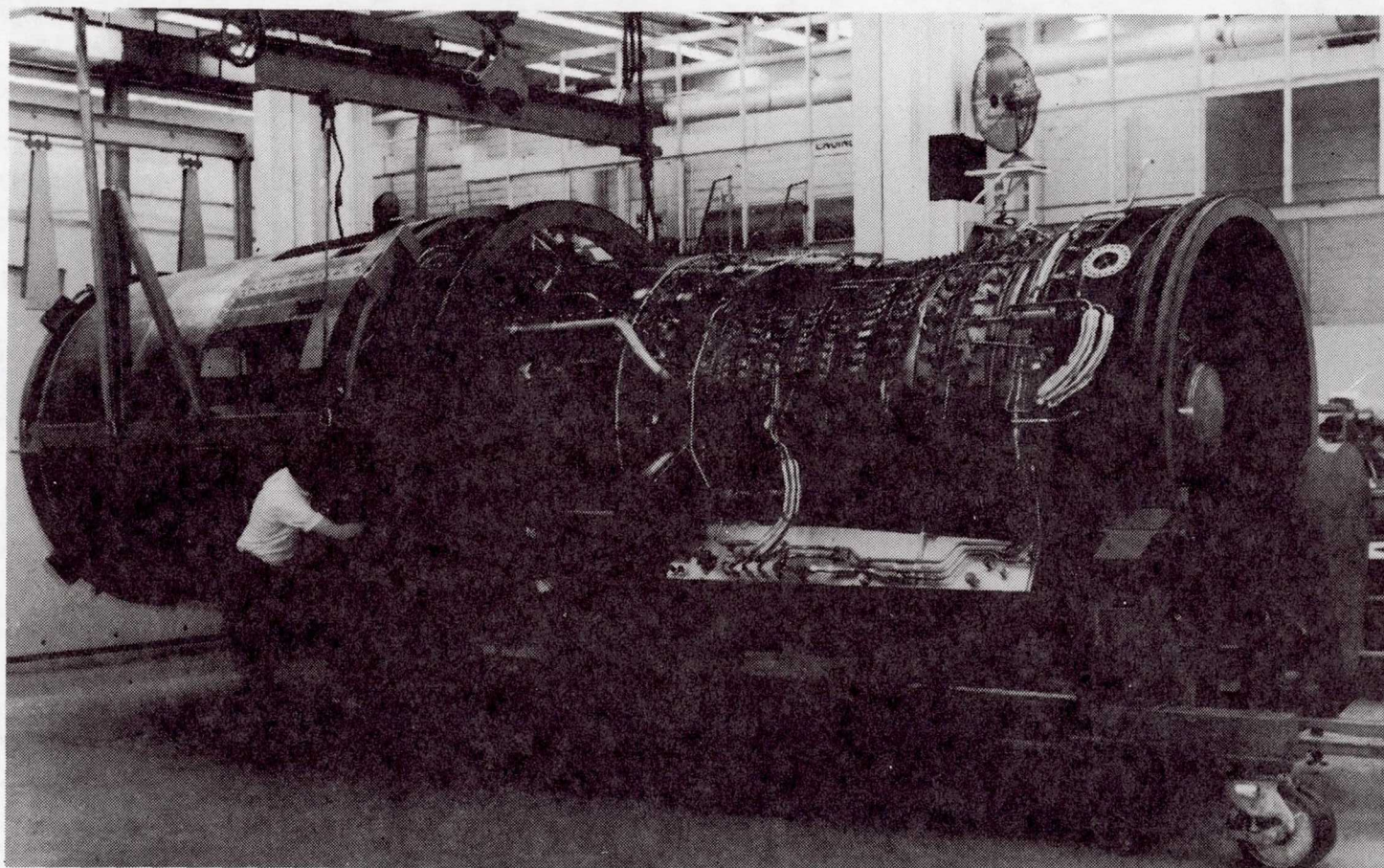
Figure 1.- GE4/J5 test engine.
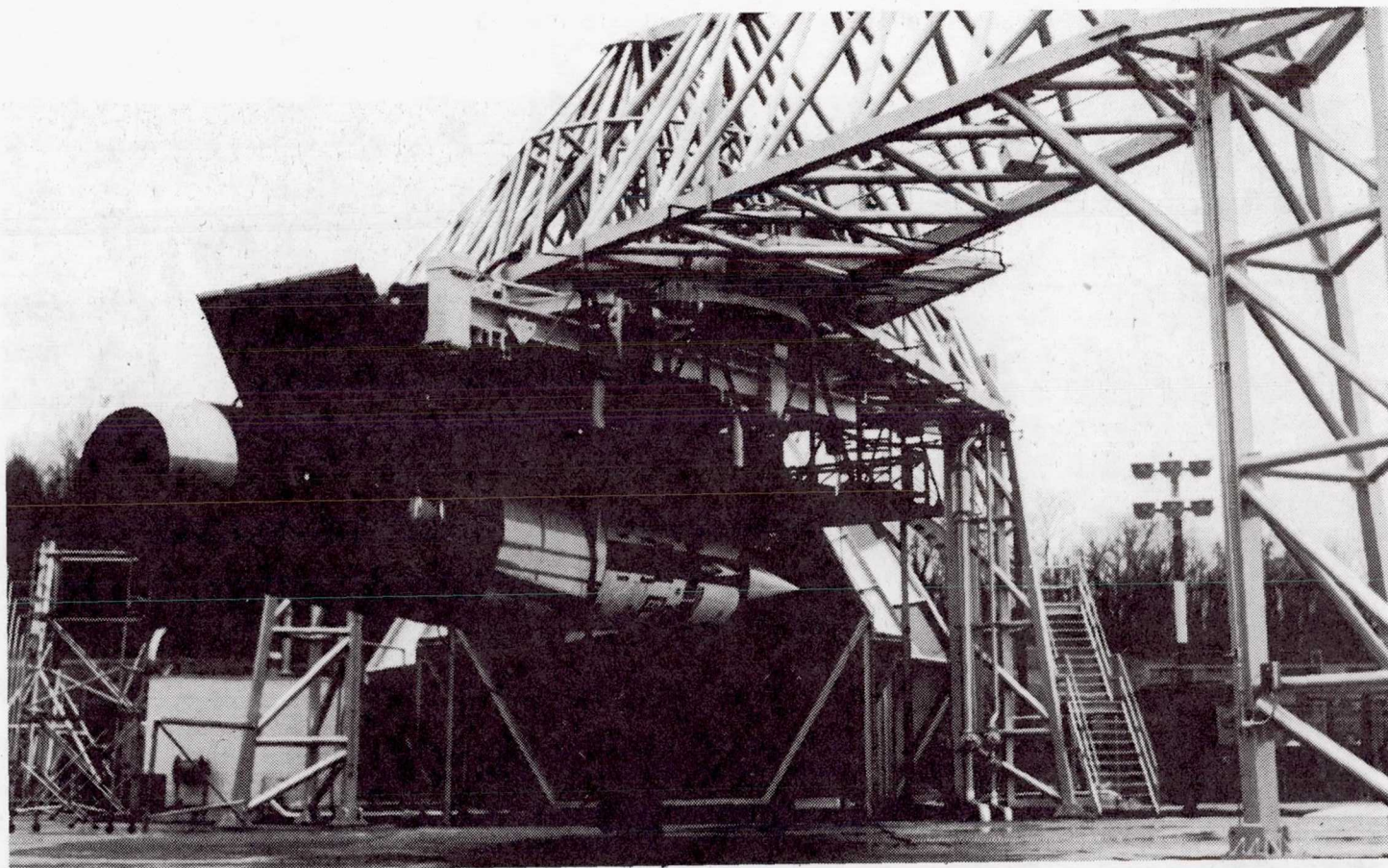
Figure 2.- GE4/J5 at Peebles test site.
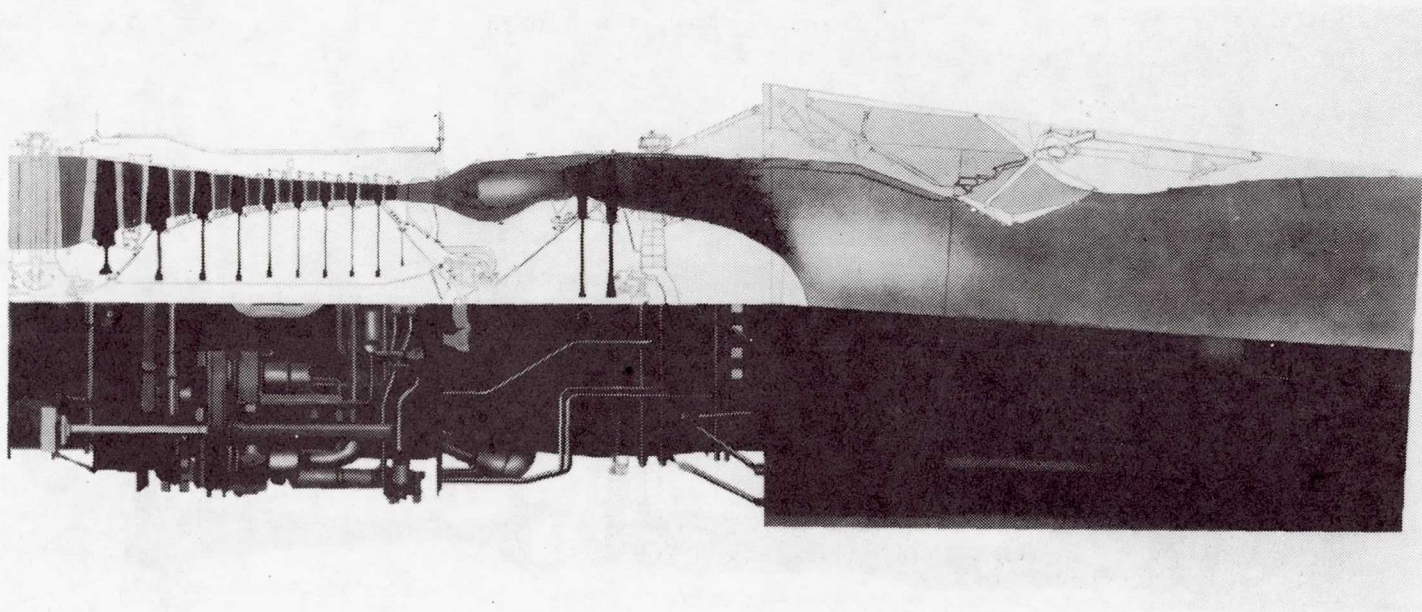
Figure 3.- GE4/J5 M2.7 turbojet.
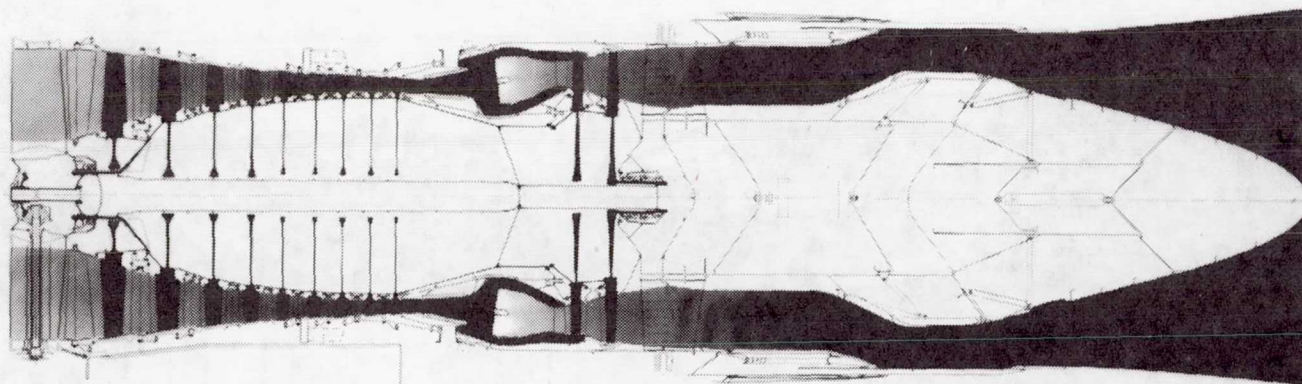
Figure 4.- GE4/J6H turbojet.
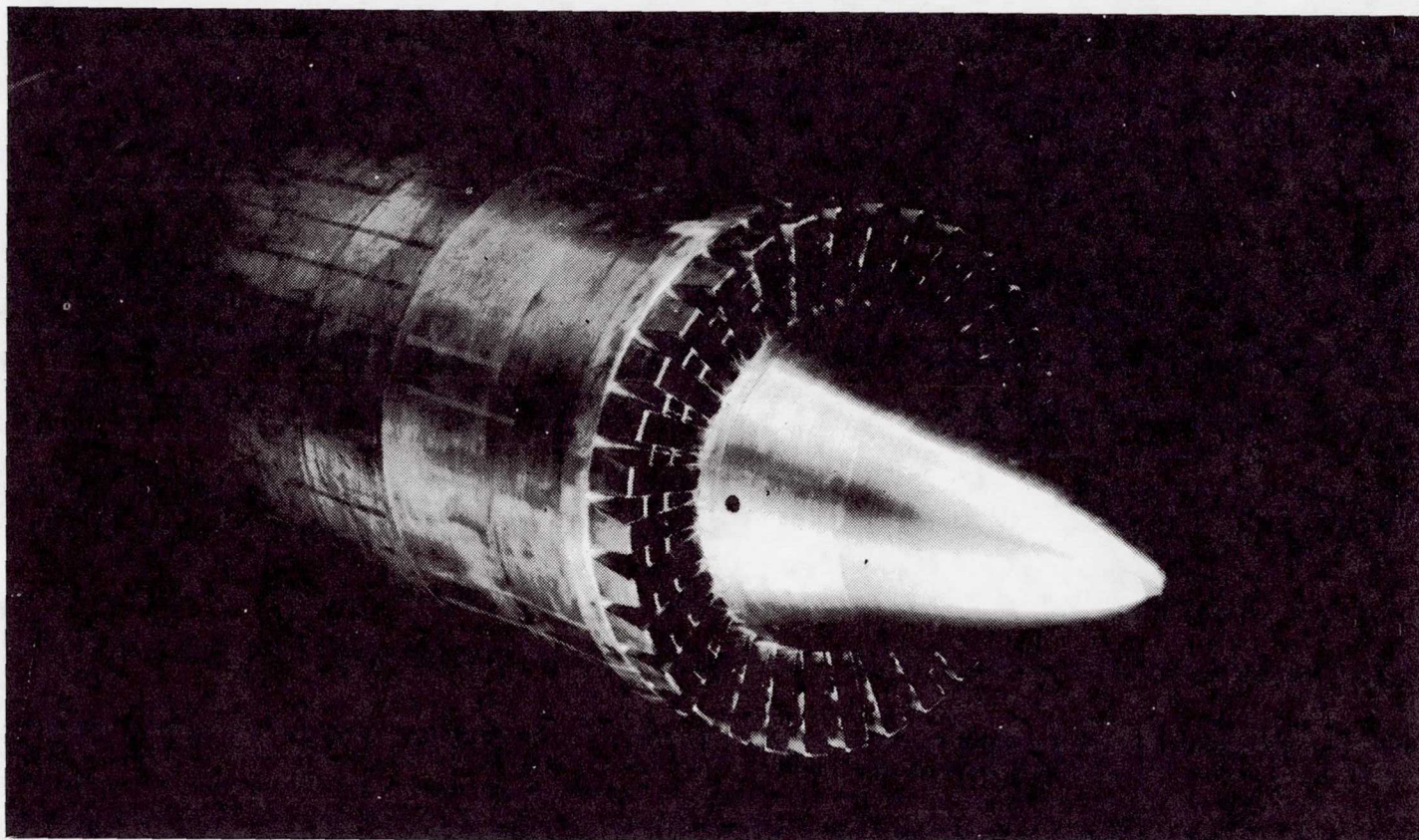
Figure 5.- GE4/J6H suppressor model — 32 chutes.
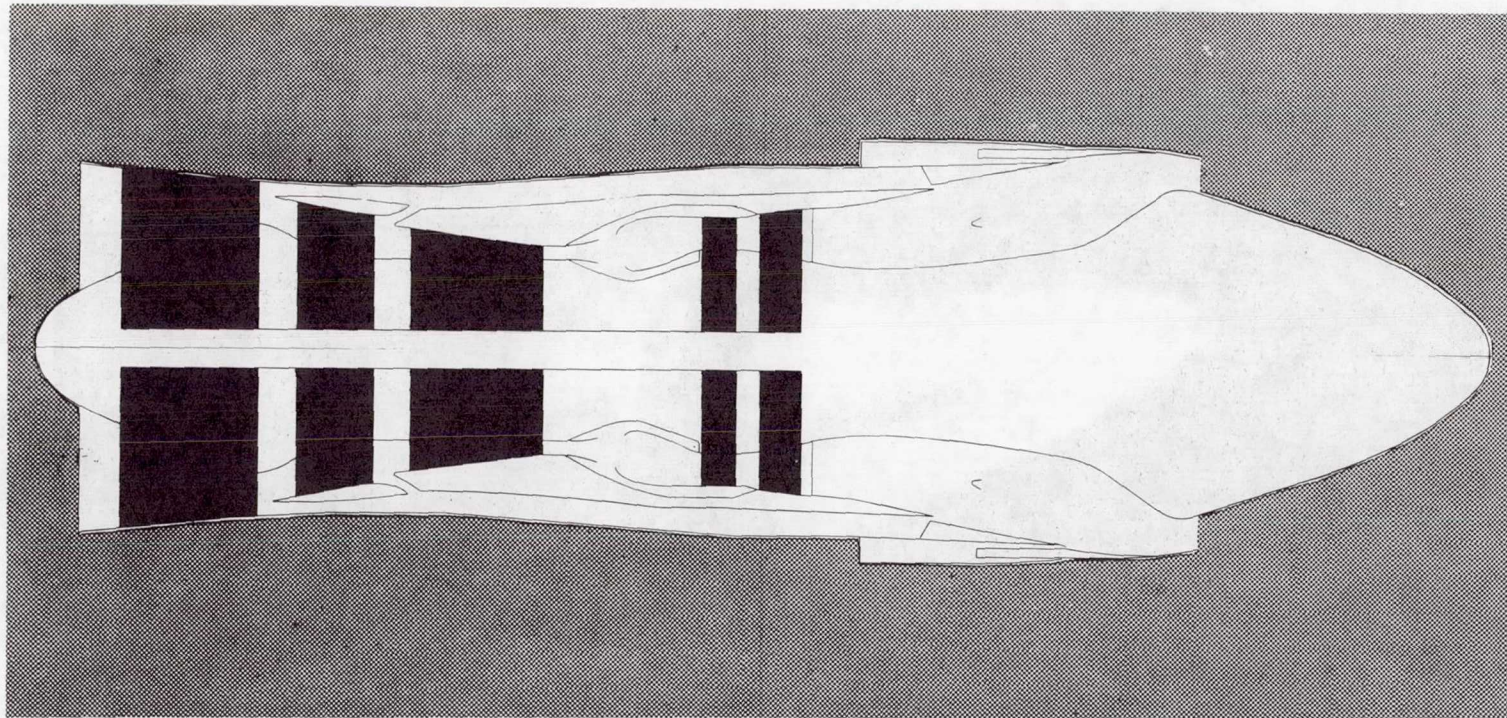
Figure 6.- AST-VCE.
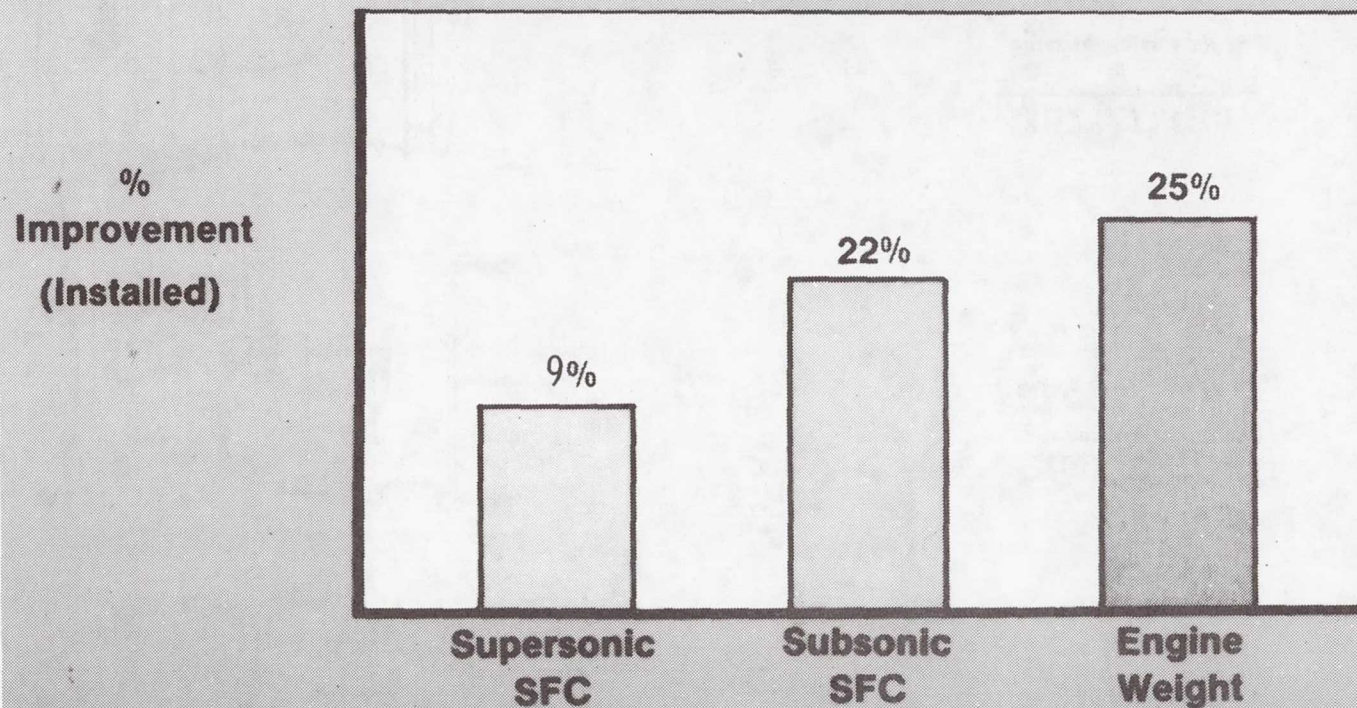
Figure 7.- Comparison of AST-VCE and GE4/J6.

GE4/J5P

Sideline Noise FAR 36 + 10

GE4/J6H

Sideline Noise FAR 36-0

GE21/J11B3

Sideline Noise FAR 36-0
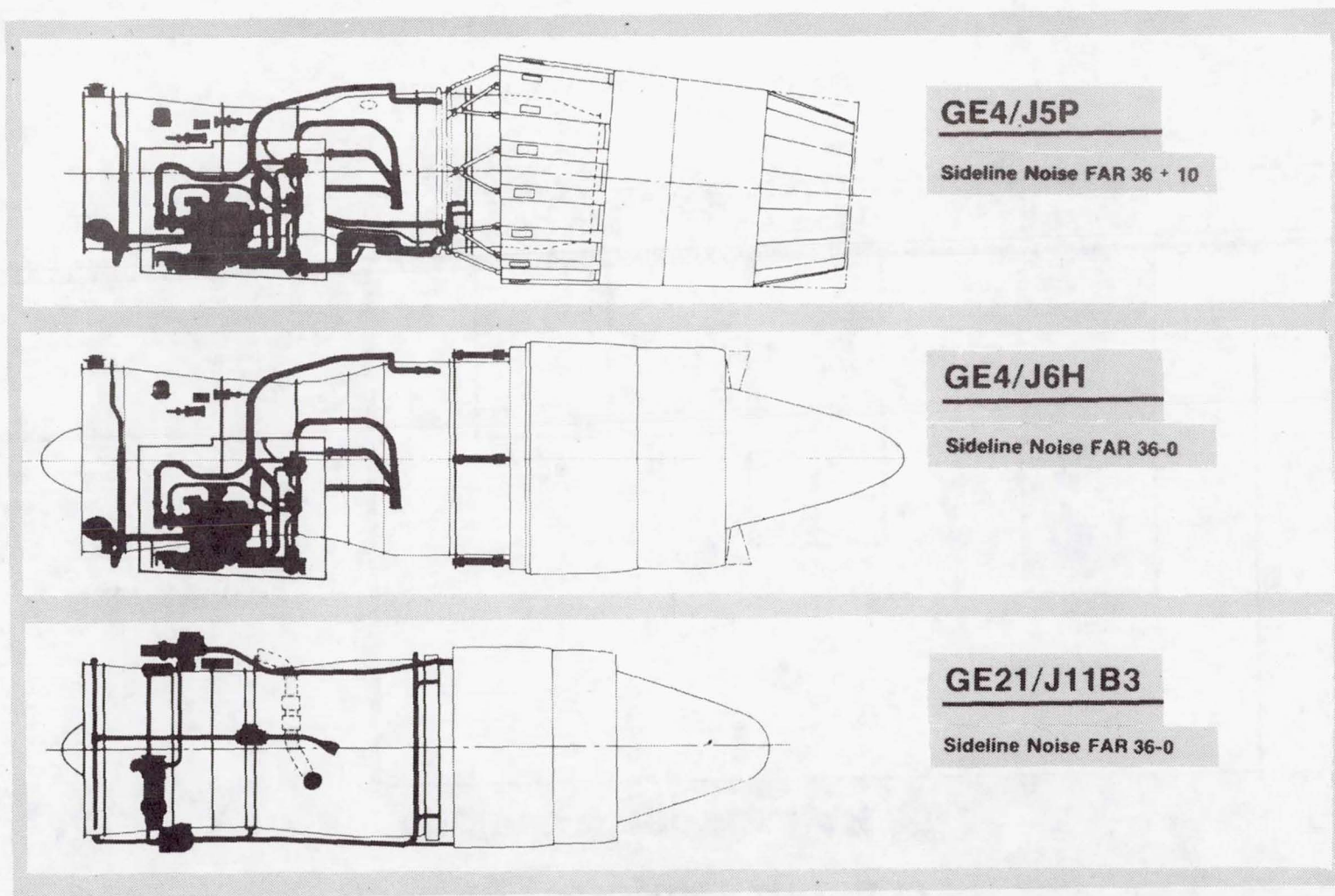
Figure 8.- Engine installation comparison.
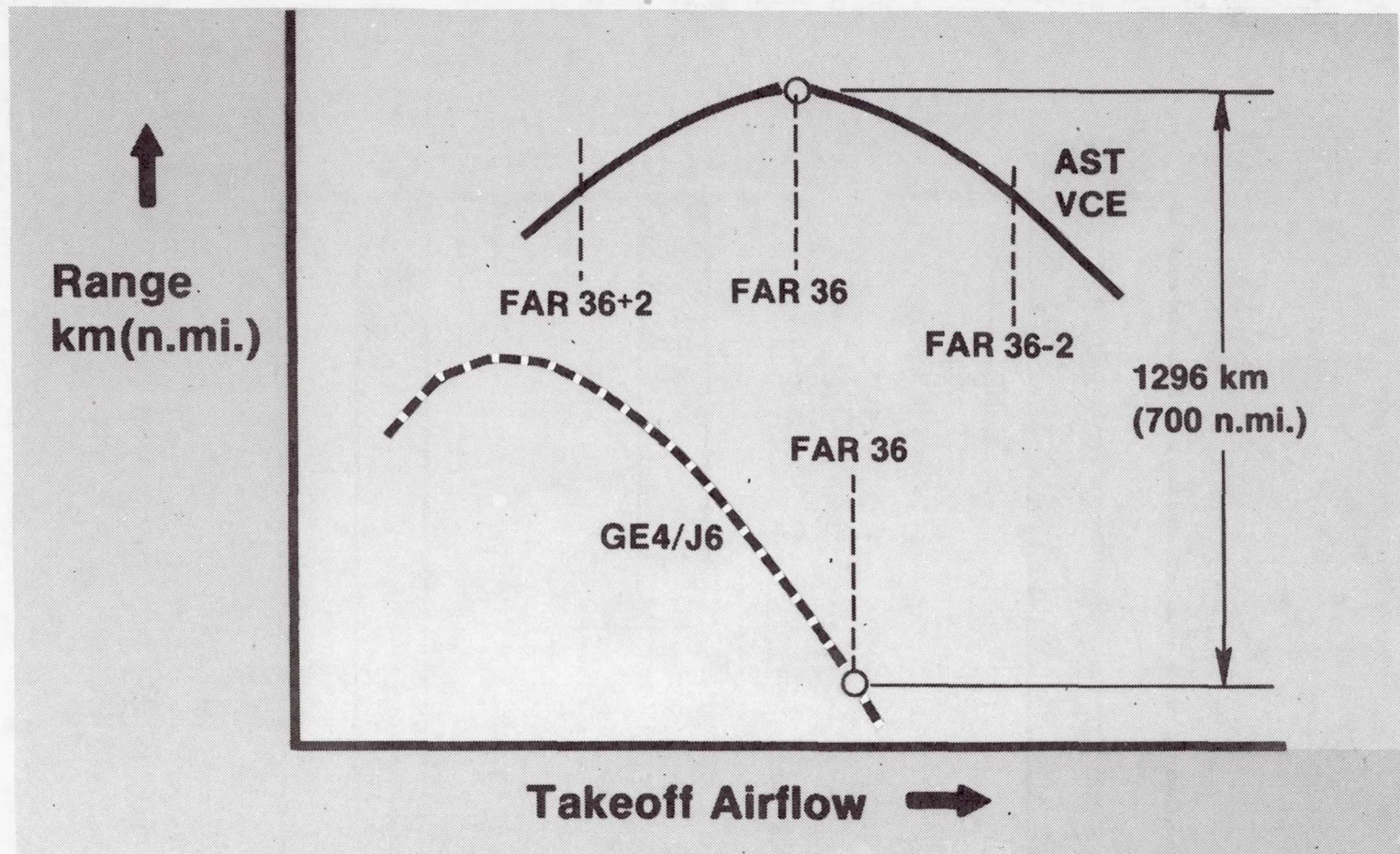
Figure 9.- VCE range improvement.
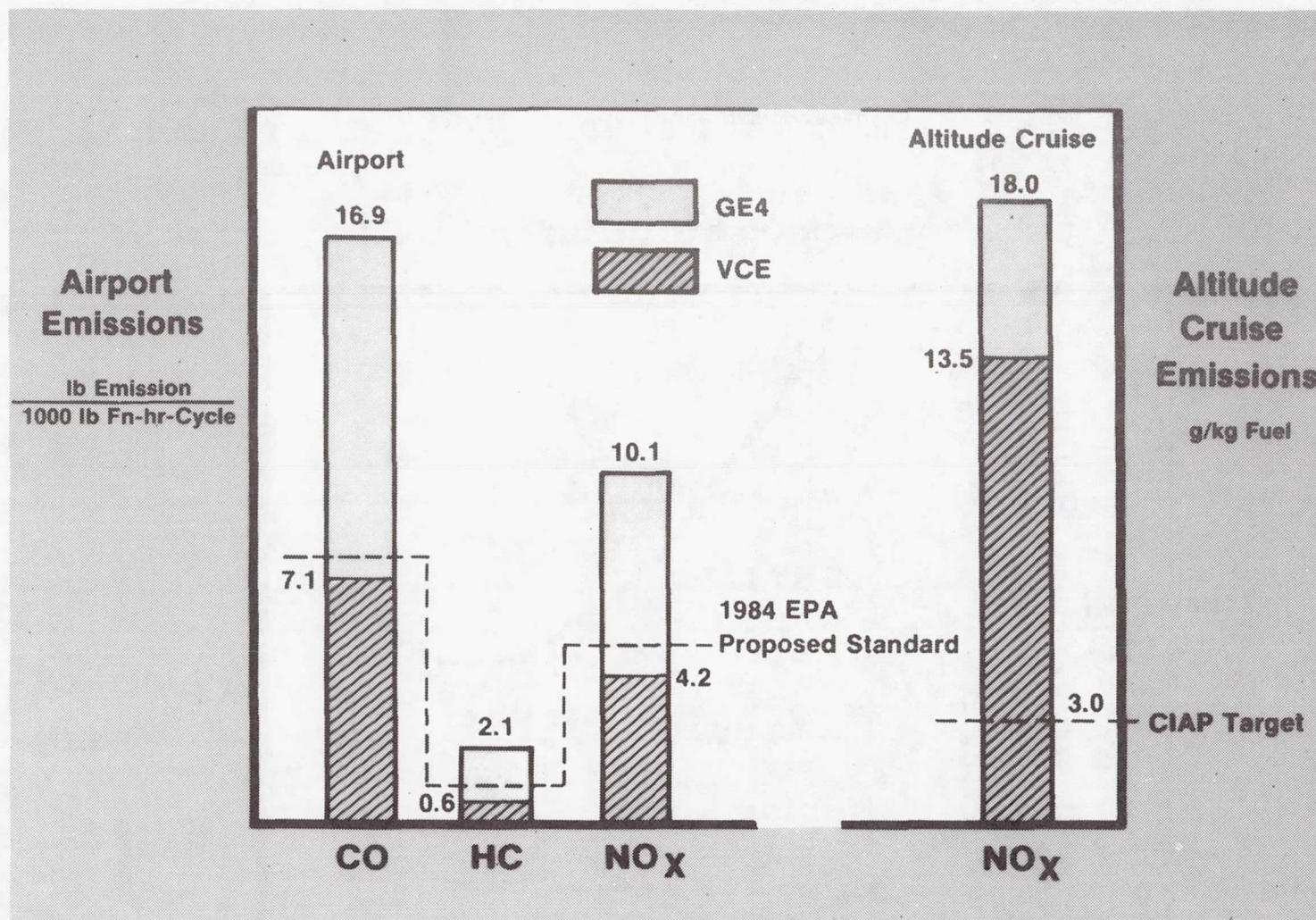
Figure 10.- Emission levels. (To convert from $\dfrac{\text{lb}}{1000 \text{ lb-Fn-hr-cycle}}$ to $\dfrac{\text{kg}}{\text{kN-Fn-hr-cycle}}$, multiply by 9.807, where Fn is engine net thrust.)

COMPONENT TEST PROGRAM FOR VARIABLE-CYCLE ENGINES

Albert G. Powers, John B. Whitlow,
and Leonard E. Stitt
NASA Lewis Research Center

SUMMARY

The NASA Lewis Research Center supersonic cruise aircraft research program (SCAR) involves propulsion study contracts with the General Electric Company (G.E.) and Pratt & Whitney Aircraft (P&WA). Through these contracts, promising variable-cycle engine (VCE) concepts for a supersonic cruise aircraft have been identified. These VCE concepts incorporate unique critical components and flow path arrangements that provide good performance at both supersonic and subsonic cruise and appear to be economically and environmentally viable.

Certain technologies have been identified as critical to the successful development of these engine concepts and require considerable development and testing. To assess the feasibility and readiness of the most critical VCE technologies, the Lewis Research Center has begun a VCE component test program through a series of contracts to the two engine companies. Large-scale test hardware will be integrated with existing high-technology core engines.

In their variable-stream-control engine (VSCE) component test program, P&WA will test and evaluate an efficient low-emission duct burner and a quiet coannular ejector nozzle at the rear of a rematched F100 engine.

In their component test program G.E. will, in addition to evaluating a quiet, coannular, high-radius-ratio plug nozzle, simulate the double-bypass engine (DBE) cycle concept using modified YJ101 hardware. The fan will be split into two blocks to provide the second bypass stream required by the double-bypass concept. Variable-geometry features will be added to the engine to provide the control necessary to demonstrate a mode-switching capability.

INTRODUCTION

Advanced supersonic cruise aircraft will be required to operate efficiently over a wide variety of flight conditions without significant impact to the environment. This creates conflicting requirements on the propulsion system that can be met most effectively by a variable-cycle engine (VCE) (ref. 1). Typically, a VCE has two or more distinct operating modes, each tailored to provide a high level of efficiency at one or more major flight conditions such as takeoff, subsonic cruise, and supersonic cruise.

After screening numerous engine cycles, including preliminary design of the better concepts, NASA and the engine companies have identified two promising

371

engine cycles from the supersonic cruise aircraft research (SCAR) studies. These engine concepts are the General Electric double-bypass, variable-cycle engine (DBE) (ref. 2) and the Pratt & Whitney Aircraft variable-stream-control engine (VSCE) (ref. 3). Each of these concepts represents a significant advance over conventional engines. They may be viewed as VCE's because of extensive flow modulation either through variable components, valving, novel control techniques, or combinations of these features. Both engine concepts use high airflow for takeoff. They take advantage of coannular flow to reduce jet noise, bypass flow to reduce engine weight and improve off-design subsonic cruise performance, and high turbine inlet temperatures to provide good supersonic performance with bypass flow.

To demonstrate the feasibility, readiness, and performance of some of the most critical technologies peculiar to these engine concepts, the Lewis Research Center has begun a component test program for variable-cycle engines through a series of contracts to the two engine companies. Phase I of this program consists of further component concept screening and rig testing directed toward achieving the goals established in the SCAR propulsion studies. Phase II will consist of modifying an existing high-performance core engine to simulate, to the extent practical, these VCE concepts. Many other technologies need further development before a VCE can be put into commercial service. However, these technologies are not unique to VCE; they are common to many other advanced engine applications.

PROGRAM OBJECTIVES AND STRUCTURE

Program Objectives

The specific objectives of the VCE component test program are as follows:

(1) Demonstrate coannular jet noise reduction in large scale and in a real engine environment. Thus far, this noise reduction has been verified only with small-scale models having diameters about one-tenth of the full size.

(2) Evaluate the performance of selected unique VCE components. Pratt & Whitney will evaluate a coannular ejector nozzle and a low-emission, high-efficiency duct burner. General Electric will evaluate a unique coannular plug nozzle together with a variable-geometry, split-flow fan and flow control valves.

(3) Provide the technical basis for future experimental VCE's. Successful completion of the current program should enable us to confidently proceed into an experimental engine program. Such a program could provide complete cycle simulation, allowing performance testing at simulated climb/acceleration and cruise conditions as well as at takeoff.

Program Structure

The overall structure of the VCE component test program is illustrated in figure 1. Results of the SCAR studies, the acoustic model tests, and the component rig testing will be used in an engine and program definition study. During this phase of the program, both contractors will continue model tests of the coannular nozzle and will refine the aerodynamic lines of the exhaust systems. Candidate duct-burner configurations will be selected and rig tested by P&WA. A variable-flow front fan will be designed and rig tested by G.E. However, because of the lengthy development time, the fan will not be incorporated in the test-bed engine. The engine and program definition study will define the details of the test-bed engine configuration and the components to be used in this program.

The two branches at the bottom of figure 1 show the test-bed engines to be built. The P&WA test-bed engine will use a rematched military F100 engine with its exhaust flow separated to provide exhaust conditions similar to those of the VSCE. An advanced high-efficiency duct burner and coannular ejector nozzle will be added. Pratt & Whitney will evaluate duct-burner emissions as well as jet noise.

The G.E. test-bed engine will be based on a military YJ101 core engine. The fan will be split into two blocks to provide the two bypass streams necessary to the double-bypass concept. Variable-geometry features will be added to provide the control necessary to demonstrate a mode-switching capability. A high-radius-ratio coannular plug nozzle will be installed to verify the jet noise suppression predicted by the model tests. This will be the first test of the systems compatibility and stability of the double-bypass VCE concept.

ENVIRONMENTAL CONSIDERATIONS

Jet Noise

An important characteristic of supersonic cruise engines is the need for high specific thrust to overcome drag at supersonic conditions with minimum weight penalty and low installation losses. Engines designed for efficient supersonic operation would therefore normally also have high takeoff jet velocities and require noise suppression to meet FAR 36 limits. The upper band of data in figure 2 shows sideline noise relative to the FAR 36 limit as a function of fully expanded jet velocity for conventional mixed-flow nozzles sized with the area variation needed to produce a constant thrust. It can be seen that the turbojet engine planned for the U.S. supersonic transport (SST) in 1970 would have required about 15 EPNdB of suppression to meet the FAR 36 sideline noise limit. It is questionable whether such a retractable mechanical suppressor could have been built. At any rate, it would have been heavy and inefficient.

Model tests of coannular nozzles by P&WA and G.E. in the SCAR and VCE programs (refs. 4 to 6) have shown that an inherent noise reduction can be obtained when the outer annulus jet velocity V_j is appreciably higher than that of the

inner stream, as shown in the nozzle sketch in the lower right corner of fig-
ure 2. This reduction can be as much as 8 to 10 EPNdB, as shown by the lower
band of data in figure 2, relative to a conventional mixed-flow nozzle having a
jet velocity equal to that of the outer annulus of the coannular system with an
inverted velocity profile. A conventional turbojet engine would require a 45-
percent reduction in jet velocity to meet the FAR 36 sideline noise limit with-
out suppression. The weight penalty involved in oversizing a conventional tur-
bojet to obtain the needed takeoff thrust with such a low jet velocity would be
prohibitive. An adverse performance mismatch with the airplane would also oc-
cur, especially at subsonic cruise. By using bypass flow in a turbofan engine
to increase takeoff thrust, the weight penalty can be reduced at these lower
jet velocities. With the coannular inverted exhaust velocity profile, the an-
nulus jet velocity can be raised to a value about 40 percent higher than for the
conventional engine at the same noise level. This therefore reduces the total
airflow (or engine size) requirement. The subsonic cruise performance match
with the airplane is also improved with the bypass engine sized in this way.

Emissions

The development of variable-cycle engines to meet acceptable exhaust emis-
sion standards will face many of the same problems currently being addressed in
on-going research for low-emissions combustors. However, in addition to the
main combustor, both candidate VCE's employ low levels of augmentation during
certain critical stages of operation. The environment for the duct burner and
afterburner is entirely different than for the main combustor, and the pressure,
temperature, and velocity conditions are less compatible for efficient low-
emission burning.

Since the VCE will cruise well into the stratosphere, major concern focuses
on the oxides-of-nitrogen (NO_x) emissions and their effect on the ozone layer.
At this condition, the pressure and temperature into the duct burner of the VSCE
favor lower NO_x emissions relative to the main combustor.

Figure 3 compares the normalized performance of several combustor concepts
in terms of the relative NO_x emission index at supersonic cruise. The normal-
izing factor may vary from 20 to 50 grams per kilogram of fuel, depending on the
cruise Mach number and the engine operating condition. Since the emission in-
dex scale presented is relative, it may, as a first approximation, be applied
to augmentors as well as main combustors. The clean-combustor concepts being
developed in the NASA/industry experimental clean-combustor program (ECCP)
(refs. 7 and 8) show the possibility of a 50-percent reduction in NO_x emissions
in burner-rig experiments. However, the emissions goal for the duct-burner ap-
plication is 1 gram of NO_x per kilogram of fuel. This extremely low level, as
well as operational considerations, may require even more advanced techniques
to be applied. Further combustion improvements are predicted for such concepts
as premix combustion. Results based on small-scale, idealized laboratory exper-
iments are encouraging and indicate potential reductions of tenfold at super-
sonic cruise conditions. However, any appreciable reduction in NO_x emissions
below the ECCP level will require extensive and costly research and development
programs to determine if they can be adapted to meet SST burner requirements.

Stringent EPA goals have been proposed for carbon monoxide (CO), total un-

burned hydrocarbons (THC), and NO_x for future airport environments. During takeoff (sideline and cutback) the duct burner presents a more difficult problem than the main combustor relative to CO and THC. The cycle parameters (low pressure and temperature) that tend to help relieve the cruise NO_x problem become detrimental during takeoff and result in a somewhat lower combustion efficiency. Advanced techniques such as staged combustion and variable geometry may be required to raise combustor efficiency and lower emissions.

COMPONENT TEST PROGRAM

Variable-Stream-Control Engine

VSCE engine concept. - The P&WA VSCE engine concept (ref. 3) is shown schematically in figure 4. It features a coannular ejector exhaust nozzle and uses a duct burner in the bypass stream to obtain the coannular inverted velocity profile. Therefore, at takeoff the turbine inlet temperature is restricted to achieve the inverted velocity profile needed for low noise. However, at supersonic conditions this temperature must be as high as the state of the art allows to obtain good specific fuel consumption (sfc) at the high thrust levels needed. Despite this high temperature, duct burning must be used to obtain adequate thrust at supersonic cruise. Also with bypass flow, some duct burning is desirable from an sfc or propulsive efficiency standpoint to equalize the jet velocities of the two streams. A higher level of duct burning is required in supersonic climb/acceleration to obtain optimum thrust margins.

A variable-area, duct-stream nozzle is required to accommodate changes in the duct-burner temperature setting. Variable geometry in the fan and compressor is used in conjunction with the variable geometry in both exhaust nozzles to schedule airflow and shaft speed in order to match engine airflow with inlet airflow and minimize the supersonic bypass ratio.

VSCE component test bed. - Figure 5 shows schematically the test-bed concept to be used in testing the two most critical and unique components of the PW&A VSCE: (1) the coannular exhaust nozzle with the inverted velocity profile, and (2) the low-emissions, high-efficiency duct burner. An existing high-technology F100 turbofan engine will be used to provide the proper gas conditions into the duct burner and primary nozzle, similar to those of the conceptual VSCE at takeoff conditions. The exhaust flow from the F100 will be kept separated by an add-on bypass duct downstream of the turbines. Although the duct burner in this test will be farther downstream than it would be in an actual flight engine, this should not have a major impact on the jet noise tests or the duct-burner emissions tests. Every attempt will be made to keep costs low by using existing hardware wherever possible. Not only is an existing F100 engine being used as the gas generator, but an existing TF30 iris nozzle is planned for the duct nozzle throat.

The duct-burner design will be selected on the basis of results from duct-burner conceptual screening and rig testing currently underway in the VCE program. The exhaust nozzle will include an acoustically lined ejector based on results from SCAR and from VCE small-scale acoustic model tests. The F100 engine will be rematched for a lower turbine inlet temperature, a higher bypass

375

ratio, and a lower overall pressure ratio to better simulate the exhaust conditions of the VSCE.

Table I compares the cycle characteristics of the rematched F100 test bed and the conceptual VSCE. As shown, the test-bed engine airflow will be about ¼ scale. However, this is about 25 times the airflow used in the acoustic model tests. Large-scale testing is important for the verification of the scaling laws that have been used to extrapolate model test data to full size. The bypass ratio of the test-bed engine is somewhat lower than that of the conceptual VSCE, and there are also some slight differences in the other parameters.

The duct-stream jet velocity can be varied by changing the duct-burner temperature through adjustment of the fuel-air ratio. Less flexibility is available in varying the core-stream jet velocity. For the duct-stream velocity indicated, the ratio of duct-stream to core-jet velocity of 1.7 should produce maximum inherent suppression. Noise measurements will be taken at both higher and lower duct-burner temperatures for a range of duct-stream to core-stream velocity ratios.

VSCE schedule. - A contract was awarded to P&WA in mid-1976 to begin the first phase of component test program. The definition study is in progress and will extend over a 1-year period, as shown by the schedule in figure 6. Technical results from the individual critical-component technology programs will be incorporated in the design of the large-scale test hardware.

A contract was also awarded to P&WA to analytically screen duct-burner concepts for the VSCE. The synthesis of 8 to 12 duct-burner concepts has been completed. These configurations were ranked and four were selected for further study and design. Follow-on segment rig tests will be made in early 1977 to select the most promising duct-burner configuration to be incorporated in the test-bed engine.

Pratt & Whitney will continue aeroacoustic model tests of coannular nozzles to identify the most promising configuration for the VSCE. Results of this technology program will be used in the design of a large-scale nozzle configuration for the F100 engine test bed. The environmental and performance tests of the duct burner and the coannular nozzle installed on the test-bed engine are scheduled to begin in early 1979.

Double-Bypass Engine

DBE engine concept. - The G.E. double-bypass VCE concept (ref. 2) is shown schematically in figure 7. It also uses a coannular exhaust nozzle with an inverted velocity profile for low jet noise. In this concept, fan discharge flow is crossducted at takeoff to the plug centerbody to get the low-energy exhaust stream on the inside, as required by the inverted velocity profile. Bypass air is also used to increase the total flow at takeoff for increased thrust at the reduced jet velocities. The maximum state-of-the-art turbine inlet temperature is used with this turbofan cycle at takeoff as well as at supersonic conditions. The high temperature is required for takeoff thrust as well as for providing the high annulus velocity.

376

The fan is split into two blocks to provide two bypass streams - hence the terminology "double bypass." The outer bypass airflow can be controlled to give the turbofan cycle additional flexibility. It is desirable in takeoff to have the maximum bypass ratio and total airflow for sufficient thrust at low noise. At subsonic cruise, the higher bypass ratio is also desirable from a propulsive efficiency standpoint. However, at supersonic flight conditions, the bypass ratio must be kept low, and the outer bypass flow is therefore eliminated. In this mode of operation, the engine behaves as a low-bypass-ratio, mixed-flow turbofan engine. Extensive variable geometry is required in the turbomachinery components to accommodate these flow swings and changing work requirements.

An afterburner is required for supplying additional thrust during climb/ acceleration. It may or may not be required during supersonic cruise, depending on the outcome of continuing engine/airplane sizing and integration studies.

DBE component test bed. - Figure 8 illustrates the test-bed engine for the double-bypass concept. In addition to demonstrating the coannular suppression benefit in large scale with a plug nozzle, this test bed will also demonstrate the system compatibility and stability of the double-bypass concept. The test bed is to be built around the advanced-technology military YJ101, a minibypass turbojet engine. The fan will be split into two blocks to get the extra by- pass stream. Variable geometry components will be added to control the bypass flow split. The turbine work split will be changed to better serve the demands of the new fan arrangement.

Table II compares some of the cycle parameters between the conceptual double-bypass study engine and the test-bed engine. The top line shows that the test-bed airflow is approximately 15 percent that of the conceptual DBE. The dual values shown for each engine represent high/low flow conditions. The sec- ond line shows that at sea-level-static conditions the high-mode bypass ratio is about double the low-mode bypass ratio. Subsequent lines in the table com- pare pressure ratios and combustor exit temperatures. The bottom two lines in- dicate that, despite slight differences in some of the cycle characteristics for the two engines, the fully expanded jet velocities are similar and provide a valid large-scale test of the inverted velocity profile desirable for inherent noise suppression. These velocities are obtained in the high-flow mode where the exhaust is separated into two distinct streams. In the low-flow mode, the exhaust would be mixed and a high jet noise condition would result. Although the test bed will be tested in both modes on the test stand, a flight engine at takeoff would be operated only in the high-flow, low-noise mode.

DBE schedule. - A contract was awarded to G.E. in the fall of 1976 to be- gin the component test program definition study for the double-bypass-cycle test bed. The study will extend over a 9-month period, as shown on the schedule in figure 9. Technical results from the on-going technology programs will be fac- tored into the design of the test-bed engine as they become available.

The two critical components being studied in the technology program are the variable-flow fan and the low-noise, coannular plug nozzle. A contract was awarded in mid-1976 to screen concepts and to conduct design and performance studies of variable-flow fans. A follow-on contract will provide for design

377

and fabrication in late 1977 and rig testing of the most-promising fan concept beginning in late 1978.

A contract was also awarded to G.E. in early 1976 to evaluate the effect of key design variables on the aeroacoustic performance of high-radius-ratio, ventilated plug nozzles. Results from this technology effort will be factored into the selection of a large-scale nozzle configuration for the test-bed engine. Evaluation of the noise and performance characteristics of the engine should begin in early 1979.

CONCLUDING REMARKS

The variable-cycle engine (VCE) component test program addresses only certain unique and critical components necessary to assess the feasibility of the concept and to evaluate the potential of the cycle for supersonic cruise applications. Test-bed engines are a next logical step following model and laboratory investigations. The current schedule calls for testing to begin in early 1979, with tests to be conducted at sea-level-static conditions approximating those encountered at takeoff. The variable-cycle test-bed engines will use existing high-technology core engines with approximately a 15- to 25-percent airflow relative to the flight engines.

Successful completion of the component test program with the two test-bed engines described in this paper will allow us to proceed confidently to an experimental variable-cycle-engine program. However, performance and environmental acceptability of a VCE depend on attaining predicted levels of technology in other areas not addressed in the component test program. Many other technologies need further development before a VCE can be considered for commercial service.

REFERENCES

1. Willis, Edward: Variable-Cycle Engines for Supersonic Cruise Aircraft.
   NASA TM X-73463, 1976.

2. Krebs, J. N.: Advanced Supersonic Technology Study — Engine Program Summary:
   Supersonic Propulsion — 1971 to 1976. Proceedings of the SCAR Conference,
   NASA CP-001, 1977. (Paper no. 16 of this compilation.)

3. Howlett, R. A.: Variable Stream Control Engine Concept for Advanced Super-
   sonic Aircraft — Features and Benefits. Proceedings of the SCAR Confer-
   ence, NASA CP-001, 1977. (Paper no. 15 of this compilation.)

4. Gutierrez, O. A.: Aeroacoustic Studies of Coannular Nozzles Suitable for
   Supersonic Cruise Aircraft Applications. Proceedings of the SCAR
   Conference, NASA CP-001, 1977. (Paper no. 22 of this compilation.)

5. Kozlowski, H.: Coannular Nozzle Noise Characteristics and Application to
   Advanced Supersonic Transport Engines. Proceedings of the SCAR Conference,
   NASA CP-001, 1977. (Paper no. 23 of this compilation.)

6. Lee, R.; Whittaker, R. W.: Coannular Plug Nozzle Noise Reduction and Impact
   on Exhaust System Designs. Proceedings of the SCAR Conference, NASA
   CP-001, 1977. (Paper no. 24 of this compilation.)

7. Rudey, R. A.; and Kempke, E. E., Jr.: Technology for Reducing Aircraft
   Engine Pollution. SAE Paper 750550, Apr. 1975.

8. Rudey, R. A.; and Reck, G. M.: Advanced Combustion Techniques for Con-
   trolling Oxides-of-Nitrogen Emissions of High-Altitude-Cruise Aircraft.
   NASA TM X-73473, 1976.

TABLE I. – COMPARISON OF CONCEPTUAL VARIABLE-STREAM-CONTROL

ENGINE WITH TEST-BED SIMULATION

[Takeoff conditions.]

Characteristic	Conceptual VSCE	Test-bed engine
Engine:		
Relative total airflow	1.00	0.27
Bypass ratio	1.5	0.85
Fan pressure ratio	2.8	3.1
Overall (fan plus compressor) pressure ratio	18.6	19.5
Combustor exit temperature, K($^{\circ}$F)	1600 (2420)	1520 (2280)
Duct-burner temperature, K($^{\circ}$F)	1710 (2610)	1390 (2040)
Nozzle:		
Duct-stream jet velocity, m/sec (ft/sec)	885 (2900)	805 (2640)
Ratio of duct-stream to core-stream jet velocity	1.7	1.7

TABLE II. – COMPARISON OF CONCEPTUAL DOUBLE-BYPASS VARIABLE-CYCLE ENGINE

WITH TEST-BED SIMULATION

[Takeoff conditions.]

Characteristic	Conceptual double-bypass VCE[a]	Test-bed engine[a]
Engine:		
Relative total airflow (high/low)	1.20/1.00	0.19/0.15
Overall bypass ratio	0.8/0.4	0.7/0.4
Pressure ratio, front fan block	3.2/2.7	3.1/2.4
Pressure ratio, rear fan block	1.2/1.5	1.2/1.4
Overall fan pressure ratio	3.8/4.0	3.7/3.2
Overall (fan plus compressor) pressure ratio	17	17
Combustor exit temperature, K($^{\circ}$F)	1870/1700 (2900/2600)	1730/1700 (2650/2600)
Nozzle:		
Hot exhaust jet velocity, m/sec (ft/sec)	750 (2450)	690 (2250)
Ratio of hot to cold exhaust jet velocity	1.58	1.45

[a]Dual values represent high/low flow conditions.
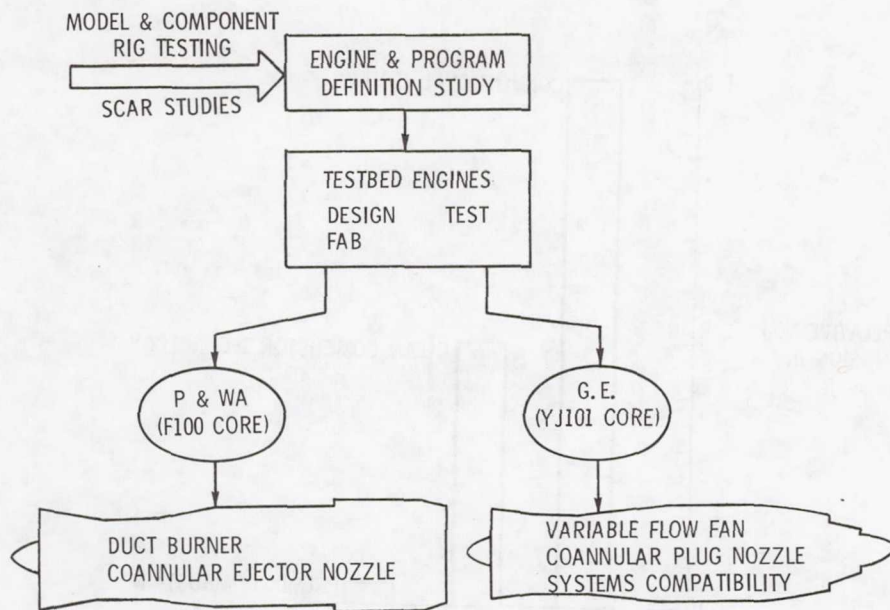
Figure 1.- Variable-cycle engine component test program.
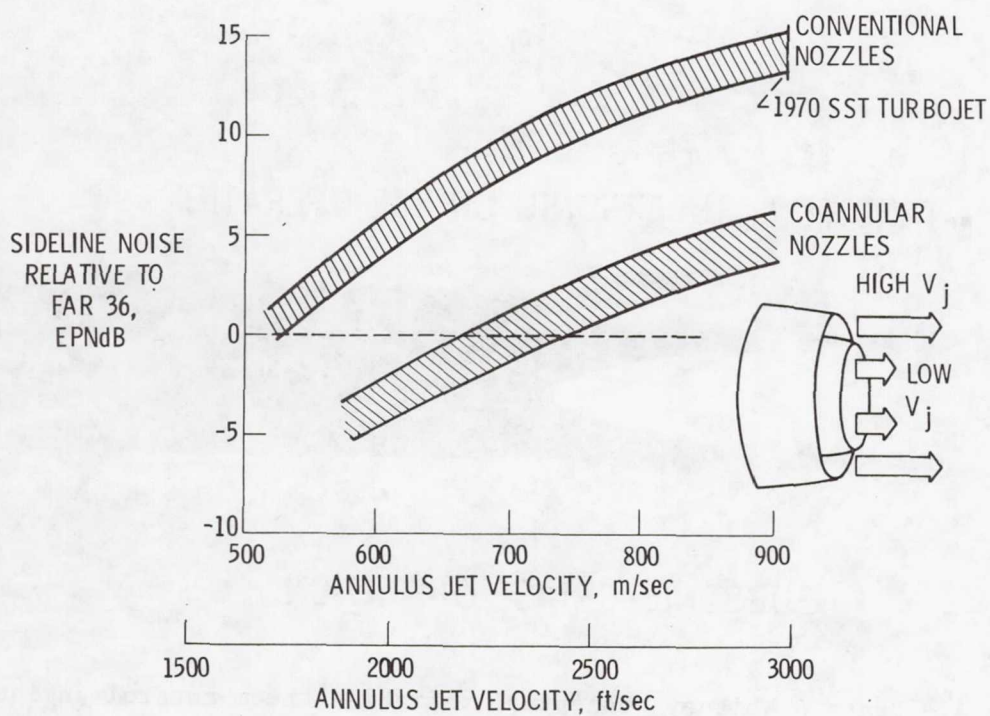
Figure 2.- Noise reduction with coannular nozzle.
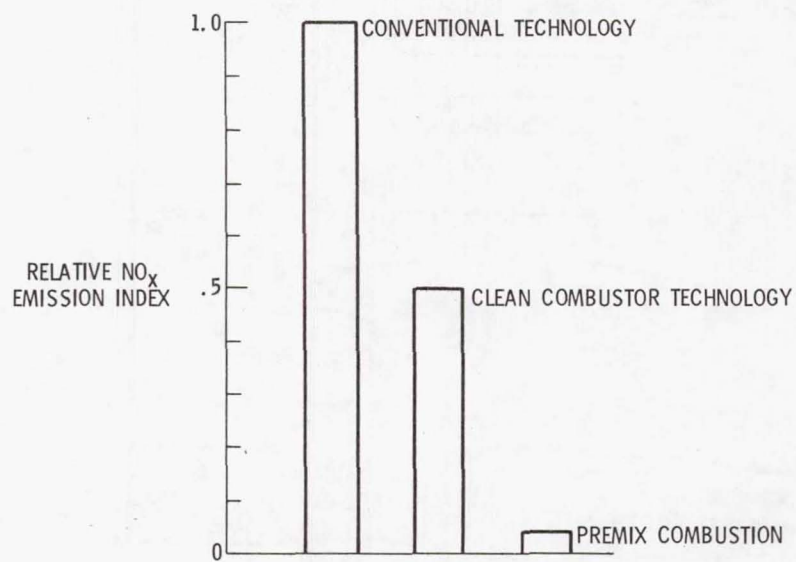
Figure 3.- Status of oxides-of-nitrogen emissions
at supersonic cruise.
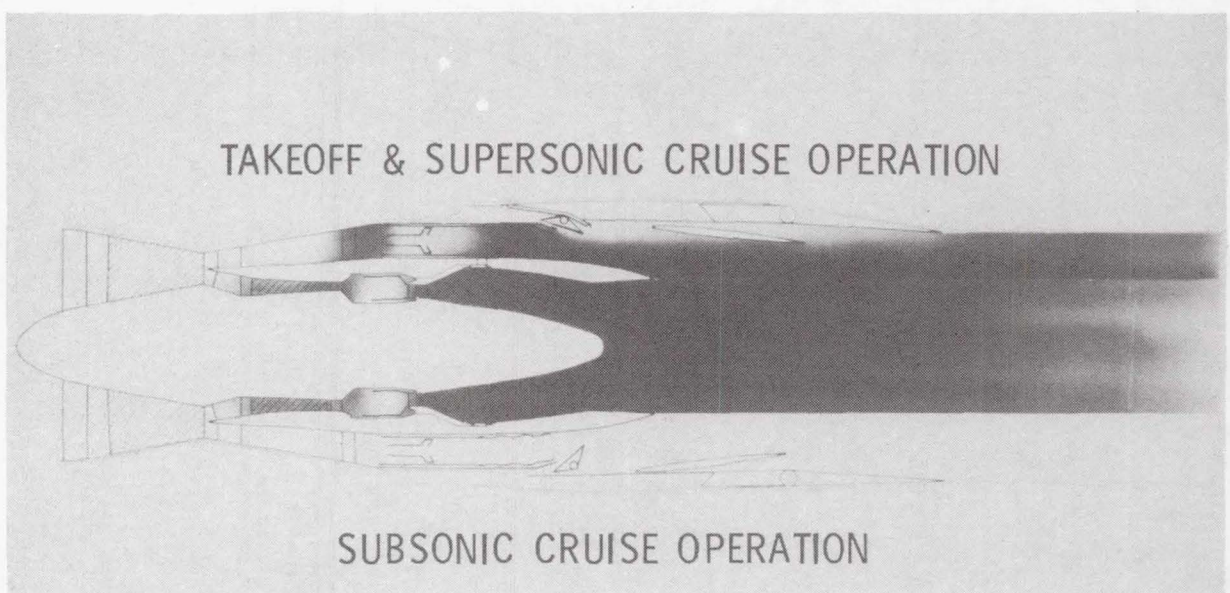
Figure 4.- Pratt & Whitney conceptual variable-stream-control engine.
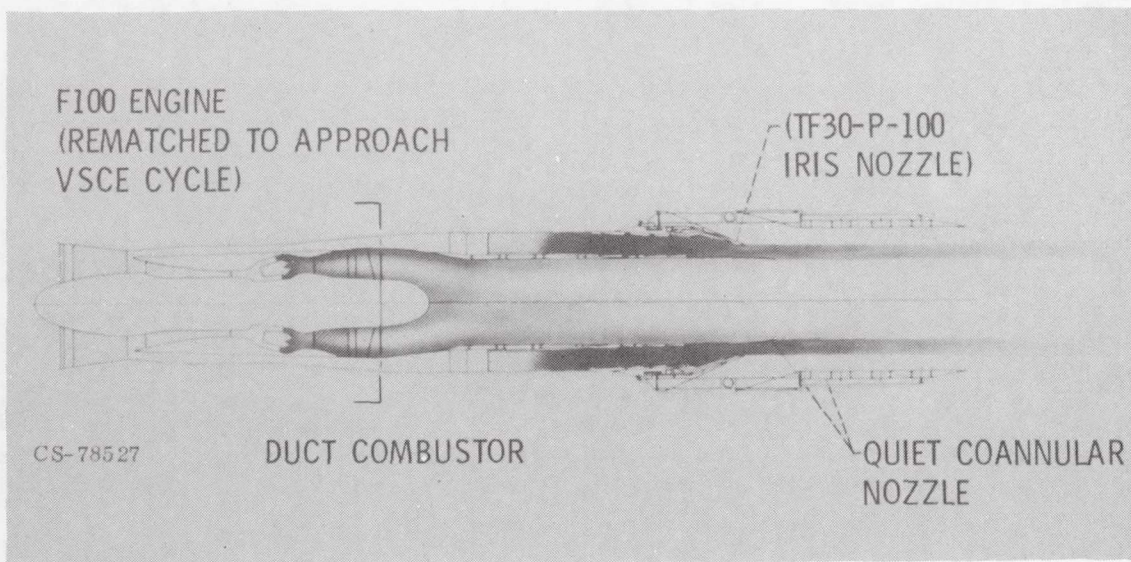
Figure 5.- Pratt & Whitney test-bed variable-stream-control engine.
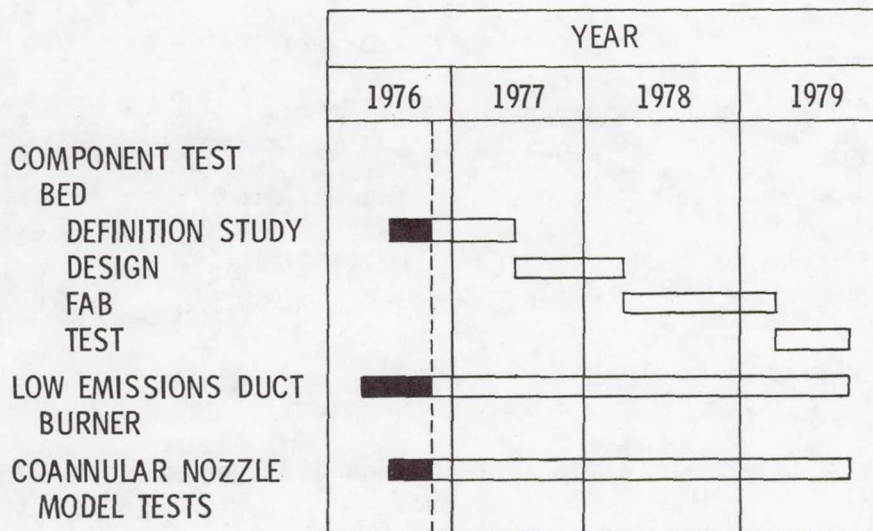
Figure 6.- Schedule of component test program for
Pratt & Whitney variable-stream-control engine.
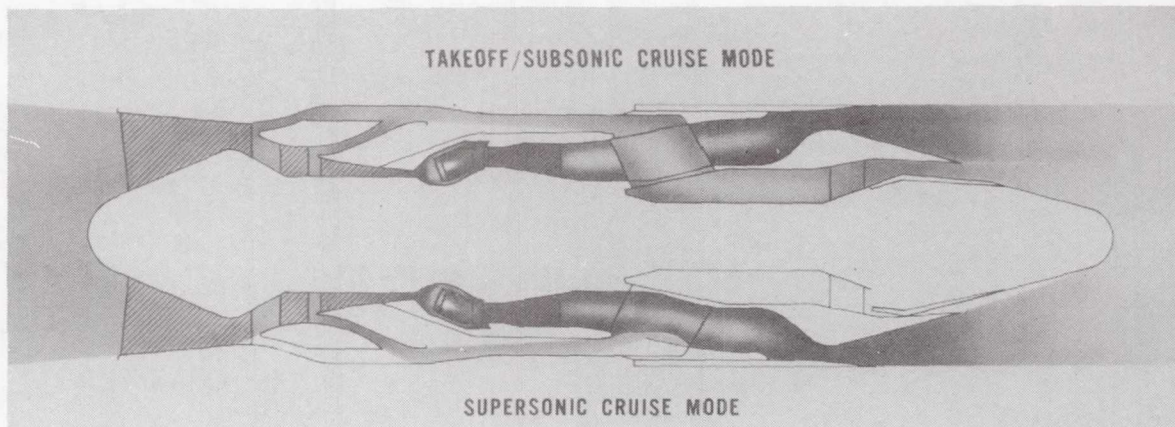
Figure 7.- General Electric conceptual double-bypass, variable-cycle engine.
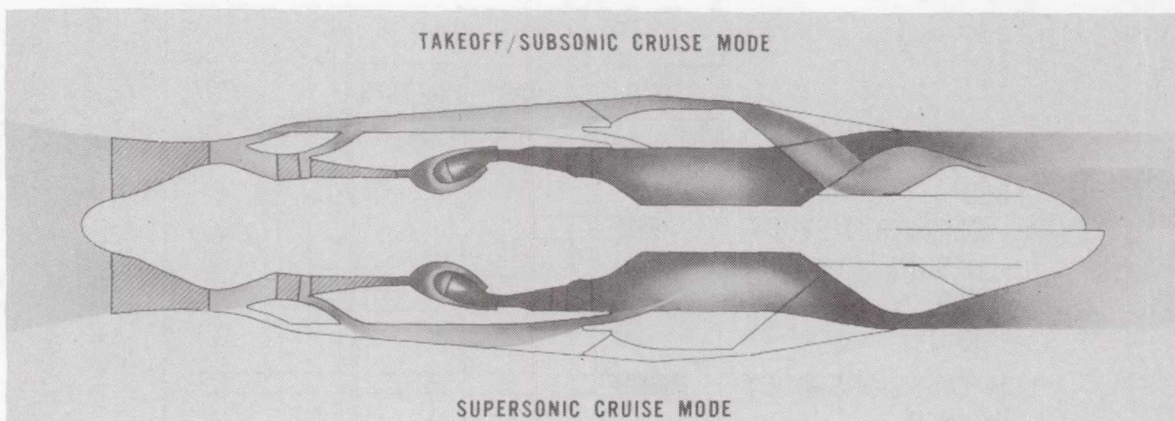
Figure 8.- General Electric test-bed, double-bypass, variable-cycle engine.

	YEAR			
	1976	1977	1978	1979
COMPONENT TEST BED				
DEFINITION STUDY				
DESIGN				
FAB				
TEST				
VARIABLE FLOW FAN				
COANNULAR NOZZLE MODEL TESTS				
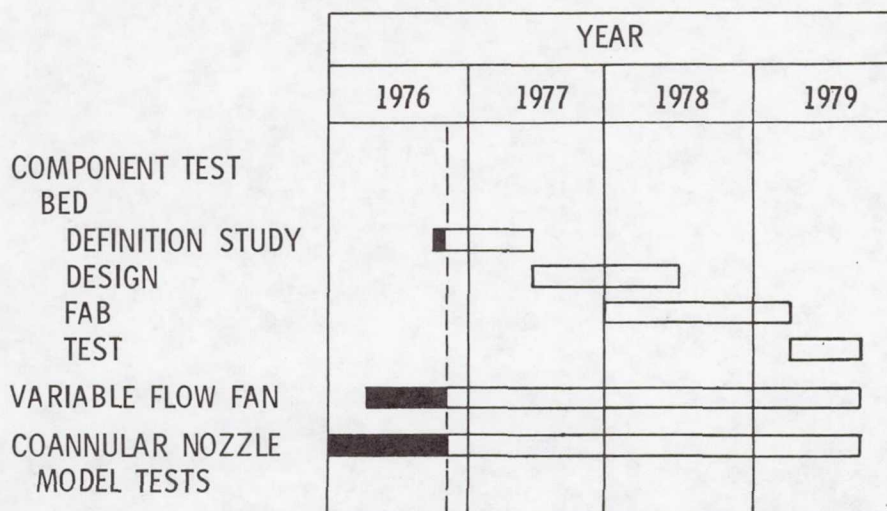
Figure 9.- Schedule of component test program for
G.E. double-bypass, variable-cycle engine.

Page intentionally left blank

SUPERSONIC CRUISE INLETS FOR VARIABLE-CYCLE ENGINES

David N. Bowditch
NASA Lewis Research Center

SUMMARY

Variable-cycle engines have the potential to operate very efficiently over
the wide speed range of a supersonic cruise aircraft. However, to choose
the optimum installed variable-cycle engine, it is necessary to determine its
performance when matched to a specific inlet. The performance of candidate
supersonic cruise inlets is reviewed and the aerodynamic installation penalties
for each type are defined. The main characteristics that affect the airflow
schedules of variable-cycle engines are defined. These schedules are compared
with the airflow schedules of the candidate inlets, and appropriate inlets are
matched to the variable-cycle engine characteristics. Auxiliary inlets are
also considered.

INTRODUCTION

Variable-cycle engines (VCE's) have the potential ability to operate more
efficiently over the wide speed range of a supersonic cruise aircraft. In their
various forms, they also have the ability to improve the matching of airflow
schedules between the inlet and the engine and thereby to reduce the penalties
normally associated with airframe installation. Since the characteristics of
the available inlet and VCE types differ significantly, it is necessary to con-
sider how the inlet and engine cycle characteristics complement each other be-
fore an optimum propulsion system can be defined. Prior to variable-cycle en-
gines, the engine airflow schedule was presented to the inlet designer, who did
his best to match it with an inlet that would incur the lowest performance pen-
alties. More recently, the engine companies have been matching their engines
to the characteristics of particular inlets. Neither approach is likely to lead
to an optimum propulsion system. As a start in the search for the optimum, the
characteristics of the existing supersonic cruise inlet types are reviewed and
matched with the major cycle characteristics of the most promising variable-
cycle engines.

INLET CHARACTERISTICS

Inlets whose characteristics are representative of those currently being
considered for supersonic cruise applications are shown in figure 1. They are
either axisymmetric or two dimensional with collapsing or translating center-
bodies to provide throat area variation with Mach number. Conceptually, the

collapsing axisymmetric inlet would have a centerbody that collapses from the beginning of the second cone to a station near the engine face inside the subsonic diffuser. This would require the circular centerbody to be constructed of overlapping leaves and seals, which would be mechanically complex but potentially feasible. In the collapsing double-wedge inlet, the centerbody consists of ramps. These can be more easily sealed and actuated but tend to be heavier because of the less desirable structural characteristics of flat cowling. Potentially the simplest mechanically is the axisymmetric inlet with a translating centerbody to provide throat area variation. This inlet should be lightweight because of its simple variable-geometry system and its structurally efficient circular shape.

Some of the characteristic aerodynamic properties of the different inlet types are associated with their percentages of internal compression (fig. 2). This term is defined as that portion (in percent) of the total supersonic area contraction from the free stream to the inlet throat that occurs inside the cowl lip at the design Mach number. Therefore, if the cowl-lip circular area is taken as the free-stream flow area, the percentage of internal contraction is 100 times the difference in the annular flow area between the cowl lip and the throat, divided by the difference between the cowl-lip circular area and the throat area.

With zero internal compression (or all external compression) the inlet throat is at the cowl lip. To achieve supersonic compression, the centerbody must turn the flow to high angles relative to the inlet axis in order to achieve a low throat Mach number. The high cowl-lip angle necessary to capture that flow incurs a large cowl drag. Therefore, to reduce the cowl drag to an acceptable level for supersonic cruise, the external compression or turning is reduced so that a relatively flat cowl can capture the flow and turn it efficiently back toward the inlet axis. With about 45-percent internal compression, the flow will be turned back to a throat with its cowl radius about equal to the cowl-lip radius. This is the location desired for a collapsing-centerbody inlet so that maximum throat area can be obtained in the collapsed position. However, for a translating-centerbody inlet, the cowl-throat radius must be significantly smaller than the cowl-lip radius so that the resulting smaller centerbody will provide an increased throat area when it is translated out to the cowl lip. Internal compression of the order of 80 percent is required to obtain the maximum off-design throat area for a translating-centerbody inlet.

At 45 percent internal compression, the flow is still turned to a relatively high angle by the centerbody. With an axial or cylindrical cowl, a relatively strong oblique shock forms at the cowl lip to turn the flow back axially. There is an associated loss in total-pressure recovery. If the cowl angle is increased to reduce the recovery loss, cowl-lip wave drag is also increased. There is a cowl-lip angle that provides an optimum trade-off between recovery and drag at each value of internal compression. Figure 3 shows the effect of internal compression on total-pressure recovery and cowl drag for the optimum cowl-lip angle at Mach 2.4. The ideal total-pressure recovery includes only the losses associated with the inlet shock structure. The cowl-lip wave drag considered here is only that associated with the immediate lip region before the external angle can be reduced to some nominal value required to reach the

388

maximum nacelle diameter. Cowl-lip wave drag downstream of this point is assumed to be offset by favorable interference with the wing. For the variable-cycle engine used in the study, the optimum internal cowl angle was the minimum angle of 0° for internal compression greater than 45 percent. The resulting low external cowl angle is close enough to the nominal nacelle angle that any cowl-lip wave drag can be recovered through favorable interference. Therefore, only cowl-lip wave drag in excess of 0.0075 is considered a penalty for installed performance. Below 45-percent internal compression the internal cowl angle had to be increased to the minimum value required to prevent subsonic flow upstream of the throat. The higher cowl angles resulted in increased drag.

High inlet total-pressure recovery and low cowl-lip wave drag favor high internal compression, where the cowl-lip angle can be low and the cowl-lip oblique shock weak. However, the bleed flow for the inlet has not yet been considered. The inlet bleed correlation of reference 1 has shown that, for previously tested inlets, the bleed flow can be related only to the ratio of inlet internal wetted area to throat area. Also, the correlation shows that inlet wetted area increased with increasing internal compression. The effect of inlet recovery, cowl-lip wave drag, and bleed on installed cruise specific fuel consumption (sfc) is presented in figure 4. The cruise sfc increase is based on the cowl-lip wave drag of figure 3, the bleed flow predicted by the correlation of reference 1, and the ideal total-pressure recovery of figure 3, reduced by 0.04 to account for viscous losses. The total increase of 10 to 15 percent is based on a Lewis version of the variable-stream-control engine. This large increase in sfc is due to the specific thrust of this type of engine being about half that of the turbojets considered before FAR 36 noise constraints were imposed. As can be seen from the variation of sfc with percentage of internal compression for axisymmetric inlets, the increased bleed at high internal compression partially offsets the better total-pressure recovery. Therefore, an axisymmetric collapsing-centerbody inlet at 45-percent internal compression would provide an installed sfc about 0.013 higher than that provided by a translating-centerbody inlet at 80-percent internal compression. Some other features of low-internal-compression inlets that tend to offset this modest penalty are better angle of attack tolerance and a smaller unstart transient.

The correlation of inlet wetted area in reference 1 also showed that previously designed two-dimensional inlets had considerably more wetted area than equivalent axisymmetric inlets. In figure 4, the increase in bleed due to added wetted area penalized the two-dimensional inlet about 0.025 in installed sfc. The level presented assumes similar pressure recovery and no cowl-lip wave drag that cannot be recovered through favorable interference with the wing.

INLET/ENGINE AIRFLOW MATCHING

To understand the airflow matching of the inlet and the engine, it is first necessary to look at the airflow characteristics produced by the major VCE features. These are constant-speed and inverse throttle schedules and the double-bypass mode of operation for takeoff. The airflow characteristics are presented in figure 5, along with the engine mechanical and corrected speeds, as a func-

tion of Mach number. The values are presented as a fraction of their value at Mach 1. For the constant-speed throttle schedule, the engine mechanical speed is constant over the Mach number range, except at takeoff where the speed is increased about 5 percent. The corrected speed varies a little subsonically as the temperature changes with aircraft acceleration and climb. However, as the aircraft accelerates supersonically to the supersonic cruise Mach number of 2.32, the increased temperature reduces the corrected speed to about 0.8 of the value at Mach 1. The airflow at constant speed remains essentially constant subsonically but drops to about 0.62 of its Mach 1 value at the cruise Mach number of 2.32. With the inverse throttle schedule, mechanical speed is varied subsonically to retain constant corrected speed. During supersonic accelera- tion the low rotor speed is increased with Mach number until a 10-percent in- crease is provided at supersonic cruise. This still allows the corrected speed and airflow to decrease but increases the flow at cruise significantly over the constant-speed throttle schedule. This increased flow will require a larger inlet. The third characteristic, double bypass, changes the engine cycle at takeoff to pump more airflow to alleviate jet noise. The flow increase in this case is 15 percent, but other values have also been considered.

To determine the effect of these airflow schedules on inlet airflow match- ing, the matching of a constant-speed throttle schedule to a translating- centerbody inlet is considered in figure 6. The inlet area is presented as a portion of the engine-face annular flow area. The upper curve presents the capture area for an inlet designed to just provide the engine airflow at each Mach number. The lower curve presents the maximum throat area obtainable with that translating-centerbody inlet. This maximum throat area is obtained by sizing the centerbody so that, when it is translated forward, the flow area between the cowl lip and centerbody is just equal to the flow area between the cowl and the centerbody support tube. The required inlet capture area varies from 0.73 of the engine-face area at Mach 1 to 1.38 at Mach 3. Comparing the maximum throat area at each Mach number with the required area of 0.73 at Mach 1 shows that a translating-centerbody inlet will provide adequate throat area for design Mach numbers of 2.7 and above. However, for the cruise Mach numbers of current interest, between Mach 2.0 and 2.5, inadequate throat area is available. Therefore, such an inlet/engine combination would require auxiliary inlets in the transonic speed regime.

In figure 7, the capture and throat areas required for matching an inverse throttle schedule engine are added to figure 6. The increased airflow demand of the inverse throttle schedule requires a larger inlet capture area at the cruise Mach number. This increased inlet size increases the throat area enough to provide adequate transonic flow for engine matching. Therefore, the translating-centerbody inlet provides a good airflow match for the inverse throttle schedule engine.

To look at the airflow matching in more detail, figure 8 compares the variation of airflow with Mach number for inlets with collapsing and translating centerbodies. The design Mach number for the inlets is 2.32. When operating with supersonic internal flow at Mach numbers below the design value, the translating centerbody moves forward relative to the cowl lip. More flow is spilled than by an inlet with a centerbody that collapses in place. Therefore,

390

because of its larger spillage, the translating-centerbody inlet provides less flow for the engine than the collapsing-centerbody inlet. Both axisymmetric and two-dimensional collapsing-centerbody inlets provide similar airflow schedules. The inlets cannot operate with internal supersonic flow at Mach numbers below 1.5, and below this Mach number the flow is governed by the maximum inlet throat size. Here again, the collapsing-centerbody inlet can provide more flow than the translating-centerbody inlet because of its larger throat area.

Figure 9 superimposes the engine flow requirements on the inlet airflow schedules. Again comparing the constant-speed throttle schedule with the translating-centerbody inlet, it is apparent that the inlet would need auxiliary inlets not only for extra flow at transonic speeds but also for speeds up to about Mach 2. A much better match for the constant-speed throttle schedule appears to be provided by the collapsing-centerbody inlet. Therefore, this conventional engine speed schedule appears to require a collapsing-centerbody inlet for design Mach numbers in the 2.0 to 2.5 range. A comparison of the inverse throttle airflow schedule with the translating-centerbody airflow schedule also shows a good match. Therefore, these two throttle schedules require different inlet types.

Another airflow matching problem occurs during takeoff, where the inlet must collect flow from a wide area. Normally either a bellmouth or the blunt lips of a subsonic inlet are available to collect the necessary flow and turn it toward the engine. However, the sharp inlet lips necessary for low drag at supersonic cruise conditions can only collect a portion of the flow required by the engine during static operation and takeoff. This problem is illustrated in figure 10. The critical parameter for this condition, the inlet mass flow divided by the mass flow necessary to choke the inlet throat at ambient total pressure and temperature, is plotted on the ordinate. Both the inverse and constant-speed throttle schedules require 0.9 of the choked flow of the translating- and collapsing-centerbody inlets, respectively. The double-bypass cycle requires 1.05 of the choked flow. Also plotted on the figure are lines of constant total-pressure recovery obtained from reference 2. As the inlet gains forward speed, the momentum of the captured flow is more alined with the inlet axis, allowing more flow to be collected by the sharp-lip inlet at a given total-pressure recovery. At Mach 0.1 for takeoff, the propulsion system should provide maximum thrust so that a high total-pressure recovery is required to minimize engine weight. If a total-pressure recovery of about 0.98 is assumed, the mass flow ratio cannot be greater than 0.45. Therefore, half of the conventional engine airflow requirement at takeoff has to be provided by an auxiliary inlet system. To provide the extra flow required by the double-bypass engine, the auxiliary inlet system will have to provide 57 percent of the engine airflow, or 132 percent of the main inlet flow.

At Mach 0.3 to 0.4, the fan noise will probably have to be suppressed to meet the flyover noise requirements. This can be accomplished with the conventional cycles by choking the main inlet, which can provide high recovery at that Mach number without auxiliary inlets. However, the increased flow requirement of the double-bypass engine would require choking the auxiliary and main inlet systems, which would incur added complexity. An alternative solution would be to reduce the engine airflow to the normal level before the flyover point is reached.

CONCLUSIONS

The characteristics of axisymmetric and two-dimensional inlets with col-
lapsing or translating centerbodies have been compared with the requirements of
variable-cycle engines with constant-speed or inverse throttle schedules and/or
double-bypass features. The following conclusions were reached:

1. An engine with a constant-speed throttle schedule will require a
collapsing-centerbody inlet for cruise Mach numbers between 2.0 and 2.5.

2. An engine with an inverse throttle schedule matches a mechanically sim-
pler translating-centerbody inlet.

3. If a total-pressure recovery of 0.98 is assumed at takeoff, the larger
airflow of the double-bypass engine requires the airflow of the auxiliary inlet
system to be increased from 100 percent to 132 percent of the main inlet air-
flow.

4. At the flyover condition, fan noise suppression for the double-bypass
engine will require choking both the main and auxiliary inlet systems or re-
ducing the double-bypass engine airflow to the conventional engine airflow that
can be supplied by the main inlet.

REFERENCES

1. Bowditch, D. N.: Some Design Considerations for Supersonic Cruise Mixed-
   Compression Inlets. AIAA Paper 73-1269, Nov. 1973.

2. Fradenburgh, Evan A.; and Wyatt, DeMarquis D.: Theoretical Performance
   Characteristics of Sharp-Lip Inlets at Subsonic Speeds. NACA TN 3004, 1953.

COLLAPSING AXISYMMETRIC   COLLAPSING DOUBLE WEDGE   TRANSLATING AXISYMMETRIC

CS-78315
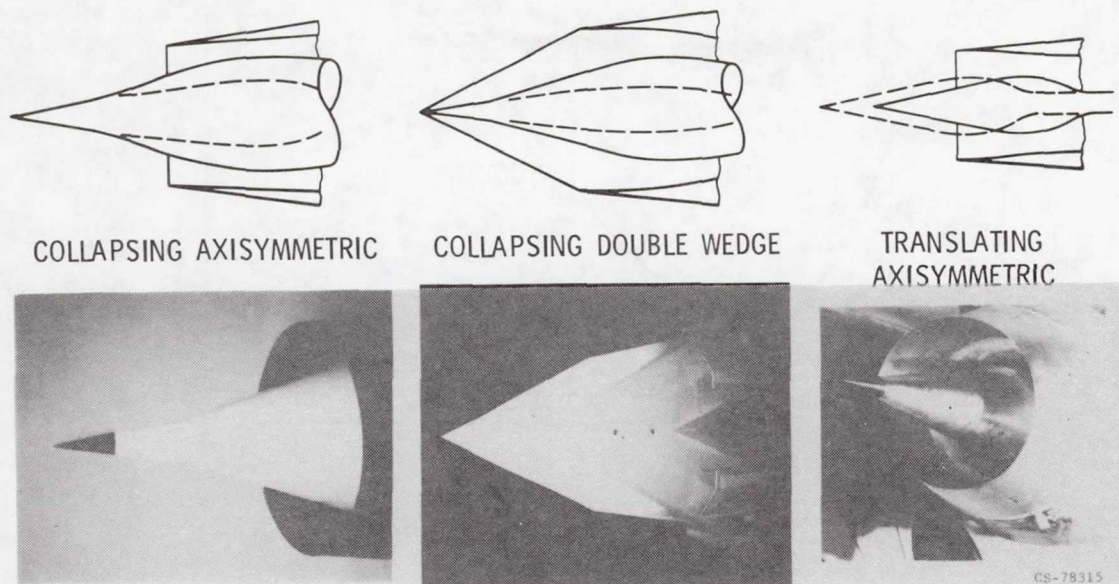
Figure 1.- Inlet concepts for use on supersonic cruise aircraft.

COWL LIP ANGLE

ALL EXTERNAL COMPRESSION   45% INTERNAL COMPRESSION

80% INTERNAL COMPRESSION
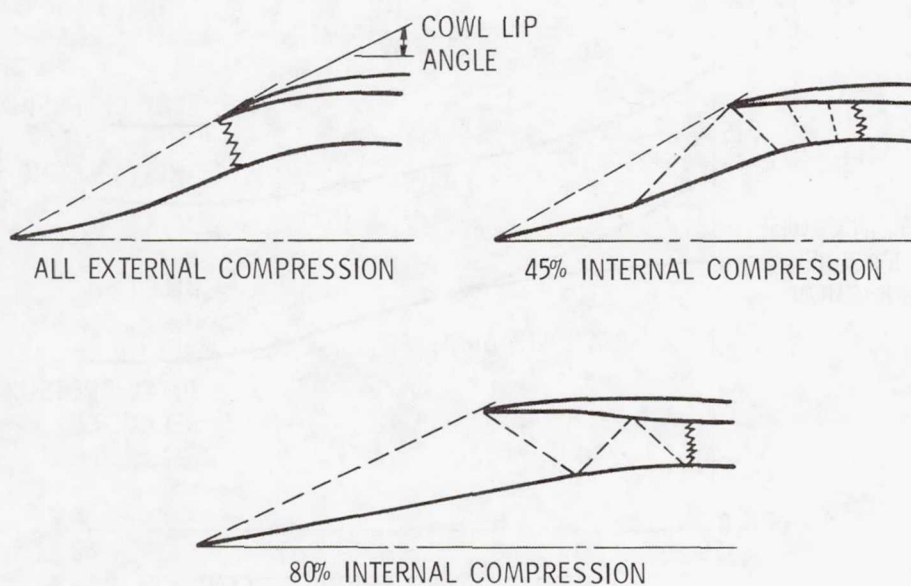
Figure 2.- Supersonic inlets with varying percentages of
internal compression.

393
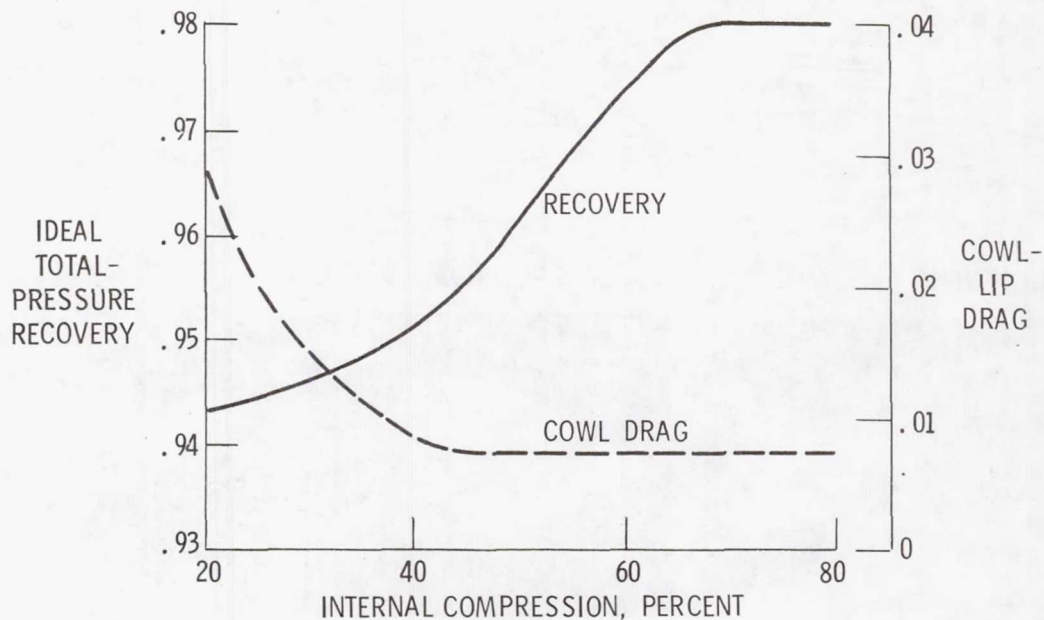
Figure 3.- Effect of internal compression on total-pressure recovery
and cowl-lip wave drag at Mach 2.4.
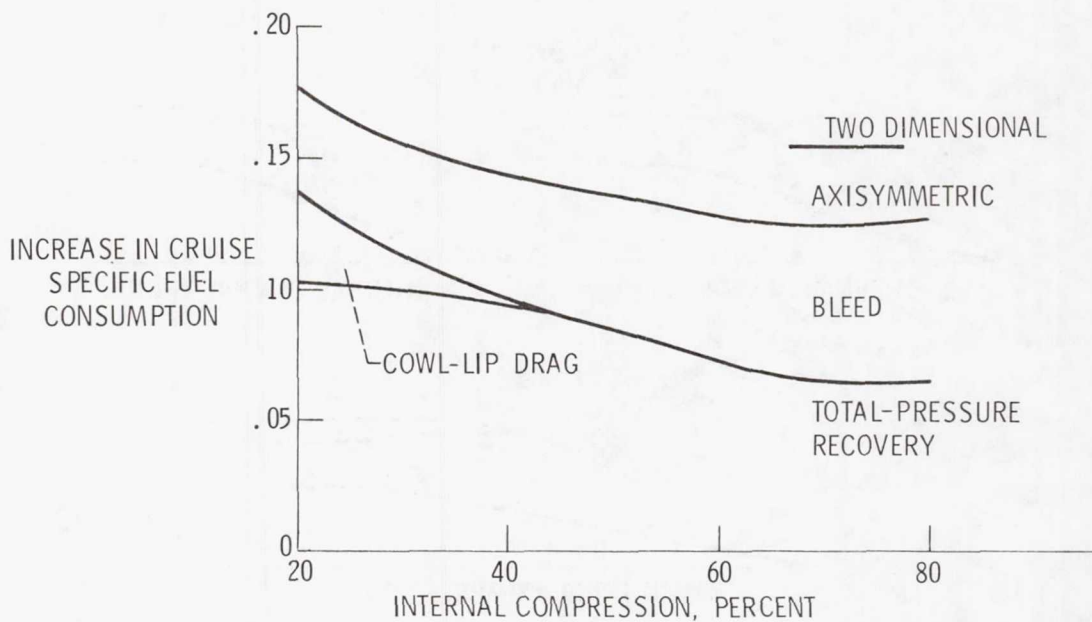
Figure 4.- Effect of internal compression on specific fuel
consumption at Mach 2.4. Reference sfc, 1.19.
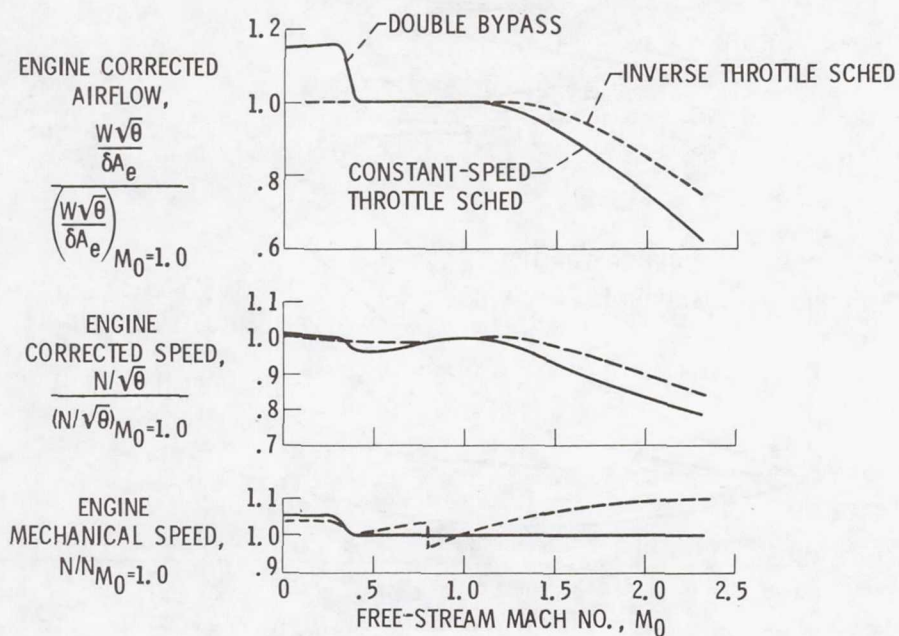
Figure 5.- Airflow characteristics of variable-cycle engines.
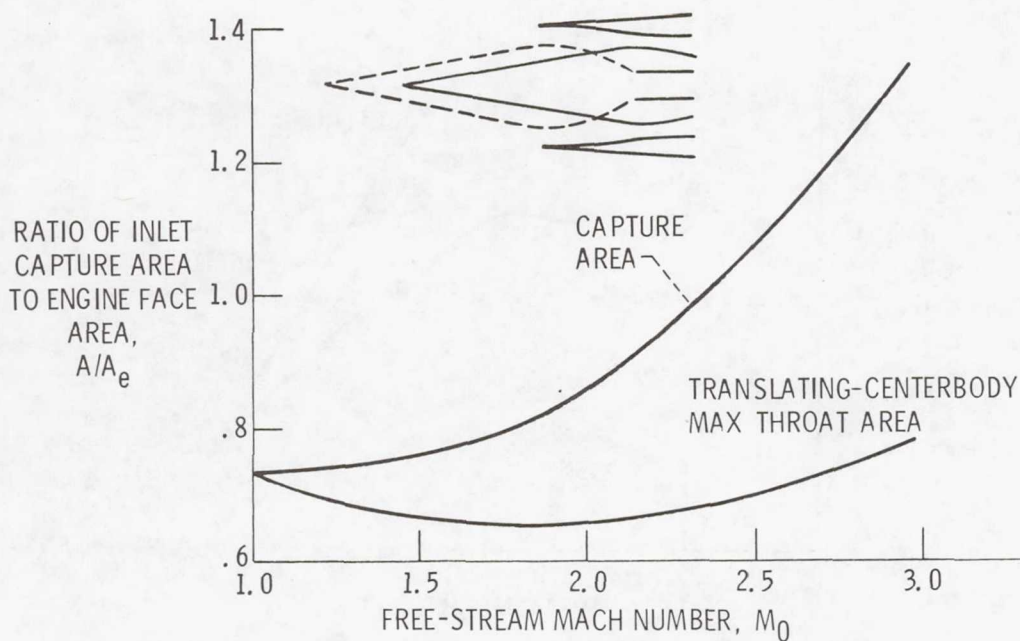
Figure 6.- Transonic airflow matching of constant-speed throttle schedule and translating-centerbody inlet.

395
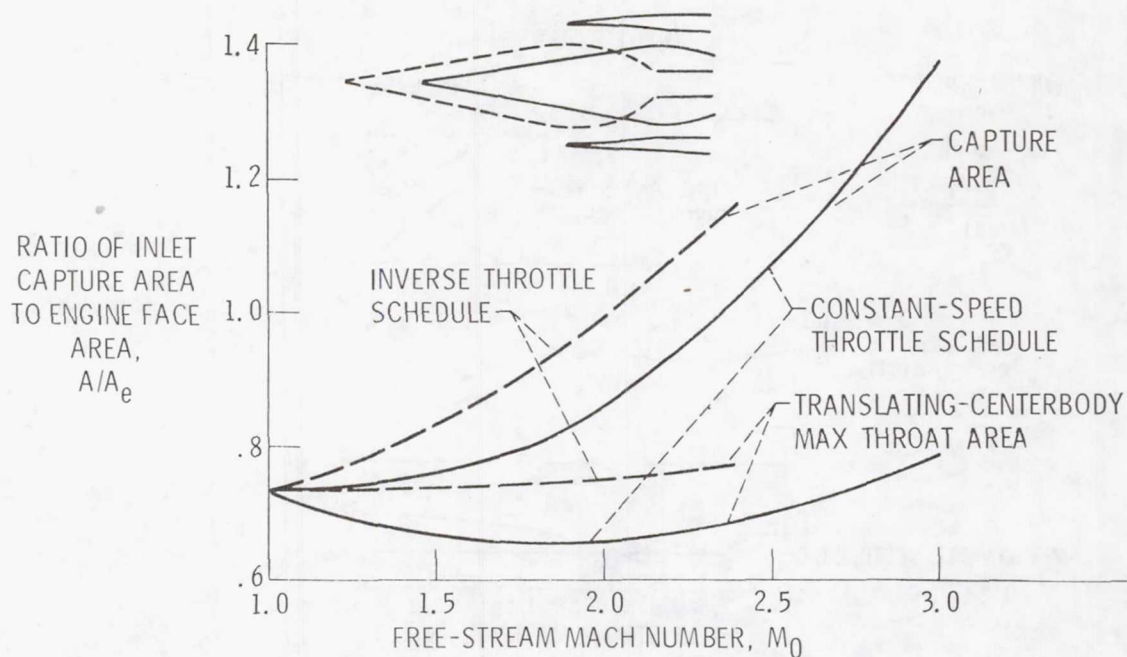
Figure 7.- Transonic airflow matching of inverse throttle schedule
and translating-centerbody inlet.
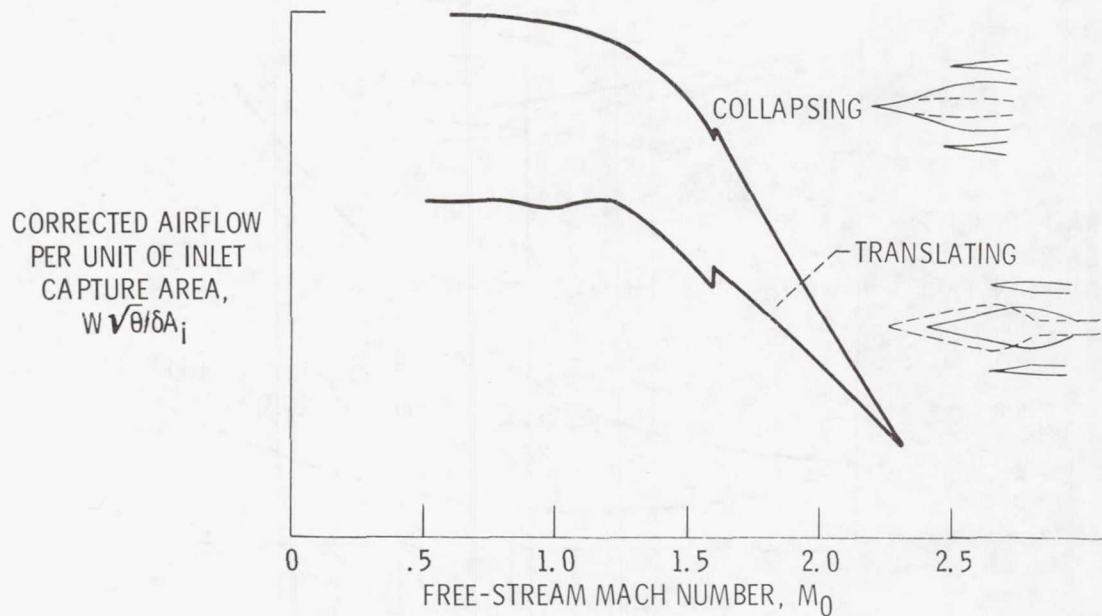
Figure 8.- Variation of airflow with Mach number for translating-
and collapsing-centerbody inlets.
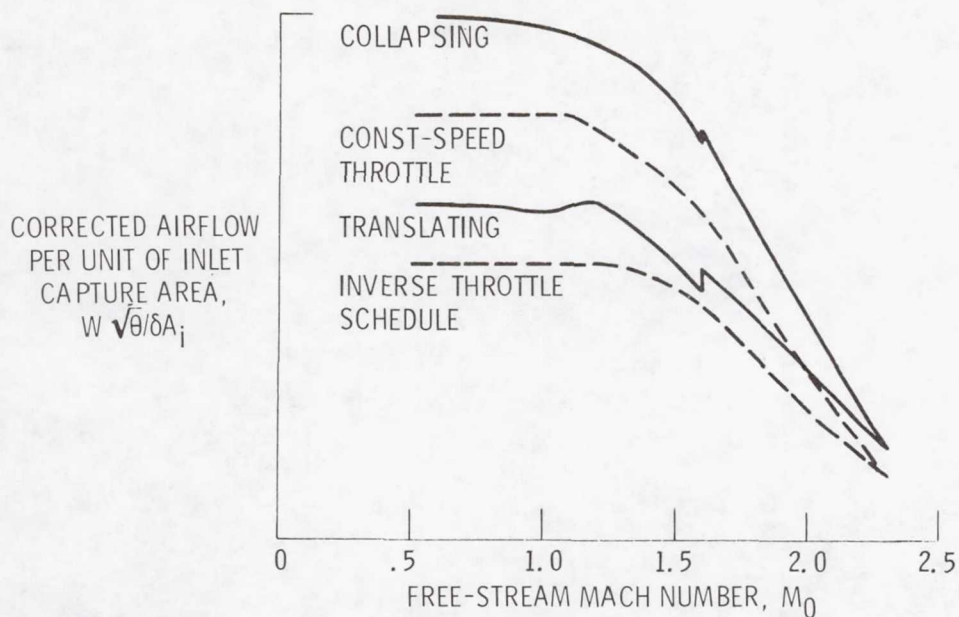
Figure 9.- Inlet/engine matching.
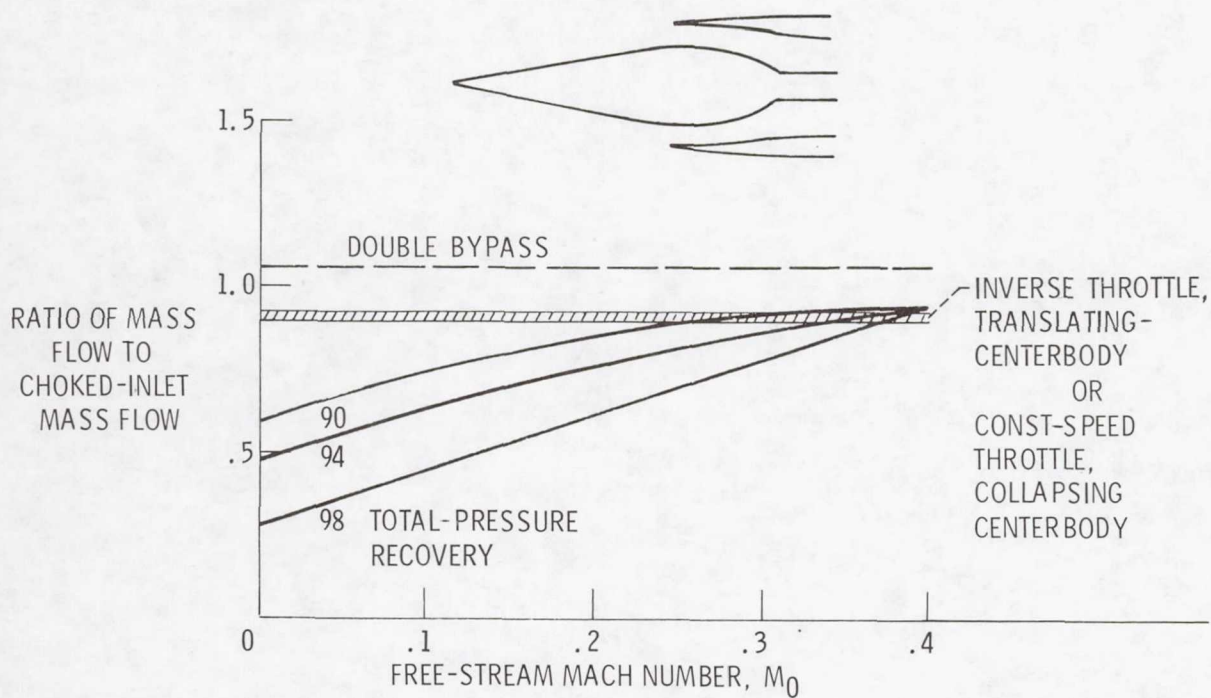
Figure 10.- Low-speed airflow matching.

Page intentionally left blank

CONTROL OF PROPULSION SYSTEMS FOR SUPERSONIC CRUISE AIRCRAFT

Kirby W. Hiller and Daniel I. Drain
NASA Lewis Research Center

SUMMARY

The unique propulsion control requirements of supersonic aircraft are presented. Integration of inlet, engine, and airframe controls is discussed. The application of recent control theory developments to propulsion control design is described. Control component designs for achieving reliable, responsive propulsion control are also discussed.

INTRODUCTION

Propulsion controls are vital to the successful functioning of supersonic aircraft. As an example of what a propulsion control is supposed to do, consider the YF-12 aircraft shown in figure 1. The YF-12 employs mixed-compression inlets and afterburning turbojet engines. When the aircraft is cruising under design conditions, the control's job is to operate the mixed-compression inlet so that it produces high pressure recovery. The engine must be operated under conditions of high efficiency while avoiding limits such as rotor overspeed and turbine overtemperature. The control must ensure stable operation so that an atmospheric disturbance does not cause the inlet to unstart. Unstart is the phenomenon where the shock pops out in front of the inlet and the pressure recovery drops. The control also has to accommodate off-design operations like takeoff, climb, descent, and landing. The control must balance high efficiency against stability. For example, this kind of inlet achieves its highest pressure recovery when it is just on the verge of unstart. Controls developments now underway may make it possible to ease the harshness of this compromise. Thus, to a degree, we will be able to improve efficiency without losing stability.

As further background, consider the elements that make up an engine speed control (fig. 2). A commanded speed is fed to a computer. There it is compared against the sensed speed. The speed error is determined by the computer and used to drive an actuator - in this case, the fuel valve. The change in fuel flow to the engine changes engine speed so as to reduce the speed error. This is called a control loop; its components, the computer, the actuator, and the sensor, appear in every control system. Other control developments now in progress are improving the type of hard-

ware that will be used in these components. The simpler notation in the lower part of figure 2 can be used to represent the control. The hollow arrow implies that several signals can be transmitted both ways. The "control" box can represent several control loops like the one above it. Even a simple nonafterburning subsonic engine can employ as many as three control loops.

INLET AND ENGINE CONTROL REQUIREMENTS

Having established this background the subject at hand, supersonic propulsion control, can now be discussed. An inlet that might be used in a supersonic aircraft is shown in figure 3. It is an axisymmetric, mixed-compression inlet with a translating centerbody. The inlet variables that a control would manipulate are called out in the figure. Two main inlet control variables are translation of the centerbody and opening of the bypass doors. Translating the centerbody controls the strength of the normal shock. Opening the bypass doors controls the position of the normal shock to a location just aft of the throat. For takeoff and acceleration, auxiliary flow doors might also be used to increase inlet-supplied airflow (ref. 1).

One type of advanced engine that might be used in a supersonic aircraft is shown in figure 4. It is the Pratt & Whitney variable stream control engine (refs. 2 and 3). The temperature and velocity of the two streams are controlled independently. The engine variables that a control would manipulate are variable geometry in the fan and in the core compressor, two independently controlled fuel flows for the main combustor and two for the duct combustor. Control of the exhaust nozzle would entail actuation of four items: ejector doors (for bringing in auxiliary airflow), the duct nozzle, the primary nozzle, and a thrust-reversing clamshell. The free-floating divergent flaps would not be controlled. This adds up to 10 independently controlled variables for the engine and three for the inlet. Other inlet and engine designs could involve more variables; additional variables could include turbine-outlet guide vanes, tip clearance controls, and additional auxiliary air intakes for the inlet.

The features of this supersonic propulsion system that present unique control requirements are as follows: First, it is obvious that the number of manipulated variables will be large. Also, the mixed-compression inlet has the inherent danger of unstart. Economics would motivate us to operate the inlet with the shock well forward, near the verge of unstart. Coupling this inlet to an augmented bypass engine could permit an airflow transient to propagate forward through the unchoked fan, resulting in an inlet unstart (refs. 4 and 5). Yet in a commercial aircraft a violent inlet unstart would be very objectionable. Also the controls must operate in a high-temperature environment. Taken together, these features imply the need for some important advances in propulsion controls.

CONTROL INTEGRATION

The most important propulsion control advancement occurring today is the use of digital control computers. Computers allow us to exercise more complex control laws and thus to more closely integrate the inlet, engine, and airframe controls. Control integration is illustrated by figures 5 and 6. Figure 5 represents the separate controls for the inlet (three control loops) and the engine (10 control loops). Most supersonic propulsion controls transmit some coordination signals between the inlet and engine controls, as illustrated by the lower arrow in figure 6. Usually, these signals are simple overrides.

Some research programs have carried integration past the point of simple overrides. Figure 7 shows a mixed-compression inlet/turbojet engine combination that was investigated at the Lewis Research Center. The inlet and engine were operated under computer control (refs. 6 and 7). We found that if the bypass doors were open, spilling a lot of air, we could increase engine airflow by uptrimming engine speed. This forced the bypass doors to close, eliminating bypass drag and improving cruise efficiency. Now we had two ways to control shock position and so could do it more effectively. In addition, the problem of inlet-engine matching was simplified. Normally, matching is done by building the inlet to close tolerances and then trimming the engine's airflow on a calibration stand. This automatic engine trimming feature has been incorporated in the controls for the B-1 aircraft.

Figure 8 shows another inlet/engine combination investigated at the Lewis Research Center, a turbofan and a mixed-compression inlet. This model was operated under digital computer control (ref. 5). It was the first time a turbofan and mixed-compression inlet had been operated together. We found that inlet operation is more sensitive to engine operation with this kind of an engine. An afterburner lightoff can feed forward through the unchoked fan to unstart the inlet (refs. 4 and 5). However, the afterburner never lights off without action initiated by the engine control. Thus, a simple anticipator, resetting normal shock position to a more aft location, could permit safe afterburner lightoff. This inlet/engine combination did not present insurmountable interaction problems. In steady operation, the afterburner did not excite inlet instabilities. However, we did have to reset inlet operation to anticipate afterburner transients.

A further step in integration studies was the Integrated Propulsion Control System (IPCS) program (ref. 8). This was a joint Air Force-NASA program involving the F-111 aircraft (fig. 9). One of the inlet/engine systems of an F-111 aircraft was operated under electronic digital control. Some of the important aspects of the program are as follows: Inlet distortion was sensed on line by five electronic pressure transducers. This distortion was converted to a distortion index and used to control the

opening of the seventh-stage compressor bleeds. Opening the bleeds reduced the pressure ratio of the front stages, increasing their distortion tolerance but reducing overall engine efficiency. Using the distortion index to operate the bleeds delayed their opening point to a higher Mach number. If both inlet/engine systems had been under digital control, the cruise range at Mach 2.2 would have been increased by 16 percent (ref. 9). A number of new control modes were incorporated into the F-111's electronic control. Two gave results of distinct importance. By sensing compressor discharge Mach num-number, tighter control of the surge margin was obtained during acceleration. With the tighter schedule, engine acceleration time was shortened. On the average, acceleration time was reduced by 26 percent. Also by including fan pressure ratio sensing and using more complex logic to control fuel flows to the afterburner fuel manifolds, the military to maximum afterburning transient time could be shortened. The transient time was reduced by 40 percent on the average.

ADVANCED CONTROL THEORY APPLICATION

In its ultimate version, integration of propulsion controls will assume a form where a separate inlet and engine control are no longer identifiable. This integration will be facilitated by the application of advanced control theory. The application of this theory to an engine alone will take the form illustrated in figure 10. Through a matrix of gains, every input will affect every output to a greater or lesser degree, depending on each element of the matrix. The resulting control is termed a "modern" control to distinguish it from conventional control designs that would be termed "classical" controls.

Modern control theory was developed to handle the problems of systems with dozens of inputs and outputs, such as process controls. It has the following advantages: It is a computer-aided design process. It results in controls that are optimal. A mathematically described performance index establishes the optimized control gains. It is especially suited to the design of multiloop controls. And, its use eliminates loop interactions, where closing one loop destabilizes another.

One of the most thoroughly developed modern control techniques is called Linear Quadratic Regulator Theory, or LQR (ref. 10). The term is derived from the facts that the plant is assumed to be linear and that the performance index uses weighting factors which give rise to matrix equations involving quadratic forms. An LQR-designed control for the F100 engine is being developed under a joint Air Force/NASA contract. The design is to be evaluated at the Lewis Research Center on an F100 engine in an altitude tank (fig. 11). The engine will be operated under digital control from a computer located in the simulation facility. At the moment, we are controlling a real-time simulation of the F100 engine from the same digital control computer in

preparation for the experimental program (ref. 11).

This program is the first experimental application of LQR theory to a propulsion system. Its objective is to see if LQR can be adapted to the nonlinear control requirements of an F100 engine. To accommodate the nonlinear effects, LQR designs for selected operating points within the flight envelope are stored in the engine controller. The control gains are blended between adjacent operating points to obtain continuous nonlinear control.

Of course, the modern control design technique is not limited to just one control at a time. As shown in figure 12, it can include the inlet, engine, and airframe controls in one formulation. As the control encompasses more of the whole system, its advantages increase. If the F100 program is successful, it may be expanded to flight demonstrations of airframe/inlet/engine controls.

CONTROL COMPONENTS

Unique to electronic control is the reliability problem with electronic hardware. Electronic sensors and actuators are remarkably less reliable than older components like a bellows pushing on a lever. Electrical transmission of signals is prone to electromagnetic interference, and electrical connectors can become unreliable in humid or salty environments. Electronic controls have the ability to process multiple signals, permitting use of more complex sensors. Also the digital computer needs sensors and actuators that communicate with digital signals or with something like frequency or pulse width, where counting or timing can be used. These characteristics of electronic control will give rise to new control sensors and actuators that are more suitable for use with electronic propulsion control. They will be reliable, may provide more complex input signals, and will communicate digitally. We at Lewis and others are working on these digital-compatible components (ref. 12).

The reliability problem of the engine-mounted electronic control is illustrated in figure 13. Mounting the computer, sensors, and actuators on the engine subjects them to high temperatures and vibration levels. For the supersonic aircraft the engine compartment temperatures will be higher and cooling fuel will be hotter. One solution is presented in figure 14. Here two steps are taken to improve reliability: the computer is off-engine mounted, and the sensors and actuators employ fiber-optic signal transmission, wherein signals are transmitted by light via bundles of optical fibers. Optical signal transmission has been found to be immune to the problems of electrical interference that plague electrical communications. The design of a fiber-optic-connected sensor is illustrated in figure 15. In the digital computer package would be a light source and lens system to illuminate the optical fiber ends. Only rugged, passive components would be mounted on the engine. The mask, whose translation is the

variable being measured, would interrupt the light beams like an encoder mask. The receiver fibers would then be illuminated, depending on the mask position. The output from the detectors would be a parallel digital word that could be used directly by the digital computer.

Although the thrust today is in the direction of greater controls sophistication, an inescapable limitation is the speed of response of the control actuator. The bypass doors shown in figure 16 would not be able to compensate for disturbances having frequencies higher than 1 or 2 hertz even though a supersonic inlet can respond to disturbances having frequencies of 30 hertz. The stability of a supersonic inlet can be improved by using self-acting valves ahead of the throat that open in response to the pressure rise across the shock. These valves can then bleed air out of the inlet in tandem with the bypass doors in order to draw the shock back to a stable location. This design is shown in greater detail in figure 17. Here, the static pressure behind the shock is higher. This higher pressure bleeds into the chamber under the valve and forces the valve piston open. Air then bleeds out of the inlet, stabilizing the position of the normal shock. A system like this was tested on a YF-12 inlet in a Lewis supersonic wind tunnel (refs. 13 to 16). It extended the frequency range of disturbances the inlet could tolerate by a factor of more than 10. This is an example of a technique that would permit operating at higher efficiency without sacrificing stability.

CONCLUSIONS

In conclusion, it has been shown that the control needs of supersonic aircraft are significantly more stringent than those of subsonic aircraft. Controlling the many variables involved will require a combination of sophisticated digital control computers, advanced-design control laws, possible use of novel inlet bleed valves, and reliable digital-compatible sensors and actuators. Military and civil programs will be advancing the state of the art in these areas. But these programs should be watched closely and special attention given to the specific needs of the commercial supersonic aircraft. These needs are likely to be in the areas of mixed-compression-inlet stability, controls for variable-cycle engines, multivariable control for an interacting inlet/engine/airframe system, and high-temperature control components.

REFERENCES

1. Sorensen, Norman E.; Latham, Eldon A.; and Smeltzer, Donald B.: Variable Geometry for Supersonic Mixed-Compression Inlets. J. Aircr., vol. 13, no. 4, Apr. 1976, pp. 309-312.

2. Weber, Richard J.: NASA Propulsion Research for Supersonic Cruise Aircraft. Astronaut. Aeronaut., vol. 14, no. 5, May 1976, pp. 38-45.

3. Willis, Edward: Variable-Cycle Engines for Supersonic Cruise Aircraft. NASA TM X-73463, 1976.

4. Baumbick, Robert J.; Batterton, Peter G.; and Daniele, Carl J.: Effect of After-burner Lights and Inlet Unstarts on a Mixed-Compression-Inlet Turbofan Engine Operating at Mach 2.5. NASA TM X-3223, 1975.

5. Batterton, Peter G.; Arpasi, Dale J.; and Baumbick, Robert J.: Digital Integrated Control of a Mach 2.5 Mixed-Compression Supersonic Inlet and an Augmented Mixed-Flow Turbofan Engine. NASA TM X-3075, 1974.

6. Cole, Gary L.; Neiner, George H.; and Wallhagen, Robert E.: Coupled Supersonic Inlet-Engine Control Using Overboard Bypass Doors and Engine Speed to Control Normal Shock Position. NASA TN D-6019, 1970.

7. Paulovich, Francis J.; Neiner, George H.; and Hagedorn, Ralph E.: A Supersonic Inlet-Engine Control Using Engine Speed as a Primary Variable for Controlling Normal Shock Position. NASA TN D-6021, 1971.

8. Bentz, Charles E.; and Zeller, John R.: Integrated Propulsion Control System Program. SAE Paper 730359, Apr. 1973.

9. Burcham, F. W., Jr.; and Batterton, P. G.: Flight Experience with a Digital Integrated Propulsion Control System on an F-111E Airplane. AIAA Paper 76-653, July 1976.

10. Special Issue on the Linear-Quadratic-Gaussian Estimation and Control Problem. IEEE Trans. Autom. Control, vol. AC-16, no. 6, Dec. 1971, pp. 527-869.

11. Seldner, Kurt: Simulation of a Turbofan Engine for Evaluation of Multivariable Optimal Control Concepts. NASA TM X-71912, 1976.

12. Kast, Howard: Fail-Fixed Servovalve. AFAPL-TR-76-24, General Electric Co., 1976.

13. Blausey, G. E.; Coleman, D. M.; and Harp, D. S.: Feasibility Study of Inlet Shock Stability System of YF-12. (SP-1964, Lockheed Aircraft Corp.) NASA CR-134594, 1972.

14. Cole, Gary L.; Dustin, Miles O.; and Neiner, George H.: A Throat-Bypass Stability System for a YF-12 Aircraft Research Inlet Using Self-Acting Mechanical Valves. NASA TM X-71779, 1975 (Also available as AIAA Paper 75-1181).

15. Dustin, Miles O.; and Neiner, George H.: Evaluation by Step Response Tests of Prototype Relief Valves Designed for YF-12 Inlet Stability Bleed System. NASA TM X-3262, 1975.

16. Webb, John A., Jr.; and Dustin, Miles O.: Analysis of a Stability Valve System for Extending the Dynamic Range of a Supersonic Inlet. NASA TM X-3219, 1975.
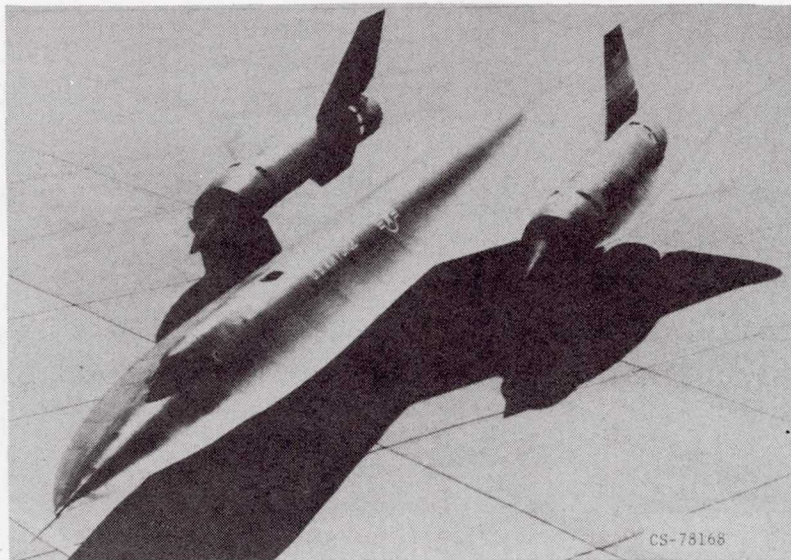
Figure 1.- YF-12 aircraft.
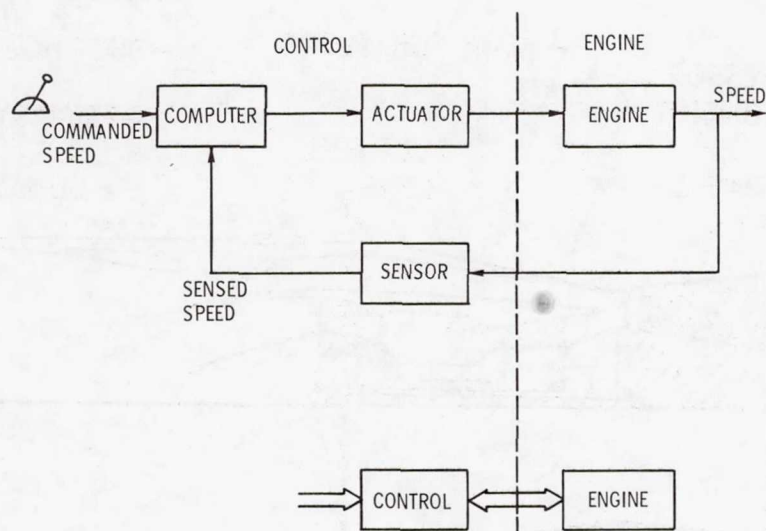
Figure 2.- Elements of an engine speed control system.
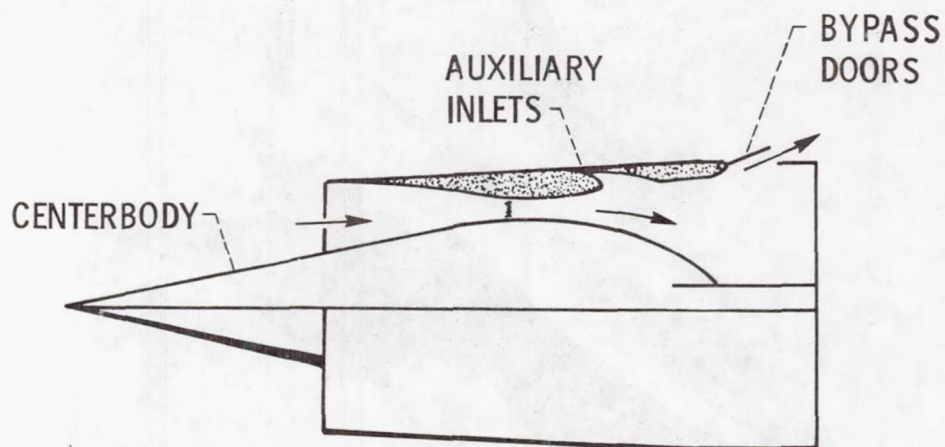
Figure 3.- Supersonic, mixed-compression inlet, showing
control variables.
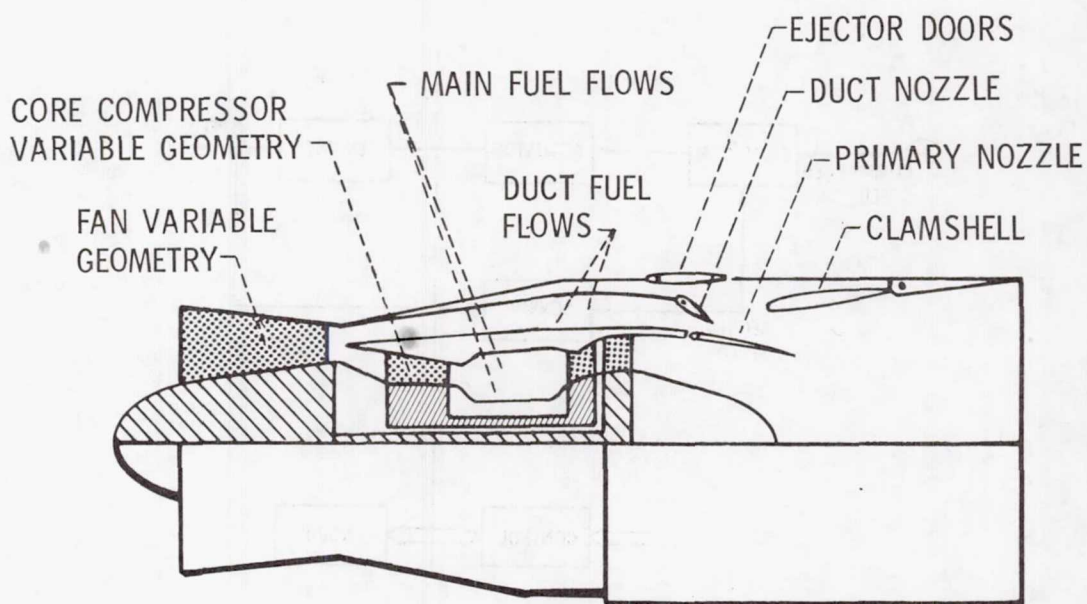
Figure 4.- Supersonic engine, showing control variables.
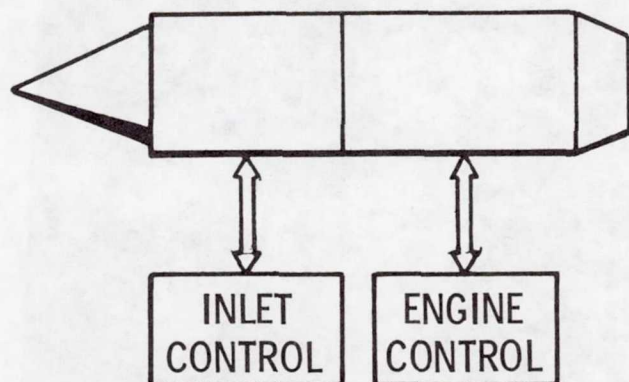
Figure 5.- Separate inlet and engine controls.
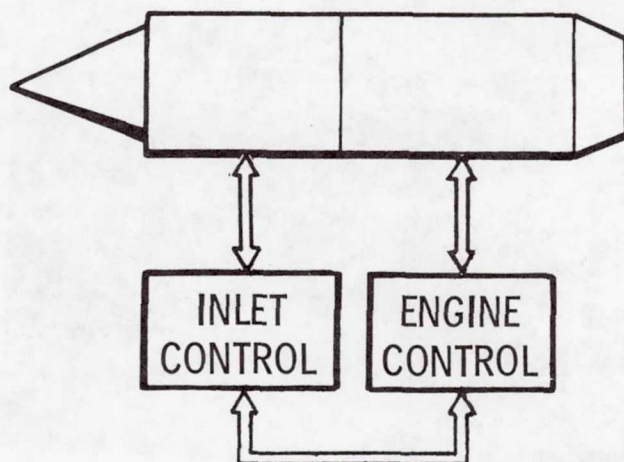
Figure 6.- Integrated propulsion control.
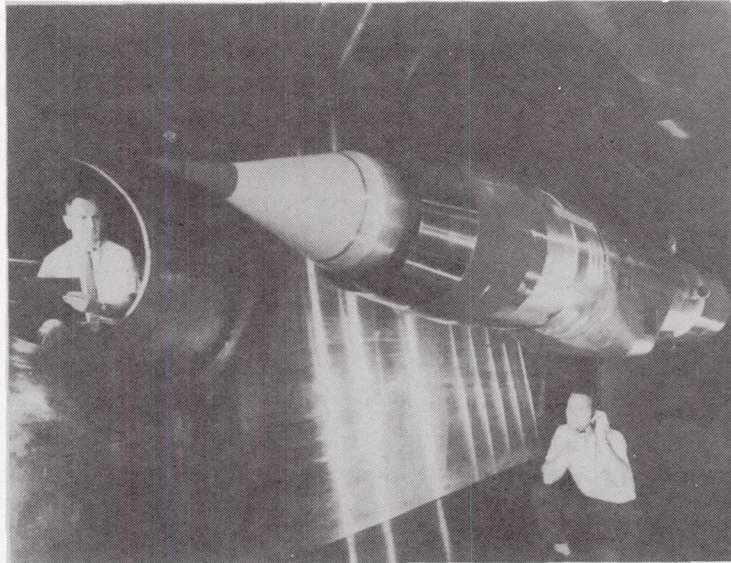
Figure 7.- Mixed-compression inlet and J85
turbojet engine in 10- by 10-foot super-
sonic wind tunnel.
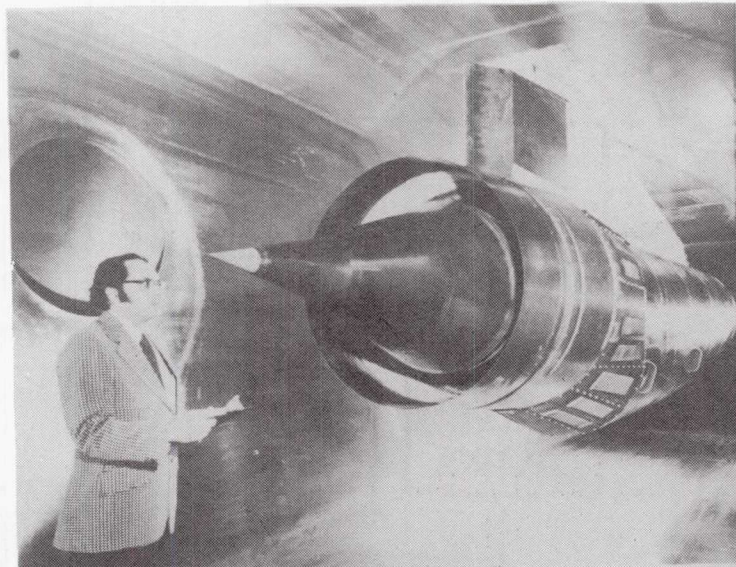
Figure 8.- Mixed compression inlet and TF-30
turbofan engine in 10- by 10-foot super-
sonic wind tunnel.

410
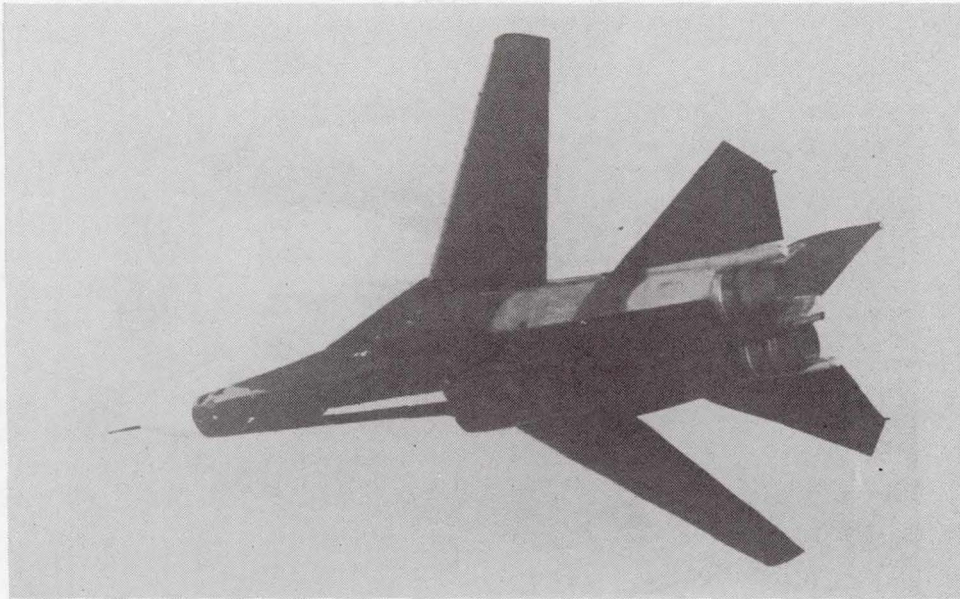
Figure 9.- F-111 aircraft.
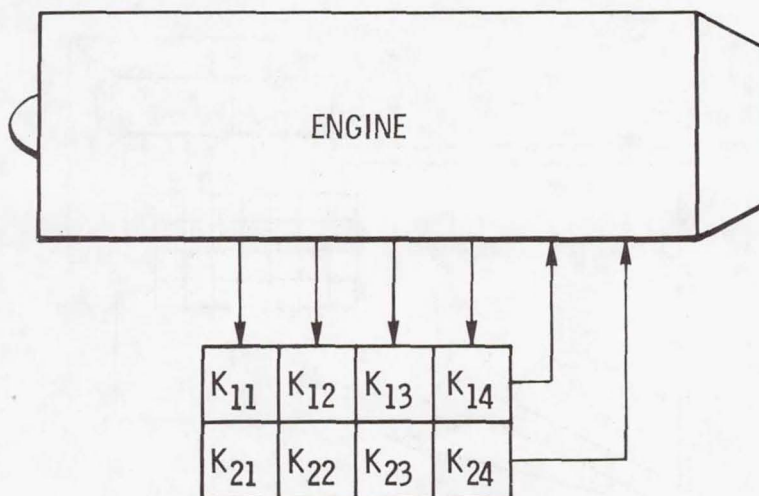
Figure 10.- Modern control theory applied to an engine.
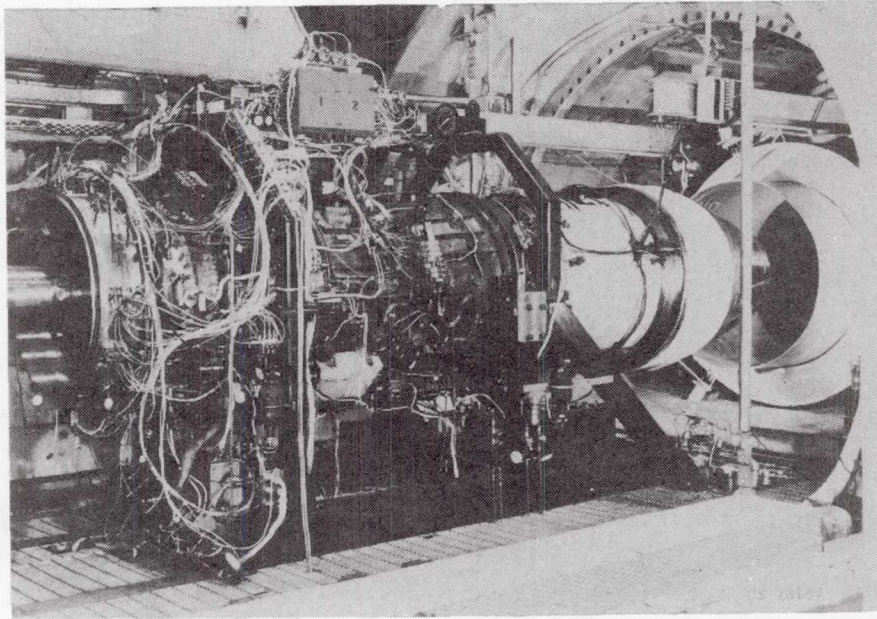
Figure 11.- F100 engine in altitude tank.
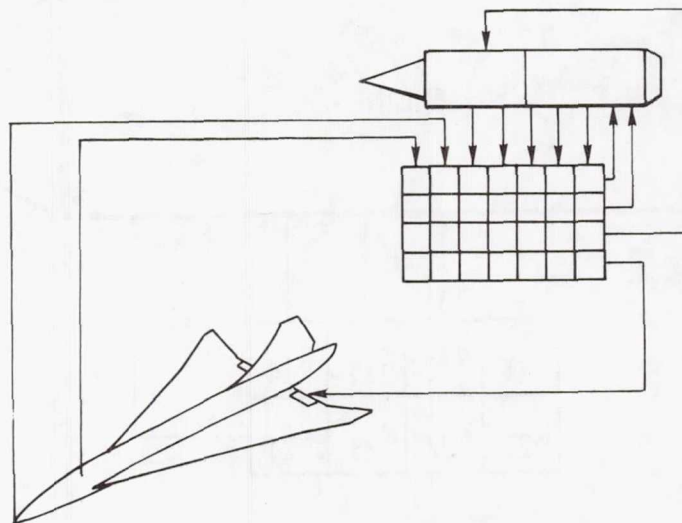
Figure 12.- Modern control of overall system.
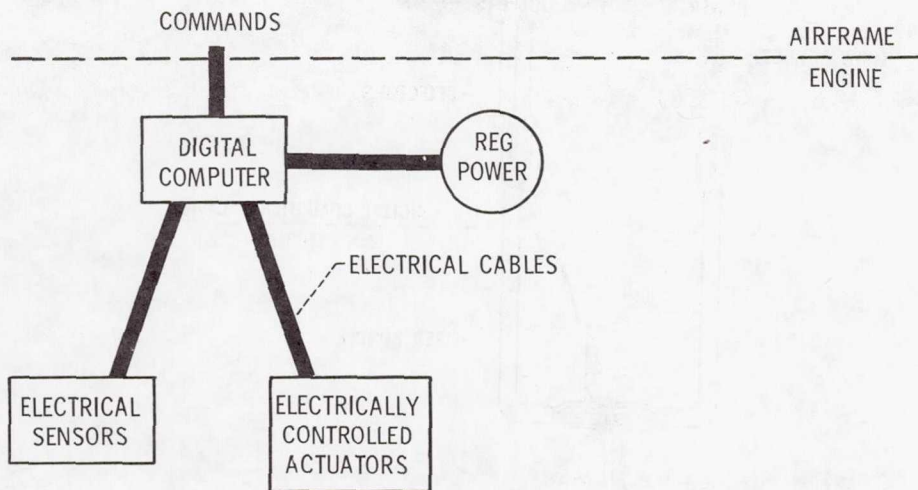
Figure 13.- Digital electronic engine control where computer
    is mounted on engine and cables are used for signal
    transmission.
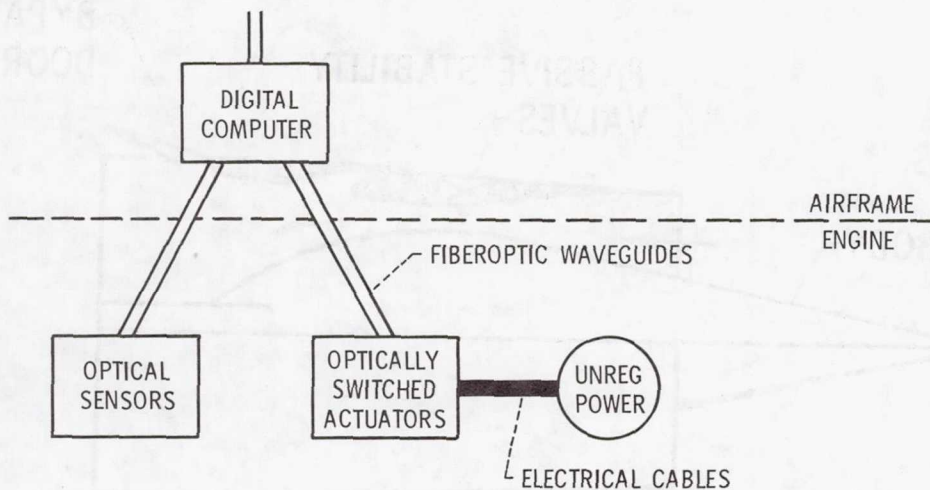
Figure 14.- Digital electronic engine control where computer
    is mounted off of the engine and fiber-optic waveguides
    are used for signal transmission.

413
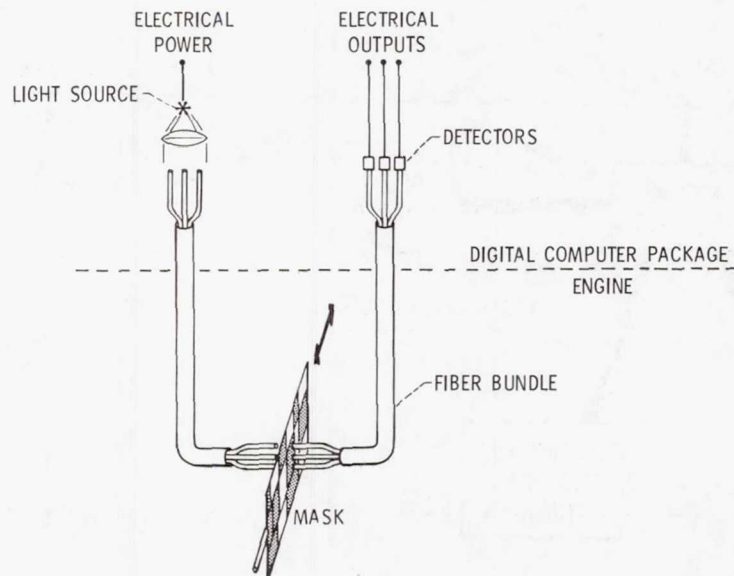
Figure 15.- Fiber-optic-connected position sensor.
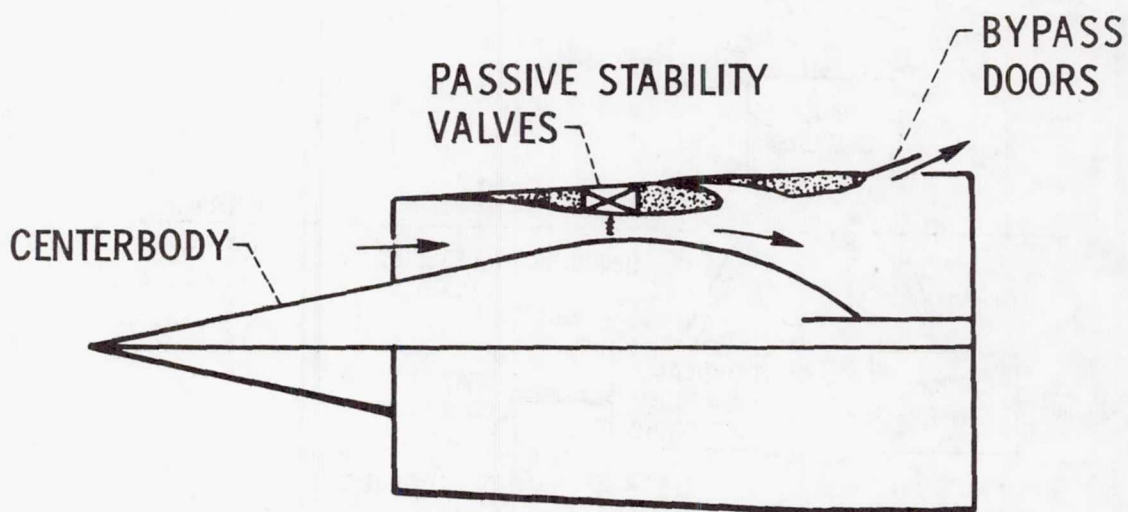
Figure 16.- Supersonic inlet with active and passive controls.
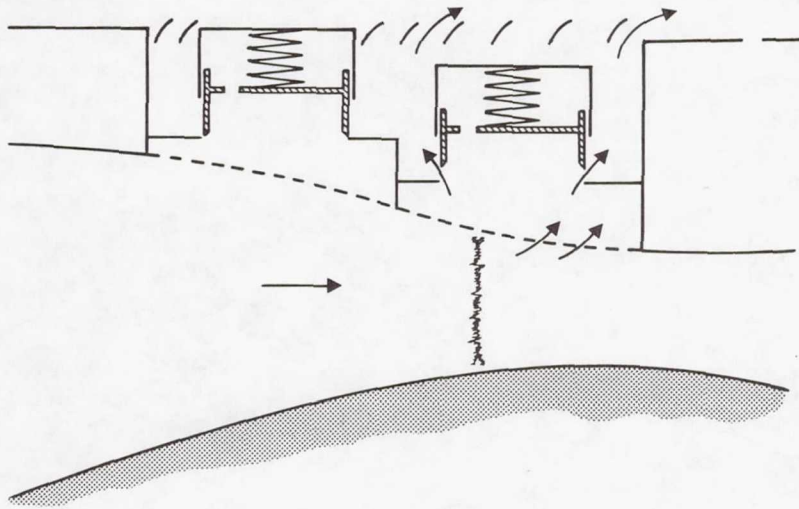
Figure 17.- Operation of inlet with passive
stability valves.

Page intentionally left blank

YF-12 PROPULSION RESEARCH PROGRAM AND RESULTS

James A. Albers and Frank V. Olinger
Dryden Flight Research Center

SUMMARY

The YF-12 propulsion research program was initiated to contribute to the technology base for the design of efficient propulsion systems for supersonic cruise aircraft. The research has been directed toward the following areas of technology: flight instrumentation, propulsion system steady state performance, propulsion system dynamic performance, propulsion system control, and airframe/propulsion system interactions. This report discusses the objectives and status of the propulsion program, along with the results acquired in the various technology areas. The instrumentation requirements for and experience with flight testing the propulsion systems at high supersonic cruise are discussed. Propulsion system performance differences between wind tunnel and flight are given. The effects of high frequency flow fluctuations (transients) on the stability of the propulsion system are described, and shock position control is evaluated. The report discusses present and future program plans and schedules.

INTRODUCTION

Supersonic cruise aircraft require propulsion systems that operate efficiently in a wide range of altitudes and at speeds from subsonic to high supersonic. To avoid penalties in engine size, weight, and fuel consumption, the inlet must supply air at maximum pressure and with minimum drag and interference. The inlet must also be able to match the airflow requirements of the engine over a wide range of flight conditions. Optimizing an inlet for a given aircraft mission requires an extensive investigation of the tradeoffs between optimum inlet performance at design and off-design conditions.

A first step in the optimization of the propulsion system is an analytical study of the various inlet geometries that match the engine requirements. Next, wind tunnel tests of scaled models are performed. These tests are followed by flight tests. It is known that, in general, wind tunnel test conditions do not exactly duplicate flight test conditions because for scaled models the Reynolds numbers and the local flow field do not always correspond to those experienced in flight. In addition, the instrumentation location and geometry of wind tunnel models are difficult to match to those of flight hardware. Because the flight hardware and its expected performance are determined from scaled wind tunnel models, scaling techniques that allow subscale inlet data to be extrapolated to full-scale flight are necessary.

Many of the current propulsion system problems of supersonic cruise aircraft involve inlet-engine compatibility. Insufficient propulsion system stability margin caused by instantaneous pressure distortion has been and continues to be a significant problem. It is at present not clear how the dynamic data from model tests should be used to predict the stability margin of the propulsion system in flight.

Another area of major concern to the propulsion system designer is the prevention of inlet unstarts, which occur in mixed-compression inlets when the terminal shock moves out in front of the cowl lip. Unstarts can take place when either internal disturbances or external disturbances occur in flight. New propulsion control concepts are needed to position the terminal shock in the inlet duct. At present, mixed-compression inlets have variable geometry features that are programed by a variety of engine, inlet, and airframe variables. For example, in the YF-12 inlet, variable bypass doors and a spike or ramp move as functions of Mach number, angle of attack, normal acceleration, and angle of sideslip. New bleed systems and shock position sensors may be required to improve the response of the present control system.

Experience to date with supersonic cruise aircraft has indicated that strong interactions exist between the propulsion system and the flight control system. These effects have been traced to the porting of bleed and bypass flows overboard around the nacelle. This porting can result in separated flow on the external nacelle and in the base and boattail region surrounding the engine exhaust. Thus, the nacelle flow interactions of supersonic cruise aircraft require further investigation. An integrated aircraft control system is needed to minimize undesirable interactions of the inlet, engine, and airframe control systems.

The YF-12 propulsion research program was initiated to contribute to the technology base for the design of efficient propulsion systems for supersonic cruise aircraft. This program is a cooperative effort among the Dryden Flight, Ames, and Lewis Research Centers. The technology areas include flight instrumentation, propulsion system steady state performance, propulsion system dynamic performance, propulsion system control, and airframe/propulsion system interactions. The status of the YF-12 propulsion program in the first quarter of 1976 was reported in reference 1. This paper updates that report and gives some results in the areas of technology indicated above. The paper also discusses present and future program plans and schedules.

SYMBOLS

$K\theta$	circumferential distortion
KRAD	radial distortion
M_∞	free-stream Mach number

418

m_0 reference captive mass flow

m_{cb}/m_0 centerbody bleed mass flow ratio

m_{eng}/m_0 engine mass flow ratio

m_{fwd}/m_0 forward bypass mass flow ratio

m_{st}/m_0 shock trap mass flow ratio

p_{t_0} inlet local total pressure

p_{t_∞} free-stream total pressure

$\bar{p}_{t_2}$ average compressor face total pressure

$p_{t_{2_{max}}}$ maximum compressor face total pressure

$p_{t_{2_{min}}}$ minimum compressor face total pressure

Δp_s change in static pressure

r_c reference cowl lip radius

ΔW change in engine airflow

W_0 reference airflow

ΔW_{dis} engine airflow decrement due to distortion

x axial distance measured from spike tip when spike is full aft

α_0 local angle of attack relative to inlet centerline of symmetry

α_∞ free-stream angle of attack

β_0 local angle of sideslip relative to inlet centerline of symmetry

θ circumferential angle measured from vertical centerline

OBJECTIVES AND APPROACH

The principal objective of the YF-12 propulsion program is to develop methods for the extrapolation of inlet dynamic performance characteristics from wind tunnel to flight. This involves determining the sensitivity of the propulsion system to such variables as scale, Reynolds number, and flow field entering the inlet. The inlet configurations and facilities used for this study are shown in figure 1. Reynolds number and scale effects can be evaluated by comparing 1/3-scale and full-scale inlet test results. In addition, the effects of aircraft forebody flow field on inlet performance can be evaluated by comparing wind tunnel inlet model data with flight results. By comparing wind tunnel and flight high frequency response data, scaling techniques can be developed that permit the extrapolation of subscale inlet dynamics to full-scale flight, and ways to use wind tunnel results for the prediction of flight performance can be established.

Another objective of the program is to determine the effects of high frequency flow fluctuations (transients) on the stability of the propulsion system and to evaluate new control concepts intended to minimize these effects. Wind tunnel models are used to investigate the effects of downstream disturbances on the dynamics of the propulsion system and to evaluate various shock position controls for mixed-compression inlets. Flight data can be used to determine the effects of both upstream and downstream disturbances, such as free-stream turbulence, on the stability of the propulsion system.

Another objective of the program is to investigate the causes of airframe/propulsion system interactions and to seek ways to minimize these effects. A control system is being developed to optimize total system performance by integrating the inlet, engine, and aircraft control systems.

Other objectives of the program include the determination of the operational range of the inlet for various geometries and flow conditions, the development of high temperature pressure sensors and other instrumentation for propulsion system testing, and use of the YF-12 airplane as a test bed for the investigation of new propulsion system concepts, such as the turbofan ramjet and variable cycle engine.

YF-12 PROPULSION SYSTEM DESCRIPTION

The propulsion system of the YF-12 airplane (fig. 2) consists of an axisymmetric mixed-compression inlet (fig. 3) and a J58 afterburning turbojet engine which exhausts through a convergent-divergent blow-in-door ejector nozzle. The inlet has a translating spike and uses a system of rotating forward and aft doors to control airflow. Throat bleed is provided by a porous slotted section on the spike and a combination flush slot and ram scoop on the cowl commonly referred to as a shock trap. The spike bleed air is ducted through struts and overboard through fixed louvers. The shock trap air is

ducted aft through the forward bypass plenum by the shock trap tubes and then ducted around the engine to the ejector nozzle. Each engine has a nine-stage single rotor compressor which is driven by a two-stage turbine. The main burner consists of an eight-can combustor. The engine is equipped with a fully modulating afterburner. The primary nozzle area is variable and is used to maintain the desired engine speed for both afterburning and nonafter-burning operation. A more detailed description of the propulsion system and instrumentation is given in reference 2.

INSTALLATION OF FLIGHT INSTRUMENTATION

Inlet performance measurements on the YF-12 inlet rely primarily on pressure measurements. Steady state measurements can be used to evaluate the overall performance of the propulsion system. Considerable interest has developed in recent years in inlet-engine compatibility, scaling effects, and the evaluation of inlet transient performance. High frequency response pressure measurements are most useful for investigating these aspects of propulsion systems.

Installing the two types of transducers used in the YF-12 flight program (fig. 4) is difficult for several reasons. The size of the steady state (less than 100 Hz) transducer, although much greater than that of the high frequency response transducer, is not necessarily a problem because the space between the internal and external skins of the inlet is adequate for mounting purposes (fig. 5). However, attaching the tubing for the transducers at a static pressure port requires access to both sides of the internal skin, and this requires the removal of large portions of the external skin. Furthermore, not all of the internal skin of the inlet can be exposed, and this makes access to these areas difficult.

Most of the measurements used to evaluate inlet performance are made in the throat region. Structurally, this region is complicated by provisions for the throat bleed and bypass airflows, which are needed to control the position of the terminal shock wave. Experience with the YF-12 airplane has shown that the throat region is one of the most difficult to gain access to for instrumentation purposes.

The smaller size of the high frequency response transducer shown in figure 4 allows the transducer to be close coupled to the measurement location. This transducer has been used for both static and total pressure measurements. Figure 6 shows the total pressure rakes installed at the compressor face. The transducers are mounted in the rakes, and the pressure and signal lines are routed into the centerbody. The lines are then collected, forming a bundle which is routed through the struts, airflow passages, and part of the wing, where it finally terminates in a cooled bay. A schematic of the installation is shown in figure 7. Approximately 10.7 meters of line are needed to reach the signal conditioning units and data acquisition system, which must be kept in a

temperature-controlled environment. Because connectors are sensitive components, they are located in open areas and the number of connectors has been minimized. Three connectors were used for the YF-12 application, one close to the transducer and the other two in the wing bays. The routing shown in figure 6 also typifies the steady state transducers. Much of the wire routing requires working blind. In some parts of the inlet it has been necessary to cut holes in the structure to accommodate the instrumentation, but this procedure should be avoided if possible to maintain the structural integrity of the inlet.

PROGRAM RESULTS

Propulsion System Steady State Performance

Many steady state wind tunnel and flight data have now been obtained with the YF-12 inlet. The approximate number and location of the pressure sensors are shown in figure 8. The steady state data include measurements of pressure recovery, airflow (bleed, bypass, and engine), compressor face distortion, duct static pressure, inlet control duct pressure, and boundary layer pressure.

Wind tunnel and engine calibration results.—A 1/3-scale model of the YF-12 inlet was tested at Ames in the Unitary Plan Wind Tunnel at Mach numbers from 0.9 to greater than 3.0 and at Reynolds numbers based on the cowl lip radius between 1.2×10^6 and 4.0×10^6. The aircraft's internal inlet geometry was completely simulated from the centerbody tip to the engine compressor face, including the variable forward and aft bypass doors and the centerbody and cowl bleed systems. The basic data are presented in references 3 and 4.

A full-scale flight inlet was tested in the Lewis 10'x10' Supersonic Wind Tunnel at Reynolds numbers based on the cowl lip radius between 2.0×10^6 and 4.2×10^6. The wind tunnel installation is described in detail in reference 5, and the results are given in references 6 and 7.

As part of the effort to obtain accurate airflow measurements in flight, an engine airflow calibration was performed at the Lewis Research Center's Propulsion Systems Laboratory (ref. 8). The engine that was installed in the aircraft was calibrated with distortion screens, which produced distortion patterns that simulated flight conditions. The engine airflow decrement due to distortion was obtained by comparing this calibration to the airflow characteristic curve that represented an average engine with no distortion (fig. 9). A decrement of up to 4 percent in corrected engine airflow was obtained for a corresponding typical maximum-minus-minimum distortion level of 20 percent. This indicates that engine calibrations should be performed in ground tests with and without distortion screens to obtain accurate airflow measurements in flight.

The local flow conditions at the inlet plane in flight must be known in order to match them with wind tunnel conditions. Wind tunnel tests of a

422

1/12-scale model of the YF-12 aircraft were conducted in the Ames Unitary Plan Wind Tunnel to investigate local Mach numbers, total pressures, and flow angles for various free-stream Mach numbers, angles of attack, and angles of sideslip (ref. 9). The local flow angles and Mach numbers are illustrated in figure 10 at a free-stream Mach number of 2.75. The flow angles are presented as vectors, with the origin of each vector the point where the data were recorded. The vector is the resultant of the local flow angles, α_0 and β_0, relative to the inlet centerline of symmetry. The lengths of the vector represent the magnitude of the resultant flow angle. Figure 10(a) indicates that the local flow changes from predominantly downwash at the low angles of attack to predominantly upwash at the higher angles of attack. In addition, there is a component of crossflow from outboard to inboard throughout the angle of attack range. Figure 10(b) indicates an increase in local Mach number gradient across the inlet plane with an increase in angle of attack. The Mach number gradient is as high as 0.14 at an angle of attack of 7.4°. The nonuniformities in inlet flow field and local Mach number, which are caused by the aircraft's forebody, could cause differences in the performance of the inlet in the wind tunnel and in flight. The wind tunnel test conditions correspond to the average of the flight test conditions at the inlet plane.

Flight test results.—Inlet performance was investigated in flight at Reynolds numbers based on the cowl lip diameter between 1.9×10^6 and 8.5×10^6 for various flight conditions and inlet geometries. The flight conditions tested were Mach number, angle of attack, and angle of sideslip. Inlet geometry was varied by changing the position of the forward bypass doors, the aft bypass doors, and the spike. The effects of these variables on pressure recovery, distortion, airflow, and shock position were investigated.

The pressure recovery and distortion at the compressor face are shown in figure 11 for nominal operating conditions. Pressure recovery varied from 97 percent at high subsonic Mach numbers to approximately 76 percent for supersonic conditions. Radial distortion (KRAD) and circumferential distortion (Kθ) generally increased with Mach number. At low Mach numbers distortion was essentially radial. At higher Mach numbers, however, circumferential distortion predominated. The high levels of distortion are due primarily to flow angularity at the inlet face. Distortion patterns at various inlet conditions are discussed in detail in reference 10.

To illustrate the effects of airflow on inlet flight performance, various inlet airflow components are shown in figure 12 for a free-stream Mach number of 2.8. As the forward bypass doors close and the forward bypass mass flow ratio decreases, the engine mass flow ratio and recovery increase. The shock trap and centerbody airflows, which account for approximately 5 percent and 3 percent of the captured mass flow, respectively, do not change during the test.

The location of the terminal shock in the inlet duct can have a significant effect on the quality of flow entering the engine. The circumferential variations of shock position for three duct pressure ratios are shown in figure 13. Duct pressure ratio is the control parameter used to control shock position.

The peak static pressure turbulence level in the throat was used as the indicator of terminal shock position. The figure indicates considerable skewing of the terminal shock within the inlet. The largest shock movement due to changing the duct pressure ratio occurred on the inboard side of the inlet, with little or no movement occurring on the outboard side. Increasing the duct pressure ratio caused the inboard side of the terminal shock wave to move ahead of the geometric throat. The skewing of the terminal shock is influenced by the Mach number gradient and the flow angularity ahead of the spike (fig. 10). The sensitivity of the shock to these variables indicates that inlet orientation is critical in maximizing inlet performance for a supersonic cruise aircraft.

Wind tunnel/flight comparisons.—Every attempt was made to match the flow conditions and inlet geometry for the wind tunnel and flight tests. Usually, one or more of the variables (Mach number, angle of attack, angle of sideslip, bypass airflow, spike position, and engine airflow) could be matched, but matching all the variables was almost impossible. Preliminary comparisons indicated some differences between the wind tunnel and flight parameters, such as engine and centerbody airflow (ref. 11). More recent comparisons also illustrate the differences between 1/3-scale, full-scale, and flight data (fig. 14). The engine mass flow ratios obtained from the 1/3-scale and full-scale tests, which agreed, differed significantly with the ratio obtained in flight. The centerbody mass flow ratios obtained from all three sets of data (1/3 scale, full scale, and flight) differed widely. The differences between the wind tunnel and flight data could exist as shown in figure 14, or they could be due to unmatched inlet parameters.

To separate the two effects, a multiple regression model based on a least-squares criterion of YF-12 inlet performance parameters was derived from the full-scale wind tunnel data. This model provided a way to derive wind tunnel data for inlet conditions that matched the flight conditions. The multiple regression model gives equations (linear or nonlinear) of the dependent inlet performance variables in terms of the independent variables of the flow conditions and inlet geometry. The dependent variables are forward bypass mass flow ratio, duct pressure ratio, percent forward bypass door opening, engine mass flow ratio, shock trap mass flow ratio, centerbody mass flow ratio, and compressor face distortion. The independent variables are Mach number, spike position, angle of attack, angle of sideslip, corrected engine airflow, and compressor face recovery. A comparison of this model with the 1/3-scale, full-scale, and flight data is shown in figure 15. A comparison of the model (for the corresponding matched condition) with 1/3-scale, full-scale, and flight data indicates no difference in the engine mass flow ratios found; however, there are some differences between the centerbody mass flow ratios. The results in figures 14 and 15 indicate the need to compare wind tunnel and flight data at conditions that are actually matched (by using a common basis for comparison like a multiple regression model) to determine which differences in inlet performance parameters are real.

To sort out the differences between the wind tunnel and flight data for all the inlet performance parameters, the statistical technique called analysis of

424

covariance was then used. Analysis of covariance uses residuals (model-predicted minus actual) for both wind tunnel and flight data and considers the combined effect of all the performance parameters. By using this analysis one can determine whether a statistical difference exists between 1/3-scale, full-scale, and flight data. When all the performance parameters were considered together, an analysis of this type indicated no difference between the 1/3-scale, full-scale, and flight data. The data are being examined further to investigate differences in the individual variables.

Propulsion System Dynamic Performance

Wind tunnel results.—Large amounts of dynamic pressure data were acquired from 1/3-scale inlet tests at Ames and full-scale flight inlet tests at Lewis. The 1/3-scale data included data from a 40-probe total pressure survey at the engine face, duct wall static pressure measurements, and bounday layer total pressure measurements (fig. 8). A statistical analysis of some of these pressure data is given in reference 12. This study includes probability density and power spectral density curves but does not include instantaneous distortion calculations.

Dynamic pressure data from a full-scale flight inlet were obtained at Lewis. The pressure data included data from a 24-probe total pressure survey at the compressor face. The number of measurements and the measurement locations were identical to those used in the flight tests. These data were recorded on magnetic tape for comparison with the dynamic data to be obtained in the flight tests.

Flight test results.—A significant aspect of mixed-compression inlet performance is the response of the inlet to transients. The effects of several types of transients have been evaluated in flight. The evaluation included an investigation of the effects of deliberately induced unstarts and compressor stalls and also the effects of the wake of a passing supersonic aircraft.

A typical inlet unstart is shown in figure 16. The unstart was intentionally induced by slowly closing the bypass doors, forcing the terminal shock wave out of the throat. As the unstart begins, pressures downstream of the throat drop rapidly, while those upstream of the throat increase. It takes about 0.01 second for the shock to move all the way to the spike tip. The inlet control system then opens the bypass doors and translates the spike forward to restart the inlet. The restart occurs 0.5 second after the unstart. The unstart transient produces large airplane rolling and yawing moments and should be avoided if possible.

In order to define the maximum pressure in an inlet duct, a stall was induced in flight at high supersonic speeds by closing the manual bleed on the fourth stage of the compressor. Duct maximum pressure is extremely important for the definition of the inlet structural load requirements. A typical compressor stall time history is shown in figure 17. The compressor stall affects

the static pressures at the compressor face first, and then, as the shock propagates forward in the inlet, the static pressures upstream of the compressor face. The induced hammershock results in a considerable duct static pressure rise, as indicated by figure 17. As shown in figure 18, the maximum normalized increase in pressure occurs in the inlet throat. The increase in pressure varies throughout the inlet duct because of the inlet's area variation. A limited quantity of flight data is now available for comparison with analytical and semiempirical prediction techniques.

Two YF-12 airplanes were flown simultaneously in late 1975 to provide a chase situation for an experiment being tested on one of the airplanes. These flights provided an opportunity to investigate the effects of passing aircraft wakes on inlet performance. The instrumented inlet of the chase airplane was used to probe the wake of the lead airplane. The maneuvers were performed with the two aircraft approximately 164 meters apart at Mach 2.5 and at an altitude of approximately 1962 meters. The chase aircraft accelerated and decelerated in such a way as to cause the bow shock wave of the lead airplane to pass across the chase airplane at least twice. The pilot reported that the disturbances caused by passing in and out of the wake were mild and that no unstarts occurred. The pressure fluctuations measured at the nose boom of the chase airplane were small. The inlet control system did not respond to the disturbances because they were of such small amplitude and short duration. The free-stream disturbances had no detectable effect on the high frequency response pressure measurements in the inlet.

A significant problem in engine development is the provision of a sufficient stability margin to allow for dynamic pressure distortion. Current methods for determining the stability margin require extensive testing with a 40-probe rake at the engine face to insure inlet-engine compatibility, and this testing is highly complex and costly. An alternative, less expensive method for determining the extreme values of instantaneous inlet distortion is proposed in reference 13. This method estimates maximum instantaneous distortion from the steady state root mean square (rms) and power spectral density (psd) measurements of only a few compressor face total pressures. This method has previously been applied only to a limited amount of wind tunnel data. In figure 19, the values of maximum instantaneous distortion estimated with this method using data from only six pressure probes are compared with the values obtained by using all 24 probes in the rake array. In general, the agreement between predicted and measured values of instantaneous distortion is excellent.

Wind tunnel/flight comparisons.—The 1/3-scale, full-scale, and flight data are being digitized and distortion parameters are being calculated for selected wind tunnel/flight match points. The effects of filters, record length, engine rake configuration, boundary layer rakes, and distortion indexes are being investigated. The statistical characteristics of distortion indexes are being calculated to establish dynamic scaling laws for wind tunnel-to-flight correlations.

426

Propulsion Controls

A rather extensive wind tunnel inlet control program has been performed at Lewis to support the overall YF-12 effort. This program included a study of normal shock and duct pressure dynamics, the digital implementation of the actual inlet's forward bypass control system, the shock position sensors, experimental shock position controls, and the throat stability bleed control system. An engine temperature control system called a turbine inlet gas temperature (TIGT) control system was evaluated in flight. The standard forward bypass door control system was used during flight tests.

Wind tunnel test results.—Open loop dynamic wind tunnel data are given in reference 14, which evaluates the response of the flight inlet to internal airflow disturbances. A comparison of these wind tunnel data with a one-dimensional dynamic model of the inlet is shown in figure 20. The dynamic model is discussed in reference 15, and the analysis is extended to upstream flow field disturbances in reference 16. An examination of the figure indicates that phase agreement is excellent and that amplitude agreement is reasonable. These examples are typical of the agreement between the analysis and the experimental data.

The full-scale YF-12 flight hardware with the duct pressure ratio inlet control system was tested in the Lewis wind tunnel (ref. 17). The digital implementation of the inlet control system is shown in figure 21. Tests consisted of open loop and closed loop frequency responses and step transients. This investigation demonstrated that a digital computer could be used to implement all the schedules and meet all the other requirements of an actual aircraft inlet control system. The data obtained from these tests, which had a duct pressure ratio control system, served as the baseline for comparison with other shock position control systems.

Various shock position sensors were tested in the wind tunnel. One of those tested was a continuous-output shock position electronic sensor (ref. 18). The frequency response of this sensor is shown in figure 22. The response is excellent out to a frequency of 60 hertz. However, this sensor may be difficult to incorporate into the hardware for the inlet control, since it requires several pressure transducers to determine the terminal shock position over an operational range.

Results from frequency response and transient testing of various experimental shock position control systems are given in reference 19. For this investigation, optimal fixed form shock position controllers of the proportional-plus-integral form were used. One of the experimental controls used the shock position sensors described in reference 18 for the feedback signal. Both engine speed and forward bypass door position were used to control shock position. Although the optimal controllers gave better response than the aircraft's inlet shock position control, the system was limited by the response of the forward bypass door hardware.

One means of providing a greater stability margin for the control of shock position is to make the throat bleed function as a throat bypass by regulating

the bleed plenum exit area. A throat bleed control system of this type was designed for the YF-12 aircraft (fig. 23) and demonstrated in the wind tunnel at Lewis. In this system, bleed airflow is removed through a porous bleed region just ahead of the inlet shock trap. Two circumferential rows of mechanical relief valves control bleed plenum exit area and hence bleed airflow. The valves, instead of being actuated directly by the bleed plenum pressure, have a shield and duct to sense an actuating pressure. Such an arrangement provides better valve response to airflow disturbances for this application. The effects of downstream disturbances on the bleed system are given in reference 20. Although limited results of external effects are given in reference 20, such effects can best be investigated by flight testing. A comparison of the response of the standard forward bypass control with that of the forward bypass control modified with these stability valves is shown in figure 24. For low airflow disturbance rates (less than 5 percent per second) the standard inlet unstarts with a 10-percent change in airflow. The stability valves provide a considerable increase in stability margin, with a 20-percent change in airflow necessary to unstart the inlet for the range of airflow disturbance rates tested.

A flight program is planned for the near future to investigate the nature of atmospherically induced disturbances and their effects on mixed-compression inlets. If the results indicate that a shock stabilizing system is needed, it will then be desirable to demonstrate that the proposed systems are feasible in a flight environment and that mixed-compression inlets operate nearer peak performance with such systems.

Flight test results.—A turbine inlet gas temperature control system was designed and developed for the J58 engine and flown on the YF-12 aircraft. This control system has a high response fluidic sensor in which output is fed to the standard J58 exhaust gas temperature (EGT) controller (ref. 21).

The fluidic temperature sensor accumulated approximately 100 hours of flight time in the range of 1200 kelvins and 1500 kelvins. The sensor was subjected to the full range of operational environments, including unstarts and throttle transients. In addition, the signal from the fluidic sensor was used for closed loop control of the engine temperature for approximately 2 hours during the flight testing. The closed loop tests were conducted only for steady state conditions, since the system was not optimized for controlling the engine temperature throughout the full range of the flight environment. The sensor operated as predicted by the ground tests reported in reference 22, and visual inspection of the sensor following the flight tests revealed no deterioration.

Airframe/Propulsion System Interactions

As part of the YF-12 performance and propulsion program, a limited amount of information was obtained on nacelle flow interactions to lay the groundwork for future flight testing.

Wind tunnel test results.—Wind tunnel tests of a 1/12-scale model were run at Ames, primarily to obtain force data. A limited number of surface static

pressure measurements were obtained during these tests. The pressure orifices were installed on the left wing and nacelle, and measurements were made with various bleed flows through the forward bypass and centerbody bleed louvers.

Subsequent testing was done with the same model to obtain loads data. Many additional pressure orifices were installed for those tests. Extensive data were obtained throughout the Mach number range and for various bleed flows. In addition, data for started and unstarted inlet conditions were recorded.

Flight test results.—To obtain an understanding of the complex flow around the YF-12 inlet in flight, tufts were placed on the inboard upper and lower quarters of the nacelle (ref. 23). High-speed cameras were used to film the flow patterns revealed by tuft movement and direction. Flow patterns were obtained for a wide range of flight conditions. The effect of forward bypass door position on the local flow around the upper surface of the nacelle is shown in figure 25. Three general types of flow could be observed from the activity of the tufts. In steady flow, the tufts were nearly motionless and lay close to the surface. In unsteady flow, the tufts oscillated slowly, with small angles of movement. In turbulent flow, the tufts oscillated rapidly, with large angles of movement. Figure 25(a) shows the nacelle flow with the forward bypass door closed. The surface flow downstream of the top bypass exit on the upper nacelle was generally turbulent. When the doors were opened 20 percent (fig. 25(b)), an area of lateral and reverse flow appeared upstream of the topmost door. However, the bypass flow apparently injected enough energy into the boundary layer to eliminate flow separation downstream of the exit. When the bypass doors were 70 percent open (fig. 25(c)), the flow downstream of the top exit remained turbulent or became separated despite the strong flow through the exit. This study indicates that the exit louvers should be designed to minimize separated flow regions on the nacelle in order to minimize external drag.

Program Plans and Schedule

The present YF-12 propulsion program (table I) includes plans to complete the flight testing being done to obtain compressor face and duct dynamic data. These flights, which began in mid-1976, are being performed primarily for matching wind tunnel test conditions and for investigating the effects of transients on inlet performance. In addition, dynamic data are to be obtained for investigating the effects of free-stream turbulence. The propulsion program is to be followed by a cooperative airframe/propulsion control system program, which is to be concurrent with flight tests for evaluating advanced shock sensors and nacelle flow interactions.

Compressor face and duct dynamics.—The objectives of the compressor face and duct dynamic pressure flight tests are to obtain dynamic pressure data with the flight and inlet parameters matched with wind tunnel settings.

The flight and wind tunnel data are to be compared to establish dynamic distortion scaling laws. In addition, the dynamic pressure instrumentation should provide data for evaluating inlet transients, such as unstarts. The dynamic data are to be used to evaluate the causes and effects of the inlet transients, and the results are to be compared with analytical prediction techniques for aircraft stability and control. The dynamic pressure measurement instrumentation includes 24 compressor face total pressure sensors and 40 duct static pressure sensors with frequency responses from steady state to 500 hertz (fig. 8).

Atmospheric effects.—Some flight tests are to be made to measure and evaluate the effects of atmospherically induced turbulence on the dynamics of mixed-compression inlets. A gust probe is to be installed on the nose boom of the YF-12 airplane, and measurements of the free-stream turbulence are to be correlated with the dynamics of the inlet flow (including boundary layer measurements in the inlet). Data from these flight tests should be valuable for the determination of realistic inlet control design criteria and for comparison with inlet performance predictions.

Cooperative control.—Strong interactions between the airframe and the propulsion systems of supersonic cruise aircraft can cause significant penalties in terms of performance, range, fuel consumption, and structural weight. The development of an integrated control system that maximizes favorable interactions and minimizes unfavorable interactions is a complex control problem. Recent innovations in flight-qualified digital computers make them ideally suited for this problem because of their speed and accuracy and because digital control is so flexible.

The cooperative control program planned for the YF-12 airplane utilizes the integrated digital control concept and is to be flight tested in two phases. The purpose of the first phase is to validate the hardware and software required to convert the existing analog systems to digital control. The systems to be converted are the autopilot, air data system, inlet control system, and autothrottle. In the second phase, these systems are to be integrated and new control laws are to be developed using optimal as well as classical control methods. A complete description of this program is given in reference 24.

Advanced shock sensor.—In current inlet control systems, terminal shock wave position is inferred from a duct pressure ratio that is independent of altitude effects. However, the value of the duct pressure ratio reference must be scheduled to accommodate various operating conditions. Sensing the shock position directly would be advantageous because it would allow closed loop control of the shock position or other primary variable, eliminate the need for normalized signals, lead to tighter control with potentially higher inlet recovery, and eliminate or greatly simplify schedules.

Studies are now being made to evaluate various logic schemes for detecting shock position from static pressures measured in the shock operating region. The schemes could be implemented on the aircraft by using instrumentation already available and the cooperative control computer. Alternatively, data

could be recorded during flight tests for evaluation in a ground-based facility. Digital pressure transducers using fiber-optic technology should ultimately replace conventional transducers. Digital fiber-optic devices are attractive because they are passive and because signals are transmitted as light (on or off) to electronics mounted off the inlet. In addition, the use of fiber-optic cables eliminates electrical wiring and the associated electrical noise. A device using digital transducers and the logic indicated by wind tunnel and bench tests is then to be evaluated on the YF-12 airplane. The flight testing should determine the accuracy and reliability of the approach in the flight environment. If successful, the device could then be used for control purposes.

Nacelle flow interactions.—Bleed and bypass airflows that are dumped overboard from the inlet create a complex flow field which can adversely affect the stability and control of the airplane. Flight tests are to be made to obtain pressure data for the external nacelle and wing. The flight data are to be compared with pressures measured on a wind tunnel model. The data should result in a better understanding of the flow field and permit the methods used to predict these interactions to be evaluated.

REQUIREMENTS AND RECOMMENDATIONS FOR FURTHER PROPULSION SYSTEM RESEARCH

Future supersonic cruise aircraft propulsion systems must meet demanding environmental and performance standards. Recent propulsion system studies have selected two variable cycle engine concepts that appear to be capable of meeting these standards. Hardware development and component testing are underway to lead to experimental engines that incorporate these concepts. New nacelles and supersonic inlets that match the airflow requirements of the engines must be designed and tested. The inlets and engines can be ground tested separately under simulated flight conditions, but the integrated inlet-engine combination will require flight testing.

The YF-12 airplane could be used as a test bed for flight testing the new propulsion concepts. As illustrated in figure 26, this aircraft is capable of carrying full-scale propulsion system experiments that are independent of the aircraft propulsion system. This method of flight testing provides an opportunity to investigate the high risk aerodynamic and propulsion system concepts that are needed for the development of technically feasible and economically competitive propulsion systems. Realistic flight environments can be obtained over a continuous range of Mach numbers to provide performance information not obtainable in ground facilities.

Noise suppression continues to be a major concern for future propulsion systems. Quiet nozzles are to be developed as part of the new engine program, however, and they can be tested separately from the rest of the propulsion system. Such nozzles can be tested on the J58 engine, which has the high pressure ratio representative of advanced engines. Flight tests

431

should provide information on forward velocity effects, which are known to reduce the effectiveness of the noise suppressor relative to the static performance.

Before accurate performance predictions for supersonic cruise aircraft can be made, wind tunnel performance must be extrapolated to flight conditions. The data obtained from the YF-12 propulsion program should prove to be valuable for this purpose. An understanding of the causes of and ways to reduce instantaneous dynamic distortion is vital if inlet-engine compatibility is to be obtained. The YF-12 program should shed some light on this problem in aircraft development. If propulsion system performance is to be optimized, new shock sensors and shock position controls must be developed. The latest developments in this area have been and will continue to be pursued in the YF-12 propulsion program. Finally, the only way to optimize total aircraft performance is to design a control system (such as the cooperative control on the YF-12 airplane) which integrates the inlet, engine, and airframe control systems. It is imperative that representatives of the various disciplines of aircraft design (aerodynamics, structures, propulsion, and stability and control) work together to create an integrated aircraft design that is competitive economically and performs well.

REFERENCES

1. Albers, James A.: Status of the NASA YF-12 Propulsion Research Program. NASA TM X-56039, 1976.

2. Burcham, Frank W., Jr.; Montoya, Earl J.; and Lutschg, Phillip J.: Description of YF-12C Airplane, Propulsion System, and Instrumentation for Propulsion Research Flight Tests. NASA TM X-3099, 1974.

3. Anderson, J. Thomas; Martin, Robert K.; and Shibata, Harry H.: 1/3 Scale Inlet Model Test Results. Vol. I – Test Definition and Steady State Data Presentation. NASA CR-114702, 1974.

4. Anderson, J. Thomas; Martin, Robert K.; and Shibata, Harry H.: 1/3 Scale Inlet Model Test Results. Vol. III – Test Definition and Steady State Data Presentation. NASA CR-114704, 1974.

5. Lewis Research Center: Wind-Tunnel Installation of Full-Scale Flight Inlet of YF-12 Aircraft for Steady-State and Dynamic Evaluation. NASA TM X-3138, 1974.

6. Cubbison, Robert W.: Wind Tunnel Performance of an Isolated Full-Scale YF-12 Inlet at Mach Numbers Above 2.1. NASA TM X-3139, 1976.

7. Cubbison, Robert W.: Effects of Angle of Attack and Flow Bypass on Wind-Tunnel Performance of an Isolated Full-Scale YF-12 Inlet at Mach Numbers Above 2.075. NASA TM X-3140, 1976.

8. Ladd, J. M.: Airflow Calibration of a J-58 Engine at Simulated Supersonic Conditions. NASA TM X-71797, 1975.

9. Olinger, Frank V.; Shibata, Harry; and Albers, James A.: Local Flow Measurements at the Inlet Plane of a 1/12-Scale Model of the YF-12C Airplane. NASA TM X-3435, 1976.

10. Taillon, Norman V.: Steady-State Inlet Recovery and Distortion of the YF-12C Airplane. NASA TM X-3382, 1976.

11. Smeltzer, Donald B.; Smith, Ronald H.; and Cubbison, Robert W.: Wind Tunnel and Flight Performance of the YF-12 Inlet System. AIAA Paper 74-621, July 1974.

12. Anderson, J. Thomas; and Edson, Ralph D.: 1/3 Scale Inlet Model Test Results. Vol. II – Dynamic Data Analysis. NASA CR-114703, 1974.

13. Melick, H. Clyde; Ybarra, Andres H.; and Bencze, Daniel P.: Estimating Maximum Instantaneous Distortion From Inlet Total Pressure RMS and PSD Measurements. NASA TM X-73,145, 1976.

14.   Cole, Gary L.; Cwynar, David S.; and Geyser, Lucille C.: Wind-Tunnel Evaluation of the Response of a YF-12 Aircraft Flight Inlet to Internal Airflow Perturbations by Frequency-Response Testing. NASA TM X-3141, 1974.

15.   Willoh, Ross G.: A Mathematical Analysis of Supersonic Inlet Dynamics. NASA TN D-4969, 1968.

16.   Cole, Gary L.; and Willoh, Ross G.: Analysis of the Dynamic Response of a Supersonic Inlet to Flow-Field Perturbations Upstream of the Normal Shock. NASA TN D-7839, 1975.

17.   Neiner, George H.; Arpasi, Dale J.; and Dustin, Miles O.: Wind-Tunnel Evaluations of YF-12 Aircraft Inlet Control System by Frequency-Response and Transient Testing. NASA TM X-3142, 1975.

18.   Dustin, Miles O.; Cole, Gary L.; and Neiner, George H.: Continuous-Output Terminal-Shock-Position Sensor for Mixed-Compression Inlets Evaluated in Wind-Tunnel Tests of YF-12 Aircraft Inlet. NASA TM X-3144, 1974.

19.   Neiner, George H.; Seidel, Robert C.; and Arpasi, Dale J.: Wind-Tunnel Evaluation of Experimental Controls on YF-12 Aircraft Flight Inlet by Frequency-Response and Transient Testing. NASA TM X-3143, 1975.

20.   Cole, Gary L.; Dustin, Miles O.; and Neiner, George H.: A Throat-Bypass Stability System for a YF-12 Aircraft Research Inlet Using Self-Acting Mechanical Valves. NASA TM X-71779, 1975.

21.   Webb, William L.; and Reukauf, Paul J.: Development of a Turbine Inlet Gas Temperature Measurement and Control System Using a Fluidic Temperature Sensor. AIAA Paper 73-1251, Nov. 1973.

22.   Webb, W. L.: Turbine Inlet Gas Temperature Measurement and Control System. AFAPL-TR-73-116, Air Force Aero Propulsion Laboratory, Wright-Patterson Air Force Base, Dec. 1973.

23.   Yanagidate, Craig: Tuft Study of the Local Flow Around the Nacelle of the YF-12A Airplane. NASA TM X-56035, 1975.

24.   Reukauf, Paul J.; Burcham, Frank W., Jr.; and Holzman, Jon K.: Status of a Digital Integrated Propulsion/Flight Control System for the YF-12 Airplane. AIAA Paper 75-1180, Sept. 1975.

TABLE I.- PROGRAM SCHEDULE

	1977 J F M A M J J A S O N D	1978 J F M A M J J A S O N D	1979 J F M A M J J A S O N D
Compressor face and duct dynamic flight tests	█		
Boundary layer rake and gust probe installation	▁███▁		
Atmospheric effects flight tests	▁▁▁███		
Cooperative control, external nacelle pressure, and advanced shock sensor installation	▁▁▁▁▁███	███▁	
Basic cooperative control flight tests		▁███	
Advanced shock sensor flight tests		▁▁▁▁█	
Nacelle flow interaction flight tests		▁▁▁▁█▁█	
Optimal cooperative control flight tests		▁▁▁▁▁▁▁▁▁▁███	████████████
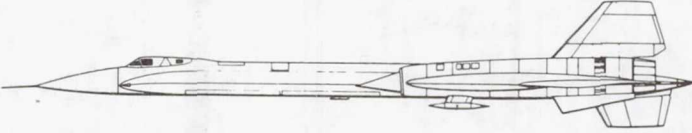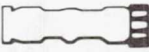
TEST OBJECT   FACILITY

AIRPLANE   FLIGHT, DRYDEN

FULL-SCALE INLET MODEL   10'x10' SUPERSONIC WIND
                                        TUNNEL, LEWIS

                    8- BY 7-FOOT SUPERSONIC
                                        WIND TUNNEL, 9- BY 7-FOOT
                                        SUPERSONIC WIND TUNNEL,
1/3-SCALE INLET MODEL   AND 11-FOOT TRANSONIC
                                        WIND TUNNEL, AMES

                                        PROPULSION SYSTEMS
                                        LABORATORY (PSL)
FULL-SCALE ENGINE   ALTITUDE TEST FACILITY,
                                        LEWIS

Figure 1.- Comparison of inlet configurations and facilities.

BLOW-IN-DOOR
EJECTOR NOZZLE

J58 AFTERBURNING
TURBOJET ENGINE

AXISYMMETRIC
MIXED-COMPRESSION
INLET
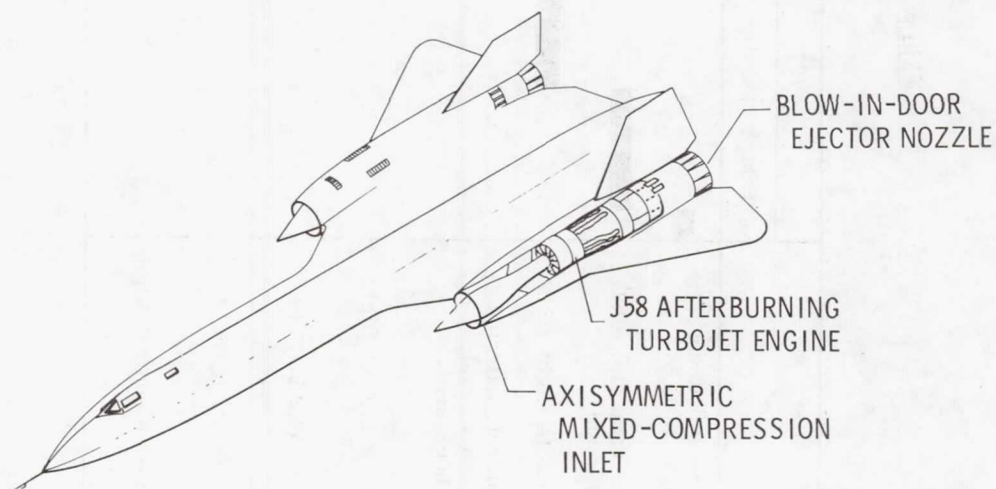
Figure 2.- YF-12 propulsion system.

436
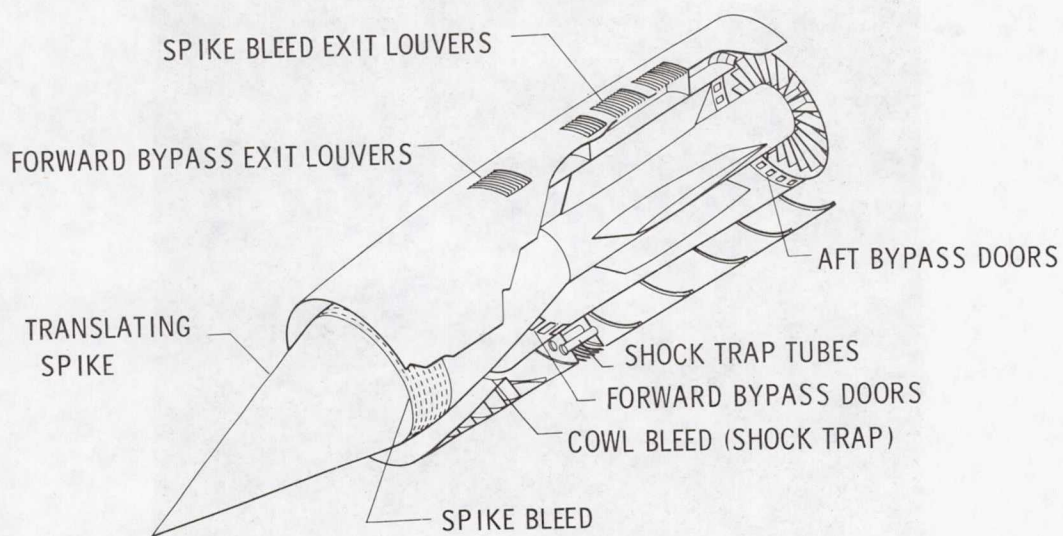
Figure 3.- YF-12 inlet.
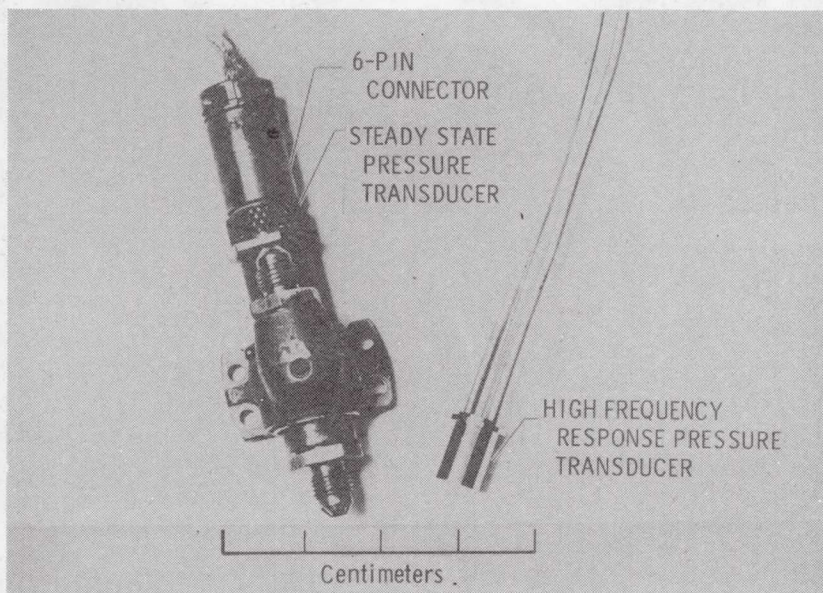
Figure 4.- High temperature pressure transducers
used on YF-12 airplane.
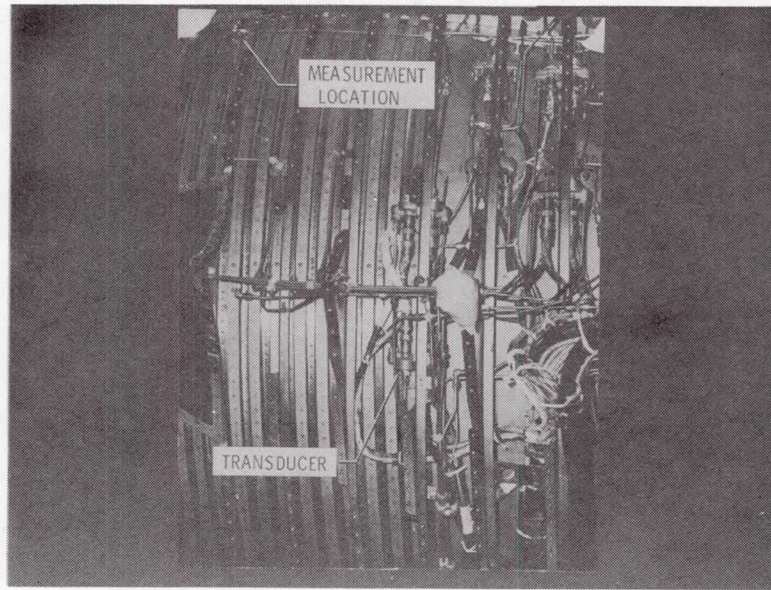
Figure 5.- Left inlet steady state pressure instrumentation (external skin removed).
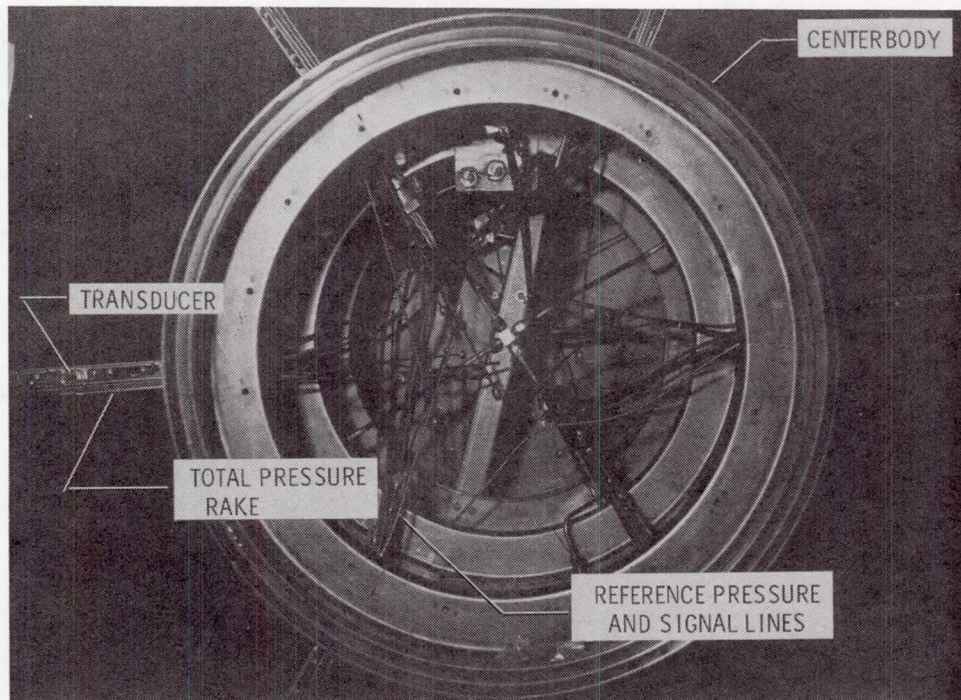
Figure 6.- Compressor face high frequency response pressure instrumentation (view looking forward).

DATA ACQUISITION SYSTEM

HIGH TEMPERATURE CABLES AND
PRESSURE LINES (APPROXIMATELY
10.7 m (35 ft) LONG)

SIGNAL
CONDITIONING

TOTAL PRESSURE
RAKE

COOLED BAY

STATIC PRESSURE
TRANSDUCER
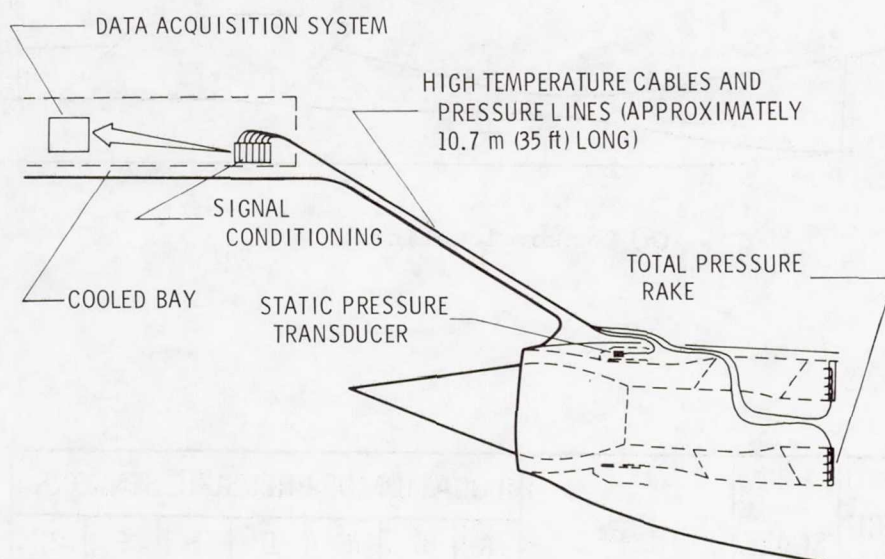
Figure 7.- Typical pressure instrumentation installation.

A FORWARD SPIKE
B FORWARD COWL
C COWL THROAT
D SPIKE THROAT
E BLEED FLOW PASSAGE
F COMPRESSOR FACE
G ENGINE
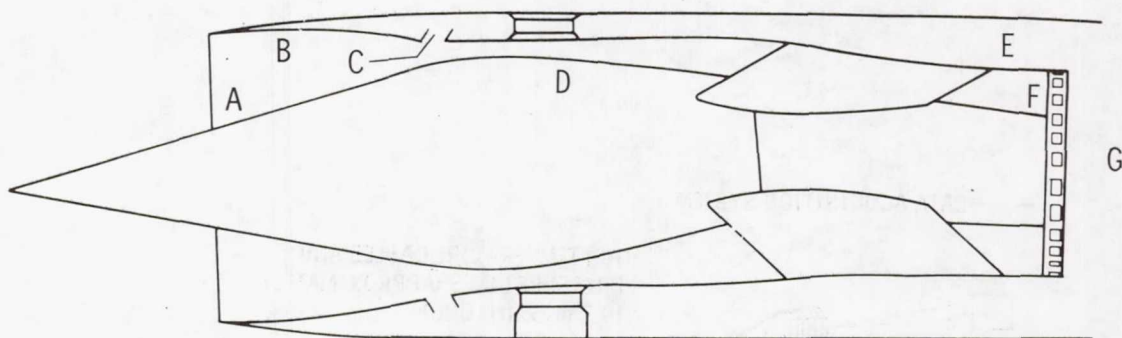
(a) Sensor locations.

NASA RESEARCH CENTER	SCALE	TYPE	LOCATION OF PRESSURE SENSORS							
			A	B	C	D	E	F	G	
			NUMBER OF SENSORS AT LOCATION							TOTAL
AMES (WIND TUNNEL)	1/3	STEADY STATE	73	32	84	44	47	40	-	320
		DYNAMIC	12	6	16	12	1	40	-	87
LEWIS (WIND TUNNEL)	FULL	STEADY STATE	75	58	128	94	45	52	-	452
		DYNAMIC	-	11	27	-	12	24	-	74
DRYDEN (FLIGHT VEHICLE)	FULL	STEADY STATE	9	17	33	8	13	50	3	133
		DYNAMIC	4	4	19	6	6	24	3	66

(b) Number of sensors.

Figure 8.- YF-12 inlet study instrumentation comparison.

440
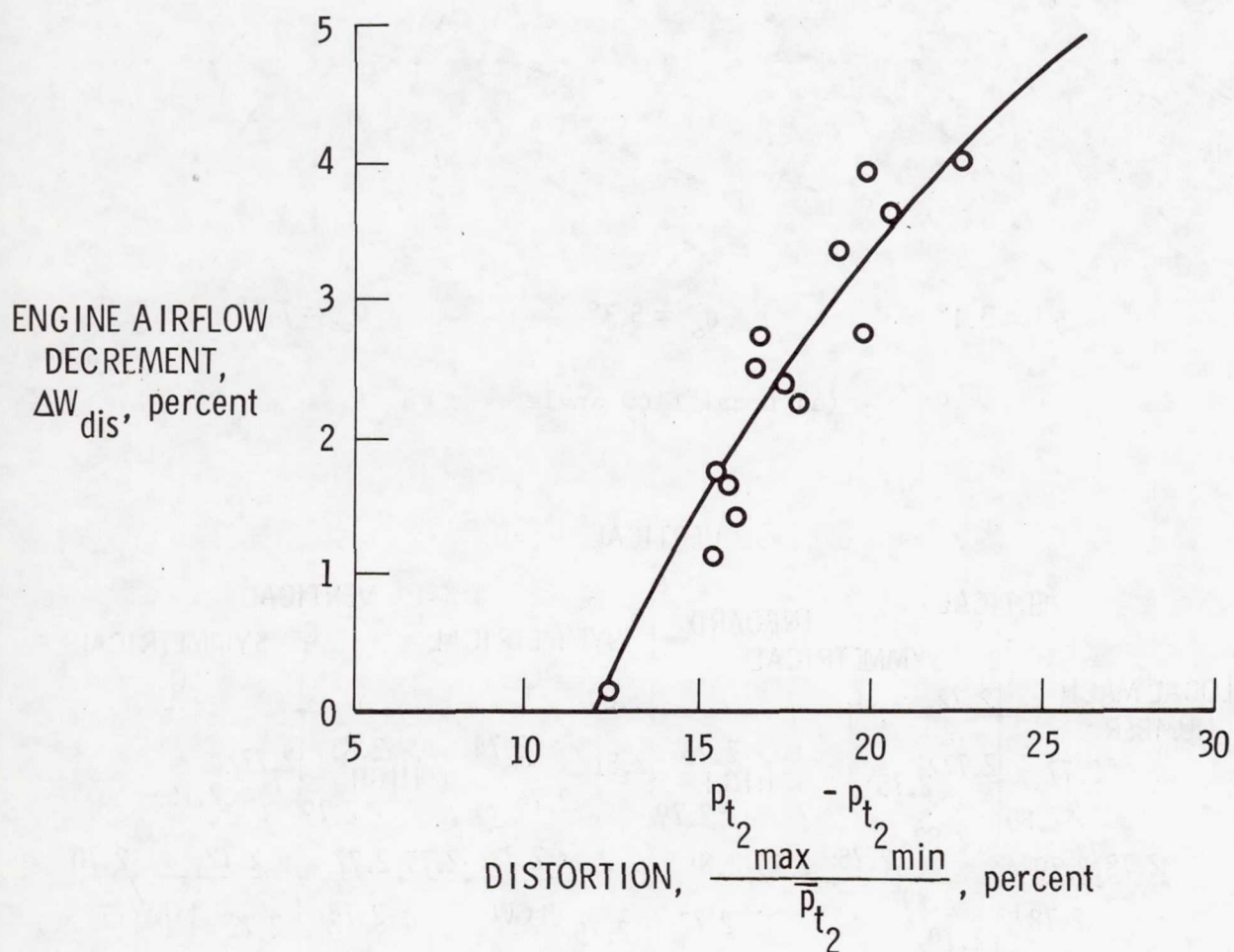
Figure 9.- Effect of compressor face distortion on engine airflow (engine airflow calibration).
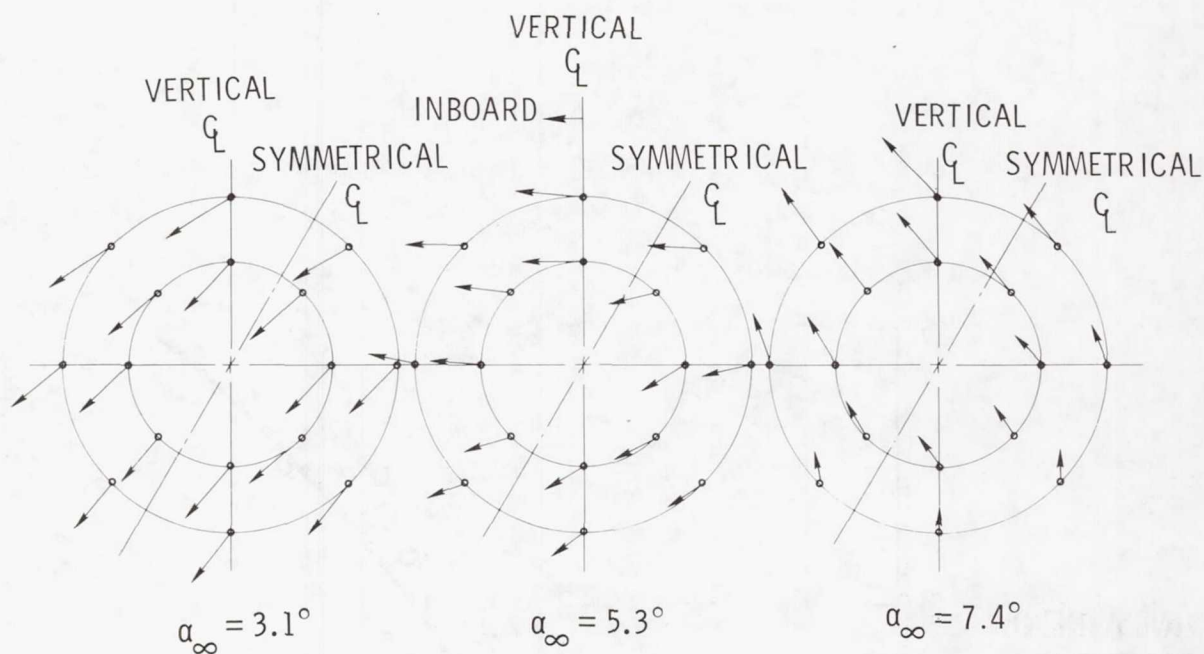
(a) Local flow angle.
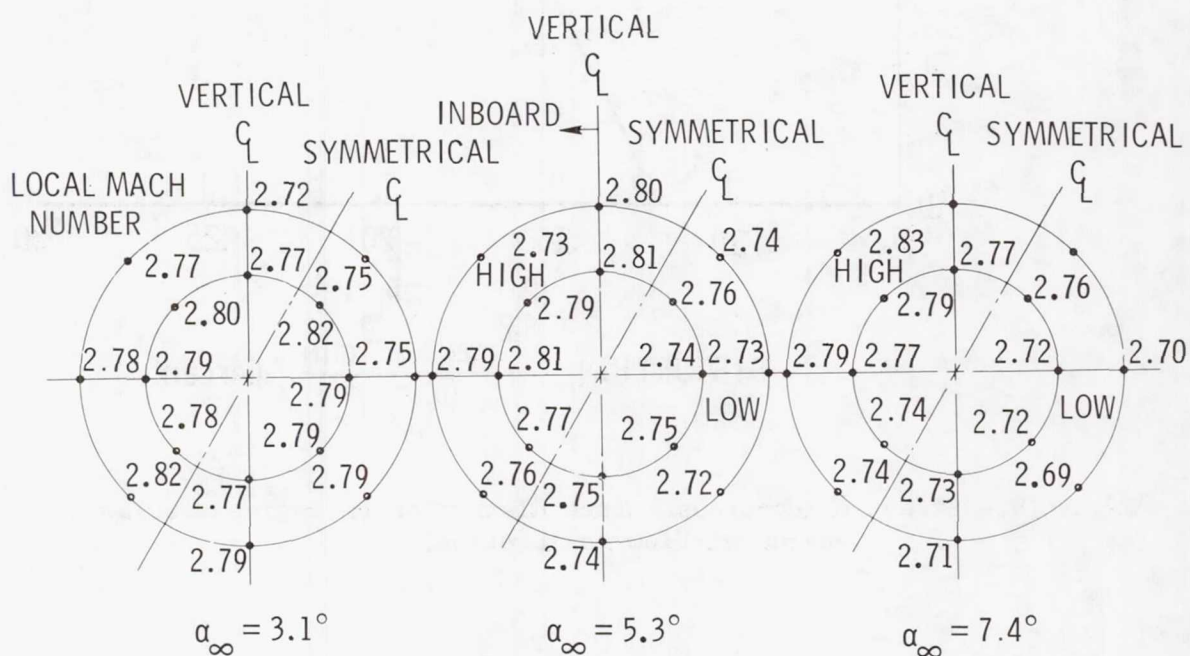
(b) Local Mach number.

Figure 10.- Local flow conditions at inlet plane of 1/12-scale model of YF-12 airplane. $M_\infty = 2.75$.

(a) Recovery.
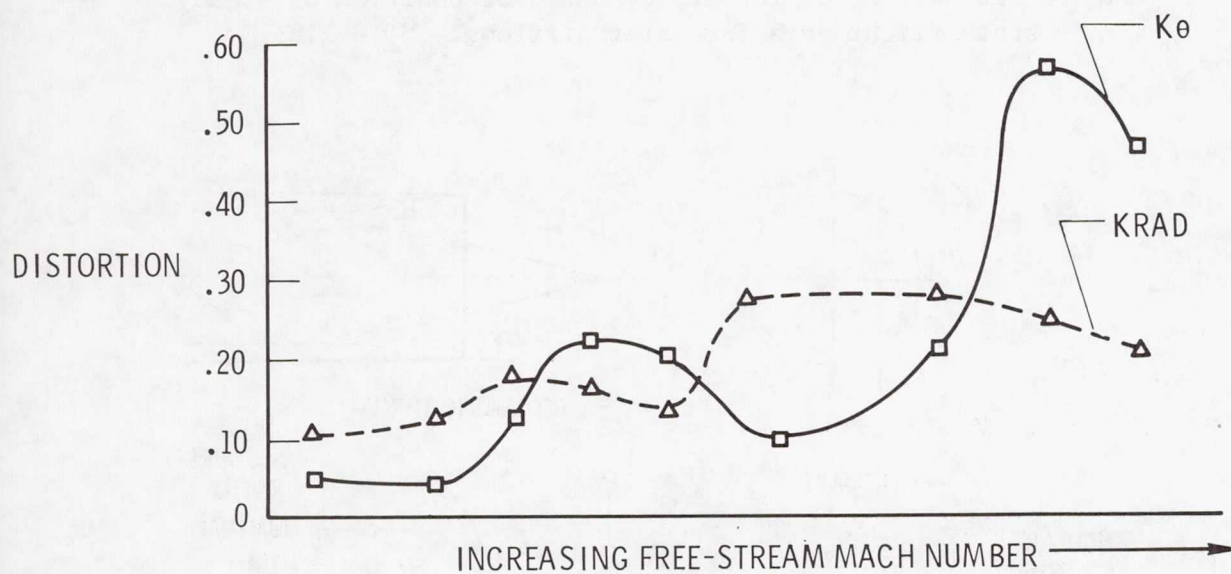
(b) Distortion.

Figure 11.- Steady state flight data of pressure recovery and
distortion at compressor face.

443
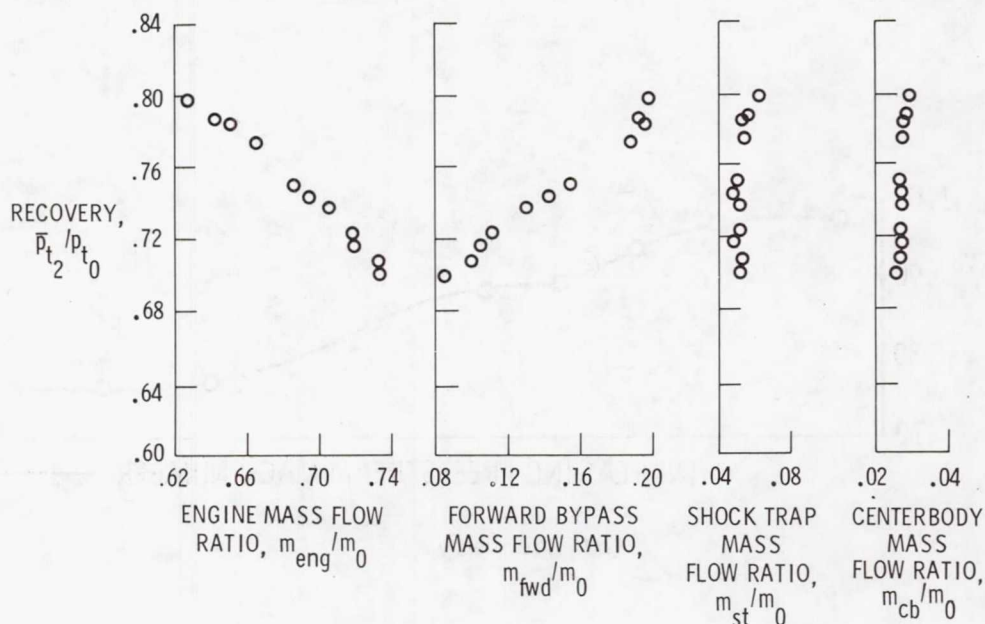
Figure 12.- Effect of forward bypass door position on steady
state flight data for inlet airflows. $M_\infty = 2.8$.
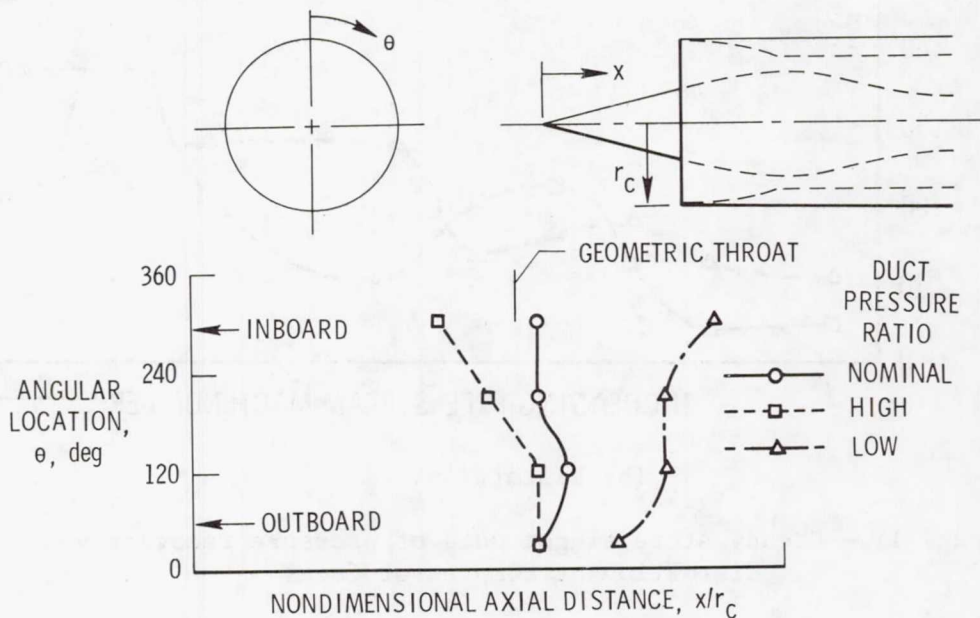
Figure 13.- Circumferential variation of shock position for
three duct pressure ratios. $M_\infty = 2.8$.
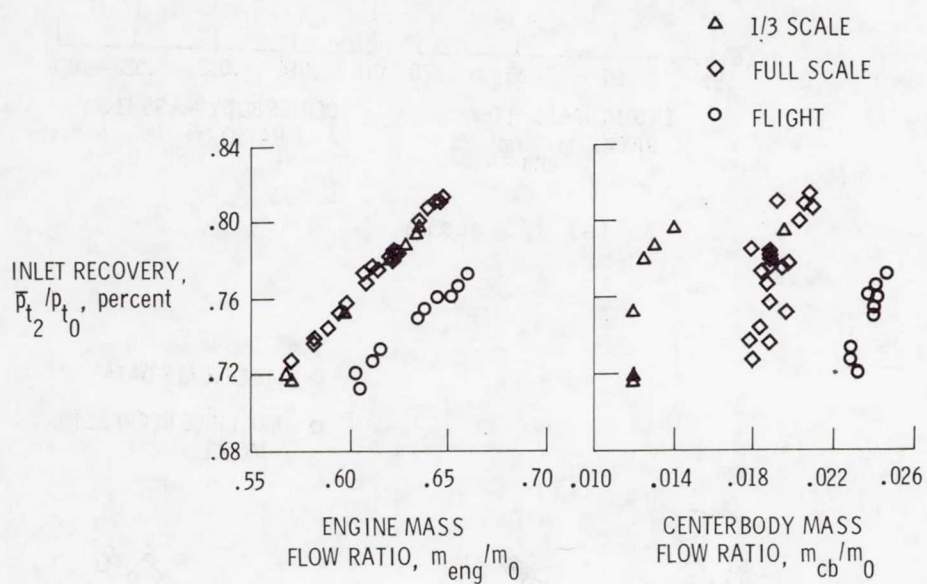
Figure 14.- Comparison of flight, full-scale, and
1/3-scale inlet performance parameters. $M_\infty = 2.8$.
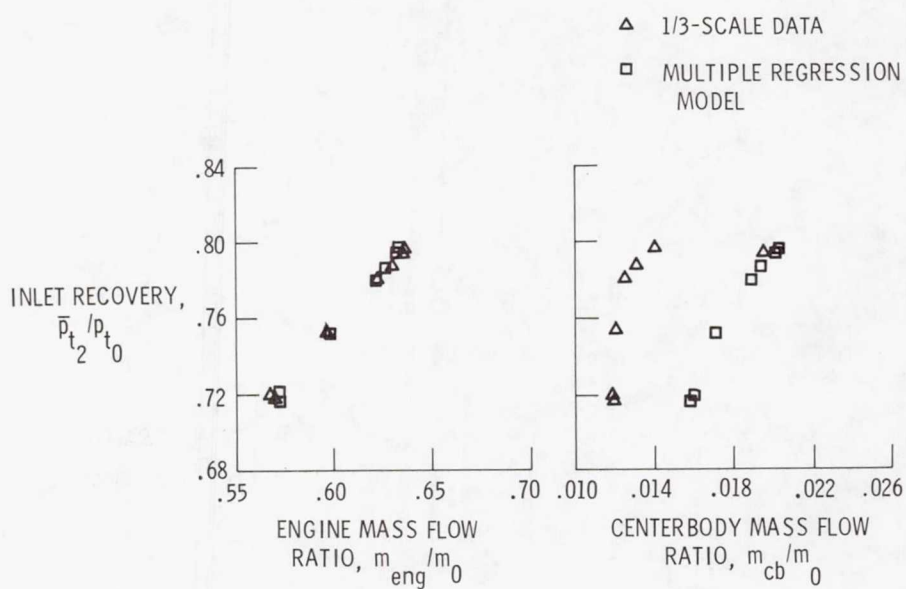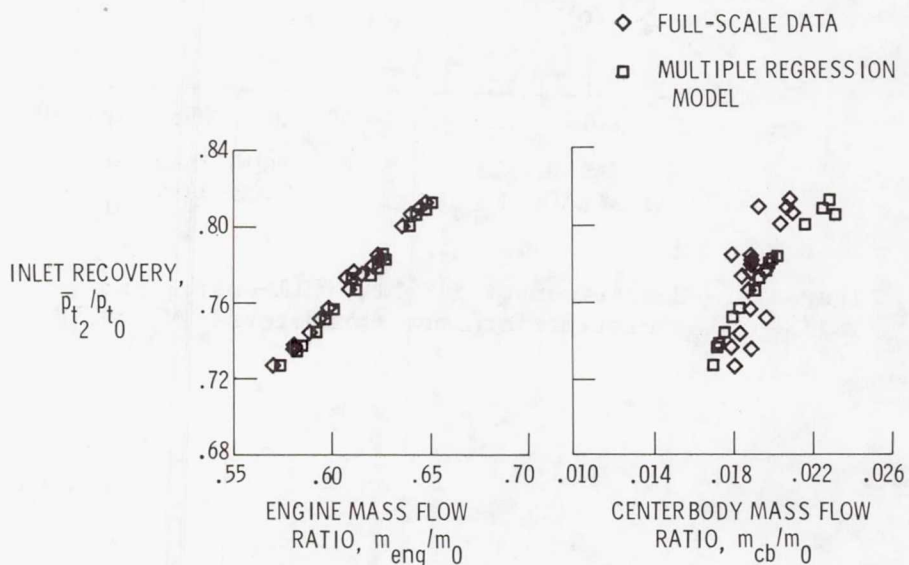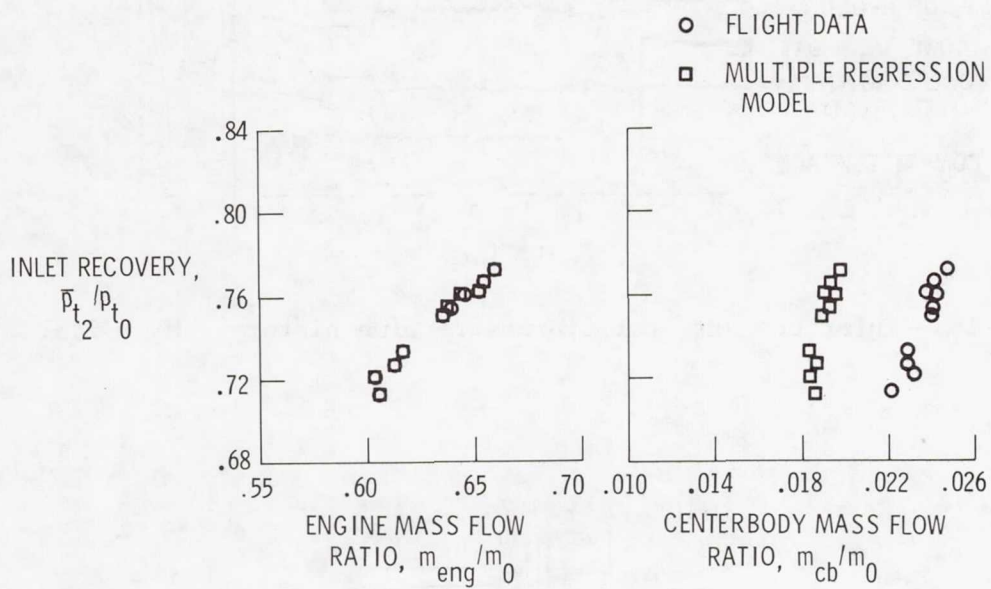
(c) Flight data.

Figure 15.- Concluded.
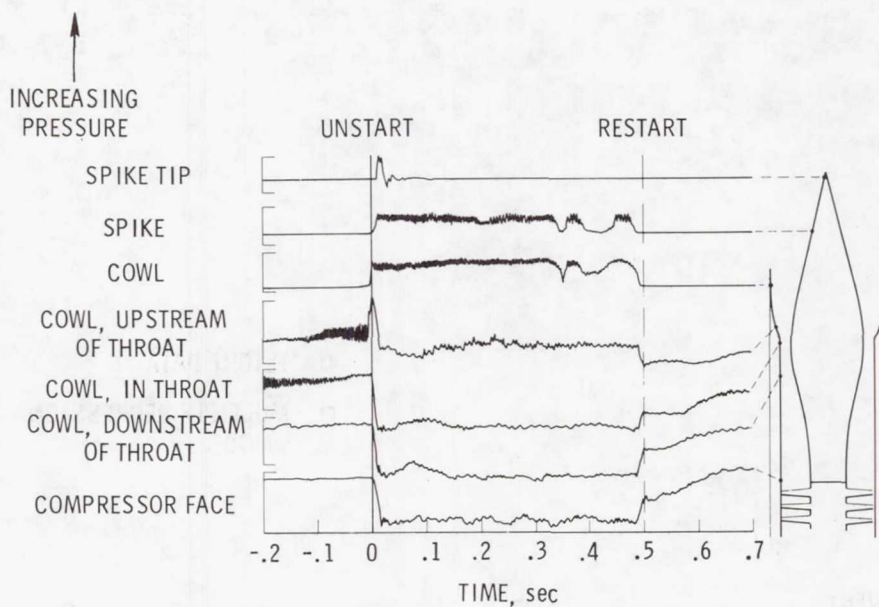
Figure 16.- Inlet unstart static pressure time history. $M_{\infty} = 2.5$.
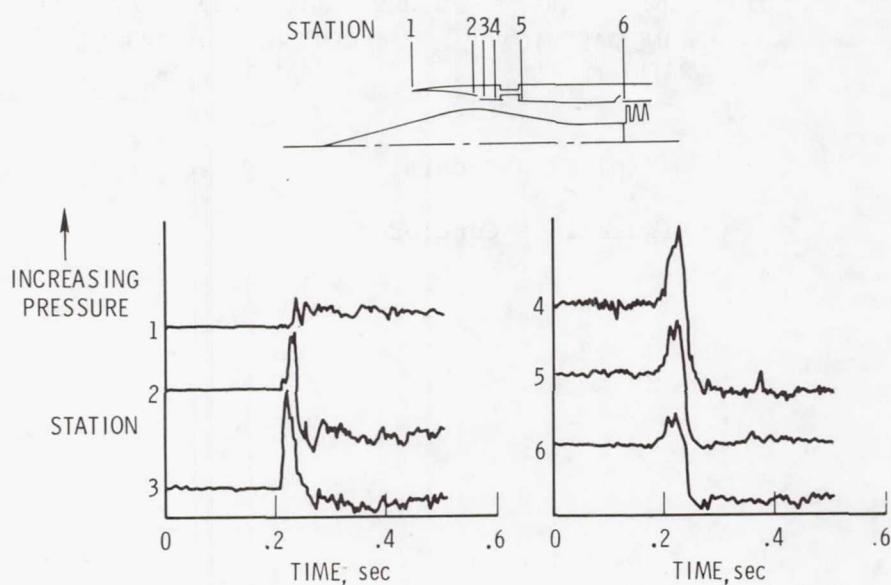
Figure 17.- Compressor stall duct pressure time history.

448
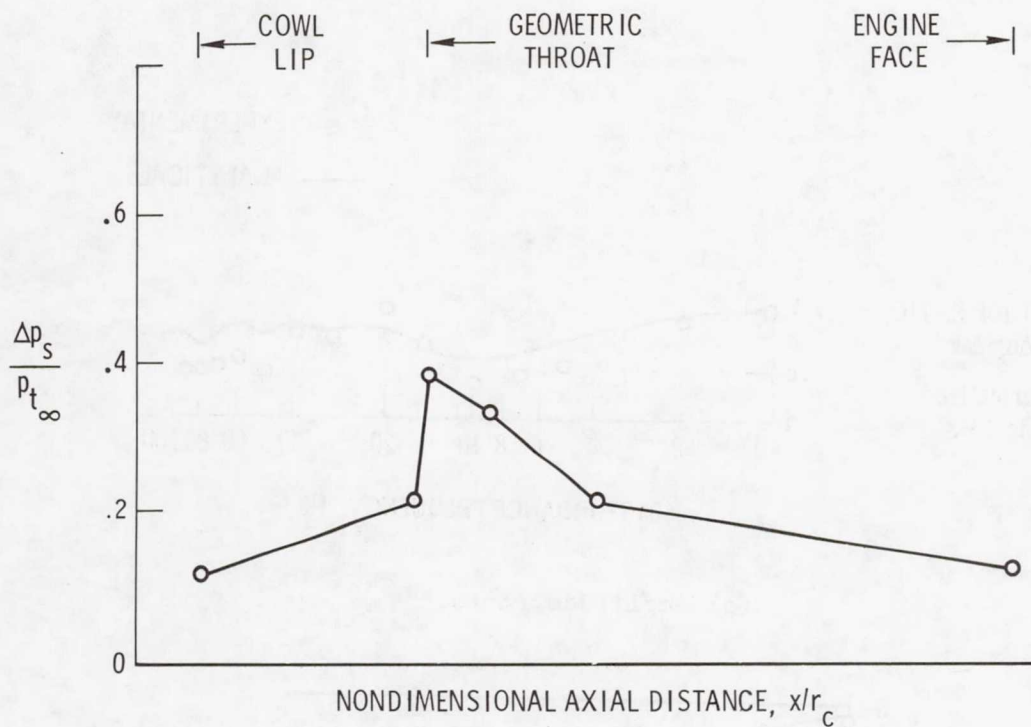
Figure 18.- Duct pressure rise during compressor stall.
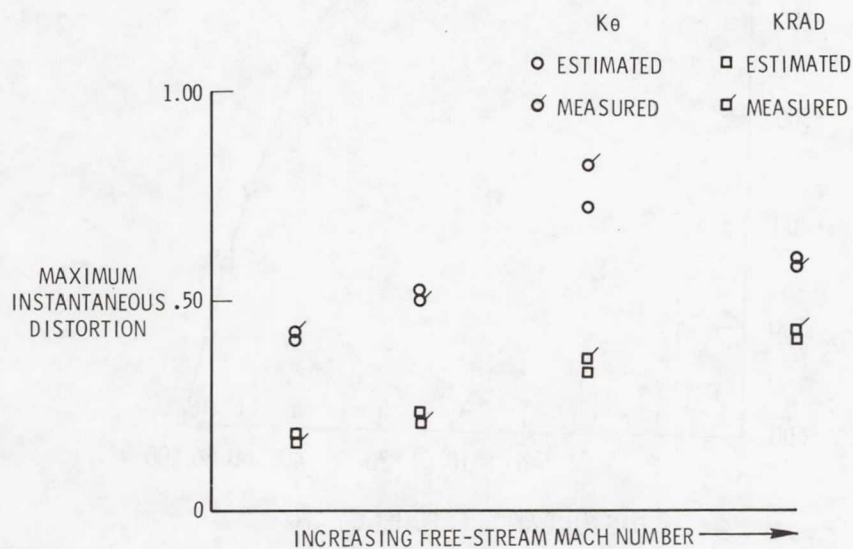
Figure 19.- Comparison of flight-measured with estimated
maximum instantaneous distortion. Estimates are from
inlet rms and psd measurements.
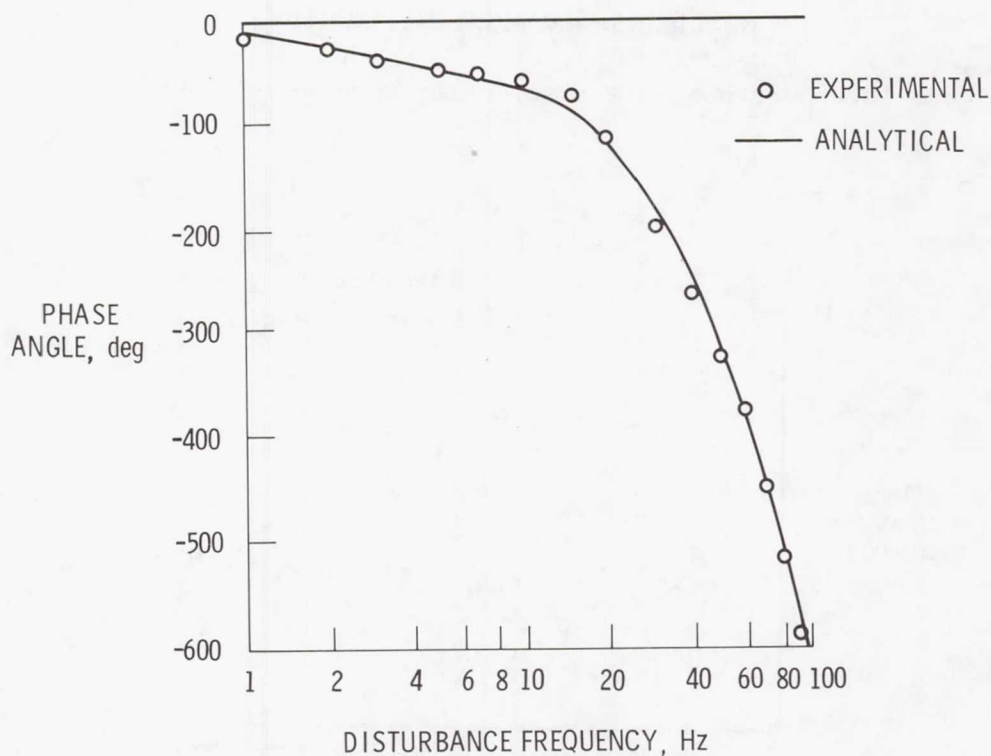
Figure 21.- Digital implementation of inlet control in wind tunnel.
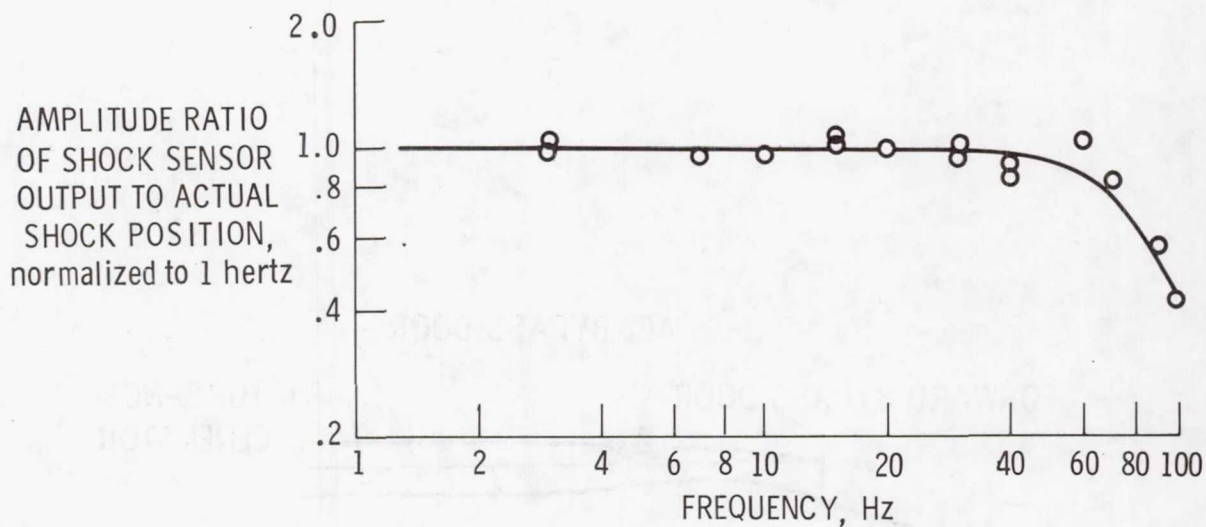
(a) Amplitude ratio.
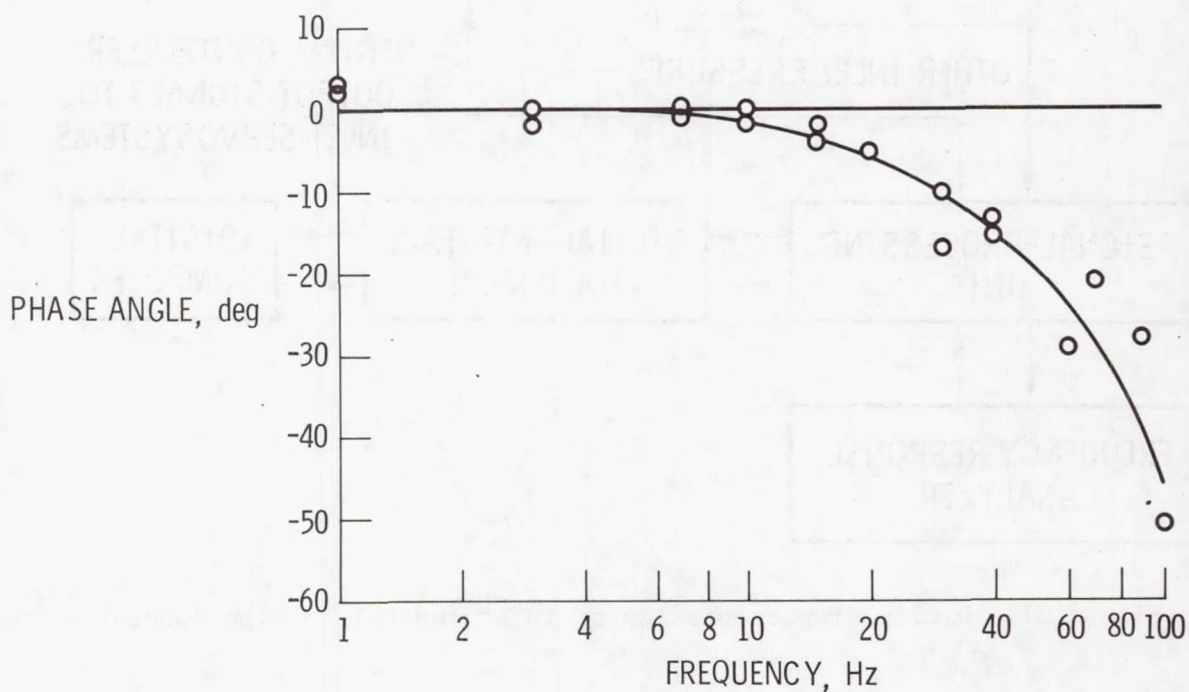
(b) Phase angle.

Figure 22.- Frequency response of terminal shock sensor output
to actual shock position for continuous output electronic
sensor.

452
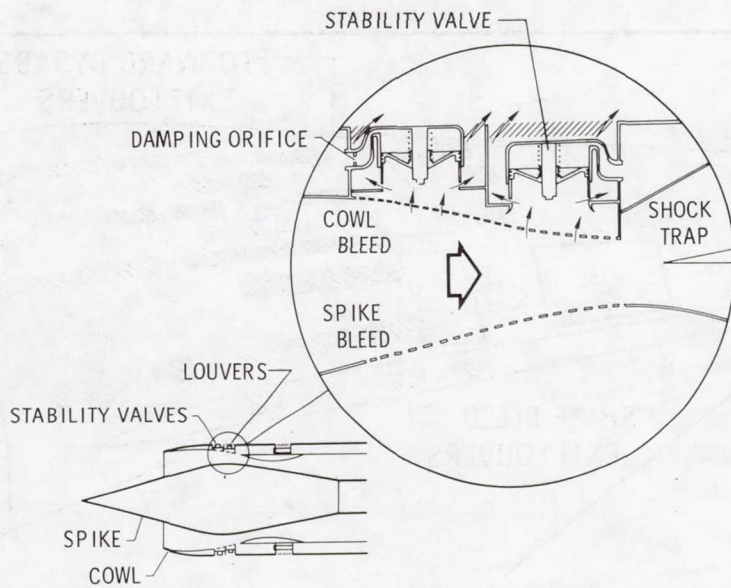
Figure 23.- Inlet configuration showing detail of
stability valve installation.
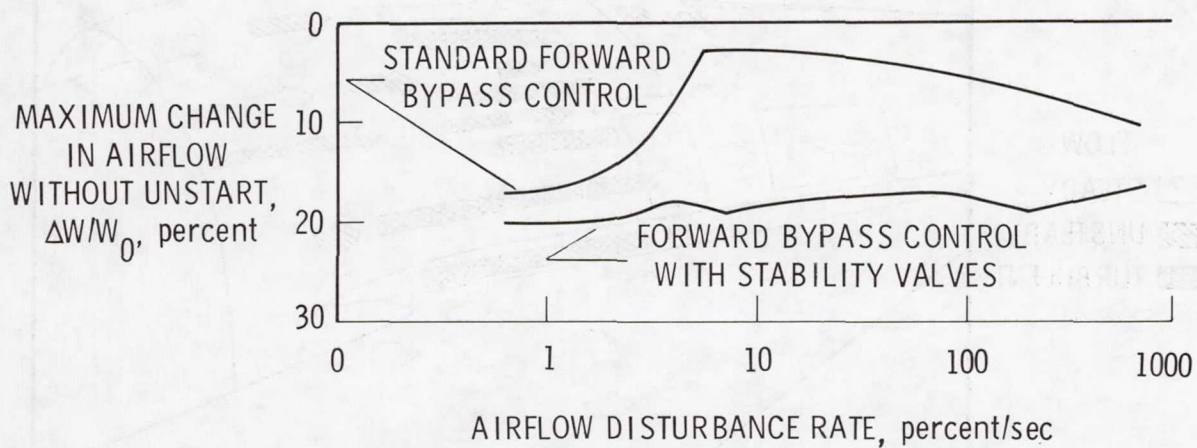
Figure 24.- Comparison of modified and standard inlet tolerance
to internal airflow transients. $M_\infty = 2.5$.
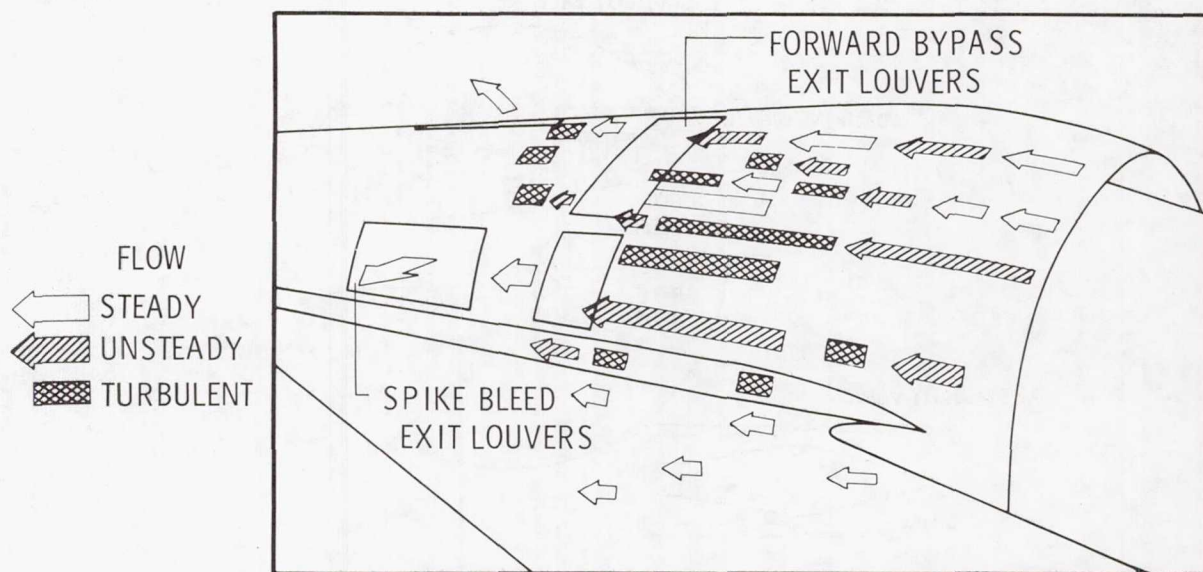
(a) Doors closed.
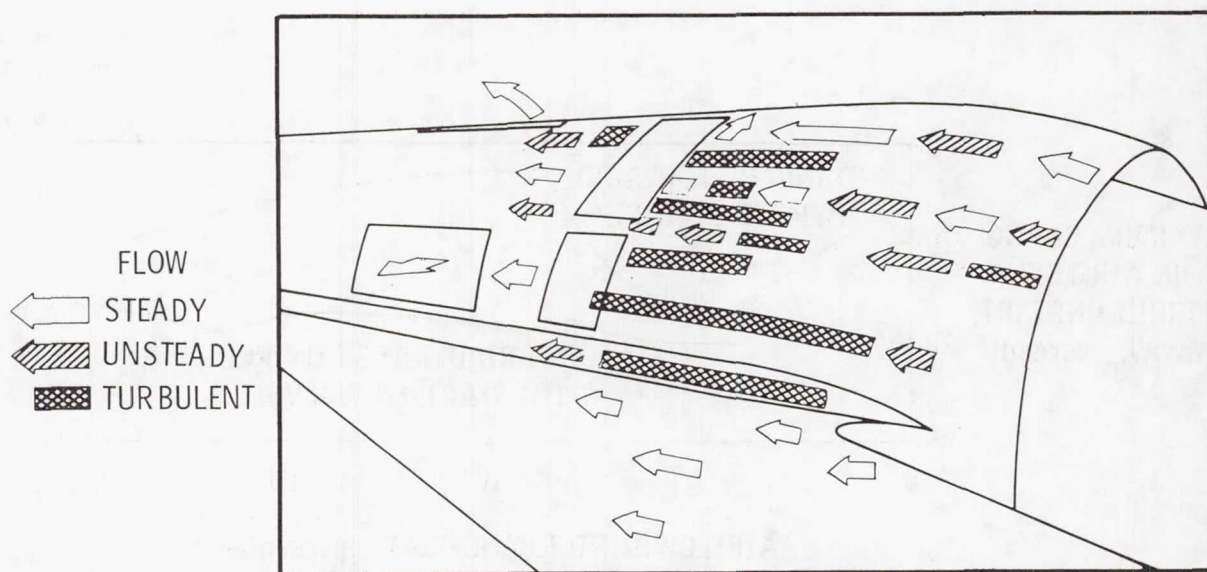
(b) Doors 20 percent open.

Figure 25.- Effect of forward bypass door position on
local flow around nacelle. $M_\infty = 2.6$.
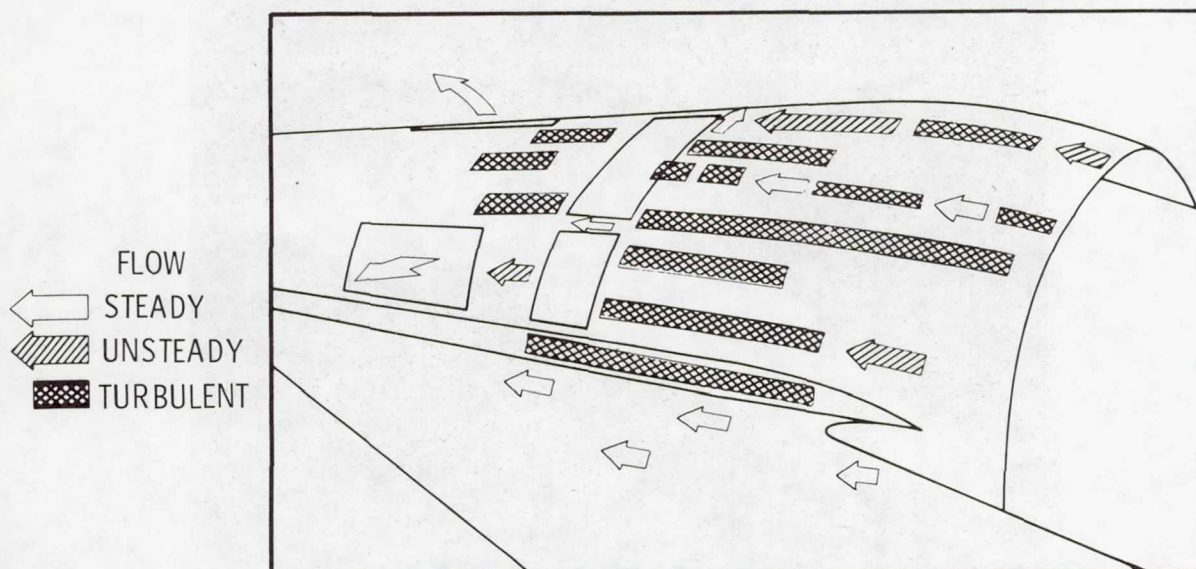
(c) Doors 70 percent open.

Figure 25.- Concluded.
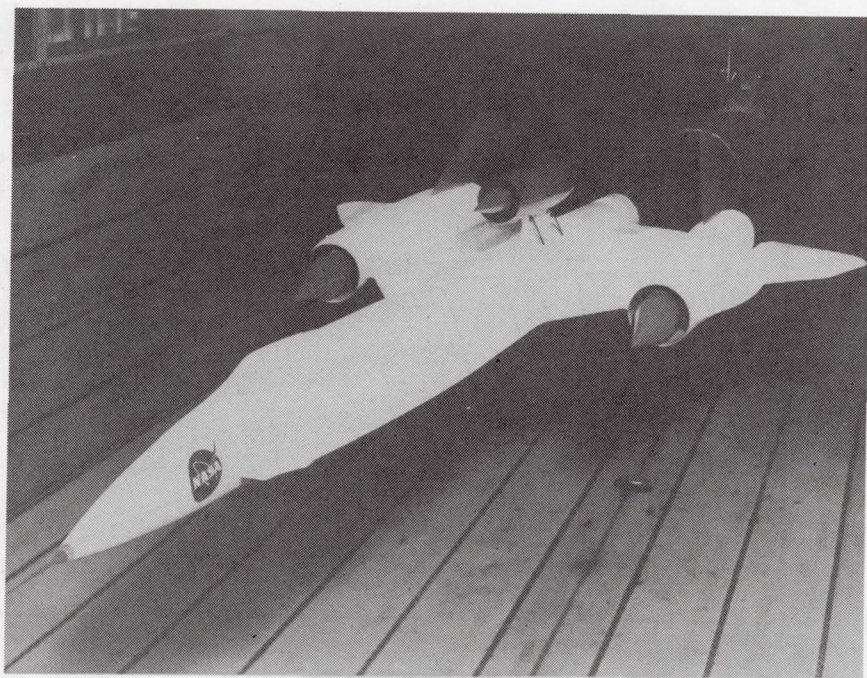
Figure 26.- YF-12 airplane as test bed for
new propulsion concepts.

COMPOSITE MATERIALS RESEARCH IN SUPPORT OF SUPERSONIC PROPULSION SYSTEMS

Robert A. Signorelli
NASA Lewis Research Center

SUMMARY

Two engine components, fan blades and exhaust systems, have been selected for composite materials development efforts in support of the supersonic cruise aircraft research (SCAR) engine program. The materials selected were boron/aluminum for fan blades and silicon carbide/superalloy sheet for the exhaust system. The current status of the research into applying these two composite materials to SCAR engines is reviewed in this paper.

Significant progress has been made in improving the impact resistance of boron/aluminum, and the improved material is being evaluated in prototype SCAR fan-blade rig tests. Reaction at the silicon carbide fiber – superalloy matrix interface has been identified as a problem area in fabricating composite sheet. Diffusion barriers appear to control this interfacial reaction, permitting composite development to proceed.

INTRODUCTION

Propulsion systems for supersonic cruise aircraft will require improved materials to achieve low ground noise on takeoff as well as efficient subsonic and supersonic flight. Some of the advanced-design engine components needed for this purpose can be achieved through the use of advanced composite materials. Composite materials offer the potential for better component performance than conventional materials because they have higher modulus, lower density, and greater strength. For example, using boron/aluminum fan blades for 275° to 375° C (500° to 700° F) service can reduce fan-blade stage weight by 25 to 40 percent from that of standard titanium alloy blades. In addition, aerodynamic performance is improved by the removal of midspan dampers, which is made possible by the greater stiffness of boron/aluminum. The lower blade weight also permits lower disk, shaft, bearing, and containment ring weights.

Silicon carbide/superalloy composite sheet will permit higher material operating temperatures than conventional superalloy sheet because the silicon carbide reinforcement retains its strength to above 1100° C (2000° F). Thus, trade-offs are possible between higher operating temperatures and decreased cooling-air requirements for the exhaust system. In addition, because the reinforcing filaments have less than half the density of conventional superalloys, the density of the composite is 20 to 25 percent lower than that of a conventional superalloy.

457

The current status of the research on boron/aluminum fan blades and silicon carbide/superalloy sheet for exhaust systems for SCAR engine applications is reviewed.

Values are given in both SI and U.S. customary units. The work was done in U.S. customary units.

BORON/ALUMINUM FAN BLADES

Composite fan blades have been fabricated in related programs and have shown excellent potential for fulfilling the requirements for advanced-engine fan blades. Fabrication processing of such blades generally involves production of monolayer composite tape by diffusion bonding two aluminum foils about a uniaxially oriented boron fiber array. Plies cut from the composite monolayer are stacked to fill a die cavity and are hot pressed to a blade shape such as that shown in figure 1. The desired blade properties are obtained by suitable orientation of the plies and selection of the stacking sequence. The relative advantages of boron/aluminum over titanium alloy, the standard fan-blade material, are also shown in the figure. The composite has better than a twofold strength/density and modulus/density advantage over titanium. Use temperature of the boron/aluminum is also greater than that of aluminum alloys (not shown in fig. 1). The boron fiber retains strength to well above 500° C (930° F) and increases the use temperature of boron/aluminum to 375° C (700° F).

While many properties of composite materials are superior to those of conventional materials, the impact resistance demonstrated has been inconsistent and, in many cases, inadequate for fan blades. Notched Charpy pendulum impact data for a titanium alloy and early boron/aluminum are compared in figure 2. The composite material has less than half the impact resistance of a typical titanium alloy used for fan blades.

Based on laboratory and rig tests of specimens and blades, it is probably safe to say that the impact resistance of boron/aluminum composites to small objects such as ice balls, gravel, rivets, and sand is acceptable. However, resistance to large objects such as birds has been less than adequate. Bird ingestion generally occurs at low altitudes because that is where most birds fly. Therefore, bird impact damage is most likely to occur during takeoff or landing of aircraft. Over half of the bird population is found at altitudes of less than 150 meters (ref. 1). Figure 3 clearly illustrates the potential danger of bird impact to aircraft engine fan blades. Even so, bird ingestion is rare, and usually does not cause severe operational changes in modern turbofan engines. However, as shown in figure 4, even standard titanium alloy fan blades can be damaged as a result of bird impact. The damage shown in this figure for a titanium alloy blade is representative of a severe impact condition. Also shown is an early boron/aluminum blade subjected to severe impact in a whirling-arm rig test. However, the poor impact resistance that led to the multiple failure of this early boron/aluminum blade does not represent the potential of this type of composite.

Studies to understand and improve boron/aluminum impact resistance have been undertaken at several laboratories (refs. 2 to 8). The major variables that were investigated in a program undertaken by the Lewis Research Center to improve boron/aluminum fan-blade impact resistance were fiber diameter, matrix alloy ductility, fabrication processing, and fiber ply orientation. The choice of variables was influenced by efforts to minimize the embrittling effects of the low strain-to-failure boron fibers in an otherwise relatively ductile aluminum alloy. Large-diameter fibers ($\leq$ 0.2 mm) were selected to increase the interfiber distance in the composite and thereby reduce the volume of the matrix constrained by the high-modulus, low-strain boron fibers and permit greater strain in the composite upon impact. Fabrication processing was improved to obtain low-porosity, well-consolidated composites and a high degree of bonding between the fiber and the matrix and between matrix fiber plies. However, the bonding temperature was kept low to minimize reaction at the fiber/matrix interface since such reaction generally degrades composite properties. In addition, the fiber ply orientation was selected to provide a viable compromise between the properties required in the various directions and the impact resistance of the composite. Significant increases in impact resistance were obtained through these approaches (refs. 8 to 10). Only some of the results are included herein for brevity.

Increasing fiber diameter from 0.1 millimeter to 0.2 millimeter increased notched Charpy impact strength from less than 40 joules to 96 joules (fig. 5). These larger diameter fibers were incorporated in specimens that had the best combination of the other beneficial effects (such as better processing and a more ductile matrix) identified in the program. Increasing the ductility of the matrix by using commercially pure, 1100 alloy aluminum increased Charpy impact strength from less than 20 joules to 96 joules (fig. 6).

The marked improvement in impact resistance is illustrated in figure 7, which compares impact values of a typical titanium alloy fan-blade material, an early boron/aluminum composite, and an improved boron/aluminum composite. A tenfold increase in laboratory pendulum impact values, as shown in figure 7, is very encouraging but not necessarily indicative of satisfactory foreign-object-damage resistance at the high-velocity impact conditions that fan blades encounter in normal service. Fan and compressor blades of the improved boron/aluminum are being fabricated and tested, and preliminary results are encouraging. Composite J-79 blades containing improved boron/aluminum material are shown in figure 8 after bird impact testing in single-blade, rotating-rig tests. These blades were included in a joint Air Force - NASA program. Each of the three blades was impacted by a real bird under conditions simulating aircraft takeoff conditions. These blades showed evidence of some deformation and delamination at the tip of the airfoil near the impact point. However, no portion of the blade was broken off by the impact.

Improved impact-resistant boron/aluminum is currently being used in a prototype SCAR blade. Figure 9 shows one of the preliminary blades fabricated from boron/aluminum for evaluation, which includes rotating-rig impact tests. Additional blades are being fabricated for evaluation in the near future. The encouraging results obtained in this impact testing suggest that foreign-object-damage resistance, the remaining major technical impediment to success-

ful flight demonstration of boron/aluminum blades, may have been overcome.

SILICON CARBIDE/SUPERALLOY COMPOSITE SHEET FOR EXHAUST SYSTEMS

Exhaust system components can be a significant portion of SCAR engine weight. The high-temperature portions of a SCAR engine, which operate at temperatures to 980° C (1800° F), have been estimated to weigh 550 kilograms (1200 lb) (private communication from R. A. Howlett, Pratt & Whitney Aircraft, East Hartford, Conn.). Substituting silicon carbide/superalloy composite sheet for the conventional superalloy could reduce that weight by about 20 to 25 percent or by about 120 kilograms (264 lb). This weight reduction is due to the lower density of the silicon carbide fiber. In addition to the lower density advantage, the silicon carbide fiber retains greater strength and stiffness at the operating temperature, 980° C (1800° F). The silicon carbide/superalloy composite sheet can be expected to have four times the tensile strength, twice the elastic modulus, and five times the 1000-hour rupture strength of conventional superalloy sheet at 980° C. These superior mechanical properties can be used to design more efficient systems that use less cooling air and to reduce weight by using thinner sections.

To make the silicon carbide/superalloy composite sheet a viable material system, certain problems must be addressed. The property advantages can be achieved only if fiber-degrading chemical interaction at the fiber/matrix interface can be minimized. Reaction rates at the 980° C (1800° F) service temperature are expected to be tolerable; however, reactions occurring during the higher temperature fabrication processing can be a problem. Typically, the composite is made by first hot pressing superalloy foils together with silicon carbide fiber arrays to form monotapes. A secondary diffusion bonding of stacked layers of the monolayer tapes forms the composite sheet. Limited fabrication processing techniques have been evolved to bend, cut, and join the composite sheet into exhaust system components.

Research has been underway to overcome the interfacial reaction through the use of diffusion barrier coatings on the silicon carbide fibers (ref. 11). Figure 10 shows the marked improvement provided by diffusion barrier coatings in reducing reaction during composite processing. The uncoated fiber has formed a thick reaction zone, but the tungsten-coated fiber has no visible reaction. Although tungsten is an effective coating, it requires a greater thickness than desired and incurs a weight penalty, being twice as dense as superalloys. Alternative carbide coatings are currently being deposited on silicon carbide fibers, and preliminary compatibility results suggest that the fiber/matrix reaction can be controlled. Composite test specimens also are being fabricated to assess the properties of the composite in high-temperature tensile and long-time rupture tests.

The properties of silicon carbide/superalloy and conventional superalloys are compared in figure 11. The data shown are projections expected from the composite currently being processed and evaluated.

In summary, considerable progress has been made, but much work remains before composite sheet can be applied to exhaust systems.

CONCLUDING REMARKS

Significant progress has been made in developing boron/aluminum and silicon carbide/superalloy sheet composites for application in SCAR propulsion systems. A marked improvement in boron/aluminum impact resistance has been obtained in laboratory tests, and this technology is currently being applied to fan blades. The progress made suggests that foreign-object-damage impact resistance, the remaining major technical impediment to the use of boron/aluminum blades in SCAR propulsion systems, may have been overcome.

Excellent progress has been made in studies of silicon carbide/superalloy sheet. Diffusion barrier coatings have been identified and applied to the silicon carbide fibers, and preliminary data suggest that these barriers can control interfacial reactions. While much work remains before silicon carbide/superalloy sheet can be used in SCAR engine exhaust systems, the potential appears promising.

REFERENCES

1. DeJong, A. P.: Their Airspace or Ours? Shell Aviation News, No. 390, 1970, pp. 2-7.

2. Kreider, K. G.; and Prewo, K. M.: Boron-Reinforced Aluminum. Composite Materials, Vol. 4, Metallic Matrix Composites. Kenneth G. Kreider, ed., Academic Press, 1974, pp. 400-480.

3. Hancock, J. R.; and Swanson, G. D.: Toughness of Filamentary Boron/Aluminum Composites. Composite Materials: Testing and Design, Second Conference. STP-497, Am. Soc. Testing Mater., 1972, pp. 299-310.

4. Prewo, Karl M.: The Charpy Impact Energy of Boron-Aluminum. J. Compos. Mater., vol. 6, Oct. 1972, pp. 442-455.

5. Olster, E. F.; and Jones, R. C.: Toughening Mechanisms in Continuous Filament Unidirectionally Reinforced Composites. Composite Materials: Testing and Design, Second Conference. STP-497, Am. Soc. Testing Mater., 1972, pp. 189-205.

6. Hoover, W. R.; and Allred, R. E.: Toughness of Borsic-Al Composites with Weak Fiber-Matrix Bonds. SC-DC-71-4467, Sandia Labs., 1972.

7. Melnyk, P.; and Toth, I. J.: Development of Impact Resistant Boron/ Aluminum Composites for Turbojet Engine Fan Blades. (ER-7806, TRW Equipment Labs.; NAS3-17763), NASA CR-134770, 1975.

8. Signorelli, R. A.: Metal Matrix Composites for Aircraft Propulsion Systems. Proceedings of International Conference on Composite Materials. Am. Inst. Mining Eng., 1976, pp. 411-432.

9. McDanels, David L.; and Signorelli, Robert A.: Effect of Fiber Diameter and Matrix Alloys on Impact-Resistant Boron/Aluminum Composites. NASA TN D-8204, 1976.

10. McDanels, David L.; and Signorelli, Robert A.: Effect of Angleply and Matrix Enhancement on Impact-Resistant Boron/Aluminum Composites, NASA TN D-8205, 1976.

11. Cornie, J. A.; Cook, C. S.; and Anderson, C. A.: Fabrication Process Development of SiC/Superalloy Composite Sheet for Exhaust System Components. (Westinghouse Electric Corp.; NAS3-18921), NASA CR-134958, 1976.
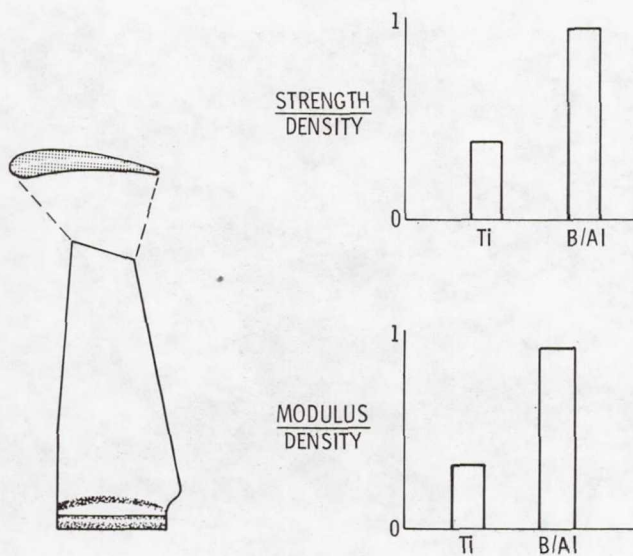
Figure 1.- Relative advantages of boron/aluminum
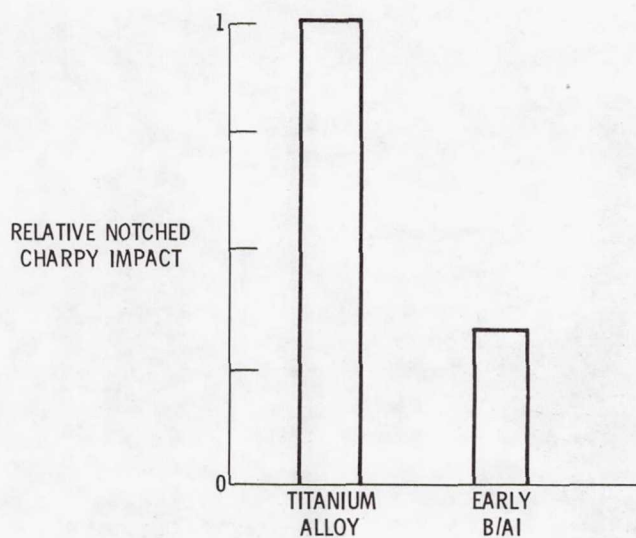composite blades over titanium alloy blades.

Figure 2.- Relative notched Charpy pendulum impact
strength of titanium alloy blades and early
boron/aluminum composites.

463

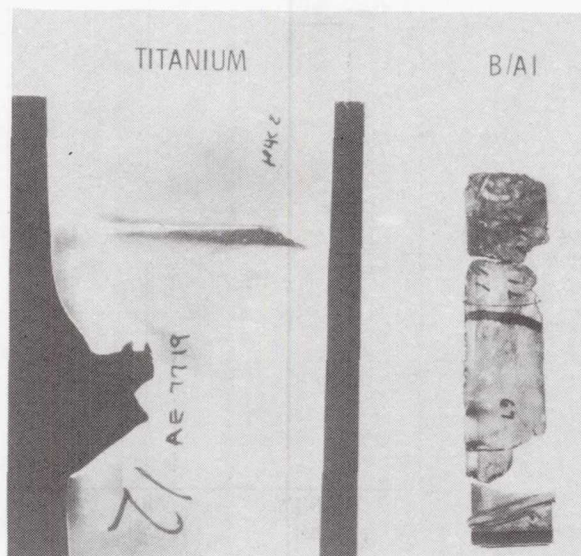Figure 3.- Example of bird density near an airport.

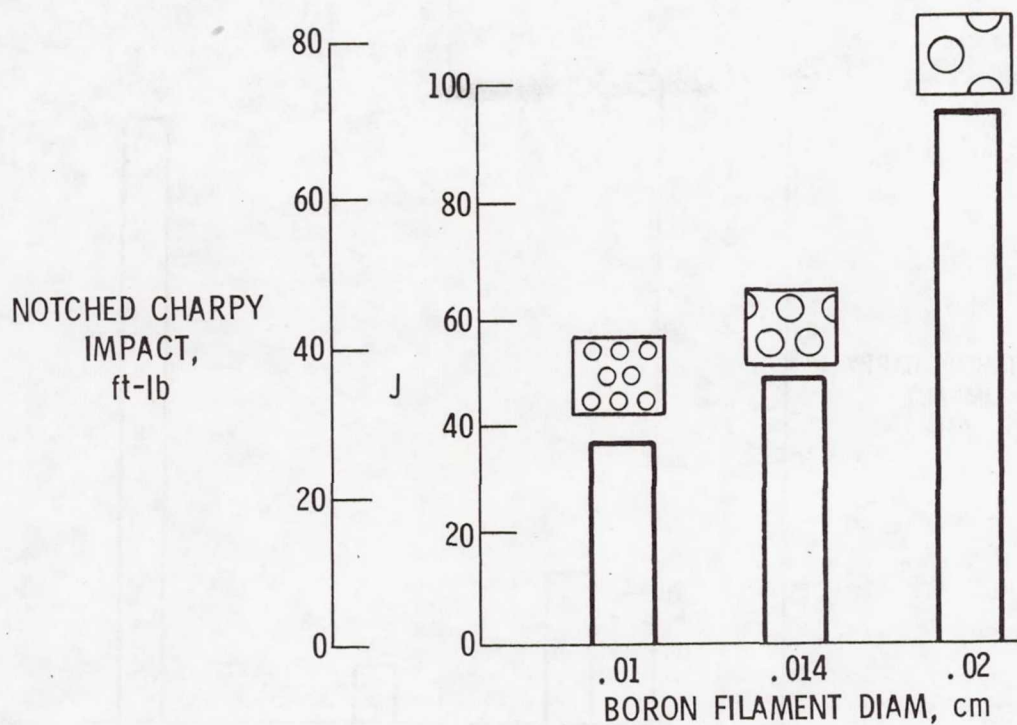Figure 4.- Impact damage to representative fan blades.

Figure 5.- Effect of filament diameter on impact strength of
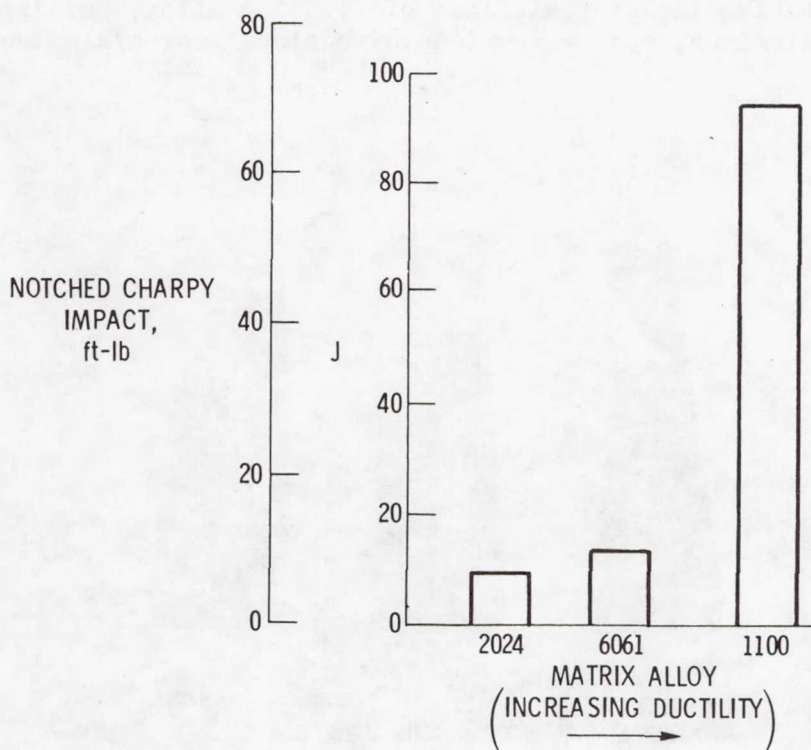boron/aluminum composites. Matrix, 50-vol % 1100 aluminum.

Figure 6.- Effect of matrix ductility on impact strength of boron/aluminum
composites. Boron fiber content, 50 vol %; fiber diameter, 0.02 cm.
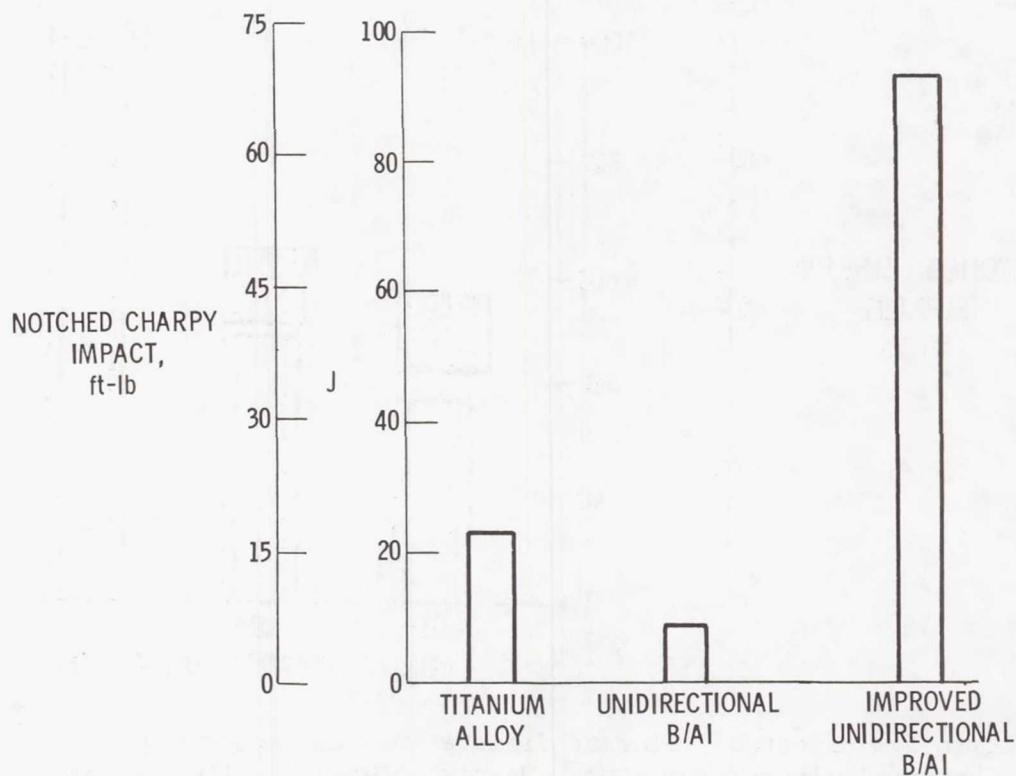
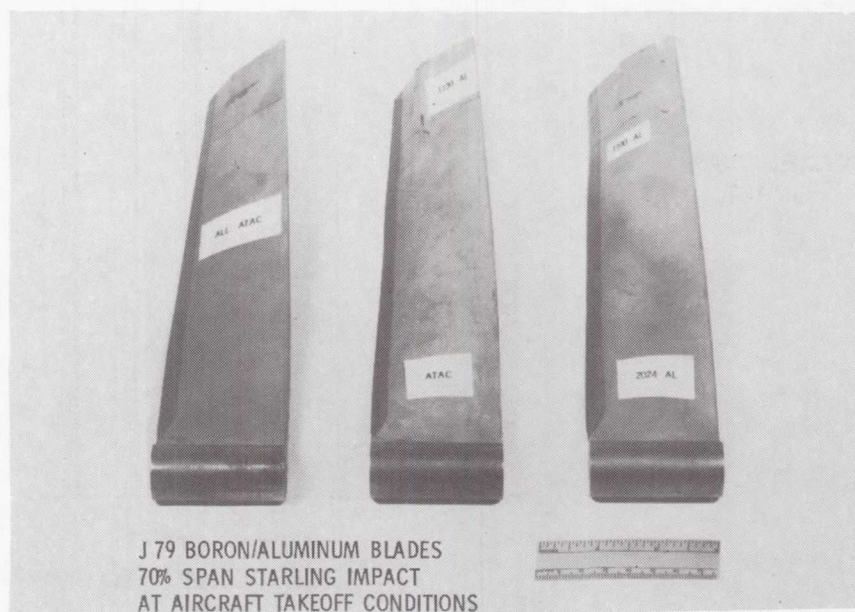Figure 7.- Relative impact resistance of titanium alloy, unidirectional boron/aluminum, and improved unidirectional boron/aluminum.

Figure 8.- J-79 boron/aluminum blades after bird impact testing at takeoff conditions. (Starling impact at 70 percent of span.)
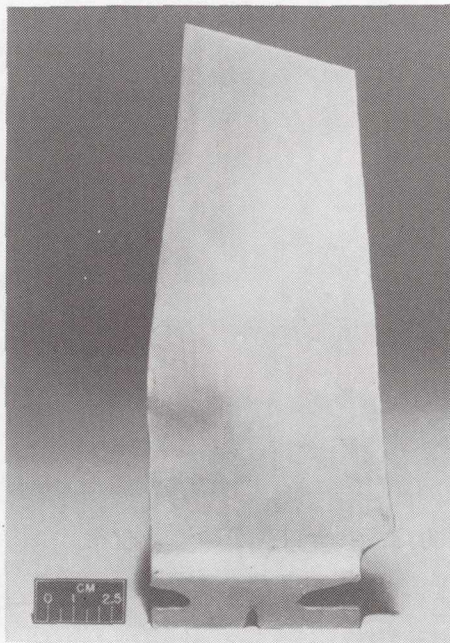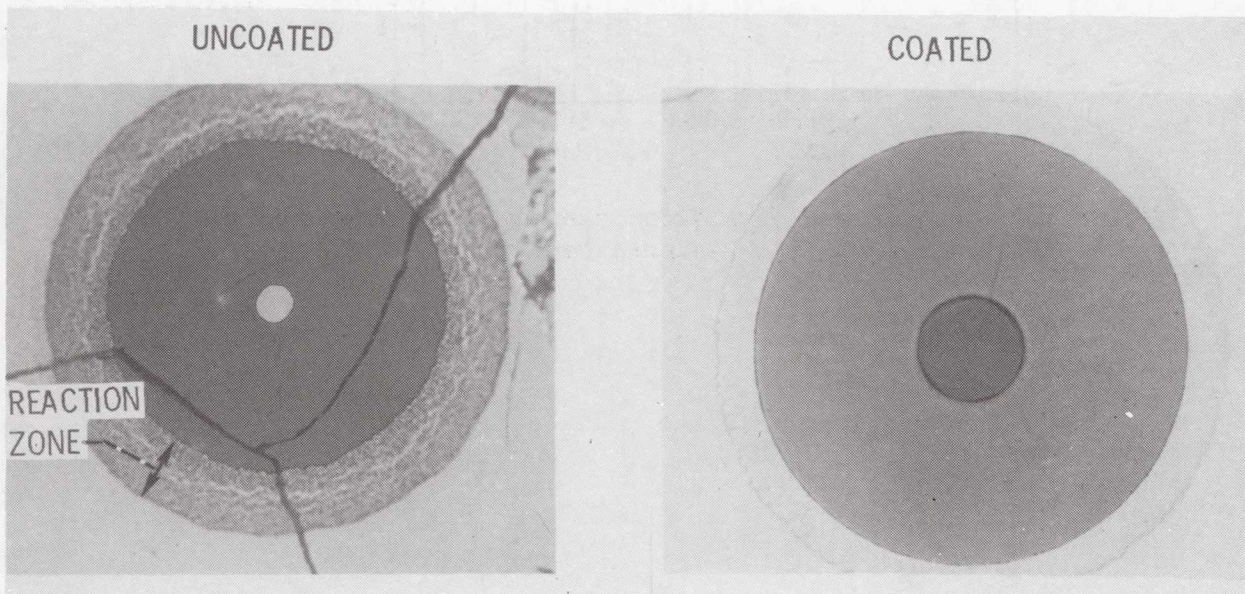
Figure 9.- Prototype SCAR boron/aluminum blade.

Figure 10.- Relative interfacial reactions of coated and uncoated
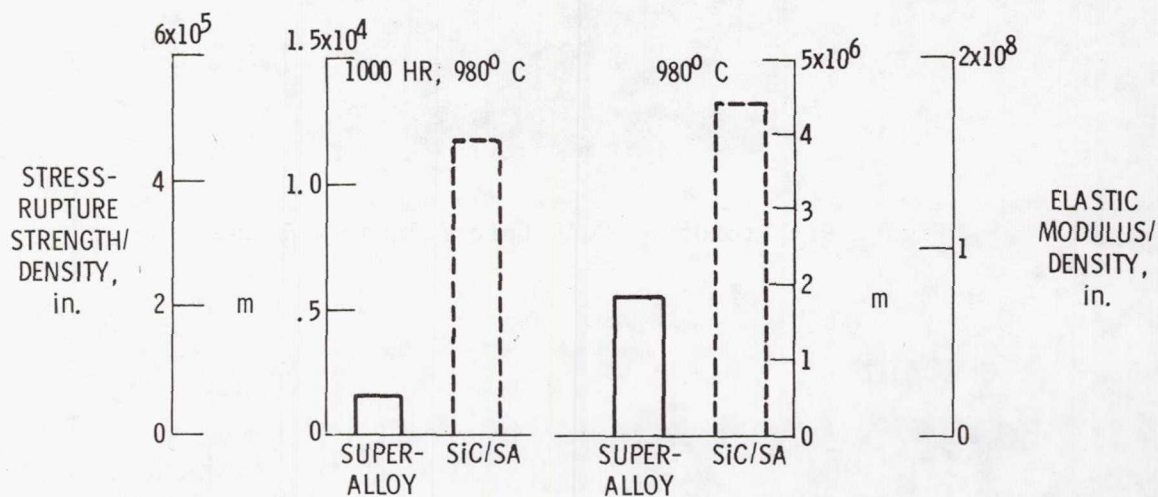silicon carbide fibers in a superalloy matrix.

Figure 11.- Properties of silicon carbide/superalloy and conventional superalloys.